Liquid Argon Calorimeter

Technical Design Report

For this edition obvious typing ans typographical errors have been corrected. Figure 1-13 has been also slightly updated. Thus layout and pagination are slightly different from those of the first, limited edition.

ATLAS Collaboration

Armenia
Yerevan Physics Institute, Yerevan

Australia
Research Centre for High Energy Physics, Melbourne University, Melbourne
Australian Nuclear Science and Technology Organisation, Sydney
University of Sydney, Sydney

Austria
Institut für Experimentalphysik der Leopold-Franzens-Universität Innsbruck, Innsbruck

Azerbaijan Republic
Institute of Physics, Azerbaijan Academy of Science, Baku

Republic of Belarus
Institute of Physics of the Academy of Science of Belarus, Minsk

Brazil
Universidade Federal do Rio de Janeiro, COPPE/EE/IF, Rio de Janeiro
Instituto de Fisica, Universidade de Sao Paulo, Sao Paulo

Canada
University of Alberta, Edmonton
Department of Physics, University of British Columbia, Vancouver
University of Carleton/C.R.P.P., Carleton
Group of Particle Physics, University of Montreal, Montreal
Department of Physics, University of Toronto, Toronto
TRIUMF, Vancouver
University of Victoria, Victoria

CERN
European Laboratory for Particle Physics (CERN), Geneva

Czech Republic
Academy of Sciences of the Czech Republic, Institute of Physics, Prague
Charles University, Faculty of Mathematics and Physics, Prague
Czech Technical University in Prague, Faculty of Nuclear Sciences and
Physical Engineering, Faculty of Mechanical Engineering, Prague

Denmark
Niels Bohr Institute, University of Copenhagen, Copenhagen

Finland
Helsinki Institute of Physics, Helsinki

France
Laboratoire d'Annecy-le-Vieux de Physique des Particules (LAPP), IN2P3-CNRS, Annecy-le-Vieux
Université Blaise Pascal, IN2P3-CNRS, Clermont-Ferrand
Institut des Sciences Nucléaires de Grenoble, IN2P3-CNRS-Université Joseph Fourier, Grenoble
Centre de Physique des Particules de Marseille, IN2P3-CNRS, Marseille
Laboratoire de l'Accélérateur Linéaire, IN2P3-CNRS, Orsay
LPNHE, Universités de Paris VI et VII, IN2P3-CNRS, Paris
CEA, DSM/DAPNIA, Centre d'Etudes de Saclay, Gif-sur-Yvette

Republic of Georgia
Institute of Physics of the Georgian Academy of Sciences, Tbilisi
Tbilisi State University, Tbilisi

Germany
Physikalisches Institut, Universität Bonn, Bonn
Institut für Physik, Universität Dortmund, Dortmund
Fakultät für Physik, Albert-Ludwigs-Universität, Freiburg
Institut für Hochenergiephysik der Universität Heidelberg, Heidelberg
Institut für Informatik, Friedrich-Schiller-Universität Jena, Jena
Institut für Physik, Johannes-Gutenberg Universität Mainz, Mainz
Lehrstuhl für Informatik V, Universität Mannheim, Mannheim
Sektion Physik, Ludwig-Maximilian-Universität München, München
Max-Planck-Institut für Physik, München
Fachbereich Physik, Universität Siegen, Siegen
Fachbereich Physik, Bergische Universität, Wuppertal

Greece
Athens National Technical University, Athens
Athens University, Athens
Aristotle University of Thessaloniki, Thessaloniki

Israel
Department of Physics, Technion, Haifa
Raymond and Beverly Sackler Faculty of Exact Sciences, School of Physics and Astronomy, Tel-Aviv
University, Tel-Aviv
Department of Particle Physics, The Weizmann Institute of Science, Rehovot

Italy
Dipartimento di Fisica dell' Universitá della Calabria e I.N.F.N., Cosenza
Laboratori Nazionali di Frascati dell' I.N.F.N., Frascati
Dipartimento di Fisica dell' Universitá di Genova e I.N.F.N., Genova
Dipartimento di Fisica dell' Universitá di Lecce e I.N.F.N., Lecce
Dipartimento di Fisica dell' Universitá di Milano e I.N.F.N., Milano
Dipartimento di Fisica dell' Universitá di Napoli e I.N.F.N., Napoli
Dipartimento di Fisica Nucleare e Teorica dell' Universitá di Pavia e I.N.F.N., Pavia
Dipartimento di Fisica dell' Universitá di Pisa e I.N.F.N., Pisa
Dipartimento di Fisica dell' Universitá di Roma 'La Sapienza' e I.N.F.N., Roma
Dipartimento di Fisica dell' Universitá di Roma 'Tor Vergata' e I.N.F.N., Roma
Dipartimento di Fisica dell' Universitá di Roma 'Roma Tre' e I.N.F.N., Roma
Dipartimento di Fisica dell' Universitá di Udine, Gruppo collegato di Udine I.N.F.N. Trieste, Udine

Japan
Department of Information Science, Fukui University, Fukui
Hiroshima Institute of Technology, Hiroshima
Department of Physics, Hiroshima University, Higashi-Hiroshima
KEK, National Laboratory for High Energy Physics, Tsukuba
Department of Physics, Faculty of Science, Kobe University, Kobe
Kyoto University of Education, Kyoto-shi
Naruto University of Education, Naruto-shi
Department of Physics, Faculty of Science, Shinshu University, Matsumoto
International Center for Elementary Particle Physics, University of Tokyo, Tokyo
Physics Department, Tokyo Metropolitan University, Tokyo
Tokyo University of Agriculture and Technology, Department of Applied Physics, Tokyo

Kazakhstan
High-Energy Physics Institute of the Kazakh Academy of Sciences, Almaty

Netherlands
FOM - Institute SAF NIKHEF and University of Amsterdam/NIKHEF, Amsterdam
University of Nijmegen/NIKHEF, Nijmegen

Morocco
Faculté des Sciences Aïn Chock, Université Hassan II, Casablanca, and Université Mohamed V, Rabat

Norway
University of Bergen, Bergen
University of Oslo, Oslo

Poland
Henryk Niewodniczanski Institute of Nuclear Physics, Cracow
Faculty of Physics and Nuclear Techniques of the Academy of Mining and Metallurgy, Cracow

Portugal
Laboratorio de Instrumentação e Física Experimental de Partículas (University of Lisboa, University of Coimbra, University Católica-Figueira da Foz and University Nova de Lisboa), Lisbon

Romania
Institute of Atomic Physics, Bucharest

Russia
Institute for Theoretical and Experimental Physics (ITEP), Moscow
P.N. Lebedev Institute of Physics, Moscow
Moscow Engineering and Physics Institute (MEPhI), Moscow
Moscow State University, Institute of Nuclear Physics, Moscow
Budker Institute of Nuclear Physics (BINP), Novosibirsk
Institute for High Energy Physics (IHEP), Protvino
Petersburg Nuclear Physics Institute (PNPI), Gatchina, St. Petersburg

JINR
Joint Institute for Nuclear Research, Dubna

Slovak Republic
Bratislava University, Bratislava, and Institute of Experimental Physics of the Slovak Academy of Sciences, Kosice

Slovenia
Jozef Stefan Institute and Department of Physics, University of Ljubljana, Ljubljana

Spain
Institut de Física d'Altes Energies (IFAE), Universidad Autónoma de Barcelona, Bellaterra, Barcelona
Physics Department, Universidad Autónoma de Madrid, Madrid
Instituto de Física Corpuscular (IFIC), Centro Mixto Universidad de Valencia - CSIC, Burjassot, and Departamento de Informatica y Electronica, Universidad de Valencia, Burjassot, Valencia

Sweden
Fysika institutionen, Lunds universitet, Lund
Royal Institute of Technology (KTH), Stockholm
University of Stockholm, Stockholm
Uppsala University, Department of Radiation Sciences, Uppsala

Switzerland
Laboratory for High Energy Physics, University of Bern, Bern
Section de Physique, Université de Genève, Geneva

Turkey
Department of Physics, Bogaziçi University, Istanbul

United Kingdom
School of Physics and Space Research, The University of Birmingham, Birmingham
Cavendish Laboratory, Cambridge University, Cambridge
Department of Physics and Astronomy, University of Edinburgh, Edinburgh
Department of Physics and Astronomy, University of Glasgow, Glasgow

School of Physics and Chemistry, Lancaster University, Lancaster
Department of Physics, Oliver Lodge Laboratory, University of Liverpool, Liverpool
Department of Physics, Queen Mary and Westfield College, University of London, London
Department of Physics, Royal Holloway and Bedford New College, University of London, Egham
Department of Physics and Astronomy, University College London, London
Department of Physics and Astronomy, University of Manchester, Manchester
Department of Physics, Oxford University, Oxford
Rutherford Appleton Laboratory, Chilton, Didcot
Department of Physics, University of Sheffield, Sheffield

United States of America
State University of New York at Albany, New York
Argonne National Laboratory, Argonne, Illinois
University of Arizona, Tucson, Arizona
Department of Physics, The University of Texas at Arlington, Arlington, Texas
Lawrence Berkeley Laboratory and University of California, Berkeley, California
Department of Physics, Boston University, Boston, Massachusetts
Brandeis University, Department of Physics, Waltham, Massachusetts
Brookhaven National Laboratory (BNL), Upton, New York
University of Chicago, Enrico Fermi Institute, Chicago, Illinois
Nevis Laboratory, Columbia University, Irvington, New York
Department of Physics, Duke University, Durham, North Carolina
Department of Physics, Hampton University, Virginia
Department of Physics, Harvard University, Cambridge, Massachusetts
Indiana University, Bloomington, Indiana
University of California, Irvine, California
Massachusetts Institute of Technology, Department of Physics, Cambridge, Massachusetts
Michigan State University, Department of Physics and Astronomy, East Lansing, Michigan
University of New Mexico, New Mexico Center for Particle Physics, Albuquerque
Physics Department, Norfolk State University, Virginia
Physics Department, Northern Illinois University, DeKalb, Illinois
Department of Physics and Astronomy, University of Oklahoma
Department of Physics, University of Pennsylvania, Philadelphia, Pennsylvania
University of Pittsburgh, Pittsburgh, Pennsylvania
Department of Physics and Astronomy, University of Rochester, Rochester, New York
Institute for Particle Physics, University of California, Santa Cruz, California
Department of Physics, Southern Methodist University, Dallas, Texas
Tufts University, Medford, Massachusetts
High Energy Physics, University of Illinois, Urbana, Illinois
Department of Physics, Department of Mechanical Engineering, University of Washington, Seattle, Washington
Department of Physics, University of Wisconsin, Madison, Wisconsin

Acknowledgements

Table Of Contents

1 Calorimeter overview

1.1 The Liquid Argon calorimeter in ATLAS

The calorimeter plays a central role in ATLAS. In the difficult environment of the LHC machine running at its full luminosity, the calorimeter is designed to trigger on and to provide precision measurements of electrons, photons, jets, and missing E_T.

The Liquid Argon sampling calorimeter technique with "accordion-shaped" electrodes is used for all electromagnetic calorimetry covering the pseudorapidity interval $|\eta| < 3.2$.

The Liquid Argon technique is also used for hadronic calorimetry from $|\eta| = 1.4$ up to our acceptance limit $|\eta| = 4.8$. This corresponds to detector radii less than 2.2 m. At larger radii, where most of the calorimeter weight is located, and where the radiation levels are low, a less expensive iron-scintillator hadronic "Tile calorimeter" is being used.

This results in the global layout shown in Figure 1-i and Figure 1-ii. The central cryostat contains the barrel electromagnetic calorimeter and the 2 T superconducting solenoid. Each end-cap cryostat houses an electromagnetic and two hadronic wheels, and one forward calorimeter.

The central cryostat, which houses the tracking system in its inner cavity, is supported by the barrel Tile calorimeter. The "extended barrel" Tile calorimeters support each of the two end-cap cryostats.

The performance of the calorimeter system has been addressed globally, and is presented as a separate volume [1-1] which contains the expected performances for electrons, photons, jets and missing E_T. The Tile calorimeter is also the subject of a separate volume [1-2], while here we deal only with the Liquid Argon detectors.

1.2 Framework of the Technical Design Report

This Technical Design Report is the result of studies carried out by the ATLAS Collaboration, in particular by the Liquid Argon community, over the past few years. This work itself is the continuation of an active R&D effort which began in 1990. Detailed simulation studies, presented in the Performance Volume [1-1], and a wealth of test beam results, summarized in Chapter 2, have convinced us that, in the framework of the approval process of LHC experiments, we are now in a position to seek approval for the starting of construction of the ATLAS Liquid Argon calorimeter.

After this approval, the construction work would be subject to a set of milestones, which we have set for ourselves, and which will be available for review. Of particular importance in this respect are the "module 0": these are modules of the detector with the final geometry, which use the materials selected for construction, and are built with the final tooling that we are presently assembling in the participating laboratories. Typically these modules will be assembled and warm-tested in 1997, with the goal of a first exposure to the CERN beams in 1997, and in greater detail in 1998. The "module 0" construction and tests appear in all our schedules, and are discussed in the various chapters.

Chapters 3 to 5 concern the cryostats and cryogenics, and Chapters 6 to 9 treat the calorimeter modules properties. Chapter 10 is dedicated to the electronics, an extremely important element in Liquid Argon calorimetry. The aspects of radiation and monitoring are treated in Chapters 11 and 12, and the forthcoming calibration with test beams in Chapter 13. Before installing the detectors in the ATLAS pit, we plan a cold test of each "ready-to-go" detector in the CERN West Hall, where they will be assembled. This activity is treated in Chapter 14, while the final installation is described in Chapter 15. Finally, the schedule and the description of work sharing (Product Breakdown Structure) is given in Chapter 16 (except for test beam activities, for which the information is given in Chapter 13).

Chapter 16 also contains the list of the Institutes and the names of the physicists and engineers proposing to carry out the work. Some technical data, and the list of acronyms used in this volume, are given in Appendix.

Before the detailed presentation of each of these aspects, an overview is given in the remaining part of this introductory chapter. It includes, at the end of the chapter, a cost summary and a brief description of the management structure of the Liquid Argon project.

1.3 Evolution since the Technical Proposal

Since the submission of the ATLAS Technical Proposal [1-3], about two years ago, the basic calorimeter design has been stable. There were, however, a number of points left open, which we have now settled:

Choice of the liquid: liquid krypton had been left as an option for the barrel calorimeter. Detailed simulations were made, using in particular the Higgs boson decays into two photons and into four electrons. The anticipated benefit in terms of mass resolution was not found large enough to counterbalance the excess in cost and complexity [1-4], therefore liquid argon was chosen for both the barrel and the two end-caps.

Presampler granularity and coverage: In the Technical Proposal, the granularity of the barrel presampler had been chosen very fine in η (0.003) so as to allow precise pointing of photons in this direction. Further simulation studies have shown that we have enough pointing accuracy using the narrow strips of the first sampling ($\Delta\eta \times \Delta\phi = 0.003 \times 0.1$) and the towers ($\Delta\eta \times \Delta\phi = 0.025 \times 0.025$) of the central sampling. The granularity of the presampler was thus reduced to $\Delta\eta \times \Delta\phi = 0.025 \times 0.1$, since its function changed to energy recovery only. On the other hand, more effort has been put into optimizing the performance of the EM calorimeter in the barrel to end-cap transition region. These studies [1-1] have led us to enlarge the presampler coverage up to $|\eta| = 1.8$.

Cold or warm preamplifiers: The fast Liquid Argon concept was born with cold preamplifiers [1-5]. Warm preamplifiers, using bipolar transistors, were later developed for the end-cap case, because of the anticipated high radiation level at large rapidity. They are more noisy than cold GaAs preamps (by a factor about 1.5, for the same peaking time); however, when evaluating the effect of both the electronics noise and the pile-up noise onto shower measurements it was realized that the penalty, measured in total noise increase, was not more than about 10%. Under these circumstances, and also considering long term reliability, we decided on the use of warm preamplifiers for the entire electromagnetic calorimeter, barrel and end-cap.

In the case of the hadronic end-cap, the situation is somewhat different. The mechanical structure (the absorber plates are perpendicular to the beam axis) does not lend itself to a simple ganging in depth of the detector gaps, and the inductances necessary to parallel

the plates of a given tower hamper somewhat the use of warm preamplifiers at fast shaping.

We have therefore selected a scheme with one cold GaAs preamplifier per double gap, followed by a summing stage to form the readout towers. These active elements are located at the wheel periphery where the radiation level is rather low (see Chapter 11). Another positive aspect particular to the hadronic end-caps, is the use of a continuous resistive layer to distribute the high voltage which gives a natural protection to the preamplifiers against sparking (see Chapter 8). Nonetheless, a number of milestones have to be met with "module 0", in particular concerning reliability, before we start the mass production of cold preamplifiers.

For the forward calorimeter, where the pile-up dominates largely over the electronics noise, warm preamplifiers have also been selected.

Choice of pipelines: Another important choice left open at the time of the Technical Proposal was the nature of the signal summation for the first-level trigger (analog or digital) and the type of pipeline (digital or analog using switched capacitor arrays). For various reasons, including power dissipation and demonstrated performance, we have selected a scheme in which the signal summation is done in an analog manner, and the pipeline is also analog. We shall also use multilinear ranges, to cover the required dynamics, as opposed to signal compression. As for the preamps, demonstrated performance with "module 0" is a prerequisite before embarking on mass production. This electronics up to and including the ADCs will sit "on detector" as close as possible to the cold-to-warm feedthroughs (see Figure 1-ii).

1.4 The electromagnetic calorimeter
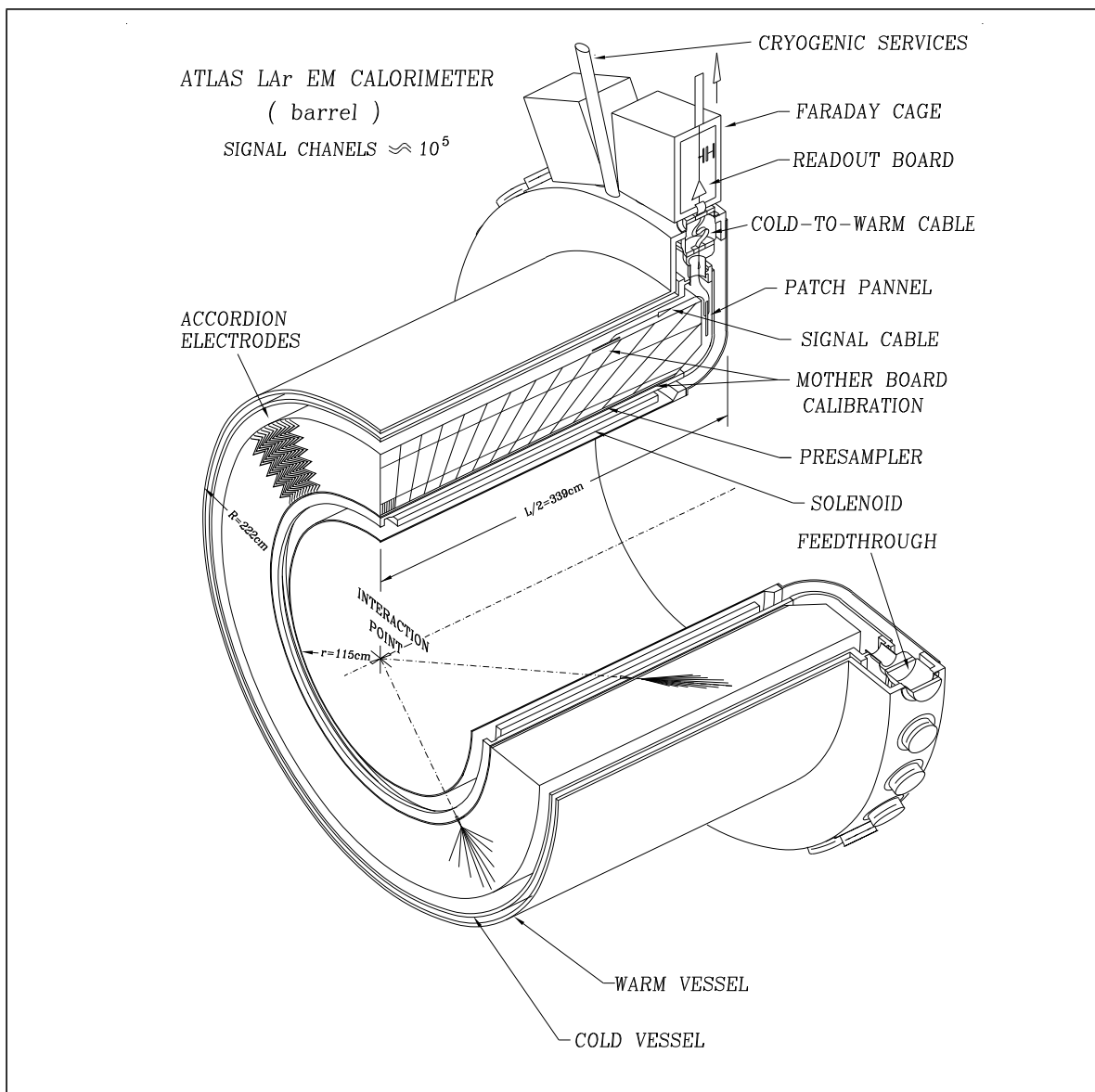
A careful optimization of the detailed calorimeter design has been carried out during the last few years using a full simulation with GEANT. The simulation code was checked against test beam studies (see Chapter 2). Particular care was taken in simulating properly the amount of material in front of the active calorimeter (tracking, cryostats, ...), however, some approximations are unavoidable. In particular the tracking material was averaged in azimuth.

1.4.1 Barrel calorimeter

A perspective view of half of the barrel calorimeter system is shown in Figure 1-1. The full cryostat is 6.8 m long, with an outer radius of 2.25 m, and an inner cavity radius of 1.15 m. Both shells are in aluminium alloy, with vacuum insulation (see Chapter 4).

The superconducting solenoid uses the same insulation vacuum as the liquid argon vessel. The winding has one layer, which is fed from the A-side (see Appendix B). The total thickness of the bare solenoid is 44 mm, and amounts to $0.63 \, X_0$. It is supported by the warm flange of the inner shell. The solenoid is the object of a forthcoming separate TDR volume.

Inside the liquid argon vessel, the calorimeter consists of two identical half-barrels, with a gap of a few millimetres in between. On account of the accordion shape, each half-barrel appears continuous in azimuth. The way to achieve this in practice has rather strongly influenced the design, and is discussed in some detail in Chapter 6. Each half-barrel consists of 1024 lead-stainless-steel converters with copper-polyimide multilayer readout boards in between. Fully pointing readout cells are defined in η by etching of the readout boards, and in azimuth by grouping together four (for the central towers) adjacent boards (see Figure 1-2). Connections are made at

ATLAS LAr EM CALORIMETER
(barrel)
SIGNAL CHANELS $\approx 10^5$
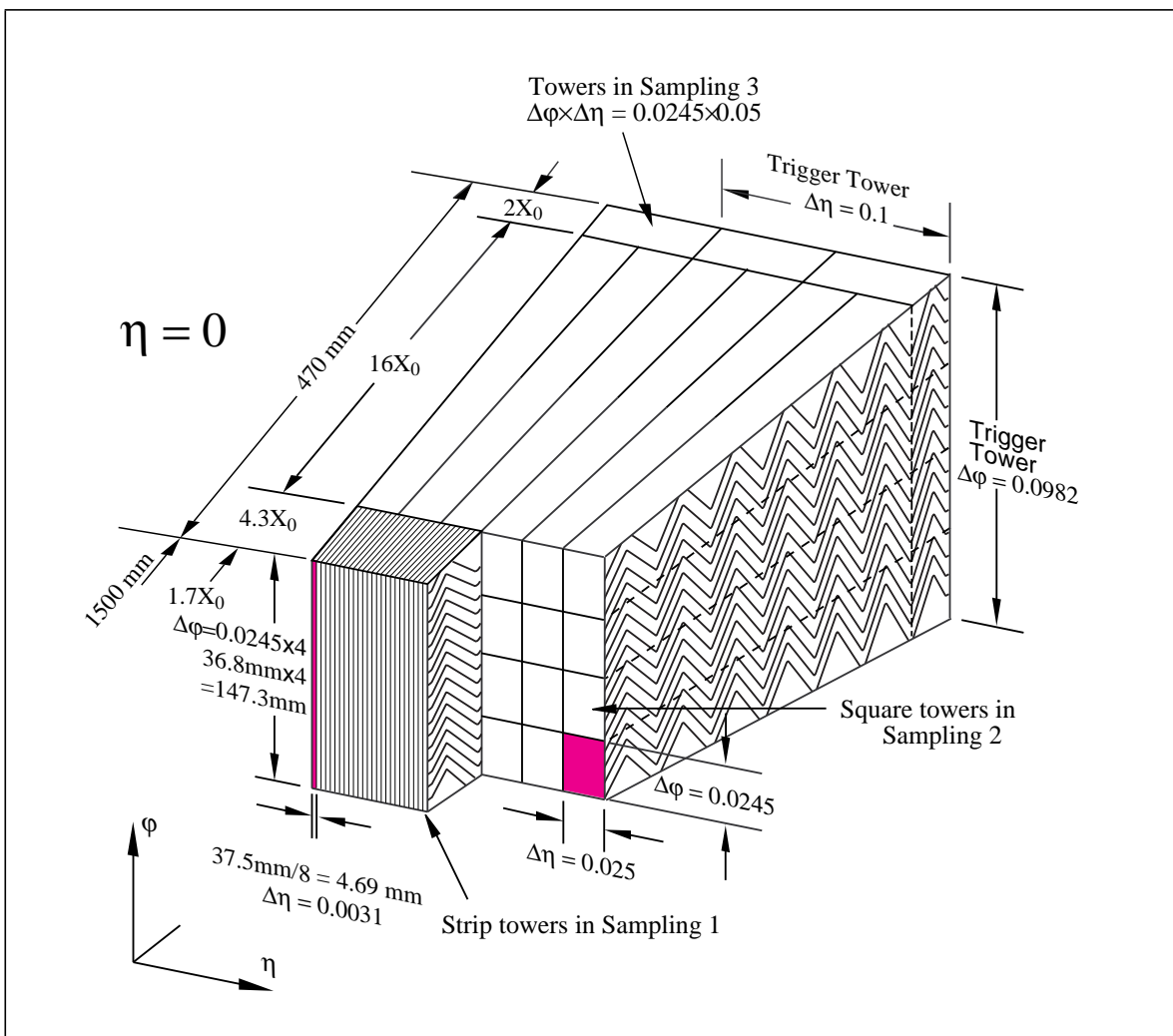
Figure 1-1 Perspective view of one half of the barrel cryostat.

the front and back face of the calorimeter using "motherboards", which also carry the calibrating element (one resistor per channel).

Read-out and calibration signals are routed through cold-to-warm feedthroughs located at each end of the cryostat. Electronics boxes containing the readout elements, up to and including the ADCs, are located on each feedthrough, and provide electrical continuity of the ground so as to form a single Faraday cage out of which come the digital signals.

1.4.2 End-cap calorimeter

Figure 1-3 shows a perspective view of an end-cap cryostat, containing the electromagnetic wheel, the two hadronic wheels, and the forward calorimeter. In the end-caps, the amplitude of the accordion waves scales with the radius. Given the practical limitations in fabricating the absorber plates (which are arranged like the spokes of a wheel), the ratio of inner to outer radius of

Figure 1-2 Sketch of the accordion structure of the EM calorimeter.
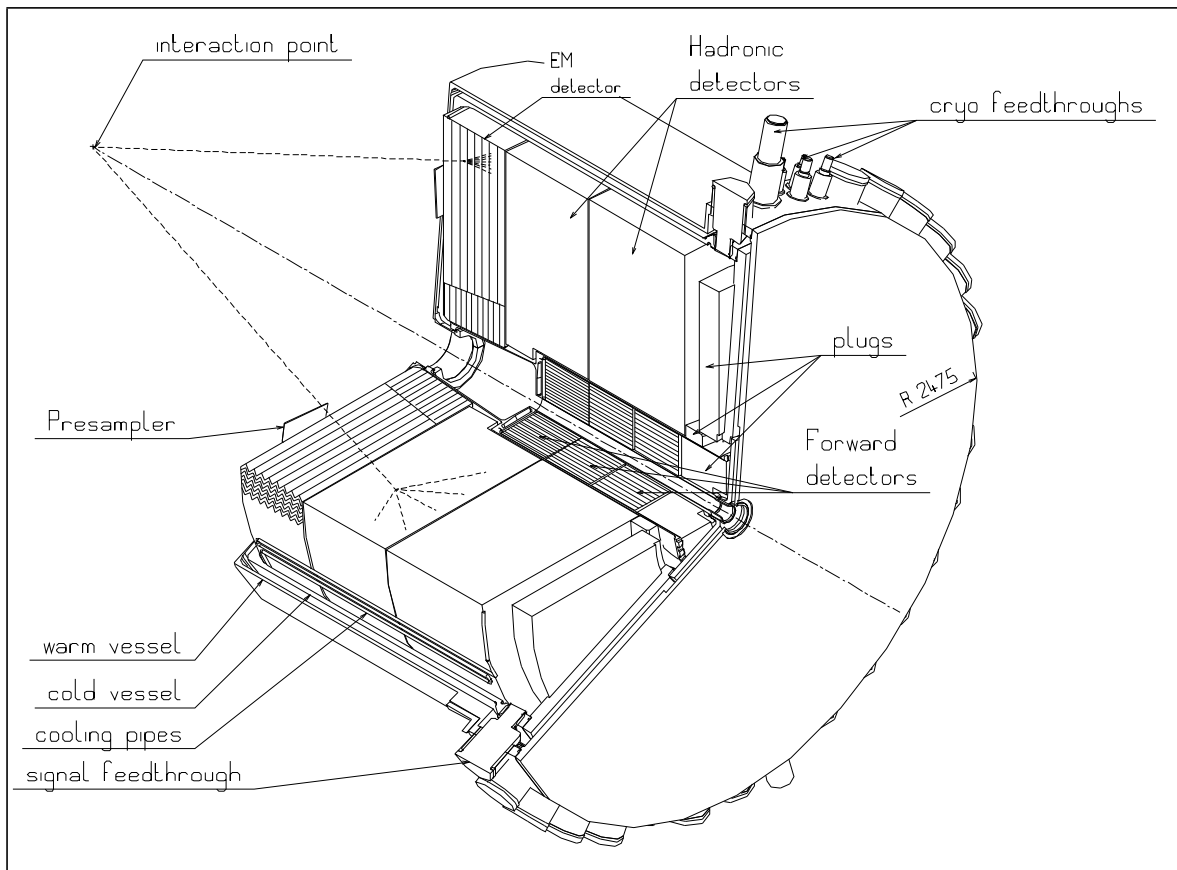
a given plate is limited to about three. As a consequence each end-cap EM wheel consists of two concentric wheels, the large one spanning the pseudorapidity interval from 1.4 to 2.5, and the small one from 2.5 to 3.2.

There are 768 plates in the large wheel (3 consecutive planes are grouped together to form a readout cell of 0.025 in ϕ) and 256 in the small wheel.

As for the barrel, the end-cap cryostats are built out of aluminium, and are vacuum insulated. The outer radius of the cylindrical warm shell is the same as the barrel (2.25 m), and the length of one cryostat is 3.17 m. In order to limit the thickness of the flat front faces of each cryostat, the warm and the cold shells can push on each other through plastic bumpers (see Chapter 5). In total the two flat walls represent, however, almost 1 X_0.

1.4.3 Presampler

The distribution of material in front of the EM calorimeter is shown in Figure 1-4. This amount of material, the way it is distributed in space, and the presence of a magnetic field combine to necessitate a presampler to correct for the energy lost in front of the calorimeter. The barrel

Figure 1-3 Perspective view of one end-cap cryostat.

(endcap) presampler feature, a 1 cm (5 mm) liquid argon active layer instrumented with electrodes roughly perpendicular (parallel) to the beam axis.

In the transition region between barrel and end-cap, around $|\eta|$ = 1.4, the situation is particularly critical, and a scintillator layer, between the two cryostats, is used to recover mainly the jet energy measurement. This also helps for electrons and photons (see Performance Volume [1-1]). Beyond a pseudorapidity of 1.8, the presampler is no longer necessary given the more limited amount of dead material and the higher energy of particles for a given p_T.

In order to avoid creating a gap in the electromagnetic calorimetry coverage (see Figure 1-5), the electromagnetic end-cap wheels have to be as close as possible to the barrel modules. To satisfy this requirement, we have tried to reduce to a minimum, in accordance with the ATLAS Technical Coordination, the gap between the two cryostats (95 mm), and the end-cap presampler, which is of minimum thickness, is encased in a notch of the cryostat cold wall. This takes advantage of the fact that at this radius the mechanical stresses in the end-cap cryostat cold wall are not too large.

1.4.4 Lead thickness and signal height

Detailed simulation of the response to high-energy electrons and photons has shown [1-1] that the total radiation thickness up to the end of the EM calorimeter must be at least 24 X_0 in the barrel, and 26 X_0 in the end-caps. On the other hand, the resolution at medium energy is better if the sampling fraction is higher, meaning fewer X_0's in the same space.
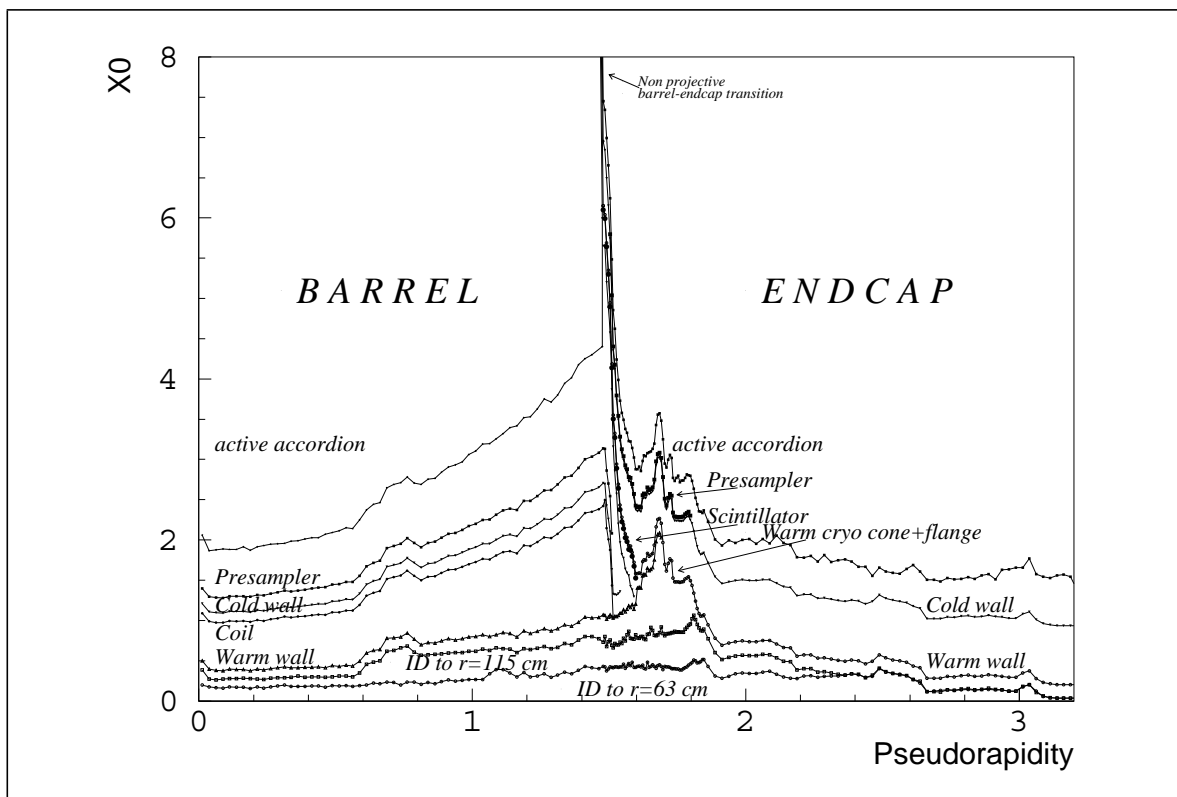
Figure 1-4 Breakdown of dead material (in X_0) up to the active EM calorimeter, as a function of η.
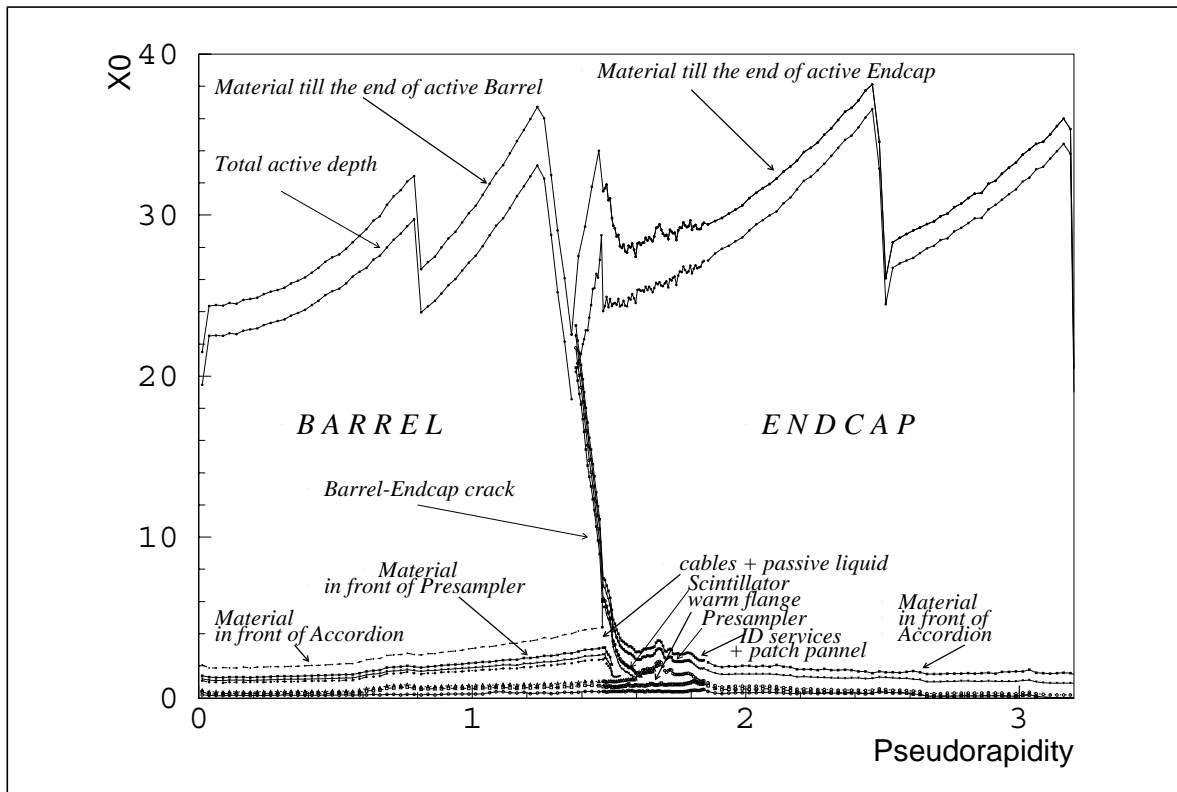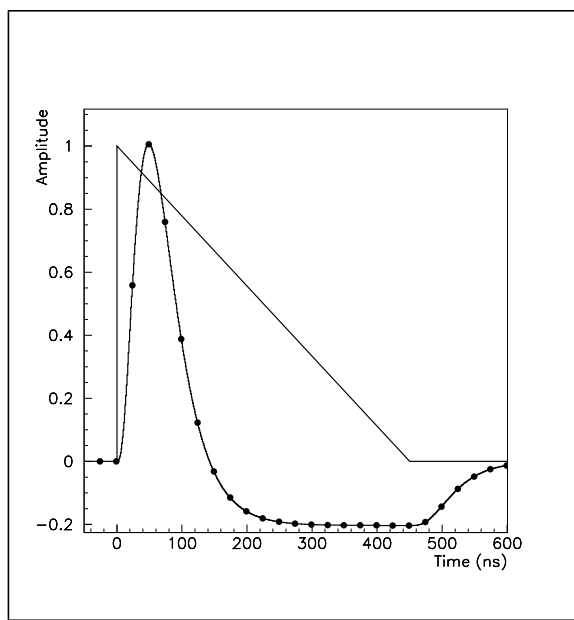
Figure 1-5 Total EM calorimeter thickness (in X_0) as a function of η.

Given the space constraints, and the shape of the calorimeters (cylinder in the barrel, flat disk in the end-caps), we have chosen to use 4 different lead thicknesses from 1.1 to 2.2 mm, as listed in Table 1-1. The sampling fractions can then be deduced in a straight-forward way from the pitch of the electrodes defining the gap ($2\pi/1024$ in the barrel, $2\pi/768$ in the large wheel of the end-caps) and the exact composition of the converter (lead and 0.2 mm stainless steel clad) and readout electrodes (see Chapters 6 and 7).

Given the fast readout used (see the sketch in Figure 1-6), the most significant quantity for establishing the scale of a signal is the peak current corresponding to a given energy deposited in a readout cell. This is expressed in $\mu A/GeV$, and is readily calculated from the sampling fraction and the drift time t_D which is typically 400 ns for a 2 mm gap [1-6]. One should note that in the end-caps, the sampling fraction and the drift time are both a function of the radius. They vary in opposite

Figure 1-6 Signal shape as produced in the detector (triangle), and after shaping (curve with dots). The dots represent the position of the successive bunch crossings.

directions and essentially cancel out, giving a response with a small variation with radius for a given, constant, high voltage over the detector. As explained in [1-1] and in Chapter 7, we have chosen to use a radius-dependent high voltage in order to obtain an *a priori* flat response.

Table 1-1 Lead thickness and detector sensitivity.

Pseudorapidity range	0.0 to 0.8	0.8 to 1.4	1.4 to 2.5	2.5 to 3.2
Lead thickness (mm)	1.5	1.1	1.7	2.2
Sensitivity ($\mu A/GeV$)	2.74	3.08	2.48	2.06

1.4.5 Granularity of the samplings

The number of samplings and the granularity in each of the samplings are summarized in Table 1-2. Physics studies showed that precision physics can hardly be extended beyond a pseudorapidity of 2.5. For this reason, the small wheel has a coarser granularity and only two samplings in depth. We also tried to reduce the number of channels wherever possible without affecting the performance in order to reduce the cost.

The main sampling for measuring energy is the "central one" of the calorimeter, for which we have selected "square towers" of 0.025 in both pseudo-rapidity and azimuth (where it is actually $2\pi/256$). The first calorimeter sampling has a fine granularity in order to allow for π^0 rejection up to E_T of 50 GeV or more. Given the fact that the magnetic field in the tracking volume opens up converted photons, thus obscuring somewhat the rejection power in azimuth, we have chosen to have the finer dimension in the pseudorapidity direction. This fits nicely with the calorimeter structure: thin cells in η are "easy" to obtain by etching correspondingly narrow strips on the readout electrodes. The selected granularity is $1/8$ of the tower size in η. In order to limit the number of channels, the cells are conversely wider in azimuth (4 times the tower size, corre-

Table 1-2 Granularity of the EM calorimeter (pseudorapidity, azimuth).

η range	0 to 1.4	1.4 to 1.8	1.8 to 2.0	2.0 to 2.5	2.5 to 3.2
Presampler	0.025×0.1	0.025×0.1			
Sampling 1	0.003×0.1	0.003×0.1	0.004×0.1	0.006×0.1	0.1×0.1
Sampling 2	0.025×0.025	0.025×0.025	0.025×0.025	0.025×0.025	0.1×0.1
Sampling 3	0.050×0.025	0.050×0.025	0.050×0.025	0.050×0.025	
Trigger	0.1×0.1	0.1×0.1	0.1×0.1	0.1×0.1	0.2×0.2
Readout channels	110 208	25 600	12 288	24 064	1792

sponding to 16 readout plates ganged together). Such a fine granularity in η in the first sampling is also well matched for measuring the pointing of photons ([1-1] and 1.10). In the end-caps, a given pseudorapidity bin becomes narrower and narrower (as does the distance between photons from a constant E_T π^0 decay) when going to large η. Practical considerations have led us, however, to limit the strip pitch to 5 mm or more. This is why above a pseudorapidity of 1.8 the strip size becomes 1/6 of the tower size, and 1/4 above 2.0.

In accordance with the choices made for samplings 1 and 2, and trying to limit the total number of channels, we have chosen for the presampler a granularity of $\Delta\eta \times \Delta\phi = 0.025 \times 0.1$, and for the last calorimeter sampling $\Delta\eta \times \Delta\phi = 0.05 \times 0.025$.
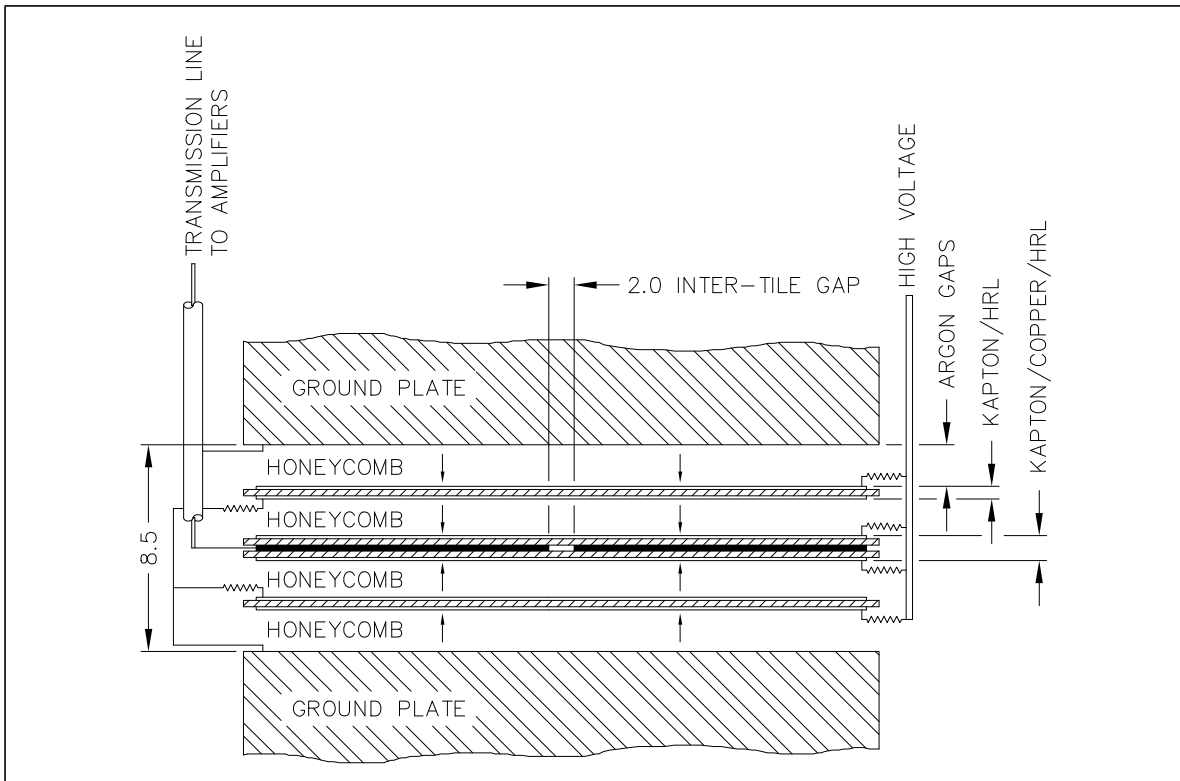
As explained in the Performance Volume [1-1] and here in Chapters 6, 7, and 10, the depth of the various samplings have been the object of a detailed optimization. Mostly based on the criterion of π^0 rejection, the depth of the first sampling (narrow strips) has been chosen to be 6 X_0 (including dead material and presampler). The end of the second (main) sampling was chosen to be 24 X_0, mainly to limit the number of channels necessary to reconstruct medium-energy photons (the back sampling is not necessary below 50 GeV E_T), and to provide the same capacitance everywhere for the preamplifiers. The depth of the back sampling (see Chapters 6 and 7) varies from 2 to 12 X_0 (for η less than about 0.6 the depth of the second sampling is limited to 22 X_0, in order to have at least 2 X_0 in the third sampling).

In total the number of channels in the electromagnetic calorimeter is ~170 000. The trigger towers, quite naturally derived from the numbers discussed above, are defined as covering 0.1×0.1 in both pseudorapidity and azimuth. In the central region 60 elementary cells are summed up to form the trigger signal. At high rapidity, according to Table 1-2, this number slowly decreases and finally becomes 8 for rapidities larger than 2.5 (where the trigger towers are 0.2×0.2).

1.5 Hadronic calorimeter

Each hadronic end-cap calorimeter - HEC - (see Chapter 8) consists of two independent wheels (see Figure 1-3), of outer radius 2.03 m. The first wheel is built out of 25 mm copper plates, while the second one uses 50 mm plates, as cost savings measure. In both wheels the 8.5 mm gap between consecutive copper plates is equipped with three parallel electrodes, splitting the gap into four drift spaces of about 1.8 mm. The readout electrode is the central one which is a 3-layer printed circuit, as in the EM part. The side ones (2-layer) serve only as high-voltage carriers (see Figure 1-7). This forms an "electrostatic transformer" with an EST ratio of 2. Such a scheme has the same behaviour as a double gap of 4 mm, but without the drawback associated

with large high voltage (which would be typically 4 kV instead of 2 kV), nor with large gaps in terms of ion build-up [1-7].

Figure 1-7 Structure of a readout gap in the hadronic end-cap.

Each wheel is built out of 32 identical modules, assembled with fixtures at the periphery and a central ring. The central (buried) layer of the readout boards features a pad structure which defines the transverse readout granularity. The other layers are made out of a high resistive coating, with a typical surface resistance of 1 MΩ per square. The first wheel has two longitudinal segments (of respectively 8 and 16 layers in depth) while the second wheel has only one segment, of 16 layers. The weight of the first (second) wheel is 67 (90) tons.

In order primarily to limit the capacitance seen by a single preamplifier, so as to allow for a fast response, only two gaps are ganged together at the pad level. A miniature coaxial cable running in between the sectors carries the signal to the preamplifier boards located at the wheel periphery. Output signals from (typically) four preamplifiers are summed together on the same board. A buffer stage drives the output signal up to the cold-to-warm feedthroughs.
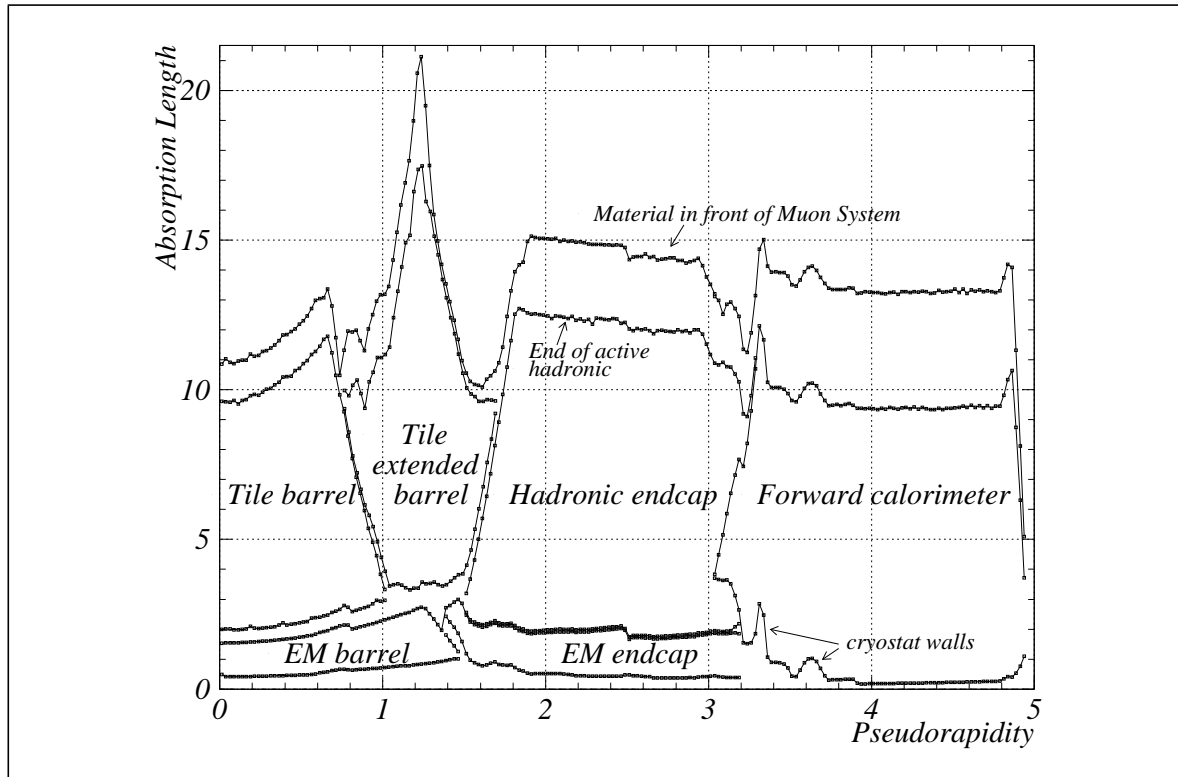
Cells defined in this way are fully pointing in azimuth, but only "pseudo-pointing" in η. The detector limits, from rather obvious mechanical constraints, are however of cylindrical shape (see Figure 1-3). To avoid a crack in material density at the transition between the end-cap and the forward calorimeter (around $|\eta| = 3.1$), the acceptance of the electromagnetic calorimeter goes down to $|\eta| = 3.2$ (see Section 1.4).

Useful numbers for the hadronic end-cap are given in Table 1-3. Trigger towers have the same transverse granularity as the readout ones. A trigger tower is thus the longitudinal sum of three read-out towers.

The amount of material seen by particles up to the back of the calorimeters and over the whole rapidity range is given in Figure 1-8.

Table 1-3 Hadronic calorimeter in numbers

	First wheel	Second wheel
Copper / LAr thickness	25 mm / 8.5 mm	50 mm / 8.5 mm
Sensitivity (μA/GeV)	0.32	0.16
Depth of samplings (λ)	1.4 and 2.9	5.7
Granularity up to $|\eta| = 2.5$	0.1×0.1	0.1×0.1
Granularity up to $|\eta| = 3.1$	0.2×0.2	0.2×0.2
Number of read-out channels	$(768 + 736) \times 2$	704×2
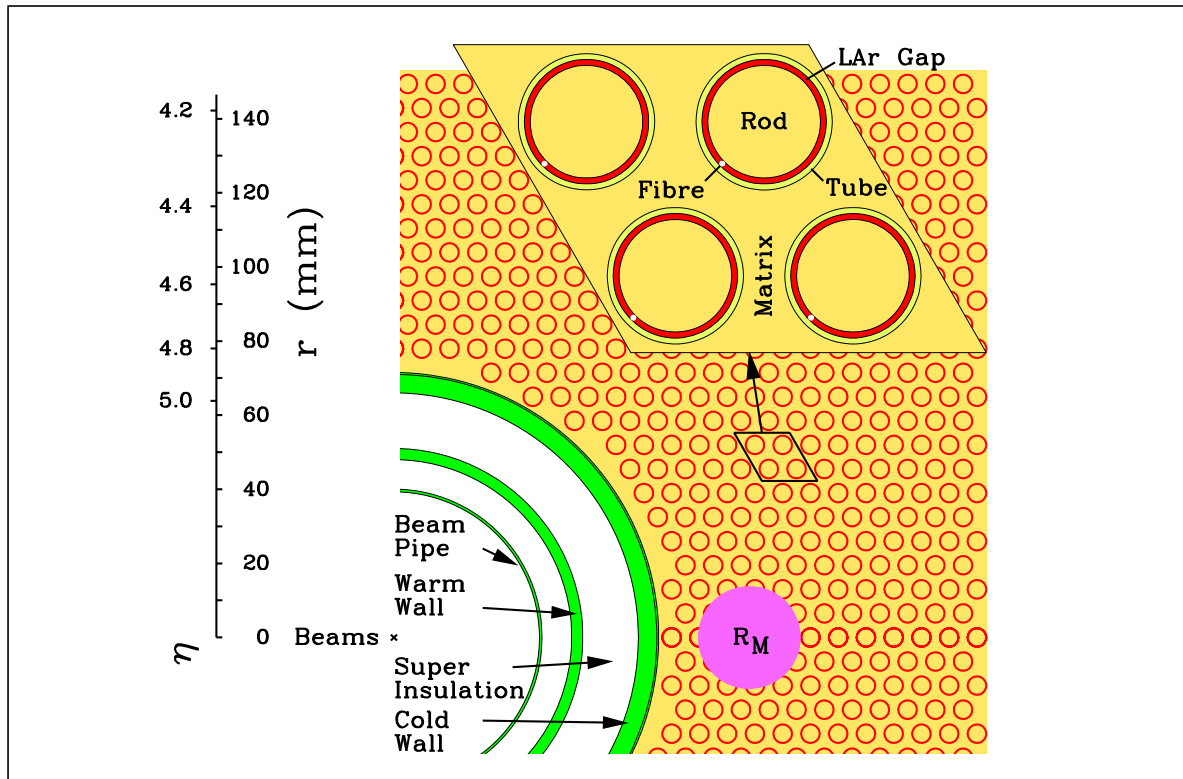
Figure 1-8 Material budget of the ATLAS calorimetry in λ_{abs} as a function of rapidity.

1.6 Forward calorimeter

The forward calorimeter - FCAL - is a particularly challenging detector owing to the high level of radiation it has to cope with (see Chapter 11). In ATLAS the forward calorimeter is integrated into the end-cap cryostat, with a front face at about 4.7 m from the interaction point. This makes dealing with radiation even more difficult (as compared to layouts in which the forward calorimeter is far outside) but, on the other hand, provides a clear benefit in terms of uniformity of calorimetric coverage (see [1-1] and Chapter 9).

A global view of the forward calorimeter is visible in Figure 1-3. In order to avoid too much neutron albedo in the central cavity (to give an example, at 47 cm radius and z less than 1 m, the albedo from the forward calorimeter contributes less than 5% [1-8] of the total neutron fluence), the front face of the forward calorimeter is recessed by about 1.2 m, as compared to the electro-

magnetic calorimeter front face. This leaves rather limited longitudinal space for integrating about 9.5 active interaction lengths, calling for a high density calorimeter. A dense calorimeter also avoids the spilling out of energy from the forward calorimeter into its neighbours. A lower density would significantly increase the pile-up seen in the end-cap calorimeter, especially in the back wheel which is otherwise rather protected. In the proposed design, the forward calorimeter consists of three sections. The first section is made out of copper, while the other two are of tungsten. In each of them the calorimeter consists of a metal matrix with regularly spaced longitudinal channels filled with concentric rods and tubes (see the inset in Figure 1-9). The

Figure 1-9 Sketch of matrix and rods in the forward calorimeter.

rods are at positive high voltage while the matrix is grounded. The liquid argon gap in between is the sensitive medium. This geometry allows for an excellent control of the gaps which are as small as 250 µm in the first section. With such small gaps, the limiting luminosity due to the ion build-up effect (which goes like $1/g^2$ at constant field) is safely high and the density is maximized.

While the construction of the copper section does not present special difficulties, building a tungsten calorimeter is rather new and challenging. After successful assembly of an engineering prototype [1-9], we have chosen a technique based on the assembly of small sintered tungsten alloy pieces. The overall density (including the liquid argon) of a section built in this way, with 375 µm gaps, is 14.5 g/cm^3.

Numbers summarizing the forward calorimeter properties are given in Table 1-4.

Another difficult point was to find a means of supporting the forward calorimeter in the endcap cryostat so that the sensitive area could be extended down to an angle as small as possible. This is achieved by having an external structural tube which carries the weight of the forward calorimeter, and withstands the force of pressure on the cryostat end-walls (see Figure 1-3), while

Table 1-4 Forward calorimeter in numbers

Section	FCAL 1	FCAL 2	FCAL 3
Material	Copper	Tungsten	Tungsten
Acceptance (edge)	$3.0 < \eta < 4.9$	$3.1 < \eta < 4.9$	$3.2 < \eta < 4.9$
Rod diam./argon gap	4.75 mm / 0.25 mm	4.75 mm / 0.375 mm	5.50 mm / 0.50 mm
Cell size (cm^2)	2.0 (4 rods)	3.5 (6 rods)	5.6 (9 rods)
Number of tubes & rods	12000	10000	8000
Sensitivity (μA/GeV)	1.9	1.2	1.1
Depth (λ)	2.6	3.5	3.4

the central cryostat tubes near the beam pipe have no structural role (see Chapter 5 for details). The acceptance limit is shown in Figure 1-8.

In terms of electronics and readout, the rods are ganged by 4 on detector, and the signal is carried out by polyimide insulated coaxial cables. Given the particular structure of the forward calorimeter, and the high dose environment, blocking capacitors could not be integrated in the calorimeter readout electrodes (unlike the EM and hadronic calorimeters). They appear as discrete elements located in the back of the second hadronic wheel. The number of channels corresponding to the granularity just described is 11 288 (for both end-caps). While the corresponding number of feedthroughs and readout channels is reserved for such a number, it corresponds to a granularity in excess of what physics requires in this pseudorapidity area. Solutions to combine channels while preserving the speed of response and the noise performance are presently being studied (see Chapter 10).
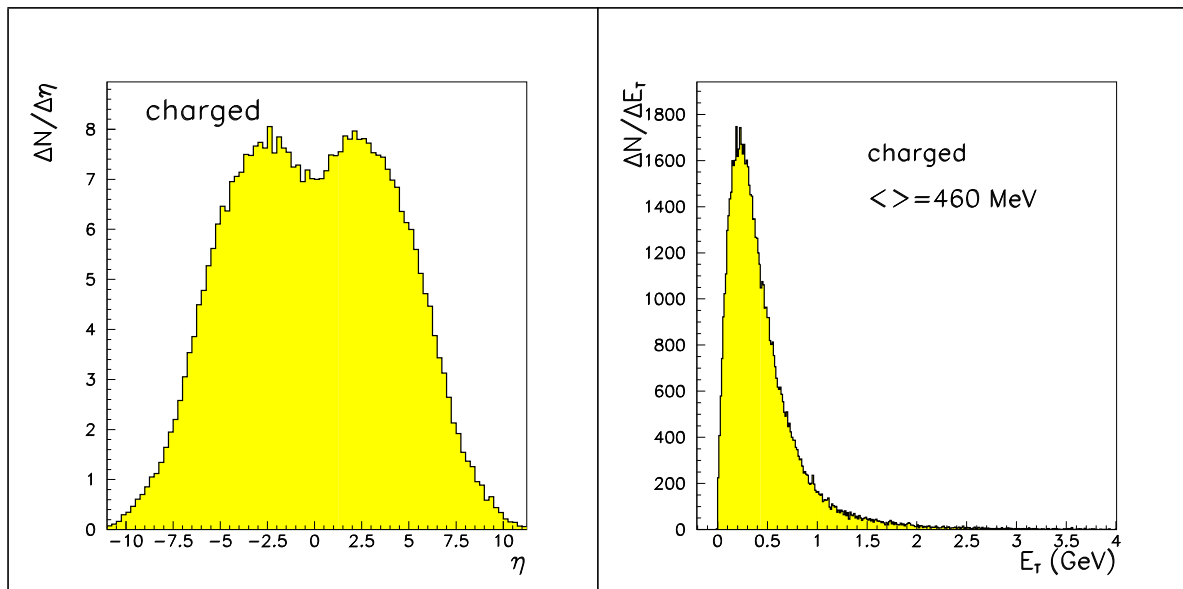
1.7 Shaping, pile-up, and electronics noise

The effect of pile-up on the calorimeter performance, as described in detail in [1-1] depends on a number of features which we briefly consider in this section, before addressing the calorimeter readout.

Primarily the pile-up results from the energy deposited in the calorimeter by the particles produced in the numerous soft interactions taking place at each bunch crossing. However, the mean energy in any calorimeter cell, and its fluctuations, depend also, and in a critical way, upon the details of the calorimeter signal treatment.

At the production level, the main parameters are the particle multiplicity distribution and the p_T spectrum. Those are given, for charged particles, in Figure 1-10 and Figure 1-11, using the PYTHIA 5.7 generator as input [1-10]. The mean number of charged (neutral, after π^0 decay) particles per pseudo-rapidity interval is 7.5 (7.9) and their average p_T (without low-energy threshold cut) is 460 (290) MeV. Due to the solenoidal field, charged particles of p_T less than 360 MeV are trapped inside the cavity.

Assuming an inelastic cross-section of 70 mb, and an average luminosity of 10^{34} cm^{-2}s^{-1}, and taking into account the average filling factor of the LHC of 2835 active bunches over 3564 clock cycles [1-11], one finds on average 23 inelastic events per "active" crossing.

Figure 1-10 Charged tracks multiplicity as a function of pseudo-rapidity for minimum-bias events.

Figure 1-11 Transverse momentum distribution of charged particles for minimum-bias events.

With the signal shape as described in Figure 1-6, which has a zero net area, the average signal in any calorimeter cell is also zero (except for settling effects at the beginning and end of a bunch train).

As a reflection of the high-p_T tail (and of the signal shape), one should however notice that the most probable value is not precisely zero. Under the above conditions its value in E_T is typically -50 MeV in an EM cluster (3 cells in pseudorapidity, times 5 cells in azimuth, defined in the second sampling). This kind of pedestal will be continuously measured by taking random triggers interspersed with the physics triggers.

The r.m.s. of the energy deposit (which is usually called pile-up) is also directly proportional to the pile-up sum I, defined as
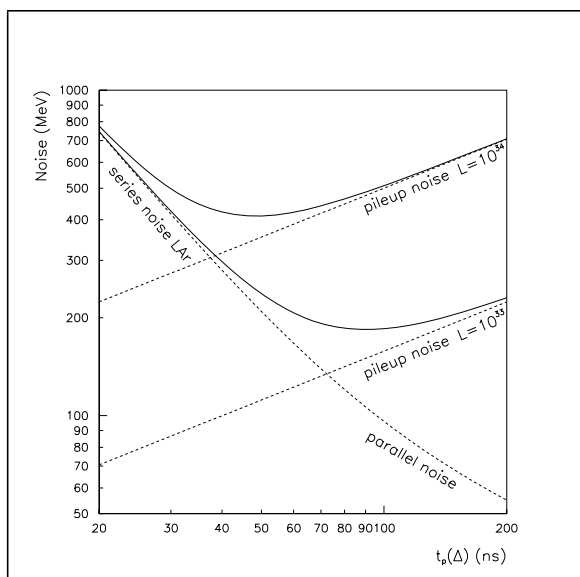
$$I = \left(\sum_i f_i^2 \, / f_{max}^2 \right)^{1/2}$$

where the sum runs over all the bunch crossings contributing to the signal, with a relative amplitude f_i normalized to the peak amplitude f_{max}. For the signal shape shown in Figure 1-6, I is about 1.5. This means that we are sensitive on average to 2.2 bunch crossings. One should note that the bipolar shape with a null net area insures "automatically" the base line subtraction.

In an EM cluster (3×5 in $\Delta\eta \times \Delta\phi$) the r.m.s. of the transverse energy deposition is typically 300 MeV (see [1-1] and [1-12]). A pile-up value like this contributes significantly to the calorimeter resolution. An obvious way to try to reduce it is to make the signal response faster (peaking time $t_p(\Delta)$ shorter), in such a way as to reduce the pile-up sum. In doing so, one increases the accepted bandwidth, and thus the thermal noise, and reduces the charge effectively sampled, thus in total worsening rapidly the effective thermal noise.

The interplay of pile-up and thermal noise as a function of shaping time is shown in Figure 1-12, and discussed in detail in Chapter 10. The shaping we have chosen gives optimum response (minimal sum for electronics and pile-up noise) when sampling at the peak for the nominal high luminosity. At lower luminosities (down to 10^{33} cm^{-2}s^{-1}) digital filtering using 5 samples around the peak properly weighted (see Chapter 10) allows to stay at the optimum performance. The same shaping time is used for the calorimeter trigger signal.

For larger clusters, the pile-up increases typically as the area to the power 0.7 [1-13]. In order not to spoil the resolution of jets nor the resolution of missing E_T, an algorithm suppressing channels below typically twice the noise can be used [1-14]. In the hadronic end-cap back wheel the pile-up is rather low,

Figure 1-12 Optimization of the shaping time for high and low luminosity.

and in order to diminish the electronics noise to be able to see muons, a longer shaping time will be effectively done, even at the highest luminosity, using digital filtering.

1.8 Electronics and trigger

As stated in Section 1.3, warm preamplifiers have been preferred for the electromagnetic calorimeters, based on various considerations, in particular long term reliability (see [1-1] Chapter 2). Using preamplifiers with a bipolar input transistor, a noise level of typically $0.4\,\text{nV}/\sqrt{\text{Hz}}$ is obtained. An important consideration at the speed retained is that the preamplifier matches accurately the cable impedance (50 or 25 Ω, depending whether the capacitance to be readout is smaller or larger than about 800 pF). Satisfactory results, although not perfect, are obtained with the common base configuration chosen.

The design of the shaping stage is driven by the interplay between pile-up and thermal noise, as briefly described above, and by the required dynamic range. While the preamplifier is designed to cover a dynamic range in excess of 17 bits, it is considered impossible to connect to the pipeline/ADC stage with such a range. Our choice is to split the range to be covered by having a shaping amplifier with 3 linear output ranges, with relative gains of typically 1, 10 and 100. With such a choice the necessary dynamic range can be comfortably covered with a 12 bit system downstream of the shaper. An ASIC with bipolar technology is employed for the shaper. For a cell capacitance of 1.5 nF, typical of the second sampling, the electronics noise is about 140 nA (at $t_p(\Delta)$=45 ns), which converts to about 50 MeV for an electron or photon energy measurement using the electromagnetic calorimeter.

Chosing a multirange output shaper forces one to have the pipeline/ADC stage physically close to the shaper. Our choice is to group onto the same front-end board the preamplifier (except for the hadronic end-caps), the shaper, the pipeline, and the ADC. A perspective view of the layout of the crates housing these boards can be seen in Figure 1-1, and details are given in Chapter 4 and in Chapter 10. This layout offers the advantage of a rather easy access, several times a year if necessary (see Chapter 15).

Particularly challenging in such a layout are the requirements on the coherent noise, for which we have set an upper limit of about 3 MeV per read-out channel (see [1-1], Chapter 3, and [1-15]). Previous experience indicates that obeying strict grounding rules is one of the key elements for success in this matter. It is our intention to establish them soon, and follow them already in our test beam set-up. Another critical point is the electrical power cabling and the extraction of the dissipated heat. Particular attention should also be devoted to possible electromagnetic interference brought in by the solenoid power supply.

As noted at the beginning of this chapter we have selected an analog pipeline using SCAs, followed by a multiplexed 12 bit ADC. Successful beam tests [1-16] with simultaneous write/read operation have convinced us that the technique chosen has the necessary potential, and satisfies the low power requirements. A further evolution of our SCA chip, incorporating the 3-gain scheme, will be produced by spring 1997, in parallel with the layout of prototype front-end boards. The next milestone is to routinely operate about 8000 pipelined channels in the readout of our modules zero in the test beam (see Chapter 13).

Downstream of the front-end board, the last stage of the calorimeter readout is the digital filtering. Its purpose is to extract the best possible information from the five samples which are digitized around the peak. The corresponding boards would sit off-detector (trigger cavern), rather far away from the front-end crates. A digital optical link, dimensioned for a LVL1 trigger rate of 75 kHz maximum, connects the two.

Signals for the first level trigger are formed by analog sums, and correspond to trigger towers of $\Delta\eta \times \Delta\phi = 0.1 \times 0.1$. Due to the large number of channels to be summed (up to 60), the sums are performed in steps (up to three): in the shaper chip, on the front-end board, and then on dedicated boards also sitting in the front-end crates. The resulting analog sums are brought to the trigger hut where they are digitized at 40 MHz. The analog pipelines have 144 cells, covering a maximum latency time of 2.5 μs, and allowing some safety margin for derandomizing.

The read-out of the presamplers, and of the forward calorimeters are essentially identical to that of the EM calorimeter. For the forward calorimeter, the number of channels to be readout (about 6000 per side) does not reflect the necessary granularity, but is more a matter of convenience in order to use the same boards as for the EM calorimeter. If ganging of cells in the cryostat with transformers, downstream of the blocking capacitors, proves acceptable, it will allow us to reduce significantly the number of channels (see Section 1.6 above and Chapters 9 and 10). For the hadronic end-cap the differences are essentially related to the fact that the preamps are in the cryostat, requiring a different input impedance for the shapers. Also, a trigger tower requires the sum of only 3 channels (see Chapters 8 and 10 for details).

The high voltage, of typically 2 kV, is brought from outside using warm feedthroughs, located on top of each cryostat. The two sides of each Kapton board are powered separately. This ensures maintaining 50% of the signal (which can be corrected for) in case of a HV problem in a given gap. Each twin HV input covers typically four trigger towers.

Preliminary studies indicate that the current drawn by the calorimeter can be used for a luminosity measurement. The "granularity" needed for these dc measurements has not yet been decided.

1.9 Calibration, monitoring

1.9.1 Electronics calibration

Being a system with no internal gain, the calibration of a Liquid Argon calorimeter can, in principle, be "factorized" in a channel to channel calibration of the electronics readout, and an overall energy scale determination. The requirements are particularly stringent for the EM calorimeter, because of its high intrinsic resolution.

To get an accurate electronics calibration, the signal has to resemble "as much as possible" the physics signal. In particular the electronics calibration signal should be fast (electromagnetic showers induce signals with rise time of 1 ns or less), and have a decay time equal to the drift time in the gap. The system we have selected sends voltage pulses to precision resistors located in the cold, close to calorimeter cells.

In the signal distribution, it is critical to avoid any inductance that would be seen differently by the physics or calibration signals. From detailed simulations of signal propagation, and past experience with prototypes (see Chapter 2), we think that the system proposed can be guaranteed to better than 0.25%, but only on detector "blocks" of typically $\Delta\eta \times \Delta\phi = 0.2 \times 0.4$ (see Chapter 10 for details). For larger detector areas, some systematic effects in the calibration will have to be corrected for.

1.9.2 Global calibration of the EM calorimeters

Before making such corrections, and in order to provide an overall relative calibration, it is necessary to consider other effects which can affect the response from place to place. Among these one can list the non-uniformity of dead material in front of the first active layer (presampler), some liquid temperature gradient, etc.

Our strategy for the overall calibration consists in relying on physics event samples ($Z \rightarrow e^+e^-$ in particular), not only for the global energy scale, but also for the type of "medium-range" effects considered above. The exact weight that physics events will carry with respect to electronics calibration is rather difficult to specify now. It will clearly depend upon the luminosity accumulated and the understanding of the detector at a given time. Further details can be found in the Calorimeter Performance Volume [1-1].

1.9.3 Temperature monitoring

For a time-integrating Liquid Argon calorimeter, the signal depends on temperature only through the liquid density, with a sensitivity of about -0.5% per K. With fast shaping, as adapted to the high interaction rate of the LHC, the signal is directly proportional to the electron drift speed in the gaps, which is also temperature-dependent. This fact was realized rather recently [1-17] and measurements done with some of our prototypes (see Chapter 2) have confirmed the effect. Globally the temperature dependence is -2% per K, of which 3/4 is to be attributed to the effect on speed. This rather strong dependence calls for a uniform liquid temperature bath, regulated very smoothly, and for accurate temperature measurements. These points are addressed in Chapter 3 and 12. Our final aim is a temperature difference smaller than 0.3 K between any two points of the calorimeter, corresponding to a contribution to the energy resolution constant term of 0.2% or less.

While the role of speed increases markedly the sensitivity of the signal to temperature varia-tions, it is to be noted that, fortunately, it also brings with it a possibility of directly monitoring the temperature in the calorimeter, as a function of time: the length of the negative lobe (see Figure 1-6) of the pulse is a direct measurement of the drift time, and thus of the speed. Simula-tions have shown that with the currently anticipated noise level, a 40 GeV energy deposit should lead to a drift time measurement with a statistical error of 0.4 ns. First test beam studies (see Chapter 2) indicate an actual accuracy about a factor two worse, due to various practical limitations [1-18]. This indicates that with a limited amount of data in which the whole pulse is read out, one can in principle follow the effect of temperature variation on the signal, in any point of the calorimeter, with the requisite accuracy (0.1%). While the details of event selection have not yet been worked out, the basic requirement of being able to read out fully (i.e. 25 bunch crossings instead of the usual 5) a given flagged event, is part of the read-out specifica-tions.

Having in mind this possibility of *a posteriori* correction, and having not completed detailed cal-culations and optimization of temperature maps in the cryostat, we have given to our cryogenic system designers a first specification of uniformity of 0.6 K, to be redefined (down hopefully to 0.3) when experience has been gained with the new test cryostat and monitoring system (see Chapters 12 and 13) and when the results of the calculations are available.

1.9.4 Purity monitoring

In contrast with the case of temperature dependence, the fast read-out diminishes the sensitivi-ty to electronegative impurities by a significant factor, equal to typically $V_{drift} \times t_p(\Delta)/gap$. Nonetheless purity should be monitored and we have foreseen a number of test cells (α and β) in various places of each cryostat (see Chapter 12).

A point specific to operation at the LHC is the possible occurrence of pollution due to outgas-sing of calorimeter material under irradiation. While the phenomenon of radiolysis at room temperature is well known, there was no data concerning pollution of noble liquids at low tem-perature. In the framework of R&D activity [1-19], a test programme was launched a few years ago, from which we now have some results (see Chapter 11). These indicate that indeed a high neutron irradiation of plastic materials does trigger the emission of some electronegative impu-rities. However the level is such that, with the careful selection of components that we plan (see Chapter 11 and Chapters 6 to 9), no alarming effect should take place.

1.9.5 Calibration of hadronic and forward calorimeters

Given the level of precision required from the hadronic and forward calorimeters, their elec-tronics calibration does not raise problems of principle once the case of the electromagnetic cal-orimeters has been solved. There are, however, a number of practical points to be considered.

In the hadronic end-cap, the calibration signals are brought down to the pad level, in a way sim-ilar to that for the electromagnetic calorimeters. However, all pads of a read-out tower are pulsed simultaneously, which forbids calibrating one by one each of the individual "pad pream-plifiers". Simulation of the effect on jet resolution of the currently obtained gain dispersion (less than 5%) has shown this is perfectly acceptable (see Performance Volume [1-1] and Chapter 8).

For the forward calorimeter, due to the high level of radiation, it was found too difficult, and furthermore not necessary to bring the calibration pulses "down to the rods". Instead the cali-bration resistors are located close to the blocking capacitors, some 1 to 3 m away from the active

cells. It is estimated that the induced calibration to physics signal distortions can be corrected to the necessary level of a few per cent.

A difficult problem remains for all hadronic calorimeters, namely the overall normalization with respect to the electromagnetic calorimeters. The use of test beam data is one of the approaches to be followed, and our plans (see Chapter 13) include a number of combined set-ups. Of particular interest for the forward region would be the possibility that we are presently exploring to expose a fully equipped end-cap, in the X5 beam line, near their point of assembly (see Chapter 14). Studies have not yet been finalized for in situ calibration with physics events. Channels investigated include W decays in two jets, in $t\bar{t}$ events, and Z^0-jet and γ-jet events [1-1].

1.10 Summary of performances

The Liquid Argon calorimeter system described in this TDR has been optimized by a constant and fruitful exchange between the simulation groups and the detectors, electronics, and cryogenics design groups.The patient process of optimization, and the resulting performances are the object of the TDR Performance Volume [1-1]. We refer the reader to this text for all details, and only give here some remarks and a few illustrative numbers.

A characteristic of the proposed calorimeter is its planned reliability and robustness, which should allow long term high luminosity running without any degradation of its performance.

Because its high intrinsic performance is easily degraded by the environment, the most difficult part of the calorimeter to optimize in the general context of the ATLAS experiment, was the electromagnetic calorimeter. Considering first the energy resolution $\sigma/E = a/(\sqrt{E}) \oplus b/E \oplus c$, the sampling term a between 8 and 11% is a direct reflection of the sampling frequency. To avoid worsening this term at low energy, a presampler has been added where necessary, in order to correct for energy losses in the dead material upstream (tracker, coil, cryostat, etc). Equally challenging was to find a layout in which the barrel to end-cap transition was not creating a large area of reduced performance (a so-called "crack"). The barrel cryostat design at which we arrived uses "isogrid" (a technique developed for space industry) in order to minimize dead materials in critical areas.
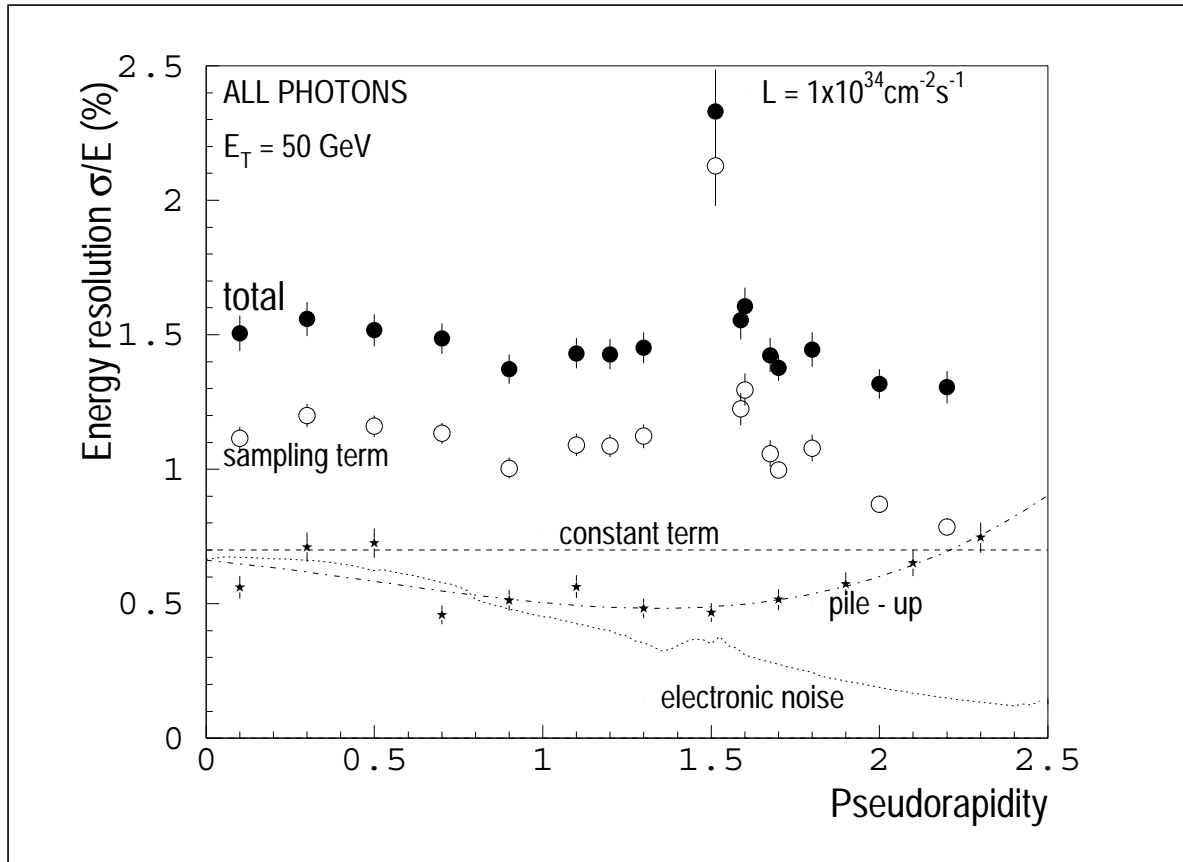
The electronics and pile-up noise terms, as explained shortly in Section 1.7, vary in opposite directions with the shaping time. A careful optimization has been done, which leads to a combined noise term b (close to $\eta = 0$, for a $\Delta\eta \times \Delta\phi = 3 \times 5$ cluster) of about 400 MeV (200 MeV) at 10^{34} cm^{-2}s^{-1} (10^{33} cm^{-2}s^{-1}). This term affects the performance of the EM calorimeter at 20 GeV and below.

At the other end of the energy range, the most important error in the energy measurement is the constant term c. Our working figure is to keep it below 0.7%. The main contributions that we expect to this term are given in Table 1-5. As opposed to the other terms, which are mostly a reflection of the design, the constant term is more sensitive to the skill put into the construction, calibration, and operation of the detector. The number finally achieved will be a direct image of this. As a summary, the various contributions to the energy resolution of 50 GeV E_T photons are shown in Figure 1-13.

Beyond energy measurement, the EM calorimeter we are proposing will provide, thanks to its high granularity, powerful electron/photon identification and rejection of the jet background. The thin strips in the first sampling are a unique feature of this calorimeter. They allow π^0 rejection, by a factor larger than 3 at 50 GeV E_T. In total, the jet rejection, at 20 GeV or above, is ex-

Table 1-5 Contributions to the constant term in the EM calorimeter energy resolution

Source of imperfection	Contribution
Local term (cluster size, accordion shape, ...)	0.35 %
Mechanics of the modules (lead, gaps)	0.3 %
Calibration sytem	0.25 %
Temperature inhomogeneities	0.2 %
Combined	0.6 %
Target figure	0.7 %

Figure 1-13 50 GeV E_T photons. Various contributions to the energy resolution.

pected to be about 5000. Such a rejection is required to eliminate huge QCD backgrounds in the $H \rightarrow \gamma\gamma$ channel. The narrow strips contribute also to the photon angular measurement in the η direction, with an accuracy of about $(50\mathrm{mrad})/(\sqrt{E})$, an essential information in the reconstruction of the channel mentioned above. The calorimeter is also an essential tool in identifying τ decays into hadrons. Combined with the tracker, a rejection of about 400 against jets is possible for about 30% efficiency, allowing to improve in an essential way the signal to background ratio in the search for MSSM Higgs bosons (A/H) decaying into $\tau\tau$.

While jet reconstruction is perceived as the task of hadronic calorimeters, it may be worth recalling that typically 50% (it is energy dependent) of a jet energy is deposited in the EM calorimeter. The good resolution for the EM component, and the high granularity, help in the overall jet performance. However, coherent noise may hamper the performance for jets and missing E_T, which

both require summing up a large number of channels. The limit of 3 MeV per channel is derived from this requirement.

The hadronic and forward liquid argon calorimeters cover a large fraction of the pseudo-rapidity space, $1.4 < |\eta| < 4.8$. This region is more difficult to instrument, as compared to the barrel part covered by the Tile calorimeter, because of the high level of radiation (see Chapter 11). The layout we are proposing, with both the HEC and FCAL calorimeters in the same cryostat, offers continuous coverage up to the acceptance limit, an essential element in forward jet tagging for the Higgs boson search in the TeV mass range [1-1].

Detailed simulations of jet energy resolution, up to the TeV range, indicate that the liquid argon hadronic end-cap calorimeter has a sampling term of about $(60\%/\sqrt{E})$, and a good constant term (possibly as low as 2%). The real performance in the medium and low E_T range will however be limited by cone size effects, and pile-up. As an illustration, and again taken from [1-1], the jet energy resolution in a cone of $\Delta R = 0.4$ or integrated over the calorimeter, is shown in Figure 1-14. The interval of rapidity $|\eta| < 1.4$ is covered by the Tile calorimeter. At 10^{34} cm^{-2}s^{-1}, the pile-up noise in a $\Delta R = 0.4$ cone is less or about 7 GeV E_T.
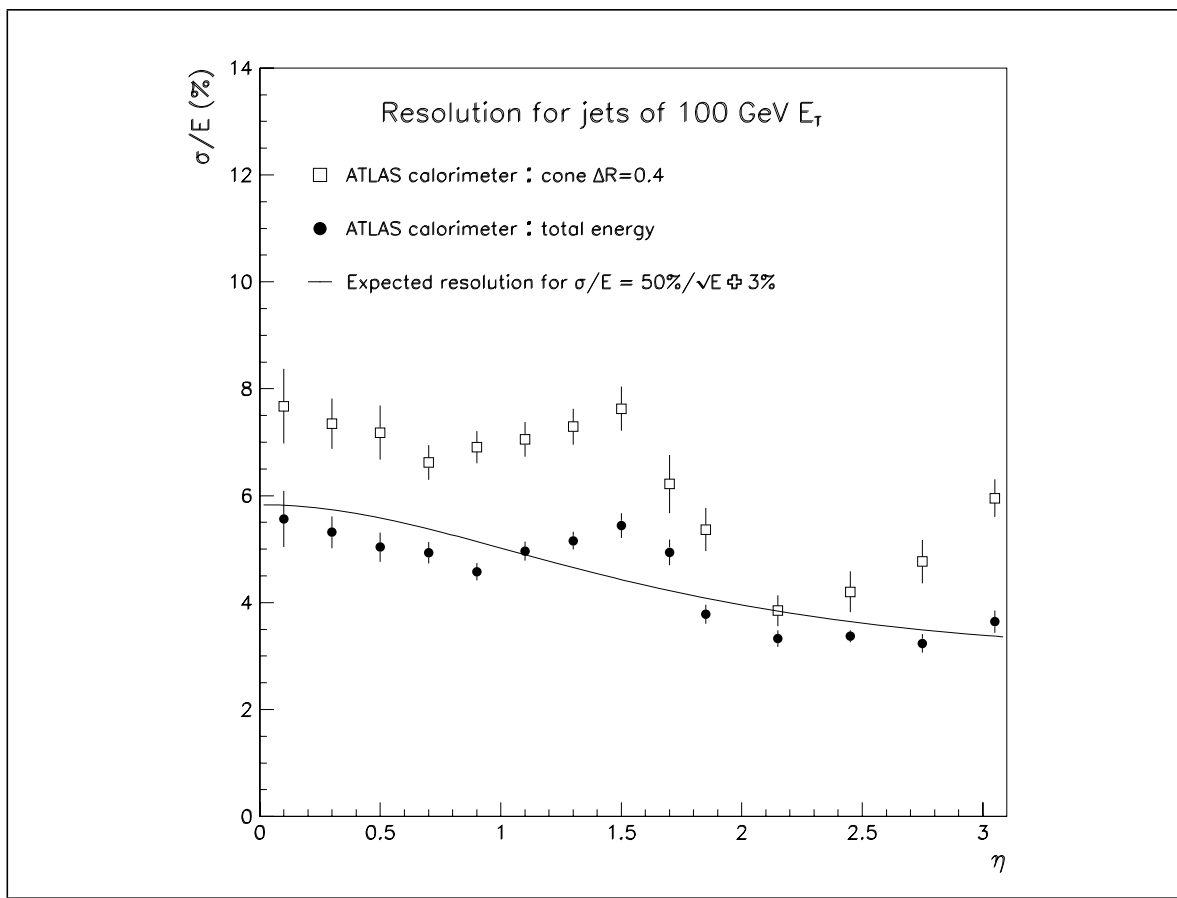
Figure 1-14 Resolution of 100 GeV E_T jets as a function of η.

The forward calorimeters have enough granularity to allow a good angular measurement down to the smallest angles, an important feature in tagging jets, measuring their p_T and measuring the missing E_T. In total, as a bench mark for the complete ATLAS calorimeter, the missing p_T resolution of $A \rightarrow \tau\tau$ events has been estimated to be about 7 GeV for each transverse component allowing at 150 GeV a mass resolution of about 20 GeV.

1.11 QAP, safety, cost, project management

1.11.1 Quality assurance plan

A quality assurance plan has been defined on the scale of the ATLAS project [1-20]. It is based on the recommendations stated in the ISO 9001 quality systems. The laboratories involved in the Liquid Argon detector construction have agreed to follow this plan, and a document more specific to this detector has been issued [1-21]. The main recommendations are already being followed for the presently engaged construction of "modules zero", and the overall final design.

Among the most relevant points, one can list:

- design complying with standards (ASME, CODAP, ..), and design reviews
- approval of drawings at the appropriate managerial level
- documentation (to become embedded in Engineering Data Management System)
- selection and radiation hardness testing of critically exposed components
- traceability of all components
- quality of processing, assembly, and handling (clean rooms, ...)
- acceptance tests before shipping and upon receipt at CERN

The design, and level of quality control, is furthermore adapted to the level of access for maintenance and repair which is foreseeable during the LHC operation (see Chapter 15). Essentially four classes of elements can be distinguished:

- cold elements of the barrel cryostat and calorimeter with access only in case of major problem, and requiring a shut-down of the experiment
- cold elements of the end-cap cryostats and calorimeters, with very limited access, requiring a transport of one end-cap to the surface area
- warm elements on detector (mainly electronics), with limited access, a few times a year
- elements accessible at any time

1.11.2 Safety

The question of safety in ATLAS will be treated coherently, in the "Technical Coordination" TDR volume, where the experimental area and its safety devices will be described together with the corresponding requirements on all individual parts of the detector and their interplay. In this section only the guiding principle will be mentioned. More details are discussed in the following chapters treating the safety information in the technical context of the components.

All elements of the calorimeter are designed to comply with the CERN Safety Rules. Beyond the problems of complex and heavy detector elements, and densely packed electronics, two elements are of particular concern in the detector described in this volume:

- The presence of large volumes of cryogenic liquids in the operating detector or in the storage tanks (about 80 m^3 of liquid argon in total) presents a potential hazard for the personnel, especially during the installation and setting up phase. The main active safety element is a design complying with the "pressure vessels safety regulation (CODAP)", and severe acceptance tests of the vessels. Beyond that, critical elements (like

feedthroughs) feature a double safety against leaks, with continuous monitoring of the intermediate vacuum. Finally, sensitive oxygen meters will be installed in close proximity to critical elements, in such a way as to allow quick evacuation in case of problems.

- Activation of some detector elements. From the irradiation levels in the calorimeter, the equilibrium concentration of ^{41}Ar in the cryostats (due to thermal neutron activation) has been calculated (see Chapter 11). At the nominal high luminosity it should be about 160 GBq. Venting some argon to the atmosphere in case of safety valve opening is well within the accepted levels of emission [1-22].

In case of access to the electronics during a planned access period, there is a potential risk that people may come too close to activated areas. The main critical points in that respect is the centre of the front and back faces of the end-cap cryostats. Estimates [1-3] have shown that a 5 cm lead plate put in place before access should bring the irradiation level at contact below 0.02 mSv/h.

Detailed work on safety aspects is ongoing, in close collaboration with the ATLAS Technical Coordination and the CERN TIS Division.

1.11.3 Cost and resources

The detail cost breakdown of the Liquid Argon calorimeter will be given in the CORE 6 document. In the brief summary given below (see Table 1-6) the numbers include the cost for manpower when institutes have to hire temporary personnel for the construction.

Discussions with the laboratories involved in Liquid Argon calorimetry (a list is given in Appendix D), in connection with the sharing of work and responsibilities described briefly in the PBS, indicate that the planned resources should be able to cover the expenses. The numbers under consideration appear in the Intermediate Memorandum of Understanding [1-23].

1.11.4 Project management

The management of the Liquid Argon Calorimeter project is organized according to the general ATLAS policy.

The management is organized by a Steering Group chaired by the Project Leader. The Project Leader is proposed by the community and formally elected by the ATLAS Collaboration Board for a period of two years. He is assisted by a Technical Coordinator and a Finance Coordinator. At the present time those positions are held by Daniel Fournier, Vincent Vuillemin, and Bernard Aubert respectively. Besides the Project Leader two other persons represent the Liquid Argon community in the ATLAS Executive Board (at the present time they are David Lissauer and Horst Oberlack).

The members of the Steering Group organize the areas of activity. At the present time the activity is split between the following groups (in parentheses the name of the person(s) holding the position):

- Simulation of EM performance: (Fabiola Gianotti and Michal Seman)
- Simulation of jet performance: (Laura Perini)
- Cryostats and cryogenics: (Pierre Pailler)
- EM barrel mechanics: (Bruno Mansoulie)

- EM end-cap mechanics: (Sylvain Tisserant)

- Readout electrodes for the EM calorimeters: (Bernard Aubert and Giuseppe Costa)

- Presamplers: (Johann Collot)

- Hadronic end-cap: (Horst Oberlack and Christopher Oram)

- Forward calorimeter : (John Rutherfoord)

- Electronics: (Jacques Colas, Christophe de La Taille and Veljko Radeka)

- Test beam: (Patrick Fassnacht)

- Irradiations studies: (Claude Leroy)

Some other activities (monitoring, slow control), are so far under the responsibility of the Technical Coordinator.

Each important decision is to be endorsed by the assembly of the representatives of all institutes participating in the building of the Liquid Argon calorimeter. When appropriate, the ATLAS Collaboration Board is also asked to formally endorse the decisions.

Table 1-6 Cost of the Liquid Argon system

Element	Cost (MCHF)
Barrel cryostat and feedthroughs	12.3
End-cap cryostats and feedthroughs	10.1
Proximity cryogenics	10.8
External cryogenics	3.3
EM barrel detector	18.4
EM end-cap detector	10.8
Hadronic end-cap detector	11.8
Forward calorimeter detector	3.3
Presampler detector	2.0
Monitoring (purity, temperature)	0.8
Off detector electronics (incl. test beam)	29.1
Test beam (mechanics, cryogenics)	2.0
General Infrastructure, radiation test,...	2.0
Total cost	116.7

1.12 References

1-1   ATLAS calorimeter Performance Volume, CERN/LHCC 96-40, ATLAS TDR1, 12/1996.

1-2   ATLAS Tile calorimeter Technical Design Report, CERN/LHCC 96-42, ATLAS TDR2, 12/1996.

1-3   ATLAS Technical Proposal CCERN/LHCC/94-43 LHCC/P2 (1994).

1-4   G. Parrour et al., ATLAS Internal Note CAL-077, 1995.

1-5   B. Aubert et al., Nucl. Instrum. Methods A309 (1991), 438.

1-6   C. de La Taille, ATLAS Internal Note CAL-035, 1995.

1-7   J. Rutherfoord, GEM Note TN-91-27, 1991.

1-8   ATLAS Internal Note, CERN/LHCC 93-21. 1993.

1-9   J.K. Mayer et al., ATLAS Internal Note LARG-057, 1996.

1-10   T. Sjostrand, preprints CERN-TH 7111 and 7112 (1993).

1-11   The Large Hadron Collider, the LHC study Group, CERN/AC/95-05(LHC), 1995.

1-12   L. Serin and V. Tisserand, ATLAS Internal Note CAL-073, 1995 , V. Tisserand, PhD thesis, Université Paris XI, 1997.

1-13   J.C. Chollet, ATLAS Internal Note CAL-075, 1995.

1-14   R.A. Davis, D. O'Neil and P. Savard, ATLAS Internal Note CAL-089, 1996.

1-15   D. Cavalli, $A \rightarrow \tau\tau$ studies, transparencies shown at ATLAS Liquid Argon Optimization group meetings, 03/1996.

1-16   J. Ardelean at al., ATLAS Internal Note LARG-050, 1996 and J. Parson at al., Proceedings of the 1st Workshop on Electronics for the LHC, Lisbon (1995), 265-269.

1-17   NA48, Internal note 1996/8.

1-18   L. Serin, "Drift time measurement with pulse shape", transparencies shown at ATLAS Liquid Argon test beam group meeting, 06/1996.

1-19   The RD3 Collaboration, CERN/DRDR/91-21. DRDC/P5-Addendum 1, 1991.

1-20   G. Bachy et al., ATL-CER-QA-001, 003, 301.

1-21   B. Mansoulié et al., ATLAS Internal note LARG-040, 1996.

1-22   Radiological Implications of the release of air from the LHC Experimental Regions, CERN/TIS-RP/96-06.

1-23   ATLAS Interim Memorandum of Understanding (Annex 4.2), ATLAS RRB-D 96-9, 1996.

ATLAS Calorimetry (Geant)
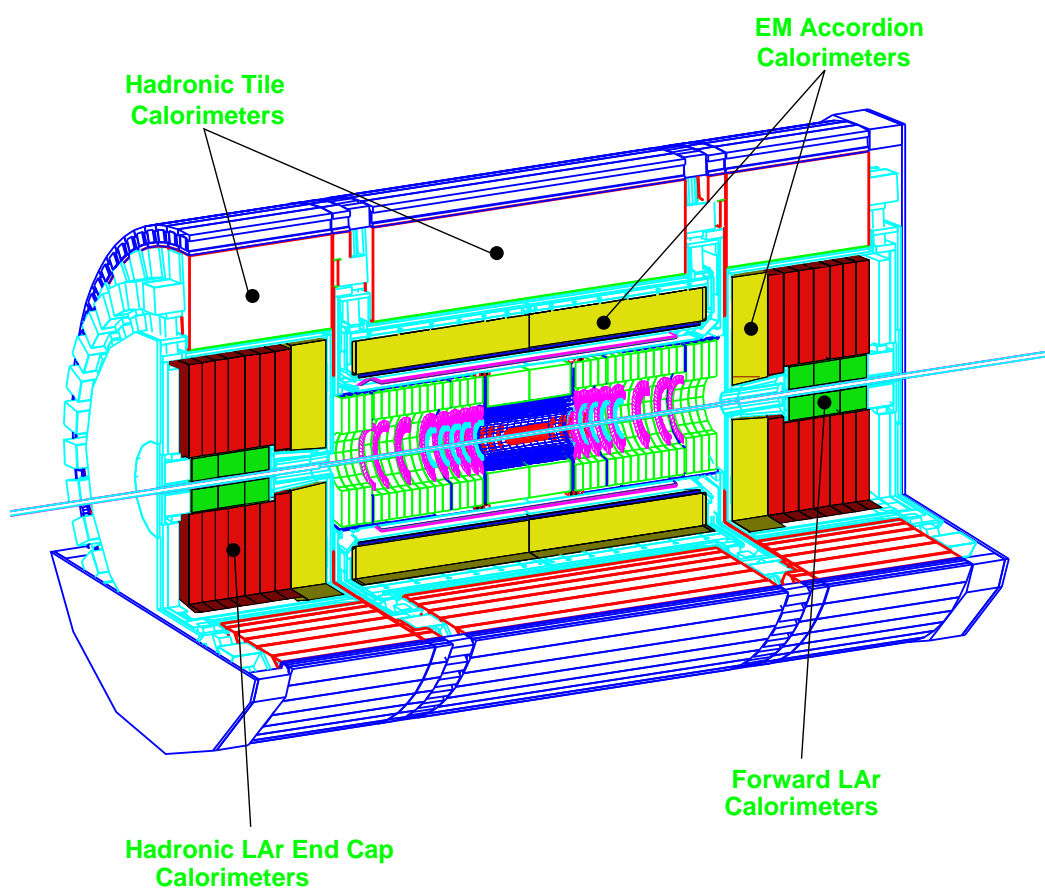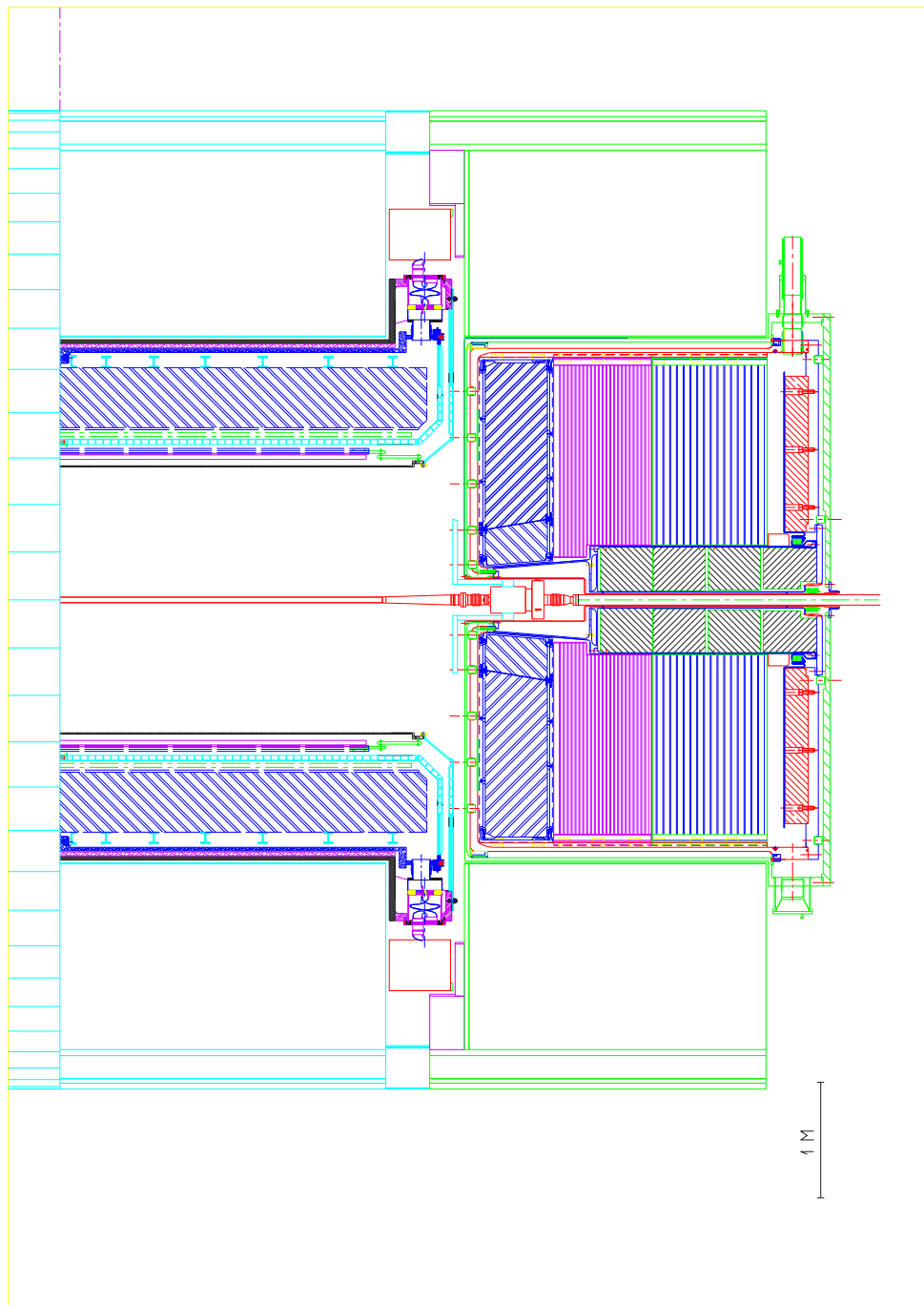
Figure 1-i 3D-view of the ATLAS calorimetry obtained with GEANT.

Figure 1-ii Longitudinal view of the ATLAS calorimeter (+z view). Engineering drawing.

2 Test beam results

This chapter presents results obtained with prototypes during the last few years. Prototype results of the electromagnetic barrel and end-cap, of the hadronic end-cap and of the forward calorimeters (brass section) are presented, as well as results from the presampler. Some data are also shown concerning signal variation with temperature and drift time measurements. The last section is devoted to results obtained with analog and digital pipelines.

2.1 The 2 m prototype of the barrel EM calorimeter

A 2 m long prototype of the EM barrel calorimeter has been constructed and extensively studied in test beam. The satisfactory response of this prototype, which was conceived as a sector of the ATLAS calorimeter, and of the EM end-cap prototype, have proved that the Accordion concept can be applied on a large scale and adapted to a fully projective geometry. The barrel prototype was operated from 1992 to 1996 and was subject to eight cool down and warm up cycles.

2.1.1 2 m prototype description

A view of the 2 m barrel prototype [2-1] is presented in Figure 2-i. The prototype is a stack of three azimuthal modules, each one covering $9°$ in ϕ and extending over the pseudorapidity range $0 < \eta < 1.1$ as seen from the ATLAS interaction point. It is fully pointing towards the nominal LHC interaction centre. The stack consists of 73 accordion-shaped converter plates interleaved with 72 accordion-shaped read-out electrodes. The 2 m long absorbers are made of Pb plates (1.8 mm thick for $\eta < 0.7$ and 1.2 mm thick for $\eta > 0.7$), which are sandwiched in between two 0.2 mm stainless steel sheets. The electrodes are multilayer copper-kapton boards 0.3 mm thick, separated from the converter plates by a 1.9 mm LAr gap. The thickness of the gap (and therefore the sampling fraction) is kept constant with depth by gradually changing the angle of the accordion folds along the depth of the calorimeter from $111°$ to $87°$ (see Figure 2-i). Honeycomb strips are used to center the kapton read-out board in between two consecutive absorbers. The mechanical uniformity of the stack has been measured: the dispersion in the double-gap thickness is 55 μm (r.m.s.).

In depth, the prototype is segmented into three compartments of 9 X_0, 9 X_0 and 7 X_0, respectively (at $\eta = 0$). Three consecutive kapton boards are grouped together in the same channel at the read-out level, giving an effective granularity of $\Delta\phi \approx 0.020$. The transverse segmentation of $\Delta\eta \approx 0.018$ ($\Delta\eta \approx 0.036$ in the third compartment) was obtained by etching projective strips out of the conductive layers of the electrodes. Cells are numbered in ϕ from top to bottom ($\phi=1$ to 24) and in η from the center to the edge ($\eta = 1$ to 60).

For the beam tests, the prototype was equipped with three different types of preamplifiers: charge preamplifiers working at the LAr temperature and based on Silicon JFETs [2-2] or GaAs MESFETs [2-3], and 'warm' current preamplifiers (the so-called '0T' scheme, [2-4]) located outside the cryostat. The last solution has been retained for the ATLAS calorimeter. In the first two cases, to allow for a fast charge transfer the preamplifiers were placed directly on printed circuit motherboards, which were mounted on the front and back faces of the calorimeter. After the preamplifiers there are the shaping amplifiers ($t_p(\Delta) \approx 35$ ns), Track&Hold circuits, and 12-bit ADCs, all located outside the cryostat.

Two calibration systems were used [2-1]. In the 'voltage driven' system, which has been chosen for the ATLAS calorimeter, the voltage pulse simulating the detector signal is brought from out-

side the cryostat, so that the only element in the liquid is a 2 kΩ injection resistor. In the 'current-driven' system, a DC current is sent inside the cryostat and the calibration pulse was generated in the cold near the preamplifier input.

The electronic noise measured in the calorimeter ranges from 40 MeV to 70 MeV per channel, depending on the compartment and rapidity region. The coherent noise is 2 to 3 MeV per channel.

The detector was operated with a high voltage of 2 kV, producing an electric field of about 10 kV/cm over the gap.

2.1.2 Test beam results

Several tests of the 2 m prototype were carried out in the H8 beam line of the CERN SPS using electrons in the energy range 10 to 300 GeV. Muon data were also collected to study the detector response to minimum ionizing particles. A signal-to-noise ratio of four was measured.
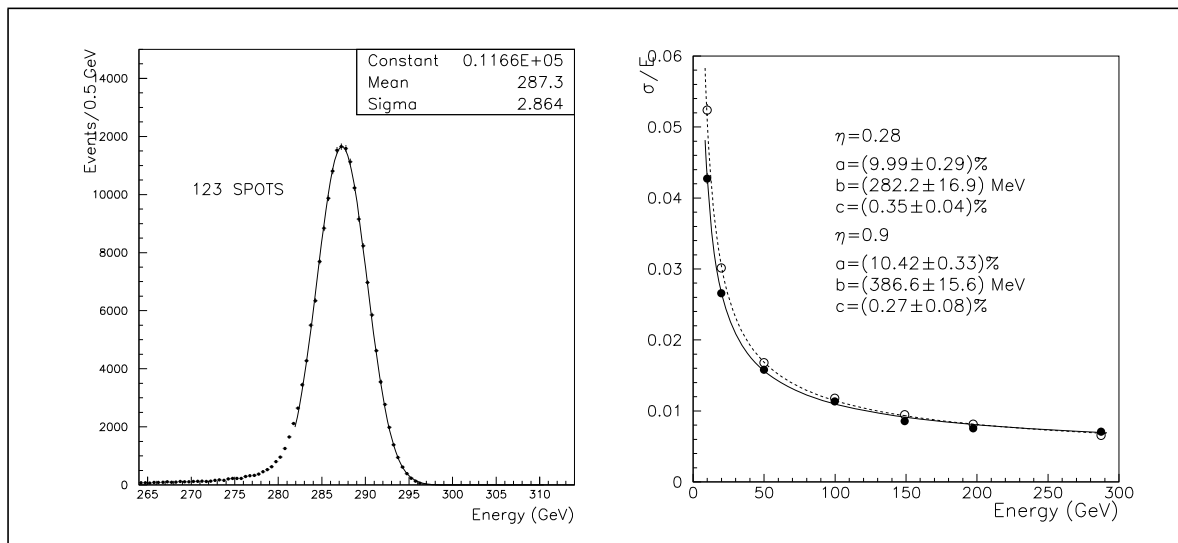
2.1.2.1 Resolution and uniformity

The electron shower energy is reconstructed in the prototype by using a region of 3 x 3 cells in $\eta \times \phi$. This energy is then corrected for known geometrical effects: the lateral leakage outside the cluster, and the modulation of the detector response as a function of ϕ, which is due to the variation of the calorimeter density in the direction perpendicular to the converter plates.

The energy resolution was parametrized as:

$$\frac{\Delta E}{E} = \frac{a\%}{\sqrt{E}} \oplus \frac{b}{E} \oplus c\%$$

where E is in GeV, *a* is the sampling term, *b* the noise term, and *c* the constant term. A typical energy distribution obtained for 300 GeV electrons and the results obtained for the parametrization at two different positions in rapidity in the region equipped with Silicon JFETs preamplifiers are shown in Figure 2-1 .

Figure 2-1 Left: line shape for 300 GeV electrons after summing over a large area (123 cells); Right: Fractional energy resolution as a function of the beam energy for electrons incident at η = 0.28 (closed circles) and η = 0.9 (open circles).
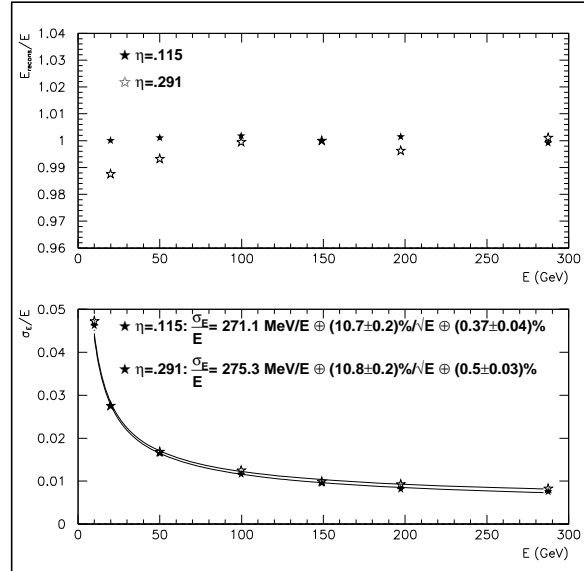
The measurements obtained at $\eta = 0.9$ show that the sampling term can be maintained at a constant value over most of the barrel coverage by using different lead thicknesses in the absorber plates. The (local) constant term is due to the residual ϕ-modulation of the response after correction. Thanks to an optimization of the calorimeter geometry, this constant term is expected to be reduced to 0.2% in the ATLAS calorimeter [2-5].

Extensive energy resolution studies were also made in the first two modules, both equipped with warm ('0T') preamplifiers. The energy resolution was obtained for two different values in rapidity: $\eta = 0.115$ and $\eta = 0.291$ using electrons from 10 to 300 GeV. Figure 2-2 (bottom) shows the experimental points as well as the fit using the quadratic sum of the three sampling, noise and constant terms. A constant term of 0.5% and a sampling term of 10.7% were achieved. These values are similar to the one obtained in the Si region (see Figure 2-1). The electronic noise contribution is typically 270 Mev for both points.
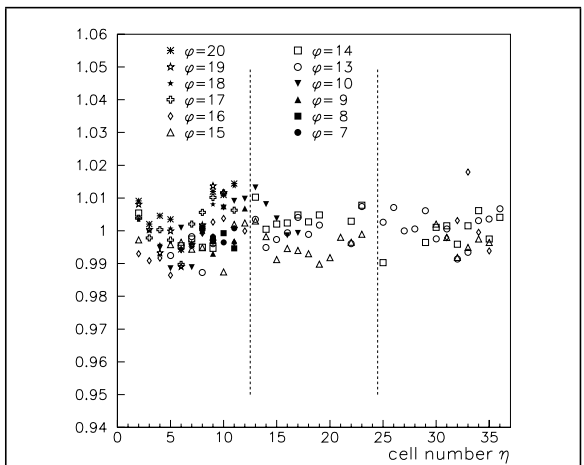
The energy response of the prototype is found to be linear within better than 1% over the full energy range and rapidity coverage, in particular in the 0T region as it is shown in Figure 2-2 (top) for the two values $\eta = 0.115$ and $\eta = 0.291$ over the range 20 to 300 GeV.

Figure 2-2 Linearity of the energy response (top) and energy resolution (bottom) for two points in η in the 0T region.

The position resolution of the calorimeter was determined by comparing the barycentre of the electron shower reconstructed in the prototype with the beam impact point given by a set of proportional wire chambers located along the beam line. The position resolution is found to be better than $5\ \mathrm{mm}/\sqrt{E}$ (GeV) in both the η and ϕ directions.

The response uniformity was studied by scanning more than 150 cells of the prototype with high-energy electron beams and is shown in Figure 2-3. The resulting r.m.s. is 0.62%. This dispersion gives rise to an overall constant term of $(0.69 \pm 0.05)\%$. Most of the constant term can be attributed to known sources of non-uniformity, arising from mechanical effects [residual ϕ-modulation (0.3%), gap non-uniformity (0.15%) and absorber non-uniformity (0.3%)] and from calibration effects [calibration accuracy (0.25%), timing precision (0.2%) and cross-talk (0.15%)]. A discussion of the strategy to achieve a constant term of less than 0.7% over the full ATLAS EM calorimeter can be found in [2-5].

Figure 2-3 Average response, normalized to the incident beam energy, obtained in the 2 m prototype for 287 GeV electrons, as a function of the hit cell position.

2.1.2.2 Performance obtained using bi-gain shapers
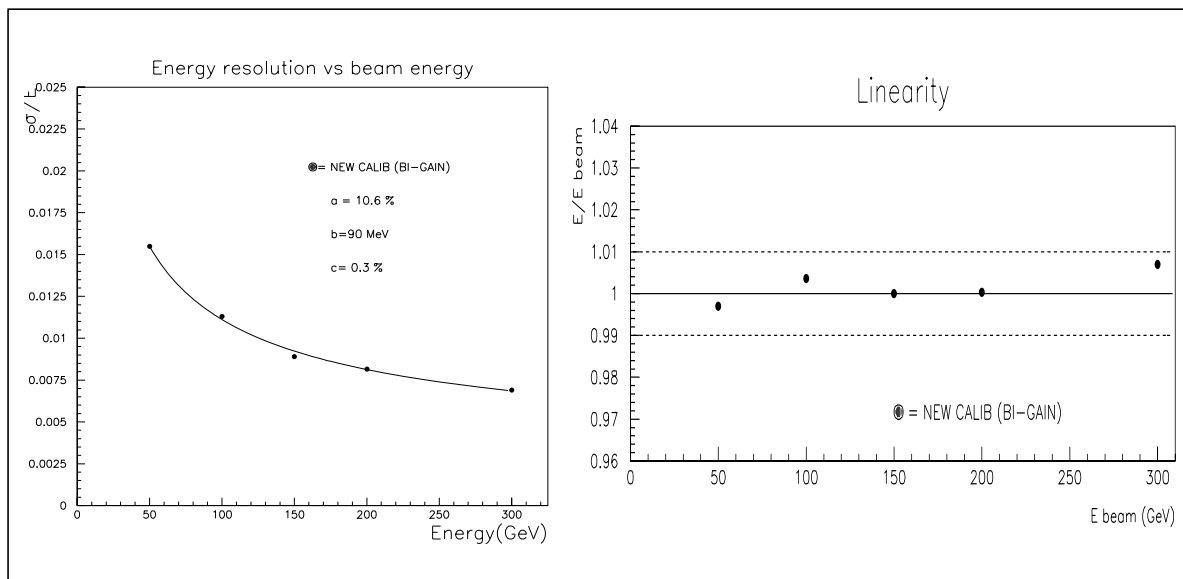
Data with double gain shapers were taken with the June 1995 test beam.

The analysis was performed in the region equipped with GaAs preamplifiers ($\eta = 29$, $\phi = 6$). The reconstructed cluster (3 x 3) is composed of a mixture of low and high gain cells: low gains are used if the high gains saturate. The cluster is then reconstructed as usual.

Moreover, a new calibration data analysis procedure was used to match the low and high gain channels. In this way it is possible to obtain smaller residuals from the fit and a better match between low and high gains.

The energy points studied are at 50, 100, 150, 200 and 300 GeV. The gain composition of the cluster, as expected, is energy dependent: at low energy (50 GeV) only high-gain ADC values are used, while as the beam energy increases (e.g. 150 GeV) the low-gain ADC value is used most of the time (86% of events) for the central cell of the cluster in the first sampling. At high energy (e.g. 300 GeV) low-gain ADC values are used not only for the centre cell of the first sampling (100% of events) but also for the two adjacent cells in the ϕ direction and for the centre cell of the second sampling (87% of events).

The standard corrections have been applied to the reconstructed energy to obtain the energy resolution and to test the linearity of response (see Figure 2-4). The dependence of the resolu-

Figure 2-4 Left: energy resolution as a function of beam momentum. Right: linearity of the energy response between 50 and 300 GeV.
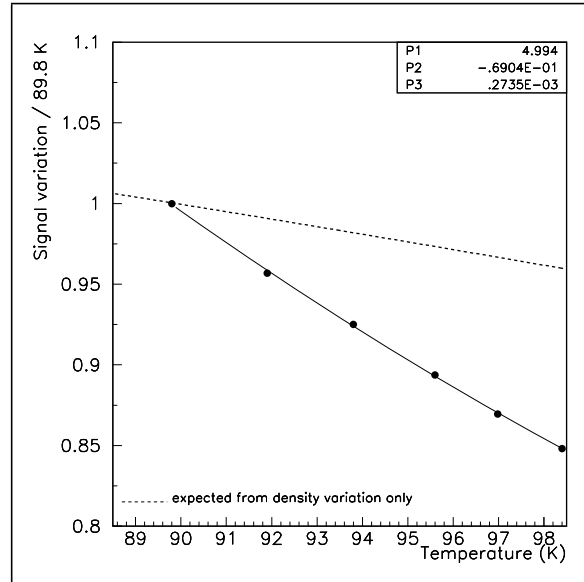
tion on the beam energy has been parametrized, as usual, as the quadratic sum of a sampling term (*a*), a noise term (*b*) and a constant term (*c*). The results obtained using the new calibration analysis and the free selection of either the low or the high gain channel is the following: $a = 10.6\%$, $b = 90$ MeV, $c = 0.3\%$. The noise term has been taken from the random trigger. The remarkable improvement of the energy resolution is given from the noise term which is low due to the use of the high gains in the cluster reconstruction and to a slower shaping time used for the GaAs preamplifiers. It is also important to notice that this result has been obtained using the same calibration constants (low and high) for runs quite far apart in time. The sampling and

constant terms are compatible with the values obtained in the past for the same η region of the prototype (see Figure 2-1).

Finally the linearity of response has been measured. Using the new calibration procedure, the response is linear to within 1% over the energy range investigated.

2.1.2.3 Effect of temperature variations

The temperature dependence of the signal of the EM calorimeter was investigated with a special data sample taken during a temperature scan over a 10 degree range, obtained by varying the gas pressure setting of the regulation system [2-6]. The temperature was measured indirectly from a pressure measurement in the gas above the liquid. In Figure 2-5 the variation of the reconstructed energy for 200 GeV electrons as a function of the temperature is shown. The slope of ~ 2% per degree comes from both a variation in density (about ~ 0.45% per ° K) and a sensitivity to the drift velocity resulting from the fast shaping (~1.55% per ° K). The temperature variation will be monitored with probes in the ATLAS calorimeter in order to control this potential source of non-uniformity (see Chapter 12). Additional measurements using the waveform of the LAr signal could also provide cross checks (see next section).

Figure 2-5   Signal variation in the 2m prototype as a function of the LAr temperature and comparison to the expected variation from the density alone.

2.1.2.4 Drift time measurements

An accurate measurement of the electron drift time, $t_{dr} = g/V_d$, where V_d is the drift velocity of the electrons in the argon and g the gap, would bring information on drift velocity non-uniformity (mainly coming from temperature variation in space and time) and about gap non-uniformity. This would give an additional tool to control or reduce the corresponding two contributions to the global constant term. The required relative accuracy on t_{dr} is 0.075% for the temperature and 1.3% for the gap control [2-6]. Monte Carlo simulations have demonstrated that such a statistical accuracy could be achieved with a few hundred high energy ($\geq$ 40 GeV) pulses per cell. However the main limitation is the systematic error which comes from the deformation and non-uniformity of the waveform.

For a drift time measurement the pulse shape has to be recorded for at least 500 ns. Data were taken using a dedicated set-up with a 2.5 ns sampling interval and with the Nevis SCA analog memory in asynchronous mode (see Section 2.6), while varying the high voltage to simulate a drift time variation. The waveform of the ATLAS EM calorimeter is similar to that of the hadronic end-cap shown in Figure 2-13, except at the end of the signal. The non-uniformity of the E field with the accordion geometry leads to longer signals due to the ionization in the folds and cannot be reproduced analytically. The drift time can still be extracted from a fit of the signal using the undershoot of the bipolar signal. The analysis of these data is currently under study. Preliminary results using the data taken with the 2.5 ns sampling interval show a good
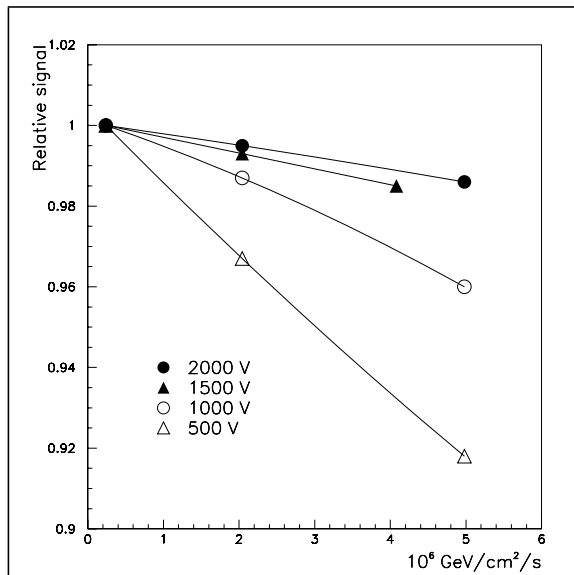
agreement with the variation expected as a function of the high voltage. An r.m.s. on t_{dr} of 4 ns has already been achieved for pulses larger than 50 GeV.

2.1.2.5 Ion Build-up

In the presence of a very high flux of incident particles, the ions which drift slowly in the gap could lead to ion loading in liquid ionization calorimeters. Such an effect induces a distortion of the electric field and thus a loss of signal. The energy density above which the signal is seriously deteriorated is characterized by the critical ionization rate, D_c, defined by the rate where the value of the ion creation pair per unit volume is equal to the rate at which ions are removed from the gap [2-7]. D_c varies as V^2/g^4 where V is the voltage across the gap of width g.

To study the onset of this effect, data were taken with the highest available intensity at the SPS beam for 200 GeV electrons and using different values of high voltage. Taking into account the measured rate in the triggering scintillating counters and the size of the beam (focused in η with a beam size 1×2.6 cm^2), the energy flux has been estimated to be between 2.10^5 GeV/cm^2/s up to $5\ 10^6$ GeV/cm^2/s. Figure 2-6 shows the relative signal with respect to the low intensity for 4 different HV values. At 2000 V, a less than 0.2% signal loss is measured for a flux of 10^6 GeV/cm^2/s.

At high luminosity the energy flux in the ATLAS EM calorimeter is estimated to be about 5.10^5 GeV/cm^2/s at $\eta = 2.5$, reaching a factor 5 more at the acceptance limit 3.2.

Figure 2-6 Relative energy response for 200 GeV electrons as a function of the incident energy flux for various high voltages.

2.1.2.6 Performances of the strip section.

Following the decision taken by ATLAS to build an 'integrated' preshower detector, which consists of fine strips in the first compartment of the calorimeter, two sectors of the 2 m barrel prototype, (each one corresponding to 8 x 12 calorimeter cells in η x ϕ) were equipped with so called 'UV strips' and tested with beam in July 1994.

Narrow strips (4 mm wide) are etched onto the kapton electrodes in the first compartment of the calorimeter [2-8]. Read-out channels are then formed by grouping strips along lines of constant U = η - ϕ and V = η + ϕ. The U and V electrodes are interleaved in the stack. The granularity in the first compartment is 1/4 of a calorimeter cell in the fine (U/V) view and four calorimeter cells in ϕ. The thickness of the three compartments is 5.5 X_0, 14.6 X_0 and 9.1 X_0, respectively at $\eta = 0.9$. The typical electronic noise in the strips is 15 MeV per channel and the crosstalk between neighbouring strips less than 2%.

The strip section provided a very precise measurement of the shower position. This is obtained by using a three-strip cluster, centred on the channel with the highest energy, in both the U and the V direction. The position resolution achieved in this way is $2 \text{ mm}/\sqrt{E(GeV)}$ [2-9]. The position in the second compartment of the calorimeter is reconstructed with a resolution of $6 \text{ mm}/\sqrt{E(GeV)}$. By combining both compartments, the angular resolution shown in Figure 2-7 is obtained.

Similar measurements were also carried out using a liquid krypton prototype [2-10]. The strips had a segmentation of $\Delta\eta = 0.004$ (4.7 mm) and $\Delta\phi = 0.156$. With a depth of 3 X_0 in the first sampling, a position resolution of 300 to 400 μm at 200 GeV was obtained, corresponding to an angular resolution of $40 \text{ mrad}/\sqrt{E(GeV)}$ at $\eta = 0$.

Figure 2-7 Angular resolution in the η and ϕ directions obtained by using the UV strip section and the second compartment of the 2 m prototype.

The tests of the UV strips in the 2 m prototype as well as the η strips in the LKr prototype have demonstrated that narrow strips in the calorimeter are feasible and that the technology is under control. Recently the ATLAS collaboration opted for an η strip section in the EM calorimeters.

2.1.3 Presampler

2.1.3.1 Geometry of the prototypes

The 1995 and 1996 prototypes were composed of two modules, each approximately 19 cm wide in azimuth and about 24 cm long, in order to match the cell size of the 2 m electromagnetic calorimeter prototype just discussed in the previous sections. In 1995 the modules were mounted contiguous in pseudo-rapidity covering 9° in azimuth and a pseudo-rapidity range from 0.48 to 0.80 (see Figure 2-i). During the 1996 beam tests new modules of the same size were used, but this time mounted to cover 18 degrees in azimuth and from 0.46 to 0.62 in η. The depth of the active layer was 10 mm instead of 11 mm as planned for ATLAS. In 1995 each of the 128 elementary cells in the fine-grained direction (η) and two in the coarse one (ϕ) were read out individually by means of preamplifiers mounted on the modules and therefore in the liquid argon. The granularity was $\Delta\eta$ x $\Delta\phi$ = 0.0025 x 0.08 for a total of 256 independent channels. The 1996 modules had eight elementary cells in the pseudo-rapidity direction grouped together into one read-out cell, resulting in a coarse granularity with eight cells in the η direction and four cells in ϕ. In this case the preamplifiers were placed outside the cryostat. Both for the granularity and the preamplifiers location, the layout is the one of the final ATLAS design.

The amount of dead material in front of the prototypes was equal to 0.83 X_0 at $\eta = 0.6$. Some dead material was added during a few runs in 1996 to simulate the real material conditions expected at larger rapidities in ATLAS.
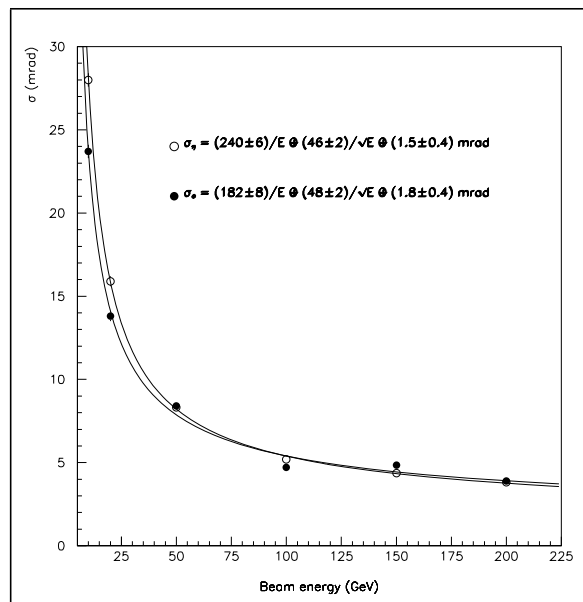
2.1.3.2 Module production technique

The 1995 modules were produced by moulding a layer of epoxy loaded with micro glass fiber on the top of the electrodes. The electrodes were spaced and stacked by means of precision shims in a hermetic mould.

In parallel, a new production technique (see Chapter 6) was developed where the electrodes are glued on both sides to FR4 plates using prepreg (i.e. pre-impregnated foils). This latter technique has been chosen for ATLAS and was used to produce the 1996 prototypes.

Both techniques allow a compact module construction featuring an overall radial thickness of only 21 mm including electrical connections.

2.1.3.3 Energy resolution for electrons

The energy resolution was measured as a function of the energy of the electron beam during the 1995 beam tests. The electron signal was collected over seven presampler cells in η centred on the most energetic channel. The total energy was calculated from the following relation: $E_{tot} = \lambda(\alpha E_{ps} + \beta E_1 + E_2 + \delta E_3)$, where E_{ps}, E_1, E_2, and E_3 refer to the signals collected in the presampler and the three calorimeter radial compartments, α, β and δ are weights introduced to minimize the width of the energy distribution, and λ is an overall calibration coefficient. Standard position-dependent energy corrections were applied to the calorimeter in order to correct for the shower containment in η and the modulation of the transverse LAr thickness in ϕ.

Figure 2-8 Energy resolution as a function of the incident electron energy measured at $\eta = 0.59$.

The energy resolution of the presampler-calorimeter system at $\eta = 0.59$ is plotted in Figure 2-8 and parametrized as:

$$\frac{\Delta E}{E} = \frac{(11.2 \pm 0.2)\%}{\sqrt{E(\text{GeV})}} \oplus \frac{0.283}{E(\text{GeV})} \oplus (0.26 \pm 0.04)\%.$$

This result gives a sampling term of 10.3%/$\sqrt{E}$ at $\eta = 0.0$, when taking into account the $\sqrt{\text{ch}(\eta)}$ scaling law. This last value is in good agreement with what was expected.

2.1.3.4 Signal response and uniformity of the coarse granularity presampler
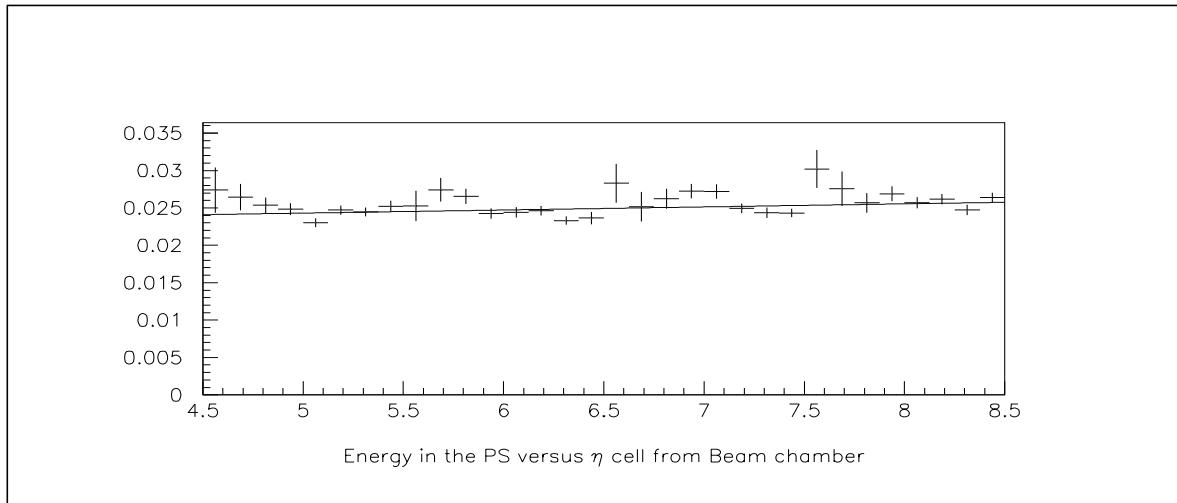
The response of a single presampler read-out cell to electrons at 200 GeV/c is shown in Figure 2-9 without and with additional lead in front. The electrons were selected by demanding a compatible signal in the calorimeter. The measured noise level is ≈ 2.9 MeV/cell (~1.4 Mips) as expected from calculations [2-11].

By using the position measurements from the beam chambers upstream of the presampler, the average response to electrons for elementary cells in the coarse granularity prototypes was obtained. All cells have a similar response within the statistical errors as seen in Figure 2-10. The

Figure 2-9 Signal for electrons compared to noise with 0.79 and 1.8 X_0 of material in front of the coarse granularity prototype.

slight increase at larger η is due to an increase in the amount of material in front of the presampler.

Figure 2-10 Response uniformity as a function of the beam impact read-out cell. Each point refers to an elementary cell. The fitted line indicates the slight increase of signal with η.

2.2 The EM end-cap prototype

The performances of the EM end-cap, measured in the H8 test beam, are very close to the one obtained for the barrel prototype. These tests have confirmed that the accordion geometry is well adapted to the ATLAS electromagnetic end-cap calorimeter.

2.2.1 Detector description

The prototype [2-12] forms a sector (1/6) of a flat disk perpendicular to the beam axis and covers the pseudorapidity range from 2.17 to 2.88, which corresponds more or less in size to the small internal wheel of the ATLAS EM end-cap. The prototype is fully pointing towards a ver-

tex point located 2.8 m from the front face. All the plates, converters and electrodes are accordion-shaped and are arranged radially like wheel spokes with the direction of the waves parallel to the beam axis.

Each absorber plate consists of a sandwich of five elements: stainless steel (0.2 mm), prepreg adhesive, lead (the converters are plates with a linearly increasing thickness from 1.3 to 2.3 mm in the radial direction), prepreg adhesive and stainless-steel (0.2 mm). The lead thickness variation is obtained with conventional machining with a precision of 0.02 mm (r.m.s.). The plates were sorted in such a way that the overall r.m.s dispersion of the lead weight from cell to cell was about 0.25%. This contributes to a signal dispersion of approximately 0.2% [2-1],[2-13].

The read-out electrodes are multilayer boards of 0.3 mm thickness, consisting of two (one double-sided and one single sided) copper-clad kapton sheets glued together. The copper layers are etched into 24 projective strips of constant $\Delta\eta = 0.03$, separated by a 1 mm gap for insulation. The electrodes are separated from the converters by a LAr gap increasing from 1.65 to 2.65 mm with increasing radius. Honeycomb strips were used to centre the kapton read-out electrodes. However, in order to cope with the variable gap between kapton and converter plates, these honeycomb strips were machined to have a variable thickness.

In the azimuthal direction, three strips from consecutive electrodes boards are ganged together and thus define cells of $\Delta\phi = 0.05$. Each strip has a longitudinal segmentation in three depth regions of $9X_0$, $9X_0$ and $6X_0$. The read-out cells are defined by $\Delta\eta \times \Delta\phi = 0.03 \times 0.05$ for the two first sampling depth regions. For the third depth region, the η strips are larger by a factor of two.

The pointing structure in ϕ is achieved by 'opening up' the absorber and read-out plates with radius. The lead sheet thickness and the gap between the electrodes and the converters increase with radius as quoted above while the wave angle increases from 57° to 110°. With this geometry, as shown with a detailed Monte Carlo simulation [2-14], the sampling fraction can be kept nearly constant in both the η and the ϕ directions.

The response can be maintained uniform by radially increasing the high voltage on the electrode boards in order to keep the drift time independent of the gap. Thus, in our standard operating conditions, twelve different HV values for the first sampling zone and twelve others for the second and third zones were defined. They ranged typically from 1000 V at low radius to 2500 V at the largest radius and were fixed according to Monte Carlo studies.

This continuous variation of the detector geometry in the radial direction is the main difference with respect to the barrel accordion prototype [2-1], see Figure 2-ii, which shows the detector during the assembly operation and just before the insertion into the RD3 cryostat. It is also different from the geometry selected for ATLAS (see Chapter 7), essentially concerning the lead thickness which becomes constant.

The mechanical uniformity was estimated by measuring the capacitance, $C_{gap,}$ of several double gaps consisting of one electrode and the two absorber plates on opposite sides. We measured an r.m.s dispersion of the capacitance values of 2.6% which corresponds to 1.3% r.m.s. on the signal of the read-out electrodes. After grouping read-out electrodes to form cells and grouping cells to form an electromagnetic cluster, this gap non-uniformity translates into a dispersion of 0.4% in the response to an electron shower.

The front-end electronics consists of a warm current preamplifier placed outside the cryostat and connected to the electrode cell through a 50 Ω cable ('0T' option). The preamplifier output is shaped with a $CRRC^2$ unipolar filter. The peaking time, $t_p(\delta)$, of the shaped response to a short current pulse is 18 ns, corresponding to about 35 ns for the triangular ionization signal from the detector. The read-out chain up to the ADC's is similar to the one used for the barrel [2-1]. The

coherent noise, usually associated with improper shielding and ground loops was measured to be 6 MeV, 6 MeV, and 7 MeV per channel in the first, second and third samplings, respectively.

The incoherent noise observed in the calorimeter comes mainly from the preamplifier noise and varies with η due to the capacitance variation. This has been measured to be between 46 and 52 MeV per channel in the first sampling and between 46 and 56 MeV in the second and third samplings.

The crosstalk between adjacent cells was measured using the calibration data and found to be at the level of 1% between neighbours.
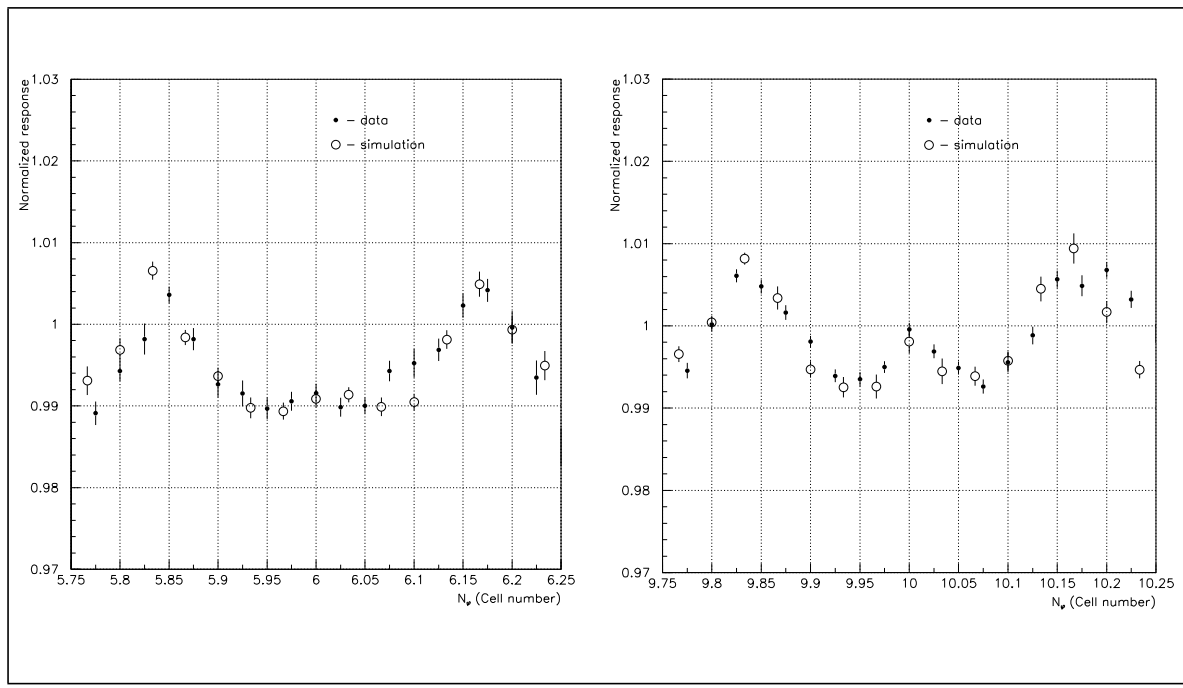
2.2.2 Simulation and test beam results

The data were taken in the H8 beam line of the CERN SPS using electrons from 20 to 300 GeV. The calorimeter was installed in the back of the RD3 cryostat in order to simulate an interaction point, in collider mode, at 2.8 m. Rohacell foam was used at the front of the detector as an argon excluder. The total amount of passive material in front of the prototype was about 0.9 X_0 at the innermost radius. The rotation in ϕ was achieved with a motor operating in the liquid argon.

2.2.2.1 Response variation across a cell

Owing to the variation of the geometry with η, a special investigation was performed to study the dependence of the corrections with η. We observed a clear signal variation over several cells in η which reflects the shower containment variation with the radius.
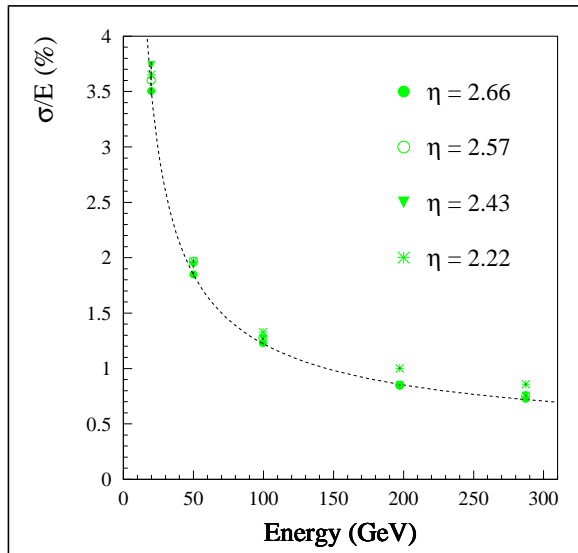
In the ϕ direction, there are modulations corresponding to the variation of the accordion shape: from the Monte Carlo simulation, it has been shown that the calorimeter response as a function of ϕ has periodic modulations due to two effects: non-uniformity of the sampling fraction near the absorber fold, and non-uniformity of the electric field near the absorber or the electrode fold. The sum of these two effects produces two sets of peaks with different amplitudes and widths at the position of the absorber and the electrode folds. The good agreement between simulated data and test beam results, in particular the set of two peaks which is very well reproduced at $\eta = 2.56$, is shown in Figure 2-11 for two different values of η.

Figure 2-11 Modulation of the signal along the ϕ direction for two different values in η (2.65 for the figure on the left and 2.56 for the one on the right), as obtained from data and from Monte Carlo simulation.

2.2.2.2 Energy resolution, linearity, and uniformity

The response is corrected for the above-mentioned variations across a cell as well as for energy losses due to early showers (material in front of the prototype). This later correction uses information from a separate presampler in front of the prototype. The energy resolution as a function of the beam energy was measured for four different η values and is shown in Figure 2-12. At a given η value, the energy resolution is parametrized using the quadratic sum of the sampling, the noise, and the local constant terms. The contribution of the beam momentum spread was subtracted. The values of the three coefficients are similar [2-12] for the four different η values. The energy resolution obtained with the detailed Monte Carlo simulation of the prototype [2-14], after correction for the ϕ modulations and the backward leakage, gives a sampling term of 10% and a local constant term of 0.25%. The measured sampling term

Figure 2-12 Energy resolution versus the beam energy for different values of η

(*a*) is of the order of 10 to 11%, in good agreement with the simulation. The noise term (*b*) was checked using random triggers and was found to be larger than the electronic noise by about 70 to 100 MeV. Using the preshower information, this excess has been attributed to the degradation of the energy resolution at small energy due to the material in front of the prototype. The constant term (*c*), typically 0.35% at large η values, mainly reflects the residual modulations in both the η and ϕ directions.

The linearity was studied using the same data and the same corrections used to determine the energy resolution. The pedestal value, extracted using randomly triggered events, is subtracted from the mean value of the fitted calorimeter response. The resulting value is then divided by the nominal beam energy and normalized at 100 GeV. The non-linearity is within $\pm$ 1.0% in the range 20 to 300 GeV at the four selected η values.

The response uniformity was studied in both the η and ϕ directions with dedicated data sets, using 200 GeV electrons. The resulting global response dispersion of these points is 0.55 ($\pm$ 0.08)%. The overall energy resolution over these 48 cells is 1.14%, taken from a Gaussian fit. After subtracting quadratically from this value the contribution of the sampling term (0.76%) and the noise term (0.26%), we obtain a global constant term of (0.79 $\pm$ 0.04)%. This number is compatible, within the errors, with the quadratic sum (0.65 $\pm$ 0.11)% of the cell-to-cell dispersion and of the local constant term. Among the various sources of instrumental non-uniformity, a large part of the constant term can be attributed to well understood mechanical effects [2-12].

2.3 Prototype of the hadronic end-cap

2.3.1 The prototype modules

One of the primary goals of the prototype tests was to define the final technology for the module construction. Various options still had to be tested for performance, reliability, cost, efficiency and optimal handling. The individual prototype modules therefore differed in some specific technological aspects, as for example:

- *the HV distribution of the electrode structure:* the HV was distributed either by a plane of high-resistive coating (HRC, high-resistive paint on a kapton layer) or by a resistor chain which connects individual pads (etched copper layer on kapton).

- *the ganging of the HV distribution lines*: either one longitudinal section was equipped with four separate lines, where the individual lines were connected to the corresponding four HV planes of a full LAr gap, or one HV line was feeding all planes of two consecutive full LAr gaps. In addition, for the HV coupling to the individual electrodes, different technologies were tested.

- *The final GaAs preamplifier and summing chip*: it was not yet available to equip all channels of all four modules. In the last test run period a complete tower (three channels) was equipped with a prototype chip of the final design. Therefore GaAs preamplifier chips which were developed in the RD33 [2-15] project were used for most of the channels. This chip was designed for application in an electromagnetic calorimeter and therefore matched to a different lateral and longitudinal segmentation: the output of eight preamplifiers is summed to one read-out channel. The longitudinal segmentation of the hadronic prototype therefore had to follow this design as well: five longitudinal sections, each with eight copper plates (thickness 25 mm), were read out separately. Also the larger pad size of the hadronic calorimeter yields a larger input capacitance and consequently an increase of the noise contribution for the RD33 preamplifier compared to the final hadronic end-cap preamplifier.

- *The shape of the interface to the forward calorimeter*: it was assumed to be conical rather than cylindrical as in the final layout.

In total four modules have been built and exposed to test beams: two modules of the 'front wheel' (HEC1) made of 3 x 8 copper plates of 25 mm thickness and two modules of the 'rear

wheel' (HEC2) made of 2 x 8 copper plates of 25 mm thickness. Because of the limitations imposed by the dimensions of the cryostat, the 'rear wheel' modules were half of the longitudinal size as designed for the ATLAS calorimeter. The corresponding total depth was about seven interaction length. The lateral segmentation was $\Delta\eta$ x $\Delta\phi$= 0.1 x 0.1 and the individual module width $\Delta\phi = 2\pi/32 \sim 0.2$ (in agreement with the final design).

The different HV distribution of the electrode structure led to different electrode thicknesses. The LAr gap was nevertheless kept uniform for all options, leading to slightly different module dimensions.

2.3.2 The test beam set-up

Beam tests were performed in the H6 beam line of the CERN SPS. A large fraction of the equipment used was originally installed by the H1 collaboration. Up to four modules forming two ϕ wedges were placed on a support structure. The horizontal frame of this support structure could be positioned at different angles, thus changing the impact angle of the beam. All data have been taken at an angle of Θ = 18.8°, corresponding to η = 1.8 in the final ATLAS detector. The support structure and the modules were placed inside a cryostat with an inner diameter of 2.50 m and a usable height of 2.20 m. Figure 2-iii shows the set up of three modules inside the cryostat.

The cryostat can be moved horizontally by ± 30 cm and a bending magnet allows the beam to be moved vertically by ± 25 cm at the entrance of the cryostat. As a result, a large area of impact positions can be scanned. The beam trigger set-up consists of three scintillator walls, a differential Cherenkov counter for particle identification, and two scintillation counters for fast timing (resolution σ = 70 ps). Six multiwire proportional chamber planes with 1 mm wire spacing allow a precise measurement of the impact position and angle.

Using either secondary or tertiary beams, the energy in the H6 beam line can be varied typically in the range 10 to 200 GeV with reasonable trigger rates for electrons, pions and muons.

2.3.3 Data

Data were taken in three run periods. In the first period only one 'front wheel' (HEC1) module was available. In the second period both 'front wheel' (HEC1) modules and one 'rear wheel' (HEC2) module were used. Only in the last third period all four modules were ready for data taking. Given the limitations due to the lateral and/or longitudinal coverage in the first two run periods, mainly electron and muon data were taken during these periods. Extensive energy scans varying the impact point over all the available area (up to 16 different pad positions) were carried out with electrons. Having the full coverage, the last run focused mainly on pion data.

2.3.4 Calibration procedure.
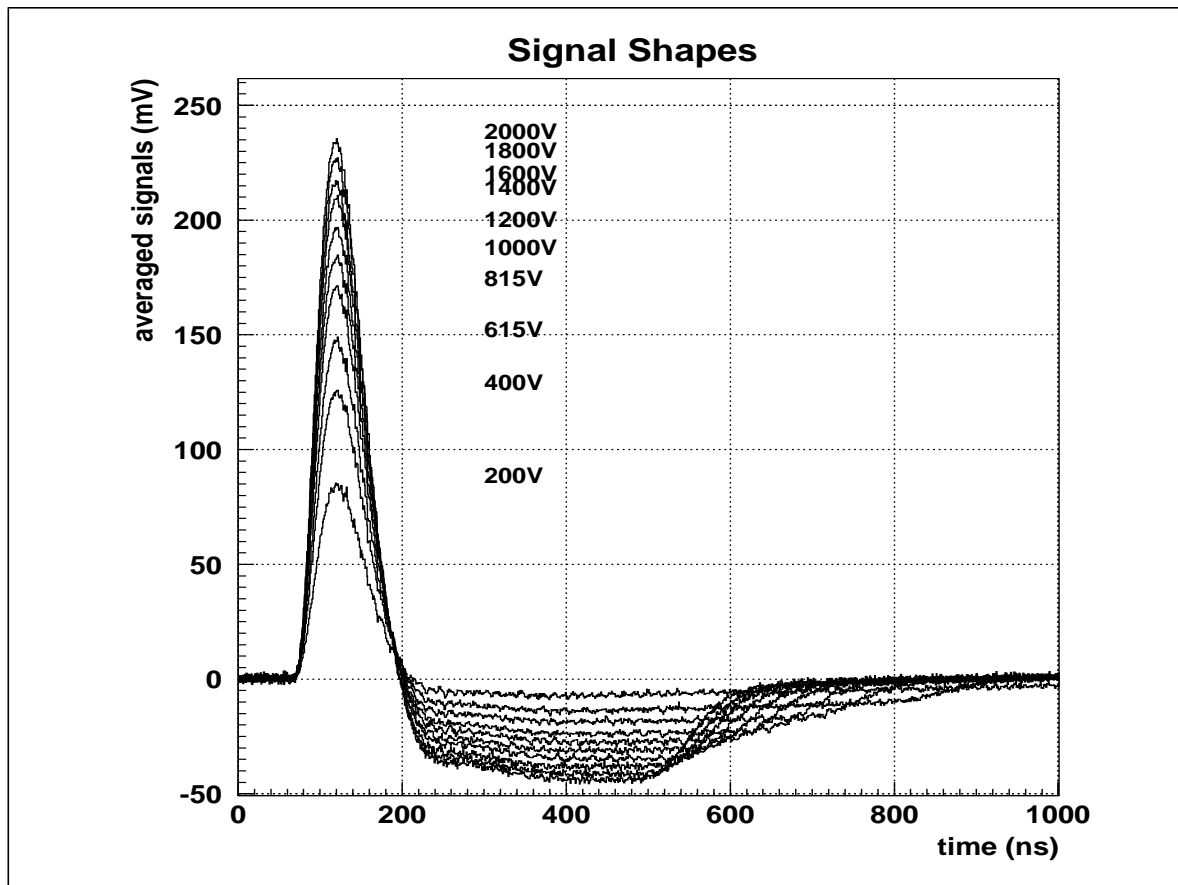
The calibration system is voltage driven, producing currents at the input of the preamplifiers or of the pads. A triangular pulse shape of 360 ns duration is simulated as closely as possible in the calibration generator via an RL-circuit feeding a 50 Ω impedance line, which runs up to the pad or preamplifier position. There the voltage pulse is transformed into a current pulse via a 10 kΩ resistor. One generator feeds up to 32 pads or preamplifiers, and in total 96 generators were in operation. The final goal is to calibrate with currents as low as 20 nA; presently the clock feedthrough is setting a limitation of ~60 nA. The maximum signal is ~300 μA per double gap.

The non-linearity of the generators and the uniformity between generators have been measured to be 0.1% and 0.3%, respectively.

2.3.5 Electronics performance

The electronic read-out system with 160 read-out channels and 1280 preamplifier channels in operation is described in detail in Ref. [2-15]. The shaping amplifiers were operated with a peaking time of 43 ns with respect to a triangular current pulse of 360 ns length[1]. The gain variation of the preamplifiers is typically at the level of ~ 3%, and the crosstalk between adjacent channels is below 1%.

The response of individual channels with respect to HV and timing has been studied in detail using electrons at high energy. Figure 2-13 shows the time evolution of the signal for various

Figure 2-13 Response of an individual channel to high-energy electrons. The evolution of the signal with time for various HV settings is shown.

HV settings for a particular channel. The signal peaking time and the variation of the drift velocity with HV can be directly extracted from these distributions. Specific delay curves taken for up to 16 individual channels with electrons confirm the peaking time obtained.

---

1. Which corresponds to $t_p(\delta) = 20$ ns.

The noise per read-out channel is typically 250 to 300 nA, which is a factor of two larger than that measured in RD33 [2-15]. This can be explained partially by the different range in capacitance of the pads with respect to RD33.
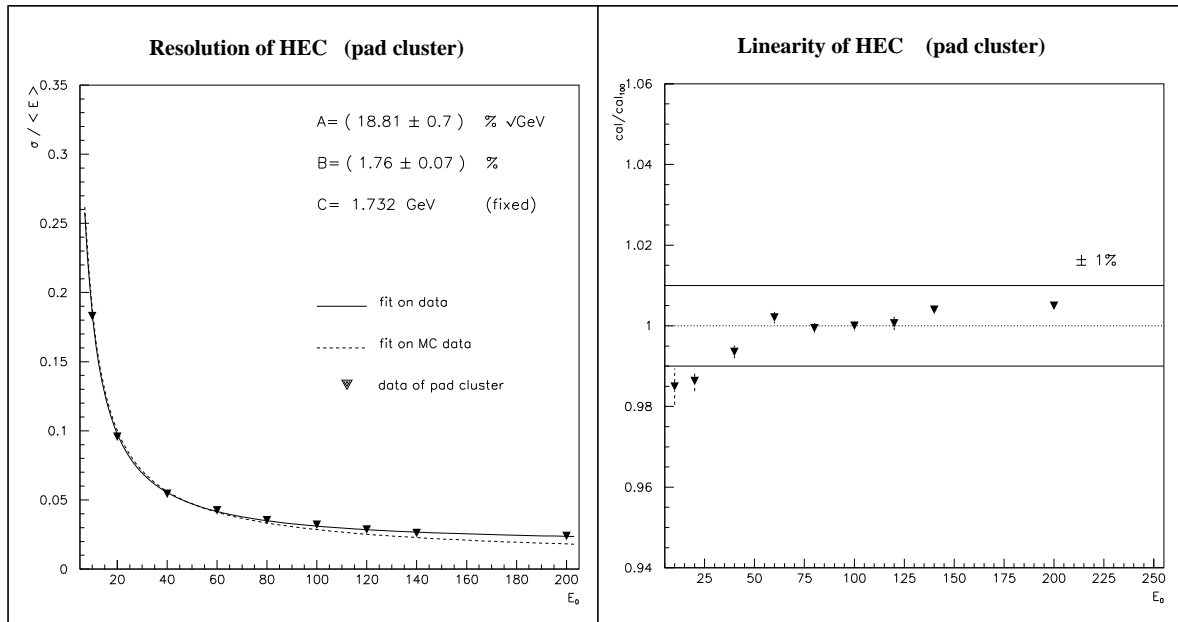
2.3.6 Results with electrons

Energy scans in the range 10 to 200 GeV were carried out with electrons in up to 16 different pad positions. The electron energy was reconstructed using three channels in the first longitudinal section and two channels in the second section. Figure 2-14 shows the energy resolution as a function of the beam energy obtained for a particular pad position. The energy resolution can be parametrized as

$$\frac{\Delta E}{E} = \frac{A\%}{\sqrt{E}} \oplus B\% \oplus \frac{C}{E},$$

where E is in GeV, A is the sampling term, B the constant term and C the noise term. The solid line in Figure 2-14 shows the result of this fit to the data. The results obtained for A, B and C are also shown in Figure 2-14. They are in good agreement with Monte Carlo expectations (dotted curve).

The linearity of the energy response for electrons is another important issue. Figure 2-15 shows
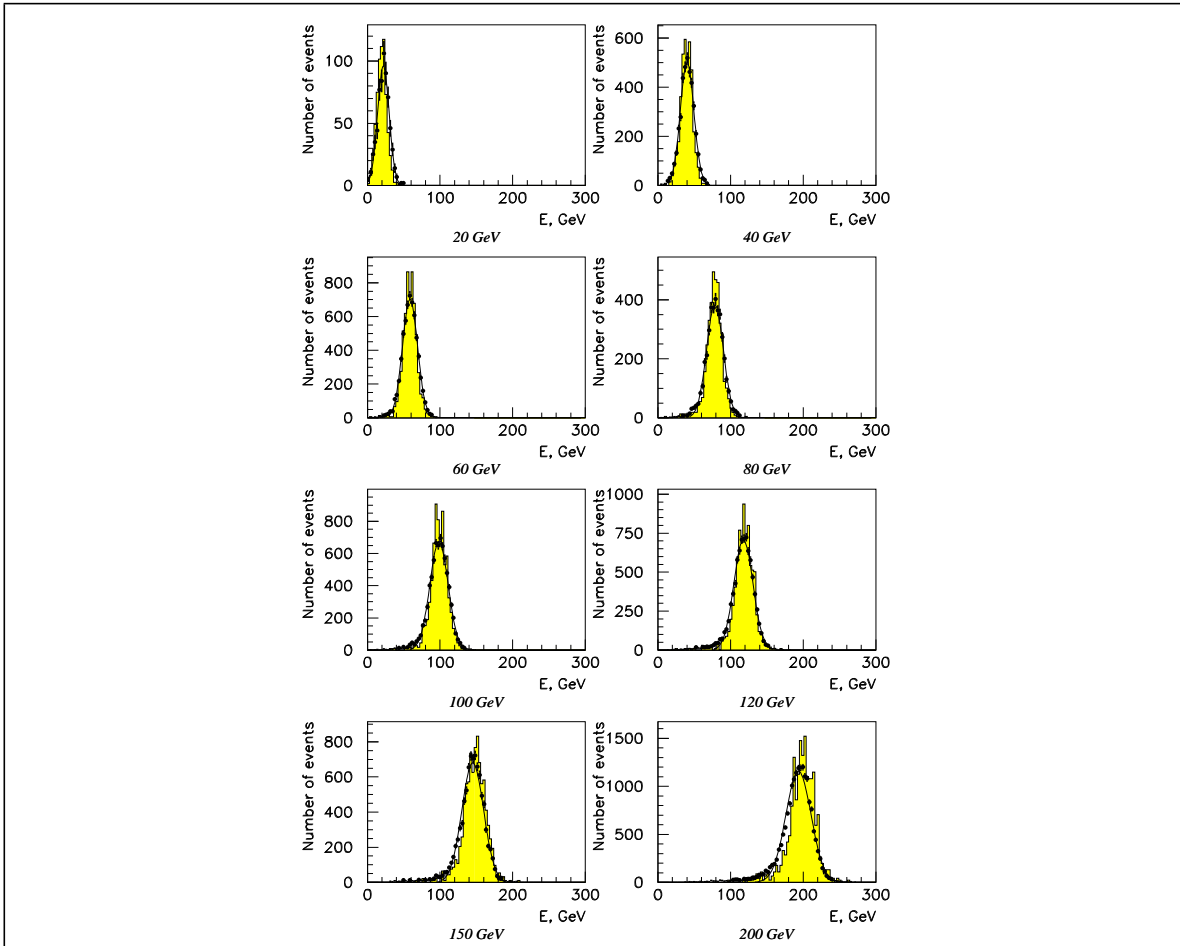
Figure 2-14 Energy resolution obtained for electrons: the solid line is the fit to the formula mentioned in the text; the dotted line is the corresponding MC prediction.

Figure 2-15 Linearity of the energy response for electrons of different energy. The ratio relative to the average response at high energy is shown.

the ratio relative to the average response at high energy for a particular pad position (pad 8 as above). At high energy the linearity stays within 1%. The deviation at low energy is due to dead material in front of the calorimeter module and due to the cuts applied in the analysis to suppress the contribution from noise. The Monte Carlo response shows a rather similar dependence; a detailed comparison is in progress.

Detailed horizontal and vertical scans with electrons at different energy were carried out. In particular the region close to the ϕ-crack between two modules was scanned with a step size as small as 1 mm. Although the analysis is rather preliminary, no significant variation of the total response or energy resolution has been observed so far.

Figure 2-16 Distribution of the reconstructed energy of pions in the energy range from 20 GeV to 200 GeV after correcting for leakage effects (see text). The solid points show the data, the line represents a gaussian fit to this distribution and the histogram shows the corresponding distribution for MC generated data.

2.3.7 Results with pions

Energy scans in the range 20 to 200 GeV were carried out at various pad positions. The analysis of the data is still in progress, and only preliminary results are available.

Horizontal and vertical scans were performed to measure the homogeneity of the calorimeter response. Given the limited longitudinal coverage in the prototype set-up (the 'rear wheel' (HEC2) modules are half the normal longitudinal size), effects of leakage strongly influence the measurement of the energy deposited. The energy is reconstructed in a cone corresponding typically to $\Delta\eta \times \Delta\phi = 0.3 \times 0.3$, yielding 36 cells in total. To correct for leakage, correction parameters were determined for these cells from a global fit minimizing the energy resolution for the combined data of all the energy points.

Figure 2-16 shows the reconstructed energy for each beam energy using this correction procedure. The solid points are the data and the line is the result from a gaussian fit to the distribu-

tion of thedata. For comparison, the same procedure has been applied to Monte Carlo data, using the GCALOR code for the simulation of the hadronic energy deposition. The histograms in Figure 2-16 show these results. In general, the width of the distributions is described rather well by the Monte Carlo data, even though they have a somewhat larger width. The mean energy reconstructed shows some deviation at low and high energy. Keeping in mind that the leakage correction parameters have been determined for all energy points together, the mean energy depends on the differential hadronic shower distributions, and in particular on the energy dependence of these distributions. The observed deviations therefore indicate some discrepancy between data and Monte Carlo simulation at the level of differential hadronic shower distributions. For comparison the GFLUKA and GHEISHA codes have been used in the simulation as well. There are preliminary indications that at low (high) energy GHEISHA (GCALOR) gives the best description of the data. GFLUKA gives the worst description of the data in the whole energy range considered. A detailed analysis, in particular the comparison with Monte Carlo simulation, is still in progress.

2.4 Forward calorimeter prototype.

2.4.1 Test beam set-up.

A full depth (45 cm) cylindrical prototype of the first section of the forward calorimeter (FCAL) was studied in 1995 at the H6 test beam at CERN using electrons from 20 to 200 GeV. This module accommodates 364 tube/rod brass electrodes in a hexagonal array, each forming a 250 μm wide tubular liquid argon gap. The electrode centre-to-centre distance is 7.5 mm. The read-out geometry corresponds to the final design of the calorimeter (see Chapter 9 for more details). The overall transverse size of the brass absorber matrix is only 18 cm in diameter, which allows for an acceptance window of about 5 x 5 cm^2 around the centre of the module with full longitudinal and lateral electromagnetic shower containment. The whole module (Figure 2-iv) is installed inside a small cryostat, which can be rotated horizontally. A Rohacell excluder is placed between the module and the inner cryostat wall (front and back).

The charge from the ionization in the LAr gap is collected at each electrode in an external field of 1 kV/mm (250 V). Groups of four adjacent electrodes are ganged together for common read-out. A G10 interconnect board at the front of the module provides the corresponding connections to the 20 Ω kapton signal cables. The length of the cables was chosen to simulate the situation in ATLAS, with 4.5 m inside the cryostat connecting the prototype to the feedthrough. Another 1 m of cables makes the connection from the feedthrough to the preamplifier box, which is installed inside a Faraday cage directly on the top plate of the cryostat.

Each of the '0T' [2-4] and [2-16] preamplifiers is connected to a bi-polar Sallen-Key (equivalent to CR--RC) shaper on a small PC board. The triangular shaping time is 40 ns, compared to a charge collection time of about 50 ns. There are fifteen or 16 of these daughterboards arranged on a common motherboard, with six motherboards providing 91 preamplifier channels in total. A warm calibration system feeding a current pulse directly to the input of each preamplifier is installed on each motherboard. A calibration control board allows every individual preamplifier or every possible combination to be addressed. It also provides converters for calibration pulse height adjustments. The evaluation of a full crosstalk matrix is possible with this system, as well as the absolute calibration for each preamplifier channel.

The amplified and shaped signals are fed into a track-and-hold (T&H) unit, which converts the signal peak amplitude to a DC level. A two-gain stage acting on the T&H output extends the

dynamic range of the following 11-bit ADCs to about 14 bits (about 10 MeV to 250 GeV). The total number of read out channels is therefore twice the number of preamplifier channels (i.e. 182).

The preamplifiers operated in a very stable way, with a channel-to-channel gain uniformity of better then 0.5% in the beam region. Incoherent electronic noise close to the theoretically expected value of 80 MeV per channel was measured. The contribution from coherent noise is about 16 MeV. It has a typical coherence length of 15 to 16 preamplifier channels (one motherboard), indicating that it is most likely generated by the specific set-up at the test beam.

2.4.2 Results for electrons

Some selected results from the study of the extended module have already been reported in Refs. [2-17] and [2-18]. They verify earlier results [2-19] for most of the parameters and show even better results for the energy resolution.
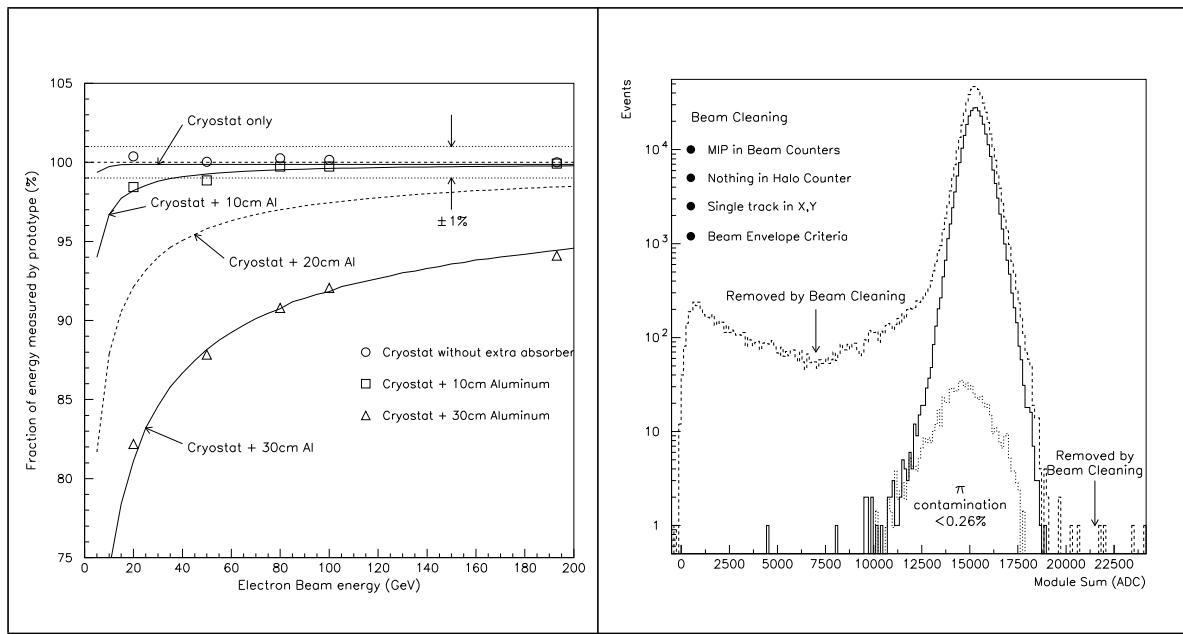
2.4.2.1 Signal linearity and energy resolution

The matrix/rod structure of the front face leads to a variation of the electron signal with the particle impact point (about ± 15% at 0.6° impact angle). This effect is less significant (about ± 8%) at larger angles, and can be corrected using the spatial signal distribution in the calorimeter itself [2-20]. The most important high-energy limit of the relative energy resolution is improved to well below 3% after the correction, with a sampling term of about 36%. The signal is also linear within better than ± 0.5% for electron momenta 20 to 200 GeV/c, basically independent of the particle impact direction (between about 0.6° and 4°). Additional studies using cylindrical cluster algorithms [2-19] show the deviation from linearity is smaller than 1% for cluster radii of about 40 mm and above.
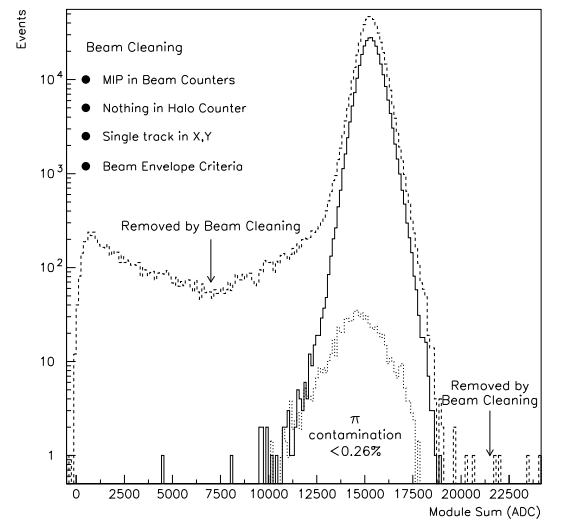
The variation of the FCAL prototype response to electrons as a function of energy with different amounts of upstream material can be understood to within ± 1% from calculations using longitudinal shower parametrizations [2-21] (no free parameters). Figure 2-17 shows the good agreement between the measurements and the simulation. The unavoidable amount of inactive material has been estimated to 0.8 radiation lengths, mostly coming from the cryostat walls.

2.4.2.2 Energy resolution function

The energy distribution at a given energy, happened to be sensitive to event selection. Electrons with the expected beam energy are selected mainly using five multiwire chambers distributed between 1 m and 14 m upstream of the calorimeter module. Each chamber has one vertical and one horizontal plane with 1 mm wire spacing. They allow events where the electron emitted bremsstrahlung to be rejected by explicitly measuring the particle direction and applying a severe cut on this variable. A small number of rejected events have a visible second neutral cluster in the calorimeter, directly indicating small-angle photon emission. This selection has the virtue of being unbiased. Figure 2-18 shows its effect on the resolution function. The pion contamination surviving all cuts is estimated from pion data taken separately, and seems to explain the low-energy tail remaining well below 10^{-4}.
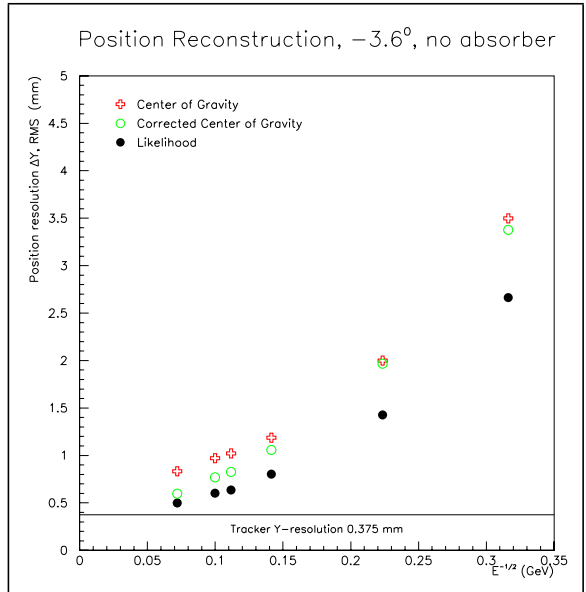
Figure 2-17 Relative signal loss due to inactive material in front of the FCAL, as a function of the beam energy.

Figure 2-18 The electron signal distribution in the FCAL prototype before (dashed) and after (solid) 'beam cleaning' (see text).

2.4.2.3 Space resolution

The same set of wire chambers has also been used for a precise determination of the impact position of each electron in the prototype. Comparing this point with the one reconstructed from calorimeter signals alone determines the space resolution shown in Figure 2-19. The important high-energy limit is about 0.4 mm and approaches the experimental limit given by the wire chambers used in this test beam. The chamber resolution has not been unfolded from the data shown in the plot. The best resolution is obviously obtained with the already mentioned correction for signal dependencies on the particle impact point.

2.5 Combined LAr-Tile test beam results
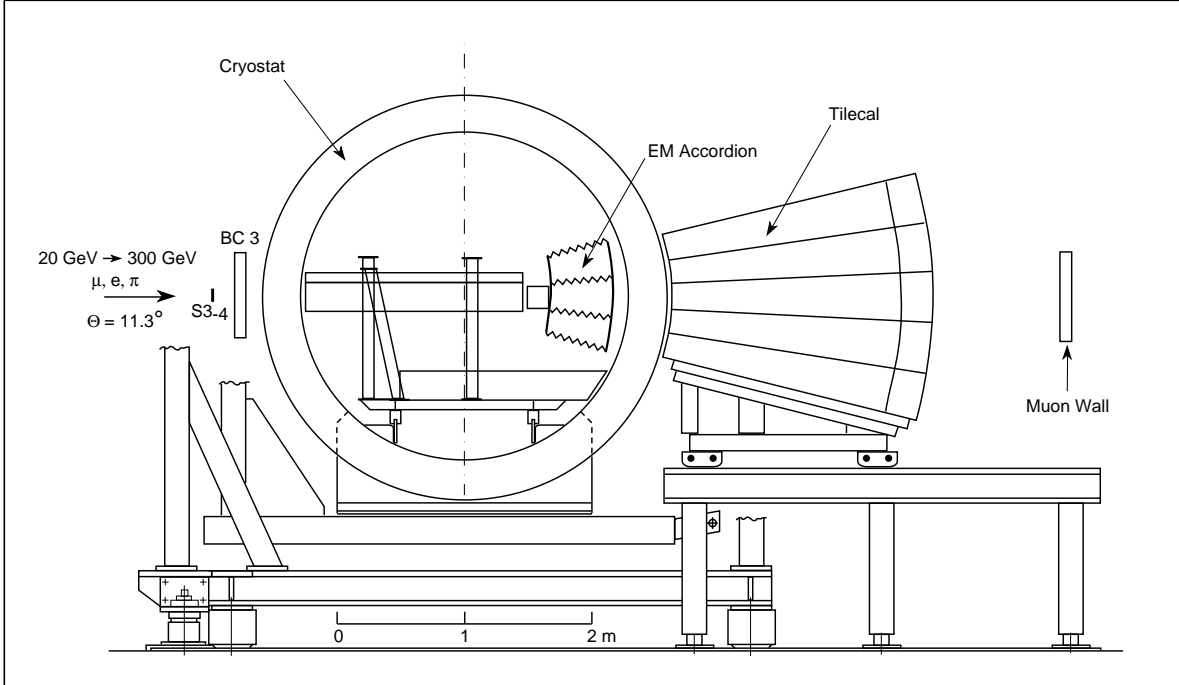
Figure 2-19 Vertical space resolution versus $1/\sqrt{E}$. The solid line indicates the experimental limit, given by the wire chamber resolution.

The detailed results of the combined LAr-Tile tests are given in the ATLAS Tile calorimeter TDR [2-22] and are only summarized here.

2.5.1 The test beam set-up.

Beam tests of the combined performance of the electromagnetic and hadronic calorimeter proto-types were carried out in 1994 and 1996. An azimuthal sector of the ATLAS barrel calorimeter was reproduced by placing the Tile calorimeter prototype downstream of the LAr cryostat as shown in Figure 2-20. In order to optimize the containment of hadronic showers the electromag-

Figure 2-20 The combined Liquid Argon and Tile calorimeter test beam set-up

netic calorimeter was installed at the back of the cryostat and the two calorimeters were placed with their $\eta = 0$ plane at 11.3° angle to the beam axis. Owing to its placement, at this angle, the EM calorimeter, no longer pointed exactly to the nominal interaction point, although cell projec-tivity along the azimuthal direction was maintained. The amount of material between the two calorimeters was $\approx 1.5\ X_0$, which is similar to the ATLAS design value, while the distance (≈ 55 cm) was a factor of two larger than foreseen for ATLAS. The total active thickness at the beam incidence angle was 10.3 λ. A muon wall located about 1 m behind the calorimeters was used to tag punch-through particles and energy leakage. The amount of structural material be-tween the active part of the Tile calorimeter and the muon wall was 0.7 λ.

The $\eta-\phi$ coverage used in the analysis corresponds at 11.3° incidence to $\Delta\eta = 0.18$ and $\Delta\phi = 0.22$ in the electromagnetic calorimeter, and $\Delta\eta = \Delta\phi = 0.5$ in the Tile calorimeter.

2.5.2 Results
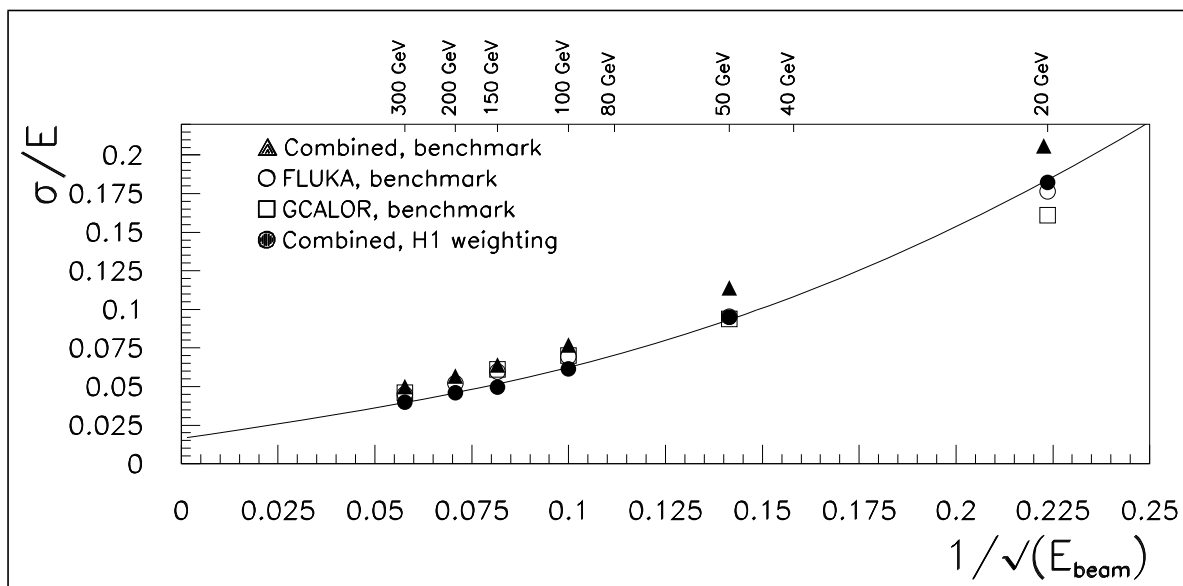
2.5.2.1 Pion energy resolution

To reconstruct the hadron energy two different algorithms were used. The first method, referred to as the 'benchmark approach', is designed to be simple [2-23]. It introduces a set of three ener-gy-independent corrections: the intercalibration between the calorimeters, a correction term for the energy lost in the cryostat wall separating the EM and the hadronic calorimeter, and a quad-

ratic term for the EM calorimeter to obtain a crude correction for its non-compensating behaviour. The parameters were determined by minimizing the fractional energy resolution of 300 GeV/c pions.

The second method [2-24] is similar to the H1 weighting method [2-25]. The total energy is reconstructed by correcting the energy in each cell of either calorimeter with a factor (typically > 1) which is a function of the energy in each cell and of the beam energy. The weights, found by minimizing the resolution, can be parametrized by simple functions using only eight parameters. No a prior knowledge of the beam energy is needed to calculate the energy dependent corrections; instead, the particle energy is estimated from the raw data with a simple iterative procedure. A new feature is that the linearity and resolution of the combined system were simultaneously optimized. Since the particle energy is not known, the energy is iteratively reconstructed with this algorithm.

The obtained resolution as a function of the pion energy is shown in Figure 2-21 compared with predictions from simulations using GEANT-CALOR and stand-alone FLUKA [2-26]. There is

Figure 2-21 Energy resolution for pions measured with the combined LAr-Tile set-up. The benchmark results are compared with predictions from the FLUKA and GEANT simulations. The result of the H1-based algorithm with a fitted curve is also shown

good agreement between the simulation and data for energies above 100 GeV. At 20 GeV the worse resolution can partly be explained by beam contamination.

Further results concerning linearity, longitudinal leakage and e/π separation can be found in the ATLAS Tile Calorimeter TDR [2-22].

2.6 Results on pipelines

In order to test read-out systems close to those required for ATLAS (i.e. a trigger latency of 2.5 μs for an interaction rate of 40 MHz, multiple samples), about 100 channels of the 2 m barrel prototype were equipped with pipeline systems. Four teams proposed such systems and all have been tested during the last two years; three of them built an analog pipeline using Switch

Capacitor Arrays (SCA) where the data wait for the LVL1 accept before digitization (OSAM (Orsay, Saclay, Annecy and Marseille), Nevis and Alberta), and one solution proposed by Paris VI/VII was based on the RD16 project where data are digitized at 40 MHz and wait for LVL1 accept in digital memories.

2.6.1 OSAM read-out system

The SCA chip has 16 channels and four reference channels used to subtract common mode noise. There are 128 capacitors per channel. In normal running conditions, the input signals are permanently sampled at 40 MHz, and the samples stored in the SCA during trigger latency or longer. We modified the test beam trigger to have a latency of 2 μs. When a trigger signal is received, five samples are read from the SCA and digitized. An internal multiplexer working at 10 MHz allows a single output pin per chip connected to a single 12-bit 10 MHz ADC (see Figure 2-22). A trigger rate up to 75 KHz is tolerated. The version of the chip that was used was produced by Austrian Micro Systems (AMS), using a 1.2 μm CMOS process. A Rad-hard version was also produced, using the "Durci Mixte Logico-Lineaire" (DMILL) process. A detailed description of the pipeline can be found in ref. [2-27].

The calorimeter cells were equipped with warm preamplifiers ('0T') and bi-gain shapers (i.e. one high gain and one low gain shaper channel for each cell, to ensure a dynamic range of the order of 16 bits) (see Section 2.1.2.2). An SCA channel was associated to each shaper channel and, for each sample in each cell, only the relevant SCA channel was digitized (see Figure 2-22).

Figure 2-22 Block diagram of the Front-End board.

Five front-end boards were built. Their dimensions are 366 x 340 mm^2. Each one treats 32 calorimeter cells (x 2 gains). This corresponds to four SCA chips, two ADC chips, plus the necessary logic. The data were read by VME and could be sent by optical fiber to a digital filtering system (MUSIP).

The whole system was operated in the test beam in June 1996.

Pedestal and test-pulse events were recorded with a synchronous trigger. The third sample (out of 5) was at the maximum of the calibration pulses. The physics trigger selected these electrons where the maximum of the pulse was within 1.5ns from the third sampling.

The noise per channel was measured to be 1.5 mV at the input of the SCA (56 MeV), out of which 0.85 mV (32 MeV) comes from the SCA and its environment on the front-end board. The noise contribution to an electron cluster is 250 MeV, out of which 125 MeV comes from the SCAs

and the front-end boards. Saturation occurs at 3 V above the pedestal for both high and low gains. The gain ratio is 10. The dynamic range of the complete read-out chain is 14.1 bits, and the dynamic range of the front-end board is 15.6 bits. The noise contribution to the calibration pulse is the same as for pedestal events, excluding a contribution of the Front-end board to the constant term in the electron resolution at the level of 0.1%.

Electrons with energy between 50 and 300 GeV have been recorded. The 300 GeV data requires both high and low gain and is currently being analysed. The measured resolution for 200 GeV and below is identical to the one obtained with the old read-out system (T/H and CAMAC ADCs): 0.8% at 200 GeV (see Figure 2-23) and 1.6% at 50 GeV. The tails at low energy, also present with the old read-out in this test period, were a consequence of some bad beam tuning.

Figure 2-23 Energy spectrum for 200 GeV electrons.

2.6.2 Nevis SCA test beam results

Through a sequence of prototypes, Nevis Labs has developed a custom switched-capacitor array (SCA) analog memory [2-28] using the HP 1.2 micron CMOS process. This SCA has a dynamic range in excess of 13 bits, DC non-linearity below 0.2%, and a timing jitter of only 9 ps.

To investigate the performance in beam conditions, two generations of 6U VME read-out boards have incorporated different versions of the SCA prototypes. These boards have been used during each of the past three summers for test beam measurements performed at CERN. The first prototype board comprised two 6-channel differential SCAs, 14-bit 5 MHz ADCs for digitization, and a programmable on-board single chip SCA Controller utilizing an Field Programmable Gate Array (FPGA). In the SCA, each active channel was paired with a neighbour pipeline which was used as a reference to subtract common mode noise. Owing to speed limitations in the SCA Controller arising from the FPGA technology available at that time, the boards were not operated with simultaneous Read and Write operations. The boards demonstrated a dynamic range in excess of 12 bits. Later tests with a newer FPGA revealed that the noise was not significantly increased when running with simultaneous Read and Write operations.

In August 1994, we used these boards to measure the response of a liquid krypton (LKr) EM calorimeter to electron beams of energy 20 to 200 GeV [2-29].

The shaped response of the calorimeter to a 50 GeV electron beam, as measured with the SCA electronics, is shown in Figure 2-24. The energy resolution (see Figure 2-25) using the SCA read-out was $(5.5 \pm 0.3)\%/\sqrt{E}$ (where $\pm$ denotes the addition in quadrature and E is measured in GeV), in agreement with results using a separate Track-and-Hold read-out and also with Monte Carlo expectations. In addition, the timing resolution for a single channel was determined to be $\sigma(t) = (1.0 \pm 0.05)$ ns/E, a result which is much better than required by ATLAS and is dominated by the noise in the calorimeter.

During 1995, we used these electronics to measure the response of the RD3 LAr barrel EM calorimeter prototype (Section 2.1) to electrons of energy 20 to 300 GeV [2-30]. The energy resolution was measured to be $(9.7 \pm 0.1)\%/\sqrt{E}$, in agreement with the best published results using this calorimeter. Additional measurements were made with the conventional front-end electronics re-
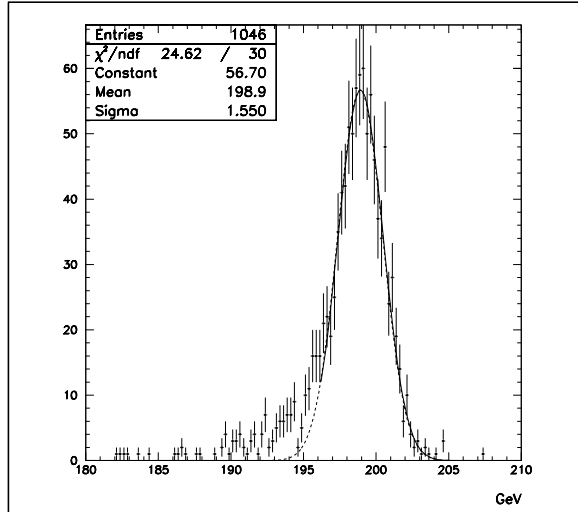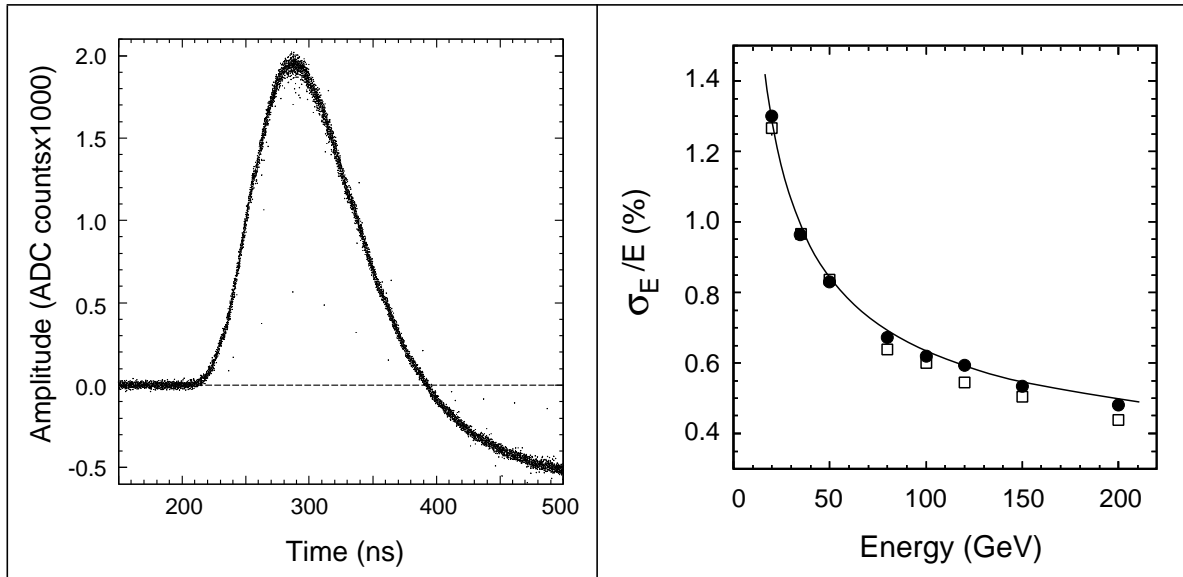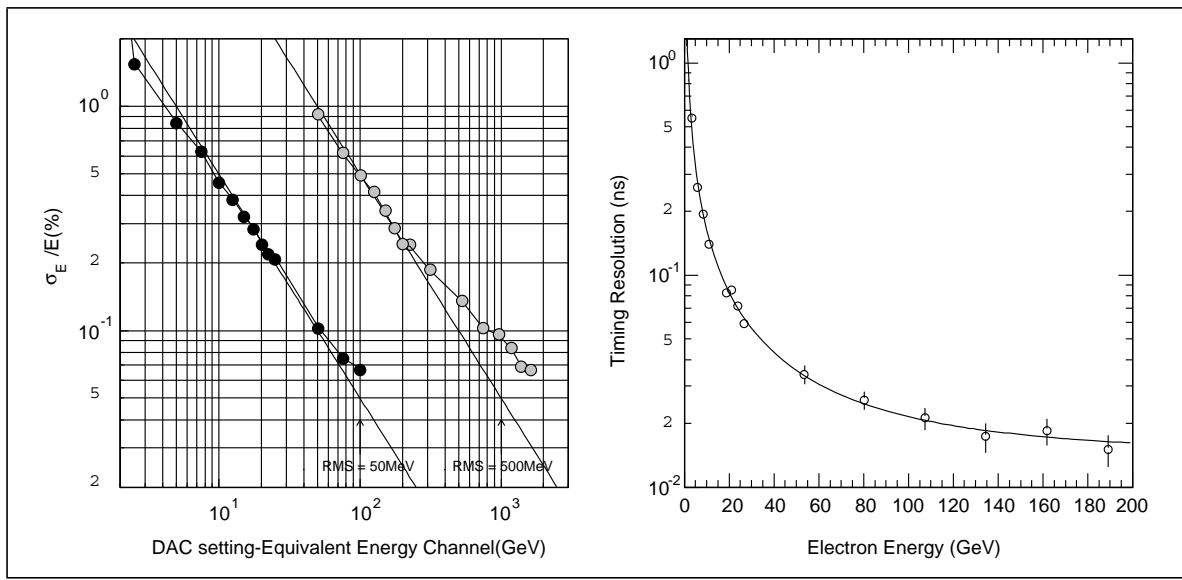
Figure 2-24 Response of the LKr calorimeter prototype to a 50 GeV electron beam, as measured with the Nevis SCA electronics. About 1000 events are superimposed on the figure.

Figure 2-25 Electromagnetic energy resolution of the LKr calorimeter prototype measured with the Nevis SCA electronics (circles), and compared with Monte Carlo expectations (squares). The curve shows the result of the fit described in the text.

placed by cryogenic silicon JFET preamplifiers with a nonlinear transfer function, as one possible means of reducing the overall dynamic range of the read-out. Analysis of the nonlinear data is complicated by the fact that the pulse shape changes with energy (for example, the position of the peak shifts by about 20 ns from the lowest to the highest beam energies in this study). However, the changing shape can be tracked and accounted for by using the multiple sample SCA data. Algorithms for extracting the optimally filtered energy were developed, and yielded an energy resolution consistent with that obtained with the linear preamplifiers [2-31]

Finally, during June 1996 we used the latest 16-channel SCA prototypes to measure the response of the RD3 prototype again. For this second generation read-out board, an SCA Controller was developed utilizing a new FPGA chip which was sufficiently fast to handle the algorithm with fully simultaneous Read and Write operations. For this beam test, the instrumented region of the RD3 prototype was equipped with warm '0T' preamplifiers and bi-gain shapers (with a gain ratio of 10). An energy resolution of 10.5%/$\sqrt{E}$ was achieved, again consistent with results from the Track-and-Hold system. With the bi-gain shapers, it was possible to test the read-out over almost the full ATLAS dynamic range, and far above the 300 GeV highest beam energy. As shown in Figure 2-26, the precision obtained in reconstructing the amplitude of calibration pulses reached levels of about 0.07% for large pulses, and followed the expected 1/E behaviour until levels of 0.1%. The single channel timing resolution was also studied (see Figure 2-26). For the calibration pulses, the timing resolution of about 1.5 GeV.ns is dominated by the calorimeter noise. The constant terms in the timing resolution are only about 45 ps and 14 ps for beam and calibration pulses, respectively.

Additional data runs were taken with the electronics reconfigured to read 32 samples per event, thereby measuring the pulse shape over the entire approximately 400 ns duration of the calorimeter signal. This data is currently being studied in order to investigate the precision with which one can determine the electron drift time in the calorimeter, as a possible method of monitoring temperature drifts and other effects which would contribute to the constant term in the energy resolution.

Figure 2-26 Energy and timing resolution measured with Nevis SCA electronics using calibration data.

2.6.3 Alberta

During the past four years the University of Alberta has performed R&D on an analog pipeline read-out system based on switched capacitor array (SCA) technology. The performance has been studied by using prototype pipeline systems to read-out regions of the electromagnetic prototype calorimeter.

In September 1993 a demonstrator system was built and tested ([2-32] and [2-33]). The modules operated successfully in the test beam and the incoherent noise was measured to be 0.73 mV of which 0.31 mV (100 MeV) was due to the pipeline system. We measured signals up to 2.5 volts. This corresponded to a greater than 11.7-bit resolution. Owing to substantial coherent noise in the system (mostly attributed to the power supply on the VME crate), the electron energy resolution was worse than expected [2-34].

The aim of the September 1995 test beam period was to run the system at the LVL1 trigger rate and test the full dynamic range with the calibration system using a dual-gain approach. The layout combined the analog pipeline and digitization circuits on the same board. A new version of the SCA chip with faster output reconstruction amplifiers and other small improvements was made. Besides the updates and improvements to the pipeline memory boards, a new controller was used. It allowed the memory boards to be operated at full speed and with all the final system functionality and programmability [2-35]. The read-out system was operated in two different modes. A slower read-out mode used the VME backplane. In a full speed read-out mode, the output from the FIFOs on the memory boards was sent directly to transmitter boards in the same crate. The signals were then transmitted to receiver boards in another crate and thus to a digital filtering system. The pipeline system operated at the required speed.

For the June 1996 test beam period a new layout of the pipeline memory board was made to correct faults observed in the operation of the previous system. To be able to achieve the required resolution, 14-bit ADCs operating at 1 MHz were used. Data were recorded over a range of electron beam energy and operating conditions with both bi-gain and mono-gain shapers. The average pedestal noise was measured to be 3.4 ADC counts of which 1.7 ADC counts were due to the pipeline system. This corresponds to a 12.2-bit resolution. The coherent contribution to the

noise was estimated to be about 1.1 ADC counts. The calibration analysis and reconstruction of the electron energy is in progress.
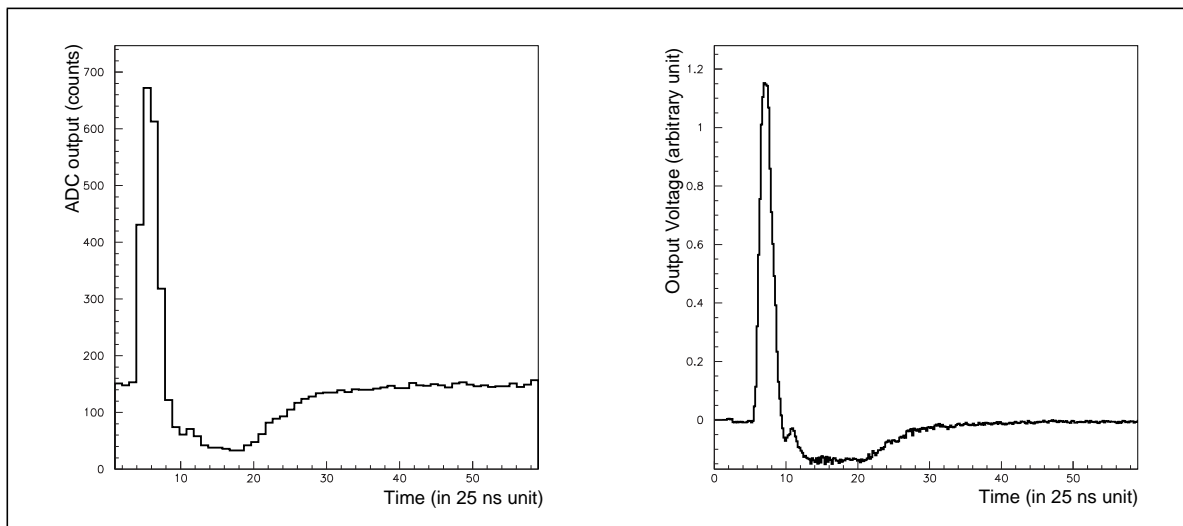
2.6.4 Digital pipelines

A generic concept of a fast digital read-out (FDR) was initiated by the RD16 Collaboration [2-36]. This has been developed within RD16 in contact with the ATLAS and CMS experiments. It is characterized by an early digitization of the incoming signals at the front-end. The key issues for an FDR in LHC experiments are: a fast digitization (40 MHz); a good coverage of the full dynamic range, at least 16 bits; a powerful digital processing that includes the LV1 trigger processing operating synchronously at 40 MHz and the DAQ processing in asynchronous mode.

So far, the two main parts of the FDR, i.e. the digitizer and the digital processing, have been tested independently. A prototype of the digitization part of an FDR has been tested in high-energy test beams (ranging from 20 to 300 GeV), at the CERN SPS since 1994 on various prototypes of the LHC calorimeters. The A/D prototype is a 10-bit 40 MHz PSA-ADC developed by RD16. It is preceded by a four-gain compressor (15/16 bits to 10 bits) also developed by RD16. It has a minimal digital processing part consisting of FIFOs read out through VME. It is located on a VME board produced by CAEN.

The performance of this specific fast A/D converter scheme has been studied in terms of noise and stability, imaging properties, linearity and calibration issues, and resolution [2-37]. With no additional gain at its input, the average noise of the overall read-out chain is ~1.2 ADC counts. When an extra gain of 10 is added, the noise increases up to 1.8 ADC counts on average. This estimate includes the intrinsic FDR noise as well as the preamplifier, shaper and externally induced noise, present in realistic test beam conditions. The pedestal measurement also gives an estimate of the stability of the electronics. Over a period of 12 days, this was demonstrated to vary at most by ±0.2 ADC count, when connected to the Tiles calorimeter read-out.

The FDR prototypes that have been tested demonstrate high imaging capabilities. They allow the pulse shape to be visualized in detail and to detect overlapping events to a high accuracy (see Figure 2-27).

Figure 2-27 Imaging properties of a fast digital read-out: Online LAr bipolar-shaped signal (left, single event) and Off-line reconstructed LAr bipolar-shaped signal (right, multiple events).

Moreover the imaging capabilities permit to measure relevant parameters characterizing both the detector and its associated very front end (VFE) electronics. To evaluate the drift time (see also Section 2.1.2.4) it is possible to fit the digitized frames with a theoretical function that includes among its parameters the drift time and the shaping time. Changes in the drift time when varying the high voltage values were clearly visible (1 ns per 20 V for a given channel) [2-37].
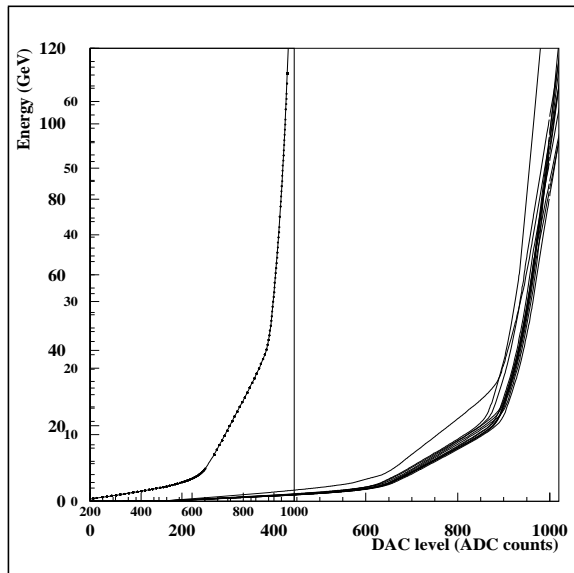
The linearity is another crucial parameter. The four-gain compression stage used implies four linear regions depending on the amplitude of the signals. Each corresponds to a different gain. The linearity is restored by the use of a Look-Up-Table (LUT) that contains the transfer function of each channel. A way to determine the LUT is by using the test pulse data delivered by the system (see Chapter 10). Detailed test pulse calibration have been performed with a large number of steps (up to 140) to cover the overall dynamic range.

The analysis of this calibration has been performed for both the 1995 and 1996 data. It gave the answer to the following questions about the calibration when a compression is applied to the incoming signals. How many points are actually needed to determine the LUTs? Is it necessary to have one LUT per channel? How dependent is the LUT on the energy estimator? How stable are the LUTs (monitoring and calibration issues)? What is the sensitivity of the results to a detailed reconstruction of the LUTs?

Figure 2-28 shows a series of LUTs corresponding to 18 different channels. It shows a clear difference in shape, indicating that one LUT per channel is needed. As the LUTs represent the transfer function of the overall electronics chain (including preamplification and shaper), they are sensitive to a variation of any element of this chain and will vary with it. The use of the compressor of course makes it more complicated to cope with these eventual variations. Furthermore, for a high-resolution calorimeter such as the EM liquid argon calorimeter, the results are sensitive to an accurate determination of the LUT, especially at high energy.

Figure 2-28 Reconstructed LUTs corresponding to the low gain channels of a 3 x 3 cluster in sampling 1 and 2. On the left side, the data and the interpolation results for one single LUT are shown.

The expected energy resolution is achieved within the limits of the presently available prototypes, i.e. the 10 bits A/D and the compression scheme currently used. The method to analyse the data as well as the results are described in Refs. [2-37] and [2-38].

The two main issues are to include the LUTs in the overall calibration and to study the sensitivity of the results to the choice of the energy estimator. This is especially true when working with fast signals such as the ones of the bipolar-shaped Liquid Argon EM calorimeter. The results quoted correspond to the 1995 data that were taken in asynchronous mode. Presently we have worked out only the high gain LUTs and therefore computed the energy response only up to 150 GeV. Figure 2-29 shows the energy response of the system for electrons of 20 GeV and 150 GeV. It can be noted that the resolution obtained at 20 GeV $(2.88 \pm 0.03)\%$, is compatible with values obtained with the standard T&H system, whereas the value at 150 GeV is slightly

Figure 2-29 Energy spectrum for 20 GeV and 150 GeV electrons.

higher. A fine adjustment, using partly the low gain LUTs, will improve the result. The determination of the full resolution curve up to 300 GeV is in progress.

The analysis of the 1996 data taken both synchronously and asynchronously, is still in progress ([2-37], [2-38]).

The full functionality of the overall FDR system, made of the presently produced ASICs, has been tested using detailed and reliable VHDL simulation. It has also been partially tested on a laboratory test bench ([2-37], [2-38]).
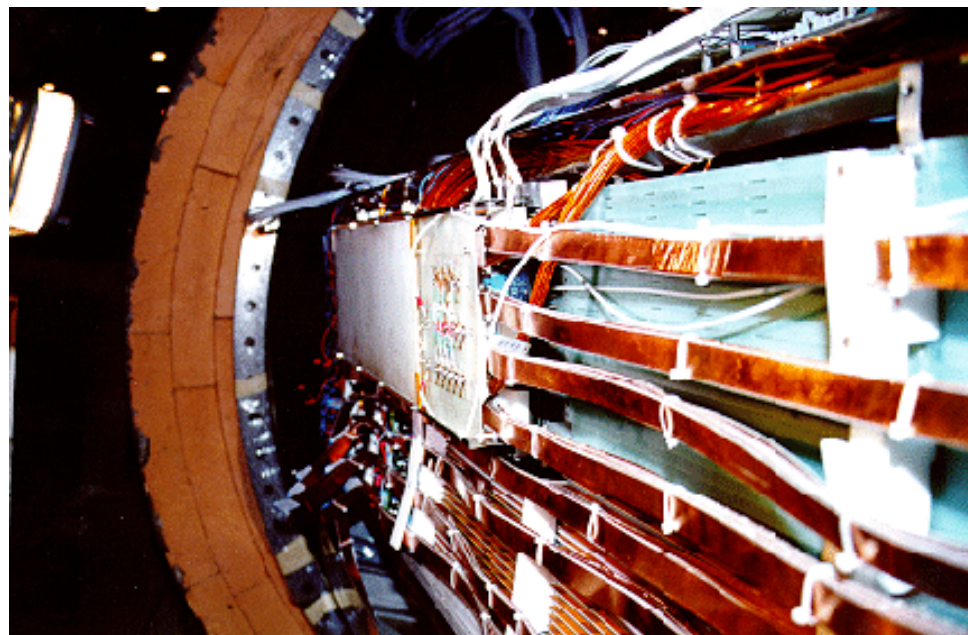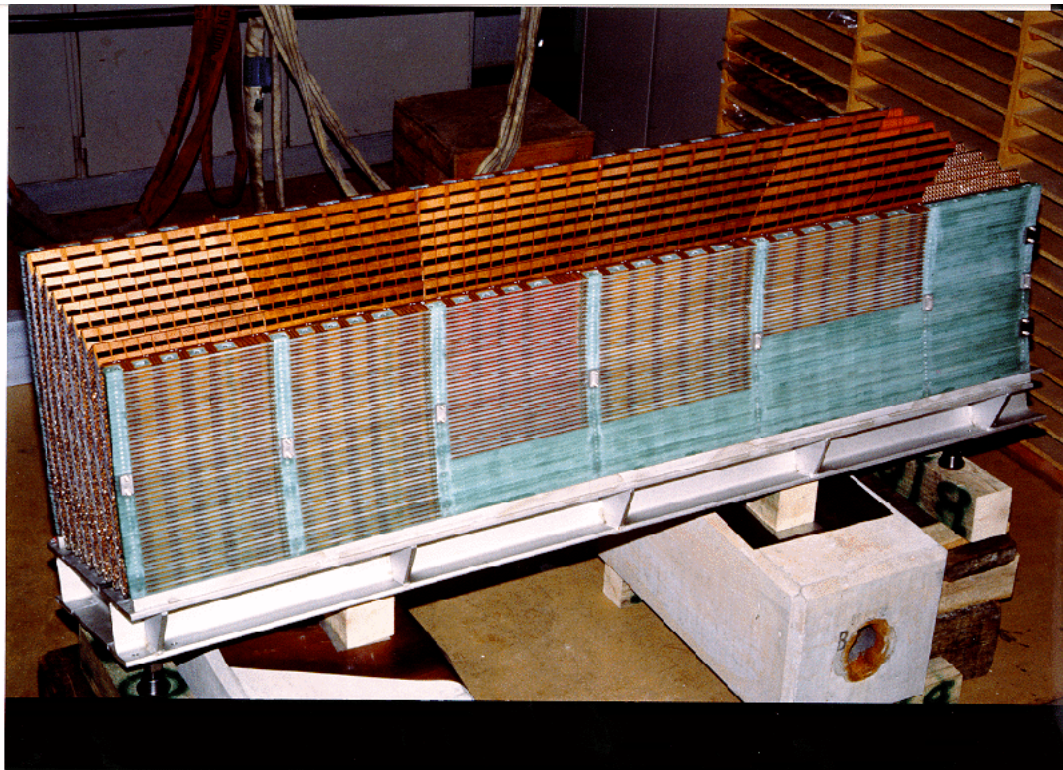
2.7 References

2-1   D.M. Gingrich et al., Nucl. Instrum. Methods A364 (1995) 290.

2-2   B. Yu and V. Radeka, BNL 52444 (1990).

2-3   D. Camin et al., Nucl. Instrum. Methods A315 (1992) 385.

2-4   R.L. Chase et al., Nucl. Instrum. Methods A330 (1993) 228.

2-5   ATLAS Collaboration, TDR Calorimeter Performance volume.

2-6   C. De la Taille and L. Serin, ATLAS Internal Note LARG-No-029.

2-7   J. Rutherfoord, GEM TN-91-27 (1991), GEM TN-93-410 (1993).

2-8   J. Colas, S.Jezequel and B.Mansoulie, ATLAS Internal Note CAL-No-40 (1994).

2-9   I. Wingerter-Seez, ATLAS Internal Note CAL-No-57 (1994) and Nucl. Instrum. Methods in preparation.

2-10   O. Benary et al., GEM collaboration, Nucl. Instrum. Methods A344 (1994), 363.

2-11   E. Albertson and J.Collot, ATLAS Internal Note, LARG-No-024, 1995.
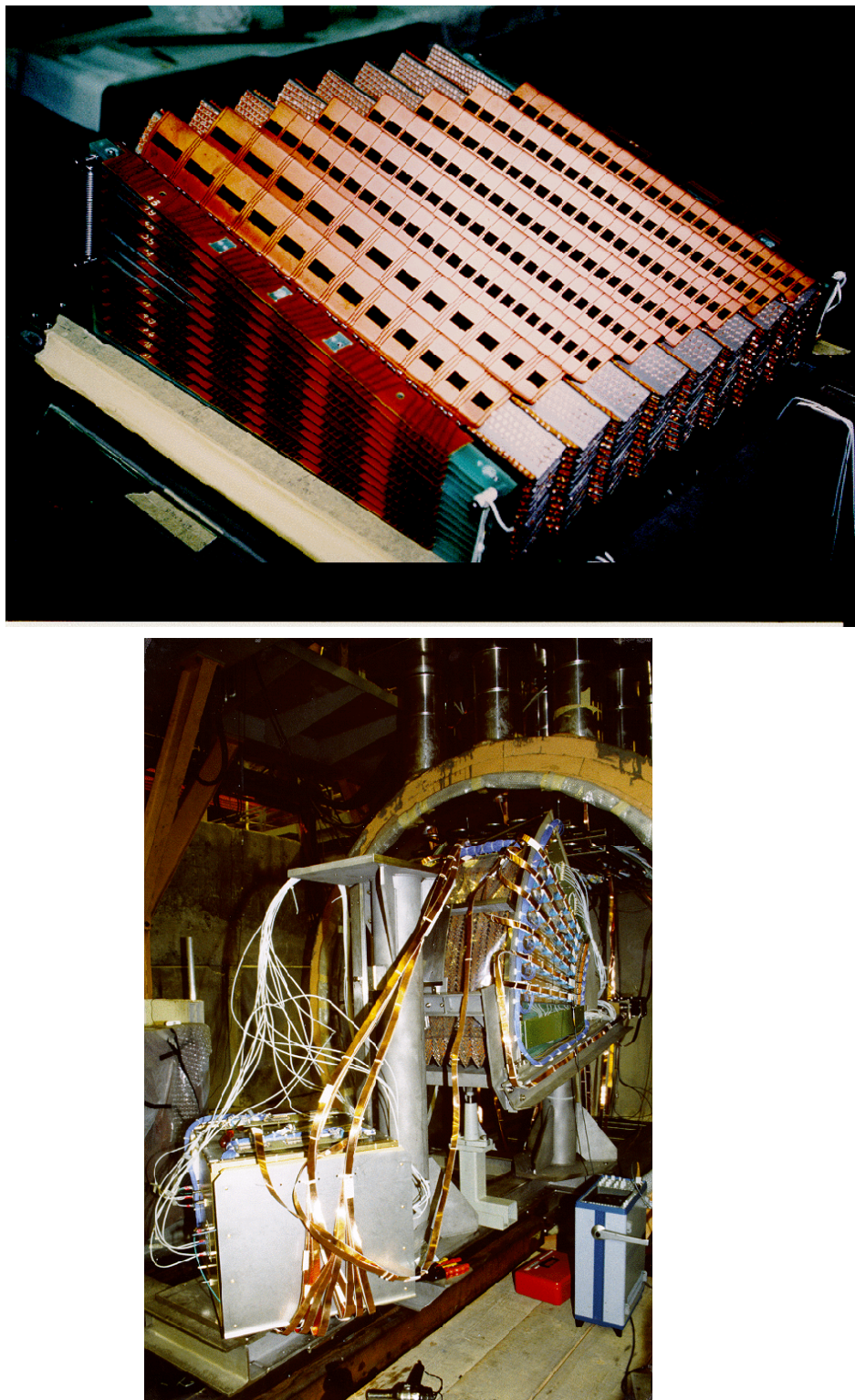
2-12   D.M. Gingrich et al., accepted for publication in Nucl. Instrum. Methods and CERN-PPE/96-175.

2-13   A. Cravero and F. Gianotti, ATLAS Internal note CAL-No-33 (1994).

2-14   A. Chekhtman, ATLAS Internal Note, LARG-No-041.

2-15   W. Braunschweig et al., Nucl. Instrum. Methods A378 (1996), 479 and C. Berger et al., Nucl. Instrum. Methods A357 (1995), 333.

2-16   R.L. Chase, C. de la Taille and N. Seguin-Moreau, Nucl. Instrum. Methods A343 (1994) 598.

2-17   J.P. Rutherfoord, to appear in Proc. 6th Int. Conf. on Calorimetry in High Energy Physics, Frascati, Italy 1996.

2-18   P. Loch, to appear in Proc. 5th Int. Conf. on Advanced Technology and Particle Physics, Como, Italy 1996.

2-19   M.I. Ferguson et al., accepted for public. in Nucl. Instrum. Methods A (1996).

2-20   A. Savine et al, Proc. of the 5th Int. Conf. on Calorimetry in High Energy Physics, Brookhaven National Laboratory, Sept. 25 - Oct. 1, 1994, ed. H.A. Gordon and D. Rueger, World Scientific (1995).

2-21   E. Longo and I. Sestili, Nucl. Instrum. Methods 128 (1975) 283 and G. Grindhammer, S. Peters and M. Rudowicz, Nucl. Instrum. Methods A336 (1993) 460.

2-22   ATLAS Technical Design Report, Tile calorimeter volume, CERN/LHCC 96-42, 1996.

2-23   Z. Ajaltouni et al., accepted by Nucl. Instrum. Methods and CERN-PPE/96-178.

2-24   M.P. Casado and M. Cavalli SForza, ATLAS Internal Note TILE-No-075, 1996.

2-25   W. Braunschweig et al., DESY internal report, DESY 89-022 (1989); H.P. Wellish et al., MPI-PhE/94-03, H1-02/94-346(1994); B. Andrieu et al., DESY internal report, DESY 93-047(1993).

2-26   A. Fasso, A. Ferrari, J. Ranft and P. Sala, Proc. of the 2nd Workshop on Simulating Accelerator radiation Environment, SARE-2, CERN Geneva, October 9-11, 1995, Yellow Report CERN in press.

2-27   J. Ardelean et al., ATLAS Internal Note LARG-No-50.

2-28   H. Cunitz et al., Proc. of the Fourth Int. Conf. on Electronics for Future Colliders, LeCroy Corp. (1994) 19-30 and J.A. Parsons et al., Proc. of the Fifth Int. Conf. on Calorimetry in High Energy Physics, BNL (1994) 430-435.

2-29   O. Benary et al., to be submitted to Nucl. Instrum. Methods.

2-30   J.A. Parsons et al., Proc. of the First Workshop on Electronics for the LHC, Lisbon (1995) 265-269.

2-31   W.E. Cleland et al., to appear in Proc. of the Int. Conf. on Calorimetry in High Energy Physics, Frascati (1996).

2-32   S.A. Kleinfelder, M. Levi & O. Milgrome, Nucl. Phys. B (Proc. Suppl.) 23A (1991) 382 and LBL preprint 30111.

2-33   D.M. Gingrich et al., Proceedings of the International Conference on Electronics for Future Colliders, 11-12 May 1994, LeCroy Corp., Chestnut Ridge, New York, 189-201.

2-34   D.M. Gingrich et al., ATLAS Internal Notes CAL-No-52-1(1995) and CAL-No-52 (1994).

2-35   D.M. Gingrich et al., Proceedings of the 1995 IEEE Nuclear Science Symposium and Medical Imaging Conference, October 21-28, San Francisco, Vol. 1, 277-279.

2-36   H. Alexanian et al., Nucl. Instrum. Methods A357 (1995) 309-317; R. Benetta et al., CERN/LHCC/95-28, April 1995 and references therein.

2-37   F. Astesan et al., ATLAS Internal Notes, in preparation.

2-38   A. Savoy-Navarro, to appear in Proceedings of the International Conference on calorimetry in High Energy Physics, Frascati, June 1996.
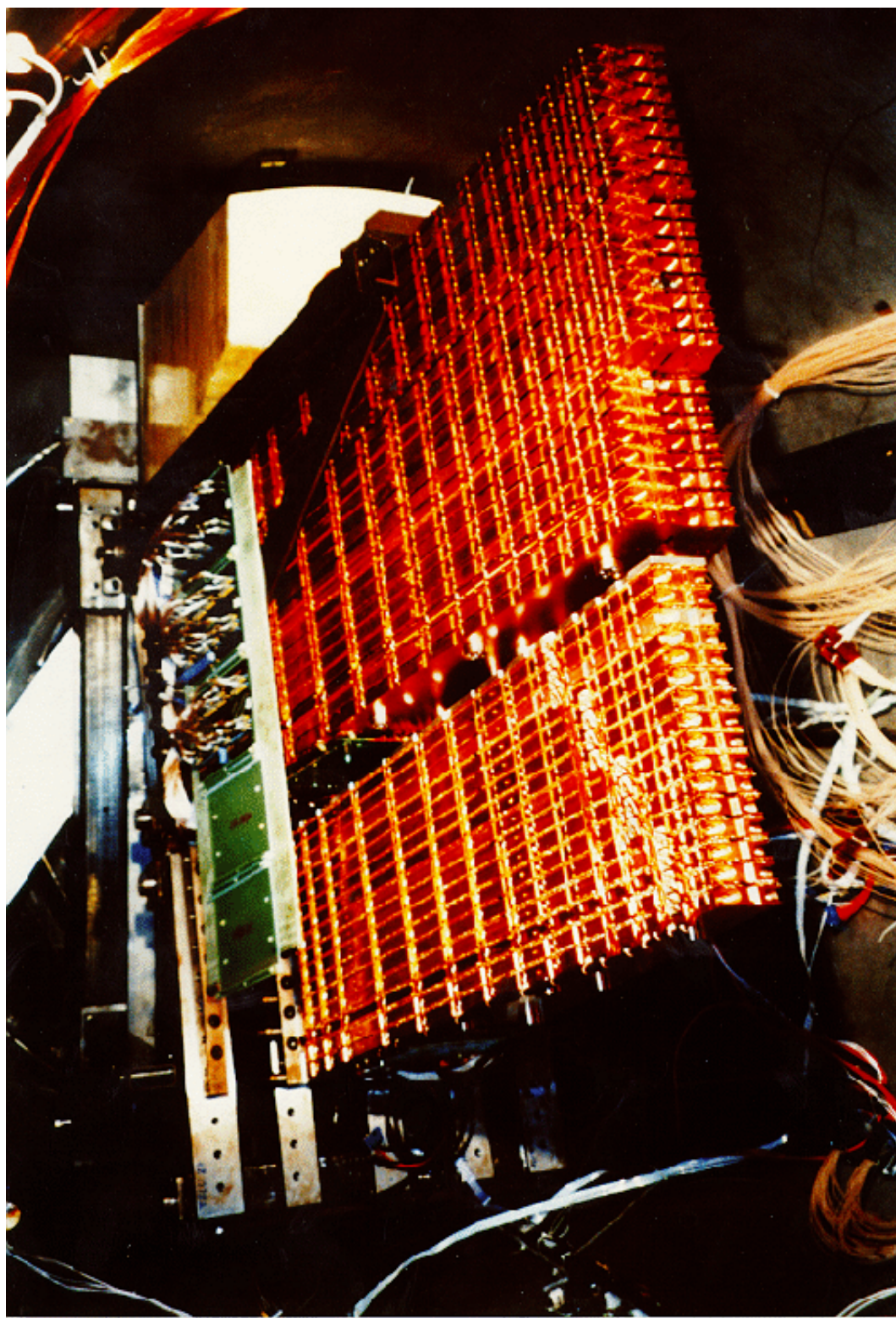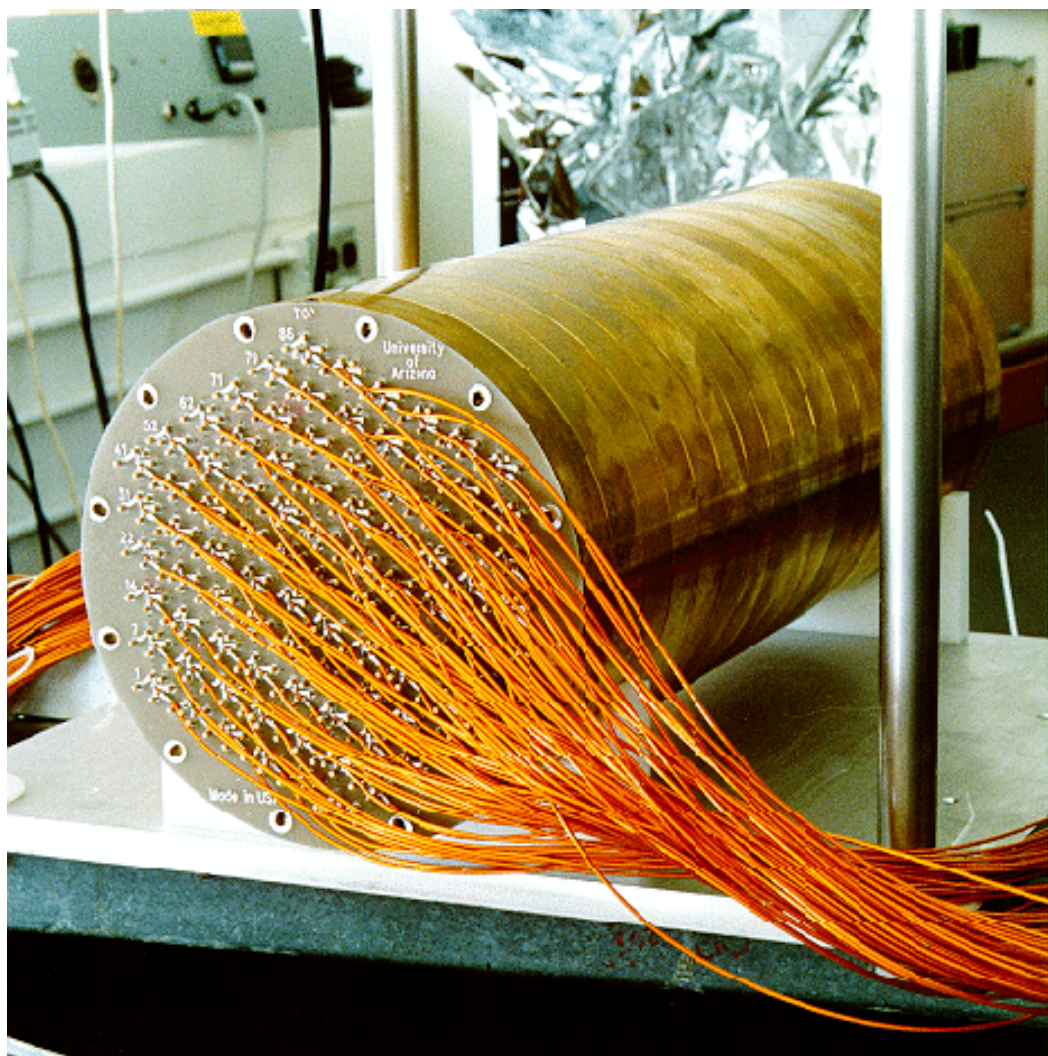
Figure 2-i View of the 2 m EM barrel prototype during assembly [only two out of the three azimuthal modules are mounted in the stack] (top view) and together with the PreSampler (PS) during insertion.

Figure 2-ii EM end-cap prototype during assembly (top) and before insertion inside the RD3 cryostat (bottom).

Figure 2-iii Set-up of the three modules (two front and one back module) positioned at the angle corresponding to $\eta = 1.8$ inside the cryostat.

Figure 2-iv The prototype of the forward (FCAL) electromagnetic calorimeter.

3 The cryogenics and vacuum system

3.1 Specification of the cryogenic system

The cryogenic system is an integrated installation for the three liquid argon cryostats. It includes the system for cooling down and warming up the cryostats and the detectors by circulation of helium. In routine operation, the cooling of the cryostats is achieved using liquid nitrogen produced in a closed loop by a liquefier located in the "cryogenics cavern".

The design of this equipment has to meet the following requirements:

- maintaining the temperature of liquid argon in the cryostats constant at approximately 89.3 K.
- maintaining the purity of liquid argon well below 2 ppm (volume) of oxygen equivalent.
- allow the movement of the end-caps for access to the inner detector and to the barrel front-end electronics.
- provide reliable service during the data taking periods.
- keep a clean environment in and out of the cryostats.
- comply with CERN safety rules.

This chapter describes the main characteristics of this installation, beginning with the parameters of the cryostats and detectors relevant for cryogenic aspects. It has been established with reference to the documents [3-1] to [3-4].

3.1.1 Masses and volumes of the cryostats and detectors

The capacity of the vessels, their weights, and the weights of the detectors are listed in Table 3-1.

3.1.1.1 Solenoid

Figure 3-1 gives the dimensions of the solenoid.
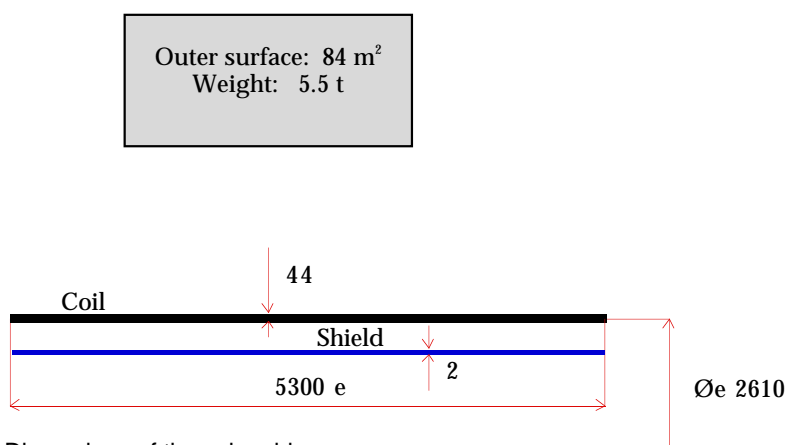
Figure 3-1 Dimensions of the solenoid.

Table 3-1 Main parameters.

Cryostats	Barrel	End-cap
Volumes (m³)		
Cold vessel	58	43
Expansion vessel	5	2
Liquid argon	45	19
Insulating vacuum	26	6
Weight (t)		
Cold vessel	12	14
Detector	110	219
Vacuum vessel	13	9.5
Solenoid	5.5	
Full cryostat	203	269
Surface areas (m²)		
Cold vessel	160	80
Solenoid	85	

Table 3-2 Barrel detector masses and heat capacity between 300 and 80 K.

Barrel	G10 & Kaptons	Cu	Pb	304	Total
Density (ton/m³)	1.7	9.0	11.7	7.9	
Weight of detector (t)	14	5.0	71.0	20.0	110
ΔH (J/g)	135.4	79.6	26.2	84.3	
Heat capacity (MJ)	1896	398	1860	1686	5840
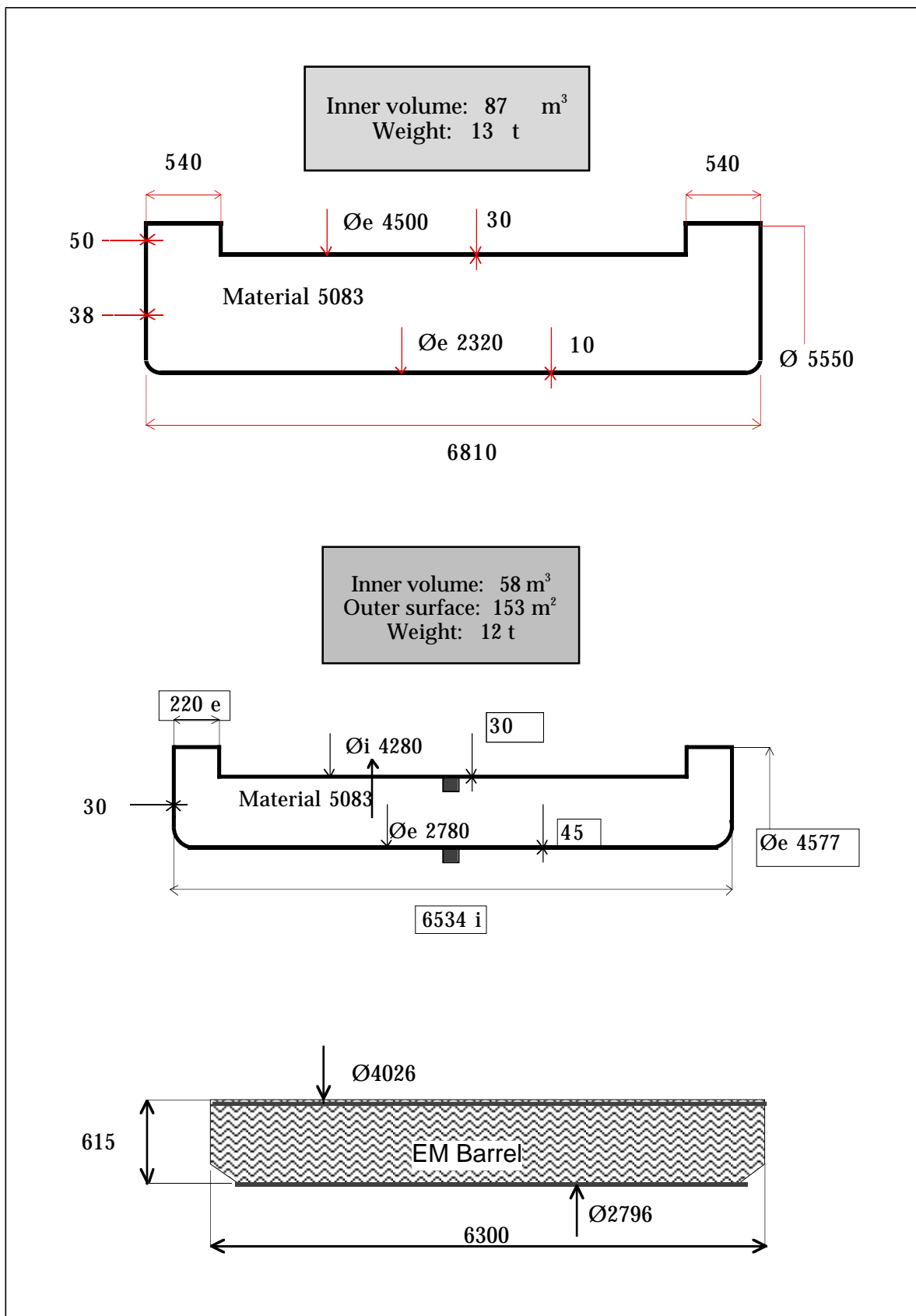
The heat capacity of the cryostat itself is $\approx$ 1900 MJ

3.1.1.2 Barrel elements
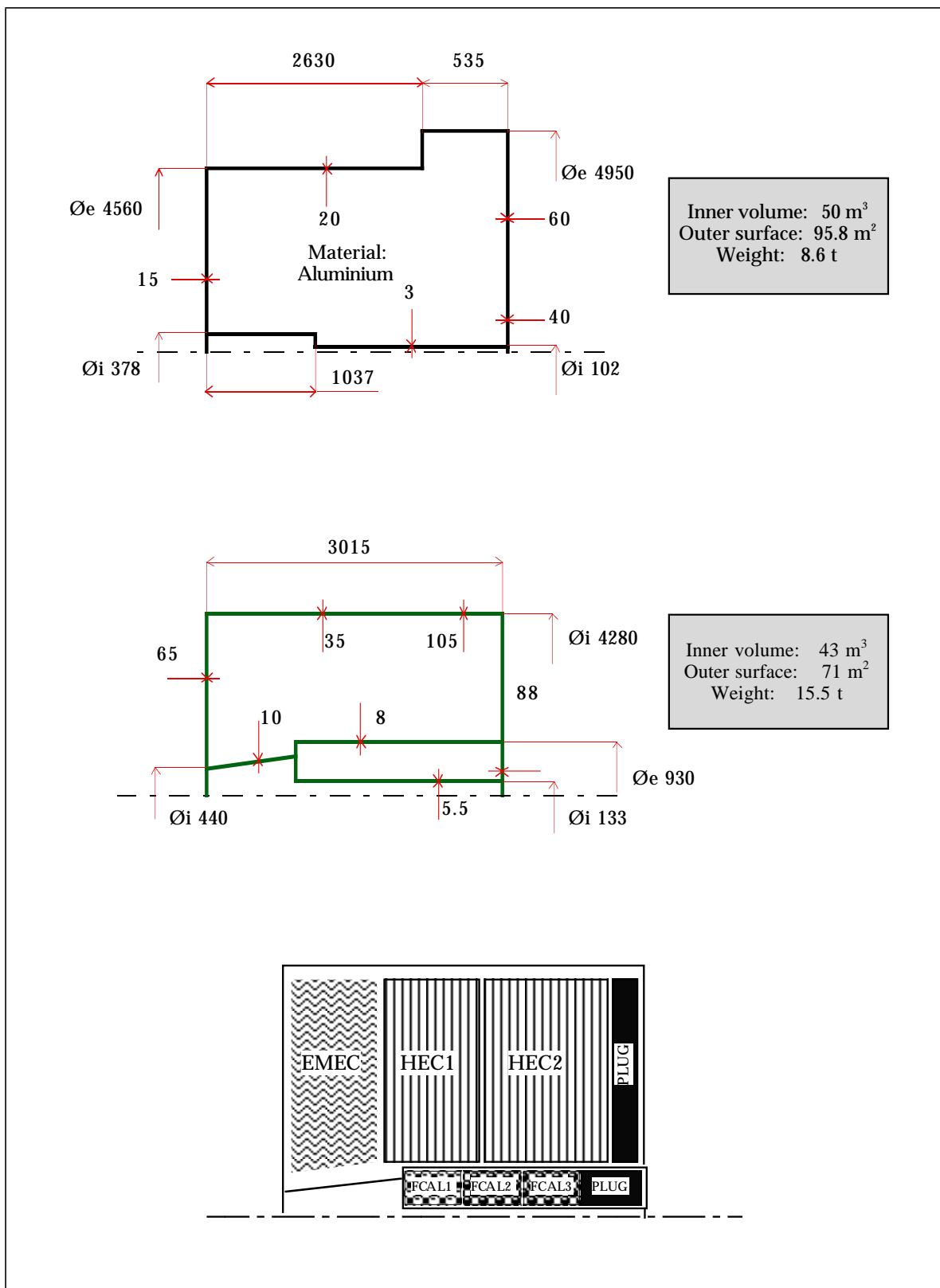
The overall dimensions of the warm and cold vessels are displayed in Figure 3-2. The overall weight of the em barrel and the fraction by weight of its main components are given in Table 3-2 which also shows how the heat capacity is distributed.

3.1.1.3 End-cap elements

Figure 3-3 shows the dimensions of the end-cap warm and cold vessels, as well as the end-cap detector layout. The detector weights are given in Table 3-3.

Inner volume: 87 m³
Weight: 13 t

540   540

50

Øe 4500   30

Material 5083

38

Øe 2320   10

Ø 5550

6810

Inner volume: 58 m³
Outer surface: 153 m²
Weight: 12 t

220 e

Øi 4280   30

30   Material 5083

Øe 2780   45

Øe 4577

6534 i

Ø4026

615   EM Barrel

Ø2796

6300

Figure 3-2 Dimensions of the barrel warm vessel (top), barrel cold vessel (middle), and barrel detector (bottom).

Figure 3-3 Dimensions of the end-cap warm vessel (top) and cold vessel (middle). The end-cap detector layout is shown at the bottom.

Table 3-3 End-cap detector masses and heat capacity between 300 and 80 K.

End-cap	G10 & Kapton	Cu	Pb	W	Al	304	Total
Density (ton/m^3)	1.7	8.9	11.7	19.1	2.7	7.9	
Mass of FCAL1 (t)		2.8					2.8
Mass of FCAL2 (t)				4.0			4.0
Mass of FACL3 (t)				4.0			4.0
Mass of FW plug (t)		2.5					2.5
Mass of EMEC (t)	1.4	0.7	18.3		0.7	3.1	24.2
Mass of HEC 1 (t)	1.2	67				1.2	69.4
Mass of HEC 2 (t)	0.8	90				1.4	92.2
Mass of plug (t)		19.5					19.5
Mass of detector (t)	3.4	182.5	18.3	8.0	0.7	5.7	218.6
ΔH (J/g)	135.4	79.6	26.2	32.1	161	84.3	
Heat capacity (MJ)	460	14 527	479	257	113	481	16317
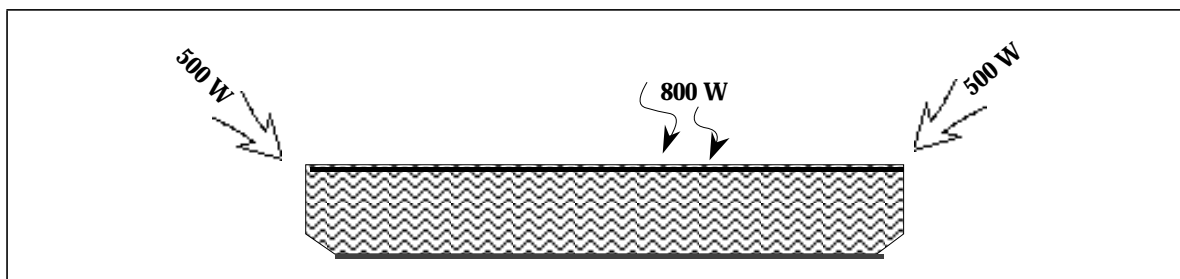
The heat capacity of the cryostat itself is $\approx$ 2200 MJ

3.1.2 Heat leaks

The heat leaks into the barrel come mainly through the external surfaces, by radiation across the vacuum insulation, and by conduction along the cables and bellows of the feedthroughs which are located at each end of the cryostat. They are listed in Table 3-4. In total this cryostat receives 2x500 W from the feedthroughs and cables at the two ends, while 800 W are transmitted through the multi-layer superinsulation and the suspension (see Figure 3-4).

For the end-caps (see Figure 3-5 and Table 3-4), the situation is different, due primarily to the presence of the preamplifiers and summing amplifiers of the hadronic end-cap detectors which contribute about 1.25 kW per cryostat. The part resulting from radiation and conduction (700 W) is also important due to the supporting of the detector on GFRP (Glass Fibre Reinforced Plastic) pads, and the use of spacers to transmit pressure forces between the warm and cold bulkheads. The contribution from the feedthroughs is smaller than for the barrel, in proportion to their respective number.

Including all of the installation in the cavern, and the "internal" and "proximity" cryogenics (see next section), the total estimated heat load on the system is 12 kW (see Table 3-5). Given these numbers, the liquifier should have a minimum production capacity of 20 kW, which is equivalent to a production of 12,000 litres a day.
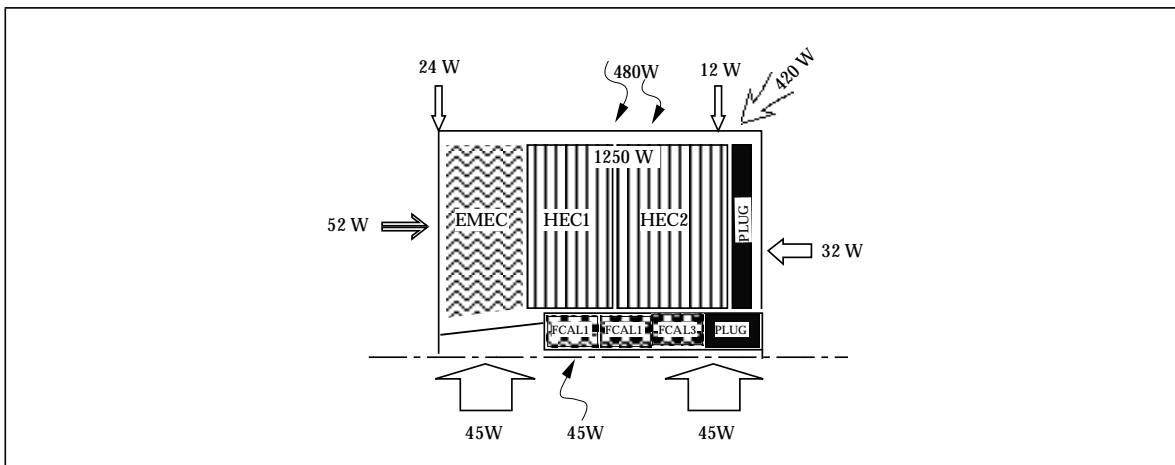
Figure 3-4 Barrel heat leaks.

Table 3-4 Heat leaks in barrel and end-cap cryostats.

Reference	Barrel				End-cap		
	P (W)	Quantity	s/s total			P (W)	Quantity	s/s total
Supports							
Suspensions	7.5	4	30	Axial rails	45	2	90
Axial and longitudinal				Bulkhead spacers	1	84	84
Stoppers	1.4	6	8	Stoppers and axial guides	6	6	36
s/s total			**38**				**210**
Radiation							
Superinsulation	6 (m^{-2})	120	720	Superinsulation	6 (m^{-2})	80	480
s/s total cryostats			**796**				**690**
Feedthroughs							
Cables	11.5	64	736	Cables	11.5	28	322
Bellows	3.5	64	224	Bellows	3.5	28	98
s/s total feedthroughs			**960**				**420**
Detector and Electronics							
Presampler			0	EMEC			0
S1			0	HEC			1250
S23			0	FCAL			45
s/s total electronics			**0**				**1250**
Total			**1756**				**2405**

3.1.3 Temperature stability requirements. Subcooling

Maintaining the temperature of the liquid in the active parts of the calorimeters uniform and stable with time is an extremely important goal, since temperature variations directly affect energy measurements (see Chapter 1, Section 1.9.3).

Figure 3-5 End-cap heat leaks.

Table 3-5 Thermal balance.

Heat Input (kW)	Barrel	End-cap
Normal working conditions[a]		
Cables	1	0.5
Preamps		1.3
Radiation and conduction	1	0.7
s/total	2	2.5
total cryostat	7	
Cryolines	2	
Dewars, valves	2	
Pumps	1	
Total heat load	12	
Vacuum breakdown	140	25

a. 1 kW $\Rightarrow$ 5.25 g/s or 24.4 l/h LN_2 @ 2.1 bars abs.
    20 kW $\Rightarrow$ 11,700 l/j

The proposed system is based on the use of subcooled liquid argon. For safety reasons (see below) each cryostat is connected by a large (and long) horizontal pipe to an overflow vessel. The gas pressure above the liquid surface in the overflow vessels will be regulated to typically 1.25 bar using a LN_2 heat exchanger. The associated temperature of the liquid argon close to the surface is 89.3 K (see Table 3-6). Thermally speaking the overflow vessel is essentially isolated from the liquid baths in each of the three main cryostats. LN_2 cooling loops, installed in each cryostat will be used to compensate the heat leaks, and to maintain the baths at the same temperature as on the surface. This is (see Figure 3-7)) between 3 to 7 K below the equilibrium temperature of liquid argon at the top or bottom of the cryostat.
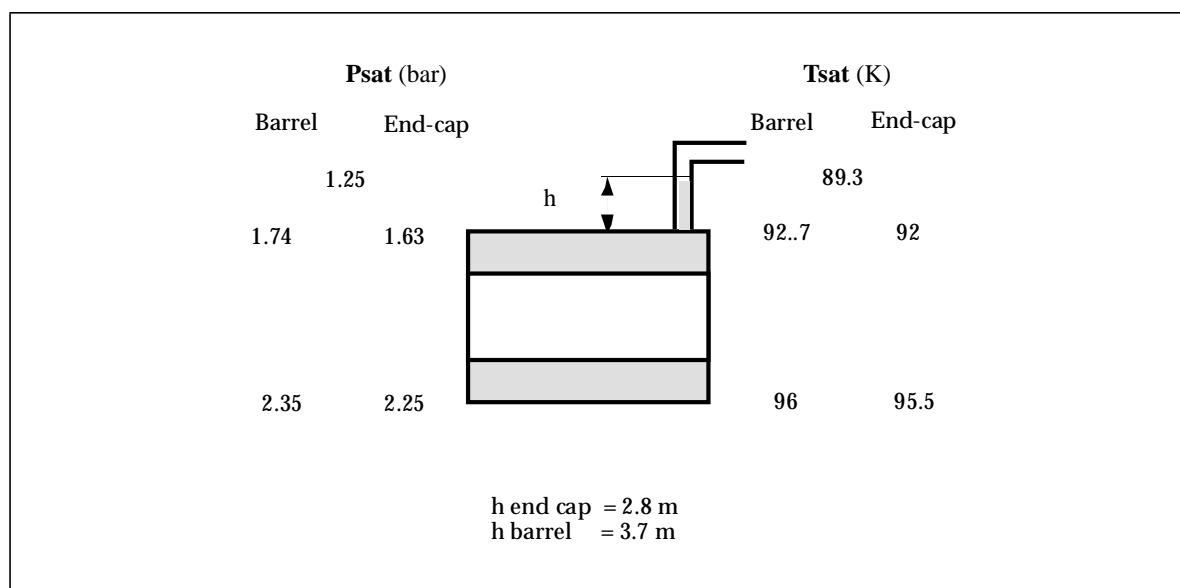
The temperature of the subcooled volume can be lowered down to 87.3K, which is the minimum to avoid the freezing of liquid argon in the region of the heat exchangers.

Table 3-6 Properties of liquid argon.

Temperature and Pressure of LAr	
Normal working temperature	89.3 K
Pressure of saturated vapour	1.25 bar abs.
Density	1381 kg/m^3
Set point of safety device	1.7 bar abs.

The minimum working temperature is 87.3 K.

Detailed calculations of the temperature maps in each cryostat, taking proper account of the heat leaks and of the parameters (position, temperature) of the cooling loops have not yet been done (for the end-caps results are expected in the first half of 1997). For the time being, we give ourselves the conservative target of 0.66 K between any two points in the sensitive volume, at any time during operation. Ultimately, our aim is to achieve a factor of two better than this, in order to be able to satisfy the requirements on the constant term in energy measurements without correction (see Chapter 1)

Figure 3-6 Diagram of saturated pressure and temperature on the cryostats.

3.1.4 List of situations[1]. Pressure for calculations

In order to design a complete and satisfactory cryogenics system and the associated vacuum system, the list of all possible situations of the major elements of the installation was established. From this list we extracted the more demanding situations in terms of stress on the cryostats. These were used for calculating the vessel parameters (see Chapters 4 and 5).

---

1. Situation: Term defined within the CODAP which means all possible combinations of stresses simultaneously exerted at any given moment on a pressure vessel.

Table 3-7 Phase parameters of the cold vessel.

Phase	Process	P_0 (bar abs.)	P_h (bar abs.)	P_b (bar abs.)	T (K)	Comments
EF1	FLUSHING warm					Normal situation
	pumping	0	0	0	300	
	pressurization	1	1	1	300	Gas: air, Ar, He
EF2	COOLING DOWN					Normal situation
	start-end	1.5	1.5	1.5	300-100	He circulation
EF3	FLUSHING COLD					Normal situation
	pumping	0	0	0	100	
	pressurization	1	1	1	100	Gas: Ar, He
EF4	LAr FILLING					Normal situation
	start barrel	1.3	1.3	1.3	89.3	height LAr = 0 m
	end barrel	1.3	1.8	2.4	89.3	height LAr = 7.98 m
	start end-cap	1.3	1.3	1.3	89.3	height LAr = 0 m
	end end-cap	1.3	1.7	2.3	89.3	height LAr = 7.08 m
EF5	RUNNING					
	Barrel	1.25	1.75	2.35	89.3	
	End-cap	1.25	1.65	2.25	89.3	
EF6	EMPTYING					Normal situation
	start barrel	1.5	2.0	2.6	89.3	
	end barrel	1.5	1.5	1.5	100	
	start end-cap	1.5	1.9	2.5	89.3	
	end end-cap	1.5	1.5	1.5	100	
EF7	WARMING-UP					Normal situation
	start-end	1.5	1.5	1.5	100-300	He circulation
EF8	COOLING FAILURE					**Exceptional situation**
	Barrel	1.7	2.2	2.8	89.3	
	End-cap	1.7	2.1	2.7	89.3	
	VACUUM FAILURE					**Exceptional situation**
	Barrel	1.7	2.6	3.2	89.3	
	End-cap	1.7	2.5	3.1	89.3	
EF9	LEAK TEST	0	0	0	300	**Exceptional situation**

In general, the total pressure calculation is the sum of three terms (see Figure 3-7):

- set pressure of the safety valve: P_o
- static head pressure: $\rho g \Delta h$.

Table 3-8 Phase parameters of the vacuum vessel.

Phase	Process	P_{ev} bar abs.	T (K)	Comments
EC1	Evacuation	1 to 0	300	Normal situation
EC2	Vacuum failure	1.3	300	Exceptional situation

Table 3-9 Maximum pressure in normal[a] situation (bar).

Normal[a]	Barrel	End-cap
P_0	1.7	1.7
P_h	2.2	2.1
P_b	2.8	2.7

a. These values are calculated, assuming that the argon gas flow in the exhaust chimney to the surface is warm.

Table 3-10 Estimated values of pressure in exceptional[a] situations (bar).

Normal	Barrel	End-cap
P_0	1.7	1.7
P_h	2.6	2.5
P_b	3.2	3.1
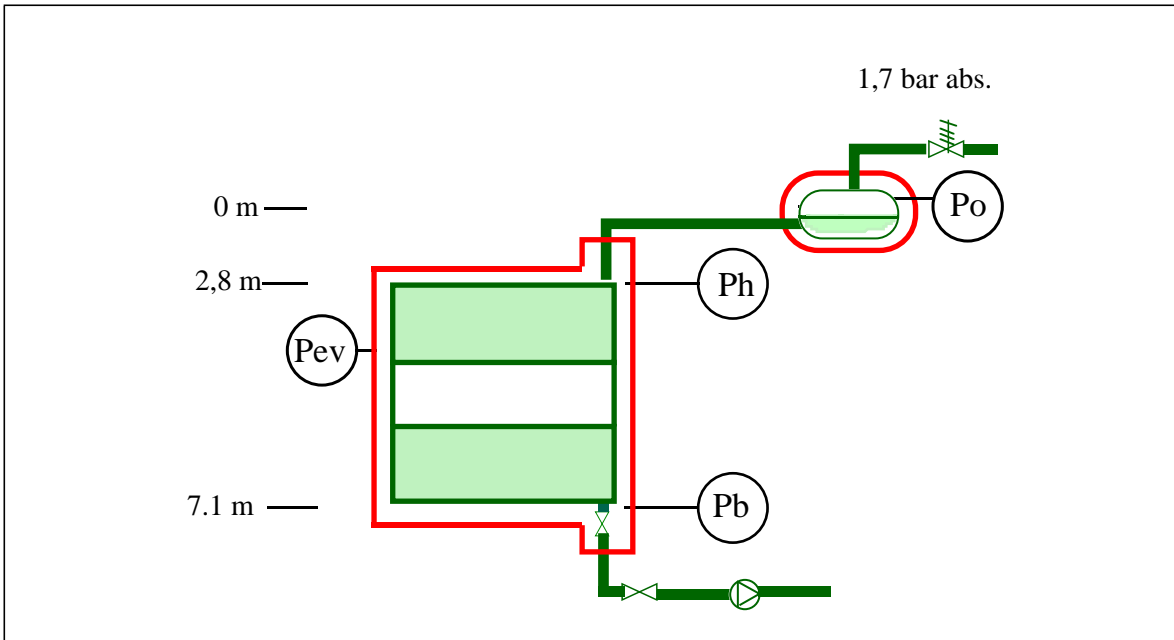
a. The pressure drop $(\Sigma\xi+\lambda L/D)rV^2/2$ in the safety pipe has been estimated at 400 mb for both cryostats.

- drop of pressure in the piping: $(\Sigma\xi+\lambda L/D)\,\rho V^2/2$

$$P_c = P_o + \rho g \Delta h + (\Sigma\xi+\lambda L/D)\rho V^2/2$$

P_0 and the static head pressure are shown in Figures 3-6 and 3-7, and the drop of pressure in the piping in Section 3.2.1.3. Maximum pressures in normal and exceptional situations are given in Tables 3-9 and 3-10.The numbers corresponding to the normal situation are relative to situation EF5 to EF6 (see Table 3-7 and Table 3-8). In exceptional conditions, the worst case would correspond to the breakdown of the isolation vacuum (EF8). In this case the pressure drop in the pipe connecting the cryostat to the overflow vessel is calculated with liquid in it, and corresponds to a sizeable contribution. The presence of liquid in the safety line results from the fact that under the large heat influx coming from the isolation vacuum breakdown an important quantity of liquid argon vaporizes and pushes the liquid upwards, at least in a transient phase. The safety lines were actually designed to limit the pressure rise to less than 0.4 bar (see Section 3.2 below).

In designing the cryostats (see Chapters 4 and 5) one has to take into account the fact that the safety factor is smaller for exceptional situations than for normal ones ($0.95\ R_{0.2}$ instead of $R_{0.2}/1.6$ for the aluminium alloy according to CODAP rules).

Figure 3-7 Diagram of pressure in the installation.

3.2 Layout and technical description of the cryogenic elements

In order to minimize the distance between the cryostats and the more important cryogenic elements, these elements have been situated in the main cavern, and constitute the so-called "proximity cryogenics". In Figure 3-i one can see that most of these elements are arranged along the cavern wall (cryo-lines), on the floor (storage tanks) or on the outer framework of the detector (valve boxes, overflow vessels). The figure also shows the end-cap flexible lines and their storage area on the framework platform.

Given the different locations and functions, the cryogenics and vacuum plant has been separated into four main parts:

1. "Internal cryogenics" elements, which are integrated into the cryostats, i.e. heat exchangers, the temperature monitors, the pressure monitors, the level monitors, the overflow vessels and the safety cryo-lines.

2. "Proximity cryogenics" directly connected to the cryostats, i.e. the argon and the nitrogen cryo-lines, the valve cold boxes, the liquid argon pumps, liquid argon storage tanks, and the cooling-down and warming-up unit.

3. "External cryogenics" which can be considered as external services, i.e. the liquid nitrogen liquefier, the liquid nitrogen storage tanks, the liquid nitrogen circulators, the cryo-lines from the surface to the cavern, the computer for control. These are actually part of the ATLAS services, in terms of PBS.

4. Vacuum system

3.2.1 Internal cryogenics

3.2.1.1 Heat exchangers

The refrigeration fluid should be a boiling liquid in order to have a two-phase flow in the heat exchanger and a quasi-uniform temperature along the exchanger. In these conditions only the vaporization heat of the fluid is being used.

Liquid nitrogen will be used as refrigeration fluid because of its thermodynamic properties which fit well our needs. Another possibility would be the use of liquid argon at low pressure.

The temperature inside the liquid nitrogen heat exchangers is fixed at 87.3 K (85.3 K min.) whereas the temperature of the bath is set at 89.3 K. In this case the pressure of the liquid nitrogen is about 2.8 bars abs. (2.4 min.) at the inlet of the heat exchanger (Figure 3-8).
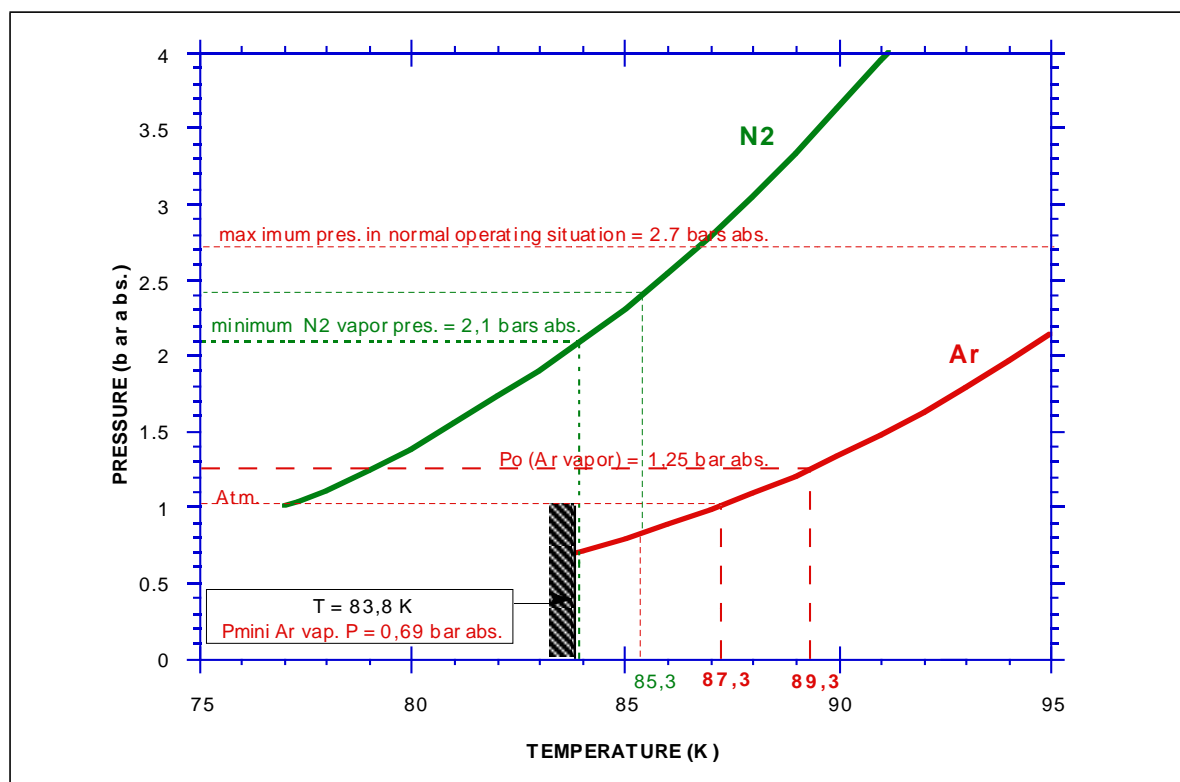
Figure 3-8 Heat exchanger LN_2/LAr, pressure and temperature diagram.

• Barrel heat exchangers

The heat leak zones are distributed mainly over the outer contours of the barrel calorimeter (Figure 1-8 and Chapter 6, Figure 6.29). The inner cold shell does not receive any radiation heat because of the presence of the solenoid (actually about 5 W are radiated towards the solenoid). In order to avoid wasting precious radial space with heat exchangers attached to the cylindrical part of the outer cold wall, we have chosen to integrate them into the calorimeter modules, given that there is some free space existing within the radial occupancy of their support rings (see Chapter 6). Given the configuration of the calorimeter (split into two 3.2 m long halves), for assembly reasons, the exchangers must be symmetrically arranged on each side (A and C). Two heat exchangers, each with a cooling capacity of 2500 W will be integrated into each half-barrel

calorimeter, one at the upper part the other at the lower part (i.e. four independent exchangers in total for the barrel).

These are built of pin-fin type tubes with a diameter of 22 mm, and a total length of 56 m for each one. Details of their layout in the barrel calorimeter modules are given in Chapter 6.

Studies are being carried out to check the possibility of removing the lower heat exchangers, which are actually not very efficient, and in turn installing two other exchangers close to the feedthroughs in order to compensate the 2 x 500 W heat leaks coming from the cables. These exchangers would be arranged in two loops at a diameter of about 4200 mm.

- End-cap heat exchangers

Unlike the barrel, the end-caps contain detectors, the hadronic wheels, which are equipped with cold preamplifiers dissipating about 1.25 kW in each cryostat (Figure 3-5). However, like for the other heat sources, the preamplifiers heat is produced mainly close to the cryostat walls thus requiring cooling loops located next to the walls. Given the layout of the detectors, coming in separate wheels, it was not felt practical to integrate the heat exchangers into the modules, as for the barrel. Therefore, two heat exchangers with a cooling capacity of 2500 W each will be fixed on the cold shell, one on the upper part and one on the lower part for each end-cap. The same type of tube as for the barrel is being used. The layout of this exchanger is described in Chapter 5.

3.2.1.2 Overflow vessels

The overflow vessels are installed on the second level platform at levels defined in Figure 3-7. The connection to the main cryostat is made with flexible cryo-lines for the end-caps and with rigid cryo-lines for the barrel, which does not have to move. A view of the barrel overflow vessel is shown in Figure 3-9.

To fulfil CODAP regulations, the size of the overflow vessels was calculated taking into consideration the following parameters:

1. expansion of the liquid from 89.3 K @ 1.25 bar abs. to 94.2 K @ 2 bars abs: 2.3%.

2. construction rules: volume occupied by gas > 5% of the main vessel volume.

3. average level of liquid for level and pressure control: 15%
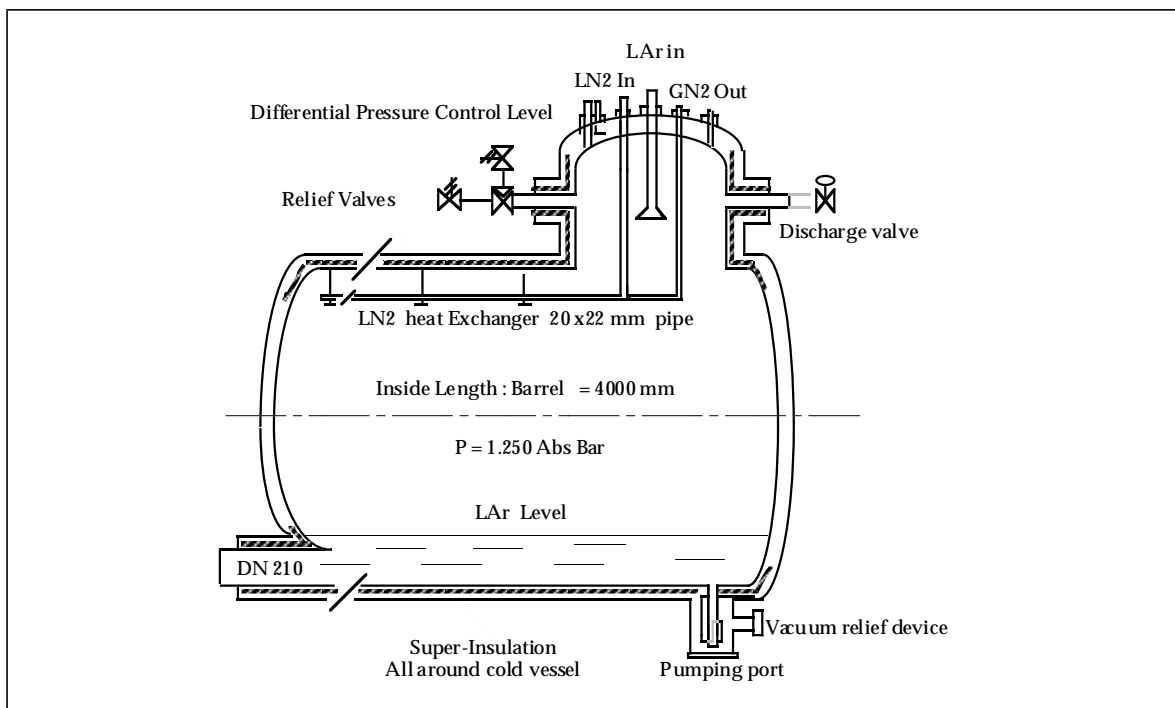
The calculated volumes are 2.53 m^3 for the barrel and 1.09 m^3 for the end-caps. The adopted volumes are respectively 4 and 2 m^3.

The overflow vessels are protected against over pressure by cryogenic-type safety valves.

3.2.1.3 Overflow lines

The calculation of the pressure drop through these lines is necessary to determine the total pressure in the barrel and end-cap cryostats. The dimensioning of these lines should not give too high a pressure drop (Figure 3-6).

For this calculation, we suppose we are in exceptional conditions, i.e. we have to face a vacuum insulation failure of the barrel or end-cap cryostats. Due to a leak of gas in the vacuum volume (helium for the barrel and air for the end-cap in the worst case), we have a heat leak which warms up the calorimeter until P_0 reaches 1.7 bar abs. (opening pressure of the safety valves in the overflow vessels). This heat leak vaporizes a large quantity of liquid argon and creates an

Figure 3-9 View of the overflow vessel.

equivalent liquid flow (in volume) in the overflow lines between the cryostats and the overflow vessels, see Table 3-11 and 3-12.

The heat flux of 925 W/m^2 and 250 W/m^2 respectively with helium and air break-down of the vacuum have been measured on NRC 2 multilayer superinsulation.

Table 3-11 Properties of liquid argon @1.7 bar abs.

Reference	Unit	Value
Temperature	K	92.5
Pressure	bar abs.	1.7
Liquid density (ρ)	kg/m^3	1360
Gas density	kg/m^3	9.3
Vaporization heat	J/kg	160 000
Viscosity	Pa.s	2.2 x 10^{-4}

3.2.1.4 Temperature, pressure and level monitoring

For the three cryostats, and for each heat exchanger, the temperature control will be achieved by means of eight temperature sensors, arranged as follows:
- two in contact with the heat exchanger (at the middle position on each side).
- six in the liquid, on the top and the bottom for each side, and for each end of the heat exchanger.

Table 3-12 Characteristics and results for the safety lines.

Reference	Unit	Barrel	End-cap
Heat flux	W/m^2	925	250
Heat capacity	kW	141.5	17.8
Liquid mass flow	kg/s	132	16.5
Velocity (v)	m/s	2.69	0.690
Total length (L)	m	17.3	32.9
Nominal diameter (D)	m	0.214	0.150
Pressure drop	mbar	215[a]	66.0[a]

a. One should add to these values the pressure drop and the static head in the chimney.
We have estimated this ΔP to be 400 mbar maximum.

This makes a total number of temperature sensors for the barrel of 8x4 = 32, and for each end-cap of 8x2 = 16.

The level control will be achieved by means of two level sensors on each overflow vessel (one capacitance and one differential pressure level control).

The pressure control of the three cryostats will be achieved by means of pressure transmitters at the top and the bottom of the cryosats.

3.2.2 The "proximity cryogenics"

3.2.2.1 Cooling down and warming up unit

The proposed system is a force flow cooling unit consisting of a circulator with its cooler, a dryer, an aluminium fin-plate heat exchanger, and an electrical heater. This unit is coupled to a vacuum pump for cleaning the system at the start and the end of operation.

The circulated gas is cooled outside the cryostats by means of an external LN$_2$ heat exchanger with a controlled and adjustable temperature difference between the inlet and the outlet of the cryostat. This system gives the possibility of removing water and other impurities contained in the detector components. These impurities will be trapped in the dryer and on the heat exchanger cold end.

Helium will be used as convecting gas, with a flow of typically 1200 m^3/h. It has the advantage of not being condensable at the temperature at which it will be used and has a good ρCp^2 factor (see Table 3-13), thus minimizing the pressure drop in the cryostat. The pressure drop is limited to 0.5 bar, corresponding to the safety valve set-up pressure, i.e. 1.7 bar.

A duration of about two weeks has been estimated for cooling or reheating one end-cap calorimeter, assuming a temperature difference of 40 K between the inlet and the outlet of the cryostat and a power of about 10 kW at 77 K. For the barrel, where the mass is lower, this will be faster.

Table 3-13 Cooling gas parameters, for T=300 K and P=1.5 bar.

Gas	ρ (kg/m^3)	C_p(J/kg/K)	$\rho.C_p^2$(SI)
Helium	0.24	5193	6.5 10^6
Argon	2.4	522.7	6.6 10^5
Nitrogen	1.7	1042	1.8 10^6

3.2.2.2 Cryo-lines

There are different types of cryo-lines in the cryogenic system:

- The liquid argon overflow lines which link the three cryostats to the overflow vessels. These lines are described in Section 3.2.1.3.

- The liquid argon and nitrogen lines for the cryogenic services.

All the cryo-lines in the cavern are multi-layer insulated, vacuum sealed, and the standard material for their fabrication is austenitic stainless steel.

Aluminium foil, non-woven glass spacer, multi layer insulation is preferred and gives the possibility of outgasing at high temperature during the initial pumping-down.

The major part of the cryo-lines is of a rigid type, while the connections between the end-cap, the valve cold box and the overflow vessel are of a flexible type to enable the movement of the cryostats during the access periods.

The dimensions and number of cryo-lines are given in Table 3-14.

Table 3-14 Dimensions and number of cryo-lines.

Reference	Quantity	Fluid	Nominal diameter	OD (mm)
BARREL				
Heat exchanger supply	4	LN$_2$	15	88.9
Heat exchanger return	4	GN$_2$	32	114.3
Emptying	1	LAr	80	168.3
Overflow	1	LAr/GAr	210	323.9
END-CAP (each)				
Heat exchanger supply	2	LN$_2$	20	113[a]
Heat exchanger return	2	GN$_2$	40	163[a]
Emptying	1	LAr	80	168.3
Overflow	1	LAr/GAr	150	363. [a]

a. Flexible lines.

3.2.2.3 Liquid nitrogen distribution

- Cooling loops

The distribution of liquid nitrogen is made from a 15,000 litres storage tank pressurized at the low pressure of the liquefier.

The pressure is raised to an adjustable value between 2.1 and 3 bar, by using a cold circulator of the immersed type.

The liquid nitrogen is then transferred to the three valve boxes where it is distributed through the inlet valves to each heat exchanger on the cryostats. The temperature control is made with outlet valves for each heat exchanger. The two-phase flow with a quality factor of ≈ 0.1 (10% of liquid) is returned to the liquid nitrogen storage tank where the two phases separate, the cold gas going through the liquefier low pressure exchange line and the liquid staying in the storage tank.

- Valve boxes

The control valves and stop valves for the distribution of liquid nitrogen are installed in three vacuum insulated valve boxes, Figure 3-10.
This prevents the production of moisture and ice and allows a better organization of the pipe work. The lower shell of the vessel is removable from the bottom and gives full access to the piping and the valves in case of maintenance.
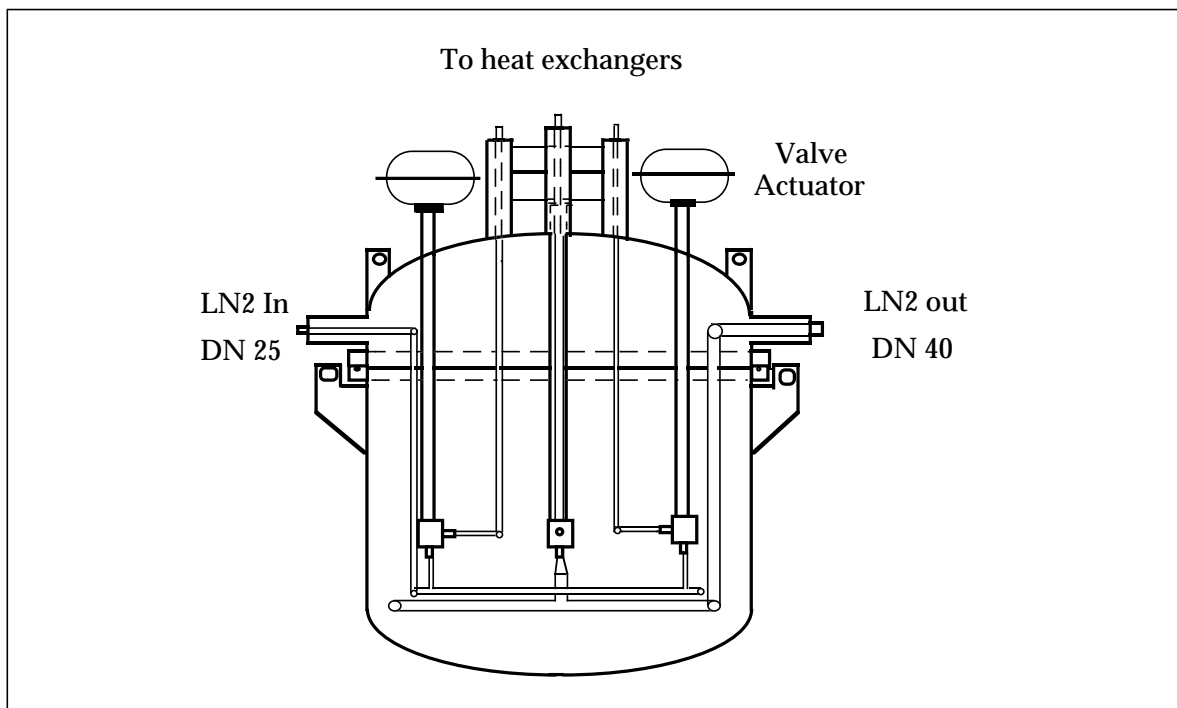
Figure 3-10 Valve box.

3.2.2.4 Liquid argon storage

Liquid argon storage tanks are installed close to the cryostats in a retention pit. The capacity of each vessel is 50,000 litres. One is used for the storage of the 44,000 litres of the barrel, the other for the $2 \times 19,000$ litres of the end-caps.

Each vessel is equipped with a liquid nitrogen cooler with a capacity of 5000 W to keep the gas at constant pressure and re-condense the gas vaporized during the cooling of cryostats, cryo-lines and the tank itself.

The construction of the tanks will be of the same type as standard custom cryogenic vessels, power and vacuum insulated. They will be equipped with a pressurizer and one of the two with a vaporizer to produce pure argon gas for flushing the whole installation.

The feet of the tanks are made of austenitic stainless steel to ensure mechanical stability in the case the retention pit is swamped by a liquid argon spill.

3.2.2.5 Circulators and pumps

Cold circulators and pumps used for the transfer of liquid are immersed in a cold box and completely isolated from the ambient air. For the liquid nitrogen circulators the control of pressure is obtained by a variable speed driving motor.

The pumps chosen for emptying the cryostats have a flow rate of 20 m^3/h which allows emptying the barrel (end-cap) cryostat in 2.5 (1.5) h. All pumps and circulators except the emptying pump for the transfer of liquid argon to the surface are duplicated for reliability and maintenance reasons.

3.2.3 The "external cryogenics"

The purpose of the external cryogenics is to provide the necessary infrastructure and associated equipment for the cool-down and the normal baseline running of the three LAr cryostats. The cooling agent is liquid nitrogen. The general flow diagram is displayed in Figure 3-ii.

The equipment is installed partly at the surface (inside and outside the SH building), and partly in the USA15 side cavern and in the main pit. Connections between the various elements pass through the access shafts PXA16 and PX15, and along the cryogenic side gallery. Depending on the fluid to be transferred connections are made via vacuum-insulated transfer lines and/or piping at ambient temperature.

The main parts of the equipment are outlined below:

At the surface:

- Two LN$_2$ dewars with a total storage capacity of 100 m^3 of liquid.

(These dewars are shared with the external cryogenics for the superconducting magnets. They are installed outside the SH building)

-LN$_2$ transfer line which permits the transfer of liquid to the main pit via the PX16 shaft.

-Filling station for truck delivery of LAr and an associated transfer line making the connection to the LAr dewars in the main pit.

-Compressor unit for the nitrogen refrigeration cycle. (The associated cold box will be installed in the underground area.)

In the underground area:

-The cold box for the nitrogen refrigeration cycle with a cooling capacity of 20 kW (current design value) is foreseen to be installed at the USA15 side cavern. (However, if possible, we would prefer the installation in the main pit close to the LN_2 intermediate storage dewar)

-LN_2 dewar with 15 m^3 capacity installed in the main pit, adjacent to the two LAr dewars.

-LN_2 phase separator and pressure reduction system for the transfer of liquid from the surface.

-Two LN_2 circulators (one for redundancy) to provide the required over pressure for coolant flow to the internal LN_2 heat exchangers of the three calorimeters.

-Transfer lines to the LN_2 distribution valve box.

3.2.4 Vacuum system

The following section describes the main characteristics of the vacuum system needed to operate the detectors and the associated equipment. A distinction is made between the "isolation vacuum" in between cold and warm vessels, for which the vacuum must be good and essentially permanent, and the inner part of the cryostat cold vessels for which pumping is to take place during the setting-up phase, or after warming up. In this latter case the vacuum can never be "good", taking into account the outgasing from the calorimeters elements. In the rest of this chapter, this is referred to as "purging".

3.2.4.1 Vacuum vessels

The volumes to be pumped down, and the proposed pumps, are given in Table 3-15. The vacuum aimed at, before the cool-down of the cold vessels, is 10^{-2} Pa or better.

The vacuum stations of the three cryostats will have to work in a non-negligible magnetic field (~ 0.1 Tesla), forbidding the use of turbomolecular devices. Instead diffusion pumps have been selected, although they require more maintenance. In this context one should note that the diffusion pump for the barrel shall be switched off as soon as the solenoid is at liquid helium temperature.

Table 3-15 Vacuum isolation.

Cryostats	Volume (m^3)	Vacuum	Pump 1	Pump 2	Pump 3
Barrel	26	Dynamic	Diffusion	Roots[a]	Rotary
End-cap	6	Dynamic	Diffusion	Roots[a]	Rotary
Overflow vessels	1	Dynamic	Turbo		Diaphragm
Valve boxes	2.5	Dynamic	Turbo		Diaphragm
Cryo-lines		Sealed			

a. used only for prepumping.

3.2.4.2 Purging

For purging, the most important criterion is a high pumping speed, at a modest vacuum in between 100 and 1 Pa. The proposed pumps are shown in Table 3-16.

Table 3-16 Purging

Purging systems	Volumes (m³)	Pump 1	Pump 2
Barrel	45		
End-cap	19	Roots	Rotary
Overflow vessels	10.5	1000 m³/h	500 m³/h
Valve boxes	5		

3.2.4.3 Barrel vacuum stations.

Two vacuum stations will be installed on this cryostat (see Figure 3-11). The purging system (station I below) is common to the three cryostats, which can be purged in sequence.

Vacuum station I:

- 1 Electropneumatic valve   DN 200
- 1 Diffusion pump 2000 l/s   DN 200
- 1 Roots pump 1000 m³/h   DN 160/100
- 1 Rotary pump 120 m³/h   DN 100

Vacuum station II:

- 1 Electropneumatic valve   DN 200
- 1 Diffusion pump 2000 l/s   DN 200
- 1 Rotary pump 65 m³/h   DN 63

3.2.4.4 End-cap stations

Each of them is identical to the barrel vacuum station II (see above).

3.2.4.5 Overflow vessels

- 1 Electropneumatic valve DN 100
- 1 Turbomolecular drag pump (300 l/s, DN 100 for the barrel, 210 l/s, DN 100 for each end-cap
- 1 Diaphragm primary pump.

3.2.4.6 Integrated primary pumping stations

An alternative solution which integrates all of the vacuum systems of the ATLAS experiment into a single system is currently being worked out.
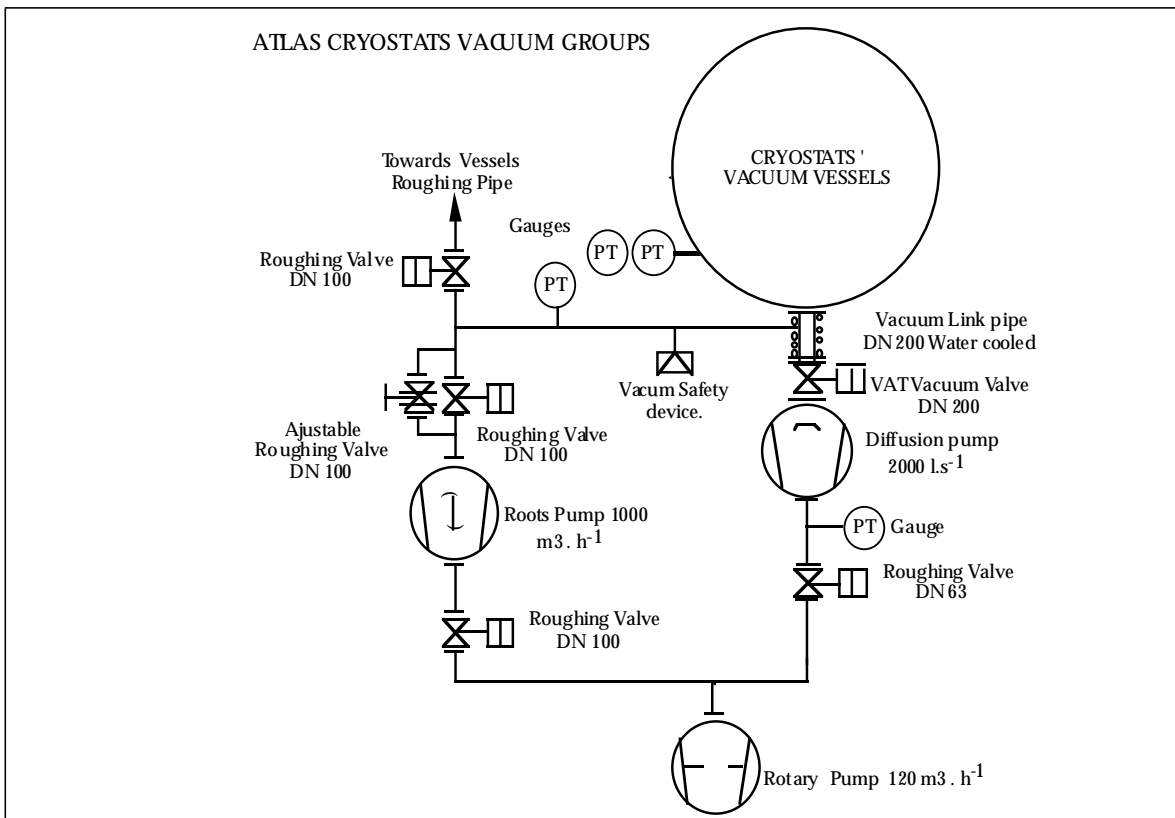
Figure 3-11   Principle of the barrel vacuum group.

3.3 Operating chart

The general flow diagram in Figure 3-ii shows the arrangement of the main components of the installation and the cryo-lines plumbing. The detailed plumbing of the different components is not always represented.

3.3.1 Storage-tank filling, flushing and purging

LN_2 tank filling: The filling of the 15 m^3 storage tank is done through a phase separator. The sequence of operations is purging and flushing of the lines, circulation of N_2 until the temperature of the tank is stabilized and then filling of the tank. The temperature inside the tank is maintained by circulating and condensing the gas using the liquefier unit.

LAr filling: To prepare the filling of the two 50 m^3 storage tanks for the end-caps and the barrel, all the lines circulating Ar are flushed. The vacuum group #201 near the cooling system is used for this operation. The liquid argon delivered from the surface goes through a pressure control valve to decrease the hydrostatic pressure. It is then transferred to the LAr storage tanks from where the flashed gas is pumped out.

A second step of flushing/filling could be carried out to ensure a good purity of LAr if necessary. The purity will be checked by analysing samples (about one litre) with a portable purity monitor system or O_2 analyser.

The precooling of the LAr tanks is obtained by the circulation of LN_2 through the heat exchangers N167 and N165. The valves PCV168 and PCV166 control the flow inside the exchangers and allow to keep constant the pressure above the liquid. It is to be noted that the pressure of LN_2 inside the exchangers is constant, independent of the position of the flow control valve. Indeed this pressure is fixed by the outlet pump of the LN_2 storage tank which feeds the general supply line and has a large flow capacity.

Cryostats flushing and purging: Before cooling down the cryostats with cooled helium in preparation for the LAr filling, it is necessary to make a few flushing/purging operations at 300 K in order to eliminate water and impurities inside the pipes and vessels.

The flushing/purging sequence could be flushing with GAr and purging to exhaust, flushing with helium and purging. This last operation should be repeated several times. In order to get enough GAr for the flushing, a LAr vaporizer functioning at about 5 bar, will be connected to the storage tanks.

3.3.2 Cooling down

The basic information is shown in Figure 3-12 and 3-13 .
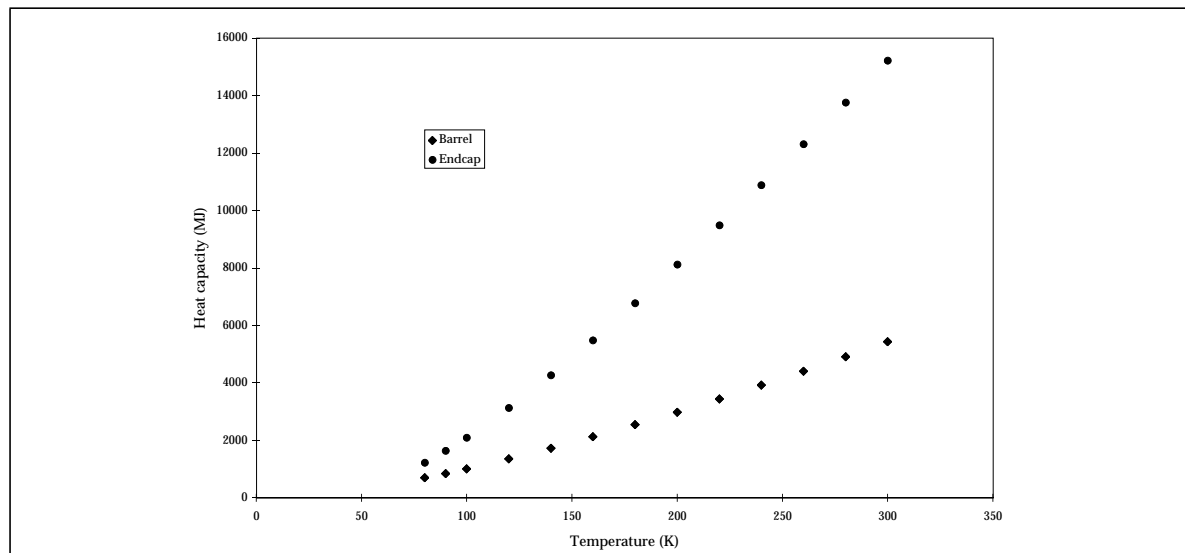
Figure 3-12 Enthalpy diagram based on weight, Table 3-2 and Table 3-3.

Cooling down with helium: From 300 K to about 100 K, the cryostats are cooled with helium gas. From the curves which show the dynamics of the cooling, it can be seen that the decrease in temperature is linear between 300 and 100 K. Due to a greater mass of the end-caps compared with the barrel, the duration of cooling is longer (15 days for each end-cap versus 6 days for the barrel).

The helium gas passing through the cooling system is cooled by a LN_2/He exchanger N169 before going into the cryostat cold vessels. LN_2 pumped from the storage tank circulates through the exchanger N169. The pressure of helium during this phase is 1.5 bar.

To gradually decrease the vessel temperature while cooling, the design of the heat exchanger allows the flow valve PCV203 to control the LN_2 flow in order to maintain a fixed difference of temperature equal to 40 K between the input flow and the output flow of helium at the cooling
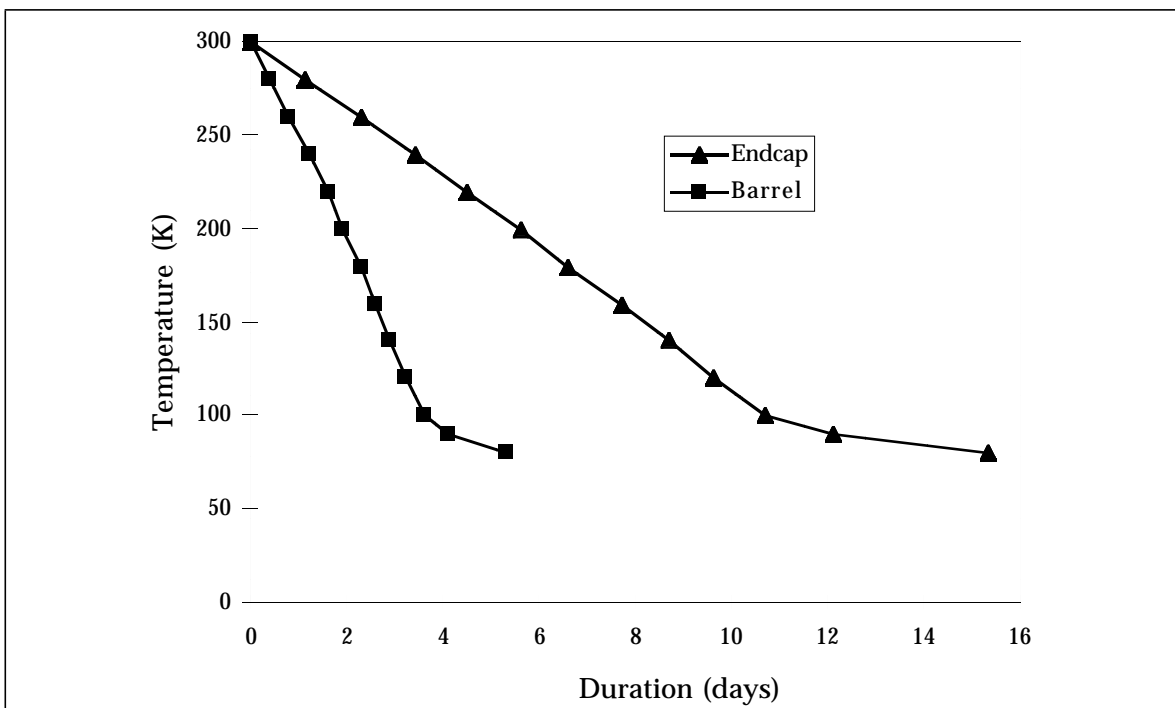
Figure 3-13 Temperature as a function of the cooling duration.

unit. The warm helium gas from the vessels is recycled again in the cooling system unit in counter flow (exchanger He/He N226).

At the end of the helium cooling phase (when the temperature is about 110 K and the cooling curve starts to slow down) it is possible to activate the upper LN_2 exchangers inside the cryostat cold vessel in order to speed up the cooling.

Filling vessels with LAr: When reaching 100 K inside the vessels, all helium is purged with the He/Ar vacuum group and the LAr lines are flushed with gas at 100 K.

The filling of LAr into the cryostats is done via the overflow vessels from the storage tanks where the pressure is increased to 3 bar. Liquid flashing into the pipes and the overflow vessels is recondensed by the LN_2 exchangers both in the overflow and cryostat vessels. During the filling phase, which should take less than one day, the pressure inside the vessels is set close to 1.25 bar. As soon as liquid accumulates in the bottom of the cryostat the hydrostatic pressure will increase gradually. This increase will be followed by a differential pressure gauge between the top and bottom of each vessel. After filling, the temperature of the liquid bath, initially at 100 K, will decrease slowly to 89.3 K by controlling the LN_2 flow in the heat exchangers (control valves in the valve boxes).

Circulation of N_2: The two-phase flow of N_2 from all vessels exchangers are collected back in the storage tank. Separation of liquid and gas is done inside the tank where gas feeds the compressor of the liquefier.

3.3.3 Running

After the filling operation has been completed and the system has stabilized, the temperature will be maintained at 89.3 K within a ΔT of 0.66 K or better (see Section 3.1.3).

To achieve better convection flow inside cryostats, the flow control inside the heat exchangers will give priority to the upper ones.

3.3.4 Warming up

Emptying liquid argon from the cryostats back into the storage tanks is done using pumps #111 or #124 after filling the drainage lines up to the pumps by gravity. All the LN_2 exchangers are purged with the vacuum group except the exchangers in LAr tanks. Warming up is done with circulating helium. The helium gas which is recycled at 1.5 bar through the cooling system unit is warmed by #Y228 heater. The same fixed difference of temperature set to 40 K is maintained between the inlet and outlet flow through the heat exchanger in order to warm up the cryostats gradually.

As for cooling, the complete warming-up operation is estimated to take approximately 15 days (end-cap).

3.4 Maintenance

The most important points for which maintenance has to be organized, and backup systems prepared are:

- Feeding of LN_2 inside exchangers: if the liquefaction unit stops, the storage tank of LN_2 at the surface will provide the necessary LN_2 for circulation in the exchangers. In this case the flash of gas will be evacuated to the exhaust.

- Backup pumps: all pumps, except the pump for raising liquid argon to the surface, will be duplicated.

- Periodical maintenance of vacuum groups: every six months all the vacuum groups will be checked.

- Follow-up of compressor inside the liquefaction unit: A supervision of this compressor by spectrum analysis is being considered.

3.5 Control command system

The cryogenic control system has to be in full time operation, whatever the operating status of the detector (maintenance, shutdowns...). It will be linked to the common field-bus system used by the slow control unit. Signal conditioning of cryogenic sensors will be done in the same way as for the other sensors, through the slow control system.

3.6 Safety considerations

Safety has been one of the main concerns in the design of the cryogenic system. Risks in the utilization of low temperature boiling fluids were identified, and preventive measures were taken:

1 - Gas, liquid argon and liquid nitrogen spills:

Special attention has been given to active prevention from the design phase of the components onwards by stressing high levels of tightness, convincing structural analysis, close follow up in industry and stringent testing and commissioning procedures. Both general and CERN-specific safety rules have been taken into account in great detail as various previous experience in H1, D0, etc. Passive prevention such as temperature monitoring of critical parts, leak detection, oxygen monitors and well controlled access and maintenance procedures will be implemented also. A powerful ventilation of the area and also special drainage of spills of cryogenic liquids to a storage pit are foreseen.

2 - Irradiation of liquid nitrogen:

Explosive behaviour of liquid nitrogen after strong irradiation has been reported but not yet explained in detail. To eliminate the risk of high concentrations of oxygen and ozone it is planned to use a re-liquefaction unit for the production of liquid nitrogen. Particular attention will be paid to the purity of nitrogen with the utilization of Oxysorb® purification cartridges in the liquefaction loop. In addition the oxygen content of the nitrogen gas will be monitored. Exposure to air will be eliminated in the installation. Furthermore the levels of irradiation resulting in explosions have been orders of magnitude higher than what can be expected in the present situation.

3.7 Schedule

The schedule for design, construction, installation and commissioning of the cryogenics system is given in Figure 3-14.

3.8 Cost

The cost breakdown of the cryogenic plant is given in Table 3-17.
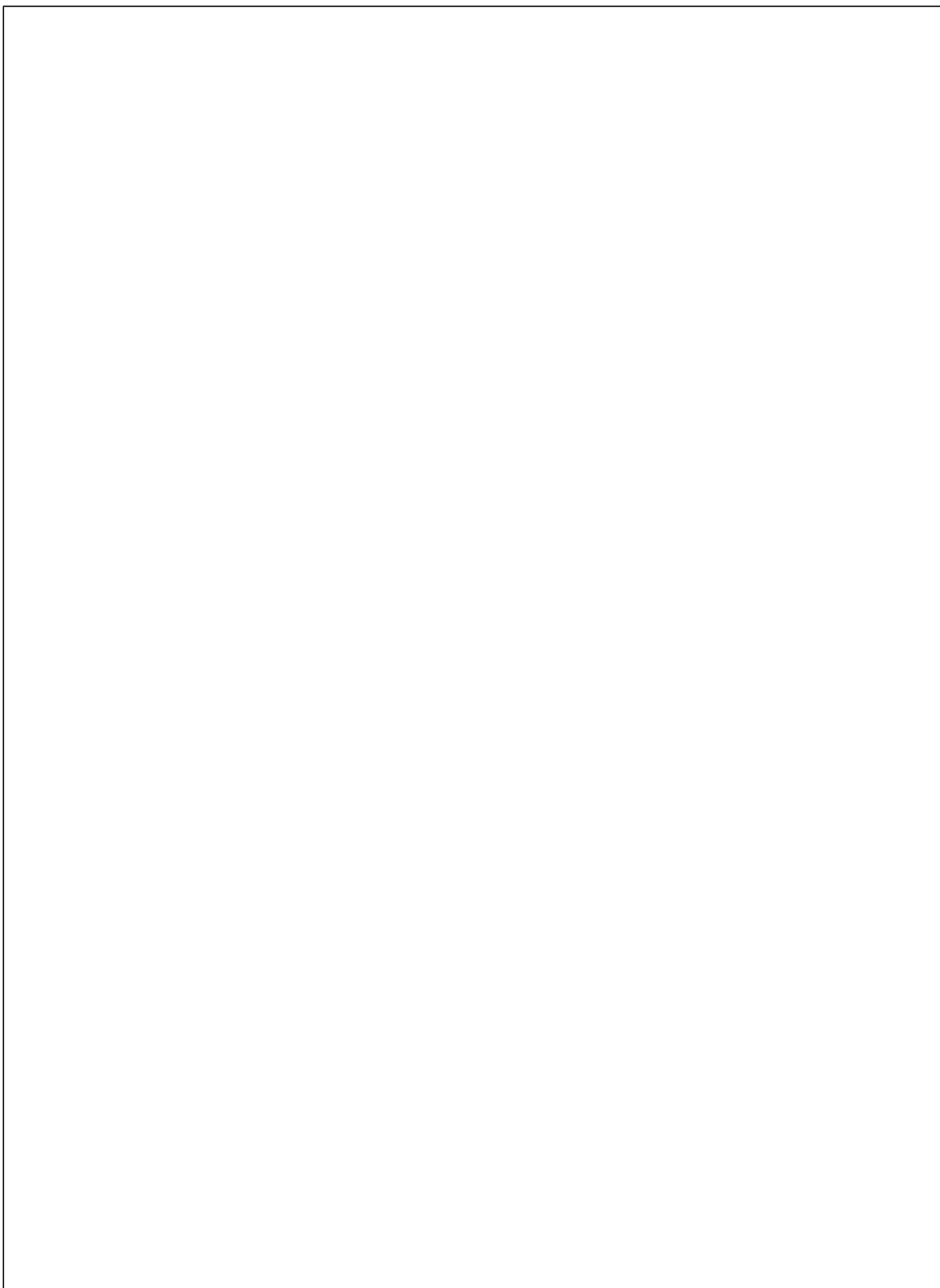
Table 3-17 Breakdown of costs (kCHF).

Cryogenic plant	Proximity	External	Total
Design	700	300	1000
Manufacturing	6600	2800	9400
Assembly	600		600
Surface test	1700		1700
Cavern installation	1200	200	1400
Total	10800	3300	14100

3.9 References

3-1   J.P. Lottin, Caractéristiques de l'installation cryogénique. Technical specifications. CEA/Saclay. Ref. 5C5720T00795 (1995).
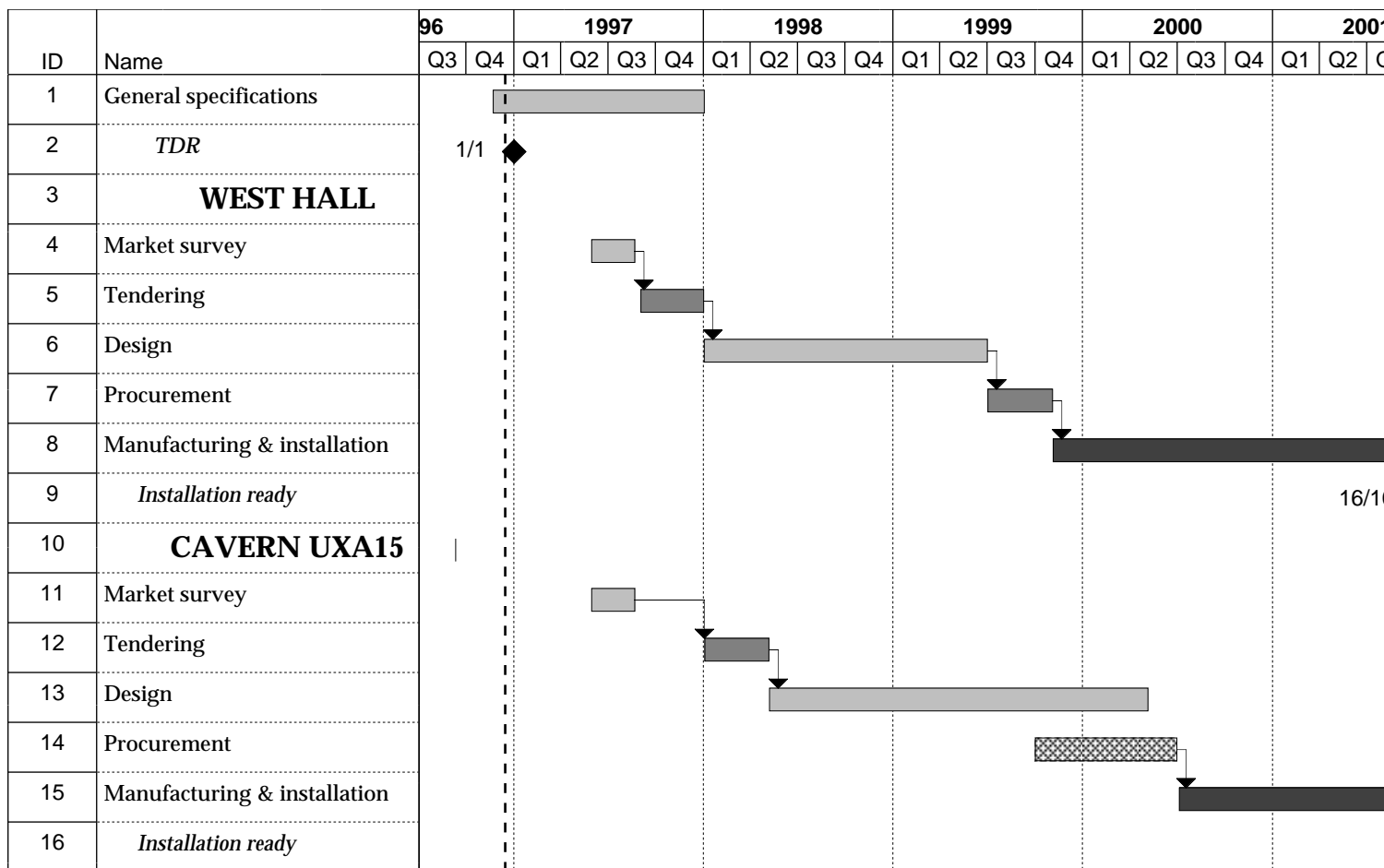
3-2   ATLAS, Livre blanc: cryostat du barrel, installation cryogénique Argon, feedthroughs. CEA/Saclay DAPNIA 21/11/1994.

3-3   CODAP: Code Francais de Construction des Appareils à Pression non soumis à l'action de la flamme. Edition 1995. SNCT/AFIAP.

3-4   Safety code, CERN.D2, issue 1988.

Figure 3-14 Cryogenic plant time schedule.

Adobe's PostScript Language Reference Manual, 2nd Edition, section H.2.4 says your EPS file is not valid, as it calls setpagedevice

CRYOGENIC PLANT TIME SCHEDULE

ID	Name	96		1997				1998				1999				2000				2001	
		Q3	Q4	Q1	Q2	Q3	Q4	Q1	Q2	Q3	Q4	Q1	Q2	Q3	Q4	Q1	Q2	Q3	Q4	Q1	Q2
1	General specifications																				
2	*TDR*	1/1																			
3	**WEST HALL**																				
4	Market survey																				
5	Tendering																				
6	Design																				
7	Procurement																				
8	Manufacturing & installation																				
9	*Installation ready*																16/1(				
10	**CAVERN UXA15**																				
11	Market survey																				
12	Tendering																				
13	Design																				
14	Procurement																				
15	Manufacturing & installation																				
16	*Installation ready*																				

Task ▬▬▬▬▬▬▬ Milestone ◆
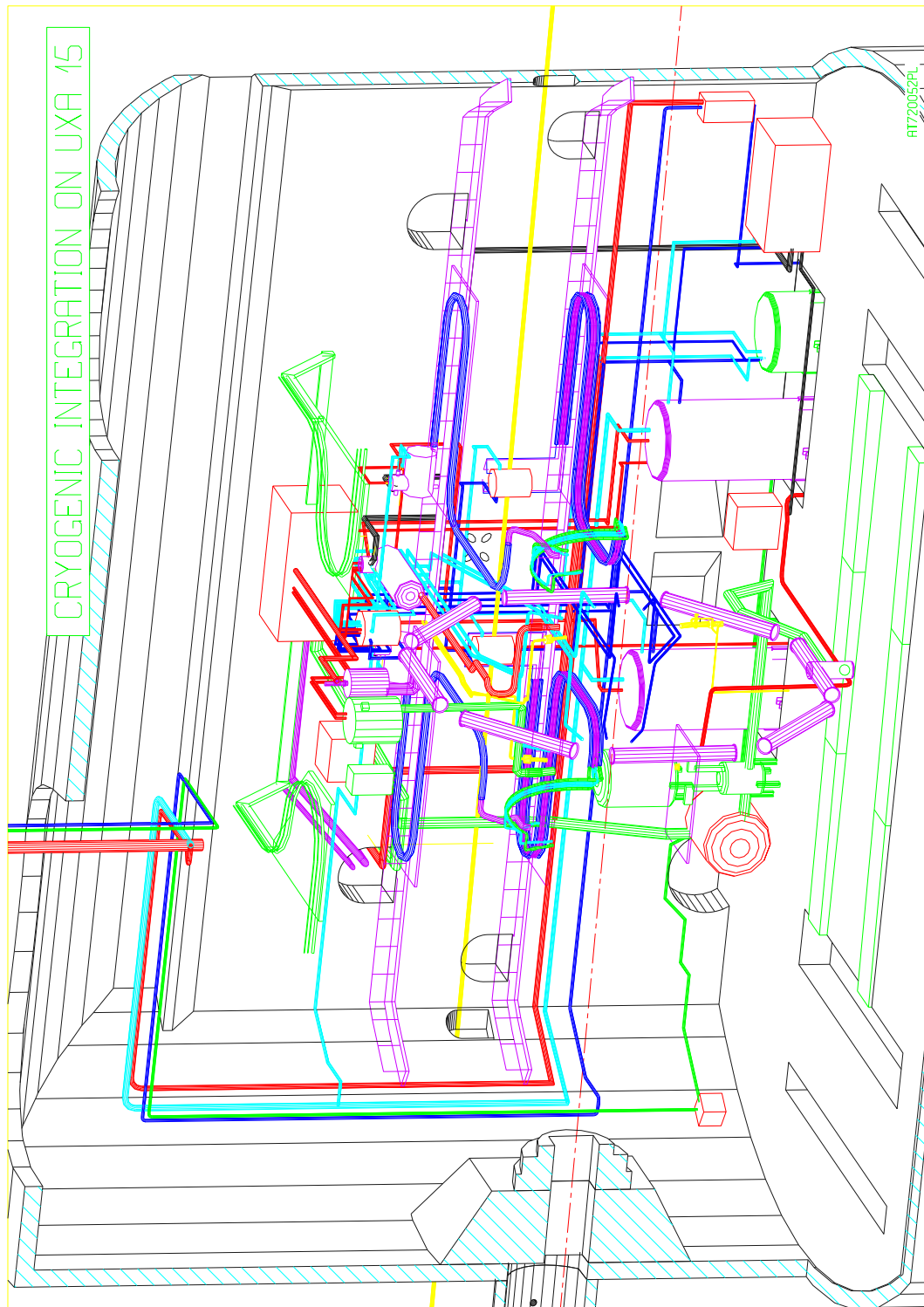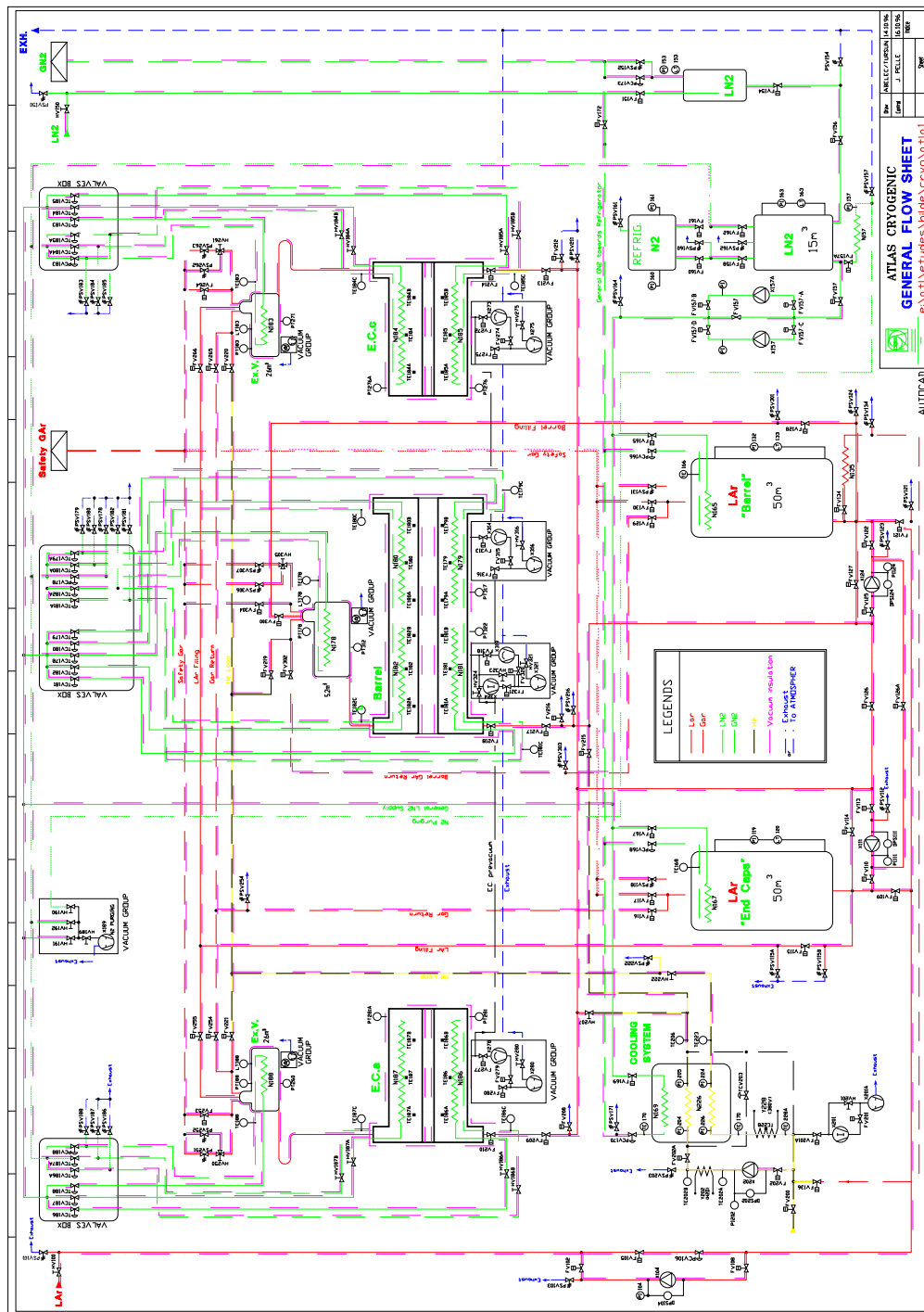
Figure 3-i Cryogenic elements in the cavern.

Figure 3-ii General flow sheet.

4 Barrel cryostat and feedthroughs

4.1 Overview

The barrel cryostat serves as the housing for the EM barrel calorimeter. In addition, it supports and provides the vacuum for the superconducting solenoid coil which serves the inner tracker. Furthermore, the cryostat supports the inner tracker and is itself supported by the Tile calorimeter.

The barrel cryostat has the general shape shown in Figure 4-i, which shows a "quarter side view": a warm vessel which forms a hollow cylinder contains a similarly shaped cold vessel, which is filled with liquid argon. The end view of the cryostat can be seen in Figure 4-ii.

The EM calorimeter is inside the cold vessel, and approx. 100 k signal lines and 2 k HV lines are required to meet the calorimeter's needs. The cold vessel is filled with Liquid Argon of high purity, and is cooled by LN_2. All the services, as well as all the support structures, are at the two ends so that there is a minimum obstruction of the Tile calorimeter which measures the hadronic components of jets.

The cryostat project can be subdivided into several parts: the bare cryostat, the signal feedthroughs, and the HV feedthroughs. The most critical interface is with the superconducting solenoid and its power leads. There are additional interfaces to consider: the Tile calorimeter supports the cryostat, the inner detector is supported by the cryostat, and the beam pipe is also supported by the cryostat. These will all be discussed in sequence.

4.2 Engineering design of the bare cryostat

4.2.1 General concepts.

All devices using cryogenic calorimetry, in particular electron/photon calorimeters, have to carefully minimize the material between the interaction region and the calorimeter. If such a device is used in a collider experiment, one also has to minimize the total volume occupied by such a device: compact construction reduces overall costs. The cryostat design is largely determined by these requirements. It is made of aluminium instead of stainless steel in order to reduce the total number of radiation lengths, and every effort is made to reduce the amount of absorbing material between the interaction region and the EM calorimeter.

A further design constraint is the requirement that the barrel EM calorimeter is constructed azimuthally in a "seamless way", with no gaps between individual modules. Thus all the cables should also leave the cryostat in a symmetrical manner, so that all signal delays from individual cells in the calorimeter are identical. This in turn constrains the locations of the signal feedthroughs: there are 32 signal feedthroughs on each end, which should be arranged in a symmetrical way, so that all the cables from the 32 EM calorimeter modules are of equal length.

In practice, since each supermodule feeds its signals to two feedthroughs, only pairs of feedthroughs have to be arranged in an azimuthally symmetric way. On the other hand, since these two feedthroughs send the signals into a single preamplifier/digitizer crate, the spacing between each feedthrough pair must be identical everywhere on the cryostat surface. In be-

tween these signal feedthroughs, space must be found for HV feedthroughs, as well as for all the vacuum and plumbing lines required to service the complete instrument.

The cryostat contains not only the EM calorimeter proper, but also the superconducting solenoid coil which provides the magnetic field for the inner tracker.

The overall dimensional limits of the cryostat are listed in Tables 4-1 and 4-2, which indicate the axial and radial extent of the cryostat. If a value cannot be any smaller or larger than indicated, we have add "min." or "max.", respectively. The rather tight constraints, in particular in the radial direction, necessitate machining of some components which in a less constrained system would be simply welded out of rolled plate.

Table 4-1 The z- coordinates of critical elements of the cryostat. (+: distance determined from thickness consideration; ## there is a bulge in both cold and warm bulkhead at the location of solenoid power line).

Reference point	Start warm	End warm	Start cold	End cold
Support end wall of warm cyl.	2850 min.	2900 +	--	--
End wall of warm cylinder	3340 +	3390 max.	--	--
Warm bulkhead near bolts	3390 +	3405 max.	--	--
Warm bulkhead midway ##	3359 +	3405 max.	--	--
Support flange cold cylinder	2936.5 nom.	2986.5 nom.	2925.4 nom.	2975
End ring cold outer cylinder	3237	3267	3225	3255
Cold bulkhead near bolts	3267 min.	3292	3255	3280
Cold bulkhead midway	3267 min.	3310	3255	3297
End flange inner warm cylinder	3050	3150 nom.	--	--
Coil support bolt location	3070	--	--	--
Transition inner cold cyl./cone	3183	3233	3171	3221

The critical parts of the cryostat, in terms of dead material, are those which lie between the interaction region and either the EM barrel calorimeter, or the EM end-cap calorimeter. These should be as thin as possible, so as to present no unnecessary absorbing material to EM showers, before they are detected by the EM calorimetry. The inner warm cylinder and the inner cold cylinder lie between the interaction region and the EM barrel calorimeter. In addition the transition between these two cylinders and the corresponding bulkheads lies between the interaction region and the EM end-cap calorimeter, and thus should also be minimized. Therefore our cryostat design has very thin walls on the inner side. In Figure 4-1 we show the exploded view of the cryostat. There are two inner cylinders, one "cold" (at LAr temperature) and one "warm" (at room temperature), whose thicknesses must be minimized. However, while the warm cylinder is subject to pressure from the inside, and thus can be just a thin shell, the cold inner cylinder is subject to the LAr pressure from the outside, and thus its failure mode is buckling.However, there are other load constraints. The EM calorimeter has a mass of about 120 tons, and the LAr adds weight. In addition, the inner warm cylinder has to support both the solenoid coil, as well as the inner detector.

Table 4-3 gives the estimated maximum loads which we assume the cryostat has to support. These are design loads, and it is hoped that the actual amount of material will be less. The cryo-

Table 4-2 Radial dimensions of cryostat components. All dimensions are in millimetres. (+: thickness is defined instead of radial dimension).

Reference point	Start warm	Start cold	End warm	End cold
warm inner cylinder	1150 min.		1160+	
Warm inner cylinder, end flange	1150 min.		1203 max.	
Coil (without inner superinsulation, but with measuring devices.)	1215 min.	1210 nom.	1305max. 1315 leads?	1300 max. (1310?)
Isogrid (inner cold cylinder) at z > 100	1345 nom.	1340 nom.	1395.3 max. 1390.3 nom.	1385 nom.
Isogrid ((flange at z = 0)	1325 min.	1320		
Presampler (innermost element of calorimeter)	1413.3 min.	1412.3		
Stainless Steel rings at outside of calorimeter	2009 nom.	2003	2109 nom.	2103
cold outer cylinder at z > 100	2140 nom	2132	2170	2162
cold outer cylinder, central flange	2050 min.	2042	2170 nom.	
Warm outer cylinder	2220 +		2250 max.	
Warm outer cylinder bulge at end			2775 nom.	
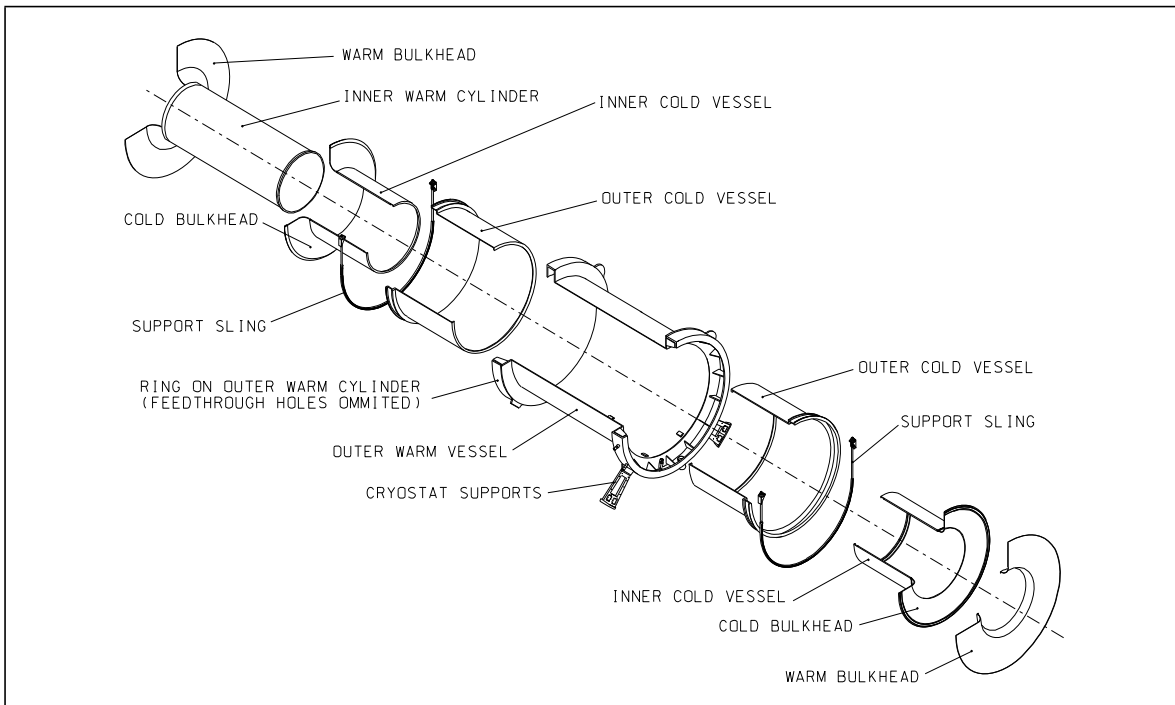
stat is to be built to (French) CODAP specifications; however, since this is very much a nonstandard vessel, there is no intention of actually asking for an attached CODAP stamp.

The space allowed in this document does not permit detailed discuission of the reason for taking certain decisions, nor discussion of other options which were investigated and discarded. The reader is referred to [4-1] for further details.

Table 4-3 Maximum mass of parts supported by the calorimeter.

Object	Mass (tons) (upper limit)
EM calorimeter	110
Liquid argon	62
Coil	5.5
Inner detector (incl. cables)	5
Cold vessel	12
Warm vessel	13

The cryostat can be considered to consist of several components, each of which is to be fabricated separately. Figure 4-1 shows the inner warm cylinder (which also supports the solenoid and the inner detector), the inner cold cylinder with attached bulkheads, the outer cold cylinder (which supports the EM calorimeter), and the outer warm cylinders. In addition there are separate warm bulkheads, which join the outer and the inner warm cylinder. We will discuss these items in sequence.

Figure 4-1 An exploded view of the barrel cryostat, identifying the individual components.

4.2.1.1 The inner warm cylinder

The inner warm cylinder supports the superconducting solenoid, and isolates the vacuum space from air on the cryostat inside. It also has a ledge which supports the inner tracker. It consists of a 10 mm thick cylindrical shell, reinforced at the end by flanges. The coil is attached to these flanges, as described in more detail later. On its inside this cylinder carries a ledge, which supports the inner detector. Since the cylinder wall is very thin, and the inner detector load distributed along its length, this ledge will not be welded to the cylinder, but epoxied with a radiation-resistant epoxy. The wall of the cylinder on the tracker side must also support all the cables and cooling lines from the tracker. A large number of such support points is required. But since each of these carries again only a light load, it is planned to attach them to the cylinder by gluing each support structure to the inside of the cylinder. The cylinder is simply too thin to carry a large number of blind taps, in particular since the exact location of many support points will not be known sufficiently in advance.

Two cylinders must be produced: one, the final one, will be shipped to KEK for mounting the coil. It will then be shipped to CERN with the coil mounted. A second cylinder will serve to temporarily stabilize the cryostat for initial acceptance tests and shipment to CERN. This second cylinder can be less accurate than the first one, and could even be made out of ordinary steel.
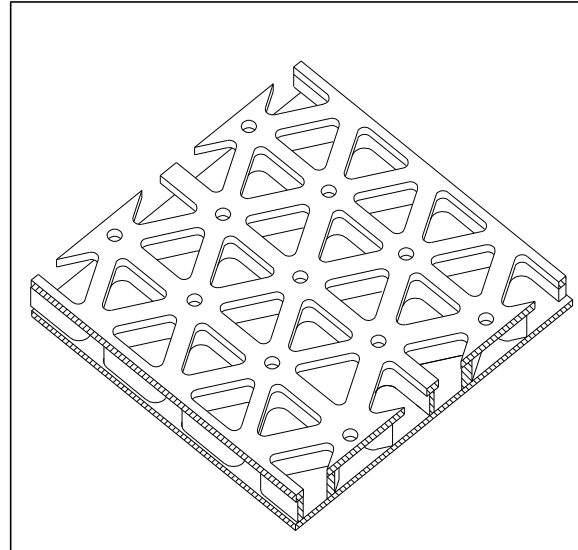
Such a thin cylinder is not stable without either being held cylindrical either by its bulkheads or by special constraining devices which we call "spiders" and whose purpose is to keep the cylinder round. These spiders will stabilize the cylinder during its shipment to KEK and from KEK to CERN, as well as during all operations of mounting and testing the coil at KEK. They will be made of non-magnetic material.

The end flange of this cylinder is in the path of particles emanating from the interaction region and impinging on the outer region of the end-cap calorimeter. Thus it has to be made as thin as is consistent with strength considerations. One way is to sculpt the flange as shown for example in Figure 4-i. However, only about 30-35% of the material can be removed - the rest is essential for supporting the coil and attaching the bulkheads.

4.2.1.2 The inner cold cylinder with bulkheads

The inner cold cylinder separates the vacuum from the LAr space which surrounds the Barrel EM calorimeter. Again this has to be as thin as possible; but it also has to withstand both the pressure of the LAr as well as the hydrostatic lift due to the liquid.

The usual failure mode of a cylinder subject to an outside pressure is buckling. In our case buckling is prevented by increasing the cylinder's radial thickness without increasing the amount of material. This can be achieved by choosing either a "honeycomb" structure, where a loose structure (honeycomb) is sandwiched (glued) between two thin sheets of metal. Or the "Isogrid" solution, where material is carved out of a single thick plate, removing some 80% of the material, but keeping as much of the stiffness as possible. The plate is subsequently bent into a cylindrical shape. This is not a new method: it was developed by General Dynamics for NASA more than 20 years ago, and is used extensively in the space shuttle and other space applications. Figure 4-2 shows an example of such an Isogrid structure. We have chosen this design as the baseline.

Figure 4-2 An Isogrid pattern is cut out of a single thick plate.

There has to be a bulkhead which connects the inner cold cylinder with the outer cold cylinder. The standard design would be to have a flange at the end of the cylinder. Unfortunately this again presents a large amount of passive absorber material where particles should be able to reach the end-cap calorimeter with minimal interference. In this context we note that any passive absorber should be as close to the active absorber as possible so as to reduce the spreading of electromagnetic showers. We therefore chose a single flange at $|\eta| = 0$ instead of one flange on each side around $|\eta| = 1.65$. This flange is traversed normally, thus presenting less absorber, and is very close to the presampler. A beneficial side-effect is that we gain in stiffness, since short cylinders buckle at higher outside pressure than long ones.

There is then no flange at the ends: the inner cold cylinder is permanently attached to the cold bulkheads. In our design the inner part of this bulkhead is also made as an Isogrid; further out, where the bulkhead is hidden behind the EM barrel calorimeter, a solid plate can be chosen. However, we still keep open the option of using a shaped cold shell bulkhead. Our calculations say that a shaped 3 cm thick bulkhead of this type satisfies the pressure rating. The final decision will be made on the basis of cost as well as ease of cable routing which is still being studied.

From Table 4-2 one can see that under ideal circumstances there is nearly 20 mm distance between the inner cold cylinder and the presampler. However, both the EM calorimeter and the cylinder deform under the effect of gravity. They deform in opposite directions, since the cylin-

der has a large "negative weight", being immersed in LAr. Thus the final clearance between the two will be about 10 mm at the worst spot, but up to 25 mm where they move apart. It may be possible to insert some "argon excluder" after all pieces have been manufactured and carefully measured.

4.2.1.3 The outer cold cylinder

The outer cold cylinder supports the EM calorimeter, and also has to hold the 50 tons of LAr which surround the calorimeter. There is a widened bulge on both ends, which is required to accommodate the various connections: signal and HV feedthroughs, LN_2 lines, the large line to the overflow vessel, and the LAr emptying line at the bottom.

This end bulge also serves a second purpose: the whole cold vessel, including the EM calorimeter, the LAr, and the inner cold cylinders with bulkhead, is supported by two "slings" which wrap around the thickened end of the bulge. This sling, discussed in more detail in Section 4.2.1.5 is a thick yet flexible Inconel structure.

This bulge prevents the whole outer cold vessel from being inserted into the warm vessel from a single end. Therefore the outer cold cylinder is constructed as two half-cylinders, joined at the centre by a flange. This flange also reinforces the cylinder, which has to transmit the calorimeter load to the outside. We discuss in [4-3] the stresses and deformations which are due to these loads.

While the outer cold cylinder itself does not have to be manufactured to tight tolerances, all the flanges have to be quite exact. In particular, the end flanges determine the position of the cold bulkheads and thus of the inner cold cylinder, which is very close to, but must never touch, the superconducting solenoid suspended from the warm outer cylinder, nor the presampler which forms the innermost component of the EM calorimeter.

4.2.1.4 The outer warm cylinder

The outer warm cylinder consists of a 5700 mm long, fairly thin cylinder of outer radius 2250 mm (max.), with two complex end sections. The long cylinder separates the outside air from the vacuum, and thus has to be strong enough to prevent buckling under 1 bar. It is subject to no other substantial loads.
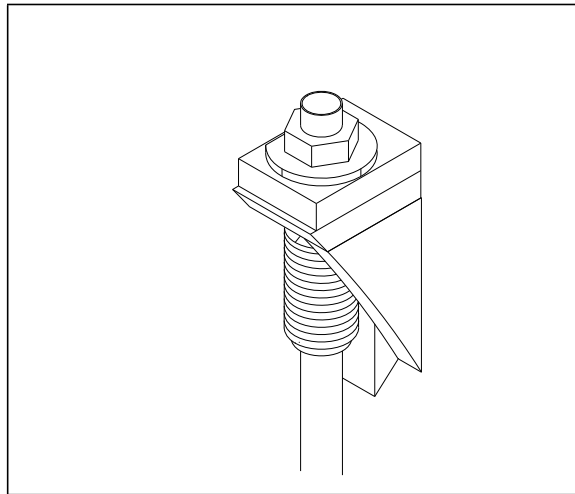
The end section starts axially at z = 2850 mm, and its first 50 mm thick plate extends to r = 2775 mm. This is the actual backbone of the whole cryostat: it transmits the load of the cold vessel to the Tile calorimeter. This plate is stabilized by the rest of the structure which extends all the way out to 3390 mm; the long cylinder has only a minor stabilizing effect. This end structure forms a large ring at each end, which not only transfers the cold vessel load, but also holds the warm bulkheads with the inner warm cylinder (and the solenoid) attached to it. It also has penetrations for all the feedthroughs, such as signal, high voltage and plumbing.

The two end sections are not identical: while the same signal and HV feedthrough number must be accommodated on each end, only one end holds the power line to the solenoid, while the other holds the connection from the cold vessel to the overflow vessel. The location of the vacuum pumpouts, LAr emptying line, and other gas and liquid lines are also not identical at the two ends. Figure 4-ii shows one of the two ends.

There are reinforcing ribs in the end sections which reinforce them against the ambient pressure when the warm vessel is evacuated. One such rib is welded between each pair of feedthroughs.
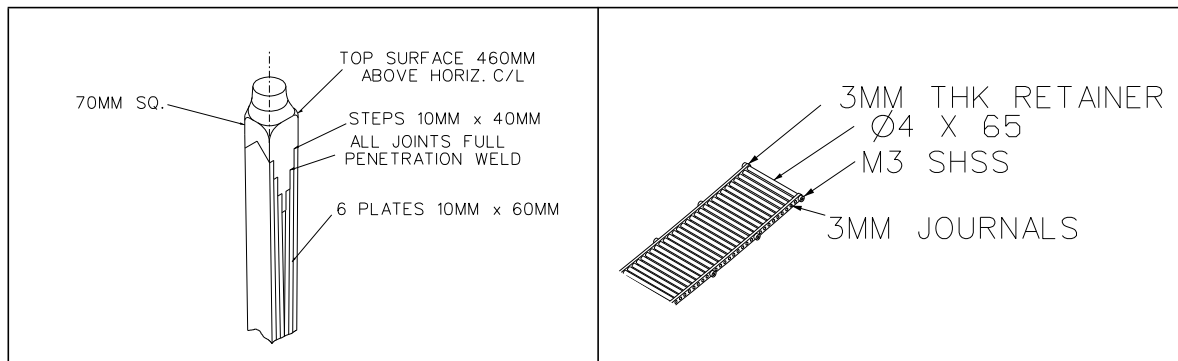
4.2.1.5 Support of the cold vessel by the warm vessel

The cold vessel is supported from the warm vessel by an Inconel structure which we call a "sling". The slings are shown in the exploded view of Figure 4-1; a more detailed view can be seen from Figure 4-3, Figure 4-4 and Figure 4-5. The top of the sling is a 60 mm diameter Inconel threaded rod, which is supported by a structure shown in Figure 4-3. A bellows attached to the rod and to the support structure provides vacuum integrity, while allowing the height to be adjusted by turning the nut. Of course, one cannot turn the nut with the whole weight (55 tons per nut) hanging on it. Therefore the threaded rod protrudes beyond the nut and the pressure on the nut can be relieved by a hydraulic device (not shown) which attaches to that protruding part.

Figure 4-3 The top of the support sling holding up the cold vessel.

The threaded rod has a transition piece shown in Figure 4-4, where it becomes subdivided into several thinner laminations to make the sling more flexible. These then wind around the reinforced end of the outer cold cylinder. In order to minimize friction, a set of stainless steel (journals) rollers is located between the sling and the cylinder. A small section of the roller assembly is shown in Figure 4-5.
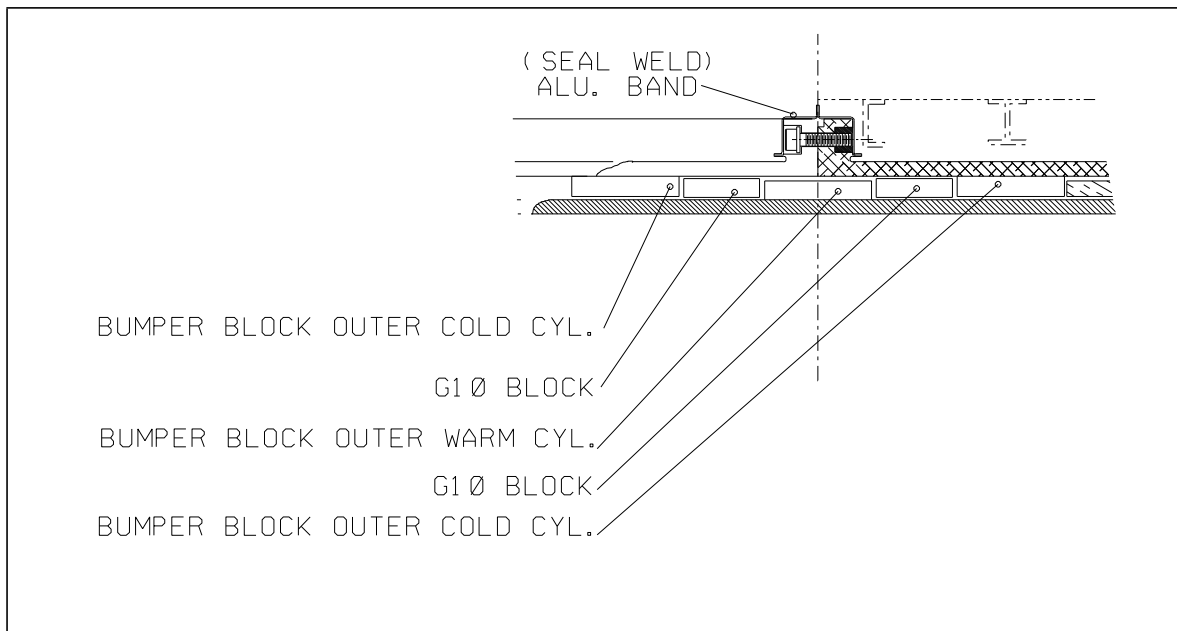
Figure 4-4 The transition from a single rods to a laminated structure.

Figure 4-5 A set of rollers between the sling and the cold vessel eliminates friction.

The sling by itself would not prevent sideways motion of the cold vessel relative to the warm one. This is accomplished with the help of "bumpers". In Figure 4-6 we show one such bumper which prevents motion of the cold vessel in the axial direction. A block is welded to the outer warm cylinder at the center bottom. Similar blocks are welded to each of the two cold half-cylinders. There are G-10 blocks mounted between them, providing thermal insulation while they also prevent motion of the cold vessel relative to the warm one.

During cool-down the sling will partially contract, and the cold vessel will contract by a full 0.38%. Since the cold vessel has to be centred when cold, a position monitoring device will be installed which measures the position of the outer cold cylinder relative to the outer warm cylinder, as well as the position of the inner cold cylinder relative to the inner warm cylinder, or to the solenoid. This will allow correction of the exact bumper locations after tests at the factory.

Figure 4-6 Bumpers locating the cold vessel relative to the warm one in the axial direction.

The vertical position of the cold vessel can be adjusted at any time by adjusting the support slings; this can be done without opening the vessel, and the slings will have to be readjusted after installing the EM calorimeter, and again after cooling the system down.

4.2.2 Cryostat interfaces to other parts of the ATLAS detector

The barrel cryostat is itself a service item, not a detector item. It serves as a repository for the EM barrel calorimeter and presampler, and the first stage of the calorimeter electronics is mounted on the outer shell of the cryostat. The cryostat also houses inside its vacuum the superconducting solenoid. It supports the inner detector, together with its cabling, and also acts as a support for the beam pipe. The cryostat is itself supported by the Tile calorimeter. In addition, there are cryogenic and vacuum services which can be considered an interface to the ATLAS cryogenic plant. Below we discuss these interfaces, reserving a discussion of signal feedthroughs and electronics for a later section.

4.2.2.1 Support of the EM calorimeter by the outer cold cylinder.

We first discuss the support of the EM calorimeter by the outer cold cylinder. Each of the two (half)-cylinders have on their inside a ledge, which is the actual support for the EM calorimeter. However, the calorimeter does not sit directly on this ledge, but on two transition pieces be-

tween ledge and the SS rings which keep the calorimeter rigid. The arrangement is shown in profile in Figure 4-7. The transition pieces serve a dual purpose:

1. While the EM calorimeter has to be positioned to an accuracy of ± 1 mm, it is too expensive to manufacture the outer cold cylinder to that precision. Thus the first transition piece will be manufactured only after the outer cold vessel has been carefully measured, so as to compensate for any manufacturing tolerances of the actual ledge. This piece, made of the same material as the outer cold cylinder (Alu 5083), will then be solidly bolted to the original ledge.

2. The second transition piece, shown in Figure 4-7, is made of stainless steel. Since the EM calorimeter shrinks axially like stainless steel (by ~ 0.28%), it will slide over the Aluminium piece which shrinks by 0.4%. This second transition piece will be fixed to the cryostat ledge in a manner to keep the EM cryostat axially aligned at low temperature.
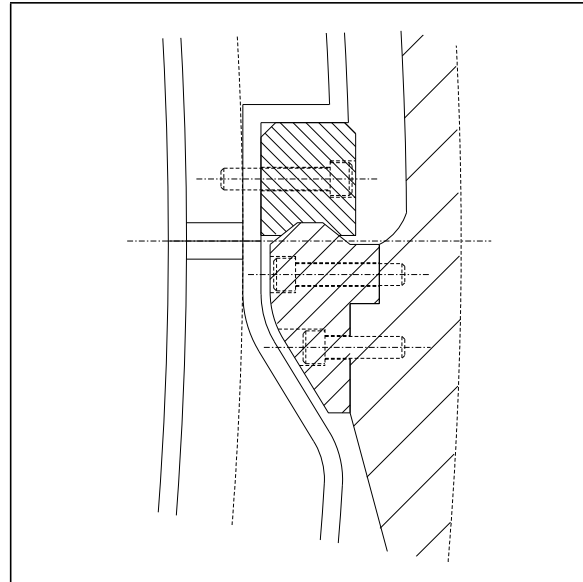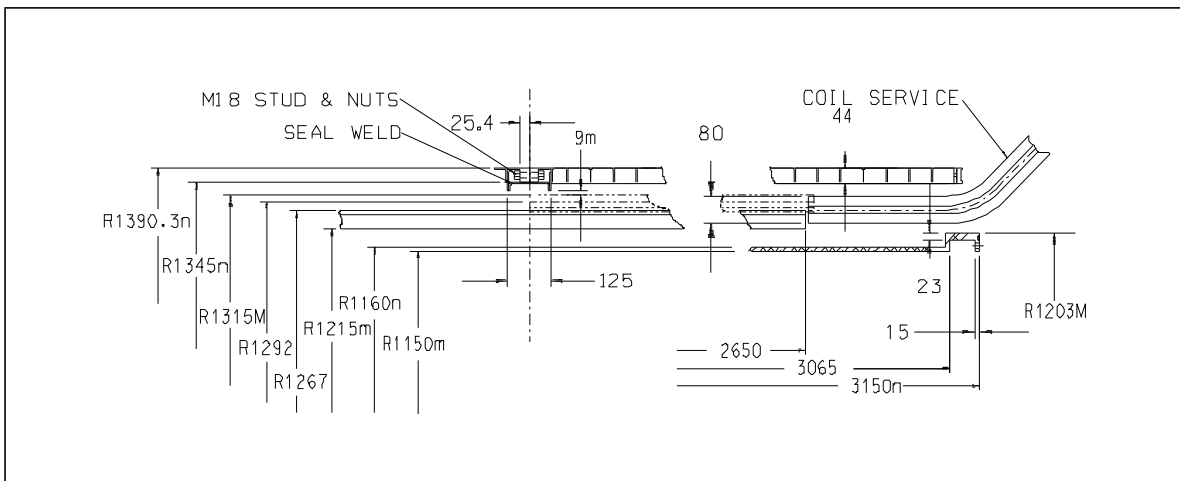
Figure 4-7 Support ledge for the EM calorimeter.

4.2.2.2 The superconducting coil

The barrel LAr calorimeter and the superconducting solenoid share a cryostat in common. One thus eliminates two vacuum walls between the solenoid and LAr calorimeter. This substantially reduces the radiation length in front of the LAr calorimeter. It also saves aprecious radial space. On the other hand, a common cryostat introduces various design as well as manufacturing constraints on both devices; it also restricts their operation. For example, the weight as well as radial and axial decentring forces of the solenoid have to be supported by the inner vacuum shell of the cryostat. The power- and cryo-service lines must penetrate through the calorimeter wall. In addition, we have decided to eliminate an outer thermal shield of the solenoid for simplicity and to save space, and therefore it is not possible to operate the solenoid when the barrel LAr calorimeter is warm. The entire solenoid system is described in the conceptual design report [4-2], and will be the object of a separate TDR volume.

Dimensional boundaries
All critical dimensions relevant to the cryostat and solenoid interfacing boundaries are shown in Figure 4-8, and are listed in Table 4-1 and Table 4-2. As one can see from these tables, both the coil and the cylinders in its vicinity have to be built to tight tolerances.
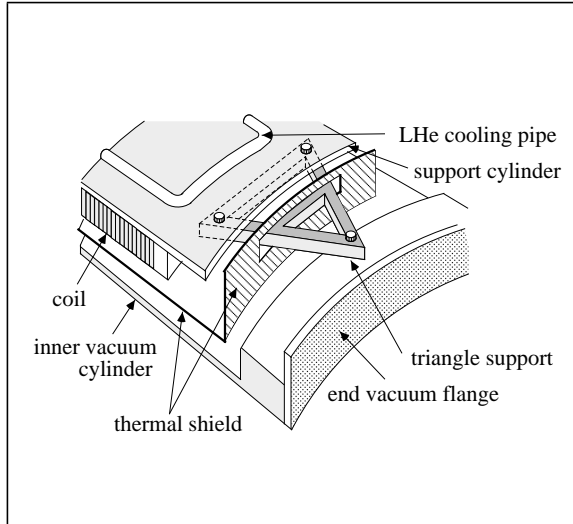
Figure 4-8 Sketch of dimensional limits between solenoid coil and inner warm cylinder. All dimensions are in mm. Suffix m=minimum; M=maximum; n=nominal.

Coil support

The coil is supported by "triangle supports" made of glass-fibre-reinforced-plastic (GFRP) material. Twelve such triangle supports are uniformly distributed at each axial end of the coil; each of them is attached to the end flange of the inner warm cylinder at z-3070 mm by two M12 or M16 bolts.   A schematic view of the triangle support is shown in Figure 4-9. The coil is axially constrained at the side where the power/cryo-service lines come out. On the opposite side of the coil, axial sliding joints between the triangle supports and the coil cylinder absorb the axial thermal contraction of the coil. The contraction is estimated to be 22 mm from room temperature to 4 K. Spherical bearings attached to the triangle support enable the coil to thermally shrink and expand uniformly in the radial direction.
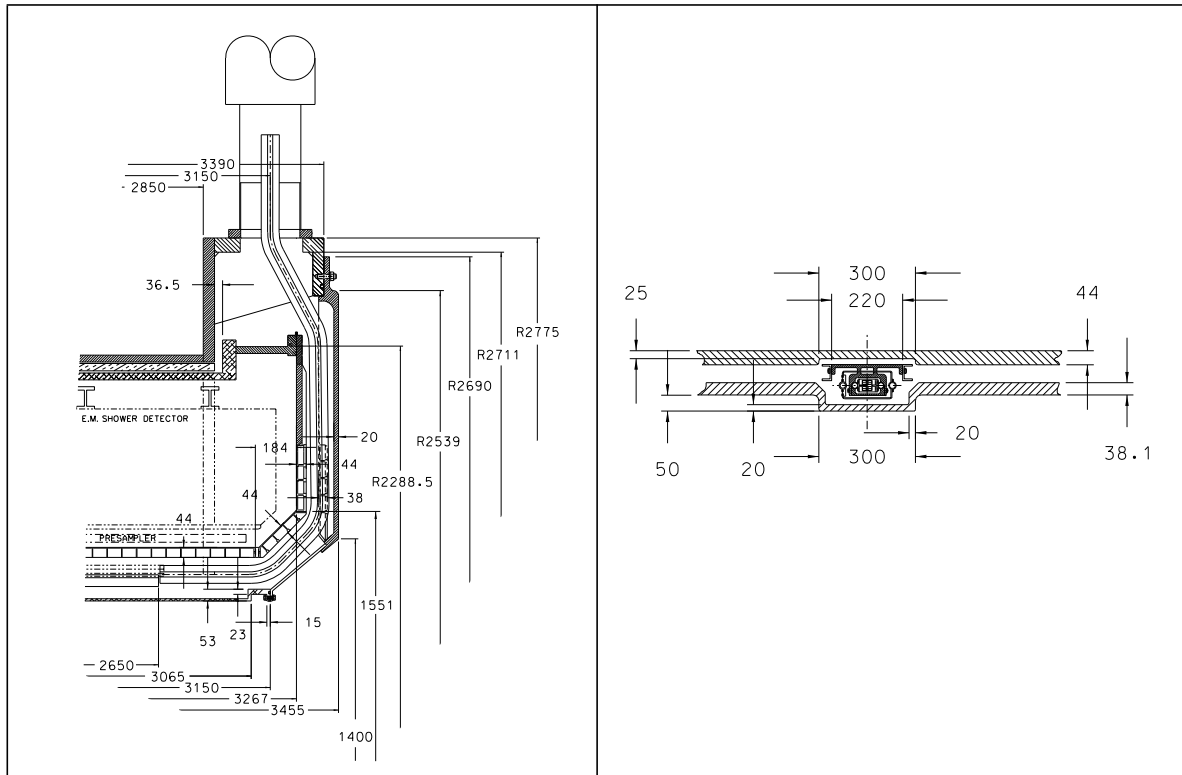
Figure 4-9 The coil is supported from the inner warm cylinder by individual fibre-epoxy triangles.

The support system is designed to be able to sustain the coil weight of 5.5 tons with a safety factor of three. We expect a radial decentring force smaller than 20 tons corresponding to a maximal radial decentring of 15 mm. The maximum axial decentring force is estimated to be less than two tons, corresponding to a maximum longitudinal misalignment of 20 mm. These forces are transmitted to the inner vacuum flange through the 24 triangle supports. However, the forces are directional and therefore not uniformly distributed among these supports. Taking this non-uniformity into account, the maximum load on the support base of the end-flange is estimated to be less than 5 tons at any one point.

Power and cryo service lines.

The superconducting power lines to feed the current into the coil as well as the cryogenic lines to supply and return the cooling helium are connected to the top part of the coil on the A-side. These service lines are bundled together and brought up in the vacuum space along the wall of the cold-vessel bulkhead to the top of the cryostat. To be compatible with the LAr feedthrough

arrangement, the solenoid service line has an angle of 11.25 degrees in the r-ϕ plane with respect to a vertical line. In order to secure the space of 220 mm (ϕ) $\times$ 120 mm (z) for the service lines, a local bulge must be introduced in the warm bulkhead as shown in Figure 4-10. Figure 4-11 shows the cross section of the service lines where a G10 holder anchors the superconductor lines so that they cannot move.

Figure 4-10 Both bulkheads must make space for the power line to the solenoid. The warm bulkhead has a bulge.

Figure 4-11 Cross-section of the power lines, showing the space spared out from the cold and warm bulkhead.

The superconducting bus lines are mechanically fixed with dedicated supporting struts. This will prevent the conductors from twisting and possibly quenching during the current charge of the coil. Figure 4-12 is a sketch of the supporting struts, showing two fixing points of the strut. The magnetic force on the conductors is estimated to be 2000 N/m or smaller. The supporting struts must be strong enough to sustain this force with a deformation of less than 1 mm. In addition, the power conductors must be well cooled via thermal conduction by the LHe cooling tube of the return flow. The conductor part is well insulated thermally from the room temperature by a shielding box which is anchored at the GHe (return) temperature. The whole service line is covered by superinsulation. The first joint of cooling tubes is made in the bulkhead region near the coil. A certain space around this joint is needed near the vicinity of the joint.

Interface to the chimney

The superconducting bus line is brought into the chimney through a 250 mm diameter flange at the top of the LAr cryostat. Figure 4-10 shows a sketch of the area around the flange. The flange must be fully accessible from the top and from the bottom for the rather complex installation work of the power superconductors and cooling tubes as well as the supporting struts. At about 50 cm above the cryostat flange there is a chimney break of 50 cm in length. This break is used as a means of access for the work of jointing superconducting cables as well as cooling pipes. This chimney break is connected to a bellows unit with vacuum flanges on both ends.

The chimney is bent twice at 90 degrees as it runs through the ATLAS detector. A control dewar is placed at the top of the ATLAS detector. Current leads for the transition from normal to super is contained in the control dewar. One should note that the LAr cryostat shares a common vacuum with the chimney and control dewar. Details of the chimney and control dewars will be described in the solenoid TDR.

Figure 4-12 The power lines have to be stabilized by additional support attached to warm vessel.

Integration of the solenoid into the cryostat

The solenoid coil will be assembled first with the inner vacuum vessel of the LAr cryostat at KEK. The inner vacuum vessel needs to be delivered to Japan for this assembly by March 1999, in order to start the magnet assembly in the latter half of 1999. During the assembly at KEK the radiation shield panel, split into two half cylinders, will be mounted on the inner vacuum wall on top of the superinsulation. Then the coil assembly is installed coaxially and fixed to the vacuum vessel at the both ends using the triangle supports. A cover cryostat will be made for the cooling and excitation tests at KEK. It is expected that the solenoid will be shipped to CERN at the end of 2001. The installation of the solenoid into the barrel LAr system will take place after the EM calorimeter has been installed and tested, towards the latter half of 2002 at the West Hall. A final excitation test of the solenoid above ground will then be done in late 2002.

4.2.2.3 Support of the inner detector by the cryostat

The inner detector will be supported by ledges glued to the inside of the inner warm cylinder along all of its length. The cylinder is too thin to expect to be able to manufacture the ledge with the cylinder in one step, and welding is also impractical because of the unavoidable deformations during the welding process.

Apart from the inner detector itself, the cryostat also has to support along the inner warm cylinder and the warm bulkheads the necessary services for the inner detector. The total weight of the Inner Detector is estimated at 3 tons, and the services may weigh another 2 tons. The cooling and signal lines are divided into two groups:

- The lines to the barrel part (SCT and TRT) are permanently mounted on the inner warm cylinder and the bulkheads, with a patch panel on the inner warm cylinder around z = 850 mm,

- The services to the forward parts (SCT and TRT) are attached to a structure, so-called "Squirrel cage", supported by the ledges, with patch panels near the end of the cryostat as shown in Figure 4-13.

From this point the services are led along the warm bulkhead to a secondary patch panel near the electronics crates on top of the cryostat. From the figure one can see that the cabling space is tightest in the region of the conical section of the warm bulkhead.

In Figure 4-14 we show a cross-sectional detail around one of the ledges supporting the inner detector. One can see the cables to the barrel part which are permanently attached to the cryostat cylinder, as well as the cables from the forward part which are attached to the squirrel cage.
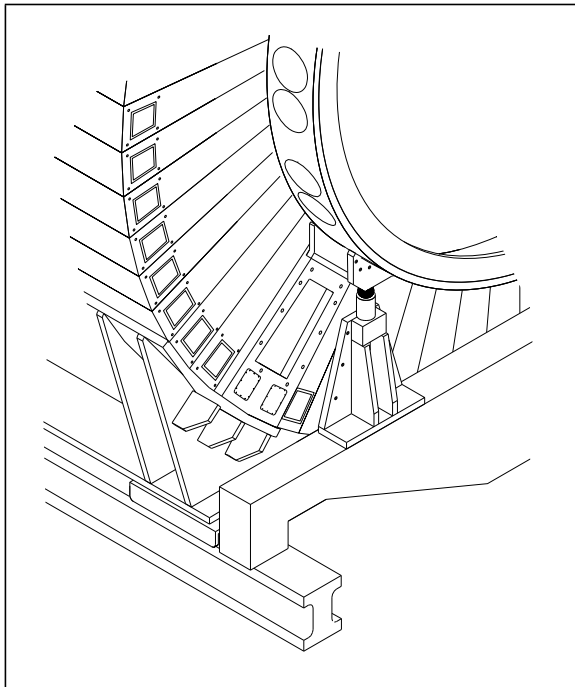
Figure 4-13 The inner detector inside the inner warm cylinder. There are other patch panels near z = 850 mm.

Figure 4-14 Support of the inner detector by a ledge on the inner warm cylinder. Also shown are the services to the central part, attached to the cylinder walls, and the services to the forward part which go to the squirrel cage.

4.2.2.4 Support of the warm vessel by the Tile calorimeter

The warm vessel is supported by the Tile calorimeter near each end as shown in Figure 4-15. A support plate is attached to the ends of the barrel Tile calorimeter at approximately 45 degrees from the bottom vertical; this supports a reinforced section of the warm outer cylinder. Stress calculations have shown that this is the position where there is a minimal deformation of the outer warm cylinder. A hydraulic jack is provided during the initial installation so that the vertical position of the cryostat can be adjusted. Once the cryostat is installed, the jack is removed. There is no need for any further adjustments later on.

The Tile calorimeter arrangement constrains the service and electronic lines from the cryostat. The Tile calorimeter electronics are inside "drawers", some of which are shown in Figure 4-15. Most of these drawers should be accessible from both sides of the Tile calorimeter, but each one *has* to be accessible from at least one side. This requirement constrains the locations of all large diameter piping from the cryostat, such as the line to the overflow vessel, the power lines to the solenoid, pumpout lines, liquid exit lines, etc.

Figure 4-15 The cryostat is supported by the Tile calorimeter at both ends.

4.2.2.5 Beam pipe

The beam pipe needs a support between the barrel and the end-cap cryostat. This will also be the location of the nearest pump station for the beam pipe. The warm bulkhead will provide a support location for the lightweight structure which will itself support the beam pipe and the pump. This structure itself does not form part of the cryostat design or manufacture.

4.2.2.6 Cryogenic and vacuum services

There are many penetrations into the cryostat. The signal and HV feedthroughs will be discussed later. Here we present the list of vacuum, gas and liquid lines which enter the cold vessel of the cryostat:

- An "overflow line" at the C-side which leads to the "overflow vessel" about 30 m away. During normal operation the LAr level will be inside this overflow vessel, so that the liquid inside the cryostat is several degrees away from its boiling point. This prevents bubble formation in the liquid due to external heat inputs. This line will also serve for pumping out the cold vessel during the initial evacuation, and as a GHe inlet during the cooldown procedure.

- He line on the opposite side from the overflow line (the A-side) allows circulation of the GHe during the cool down .

- An argon emptying line near the bottom at the C-side.

 • LN$_2$ cooling lines and return lines at both ends.

The LN$_2$ cooling lines will be attached to cooling pipes which are an integral part of the EM cal-
orimeter assembly. It is still undecided (although likely) whether one or more of the LN$_2$ lines
will have to be used to cool the region near the feedthroughs, which by themselves introduces
about half of the total heat load into the cold vessel, see Table 3.5.

The warm vessel will have additional openings: a separate monitoring feedthrough will allow
wires to enter the vacuum. Some of these will lead to the solenoid and serve to monitor strains
and temperatures of the solenoid, some will go to strain gauges attached to the outside of the
cold vessel, and some will go to location monitoring devices which accurately locate the cold
vessel relative to the warm one.

All penetrations, in particular those entering the cold vessel, have to be protected against intro-
ducing pick-up noise ("coherent noise") into the cold vessel. All of these lines to the cold vessel,
and many of the lines to the warm vessel, are stainless steel lines, connected to the cryostat by
aluminium/stainless steel transitions. In practice this implies that each of these lines has to
have a short section made of insulating material, close to but before the aluminium/stainless
steel connection.
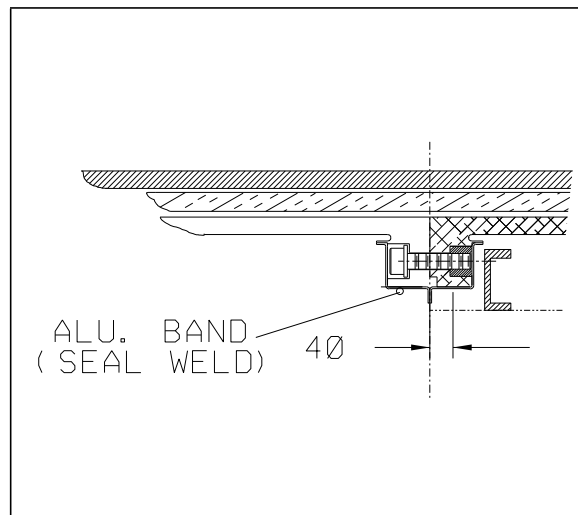
4.2.3 Operating conditions, vacuum and pressure

The cold vessel is subject to the pressure of the LAr, and there has to be a vacuum between the
cold vessel and the warm one. This affects the design of the cryostat itself, but also the sealing
methods used around the many penetrations.

4.2.3.1 Vacuum seals

We require an excellent vacuum between the cold and warm vessels. One should note that once
the solenoid has cooled down to LHe temperatures, it acts as a cryopump for argon, nitrogen or
oxygen. The barrel cryostat is designed so that all cold vacuum seals are done by seal welding,
while warm vacuum seals use O-rings, and preferably double O-rings.

Figure 4-16 shows the seal weld around the
central flange of the outer cold cylinder. In
this case the seal is under compression; the
LAr pressure forces the sealing sheet to-
wards the flange. In contrast, in Figure 4-17.
we show the seal between the outer cold cyl-
inder and the cold bulkhead. This seal is un-
der pressure from the inside, and therefore
one has to use a more complex scheme: the
flange is sealed along a lip, while a separate
channel seals the whole set of bolt holes.

Figure 4-16 The seal welds around the central flange
of the outer cold cylinder.

Apart from the main flanges, the cold vessel is penetrated by the signal and high voltage feedthrough connections, as well as by the connections for LN_2, the line to the overflow vessel, and the argon emptying line. All of these lines have an aluminium to stainless steel transition tube as their first element. The aluminium side of each of these tubes are welded into the end sections of the outer cold cylinder, while the stainless steel sides are welded to whatever connection is at the other end. We show here only one particular example: the connection to the signal feedthrough units. Since these units will be attached only after the cryostat arrives at CERN, they have to be welded from the inside. In Figure 4-18 we show one of the transition pieces welded on the aluminium side.

Figure 4-17 The seal weld between the cold bulkhead an the outer cold cylinder.

On the stainless steel side a tube is welded to the unit which protrudes back to the inside of the outer cold cylinder. The feedthrough itself ends in a tube which slides snugly inside and the final weld is made from the inside of the vessel. Of course, there will be cables dangling out from the inside of the feedthrough, and these will have to be protected during the welding process.

In contrast to the cold vessel., the warm vessel uses O-ring seals wherever appropriate: for the signal feedthroughs, for the connection of the power leads to the solenoid, and for some slow signal feedthroughs which will provide monitoring to the solenoid and the outside of the cold vessel. To the extent that this is possible, all of these will use double O-rings, with the space between them being connected to a small line so that it can be pumped out. This will allow initial testing of whether both O-rings seal properly; for all the feedthroughs this allows the testing of the seals at any single penetrations during installation, before the warm vessel is even closed.

Figure 4-18 Aluminium/stainless steel transition piece welded into aluminium vessel.

The main connections of the bulkheads to the inner and outer warm cylinders will also use double O-rings, which allows testing. But even more importantly, should a large leak develop later in *both* O-rings, one can still pump on this in-between space and reduce the effect of the leak by several orders of magnitude. This is important since to first order a leak will not produce a poor vacuum, but instead increase the heat load onto the solenoid. In this context we note that 10^{-6} cm^3/s can still be considered a small leak which would not prevent operation of the detector or use of the coil.

4.2.3.2 Pressure operating conditions

Under normal operating conditions the cryostat is completely filled with liquid argon, and there are heat exchangers inside the cryostat to compensate for the heat inputs due to the feedthroughs, the supports and the superinsulation. The liquid surface is ~ 3.7 m higher in the

overflow vessel, which is attached to the cryostat by a 17 m long line. The overflow vessel has a pressure relief valve set at 1.7 bar abs., but the normal surface operating pressure is 1.25 bar, regulated by a heat exchanger above the liquid surface. Thus under normal operating conditions the pressure is 1.7 bar at the cryostat top and 2.35 bar at the cryostat bottom (see Chapter 3, Table 3.7). Should for some reason the cooling of the liquid surface fail, the surface pressure could rise to the limit of the pressure relief valve, and the pressure inside the vessel would rise everywhere by 0.45 bar. One should note that this can happen even if the cooling of the cryostat itself continues to function; the pressure in this case is governed by the higher temperature at the liquid surface.

One should note that this is not the critical value for determining the pressure limit for designing the cryostat. This happens when for some reason there is a complete failure of the cryostat vacuum, and an ensuing large heat input into the cryostat. The liquid will start boiling, but the 17 m long line between the cryostat and the overflow vessel is still full of liquid.

The worst case occurs if there is a major helium leak from the supply lines to the solenoid. Tests with a similar multilayer superinsulation indicate that in such a case the heat loss could be as high as 925 W/m^2 of surface, which in our case amounts to a total heat input of 140 kW. Initially gas would form inside the cryostat and push the liquid out into the overflow vessel at a high rate; the ensuing pressure drop would be as high as 400 mbar. Since in such a situation the LAr level in the overflow vessel could be near its maximum, and the pressure at the relief valve could be 1.7 bar, the pressure at the top of the cryostat could be as high as 2.6 bar, and in consequence the pressure at the bottom of the cryostat could reach 3.2 bar (see Chapter 3, Table 3-10).

We are designing the cryostat as a pressure vessel with an on-axis pressure of 2.5 bar, corresponding to 2.2 bar at the top and 2.8 bar at the bottom (Chapter 3, Table3.7). In all of our calculations we are using the usual safety factor of three in both stress limits and buckling limits. This is as required by the CODAP rules. Thus, in the exceptional situation above, the nominal pressure rating could be exceeded by 0.4 bar or 14%. However, this is an exceptional situation in the sense of CODAP (CODAP C1.1.5.2), where the limits on stress and buckling safety factors are somewhat relaxed. For us the critical limit is the possibility that the inner cold cylinder might buckle. We have designed for a buckling safety factor of three at the design pressure demanded in CODAP C1.1.7.3. We note, however, that CODAP also allows a buckling safety factor of 2.2 to be used in exceptional situations. In any case, the cryostat will be subject to a hydrostatic test pressure of 1.5 times the calculation pressure.

4.3 Signal and high voltage feedthroughs

The EM calorimeter and the presampler inside the barrel cryostat will require ~ 120, 000 signal and calibration lines. In addition, there will be temperature monitors, purity monitors and probably strain monitors inside the cold vessel, in order to ensure proper behaviour of all components. In addition, a large number of HV leads are required, both to the calorimeter proper, as well as to test cells which monitor the argon purity.

There will be a total of 64 signal feedthroughs of 1920 signal lines each, connecting the inside of the cold vessel to the outside. In addition there will be two HV feedthroughs, one on each A and C side, which will each provide ~ 1000 filtered HV lines to the interior.

4.3.1 Signal feedthroughs

The ATLAS Liquid Argon calorimeters have approximately 200, 000 signal and calibration lines which must be brought out of the cryostat at all orientations in ϕ. This requires the feedthroughs to be cold. In addition to the electrical constraints of total resistance, impedance, and limited crosstalk, these feedthroughs must be robust because any leak of the liquid or vacuum could jeopardize the entire experiment. The signal feedthroughs must be fully assembled and tested with the appropriate length of pigtail cable and then brought to CERN to be welded to the aluminium cryostat.

4.3.1.1 Design considerations and specifications

The specifications that drove the technical design of the feedthroughs were quite complex. They involved geometrical and space constraints in the cryostat design, physical limitations on the space which are allocated to the feedthroughs, signal transmission quality, vacuum integrity, access, and reliability issues. We summarize the specifications below:

Density The present design has 1920 signal and calibration lines per feedthrough. There are 32 feedthroughs on each side of the barrel and 28 feedthroughs on each end-cap. The feedthroughs will have to be leak tight against a pressure of 3.5 bar of liquid argon. The aim is to have a common design for the barrel and end-cap calorimeters.

Space constraints The feedthroughs, in particular the barrel feedthroughs, are located in a prime real-estate area. They compete with the space requirements of the hadronic calorimeter and the requirements of the central detectors for space required for services and signals. In the end-cap they are in conflict with the needs for adequate shielding of the muon chambers. In addition there are the requirements in the same space for the cryogenic and vacuum services. The overall dimensions of the feedthroughs have to be minimized. The present design allows a flange size of 300 mm which is close to the maximum size that the present cryostat design concept can accommodate.

Symmetry considerations The feedthroughs have to be distributed in pairs in equal steps of $\Delta\phi$ around the perimeter of the barrel cryostat, so that the cable assemblies used in the calorimeter can be as uniform as possible. In addition, the space allocated above the feedthrough should be sufficient to accommodate the electronics boxes needed for placement of the read-out electronics. This imposes constraints on the location and extent of the routing of cryogenic services, the calorimeter support structures, and the space available for tracker services.
The situation is analogous, but not quite identical, for the end-cap feedthroughs. More details can be found in Chapter 5.

Relative movement of the two flanges: The feedthroughs will be installed at room temperature. When the barrel cryostat is cooled down, there is a relative movement of the cold and warm flanges of about 1.5 cm. Stainless steel bellows were chosen so as to accommodate this motion and to offer a high impedance for heat transmission.

Signal integrity The feedthrough cables are used to carry low level analog signals from the cryostat to the electronic box as well as calibration signals into the cryostat. Because of the fast shaping the signal integrity in this calorimeter is a major concern and special care is needed to make sure that the cables have the correct impedance. The grounding and shielding should also be adequately dimensioned to avoid signal deterioration.

Heat Loss Considerations The feedthroughs are a source of heat into the cryostat, creating a load on the cooling system and may as well create bubbles and pockets of gas. On the outside, the heat transfer into the cryostat can cause condensation if the temperature is allowed to drop below the dew point. To minimize these effects there is a limit on the allowed heat loss through a feedthrough. The heat loss allocation per channel is of the order of 7 mW, so that a feedthrough assembly including cables, bellows, etc. should have a heat loss of no more than ~ 15 W.

Vacuum system The feedthroughs are mounted between the cold and the warm vessels and have to be both pressure and vacuum tight. Each feedthrough has its own vacuum volume, so that even if there is a leak there will be no contamination of the main cryostat vacuum. There will be two vacuum manifolds for pumping out the interior of all the feedthroughs at one end of the cryostat; the "good" and the "bad" vacuum, with valves so that each feedthrough can be connected to either of the manifolds. Normally they will be connected to the good vacuum, but in the case of a small leak, a feedthrough can be connected to the bad vacuum manifold and pumped separately. In order to reduce the sensitivity to leaks, both thermal and gas, the feedthroughs may be filled with an insulating material such as Perlite.

Condensation Condensation is a problem for the electronic connections. To insure that there will be no condensation we have specified the maximum allowed heat loss per feed-through. In addition each feed-through will be equipped with a heater to make sure that the temperature at the surface is above the dew point. The dew point for the cavern should be about 12°C, corresponding to 50% humidity at 24°C.

Reliability The selected technology for the feed-through is a glass/ceramic seal to a metal pin housed in a stainless steel carrier. This is by itself a mature technology that has shown good results in applications that require extreme temperature and pressure conditions and high reliability. Still, the application that we are considering is pushing the limits of this technology for the required density.

4.3.1.2 Feedthrough design

In Figure 4-iii we show an overview of an assembled feedthrough. The warm and the cold flanges are connected by a stainless steel bellows assembly providing its own vacuum, while avoiding heat conduction. The cold flange is mounted on top of an assembly which is welded to the cryostat. The drawing also shows the path of the electric signals through the feedthrough assembly. Pigtail cables relay the signals from the calorimeter to the cold flange. Transition cables located between cold and warm flanges in vacuum carry the signals to the exterior part of the assembly. We describe briefly in the following sections each of the components.

Warm flange
The warm flange is composed of four main components: four pin carriers, a round stainless steel flange to which the pin carriers are welded, an outer ring which mates to the bellows and contains an O-ring groove, and an aluminium outer flange which provides good electrical connectivity to the electronics boxes.
In the pin carrier, metal pins are insulated and sealed by ceramic inserts. The materials are heated until the ceramic melts and bonds to the pins and the carriers. The pins are arranged in double rows of 32 pins each so that they mate standard connectors. For reasons of manufacturing convenience (machining, yield, etc.) the maximum number of pins in one carrier is about 512. We are using pin carriers with 7×64 and 8×64 pins. Two carriers of each type, mounted on a single flange, provide the required 1920 pins per feedthrough.

Cold flange

The cold flange also holds four pin carriers, which are of the same type and make as the warm flange pin carriers. The cold flange outer diameter is the size of the outer diameter of the bellows, and thus is somewhat bigger than that of the warm flange. This leaves more space between the pin carriers. This is important as the cold flange is designed to take the added pressure difference between the liquid and the vacuum which can amount to 2.8 bar in normal conditions at the bottom of the cryostat.

Attached to the cold flange is the transition piece. This will be welded on only after the pigtails have been connected to the pin carriers. It allows the feedthrough to be welded to the Al/SS transition piece which had previously been welded into an opening of the cold outer cylinder.

Bellows and vacuum connections

The stainless steel bellows connect the warm and the cold flanges and provides a separate vacuum for the feedthroughs. The separate vacuum is needed, both at the testing stage to certify the integrity of the feedthrough assemblies, and to give protection against possible small leaks past the pins.

As mentioned earlier, the bellows have to be able to allow motion between the warm and the cold flanges in two dimensions. The thickness of the stainless steel is 0.38 mm. The heat loss through the bellows is kept to a minimum and is calculated to be < 10 W per feedthrough.

Even the minimal heat loss at perfect vacuum could lead to condensation on the warm flange, unless heaters are applied to this flange. There exist commercial cables whose heating capacity is in the range that we require. These will be run on DC current and the temperature of each flange will be monitored by thermocouples so that the voltage on the heaters can be adjusted to the proper range.

4.3.1.3 Electrical connections

The electrical connections in the feedthroughs need to carry the presampler and calorimeter signals to the electronics box located on the outside of the cryostat, where the preamplifiers are located. In addition, connections for signals and power for various instrumentation inside the calorimeter will be provided using the same type of pins. There are three layers of cables which together provide a complete link between the inside and the outside.

Pigtail cables go from the cold flange to a patch panel located on the ends of the EM calorimeter. These are polyimide miniature coaxial cables in 64-cable assemblies. The cables going to the front section of the calorimeter are 50 Ω and those going to the back section are 25 Ω. Calibration cables are all 50 Ω.

Vacuum cables transfer the signals from the cold flange to the warm flange. They will all have an intermediate impedance of 35 Ω since they are short and thus their exact impedance is not critical. As the cold vessel contracts during cool down, these cables have to move both in the z and r coordinates without exerting too much force on the connectors. The heat loss through the cables has to be limited to ~ 6 mW per channel. To satisfy all of the above, a polyimide strip-line flexible cable has been designed and prototyped. It satisfies all of the above requirements.

Connection cables are short polyimide strip-line cables which connect the pins on the warm flange with the electronics crates just above. Electrically these electronics crates are inside the Faraday cage formed by the warm vessel; this serves to minimize the coherent noise (pick-up) in the detector.

4.3.1.4 Design validation and testing

The present design has undergone a detailed finite-element analysis. We show in Figure 4-iv and Figure 4-v the stresses and strains in the cold flange, which is subject to the larger pressure of 5 bar max. Both are quite small: the maximum deformation of the flange is 79 µm. The stresses are also quite modest, and this validates the concept of welding the pin carriers into the flange in a way which does not stress them.
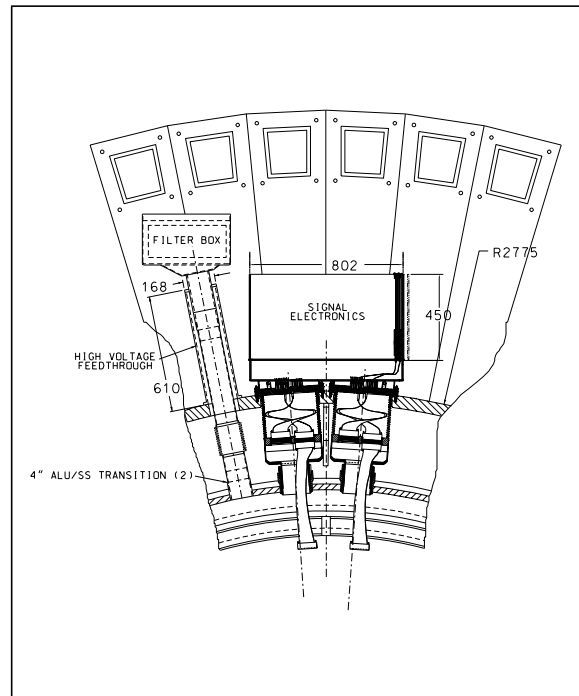
In production, each pin carrier will be tested at the factory before delivery, and after each flange has been assembled, it will again be tested. A final test of the completed feedthrough will be carried out with the cold flange cold. The test facility has a sensitivity of 10^{-10} atm.cm^3/s.

4.3.2 HV feedthroughs

There will be two HV feedthroughs on the barrel cryostat, and each will serve 1000 separate HV lines. These HV lines into the EM calorimeter will each carry 2 kV   for individual subsections. The large number of HV lines was chosen so that only a small part of the overall detector is lost should there be a broken line or a short circuit.

In principle, the HV leads can be similar to one for the signal feedthroughs, where each line goes through a vacuum region which provides thermal insulation. However, it is well known that argon, or even air, at low pressure has a very low breakdown voltage, and thus even a small gas leak into the vacuum space would lead to corona discharges or even sparks. It was therefore decided to make the HV feedthroughs in such a way that they penetrate directly from air into argon gas at 1 bar or higher pressure. Such a "warm feedthrough" has the obvious advantage that no part of the circuitry ever encounters anything except air or argon at ordinary pressure, and no breakdown will occur at electric fields below 10 kV/cm. Of course, although the actual feedthrough is never cold during normal operation, it is in principle possible that it could be touched by LAr, and so it has to be able to withstand this. We have located a company (Pave Technologies, Dayton, OH) which manufactures such feedthroughs, and we plan to use their product.

Figure 4-19 A high voltage feedthrough for 1000 HV lines. The feedthrough is from air to argon gas. The filter box contains separate RC filters for each line.

The HV lines will arrive at the cryostat surface unfiltered. Thus, the feedthrough units also have to provide RC filters for each line, situated inside a metallic enclosure which is electrically part

of the cryostat warm vessel. This filter box is positioned slightly above the electronics boxes near the top of the cryostat. After passing through the filter, each HV line is fed through the actual feedthrough layer into gaseous argon at room temperature. The fairly large total cross section of the 1000 (# 28) wires necessitates a fairly long distance before the wires touch the cold liquid. It is imperative that there be never any water condensation on the feedthrough or inside the filter box. The overall view of such a feedthrough can be seen in Figure 4-19.

4.4 Deformations and stresses in the cryostat components

The cryostat is not an ordinary pressure vessel, since it has to support a detector of 140 tons, which dominates the stress distribution and deformations in both the warm and cold vessels. In addition, the location of all the critical components has to be known to an accuracy of about 1 mm.
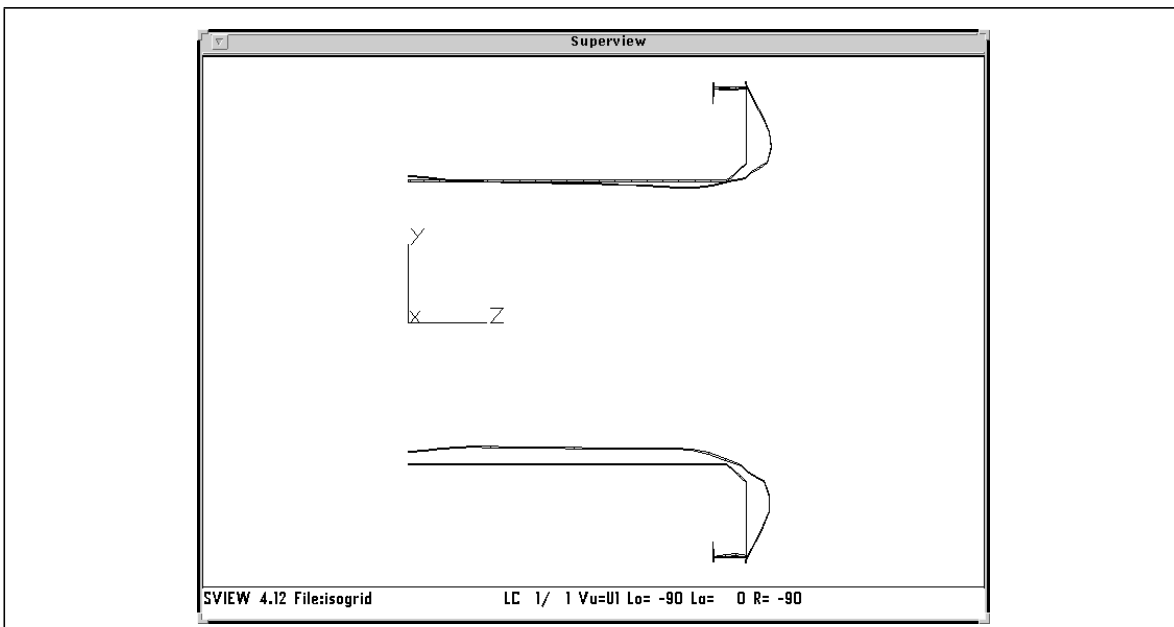
Such a device requires a detailed Finite Element Analysis (FEA), and such an analysis has been performed taking into account the various stresses and pressures due to the components. We mention here only the large weight of the EM calorimeter, and the possible large decentralizing forces due to misalignment of the solenoid or of the return path iron. The results of the calculations are described elsewhere [4-3] to [4-7]. Here we only highlight the detail to which such an FEA has to go in order to correctly show deformations and stresses.

In Figure 4-vi we show the deformations, and in Figure 4-vii the stresses, of the inner warm cylinder and the warm bulkhead under the loads of the solenoid, the inner detector and the pressure differential between ambient air and vacuum. We have repeated this calculation, adding the various possibilities of axial or transverse forces which can occur due to misalignment between the solenoid and the return iron in the Tile calorimeter.

Another critical item is shown in Figure 4-20, where we illustrate the deformation of the inner cold cylinder and the cold bulkhead. The cold cylinder - and with it the cold bulkhead - is subject not only to the average pressure of 2.5 bar, but also to the hydrostatic lift due to the argon. In consequence the bulkhead bows out by 3.0 mm maximum. The cylinder itself is stretched longitudinally, and thus its average diameter is slightly reduced. At the same time it is lifted upwards by hydrostatic force. As a result the topmost part of the cylinder hardly moves, while the lowest part of the cylinder moves upwards by about 1 mm over most of its length. The motion of this cylinder is critical since it is very close both to the inside edge of the presamplerand to the outside of the solenoid coil.

We have by now gone at least once through the analysis of each component of the cryostat. These calculations have strongly influenced the design itself; we will illustrate this here on only one example:

In Table 4-4 we show the maximum deformations and stresses of the outer warm cylinder as the support point of the cryostat is varied. At the support point the dominant force is radial; thus it itself tends to deform the cylinder. One notices a sharp minimum in the overall deformation if the support is at 45 degrees. This was the support angle chosen for the design.

Figure 4-20 Deformation and stresses of the cold inner cylinder and bulkhead under pressure. We show a cut in the Y-Z plane of both undeformed and deformed shape. The deformations are exaggerated 100 times.

Table 4-4 Maximum deformation and stresses of the outer warm cylinder when the angle of support by the Tile calorimeter is varied.

Angle (degrees)	Maximum deformation (mm)	Maximum stresses (MPa)
30.0	7.92	65.5
37.5	4.45	53.7
45.0	1.74	58.25
52.5	5.39	86.7

4.5 Testing and assembly of the cryostat

The cold vessel of the cryostat will be tested at the factory by a hydrostatic test up to 3.5 bar. This will be before any of the seal-welds have been applied. Instead temporary seals are to be used. During the test, deformations will be measured and compared with predictions by FEA. Since the signal, HV and other feedthroughs are not yet installed at this point, temporary covers will be installed. At this point the inner warm cylinder is the "spare" unit: It has neither the mounts for the solenoid nor the inner detector, it is less accurate and it may be constructed of ordinary steel.

Following this the cold vessel is disassembled and inserted into the warm vessel. The central flange on the outer cold cylinder is seal welded, but temporary seals are reinstalled at the other flanges. Both vessels are closed and the inner vessel is cooled down by a partial fill with LN_2. The deformations and motions of the cold vessel are monitored. At the conclusion of these tests the cryostat is shipped to CERN and installed in a temporary installation facility in the West Area.

After acceptance tests and opening of the cryostat, the signal and HV feedthroughs are all installed and tested. Then the EM calorimeter is installed, all cables are hooked up, and the elec-

tronics crates which mount on the warm vessel are all installed. After a thorough test of all the components of the calorimeter and read-out cables, the cold vessel is closed up, and the final inner warm cylinder with the coil already mounted on it is brought in and one of the warm bulkheads is installed. On the other side the inner warm cylinder is accurately located in the correct place. The leads to the coil are threaded through the exit opening in the outer warm cylinder, and the supports for the leads are mounted. Finally the second warm bulkhead is installed, anchoring all components in place.

4.6 Safety considerations

4.6.1 Personnel safety

A cryostat filled with liquid argon can present both a cryogenic hazard and an oxygen deficiency hazard (ODH). A broken LN_2 line or LAr line could spill liquid on personnel near or below the cryostat. The cryostat, once installed, will not move, and all lines to it will be permanently installed. Leaks in welding joints develop very slowly, if at all, and usually stay too small to endanger personnel. Thus a cryogenic hazard is likely only if a line breaks due to external impact of a foreign object. The barrel cryostat will almost certainly not be emptied, even during major maintenance such as extracting the inner detector. Neither is it likely that the LN_2 supply can be turned off during such operations. It is thus imperative that any operation inside the cave be carefully planned so that all those involved know exactly where all cryogenic lines are located, and take precautions not to damage any while moving heavy objects. Similar precautions must be taken during tests above ground.

Should the main line between overflow vessel and cryostat develop a major break, the overflow vessel will empty, but the LAr inside the cryostat will not be affected. The only outlet near the bottom is the emptying line for LAr. The valve there which is inside the cryostat requires positive He pressure to open, and thus will not spill any liquid even if the line outside the cryostat is completely open.

Another uncontrolled liquid spill could occur during a break in one of the LN_2 lines. One should consider the use of safety valves which shut off the flow during a sudden pressure drop in the line. Since the LN_2 used for cooling will normally be at a pressure of 2-3 bar, such a control device is easy to install.

Another unlikely (but in principle possible) catastrophic failure occurs if for some reason the cold vessel spills major amounts of liquid into the vacuum space between warm and cold vessel. There is a pressure relief valve near the top of the warm vessel, which will open at any positive pressure relative to ambient air, and so no liquid spill is likely in such a case. However, any major argon spill would generate many m^3 of argon gas, which will congregate below the cryostat and generate an ODH. Thus all personnel working under or near the cryostat should have ODH training, and the possibility of an ODH should be assumed in any emergency situation or warning.

The use of optical fibres around the end-flanges and feedthroughs will allow temperature drops to be monitored and LAr leaks to be localized.
Moreover, monitoring the vacuum in the feedthroughs allows a rapidly growing leak to be detected.
In both cases, one starts transferring LAr to the storage tank, an operation which takes 2.5 hours.

4.6.2 Equipment protection

Any major liquid spill will produce water condensation, which could endanger the electronics unless power is immediately turned off, and all water removed from electronics crates, feedthroughs and signal or HV cables. One should note that even minor leaks can produce significant water accumulations and damage the electronics by producing short circuits or just by slow corrosion of signal lines or connectors. This is most likely to occur at the signal feedthroughs, whose temperature could drop below freezing if the heaters fail, or if there is a bad vacuum in the feedthrough itself. Thus the temperature monitors on the feedthroughs should be able to sound an alarm or even shut off the power to the electronics .

4.7 Schedule

Figure 4-21 gives an overview of the design, manufacturing and initial installation schedule of the cryostat. Our schedule ends when the installation of the EM calorimeter begins.

4.8 Cost estimates

The CORE cost estimates, see Table 4-5, have been refined further since their last publication; the cost of the cryogenics in the cavern has decreased, while the cost of all cryostats (barrel and end-cap) has increased. In particular the cost of installation tooling was underestimated in earlier attempts. The overall sum of cryogenics plus cryostats remains the same.

Table 4-5 CORE cost estimates for the barrel cryostat.

Barrel	CORE version 6 (kCHF)
Design	1950
Manufacturing/shipping	4800
Feedthroughs	4400
Tooling	900
Installation	100
Tests	150
Total	12 300

4.9 References
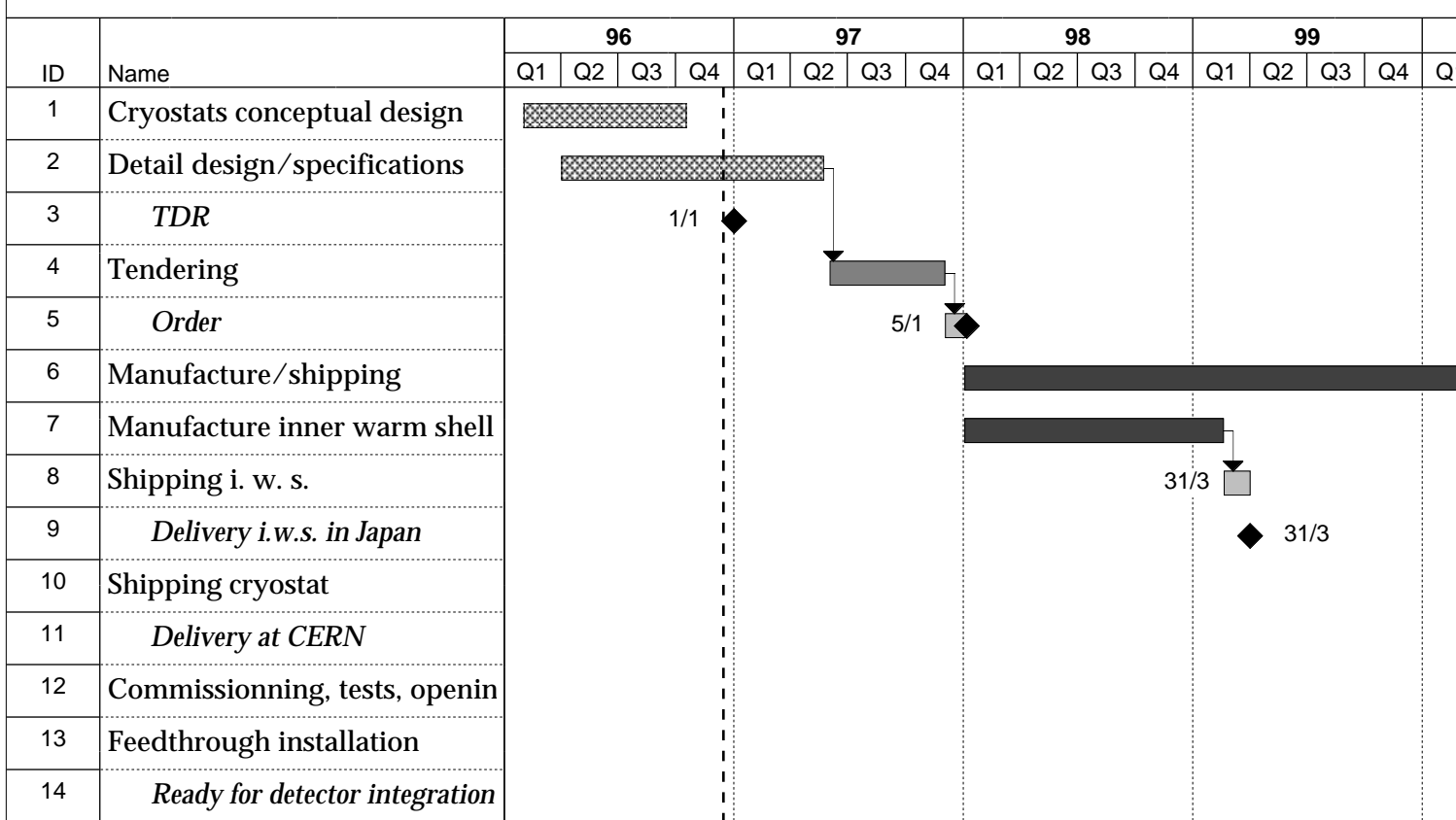
4-1   F. Lobkowicz, "Design of the ATLAS Barrel Cryostat", ATL-ABC-URO-DES-001.

4-2   A. Yamamoto et al., Conceptual Design Report of the ATLAS Superconducting Solenoid, ATLAS Internal Note TECH-020, 1996.

4-3   V. Glebov, "Finite Element analysis of the outer cold cylinder of the Atlas Barrel Cryostat," ATL-ABC-URO-FEA-001. An earlier version of this calculation was published as Atlas note LARG-NO-30.

4-4   V. Glebov: "Finite Element analysis of the outer warm cylinder of the Atlas Barrel cryostat", ATL-ABC-URO-FEA-002.

4-5   V. Glebov: "Finite Element analysis of the inner cold cylinder and bulkhead of the ATLAS BarrelCryostat" ATL-ABC-URO-FEA-003.

4-6   V. Glebov: "Finite Element analysis of the Inner Warm Cylinder and Bulkhead of the Atlas Barrel Cryostat" ATL-ABC-URO-FEA-004.

4-7   V. Glebov: "Finite Element analysis of Seal welds of the ATLAS Barrel cryostat"ATL-ABC-URO-FEA-005.

Figure 4-21 Overall barrel schedule.

Adobe's PostScript Language Reference Manual, 2nd Edition, section H.2.4 says your EPS file is not valid, as it calls setpagedevice

BARREL CRYOSTAT B   TIME SCHEDULE

ID	Name	96				97				98				99				
		Q1	Q2	Q3	Q4	Q1	Q2	Q3	Q4	Q1	Q2	Q3	Q4	Q1	Q2	Q3	Q4	Q
1	Cryostats conceptual design																	
2	Detail design/specifications																	
3	*TDR*			1/1														
4	Tendering																	
5	*Order*						5/1											
6	Manufacture/shipping																	
7	Manufacture inner warm shell																	
8	Shipping i. w. s.											31/3						
9	*Delivery i.w.s. in Japan*													31/3				
10	Shipping cryostat																	
11	*Delivery at CERN*																	
12	Commissionning, tests, openin																	
13	Feedthrough installation																	
14	*Ready for detector integration*																	

Task ▭   Milestone ◆

Figure 4-i Side view of the barrel cryostat. We show a "quarter view".

Figure 4-ii End view of the barrel cryostat.

Figure 4-iii Side view of a feedthrough.

Figure 4-iv Deformation of the feedthrough cold flange under 5 bar argon pressure. Deformations are in m.
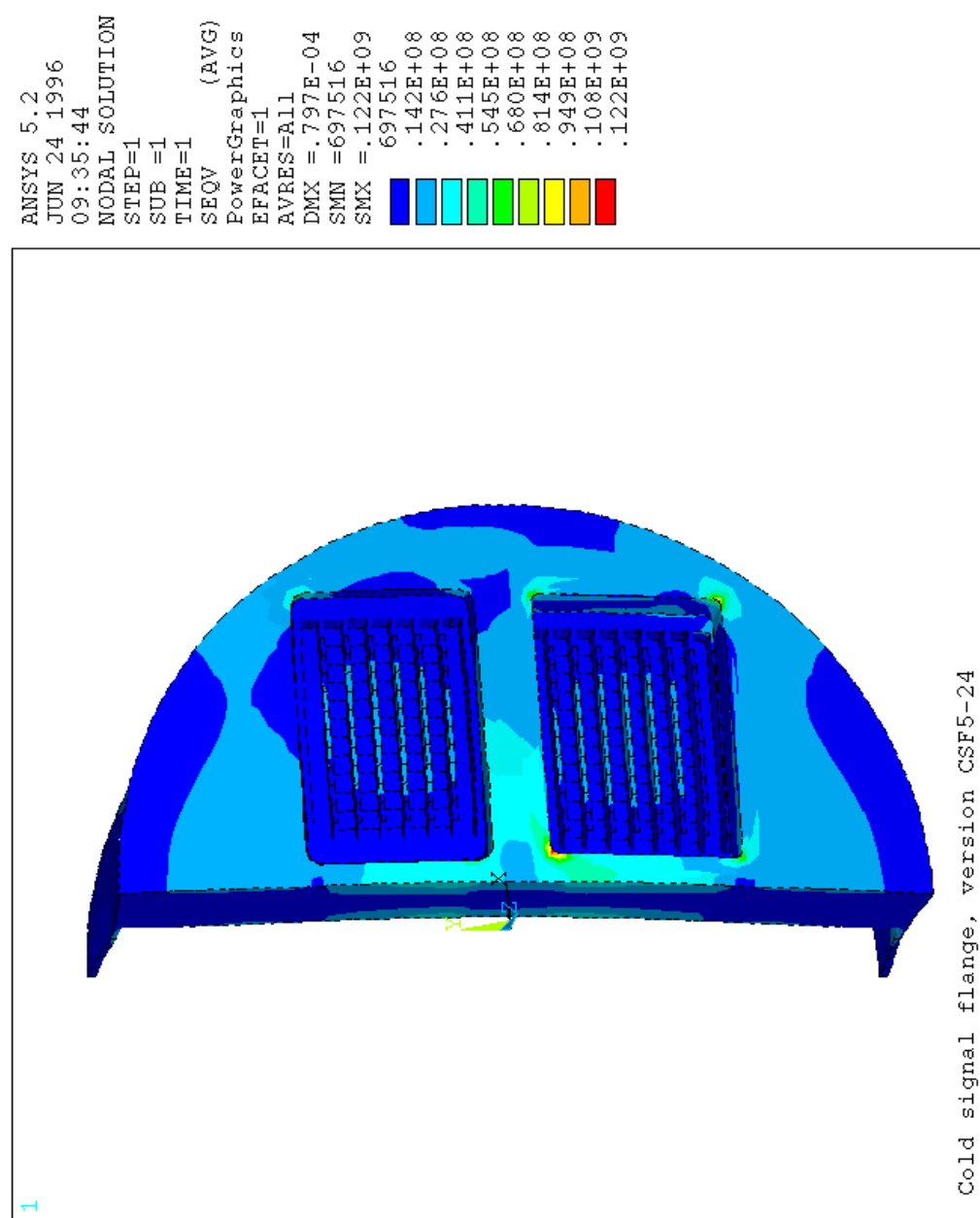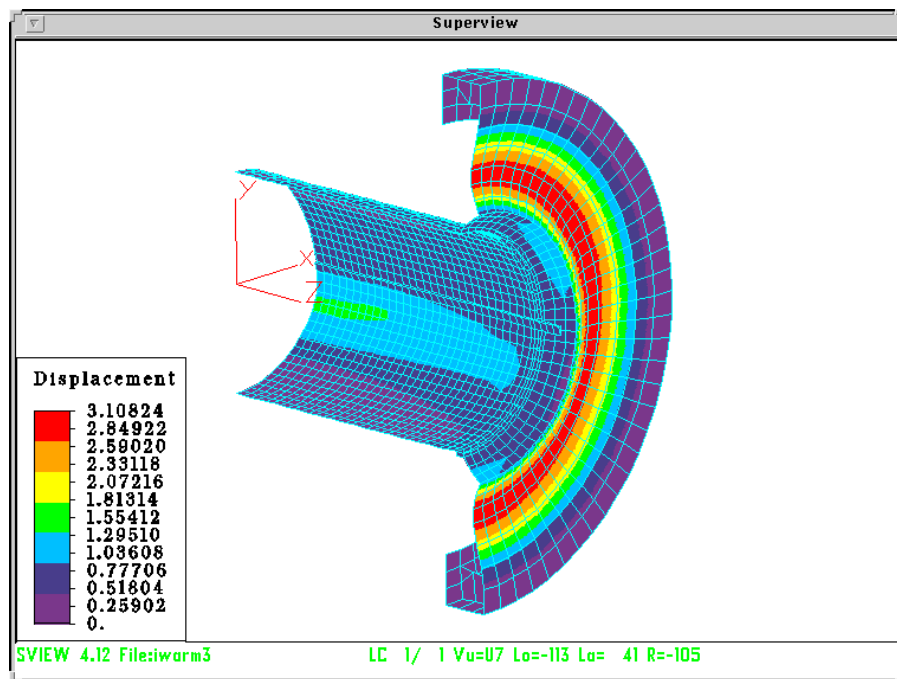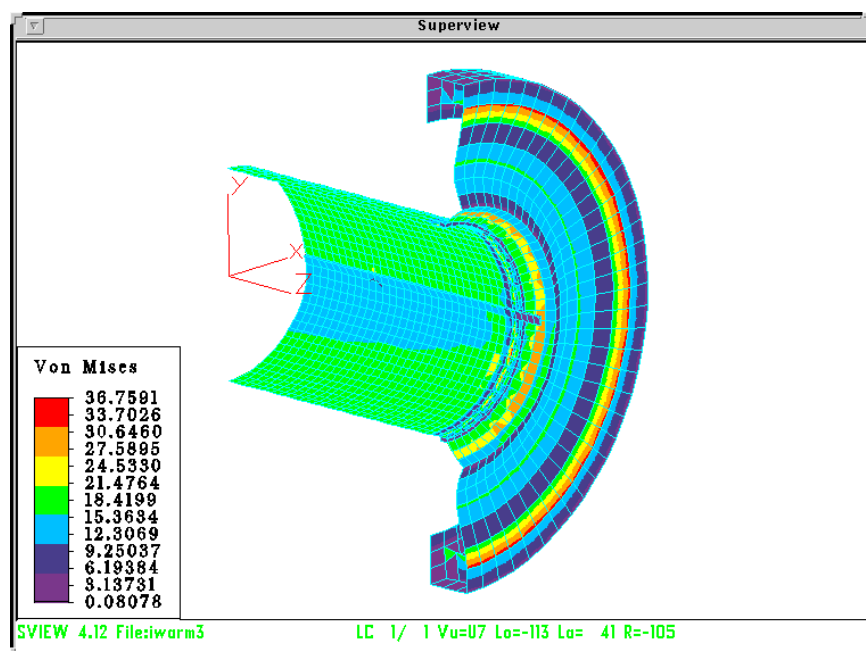
Figure 4-v Stresses in the feedthrough cold flanges. Units are in Pa.

Figure 4-vi Deformation of the inner warm cylinder with the bulkhead under the load of the inner detector, the coil and the atmospheric pressure. The deformations are in mm.

Figure 4-vii Stresses in the inner warm cylinder with bulkhead. Units are in MPa.

5 End-cap cryostat

5.1 Overview and purpose

Each end-cap cryostat contains an electromagnetic calorimeter, two wheels of a hadronic calorimeter, and a forward calorimeter. For these detectors to give the best performance, the cryostat has the following functional requirements:

- Make the best use of the allocated volume and its partitioning for the different detectors according to the physics simulation results and the boundary conditions of the   mechanical implementation.

- Minimize number of radiation lengths (structure of the cryostat and liquid argon) upstream of the detectors.

- Support the detectors by:

  - taking into account their architecture and minimizing the stresses on their structure.

  - ensuring the alignment with respect to the global apparatus and minimizing the variations caused by the different working situations (in particular during cooling-down).

- Provide the appropriate feedthroughs for the various signal, high voltage (HV), and calibration lines.

- Provide a stable and homogeneous liquid argon bath.

Additional functional requirements are related to the cryostat itself:

- Use double vessel structure for minimal heat leaks.

- Support the internal and external pressures.

- Satisfy the safety requirements due to pressurized vessels, risk of liquid argon leakage, and utilization of materials at low temperature, in accordance with the relevant CERN [5-1] and CODAP [5-2] rules.

In order to integrate the end-cap cryostat into the ATLAS experiment one has to:

- Respect the maximum volume envelope as specified by the experiment [5-3] for all operating conditions.

- Provide an opening in the centre of the cryostat for the beam tube and the associated pump station. The choice of materials in the proximity of the beam pipe should also take into account a periodical bake-out of the beam tube (during shutdowns).

- Allow the cryostat to be mounted onto the Tile detector with minimal stresses for both structures.

Furthermore, the choice of materials has been made to minimize activation under radiation. Other constraints include the seismic stresses and those resulting from transportation, handling, and installation at CERN. Finally, to accommodate movements in the ATLAS cavern together with the Tile detector for access to the inner detector and to the barrel calorimeter electronics, all supply lines include a flexible section.

5.2 Engineering design of the cryostat

The following description refers to the drawings in Figure 5-i, showing the upper half of an end-cap cut vertically, and Figure 5-ii, showing an end view of the end-cap.

The coordinate system used for the two end-cap cryostats is the one of the ATLAS experiment shown in Appendix B:

- The interaction point is the origin, Y points upwards, X is directed towards the accelerator centre, Z is along the beam.

- End-cap A is defined to be the one at positive Z, end-cap C at negative Z.

5.2.1 General concept

The cryostat is composed of two vessels made of aluminium alloy 5083. The cold vessel is filled with liquid argon at a pressure defined in Section 5.4.2. The warm vessel is loaded by the external atmospheric pressure. The space in between the vessels is evacuated to at least 10^{-2} Pa and contains multilayer superinsulation.

The cryostat vessels form a cylindrical torus around the beam axis with a flat wall in front (towards the interaction point) and a removable cover plate in the back (away from the interaction point). All cryogenic and electrical feedthroughs are integrated onto the back-end, which as a result extends to a larger cylindrical radius. The outer warm vessel of the cryostat is embedded in the Tile detector, which provides four support bearings (two at each end) slightly below the middle plane OXZ.

The inner warm tube provides space for the beam pipe and an associated pump station. It is bolted to the warm front wall. It is fixed to the warm cover plate at its backend by means of a stainless steel flange. A flexible connection between the tube and the back flange is provided by a seal welded stainless-steel bellows.

The cold inner tube surrounds the inner warm tube. The inner part of it is a double tube, called the FCAL. The smaller tube forms the wall of the cold vessel along the axis. The larger tube supports the FCAL structure detector, composed of:

- the electromagnetic forward calorimeter FCAL1
- the hadronic forward calorimeter FCAL2
- the hadronic forward calorimeter FCAL3
- the copper absorber PLUG3
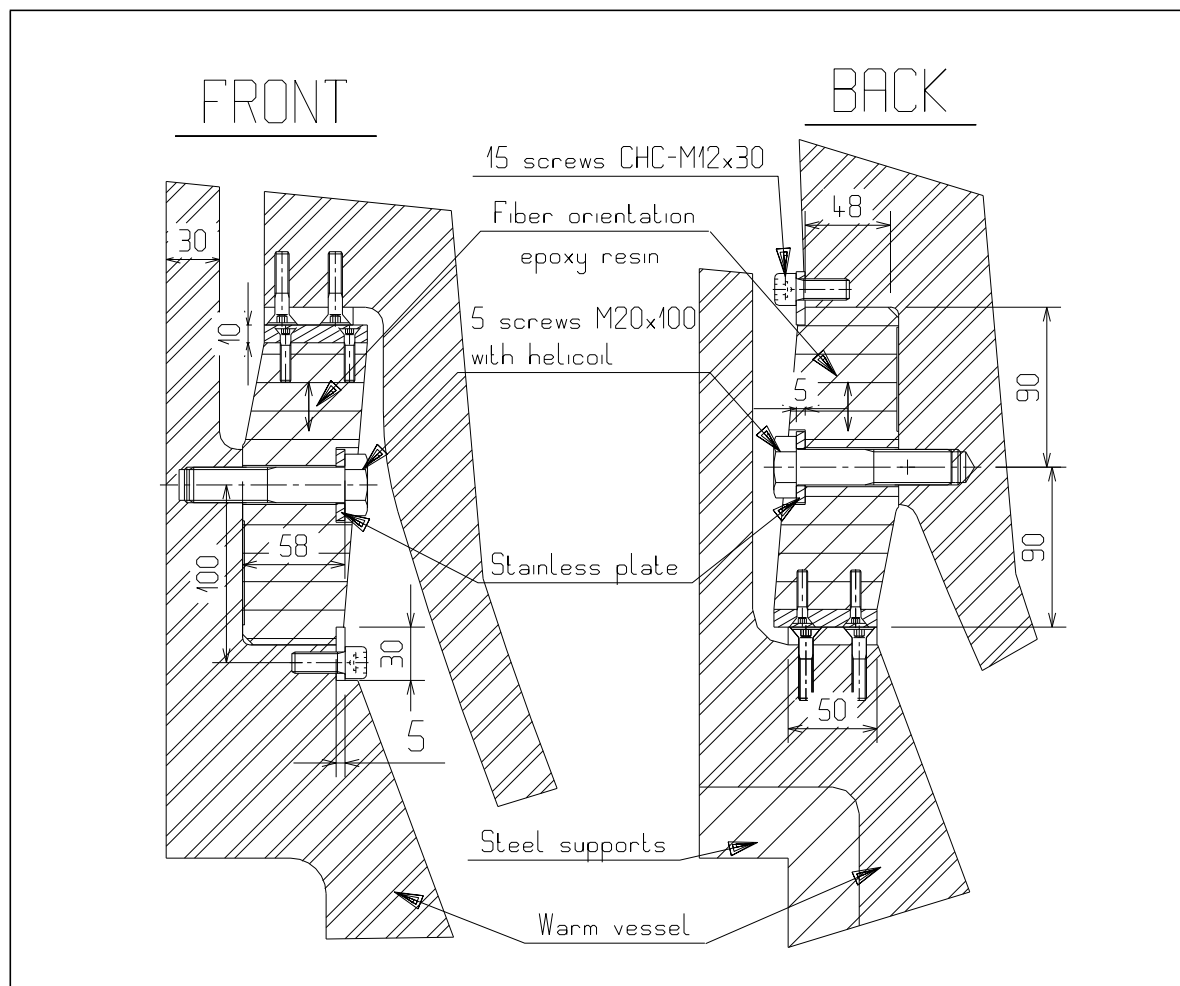
The outer tube can be removed from the FCAL structure for the mounting of the FCAL detector. It features a number of holes allowing free circulation of liquid argon. The backend of the outer tube holds the copper absorber PLUG2 on the outside.

The FCAL structure is an important element for providing mechanical stiffness of the cold vessel. The conical forward extension of the FCAL structure is bolted to the cold front wall by means of a flange. In the back the FCAL structure is closed by a cover plate. The FCAL outer tube end is bolted onto the FCAL cover plate. This plate is seal welded at its smaller radius to the inner cold tube back-end, using a bellows (equipped with a stainless-steel junction).

The electromagnetic calorimeter (EMEC) and the two hadronic wheels (HEC1, HEC2) are housed in the main part of the cold vessel. The copper absorber PLUG1 is built from segments which are bolted to the inner side of the cold back-end plate.

A region of the inner front surface of the cold vessel is counterbored to house the end-cap presampler detector (see Figure 5-i, Detail A).

Four insulating bearings made of GFRP (Glass Fiber Reinforced Plastic) support the cold vessel within the warm vessel. They are placed such that the forces are transmitted vertically to the supports of the cryostat on the Tile detector (see Figure 5-1). In order to facilitate the mounting

Figure 5-1 Cut showing the Insulating GFRP bearings to support the cold vessel within the warm vessel.

of the cold vessel, which is covered with multilayer superinsulation, the two front bearings are fixed to the warm vessel and the two back bearings are fixed to the cold vessel. The bearings are equipped with low friction stainless steel pads to allow movement during cool-down and warm-up periods.

The cold vessel positioning within the warm vessel is given:

- in X by four insulating GFRP stoppers placed top and bottom at the front and the back of the cylindrical body (see Figure 5-i Detail B and C).
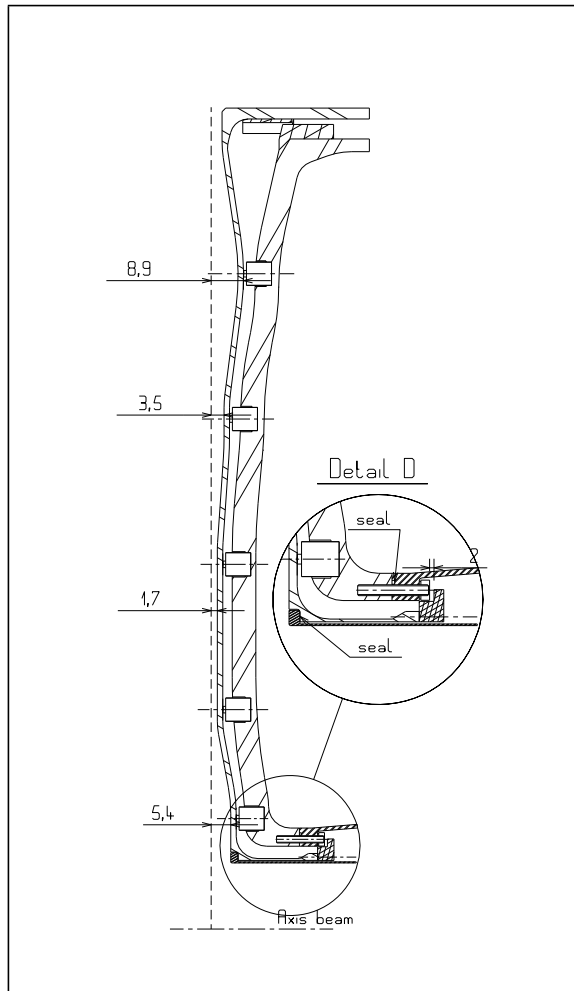
• in Z the backend flange of the cold vessel is fixed to the back-end flange of the warm vessel by four GFRP stoppers at the front face of the flange and by GFRP spacers placed between the cold and warm backend cover plates.

During cool-down and warm-up, the cold vessel and the detectors remain horizontally centered with respect to the beam axis. However vertically the detectors move downwards by 2 mm. In Z, as the detectors are fixed from the back to the cryostat rails, they move backward proportionnally (see Tables 5-1 and 5-2).
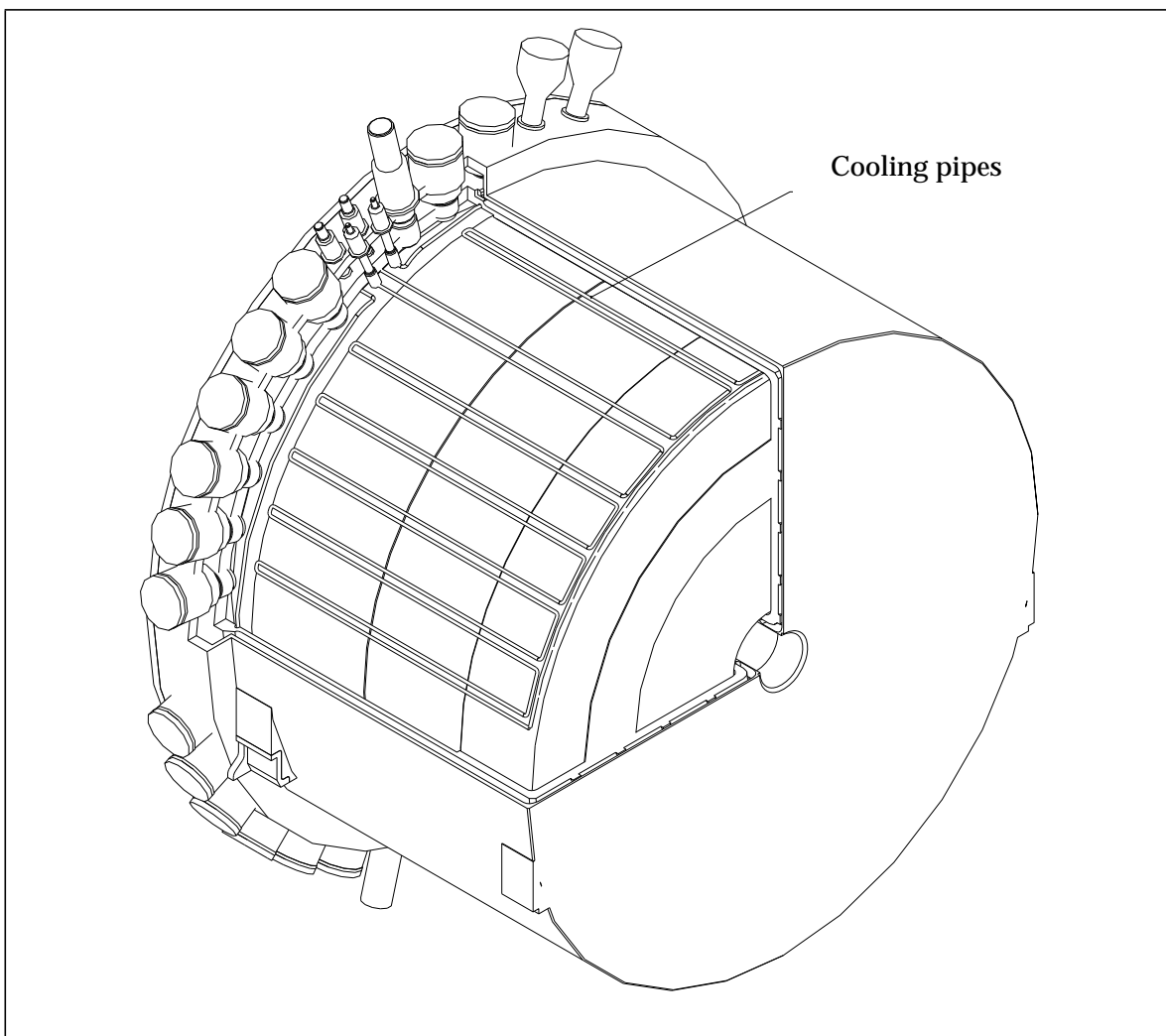
Between the front wall of the cold and warm vessels, a set of insulating spacers allows the warm wall, subjected to the external atmospheric pressure, to rest on the cold front wall. The contact between the spacers and the two walls is maintained by both internal and external pressures and by the pre-load resulting from the FCAL structure mounting (see Figure 5-2).

An inner stopper, made out of two half rings (see Figure 5-2, Detail D), is positioned during assembly after pre-loading. This stopper maintains the contact between the central part of the two end walls in case of vacuum failure. With this stopper the maximum outward deformation of the warm end wall is considerably reduced and thus stays within the design envelope [5-3].

The LN$_2$ heat exchanger piping is fixed to the inner cylinder wall of the cold vessel (see Figure 5-3). The piping consists of two independent parts, one fixed on the lower half cylinder and one in the upper half cylinder. Each of them is connected to feedthroughs for the LN$_2$ inlet and outlet.

Figure 5-2 Deformations of the cryostat front walls under pressure after cool-down (x10 magnified along the beam axis).

Cooling pipes

Figure 5-3 Open view of the end-cap cryostat, showing the heat exchanger pipes.

5.2.2 Cryostat interface

5.2.2.1 Mechanical interface to the Tile calorimeter

The cryostat is supported by the Tile detector on four bearings. Assuming the nominal vertical position, the loads are 37 tons per bearing in the front and 83 tons per bearing in the back. However in the case of a vertical misalignment, the stiffness against deformation is such, that a vertical offset of about 0.6 mm of one bearing transfers the load onto three bearings, two in the back and one in the front. The loads are consequently higher than nominal. The two front bearings of 280 x 50 mm^2 surface are free to move horizontally and are supported vertically by the Tile detector modules. These bearings are an integral part of the warm vessel structure. The bearing surface has been machined out to allow the crane adapter to be hooked on. This is secured by lateral fixing screws (see Figure 5-4).
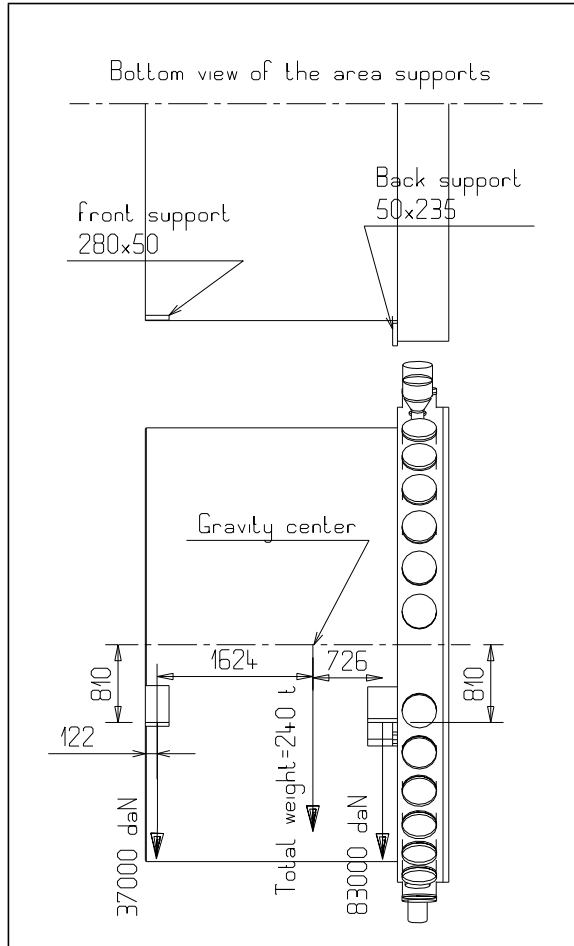
The two back feet are made of stainless steel and bolted to the aluminium warm vessel structure. Their rectangular foot surface of 235 × 50 mm^2 has its longer side aligned along X, corresponding to the support surface of the Tile detector.

The cryostat is locked in Z and X in the horizontal plane on the Tile calorimeter at the location of one bearing in the back. The other back bearing locks in Z only. As the front feet, the back feet are machined to provide a surface for the crane adapter.

Figure 5-4 Mechanical interface of the end-cap cryostat.

5.2.2.2 Beam pipe interface

The internal diameter of the central tube of the warm vessel is 102 mm. Taking into account imperfections (parallelism, cylindricality, bending), the available diameter for passage of the beam pipe is 97 mm. This diameter does not take into account the geometrical profile defined by beam pipe tolerances, relative alignment tolerances between the beam pipe and the cryostat, and movement tolerances of the Tile-cryostat assembly.

The alignment of the detectors with respect to the beam axis is carried out according to the description given in Section 5.2.3.

5.2.3 Detector interface

5.2.3.1 Forward calorimeter (FCAL)

It is mounted within the FCAL tube and sup-
ported directly by the inner cylindrical sur-
face of the tube. In fact the outer diameter of
the detectors almost fits the inner diameter of
the tube ($R_{detector}$ = 456.4 mm and
R_{tube} = 457.3 mm). The difference in diame-
ters gives space for mounting and for the
shrinkage differences between the detectors
and the tube. The positioning and fixation in
Z is given by two pins (top and bottom) for
each detector (see Figure 5-5).

The detectors have longitudinal grooves in
their outer surface to give room for the cables
running along the FCAL tube. These cables
exit the back-end between the tube and the
FCAL cover by notches in the flange of the
tube (see Figure 5-i Detail E) to allow the

Figure 5-5 FCAL detector locking mechanics.

tube to be attached onto the FCAL cover plate. The cables are terminated by connectors, which
are fixed to the tube with the help of patch panels all around the circumference of the tube.

With the back-end cover of the cold vessel mounted and the FCAL assembled (structure, detec-
tors and PLUG2), the FCAL can first be moved into the cryostat through the back-end to about
500 mm of its final position. In this position the cable ends coming from the feedthroughs can be
connected to the corresponding ones of the FCAL detector. After this operation the assembled
FCAL can be pushed into its final position, where it is centred and fixed to the front and back
plates of the cold vessel structure.

The FCAL structure coordinates are surveyed and referenced to alignment markers on the ex-
ternal part of the cryostat. The Tile-cryostat assembly will then be positioned in Z and adjusted
in X and Y within the ATLAS experiment by using the reference markers on the outside of the
cryostat, such that the FCAL detectors are centred on the beam.

The precision of the mechanical adjustment of the detectors, with respect to the beam in X,Y and
with respect to the locking device of the cryostat which positions it on the Tile in Z, is given in
Table 5-1.

Table 5-1 FCAL position tolerances (mm)

Deviations	X	Y	Z	Comments
Tolerances due to mechanical mounting precision (at 300 K without deformation)	± 0.4	± 0.6	± 0.5	
Tolerances due to reference markers on the external warm vessel with respect to the FCAL	± 0.6	± 0.6	± 1.0	
Stability after disassembly / reassembly	(see comment)	(see comment)	(see comment)	Alignment and reference markers to be redone
Stability after warm-up / cool-down	± 0.5	± 0.0	± 0.5	Due to the guidance of the cold vessel within the warm vessel
Total precision for the position of the FCAL detectors	± 1.5	± 1.2	± 2.0	
Change of position of the fixation point due to deformation and cool-down (nominal values correspond to cold status)	+ 0.3 opposite side of the anchor point of the warm vessel	- 2.0 [a]	- 5.0 (FCAL1) -2.0 (FCAL2 and 3)	The warm vessel is considered to be thermally stable

a. This value is compensated by a corresponding offset in the position of the FCAL structure with respect to the beam axis (+ 2 mm). Variations in position due to the Tile sagging under the load are compensated by shimming during integration of the end-cap cryostat on the Tile. Variations due to the moving mechanics are not included.

5.2.3.2 Electromagnetic (EMEC) and hadronic (HEC1, HEC2) calorimeters

At 75 mm below the middle plane OXZ, the cold vessel is equipped with a rail along the inner wall on both sides which serves as support for the feet of the EMEC and HEC detectors (see Figure 5-ii Detail F). The lateral positioning (centring in X) is provided by a guiding rail fixed to the top of the cold vessel (see Figure 5-ii Detail G). The Z position of the detectors is given at their backend face by stoppers in Z.

Prior to their mounting into the cryostat, the detectors are equipped with their cables, which are terminated by their connectors mounted on patch panels. Each detector slides in, is positioned in place, and fixed by two screws. Its cable harness is mounted from the front to the back onto the cold vessel and guided towards the feedthroughs. Shields are mounted to protect the cables. The patch panels are then fixed into place in the proximity of their corresponding feedthrough.

The alignment of the EMEC, HEC1 and HEC2 detectors is given by the mechanical positioning within the cold vessel, which in turn is aligned in reference to the FCAL structure, positioned on the beam axis, as described in Section 5.2.3.1.

5.2.4 Mechanical structure response under load

The cryostat is subjected to the following pre-loads:

Table 5-2 EMEC, HEC1 and HEC2 position tolerances (mm)

Deviation	X	Y	Z	Comments
Tolerances due to mechanical mounting precision (at 300 K without deformation)	± 2.0	± 2.0	± 1.0	
Tolerances due to reference markers on the external warm vessel with respect to the FCAL	± 0.6	± 0.6	± 1.0	
Stability after disassembly/ reassembly	(see comment)	(see comment)	(see comment)	alignment and reference markers to be redone
Stability after warm-up/ cool-down	± 1.0	± 0	± 1.0	due to the guidance of the cold vessel within the warm vessel
Total precision for the position of the EMEC, HEC1 and HEC2 detectors	± 3.6	± 2.6	± 3.0	
Change of position at the fixation point due to deformation and cool-down (nominal values correspond to cold status)	+ 0.3 opposite side of the anchor point of the warm vessel	- 2.0 [a]	- 7.0 (EMEC) - 4.0 (HEC1) - 0.0 (HEC2)	the warm vessel is considered to be thermally stable

a. This value is compensated by a corresponding offset in the position of the support rails in the cold vessel (+ 2 mm). Variations in position due to the Tile sagging under the load are compensated by shimming during integration of the end-cap cryostat on the Tile. Variations due to the moving mechanics are not included.

- internal and external pressures,
- weight of the different elements,
- assembly pre-load corresponding to an extra length of 15 mm of the FCAL structure,
- the loads on the spacers and stoppers between the vessels and between the detectors and the cold vessel, including the tangential friction forces due to the retraction and shrinkage differences during cool-down and warm-up phases,
- the loads on the four insulating support feet between the vessels, including the tangential friction forces on the support surfaces,
- handling and transportation loads,
- seismic stresses.

The design principle followed is to minimize the number of structural parts which are affected by the transfer of the detector loads onto the supports of the Tile detector. This was carried out allowing for thermal retractions and shrinkage differences:

- The support feet of the principal detectors are positioned in the same vertical planes as the feet on either side of the cold vessel. The detectors sit on reinforced zones of the cold vessel. These zones bend without torsion moments. In addition, the ovalization of the

back flange when the back-end cover is removed, is practically zero. This in turn allows to mount the cover without difficulty.

- The support of the FCAL detector within a tubular structure, whose ends are embedded into the front and the back of the cold vessel, also minimizes the deformation caused by the weight within the structure. Chapter_5.ps

-

Non-negligible stress-induced displacements come from the pressure loads, because of the large dimensions. In order to minimize displacement without increasing the thicknesses excessively, which would contradict the request of transparency to particles, the following principles have been adopted:

- Linkage of the front-end to the back-end of the cold vessel by means of the FCAL structure.

- Support of the end plates of the warm vessel by those of the cold vessel by means of insulating spacers. This consequently reduces the thickness of the front warm end plate to 15 mm.

- Application of compression pre-load of about 30.000 daN to the FCAL structure, due to the mechanical assembly of the FCAL structure. This pre-load reduces the final pull stress in the FCAL structure.

5.2.5 Electrical and cryogenic feedthroughs

There are four kinds of feedthroughs for which the repartition is given in Figure 5-ii:The feedthroughs for the measurement and calibration signals coming from the different detectors. In total 28 of them are grouped into four sectors of six feedthroughs each and a pair of feedthroughs at the top and at the bottom. They are pairwise connected to 14 standard electronic boxes (identical to the ones used for the Barrel cryostat), using a special pedestal base as an adapter.

- Two HV feedthroughs, integrated in the upper part of the cryostat near the top.

- Feedthroughs for the cryogenic lines:

  One of large diameter to connect the cryostat with the overflow vessel. This is mounted near the top of the cryostat.

  One LAr feedthrough connected to the bottom and used to empty the cryostat by means of gravity.

  Two inlets and outlets of LN_2 connected to the two heat exchangers are also positioned in the upper part of the cryostat.
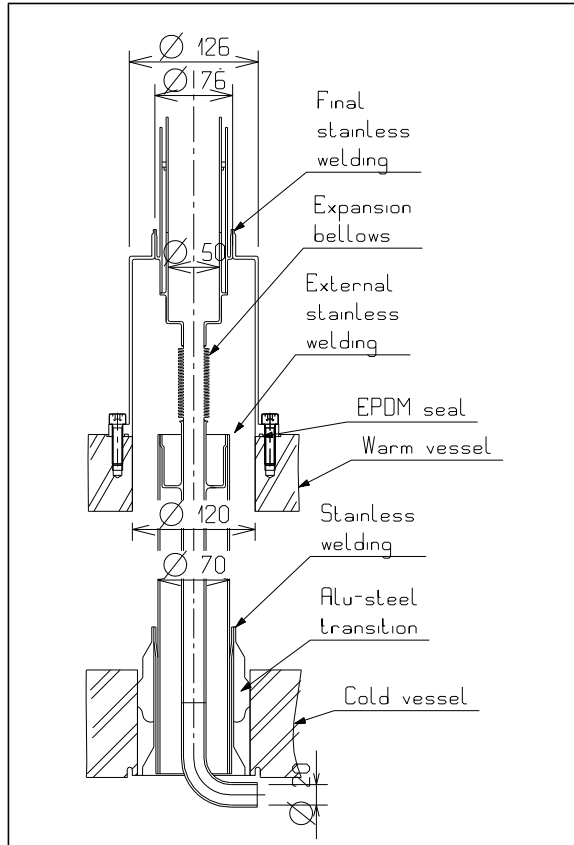
Figure 5-6 Cryogenic feedthrough (LN_2 outlet).

- The evacuation flange of the warm vessel is positioned in the bottom part. A safety relief valve, which opens at 50 mbar overpressure, is mounted onto the pipe connection to the vacuum pump.

The cryogenic feedthroughs are all fixed to the cold and warm vessel side in the same way as for the signal feedthroughs. A bellows is integrated into the structure which allows shrinkage. On the outside of the cryostat the cryogenic feedthroughs are equipped with a double wall insulated by vacuum, which interfaces to the external transfer lines (see Figure 5-6).

All feedthroughs are designed in such a way that only the aluminium weldings have to be done at the workshop, and that the stainless steel weldings can be carried out in the assembly hall at CERN. The latter kind of weld can be milled and redone several times if necessary for installation and maintenance.

5.2.6 Cryogenic and thermal considerations

With the vacuum multilayer superinsulation placed between the warm and the cold vessel, the insulating performance is mainly determined by the number of thermal bridges between the two envelopes and by the imperfections they introduce in the superinsulation coverage. The thermal bridges, which are the support feet, the spacers and stoppers, and the electrical and cryogenic feedthroughs, constitute heat sources (warm points) for the cold vessel. The electronics of the HEC1 and HEC2 detectors also introduce heat sources within the LAr bath.

The total heat flux has to be globally compensated by the two heat exchangers inside the cold vessel. The layout of the heat exchanger, within which a nitrogen gas/liquid mixture is circulating, has been chosen in accordance to [5-4]. Also the cooling has to be managed in such a way, that the heat sources taken individually do not create bubbles of argon gas, which are likely to produce short circuits between the detector electrodes. The local compensation without bubbling is based on the following arguments, which will have to be verified and quantified by thermal calculation and/or tests:

- The heat leaks through the supports, the spacers, and stoppers is distributed over a large effective exchange surface with the LAr because the structure aluminium is an excellent heat conductor.

- Effective local convection takes place within the subcooled (overpressured) liquid argon in the neighbourhood of the internal electronic heat sources [5-5], given that enough global cooling power is provided by the heat exchangers.

- The heat sources caused by the feedthrough cables are in an area which, if necessary, can be separated from the detectors by a shield, keeping potential bubbles in the zone at the extreme back-end.

- The heat exchange and temperature homogeneity of the LAr bath, specified to be better than 0.66 K, can be improved by convection which is introduced by an appropriate cooling capacity difference between the upper and the lower heat exchangers.

5.2.7 LAr and vacuum tightness

The sealing of the cold vessel is performed in four different ways, depending on the location:

- by aluminium welds for the structural parts and for the connection to the different bimetallic junctions. These welds are planned to be carried out by a certified welding crew, in an industrial environment.

- by stainless steel welds for the connection of the bimetallic junctions to the different feedthroughs and bellows.

- by the bimetallic junctions stainless steel - aluminium themselves.

- by metallic HELICOFLEX® seals for the three bolted structural parts of the cold vessel.

The fixture of these seals (see Figure 5-7) uses stainless steel bolts and INVAR® rings, which by their small expansion coefficient, allow differential shrinkage between the stainless steel and the aluminium to be compensated during and after cool-down.

The reliability of HELICOFLEX® seals of less than 1.20 m diameter, as is the case for the sealing of the FCAL end plates, has been qualified by similar applications, usually, however, with stainless steel flanges.

The new aluminium barrel test beam cryostat (see Chapter 13) is equipped with seals of 1.50 m in size and will serve as a test for validation.

A larger metallic sealing of about 4.50 m in diameter is needed in order to be able to remove the cold end plate, when access to the detectors is needed. If a leak develops, a repair procedure using seal welded aluminium profiles over the end plate connection and boltings, in a similar way as for the barrel, would be applied.

Figure 5-7 Fixure and sealing of the coverplate on the cold vessel.

However, this option still has to be designed and tested.
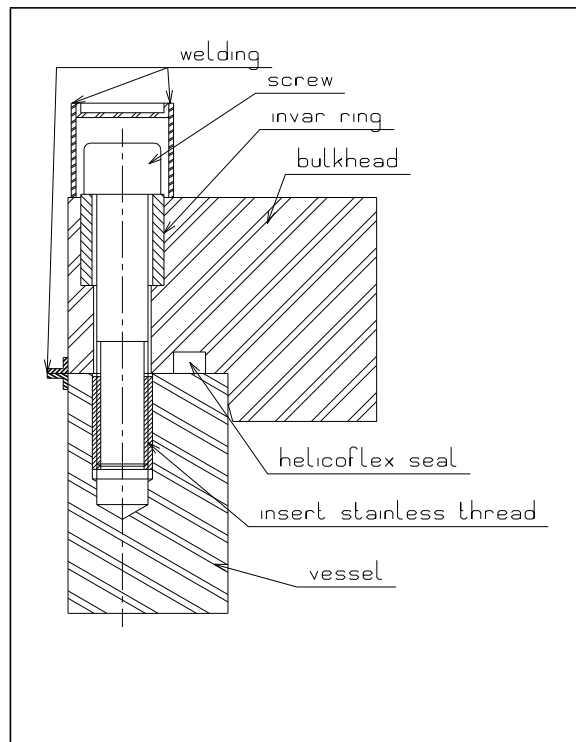
The seal for the warm vacuum vessel are always done by using EPDM[1] O-ring seals.

5.2.8 Monitoring equipment

The equipment foreseen to monitor the cryostat during the various working situations consists of different sensors for the measurement of temperature, stress and position. These are installed in the inter-vessel space.

The stand-alone vacuum of the feedthroughs will be monitored in order to be able to detect any possible leak of liquid argon coming from the cold flange.

An optical fibre will be wound around the warm flange of the feedthroughs to monitor their temperature, as a mean of early detection of leaks from cold to warm.

---

1. Ethylene-Propylene Difunctional Monomer copolymer

5.3 Design of the electrical feedthroughs

The feedthroughs for the signal and calibration lines are the same as for the barrel calorimeter. They consist of a cold flange (in contact with the LAr) and a warm flange (in contact with the external cryostat) which are separated by a monitored vacuum, which is independent of the envelope vacuum and have a pumping flange connected to the warm flange (see Chapter 4, Section 4.3.1). The layout is the same as on Figure 4-iii. The connection on the cold side is made by a stainless steel weld to a bimetallic junction, which is in turn welded to the cold vessel side by an aluminium weld. The link to the warm vessel is made by means of a chimney with one end bolted to the warm flange of the feedthrough. The leak tightness is provided by an elastomeric joint. The other end of the chimney is bolted to the warm vessel, again using an elastomeric joint to seal the connection.

The internal cables, coming from the feedthroughs, are terminated by connectors and are long enough to allow placing them outside of the cold vessel towards the backend during the mounting of the detectors, and then connecting them to the detectors. The cables are standard, (see Chapter 10), apart from some connected to the FCAL, which need to be longer.

The HV feedthroughs are built according to a different principle (see Chapter 4, Section 4.3). They have a single warm flange, which is insulated from the liquid argon by a layer of argon gas, created by heating the liquid argon in contact with the warm flange. This works, unlike the other feedthroughs, by positioning the two HV feedthroughs on top of the cryostat. The connection to the cold and warm vessels is made in the same fashion as for the feedthroughs described previously: by a stainless steel weld to a bimetallic junction on the cold side and by a bolted connection with an O-ring seal on the warm side.

The HV and signal feedthroughs will also be equipped with printed circuit heaters, to prevent condensation and icing, which might cause O-rings leaks..

5.4 Working situations and load cases

5.4.1 Specifications and mass table of cryostat materials

The total mass of the cryostat of 23.6 tons plus the mounted detectors of 218.6 tons (without liquid argon) amounts to 242 ± 2 tons. For the crane load one has to add the mass of the crane adapter of 10 ±2 tons. The mass of the liquid argon filling is 26 tons. A detailed list of the masses is given in Table 5-3 for the detector masses and in Table 5-4 for the cryostat masses. All materials used to build the cryostat are given in Table 5-6.

5.4.2 Description of situations and load cases

The operation of the cryostat can be described in terms of different working situations given in the following list. The situations are put, according to the CODAP rules, into the three categories: normal situation, exceptional situation and test situation.

Table 5-3 Detector masses (in tons)

Qty	Detector Part	Material	Mass
1	EMEC Electromagnetic calorimeter	Lead - stainless steel	24.2
1	HEC1 hadronic calorimeter	Copper	69.4
1	HEC2 hadronic calorimeter	Copper	92.2
1	Absorber (PLUG1 fixed on the cold end cover)	Copper	19
1	FCAL1	Copper	2.8
1	FCAL2	Tungsten	4
1	FCAL3	Tungsten	4
1	FCAL absorber (PLUG3)	Copper	2.5
1	FCAL absorber (PLUG2)	Copper	0.5
	Total mass of detectors without LAr		**218.6**

Table 5-4 Cryostat masses (in tons)

Qty	Cryostat Part	Material	Mass
1	Cold vessel (feedthrough interface and welding seams included)	Alu 5083	7.3
1	Warm vessel (feedthrough interface and welding seams included)	Alu 5083	5.3
1	FCAL structure in two parts + cover	Alu 5083	0.45
1	Cold cover plate	Alu 5083	3.6
1	Warm back cover plate	Alu 5083	3
1	Warm inner tube	Alu 5083	0.019
28	Electrical signal feedthrough		0.04
28	Cable harness		0.054
2	HV feedthrough		0.04
1	Cryogenic safety feedthrough	Stainless steel	0.02
2	Return feedthrough for liquid and gaseous N_2	Stainless steel	0.02
2	N_2 input feedthrough	Stainless steel	0.02
1	LAr emptying feedthrough	Stainless steel	0.02
1	Vacuum pumping feedthrough to the inter vessel volume	Stainless steel	0.02
1	General nuts and bolts (about 500 all diameters)	Stainless steel/ Alu 2219	0.5
	Miscelleaneous		0.5
1	Cooling pipes (total length = 170 m)	Stainless steel	0.08
	Total cryostat mass without detectors and without liquid argon		**23.6 $\pm$ 2**

Normal situation:

1. Standard run condition (including a deregulation up to 1.7 bar of the nominal expansion vessel pressure of 1.25 bar)

2. Purging (successive application of 0 to 1 bar helium pressure in the cold vessel in order to purge it before cool-down and filling with LAr)

3. Cool-down with helium ∕ warm-up with helium

4. Filling with LAr ∕ purging LAr

Exceptional situation:

5. Transport of the empty cryostat from the factory to the assembly hall at CERN

6. Mounting ∕ dismounting of the different detectors

7. Surface transport at CERN from the assembly hall to the pit (warm cryostat with mounted detectors)

8. Lowering by crane into the pit

9. Displacement for access of the complete cryostat filled with liquid argon and hooked to the cryogenic lines

10. Rupture of the inter vessel vacuum with the pressure maintained at about atmospheric pressure

11. Leakage of liquid argon into the insulating vacuum space

Test situation:

12. Helium leak test under vacuum of the cold vessel with its bimetallic junctions welded in at the aluminium end and obturated at the stainless steel end.

13. Helium leak test under vacuum of the warm vessel with obturated feedthroughs and the cold vessel mounted inside to hold the cover.

14. Helium leak test under vacuum of the assembled cold and warm vessel equipped with cabled feedthroughs.

15. Hydraulic pressure test.

With regard to the mechanical stiffness and taking into account the safety factors corresponding to the different situations one can cover the situations by five different load cases described in Table 5-5. Each of these load cases has to be verified by structural calculations. To be on the safe side, situation 1 must be validated with only one front foot in contact with its Tile support and in addition under consideration of seismic stresses specified by 0.15 g in all directions.

Table 5-5 Load cases, refering to the situations described in the text

Load case	P_{total} [a] (bar)	Inter vessel Pressure (bar)	T cold vessel (K)	T warm vessel (K)	Detectors mounted?
Normal situation					
1 + one front foot without contact	1.7 + 1	0	87	300	yes
2	0 to 1	0	300	300	yes
Exceptional situation					
1 + one front foot without contact + seismic effects	1.7 + 1	0	87	300	yes
11	1.7 + 1 + 0.2	1.05	87	300	yes
Test					
12	0	1	300	-	no
15	3.1 / 4.05 [b]	0	300	300	yes

a. The total pressure in the cryostat results from the regulated gas pressure in the expansion vessel plus the pressure of the LAr column plus the pressure loss in the connecting cryogenic line

b. P_{test} hydraulic = 1.3 x P_{ns} x f / f_t = 1.3 x 2.7 x 78/87.5 = 3.1 bar with P_{ns} = maximal calculated pressure in the normal situation according to CODAP and with f, f_t = admissible calculated stresses in the normal situation at 300 K and at 87 K respectively
P_{test} hydraulic = 1.5 x P_{ns} = 4.05 bar according to TIS

5.5 Structure analysis

5.5.1 Calculations based on dedicated models

In order to validate the design principles adopted and described in Section 5.2.4 (stopper support of the warm front cover on the cold front cover, application of pre-loads) and in order to optimize the structure thickness and reinforcements with spacers, dedicated models are used.

- 2D axi-symmetric model of the two vessel envelopes for the pressure calculation.

    In this model one considers the cold vessel zone with the highest stresses (see Figure 5-iii). This high stress zone is shown in part 1 of the figure for which the maximal stresses of the two dimensioning cases are:

    - case 1: $\sigma_{von\ Mises}$ = 85 MPa with 87.5 MPa admissible

    - case 15: $\sigma_{von\ Mises}$ = 106 MPa with 119 MPa admissible
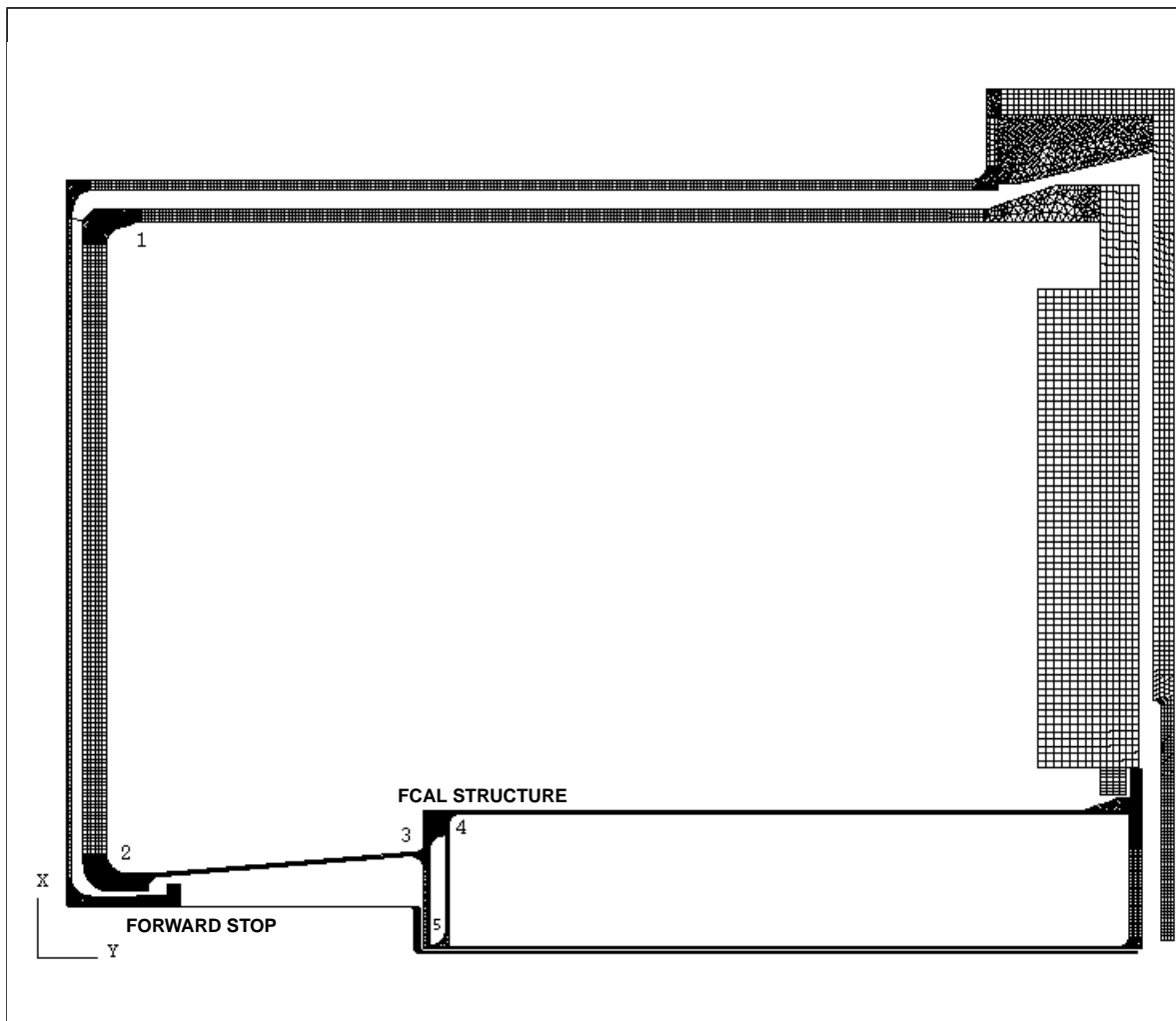
    The model is used to validate the following design principles:

    - support of the thin warm front cover on the cold front-end of enhanced thickness. In fact, the results show, that on one hand the warm front end is subjected to small stresses only and on the other hand reduces the stresses in the cold front end by transmitting the outer atmospheric pressure onto it.

Table 5-6 Cryostat materials.

Material	used for	$R_{ultimate}$ in MPa 300 K / 87 K	$R_{0.2}$ in MPa 300 K / 87 K	A in% 300 K / 87 K	E in MPa	Thermal conductivity in W / m K 300 K / 87 K	Performance under 20 years radiation load at 10^{12} to 10^{16} Neutrons/cm^2/ year
Aluminium 5083 H111 (AlMg 4.5 Mn)	the structure of the cold and warm vessel	275 / 390	125 / 140	16 / 34	71,000 / 78,000	150 / 80	good
Stainless Steel 304L (Z 2 CN 18- 10)	nuts and bolts	600 / 1320	210 /350	60 / 40	200,000/2 10,000	17 / 9	good (activates)
Stainless Steel ASTM XM14	cryostat support	805 / 1644	430 / 955	59 / 33	200000 / 210000	17 / 9	good (activates)
Aluminium alloy 2219 T 851 or T 6	insert bolts	410 / 610	300 / 300	10 / 12		- / -	good
cryogenic INVAR	fitting rings	470 / 980	280 / 680		14,500 / 13,800	10	good
GFRP STESALIT 4411 W	spacers and insulating supports	410 under compression 270 under traction			24,000 / -	0.8 / 0.4	
EPDM	warm seals						good
HELICOFLEX (Alu + Inconel 600 + NIMONIC 90)	cold seals						good (activates)
Superinsulation (aluminized Polyester + Polyethylene Terephalate)	filling of the inter vessel space					average value 6 W / m^2	good
Copper	absorber	23 / 37	7 / 12	- / -	12,500 / -		good

- pre-load of the FCAL structure at time of assembly. In fact, this pre-load reduces the stresses in the FCAL structure (zone 2, 3, 4 and 5), at the cost of zone 1. In consequence zone 1 has to be reinforced (see Figure 5-8).

- holding the warm front end by the front spacers (in the case of situation 11 of over pressure in the inter vessel space) within acceptable limits.

Figure 5-8 Dedicated axi-symmetric 2D model for calculation of the cryostat under pressure load only.

- 3D model of the cold vessel.

  This allows the support of the detectors within the cold vessel and the balancing of the load by the four feet supports between the cold and warm vessels to be verified. This introduces small additional stresses into the cold vessel in the vicinity of the thickened median zones (below 12 MPa), apart from the reinforced zone at the very feet, where the stresses amount to 43 MPa (without adding the stresses coming from the vessel pressure load). In addition, the deformations stay within small limits, such that the back flange of the cold vessel deviates only 0.7 mm from a circle shape. Based on this result one can plan for the mounting of the detectors and the closing of the cold back cover without auxiliary support tools.

- simplified 3D model of the cold vessel

  This is used to evaluate the overstresses and the corresponding deformations of the cryostat supported by three feet only (one front foot off contact).

  The stress of the double vessel under torsion turns out to be:

  - $\sigma_{\text{von Mises}}$ = 10 MPa within the cylindrical part

  - δ_{vertical} = 0.6 mm plus the displacement of the foot

- 3D model of the steel fittings which support the back end of the cryostat

  The calculations shows, that for a load of 120 tons on these iron fittings (a very conservative limit), one obtains:

  - $\sigma_{\text{von Mises}}$ = 264 MPa.

5.5.2 3D finite element analysis

A finite element model as shown in Figure 5-iii has been established using the SYSTUS program package. This allows a simulation of both vessels with the different stoppers and spacers between them with the consideration of the corresponding tolerances. It has the possibility to load the structure with all kinds of stresses to which it is subjected: pressure, weight, pre-load and seismic stress.

The shell model approach is used to determine deformations and reaction forces on bearings and fixations. The reaction forces are used as boundary conditions in local 3D models, which are used to calculate stresses in zones under high loads.

The analysis is not yet complete. However preliminary results are shown in Figure 5-iv. Stresses calculated using the shell model for load case 1 are shown. Some very local stress concentrations are too high and will be analysed using a local 3D model, which is better adapted to stress analysis.

5.6 Planning, manufacturing and assembly

There are three levels of responsibility in connection with the development and production of the complete end-cap. These levels correspond to the PBS scheme and are described below.

- First level:

  Structure elements of large dimensions made out of aluminium alloy are going to be built by a manufacturer specialized in vessel construction and aluminium welding. Also the welds to the aluminium end of the bimetallic junctions are supposed to be carried under the responsibility of the manufacturer, as are the leak tests and the hydraulic safety tests.

- Second level:

  The cold and warm vessels assembly work could be done, either at the manufacturing plant to benefit from its infrastructure and logistics and to avoid costly transportation, delays and risks of damage, or in another place to be defined (CERN for example). The set of parts needed to equip the vessels can be built elsewhere.

- Third level

  The cryostat will be delivered to the CERN assembly hall, where the feedthroughs will be mounted, the stainless steel welds performed, and the detectors mounted (under the responsibility of CERN together with the detector builders team). Details of the integration work planning connected with this third level are given in Chapter 14, Section 3.

5.7 Safety considerations

5.7.1 Risk cases

The risks are of different nature and origin owing to:

- the fact that the structure is pressurized

- the behaviour of the different materials at LAr temperature

- the use of liquid argon and nitrogen, which can be dangerous to people in case of spill out

- the aging of materials submitted to high doses of radiation, which can compromise their mechanical performance

- the activation of materials by radiation, which presents a hazard to the maintenance personnel.

5.7.2 Treatment of risk cases

5.7.2.1 Mechanical stiffness

The end-cap structure has been checked with respect to its behaviour under load by reference to the CODAP rule C10 for all the operational situations.

The finite element calculations have been done using two different program packages:

- SYSTUS (ISO 9001 certified), which allows on one hand the predimensioning and optimization of the structure by means of shell elements of the 3D type or the simplified axisymmetric type, and on the other hand the validation of the structure by means of a combination of shell elements and volume elements (not yet finished).

- ABACUS (ISO 9001 certified), which is used for a second calculation and independent validation (not yet finished).

The safety coefficients between maximal stresses and admissible stresses are taken in accordance to the CODAP safety code and are different for the normal and exceptional situations. In addition all aluminium welds will be certified according to the CODAP rules (see Table 5-7).

Table 5-7 CODAP criteria for admissible stresses depending on the type of situation.

Situation	Structure parts	Nuts and bolts
Normal situation	$\mathrm{Min}(R_{0.2}/1.6 , R_{\mathrm{ultimate}}/3)$	$R_{\mathrm{ultimate}}/5$
Exceptional situation	$\mathrm{Min}(0.95xR_{0.2} , R_{\mathrm{ultimate}}/2)$	$R_{\mathrm{ultimate}}/3$

All materials used are cryogenic compatible, even those of the warm vessel, in particular the two steel fittings and bearing fixation bolts, which support the back end of the end-cap cryostat.

At the time the different loads are established, the variations of the stresses can be measured and checked in place by means of the stress gauges installed on the structure. The measured values can be compared with the results of the calculations.

5.7.2.2 Leakage of cryogenic liquid

There are three possible causes of leakage:

- porosity of the material
- defective welding
- leaking seal

The non-porosity of the materials (grain size, cracks, etc) will be assured by specifying the supply and by the global leak test once the assembly is finished.

The design of the aluminium and stainless steel welds as well as that of the bimetallic junctions, will be subjected to development tests during 1997.

The welds will be X- rayed, 10% of the circular ones and 100% of the longitudinal ones, and all knot welds. Ultrasonic tests will be done if necessary before the leak tests of the vessels and the completed cryostat, which provide the ultimate verification.

The design of the cold seals has been discussed in Section 5.2.7. Some tests have to be done to justify the reliability of these solutions.

During the operation, any possible leak at the level of the feedthroughs will be detected by monitoring the temperature with optical fibres.

5.7.2.3 Radioactivity

The materials have been chosen by considering their satisfactory behaviour under long term irradiation. With reference to maintenance, the problem of residual radiation needs further studies. However, a first qualitative study has been done (see Chapter 11).

5.8 Schedule for procurement, fabrication, transport and tests at CERN

The overall schedule is given in Table 5-8 below.

END-CAP CRYOSTATS A&C   TIME SCHEDULE
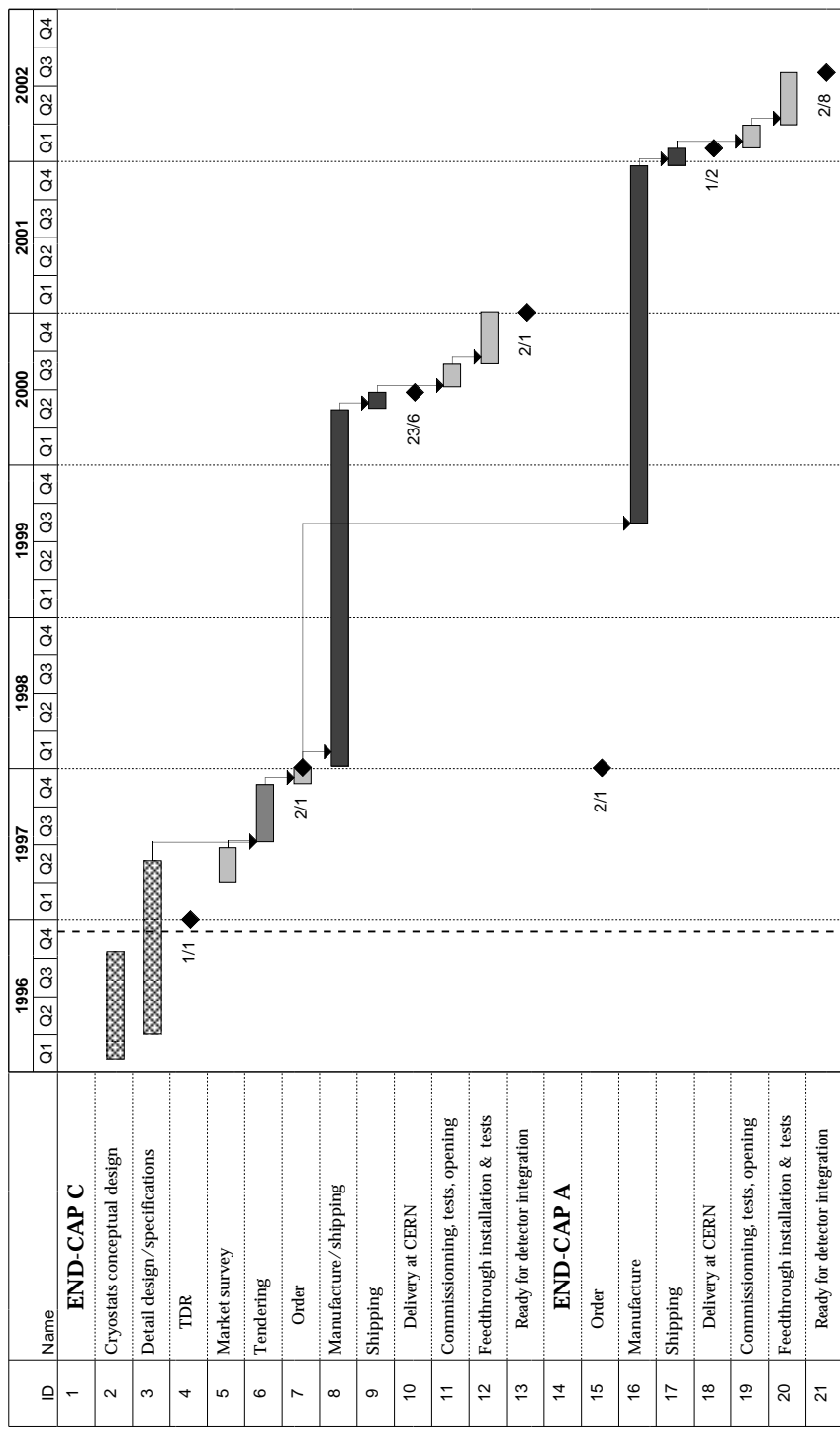
Table 5-8 Time schedule for the end-cap cryostats A&C

5.9 Cost

Table 5-9 End-cap A&C cost (kCHF)

End-cap	TDR
Design	960
Manufacturing	4000
Feedthroughs	4000
Transport	
Tooling	900
Installation	100
Tests	150
Total	10110

5.10 References

5-1   CERN Safety Code D2, Issue 1988.

5-2   CODAP, Code Français de Construction des Appareils a Pression non soumis a l'Action de la Flamme, Edition 1995, SNCT AFIAP.

5-3   Space occupied by the end-cap in ATLAS: CERN drawing AT280151PL, 24/01/1996.

5-4   Caractéristiques de l'installation cryogénique, Technical Specifications, Note CEA ref.: 5 C 5720 T 00795 A.

5-5   D.H. Jung, H. Laskus, H. Stenzel, Atlas Internal Note LARG-049, 1996.

,

.
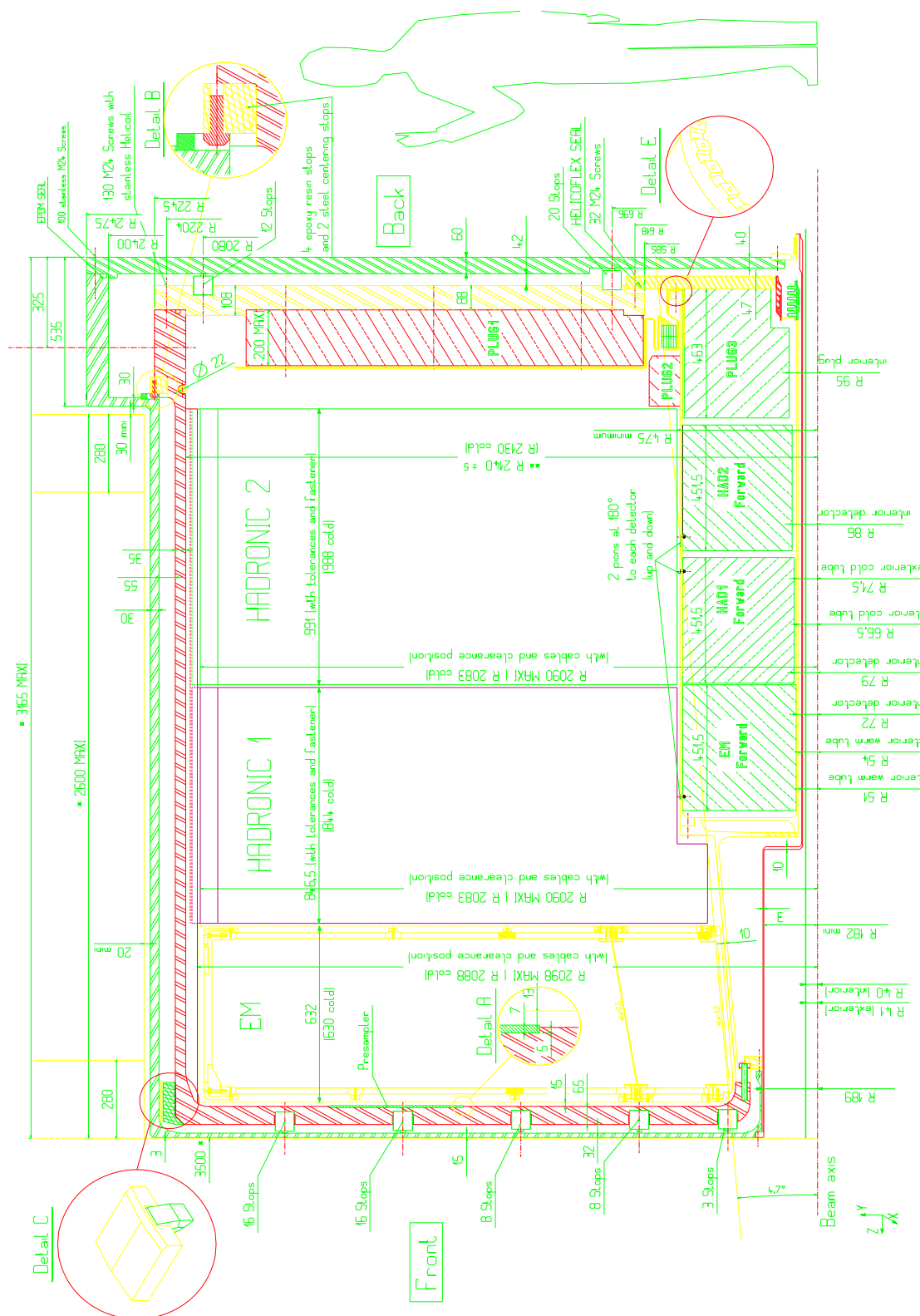
Figure 5-i Upper half of an end-cap (cut vertically).
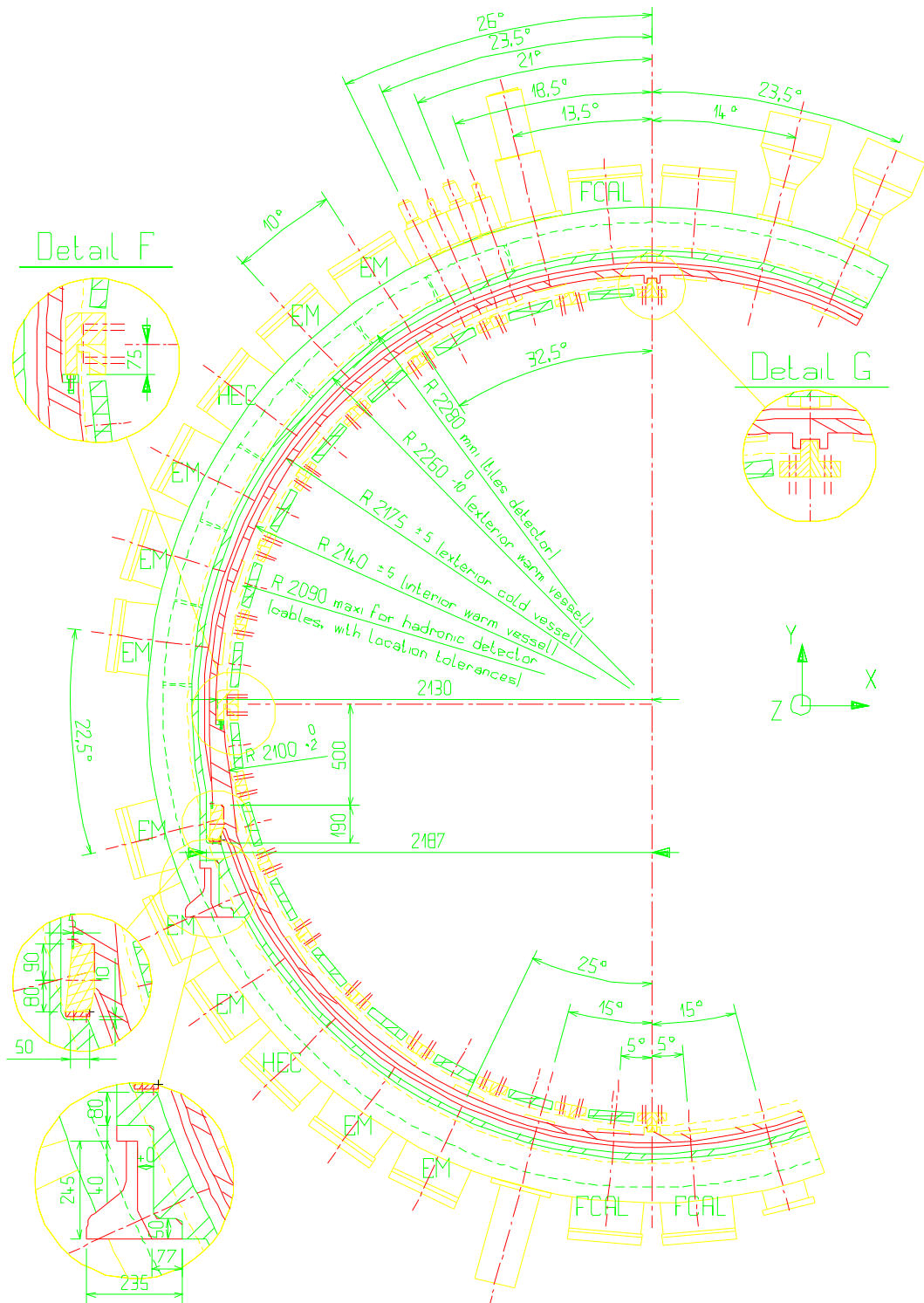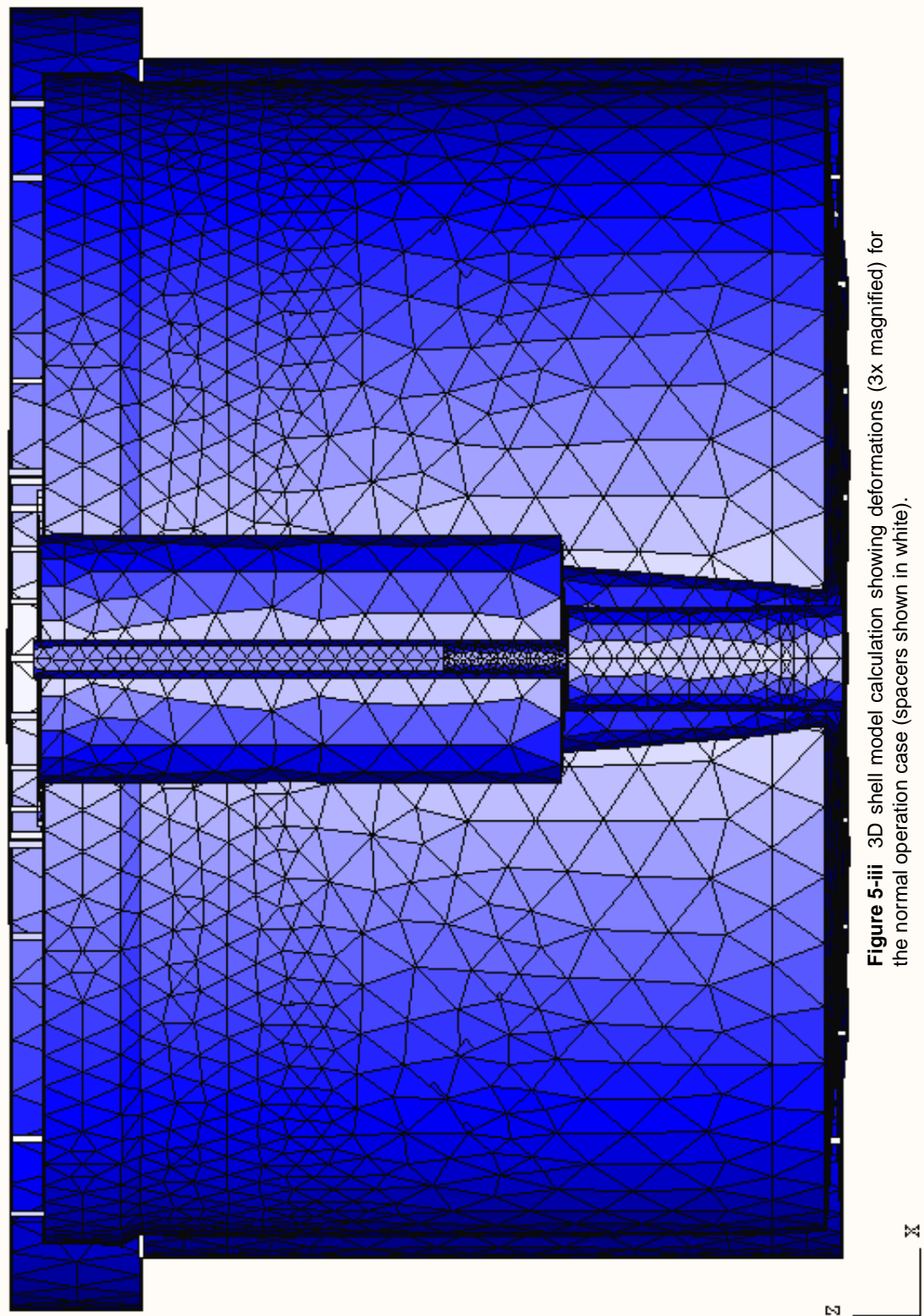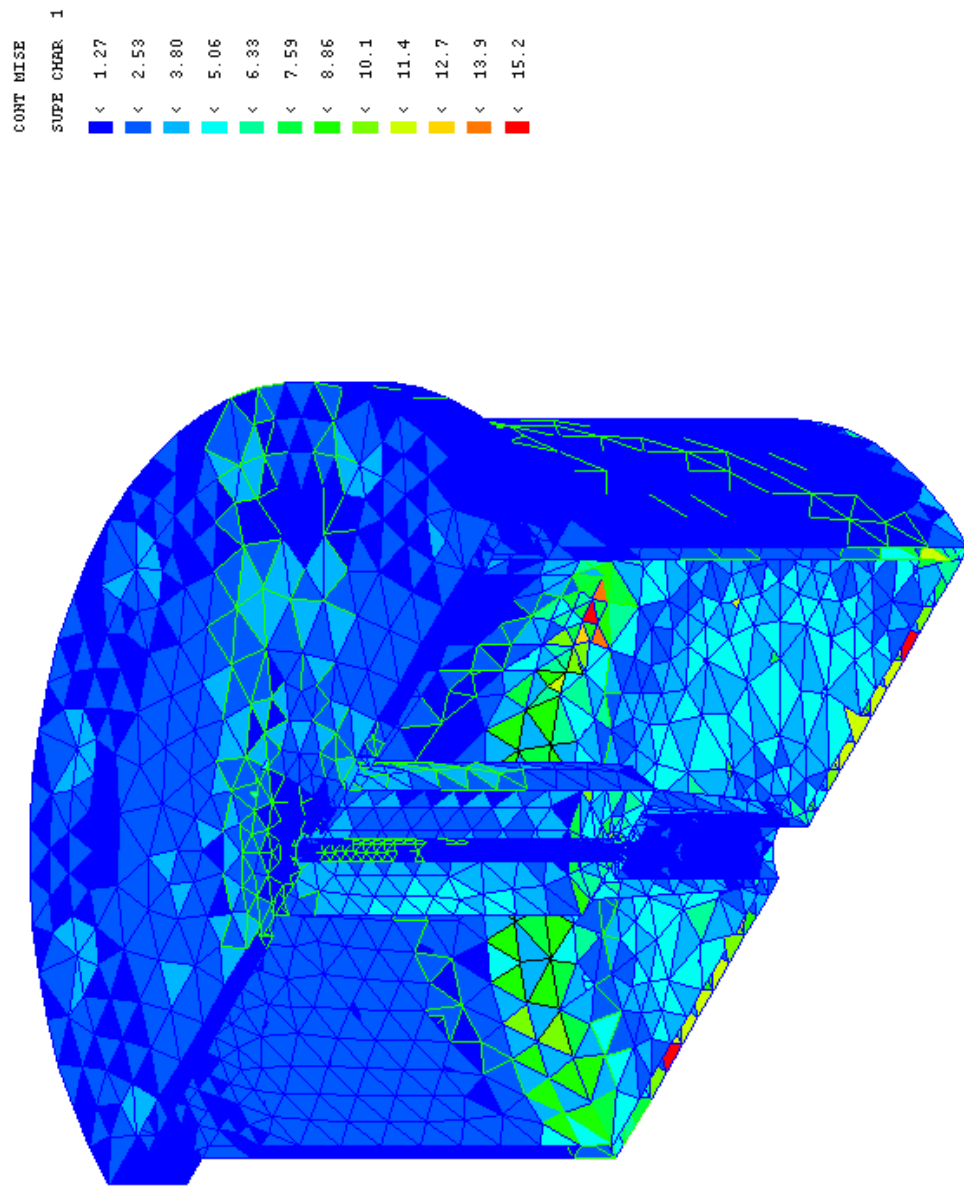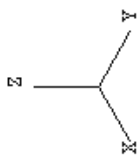
Figure 5-ii End view of the end-cap cryostat.

Figure 5-iii 3D shell model calculation showing deformations (3x magnified) for the normal operation case (spacers shown in white).

Figure 5-iv 3D shell model calculation showing stresses for the normal operation case (the high stress concentrations, shown in red, need a reevaluation using a local volume model).

6 Electromagnetic barrel calorimeter and presampler
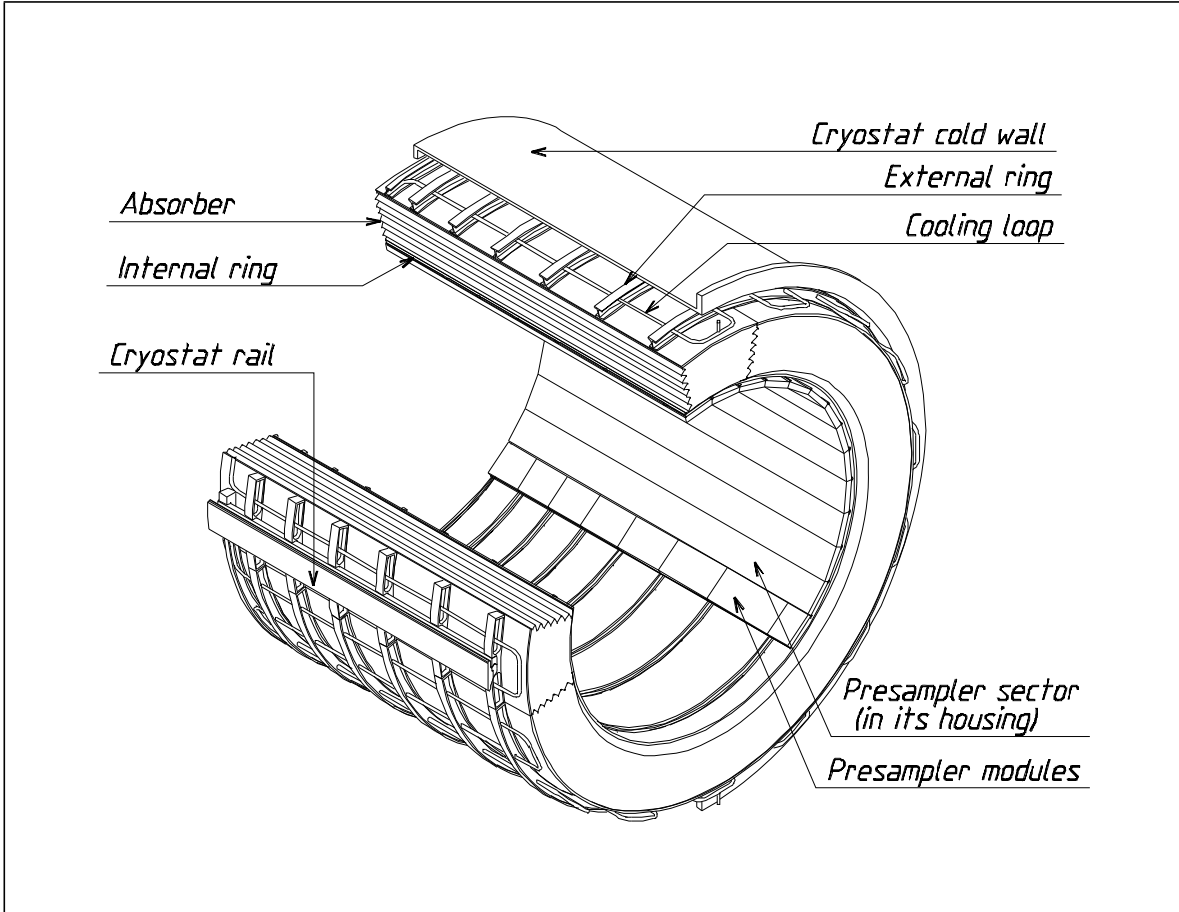
Figure 6-1 General layout.

6.1 Global engineering design

The barrel electromagnetic calorimeter consists of two identical half-barrels (Figure 6-1) covering the rapidity range $|\eta| < 1.4$. Each half-barrel is independent since its connections to the outside are made at its respective end of the cryostat.

The detector is made of two distinct devices and their services: the dense accordion calorimeter, and in front of it the presampler, a 1 cm active liquid layer used for correcting the energy lost in the coil and cryostat walls.

For each half-barrel, the calorimeter is made of 1024 accordion-shaped absorbers alternating with 1024 read-out electrodes, arranged with a complete ϕ symmetry around the beam axis. The calorimeter half-barrel has been divided into 16 modules for fabrication, supporting and connection purposes. The presampler is made of 32 sectors in ϕ, and two sectors are fixed to one calorimeter module. The barrel cryostat has 32 feedthroughs at each end: each feedthrough services half a calorimeter module and its associated presampler sector.

6.1.1 Mechanical design

6.1.1.1 Space attribution

The overall radial space available in the cryostat is from 1385 mm to 2132 mm (nominal dimension, cold). After their best design, some items occupy a fixed radial space: inner clearance and tolerances (27.3 mm), presampler (35 mm including connectics), calorimeter front-face connectics (25 mm), outer clearance and tolerances (29 mm). The space left must then be shared between the absorbers and their supports, trying to minimize the latter.

The minimum number of radiation lengths at the end of the active part of the EM calorimeter (measured from the vertex) is 24 X_0 [6-1]. This dictates the amount of lead in the absorbers, which make for most of the weight of the calorimeter. To keep dead material outside the active region, this weight must be taken by a mechanical structure at the back of the calorimeter.

Seven stainless-steel external rings distributed in z support the half-barrel and transmit its weight to the cryostat's inner wall. The width of these rings (80 mm in z) is constrained by the need to leave space for connections. Allowing for a maximum deformation of the barrel calorimeter in the vertical plane of 4 mm, the rings must take 100 mm of radial space. The radial space left for the absorbers is then from 1472.3 mm to 2003.5 mm, and a ratio of lead to liquid argon of 0.36. The shape of the accordion is then optimized (see Section 6.2.1.1) for the best energy resolution. This leads to 14 folds and lead thickness: 1.5 mm at $\eta = 0$.

Since the thickness of the calorimeter seen from the vertex increases with rapidity, the lead thickness can decrease with rapidity thereby improving the energy resolution. For technical and cost reasons, there is only one change in the lead thickness which is 1.5 mm for $|\eta| < 0.8$ and 1.1 mm for $0.8 < |\eta| < 1.4$; in the absorber this change is compensated to keep the same argon gap.

In the longitudinal direction, at large rapidity the calorimeter extends as much as possible towards the cryostat end-wall, and care is taken that the overlap with the active part of the end-cap electromagnetic calorimeter be satisfactory. For the corner at the inner radius and largest rapidity, a choice could be made about the best possible shape, such as right angle or projective cut; the simulation result was to put as much calorimetry as possible in the barrel, hence the corner simply follows the curve of the cryostat's end-flange.

On the inner radius (front face), there are seven internal rings made of light material located along the half-barrel, in the same radial space as the connections. They hold the absorbers together while accommodating their thermal contraction. The presampler sectors are fixed to these internal rings.

6.1.1.2 Tolerances

A clearance of 10 mm has been taken from the positions of the cryostat inner, outer and end-wall.

The tolerance on the shape of the end-wall of the cryostat is 10 mm at every point.

The radial tolerances and deformations relevant to the general design are listed in Table 6-1.

Table 6-1 Radial tolerances in the barrel EM calorimeter

Cryostat inner wall out-of-roundness	5 mm
Cryostat outer wall out-of-roundness	10 mm
Cryostat rails and calorimeter rings alignment	4 mm
Cryostat outer wall deformation under load	3 mm
Calorimeter gravity sagging	4 mm

6.1.2 Signal collection in the calorimeter

The absorbers have an accordion shape with a ϕ amplitude of $(2\pi)/256$. The folding angles decrease with increasing radius, so as to leave an approximately constant gap between two neighbours (4.5 mm). The read-out electrode (300 μm thick) is centred in this gap by light honeycomb spacers, defining two liquid argon gaps of 2.1 mm. The electrode has three distinct conductive layers: high voltage is applied to its outer layers, creating an electric field in the gaps, and currents induced by electrons drifting in the gaps are read from the central layer, thus summing both sides.

The granularity of the calorimeter for reading out signals is obtained in η and in radius by etching separate pads or strips on the electrode layers. Etched leads route the signals out to the front and back face of the barrel calorimeter.

There are three compartments in depth. Strips in the front compartment are read from the front face, whereas pads in the middle and back compartments are read from the back face. At the front and back faces, printed circuits connect to the electrodes and provide the connections, first between neighbour electrodes in ϕ to make the suitable ϕ granularity, then to the output cables. These circuits are also used to bring in calibration signals and high-voltage supplies from the outside.

In the middle compartment the width of the pads is $\delta\eta = 0.025$, and four adjacent electrodes are summed in ϕ, giving a segmentation of $\delta\phi = (2\pi)/256 \cong 0.025$. In the back compartment, the pad width is $\delta\eta = 0.05$, double the middle one, and the ϕ segmentation is as in the middle. In the front compartment, the width of the strips is $\delta\eta = 0.025/8$, and 16 adjacent electrodes are summed in ϕ, giving a segmentation of $\delta\phi \cong 4 \times 0.025 = 0.1$.
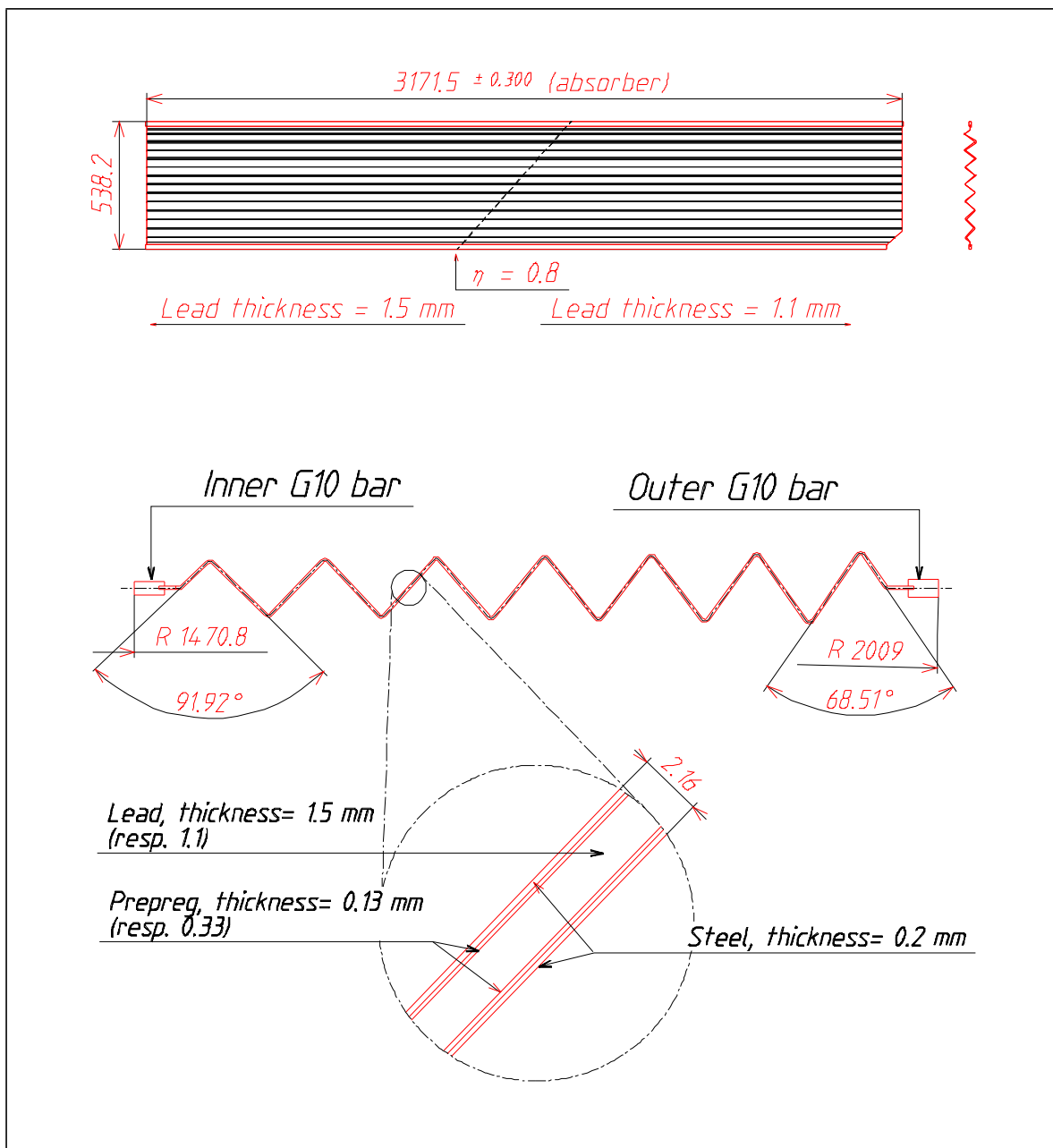
The output cables on the front and back faces of the calorimeter run over the printed circuits, parallel to the beam axis towards the end of the barrel; on the back face they pass through holes cut in the external rings. On the vertical ends, connectors at the cable ends are arranged in patch-panels, into which pigtails from the feedthroughs are connected.

The same scheme is followed for the routing of presampler signals.

6.2 Absorbers

6.2.1 General design of the absorbers

The lead sheet is sandwiched between two 0.2 mm thick stainless-steel plates for high mechanical strength. The gluing is done by a layer of 'prepreg' adhesive on each face. At the inner and

Figure 6-2 Barrel EM calorimeter absorber.

outer edges, the sandwich is encased in a groove in a wedge-shaped fibreglass (G10) precision bar which is used to hold it in place. The bars have machined notches through which the connecting end of the electrodes protrude.

6.2.1.1 Radial geometry

The geometry of the accordion is first determined at operating temperature.

With the fixed radial space, lead-to-liquid ratio, and ϕ amplitude of the accordion, one can still choose the number of folds, which will then imply the lead thickness. The chosen number (14) provides reasonable folding angles (92 to 68° from inner to outer radius) and a lead sheet not

too thin for handling. Simulations have shown this configuration to be optimal for energy resolution.

If the folding angles were sharp, a ϕ amplitude of the folds strictly equal to 4 times the absorber spacing $(2\pi)/1024$ would ensure a calorimeter thickness constant with respect to phi. In fact the folds have a 3 mm radius of curvature, which introduces a ϕ modulation of the thickness. This modulation is minimized by adjusting the ϕ amplitude of the folds to 4.067 times the absorber spacing.

Then the absorber geometry is computed at ambient temperature.

The thermal behaviour of the sandwich is not simple. This has been studied by finite element modelling and measurements of 2 m absorbers from the 1992 prototype and of 60 cm long assembled modules [6-2]. In the longitudinal direction, the contraction is described by a simple coefficient of –3.1 mm/m (ambient to liquid argon temperature). In the transverse view, the folds are subject to the same contraction, but in addition the folding angles decrease with decreasing temperature ($\delta\alpha = 0.2 - 0.0022\alpha$), and the radial extension of a free absorber contracts by 5 mm. The transverse profile of the accordion is then completely recomputed for drawing the lead and stainless-steel sheets and the bending tools; the same computation is carried out also at 125°C (the polymerization temperature).

6.2.1.2 Longitudinal geometry

Close to z = 0, the G10 bars start at z = 2 mm, the lead/steel sandwich at z = 3 mm. This clearance between the two half-barrels is made necessary by the tolerance on the flatness of each half-barrel's end-face and the possible changes in length during cooldown.

At large z, the external G10 bar is 2 mm longer than the sandwich for protection. The internal bar is cut in front of the cut corner to ease the passage of the cables around the corner.

6.2.1.3 Mechanical properties and fixation devices

At the outer radius, the G10 bars are fixed to the external support rings. The bars are in contact at ambient temperature, and will remain so when the rings contract, since their coefficient is the same as the rings'. When the calorimeter is cooled, the external rings contract like stainless steel: the outer radius decreases by 5.5 mm. The free accordion contracts by 5 mm, hence the inner radius of the calorimeter would contract by only 0.5 mm for a 1.5 m radius. The inner rings provide some traction on the absorbers, extending them by 0.5 mm, so the inner radius decreases by 1 mm. This is much less than the contraction coefficient of the inner bars, which means that some space will open between the bars. As shown in Section 6.6.2 below, the inner rings ensure that this space is evenly distributed among the absorbers.

The important aspect is that the inner bars are no longer in contact when cold.

Besides, the sagitta of an absorber located in the horizontal plane $\phi = 0$ has been computed for different conditions of attachment: it amounts to 0.9 mm if the inner and outer bars are rigidly fixed, up to 4.9 mm if the bars are free to rotate. This latter situation was considered unacceptable, since our target is 1 mm (see the effect of sagging simulation in [6-1]).

To prevent the bars from rotating although they are not in contact, there are pins in between neighbour G10 bars, with a very tight tolerance (20 µm) transverse to the bar.

From the same modelling, the radial elasticity coefficient has been computed: a piece of accordion absorber 100 mm long in z, extends radially by 0.15 mm for a traction of 10 N. This figure is important for the design of the internal rings, as described later in Section 6.6.2.

The weight of a complete absorber is 46 kg.

Table 6-2 General table for barrel calorimeter.

Absorber	
Lead/steel sandwich length (warm/cold)	3171.5 / 3162 mm
Absorber radial dimension (warm/cold)	538.2 / 533.2 mm
Absorber weight	46 kg
Lead/steel sandwich thickness	2.16 mm
Lead thickness ($|\eta| < 0.8$ / $|\eta| > 0.8$)	1.5 / 1.1 mm
Steel thickness	0.2 mm
Prepreg thickness ($|\eta| < 0.8$ / $|\eta| > 0.8$)	0.13 / 0.33 mm
Absorber sagitta (horizontal plane)	1 mm
Read-out electrode thickness	0.275 mm
Liquid gap (nominal / min. / max)	2.12 / 2.04 / 2.21 mm
Spacer thickness (warm)	1.82 mm
Module weight	~ 3.4 tons
Half-barrel weight	~ 55 tons
Barrel deformation under gravity (top and bottom)	4 mm

6.2.2 Lead

6.2.2.1 Thickness uniformity requirements
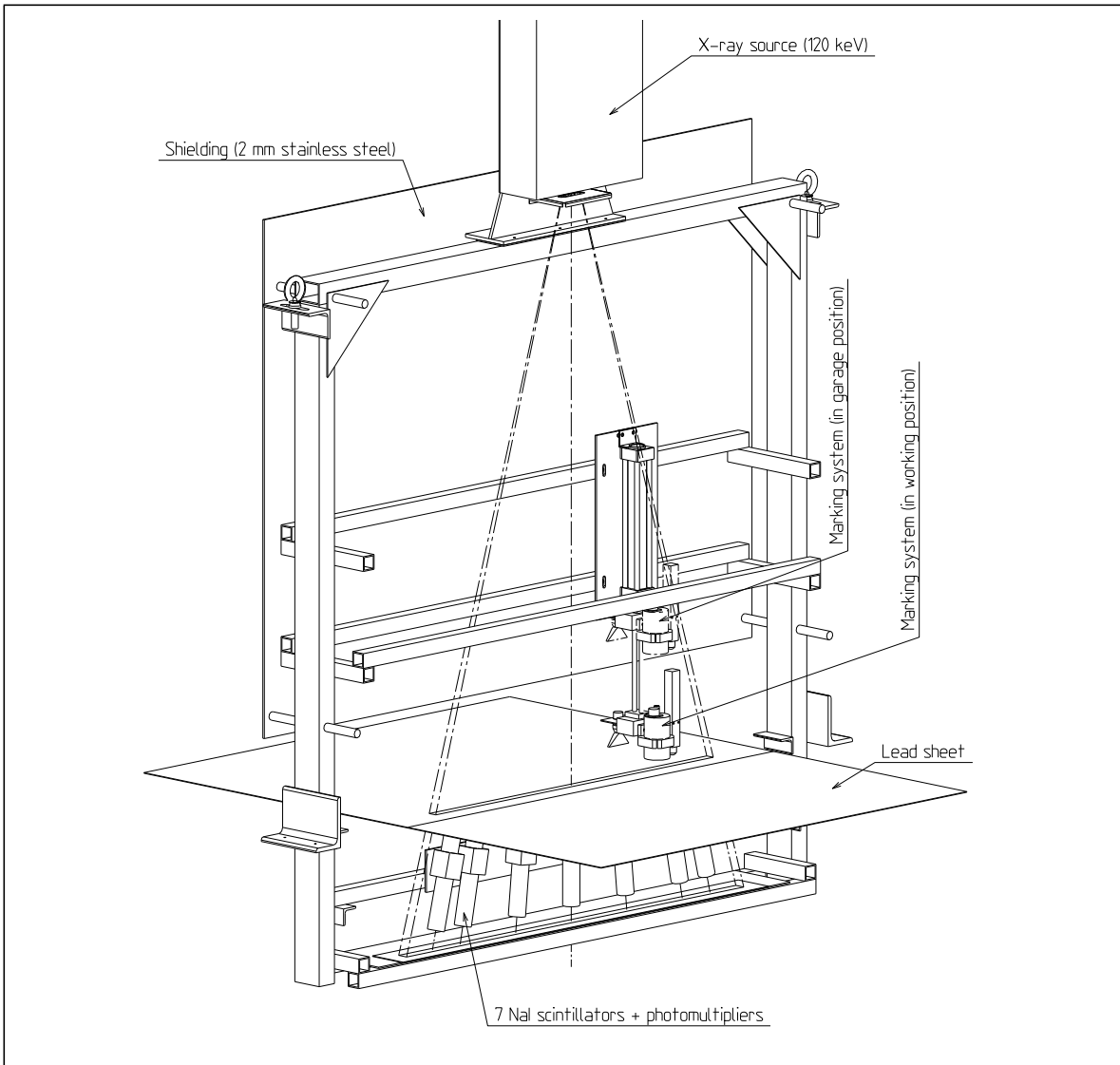
Non-uniformities in the thickness of the lead plates used to make the absorbers lead to local variations of the calorimeter response. An increase of 10 microns on the lead thickness leads to a decrease of 0.4% of the measured signal.

The flat lead sheets (99.9% pure) are produced in industry by rolling, with a thickness tolerance of ±30 microns in the best case, which would correspond to a contribution to the constant term of almost 1% in the worst case, where neighbour absorbers would have correlated thickness fluctuations. To decrease this effect, two steps are taken. First, an X-ray measurement system is used during the rolling to help reduce the fabrication tolerance. Second, an ultra-sound measurement system is used offline to confirm the online measurement, and the plates are sorted so that neighbour absorbers receive plates of opposite fluctuations, thin and thick; this reduces the effective density fluctuations, as showers average over about four absorbers.

6.2.2.2 Production and online measurement

The purpose of this measurement is to reject unacceptable lead plates, where part or all of the lead is out of tolerance, and to obtain as early as possible a knowledge of the thickness distribution, in order to prepare the sorting and the ordering of the lead plates at later stages of the absorber production process.

The device used is shown in Figure 6-3. It consists of an X-ray tube, emitting 120 keV X-rays

Figure 6-3 X-ray device used for lead thickness measurement.
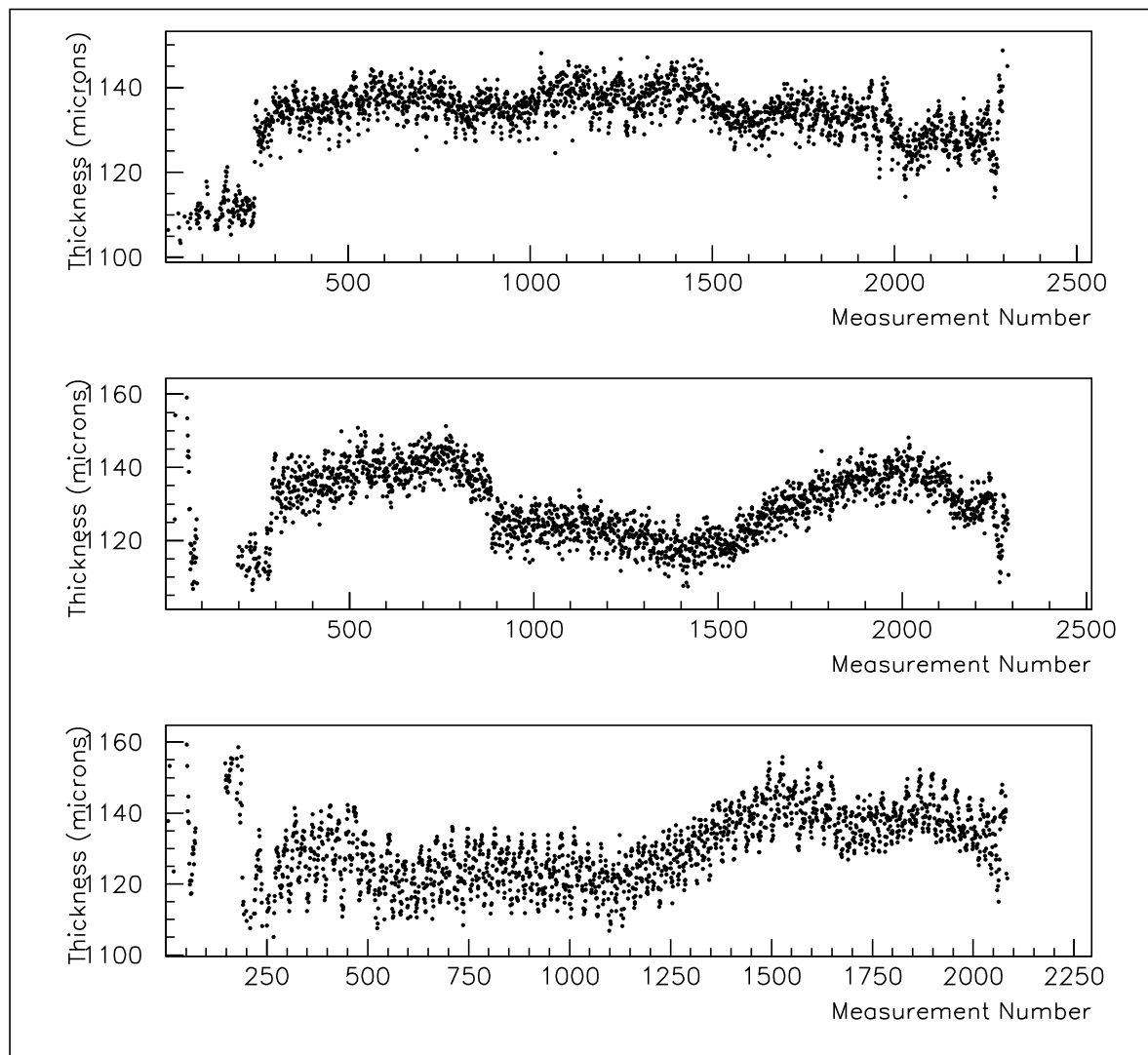
with adjustable intensity. The radiation passes through the lead sheet just being rolled and is then detected by seven NaI scintillators connected to photomultipliers. The photomultipliers count rates are used to compute the lead sheet absorption coefficient, from which the lead thickness is deduced. The accuracy is limited by the X-photon statistics, and the measurement time has been adjusted to 0.15 second for the barrel plates (1.1 and 1.5 mm thick), and 0.3 seconds for the end-cap plates (1.8 mm). During the measurement time, the length of lead that passes between the X-ray source and the detectors is of the order of 5 to 10 cm. The reproducibility of the measurement has been estimated to be about 5 microns. As soon as the thickness measured by

any of the seven detectors goes out of the tolerance interval, a printing head draws a green line on the lead itself, marking it for rejection.

The lead is rolled at a variable speed; to correlate the measurement with the position on the sheet, a printer prints the measurement number every ten measurements, directly on the sheet. These numbers stay on the lead plate until cleaning of the lead, just before it is used to build an absorber.

The rolling of the lead for module 0 (Figure 6-i) took place on October 2nd 1996: 11 rolls about 115 m long each were processed in half a day. The X-ray system performed as expected, with a resolution of about 5 microns per detector. The cross-calibration of the detectors was only good to 5 microns, this will be improved for the series production by using a larger reference sheet.

The average thickness as a function of the measurement number is shown in Figure 6-4, for three different rolls of 1.1 mm thick lead. The thickness stays approximately constant, with sometimes a slow drift, over a number of consecutive measurements of the order of 500, corresponding to a lead length of 25 m, i.e. 12 absorbers. The drift can be controlled only by a step correction, of the order of 20 microns.

Figure 6-4 Lead thickness for three rolls (online measurement).

Figure 6-5 shows the variations of lead thickness over a short range. The oscillations have a period of 1.8 m, corresponding to the rollers' circumference, and are probably due to defects of the rollers themselves. Since 1.8 m is close to the length of one plate, one could try to cut the plates in phase with this oscillation, or on the contrary to match neighbour absorbers not only in average but also for the best homogeneity at all positions in z. Measurements taken with module 0 production are still under study to decide the best strategy.

The distribution of the average thicknesses for all the 1.1 mm thick rolls is given in Figure 6-6. The r.m.s. obtained corresponds to 9 microns, dominated by the short-range variations of Figure 6-5. Similar values have been obtained for the 1.5 and 1.8 mm thick sheets. This is about twice as good as expected from the contractual tolerance [-0,+60 microns].
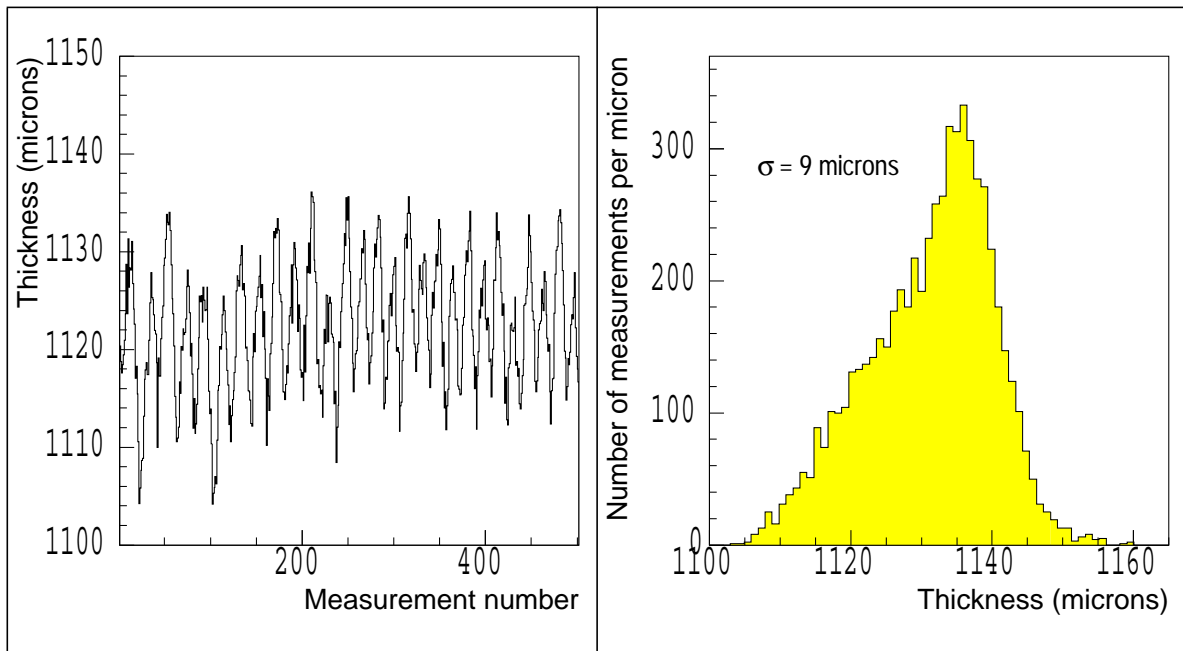
Figure 6-5 Lead thickness short-range variations.   **Figure 6-6** Lead thickness distribution.
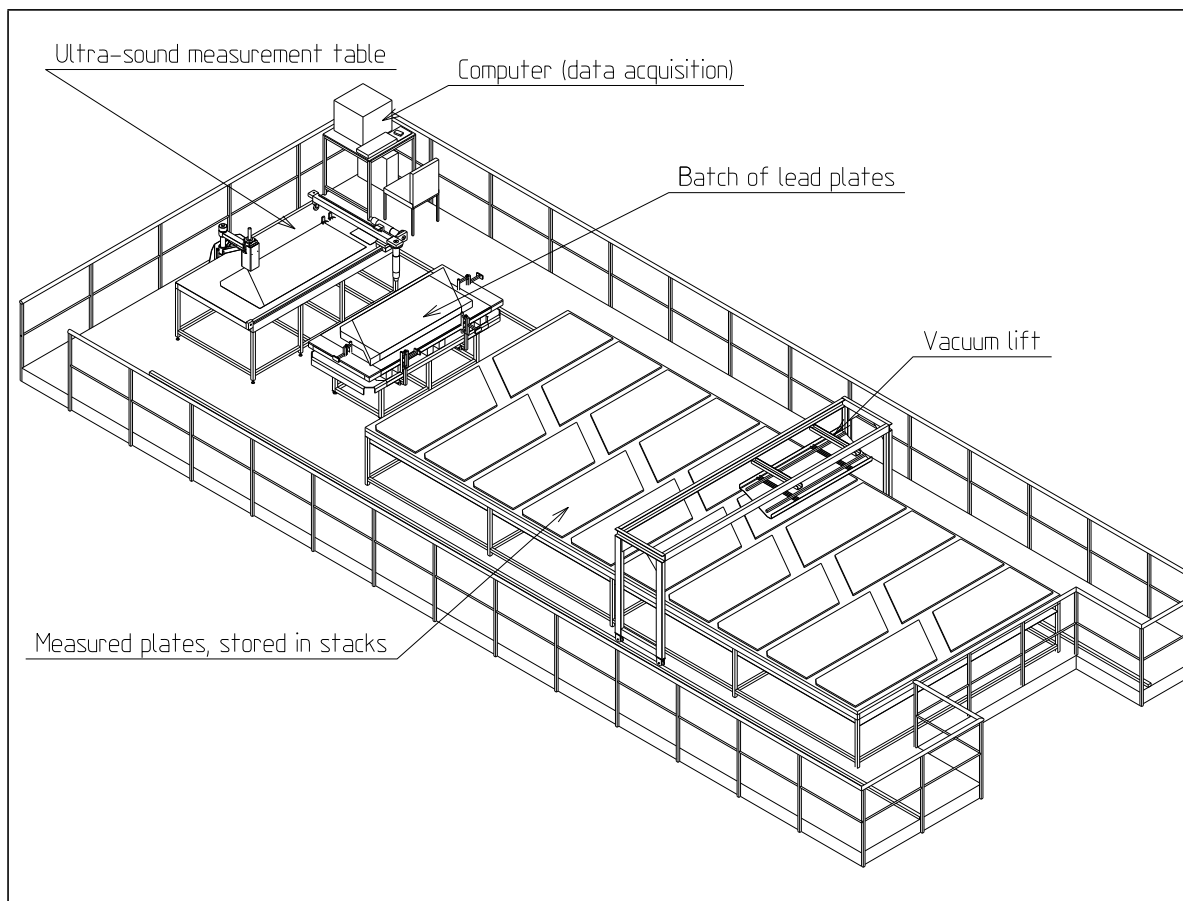
6.2.2.3 Offline measurement and sorting

This measurement will be done just before cleaning and bending of the lead into finished absorbers; it uses a x-y measurement table, equipped with an ultrasonic probe.

The accuracy can be pushed down to a few microns, with measurements recorded every few cm in both directions. The time needed to perform the measurements is estimated to be about one hour per plate, including handling. The measurements will be checked against the online measurements, and will be used to build detailed maps of each plate.

All the thickness measurement informations (online and offline), the serial number of a plate and its position in the calorimeter will be stored on a database.

The information needed to decide where to place the plate in the final calorimeter will be at hand. As can be seen in Figure 6-7, the plates will be sorted according to their thickness and stored on ten different stacks, to build two consecutive absorbers with plates with matching thicknesses. Several algorithms are presently under evaluation to do this plate matching.

Figure 6-7 Implantation of sorting process.

6.2.3 Steel

The role of the two steel sheets in the absorber is mainly to provide mechanical strength, acting as the skins of the composite material. They also offer a clean and rust-free outside surface which constitutes the ground plane facing the electrode at high-voltage.

The sheets are stainless steel AISI 304, 0.2 mm nominal thickness. The tolerance on thickness must be good, since the response of the calorimeter depends on it as for the lead, though this effect has not actually been measured. Simulation results show that increasing the steel thickness uniformly by 10 microns decreases the response by 0.4%. One company proposes to provide sheets with a ±6 microns tolerance, corresponding to a r.m.s. better than 4 microns, hence to a contribution to the constant term below 0.16%. The sheets will therefore be used without sorting them. In case a slightly worse distribution were obtained, it would be easy to sort the sheets into two different sets and match them to make uniform the effective thickness per absorber.

The specification demands no scratches deeper than 5 microns, no bending marks, and the production will be followed in-situ to make sure there are no local imperfections.

The sheets will be cut to their final dimensions by water jet. Tests have been performed to cut a stack of 45 sheets separated by 50 microns paper; the burr is about 30 microns, non cutting.

The sheets are then surface treated, with a process optimized for gluing, as explained in Section 6.2.7.

6.2.4 Epoxy-impregnated fabric (prepreg)

The prepreg is a fibreglass fabric in two thicknesses: 0.13 mm (weight ~100 g/m^2) and 0.33 mm (weight ~300 g/m^2), impregnated with epoxy resin (40 to 50% resin). The amount of resin has been optimized to have a good filling and fluidity but not too much extra glue which makes tool cleaning difficult.

The specification mentions the polymerization cycle (described below Section 6.2.7), a radiation resistance to 1 MGy, and aspects related to handling (stickiness, protection papers). The delivered prepreg will be stored at -18°C. Several companies can deliver this product.

6.2.5 Bars

On both sides, each absorber is glued, over its full length, in a groove machined in a G10 bar. These bars are azimuthally in contact with each other and define the exact cylindrical geometry of the whole calorimeter at warm temperature. Their role is multiple: they maintain the read-out electrodes at their correct z-position, they protect and hold the signal connectors, they fasten the embedded absorbers radially ensuring a minimal sagitta under gravity.

The ultimate geometrical accuracy of the cylinders is a direct consequence of the precise machining of the azimuthal contact surfaces of the bars. The thickness of the bars as well as the projective angles of both faces have to be mastered. The bars have to be rectified with ultimate accuracy. We already achieved on 3 m long G10 bars a cumulative thickness precision of 0.02 mm for 10 bars. From our experience in assembling several 2 m prototypes of 24 absorbers each, it appears sufficient to adjust the correct azimuth of the G10 bar arc with thin shims every 8 absorbers or more. The bars are exactly positioned in z and radius with respect to each other by pins passing through precision holes drilled in the bars. A precision of 0.01 mm in radius and 0.03 mm in z should be achievable (Figure 6-8). Tests conducted in the lab have achieved such accuracy, provided that the jig used for drilling the bars be of the same material as the bars themselves, in order to minimize the effect coming from possibly different temperature expansion coefficients.

Another function of the bars is to provide a cantilevering of the absorber guaranteeing the smallest possible sagitta under gravity. For that a sizeable contact surface in between bars should be maintained. The contact surface connecting the outer G10 bars is quite large, while the contact in between the inner bars increases from z = 0 towards the outside edges of the absorbers. On average this contact is adequate to guarantee an intrinsic correct geometry at warm temperature, however inner contact is less important given the fact that the bars are indexed by the inner rings.
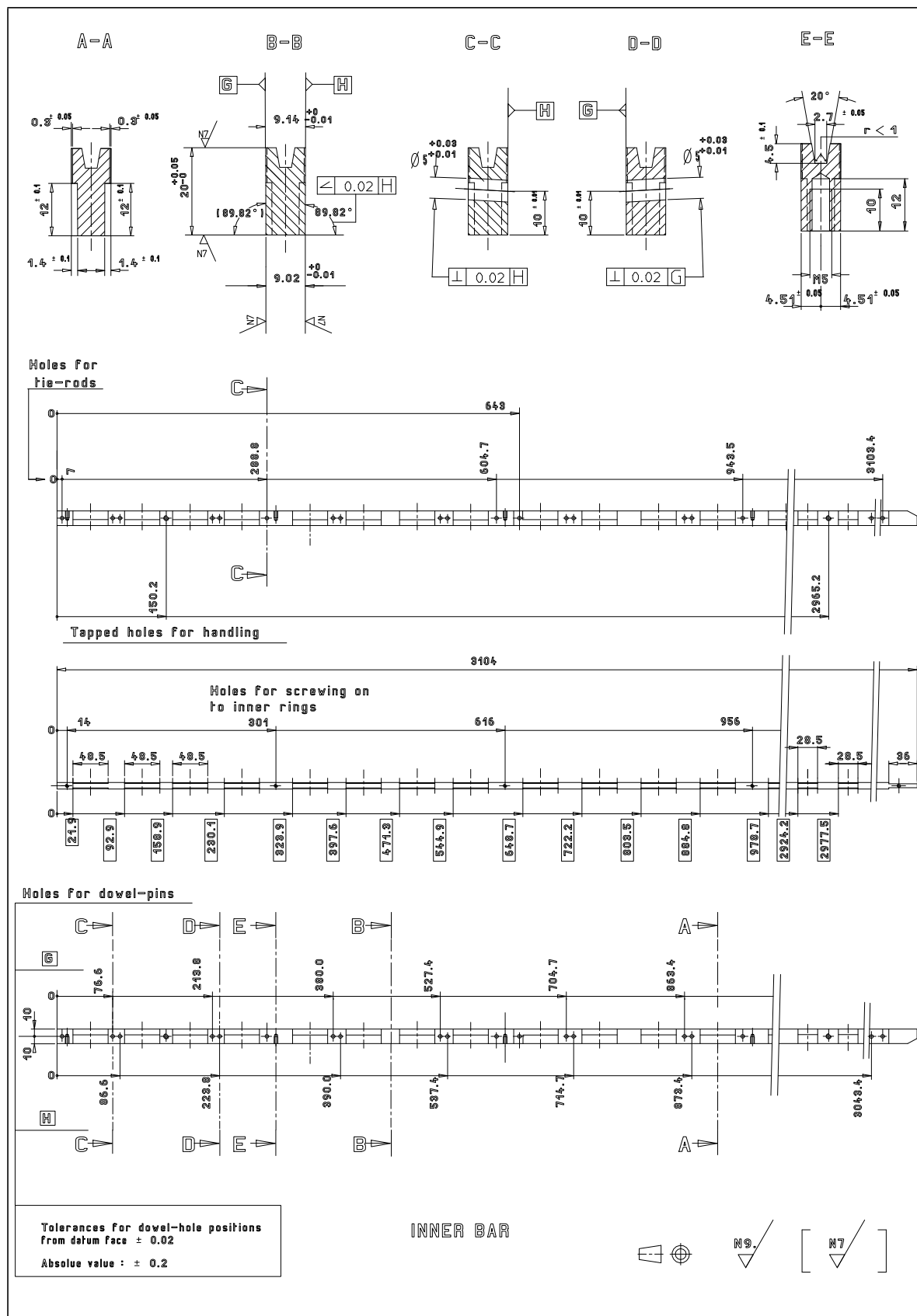
Figure 6-8 Engineering drawing of the bars.

The signal outputs of the read-out electrodes pass through grooves machined radially in the bars. Cut-outs are machined on the outside faces (inner and outer radius of the detector) to fit the connectors (Figure 6-9). These cuttings do not require high precision and will be done on a numeric milling machine.

The material for the bars is fibreglass-epoxy, but with quite specific requirements on the temperature expansion coefficients. The external bars must have the same longitudinal contraction as the absorbers' ($3 \cdot 10^{-3}$) and the same contraction coefficient in ϕ as the outer rings' which are stainless-steel: $2.5 \cdot 10^{-3}$. This is easily achieved with a material with two symmetric glass-fibre directions, by choosing their angle, as shown in Figure 6-10.

The case is more difficult for the inner bars: they should also have the same longitudinal contraction as the absorbers; however, in the ϕ direction the ideal situation would be to have such a small contraction coefficient that the inner bars would remain in contact when cold. The large contraction of the accordion absorbers could be attenuated partially by tensionning them by the inner rings, but a coefficient lower than $6.8 \cdot 10^{-4}$ would anyway

Figure 6-9 3D view of a section of a bar.

be necessary. The lowest coefficient attainable, even with a very special material, is about $1 \cdot 10^{-3}$, which means that opening-gaps between the bars at cold are unavoidable. Given this, we have chosen to have the inner bars made out of the same material as the outer bars, for low cost and easy procurement.
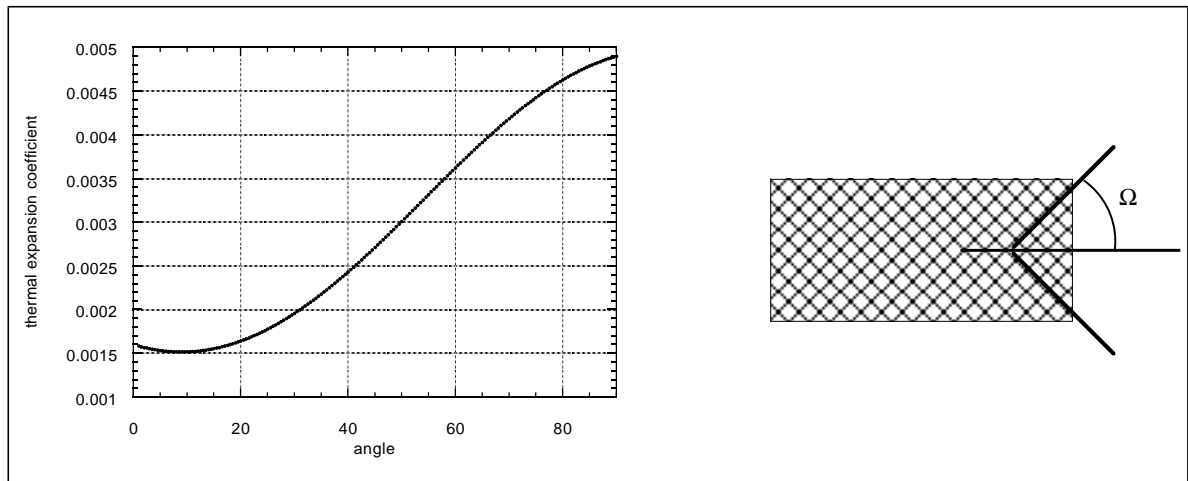
Figure 6-10 Thermal dilatation of G10 bars.

An order will first be placed for 100 bars of each kind (front and back) to build the module 0 and the final order for the 4096 bars will be placed as soon as the module 0 has proven its correct mechanical behaviour. The strategy at this moment is the following: the rectangular raw bars, including the groove to glue the absorber, are produced by industry. The grinding of both faces can be done at CERN unless proven to be feasible in industry as well as the precise hole drilling. Notches and cut-outs will be done in industry with a numeric milling machine. For the totality of the bars, we will probably transfer the rectification and the precise drilling to the factory provided a strict quality control be observed. The bars will be delivered in batches following the production of modules. The overall production and machining will take two years.

6.2.6 Bending

The bending press to fold the absorbers into the final ATLAS accordion geometry represents an upgrade of the 2 m bending press which was built and operated successfully for the barrel prototype. From the original design, many modifications in view of the manufacturing of the press of the final dimensions were implemented and tested in fabricating mock-ups for mechanical studies. All the experience accumulated in the folding of about 200 absorbers was used for the present design.
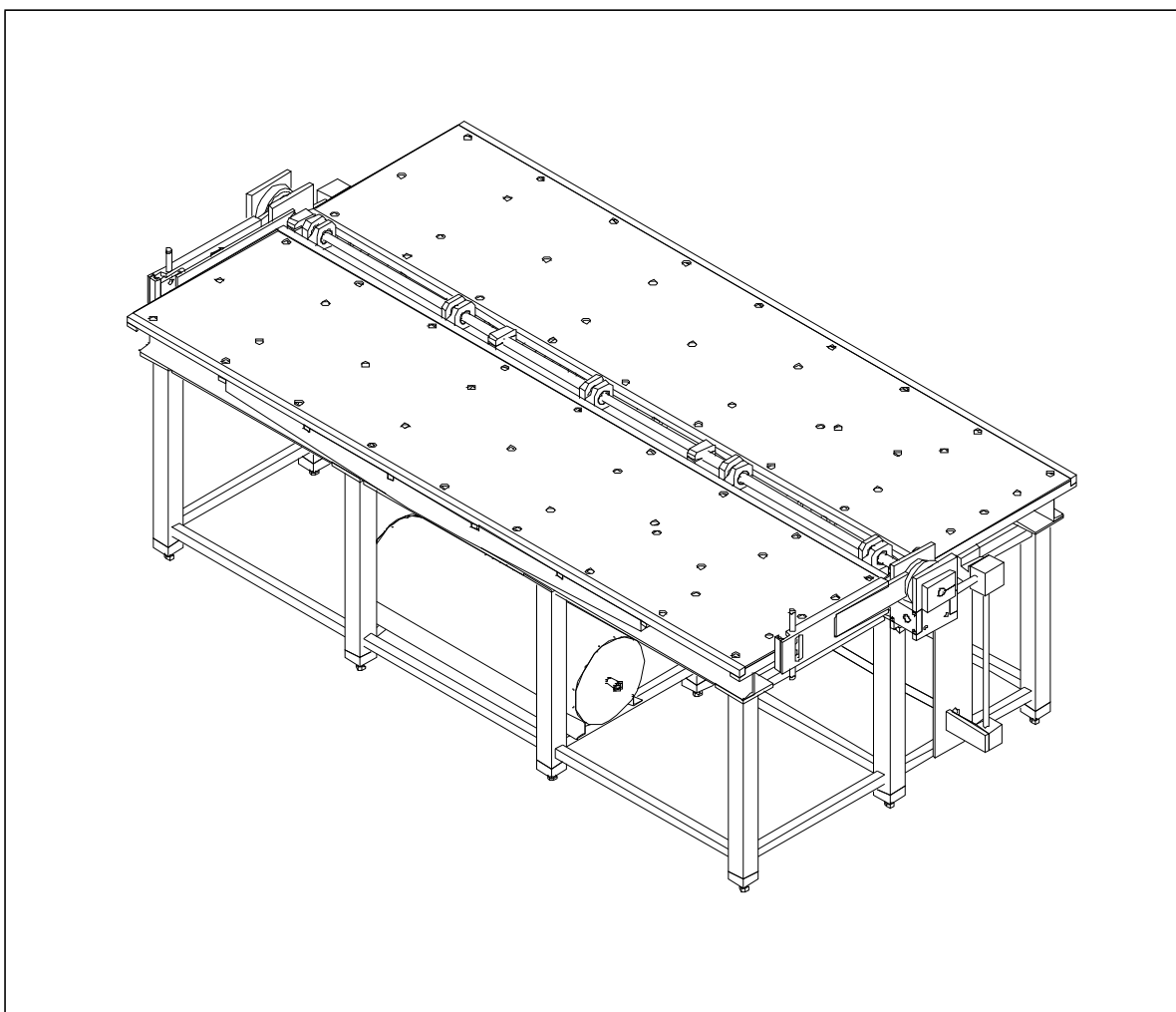
Figure 6-11 Tool for absorber sandwich preparation (see also Figure 6-ii)

Before bending, the sandwiches of stainless-steel, lead and prepreg should be assembled from the separated parts. In order to lift the thin lead and stainless-steel sheets, a special lifting beam has been constructed. A large number of vacuum suction-cups are required to avoid deformations of the foils. Given the large dimensions and the weight of the sheets, a specific semi-automatic assembly tool has been designed to form the multi-layer sandwich to guarantee the flatness of the plates during operations (see Figure 6-11 and Figure 6-ii). It works like a waffle-iron with two trays which can be rotated around a central axis, allowing the automatic superposition of the different layers on one side or the other. First the stainless-steel flat sheet is held on one tray by vacuum, positioned in a frame machined in the tray, the prepreg sheets are laid on it while the two lead sheets, of 1.5 and 1.1 mm thicknesses, rest on the other tray. The two parts are then put in contact by rotating the tray supporting the steel and prepreg. Successive multiple operations are needed to form the full flat absorber. It is then pushed on air-cushions into the jaws of the bending machine and adjusted by hand in position.

The principle of the bending machine is the following: the upper and lower knives of the machine get positioned at a precision of 0.1 mm with respect to each other and to the central top knife which is fixed. The sandwich is then pinched between the two sets of knives. There are ten rails on the top and the bottom of the main structure (see Figure 6-12) on which roll several two-wheel carriages fixed to the knives. The upper knives are pushed down by the press and simultaneously all the knives move towards the fixed knife in the centre. The driving force is the friction between the surface of the sandwich and the tips of the knives. Left and right ends of the sandwich are pinched in two supporting pieces tightened by pneumatic balloons. The overall process is controlled via the applied pressure on the hydraulic system of the press. End-of-course switches limit the final excursion of the knives and assure a uniform final thickness of the sandwich. Rollers are provided to ease the extraction of the bent absorber from the press after release of the pressure and opening of the jaws. Tooling will be designed to handle the absorber between the bending and gluing press.

Safety regulations have to be applied during the bending so that nobody can approach the press while in operation. Light beams entering photocells will fence the neighbouring area. The cutting of light beams will automatically switch off the power of the press.

The accuracy of the knives over the full length should be 0.03 mm. This is required to ensure that the bends will be at the correct radius inside the accordion detector. Effectively our experience shows that it is not possible to correct these positions afterwards with the gluing press even at high pressure. The accuracy of the bending is fixed and known solely from the precision of the knives and of the overall press, as it is not possible to check any parameter of the absorbers after bending. At this step, the multilayers are not yet glued together and are quite elastic along the direction of the bends, so the positions of the apexes of the bends as well as their angles are not fixed.

The total time of the operations is dominated by the preparation of the sandwich, namely by the cutting of the two prepreg sheets of 0.13 and 0.33 mm thickness and the exact positioning of the different elements, the stainless-steel sheets, the two lead plates, the prepreg. Adjusting the position of the sandwich in the press is also quite a delicate operation. Bending itself takes only a few seconds. The intention is to bend four absorbers per day. The total production will then take less than three years.

R 2562.6

2848

3487
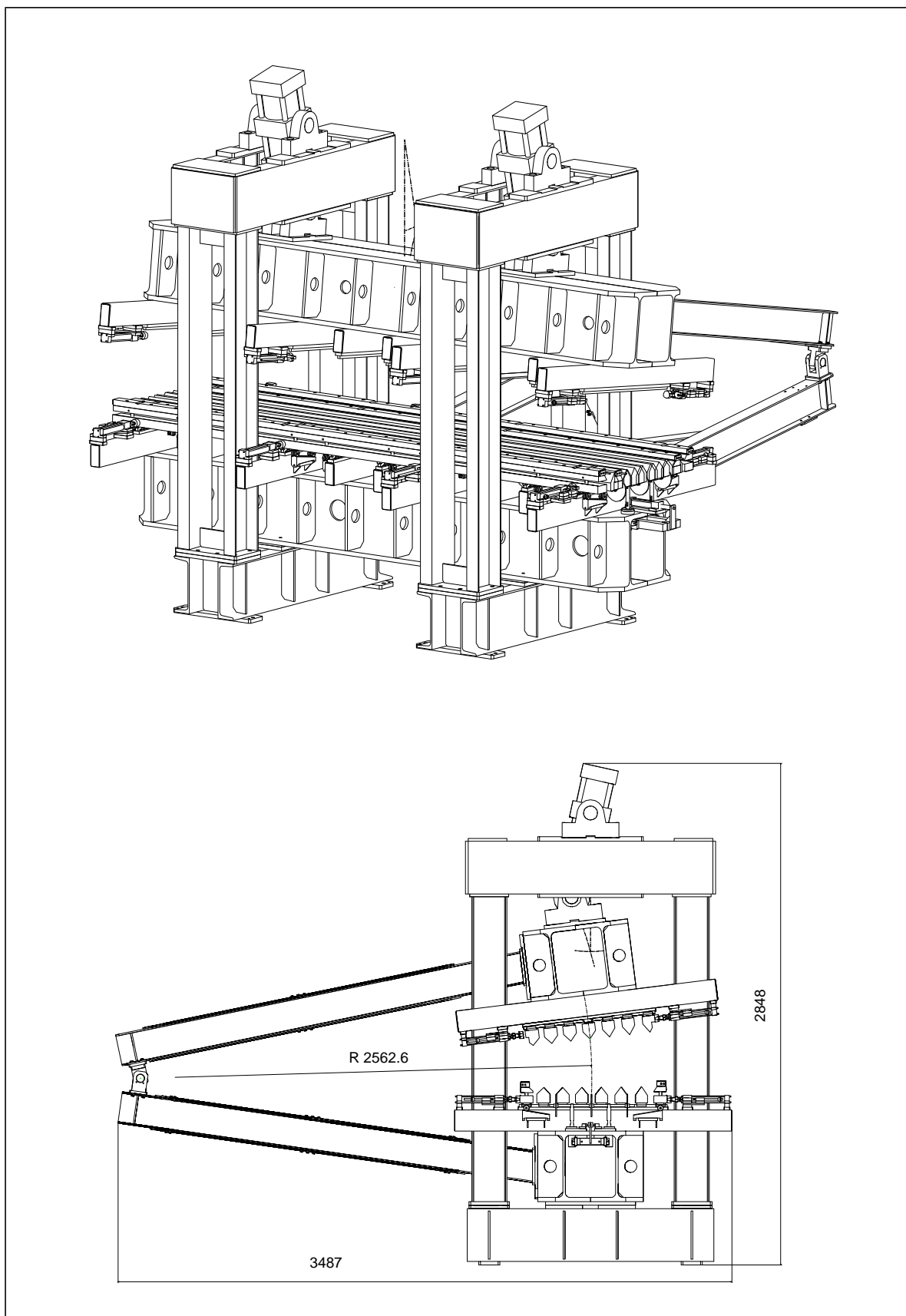
Figure 6-12 3D view of the bending press.

6.2.7 Absorber gluing

6.2.7.1 Gluing of the sandwich
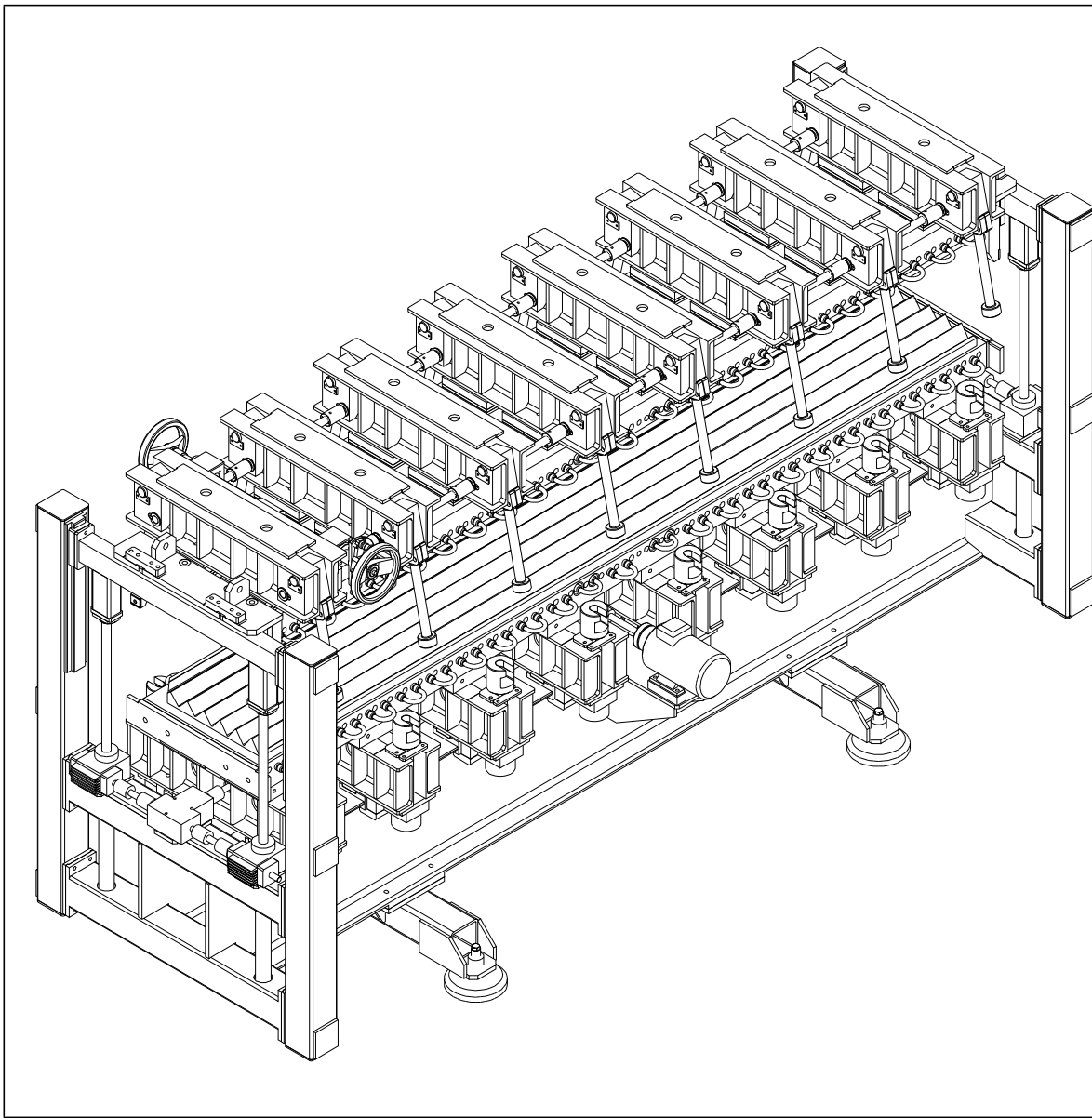
Figure 6-13 Gluing press (see also Figure 6-iii).

The lead-stainless steel sandwich is glued by a fibreglass cloth pre-impregnated with epoxy resin (prepreg). The prepreg thickness is 0.13 mm or 0.33 mm corresponding to the lead thickness 1.5 and 1.1 mm, respectively, to obtain a constant thickness of 2.16 mm for the absorber.

The process for the preparation of the lead and steel surfaces for an optimal gluing, have been tested by measuring the value of the peeling force, by the methods of mobile rollers (standard NFT 76112).

The process for the steel is a chemical degreasing (FINOX), then passivation (NETINOX), rinsing and drying; this treatment has a lifetime of several months and will be done by a specialized company.

The process for the lead is a brushing under water loaded with alumina powder, then rinsing and drying. Contrary to the steel, the lead oxidation is fast, hence this treatment will be done at the absorber fabrication site a few hours before use. The processing machine is commercially available for cleaning printed circuits.

The processed plates are assembled in a sandwich and bent as described above in Section 6.2.6.

The prepreg polymerization cycle as explained by the suppliers is a temperature rise of 3°C/minute, followed by a one-hour plateau at 125°C, then back to ambient temperature by 3°C/minute. The indicated gluing pressure is between 1 and 2 bars.

The tooling for this operation is a heating press (Figure 6-13) made by two single-piece matrices. The matrices are made of steel, machined to the absorber profile (computed at 125°C) with a tolerance of 0.02 mm over their area of 3200×525 mm. They are equipped with a 140 kW electrical heating system and a water cooling system.
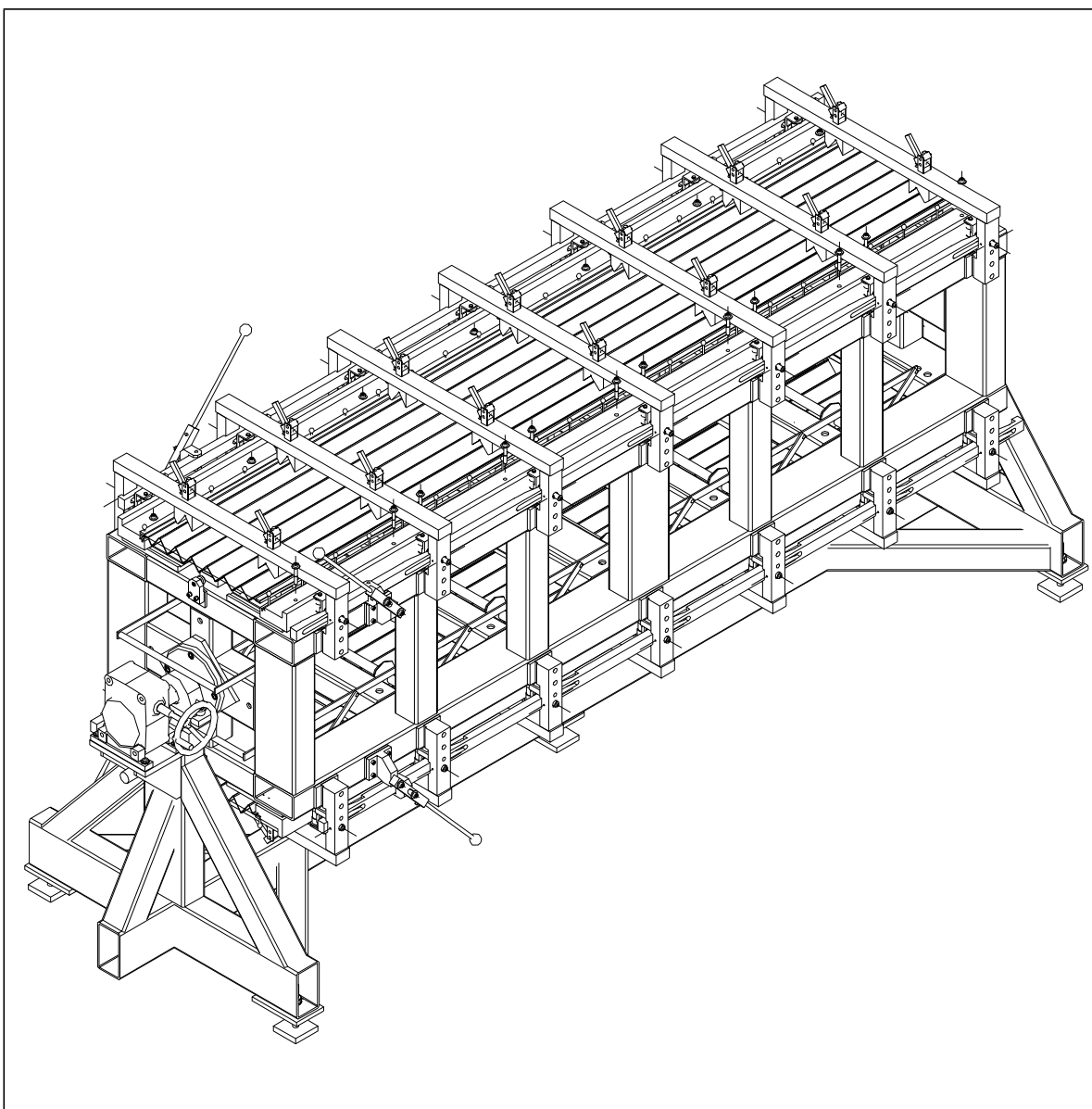
The bottom matrix (Figure 6-iii) lies on eight metal trays, themselves supported by a stand. The trays are cooled to prevent heating and deforming the stand. The trays can slide with respect to the stand, to accommodate the dilatation of the matrices. The system guarantees a good inherent flatness (±0.02 mm) of the bottom matrix's mid plane. Eight counter-trays are fixed to the top matrix, and the gluing pressure is provided by 16 hydraulic jacks which actuate 16 rods which interlink the top and bottom trays. The total force applied is 160 tons. The opening and closing of the press for loading and unloading is electrically powered.

The temperature is computer controlled in six zones, from gauges implanted in the matrices, with a ±1°C accuracy at the level of the absorber. The data will be recorded for each absorber.

6.2.7.2 Gluing of the bars

The link of the G10 bars onto the absorber is done by a glue joint, with a standard epoxy (AW106). The cohesion is good both at ambient and low temperature: after several cool-down cycles it has been measured to 50 kg per cm of bar. The profile of the slot in the bar allows both a good rigidity and an easy positioning and gluing.

Two rotating stands allow four absorbers to be equipped simultaneously. Seven pairs of screws ensure the flatness of the absorber during the gluing. The distance between the screws of each pair can be trimmed to compress or extend the accordion to its nominal profile, since a fluctuation of 0.2 mm can be expected after fabrication, in this dimension, as seen with the 1992 prototype (this spring effect is much larger than the actual accuracy on the folds' position and length). The bars are held on machined rulers by pins and screws, using the bars' holes, and the glue is deposited mechanically, adjusting the quantity to the actual penetration of the sandwich in the bar. The bar is then set in position and fixed with respect to the absorber on the stand, oriented vertically. After half a day the stand is flipped over and this operation is repeated on the other side. After dismounting, the polymerization is completed by a one-day cure in a simple oven at 35-40°C.

Figure 6-14 Absorber bars gluing stand.

6.2.8 Control

The geometry of the finished absorbers will be controlled, as shown in Figure 6-15. If necessary, each absorber can be measured in one hour, at about 100 points with an expected accuracy better than 20 microns. In addition, a certain number of the absorbers (typically 10%) will be measured more in detail (500 measurement points or more).

The measurements will be used to monitor the behaviour of the bending press, and to help to correct it if necessary; they will be stored on a database.

Absorber, attached to a frame by the G10 bar

Figure 6-15 Control.

6.3 Read-out electrodes

6.3.1 Introduction

The read-out electrodes are flexible three-layer Cu-polyimide printed circuit boards. The two Cu outer layers are connected to the HV, while the inner Cu layer, connected to the read-out channel, collects by capacitive coupling the current induced by electrons drifting in the LAr gap. In order to protect preamplifiers from accidental sparking, these outer layers consist of alternating pads of copper and resistive coating. This electrode structure combines the function of the charge collection anode and of the blocking capacitor.

In the calorimeter, signal electrodes are alternated with the absorber plates. For each half-barrel ($0 \leq \eta \leq 1.45$), the electrode is divided into two separate elements, of size ~1800 mm $\times$ 800 mm each, covering $0 \leq \eta \leq 0.8$ and $0.8 \leq \eta \leq 1.45$, respectively. The capability to build Cu-polyimide large-size electrodes with requirements for the ATLAS LAr calorimeter was demonstrated in 1996. Two series of prototypes with the barrel geometry were produced by three firms, see Figure 6-v.

The electrode board consists of two components, one double-sided and one single-sided Cu-clad polyimide sheets glued together. The overall thickness of the circuit is ~275 microns. The adhesive chosen is a thermosetting epoxy type. This kind of glue has good characteristics for cryogenic application.

The copper is a HD (high-ductility)-treated ED (electro-deposited) type. Owing to the dimension of electrode elements it is not possible use polyimide laminated with Cu RA (rolled-annealed). Kapton E[1] has been selected as polyimide support, in order to have the same elongation thermal coefficient for the Cu and the polyimide layer. In Figure 6-16 the structure of the electrode board assembly is shown.

---
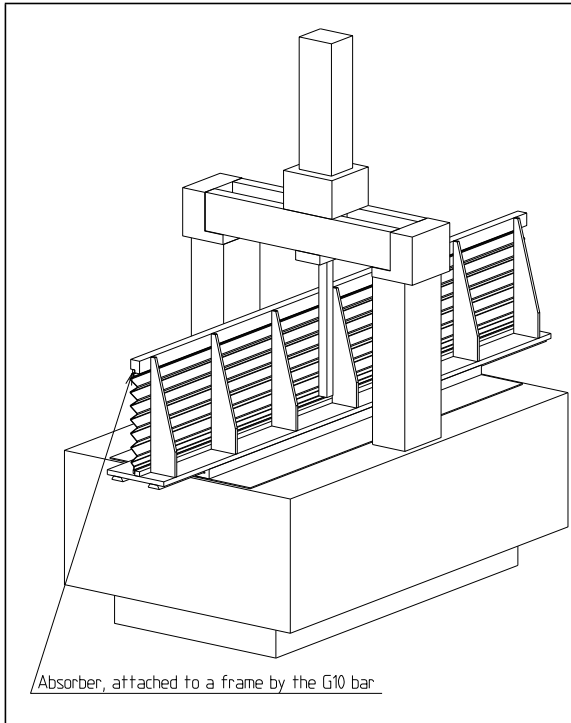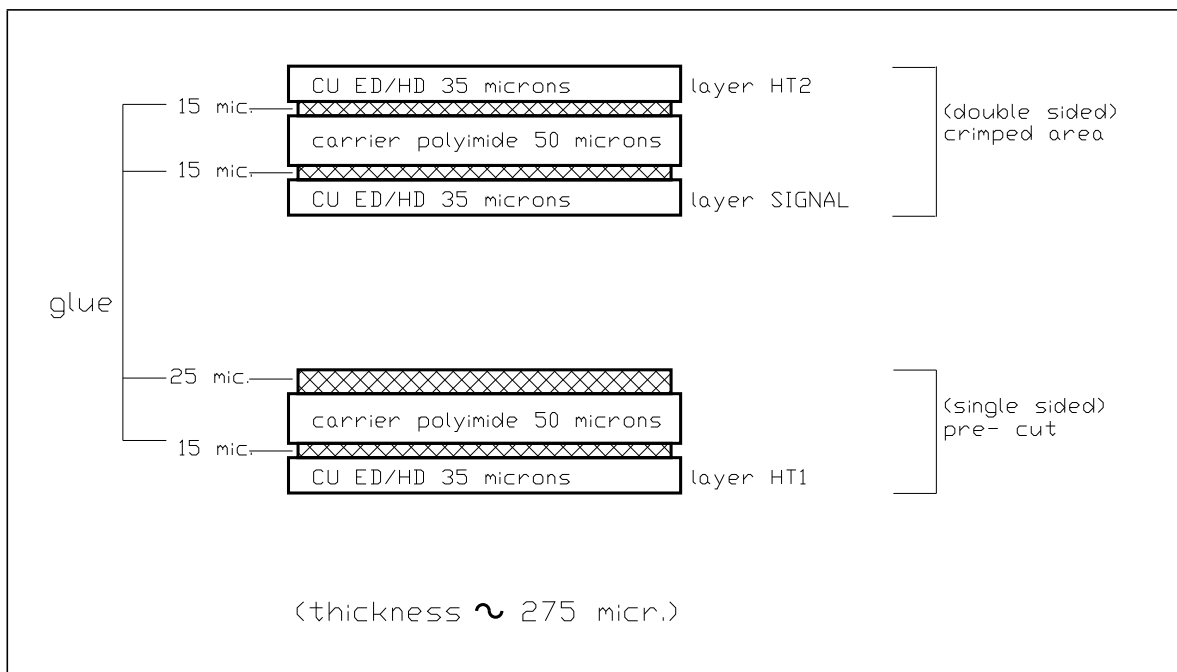
1. Kapton E is a trade mark of Dupont Corporation.

Figure 6-16 Cross-section of the double-sided and single-sided Cu-clad polyimide sheets used for the electrode assembly.

A preliminary study of radiation hardness for the raw materials used in the RD3 electrodes has been made. Peel-off measurements before and after neutron irradiation (**n** fluence of 10^{15} n/cm^2) show no significant variation in a short time-scale. Measurements of radiation hardness on the final materials selected for the electrode construction are foreseen in parallel with module 0 construction and tests.

6.3.2 Pattern design

The two electrode elements are mounted in the calorimeter module separated by 0.9 mm space at room temperature, each element is fixed close to its mid-point to the G10 bars of the absorbers through pins of 5 mm diameter. During the cool-down of the calorimeter, the electrode will not move with respect to the G10 bars at these points, while the end of the electrode will contract by less than 0.4 mm, (a relative electrode/absorber thermal contraction in the LAr of ~0.3 mm/m is expected).

The design of the electrodes was driven by physics requirements, the uniformity of the read-out of the signal over all the cells and the crosstalk constraints.

The three longitudinal samplings have the following characteristics:

- The first sampling (front), optimized for the rejection of γ/π^0, ends at 6 X_0 including ~1.6 X_0 of dead matter in front of the active part of the calorimeter; the granularity is $\Delta\eta = 0.025/8$.

- The second sampling (middle) from 6 to 24 X_0, has been optimized to contain photon showers up to 50 GeV and has a granularity of $\Delta\eta = 0.025$.

- The third sampling (back) covers the remaining depth $\geq 2 X_0$ and has a granularity of $\Delta\eta = 0.050$. Close to $\eta = 0$, the total depth is 24 X_0; in order to leave a minimum of 2 X_0 in the third sampling, the second is reduced to 22 X_0.
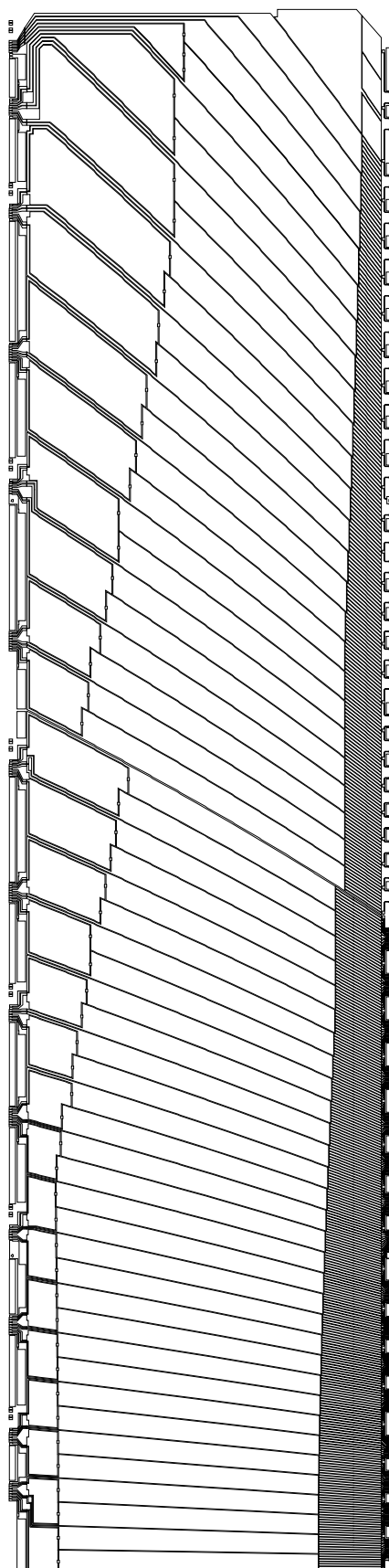
Figure 6-17 Signal layer for barrel electrode.

Figure 6-17 shows the electrode signal layer ($0 \leq \eta \leq 1.45$). The space between cells of the HV layer is 0.5 mm for strips and 1 mm for cells of middle and back samplings. In the signal layer, the space between cells is larger by 0.5 mm to cope with a misalignment between layers. The width of the output strip from the cells of the middle sampling, read out from the back edge of the electrode, increases with η to compensate for the increase of its length. The goal is to have a constant inductance of this line over all the barrel: this is necessary for the accuracy of the calibration (see Chapter 10).

Each high-voltage line supplies a face of a zone covering $\Delta\eta = 0.2$. It is distributed at large radius through a bus of 6 mm minimal width. It is brought over the electrode through resistive bridges made of silk-screened ink. Two resistors in parallel, each of 1 MΩ, connect the bus to each cell of the middle or back sampling. The two samplings are connected together by a resistor of 1 MΩ to compensate a possible failure of the resistors from the bus. The HV layers of these samplings are divided in half oundulations of copper connected by resistors of 500 kΩ to protect the read-out chain from sparks occurring in the liquid argon. The front sampling HV is supplied from the second sampling through 400 kΩ resistors.

6.3.3 Electrode construction

The process used in industry for the board construction is based on chemical etching of the Cu layers to generate the cell segmentation and the fan-out structure. In order to have the best quality for the electrode surface and precise dimensions of the board, the etching of the Cu inner layer is done as a first step. After bonding of the Kapton with double-Cu clad to the Kapton with single-Cu clad, the etching of the two Cu outer layers is done. The construction of the large-size prototypes shows a good reproducibility for the overall dimensions of the circuits. Therefore possible systematic discrepancies due to materials shrinkage could be compensated by properly biasing the masters. The required dimensional tolerances are:

- 0.4 mm on the overall size;

- 0.2 mm for the local accuracy of the etching on a given pattern;

- 0.2 mm as precision of alignment of the three Cu patterns (HV1, HV2, Signal) relative to each other;

- 0.1 mm is the precision in the clearance between adjacent cells.

In the outer layers of the electrode at high voltage, the HV distribution resistors, resistive pads along the cells, resistive bridges between different samplings are silk screened. The ink[1] used has a resistivity $\rho = 1$ MΩ/square) and after silk screening requires a curing stage of ~2 hours in an oven at 170°C.

The signal is extracted from the signal copper cells and brought to the front (front sampling) or back edge (middle or back sampling) of the electrode. Crimped connectors[2], reinforced with soldering to assure the contact at cold temperature, extract the signal from the electrode, go through the absorber G10 bars and are connected to the electronic boards. On the back, for reliability, one signal line reaches two crimped connectors. On the front side, only one connector can be used.

---

1. Resistive ink: D-RS-12116 from ESL SNC (USA).
2. Crimped connectors: Nicomatic CRIMPLEX 10025-32.

Copper beryllium springs, soldered on the electrode board, extract the ground from the absorber and transmit it through crimped connectors to the electronic board. The high voltage is brought through two crimped connectors.

6.3.4 Bending machine
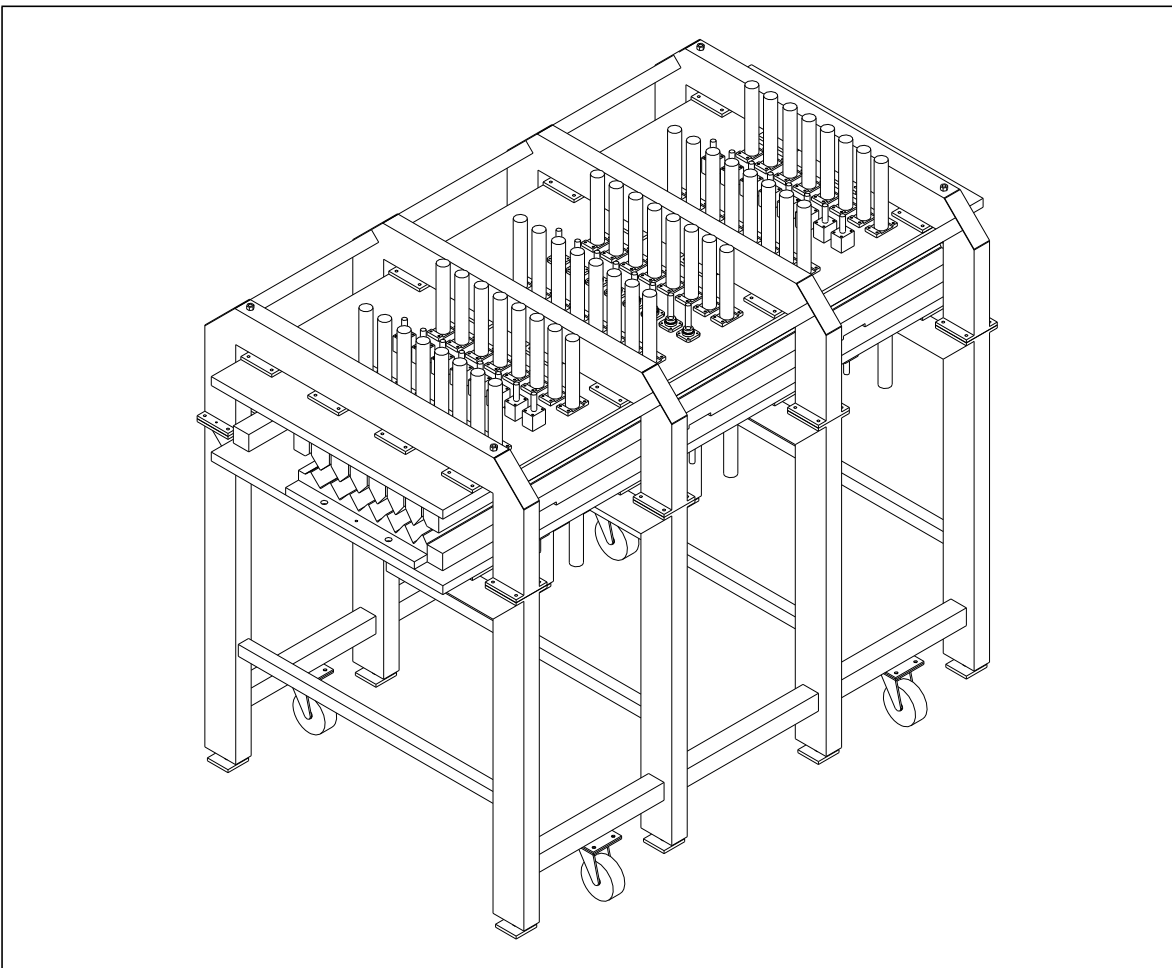
Figure 6-18 General view of electrode bending machine.

The bending machine bends the electrode from flat to accordion shape. The position of the folds has to be precise in radius and constant along the η direction. The final shape in the calorimeter is defined mostly by honeycomb spacers and the absorber. For the module assembly, the electrode element must have a shape close to the neutral fibre of the absorber.

Since both electrode elements have the same accordion shape, only one machine is needed to bend them. A general view of the bending machine is shown in Figure 6-18. The board is positioned using a set of holes at both edges. It is held at one edge and the other one is left free. The electrode element is pressed with knives one after the other to the theoretical shape with a pressure of a few tens of kilos. After bending, to cope with the elasticity of the board in the bent regions, a curing step of a few hours at 140°C in a mould stiffens the electrode element in its final shape. Air is removed during heating to prevent copper oxidation. The mould used is made of elastomer; for reasons of weight and cost, several electrodes are heated at the same time. Since the electrode was already cured at higher temperature for the resistive ink coating, this phase

does not damage the electrode structure. With only one bending station, an average production of eight bent electrode elements per day is foreseen.

6.3.5 Electrical tests

Electrical tests for the electrodes are foreseen in three phases:

- Electrical test in industry: for each electrode element the resistance of a subset of pads and the leakage current at HV are measured.

- Electrical test in the laboratory for flat electrodes, in the initial production phase. This test will be useful mainly to trace and understand possible damage done in the laboratory by handling, bending etc. For these tests the measurement technique will be the same as for the tests on bent electrodes described below.

- Tests at the laboratory on all electrodes (fully equipped and shaped).

The resistance and capacitance will be measured with a system composed of two test fixtures, a switching system, a RLC bridge, a digital voltmeter interfaced to a computer. The test fixtures will be made by two frames, one for each type of electrode element, equipped with golden spring probes having a hemispherical head and a strength of 1 N (see Figure 6-19). The map of the contacts will allow to measure on each outer side (HV layer) of the electrode:

- the resistance of the individual silk-screened resistors of the front sampling;

- the resistance between the first Cu pad of the cells of the middle sampling and the HV common distribution;

- the resistance between each Cu pad of the cells of the back sampling and the HV common distribution.
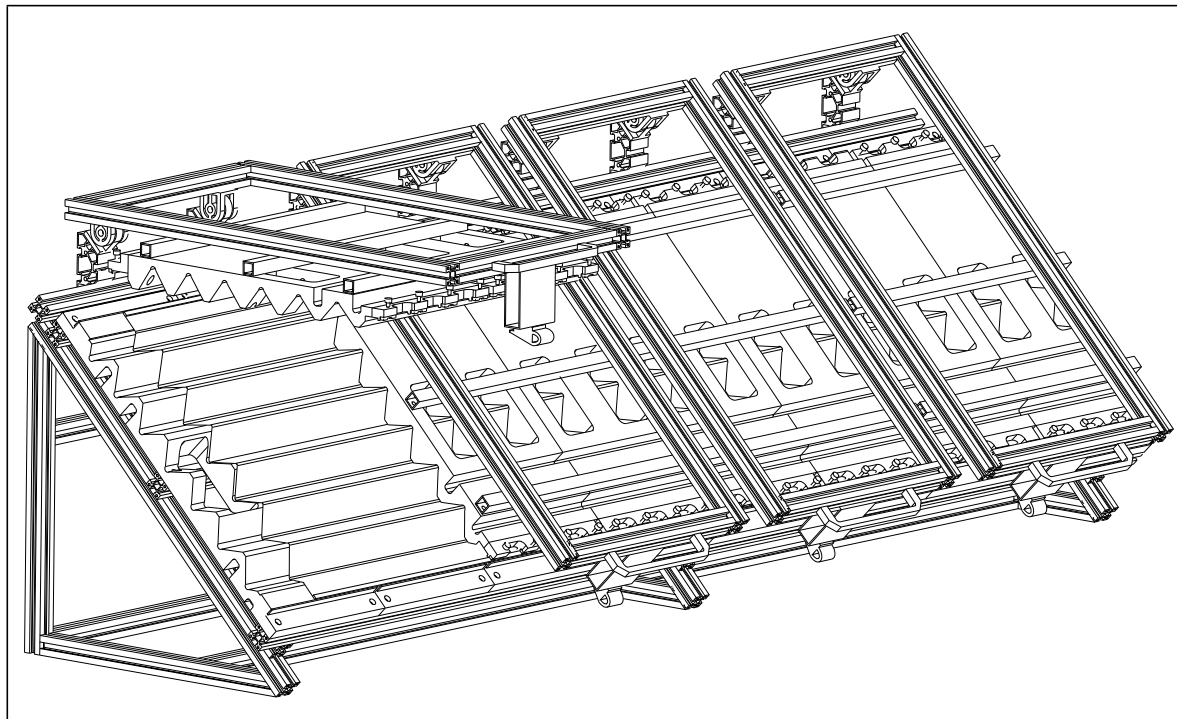
Figure 6-19 Test fixture for R,C tests on barrel electrodes.

This set of R measurements on the bent electrodes is the 'Minimal R test'. A more extensive test, i.e. the full map of R across each resistive pad, is optional. The capacitance test is intended mainly to check the integrity of the signal layer up to the connectors. It will be able to detect at least interruptions in the inner Cu layer of the cell, in the signal fan-out, in the crimped connectors and shorts between adjacent cells. Large misalignments between the HV and signal layers or inhomogeneities in the dielectric thickness can also be detected.

A subset of probes of the R test and a set of connections with the signal layer cells will be used for the capacitance test. From experience with prototypes the optimum value of the test frequency will depend on the resistance of the HV layer.

The HV test will be done on a batch (1 to 4) of electrode elements at the same time to allow a reasonable sampling frequency of the 'leakage current'. It will use a dedicated system composed of a multichannel HV system with current trip capability and a current monitor with about 10 nA resolution, a suitable bus for the monitor and control of the HV supply. The electrodes will be stored for some hours, before and during the HV test, in a room with controlled relative humidity below 40% to reduce the risk of surface current leaking and sparking. The HV ($\geq$2 kV) will be applied with a slow ramp (e.g. 10 V/s) between the two HV layers and the signal layer (all the cells clamped to ground).

The leakage current will be sampled with a frequency around 1 Hz to check for small discharges. The test will last from 3 to 4 hours. In addition to these tests, some electrodes could be kept under high voltage over a long period of time, to study ageing effects.

6.3.6 Database

All the measurements will be stored in a database so that the dimensional and electrical information of a given electrode element can be retreived.

6.3.7 Spacer

The spacers (Figure 6-vi) keep the electrode centred between two absorbers. The spacer consists of strips of honeycomb (9.6 mm wide cells, density 32 kg/m^3) laid in the flats of the accordion, on both sides of the electrode. To make the assembly process of the modules easier, the strips are first arranged in accordion-shaped sheets, where they are linked by a fine glass-fibre thread. For technical reasons, a sheet is about half as long as a module, and two sheets are juxtaposed in z to make a full spacer.

6.3.7.1 Tolerance on the spacer thickness

The liquid gap opens slightly (from 2.05 to 2.21 mm) along a fold with increasing radius, because the fold is a straight line. However, for simplicity the spacer is cut with parallel faces. The standard tolerance available from industry for cutting honeycomb sheets is ±0.13 mm on the thickness. In addition a 0.1 mm clearance is left on each gap.

The nominal thickness of the spacer is then $2.05 - 0.13 - 0.1 = 1.82\text{mm}$.

The tooling for gluing the thread has a projective gap; the thread can be more or less pressed into the honeycomb, so that it occupies the space left by the opening of the gap with radius.

6.3.7.2 Fabrication process
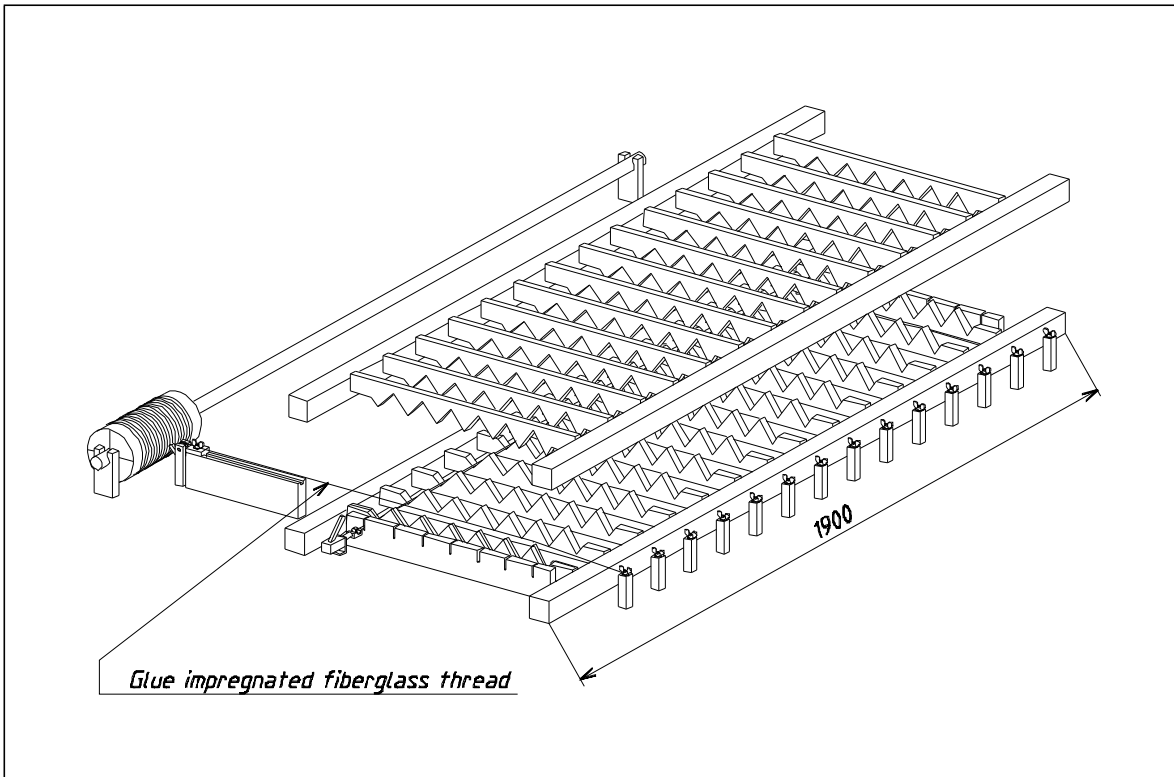
Figure 6-20 Tooling for honeycomb spacer fabrication.

A tooling (see Figure 6-20) and a process have been developed for the fabrication of spacer sheets. The honeycomb strips are disposed in the tool, with the pre-impregnated thread across them. Clamps are closed on the thread with the desired gap value; then the set-up is heated in an oven to polymerize the epoxy on the thread, which will adhere to the honeycomb strips and keep the accordion shape. The cycle takes two hours, and four such tools can be cooked together to produce 16 spacer sheets per day, compatible with the absorber production rate.
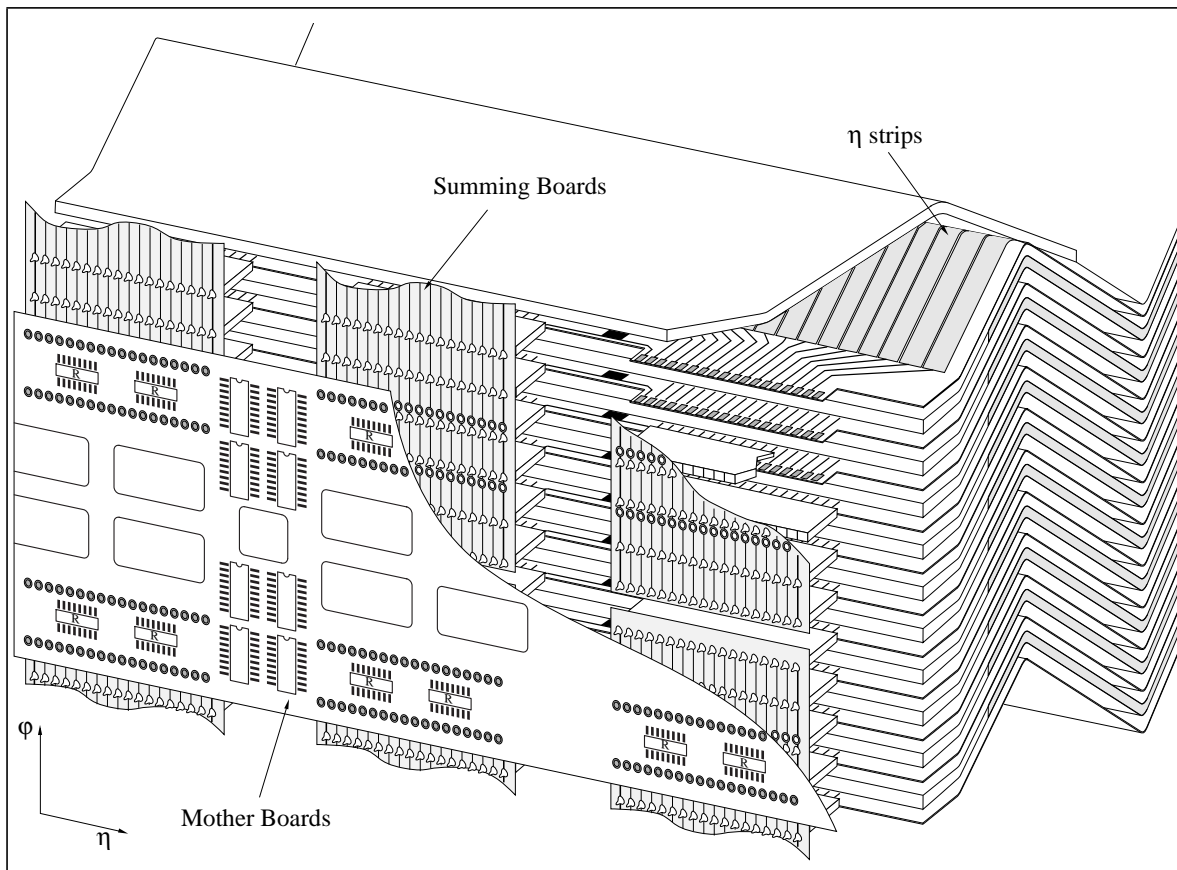
6.4 Electrical connections

6.4.1 Introduction

The interconnects that are needed to collect the signals from the read-out electrodes and carry them to the feedthroughs need to be very reliable. The impedance of the lines need to be maintained and the connection reliability goal is to be at the level of 1 in 10^5 per connection. In addition to the signal path we need to distribute calibration signals to the individual towers and HV to the read-out electrodes.

6.4.2 Calorimeter Signals

The calorimeter signals which are deposited in a different read-out electrode but belonging to the same read-out channel are added by summing boards. From there the charge is transferred

Figure 6-21 Isometric view of the accordion showing the placement of the electronics.

via the motherboards to the cables that carry the signal to the feedthroughs. The motherboards also fan out the calibration signals to the different read-out channels according to a preset pattern. Figure 6-21 shows an isometric view of the accordion barrel calorimeter with the placement of the summing and the motherboards.

There are special requirements that need to be satisfied by the summing and motherboard system:

Space Limitation

The minimization of dead space is critical especially in the front motherboard and cables.

Connection reliability

There are a large number of connections between the summing boards and the Kapton.

The electronic requirements of the read-out are discussed in the electronic section. Here we give a short description of each of the components in this part of the read-out chain.

6.4.3 Summing Boards

The summing boards in the front integrate the charge from 16 cells in azimuth. They are of two types corresponding to the two different read-out electrode types. There are 56 summing boards in Z covering a rapidity region $\eta < 1.4$ and 32 in ϕ for a total of 1792 boards for the front section. Owing to a difference in granularity at the end of the barrel covering the rapidity region $1.4 < \eta < 1.475$, a special summing board covers this region accounting for an additional 64 boards. In the back section, the summing boards span 16 cells in ϕ but they need to integrate the charge for only 4 cells thus the distribution of the channels is somewhat more complex.
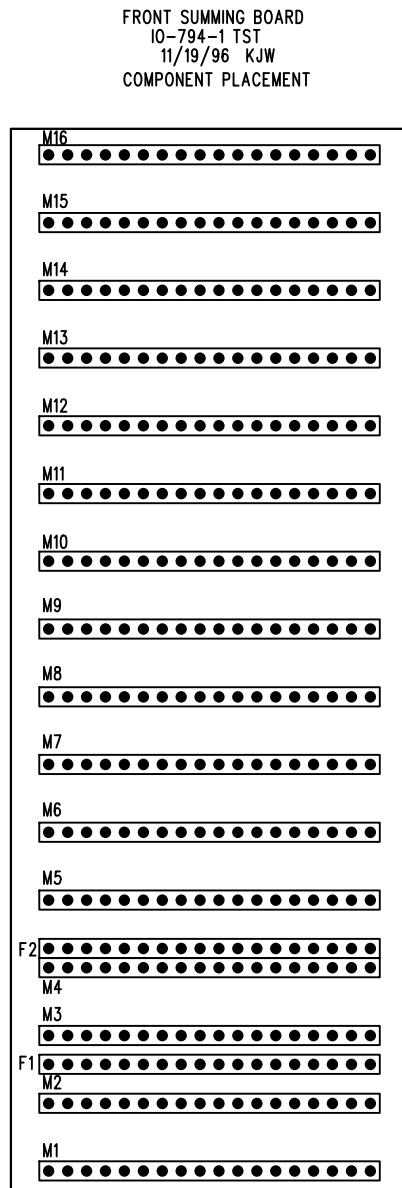
Figure 6-22 shows the design of a front summing board. The summing boards are flexible G10 boards making contact with the Kapton electrode with a 0.025'' square post soldered on to it. They provide a summation over 16 ϕ cells, M1 through M16. There will be two open bottom receptacles offset from the third and fourth pins (F1 and F2) on the summing board which will be used to make contact with the motherboard. There are two contacts provided to the motherboard for redundancy.

6.4.4 Motherboards
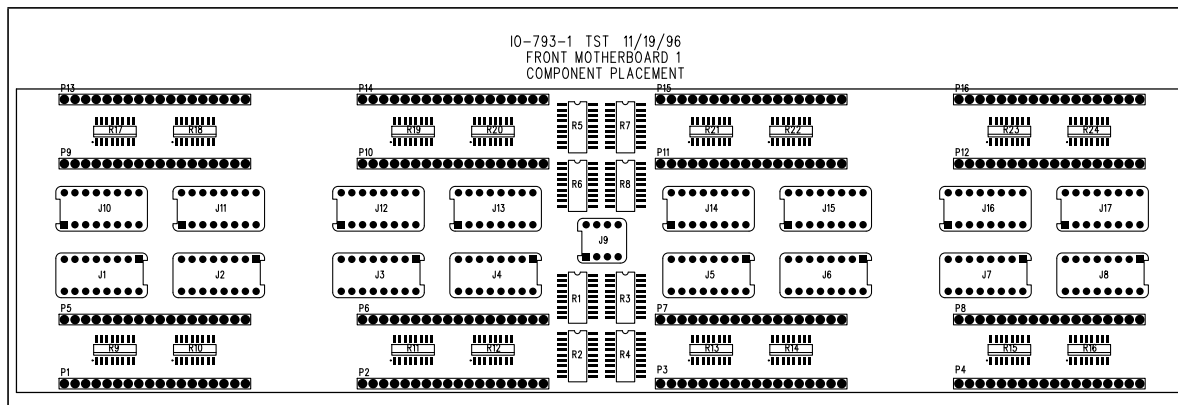
The front motherboard services 64 read-out cells in Z (corresponding to 4 summing boards) and 2 summed units in azimuth for a total of 128 read-out channels. The routing of signal and calibration pulses is achieved using an eight layered motherboard. Figure 6-23 shows the placement of the components on the front motherboard for the central rapidity region. There are seven different types of motherboard for each barrel in the front section covering a rapidity region $|\eta| < 1.4$. There is an additional special motherboard for the end barrel region $(1.4 < |\eta| < 1.475)$. Each motherboard in Z differs primarily in the relative positioning of pins as they change with rapidity. There are an equivalent number of types of motherboards for the back section.

FRONT SUMMING BOARD
IO-794-1 TST
11/19/96 KJW
COMPONENT PLACEMENT

Figure 6-22 Design of the summing board for the front section of the barrel calorimeter.

The input to the motherboard is an open bottom receptacle with an Augat Holtite socket type (part number PN 8134-HC-8P2). The connection to the summing boards is made via pins which are inserted through the motherboard into the open bottom receptacle in the summing board. This feature is advantageous as it removes the necessity to align the Kapton electrode, the summing board, and the motherboard simultaneously.

The socket for the cable header will be a closed bottom receptacle of type Mill-Max 0680-0-15-15-32-14-10-0. This socket provides a six-fingered contact which increases the reliability of the contacts and requires minimal insertion force.

Figure 6-23 Front motherboard with the placement of components.

6.4.5 Cold signal cables

The signal cables carry the signal from the motherboards to the patch panel that is located at the ends of the calorimeters. The impedance of the cables for the front is 50 Ω and the back 25 Ω. The cables need to be of high quality with very uniform impedance in order to keep the signal shape constant. The cable selected for the cold cable is a Kapton-base mini coax manufactured by Axon. Industry will deliver the cables in harnesses cut to size with the eight channel low profile connector on the motherboard side and a µD connector on the patch panel side. The µD connector has 96 pins and services 64 read-out channels. Thus every two neighbouring channels share a ground.

6.4.6 Patch panel

The patch panel fixes the µD connectors at the end of the cable to a fixed location on the calorimeter so that they become an integral part of the calorimeter mechanical structure. This is especially important during transport, module handling for tests before the installation, and during the assembly of the calorimeter into a 2π structure. The patch panel is designed so that it takes a minimum amount of space in Z and will have easy access for connections to the feedthrough cables after installation.

6.4.7 Calibration distribution

The calibration requirements for the motherboards are the following:

Calibration signals will be distributed via a network of resistors. To achieve the necessary resolution the network will be laser trimmed to an accuracy of 0.1%.

The calibration pulse received from the pulser system at the centre of the motherboard (J9) is distributed to the different channels using a resistive network split into two sections. The first of these sections consists of a 950 Ω resistive network, R1 through R8. The second 50 Ω resistive network, R9 through R24, is located at the point of injection at the motherboard as shown in Figure 6-23. The splitting of the network reduces the sensitivity of the pulses arriving at the motherboard input to the routing (length) on the board that carries the pulse.

For accuracy of calibration it is necessary to maintain the relative timing between the trigger system and the signal identical for calibration and for particles. The differences in the time-of-

flight of particles coming from the vertex to different places on the calorimeter (in rapidity) are balanced by adjusting the path length of the calibration signals on the motherboard.

6.4.8 High-voltage cables and distribution

The high voltage is supplied to the barrel electrodes from two HV feedthroughs one on each side of the barrel. The HV cables are routed on the edge of the calorimeter to HV motherboards. Each motherboard serves 64 read-out cells. Each motherboard is supplied from both ends as a redundancy. Each read-out electrode has two independent HV supplies, one for each face.

6.5 Presampler

6.5.1 Overall geometry
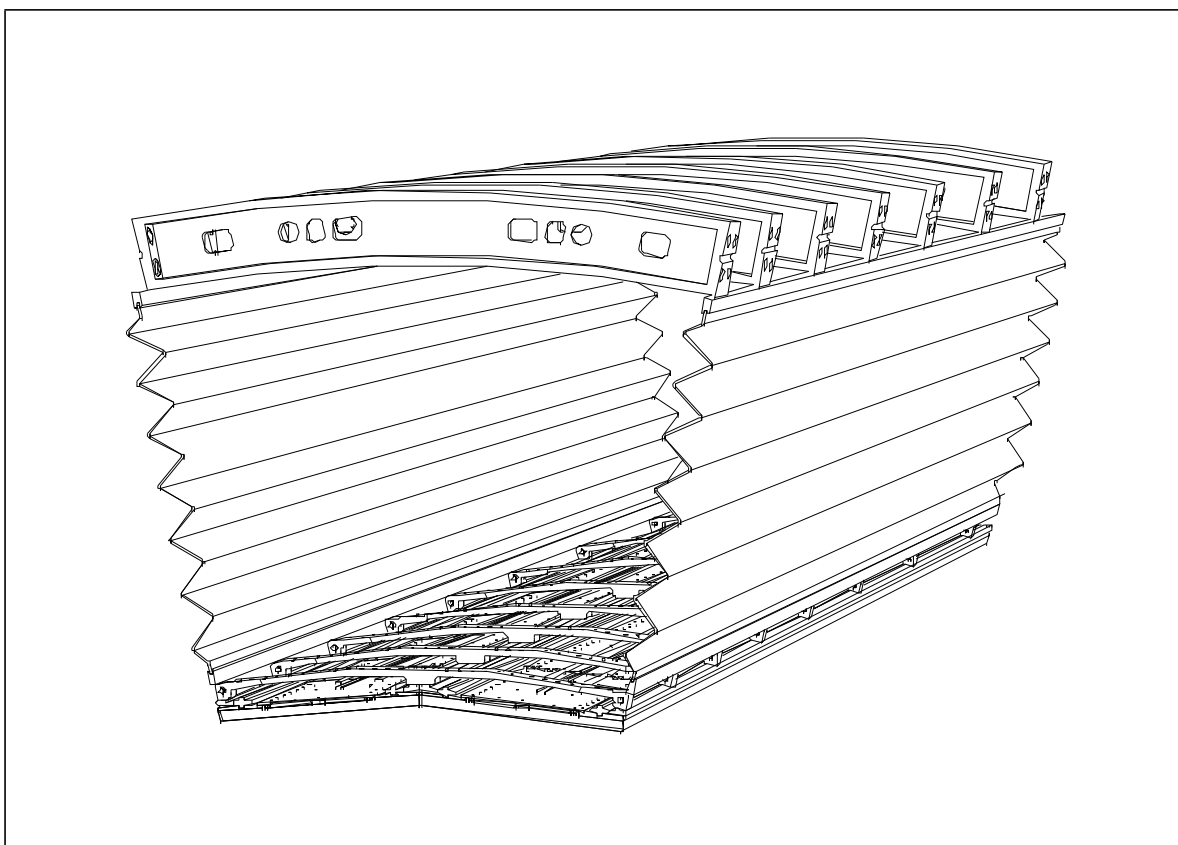
The presampler acts as a thin (11 mm) active layer of liquid argon, which provides a first sampling of the showers in front of the accordion electromagnetic calorimeter. In the transverse (R,ϕ) plane, it has a polygonal shape formed by 32 identical azimuthal sectors per half-barrel, each sector spanning 0.2 in ϕ and 1.51 in η. The two barrel halves are identical. The sectors are mounted on rails which are fixed on the barrel internal rings. Figure 6-24 shows a view of a barrel module with its two presampler sectors suspended at the front. The granularity of this device corresponds to one electromagnetic cell in the η direction (0.025) and four in ϕ (0.1). The opening of the showers in ϕ due to the solenoid's field led us to choose a coarser granularity for this coordinate. The external envelope of a presampler sector consists of a 0.4 mm thin glass-epoxy shell (3068 mm $\times$ 281 mm $\times$ 21 mm) which houses eight modules of unequal length secured together by 3 m long G10 bars. Each module covers a constant region of 0.2×0.2 in the (η,ϕ) space with the exception of the modules located at the extremities of the EM barrel for which the η coverage is reduced to 0.11. The total number of channels needed to read out this device is 7808 (122 per sector).

6.5.2 Presampler modules and electrodes

6.5.2.1 Module geometry

Since a presampler module covers a constant interval in pseudo-rapidity, its longitudinal length increases as a function of its z position in the barrel. Consequently, there are eight different types of modules of 64 identical units each. In total, 512 modules (plus 48 spare ones) will have to be produced.

The charge deposited by the showers in the 11 mm active layer is collected by 277.5 mm long electrodes which are arranged transversally with respect to the longitudinal axis. The liquid argon gap is kept approximately identical at a value of 2 mm throughout the device allowing us to operate the presampler with a fixed high voltage of 2 kV. The number of electrodes per module type varies to keep the liquid gap constant. The electrodes are strictly perpendicular to the longitudinal axis, except for the modules covering the $|\eta|$ range up to 0.4 where the electrodes are slanted with respect to the normal axis to avoid a local dependence of the signal upon the shower impact position. The read-out cells of the required granularity ($\Delta\eta = 0.025$, $\Delta\phi = 0.1$) are obtained by ganging in the longitudinal direction the appropriate number of electrodes on the
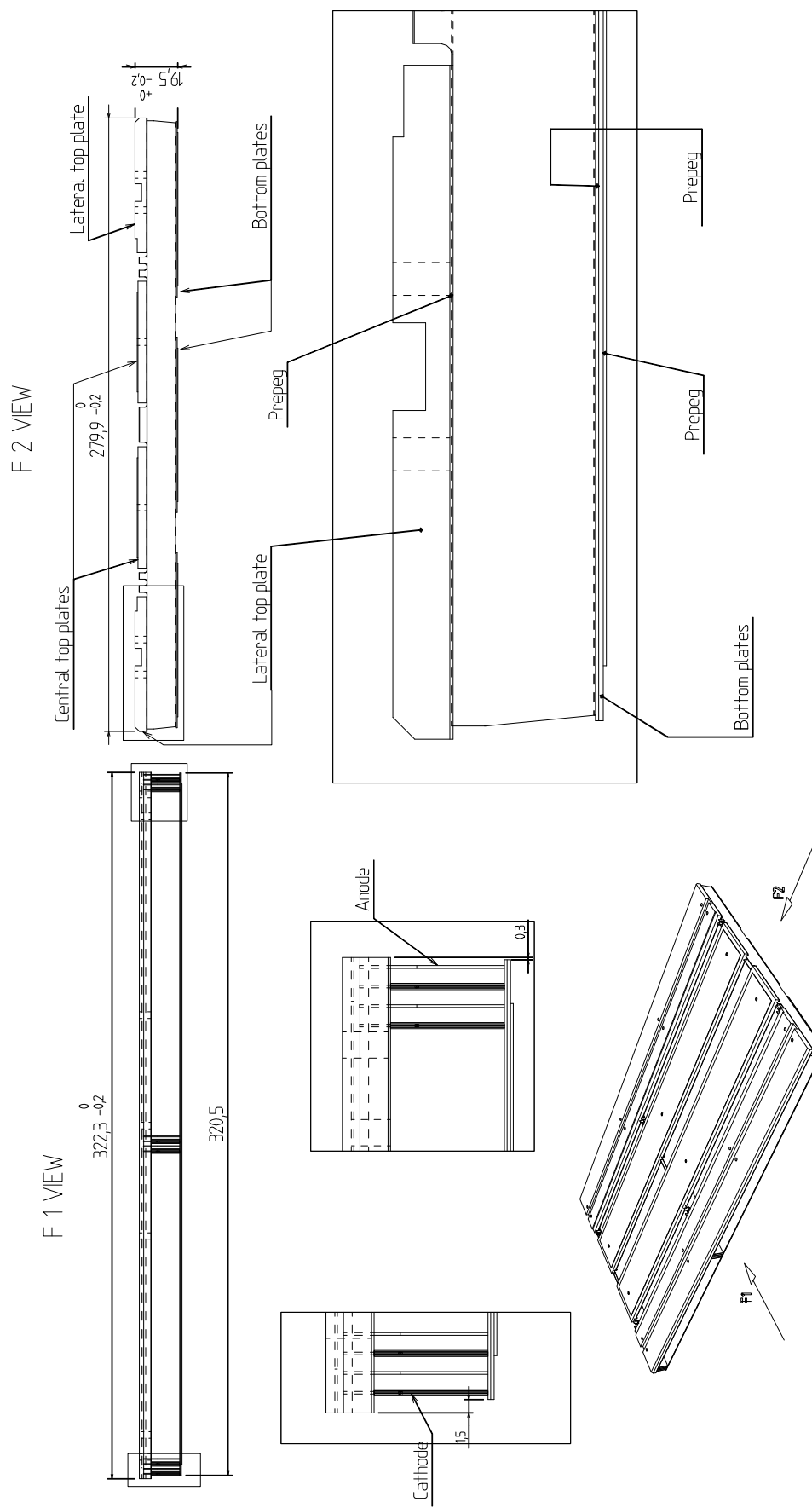
Figure 6-24 EM barrel module with two presampler sectors.

modules themselves. In φ, each electrode is subdivided into two 0.1 compartments by etching. Thus on each module there are 8 cells in η and 2 in φ, i.e. 16 in all except for the shorter modules located at the barrel edges where there are only 10 cells (5 × 2). Table 6-3 summarizes the geometric dimensions of these modules while Figure 6-25 shows the drawings of the type 3 modules.

Table 6-3 Characteristics of the presampler modules at 293 K.

Module No.	Length (mm)	Gap (mm)	No. of anodes	No. of cathodes	Ganging factor	No. of cells	Inclination angle wrt normal in °
1	281.4	1.96	56	56	7	16	25
2	298.4	1.96	64	64	8	16	12
3	322.3	1.93	72	72	9	16	0
4	356.8	1.93	80	80	10	16	0
5	404.8	2.00	88	88	11	16	0
6	478.4	2.00	104	104	13	16	0
7	563.2	1.90	128	128	16	16	0
8	363.0	1.90	82	83	18 (+10)	10	0

Figure 6-25 Type 3 presampler module.

6.5.2.2 Electrodes

The electrodes are glass-epoxy (FR4 or G10) multi-layered circuits. They are of two different kinds: cathodes which are simple 270 μm thick double-sided boards (200 μm of FR4 (or G10) plated with 35 μm of copper on each side); anodes which are 327.5 μm thick 3-layered circuits (17.5 μm of copper + 150 μm of FR4 (or G10) + 17.5 μm of copper + 125 μm of prepreg and 17.5 μm of copper). A positive HV of 2000 V is applied to the external anode layers, while the shower signals are read out by capacitive coupling to the central anode layer. Many tests including a long-term survey were performed on the anodes up to 4000 V in liquid nitrogen to check their high voltage resistance. In June 1996, two module prototypes of 128 electrodes each were operated for a month at CERN in a liquid argon cryostat installed in the H8 beam facility. A photograph of one them may be seen in Figure 6-iv. In both cases, no failure was ever detected.
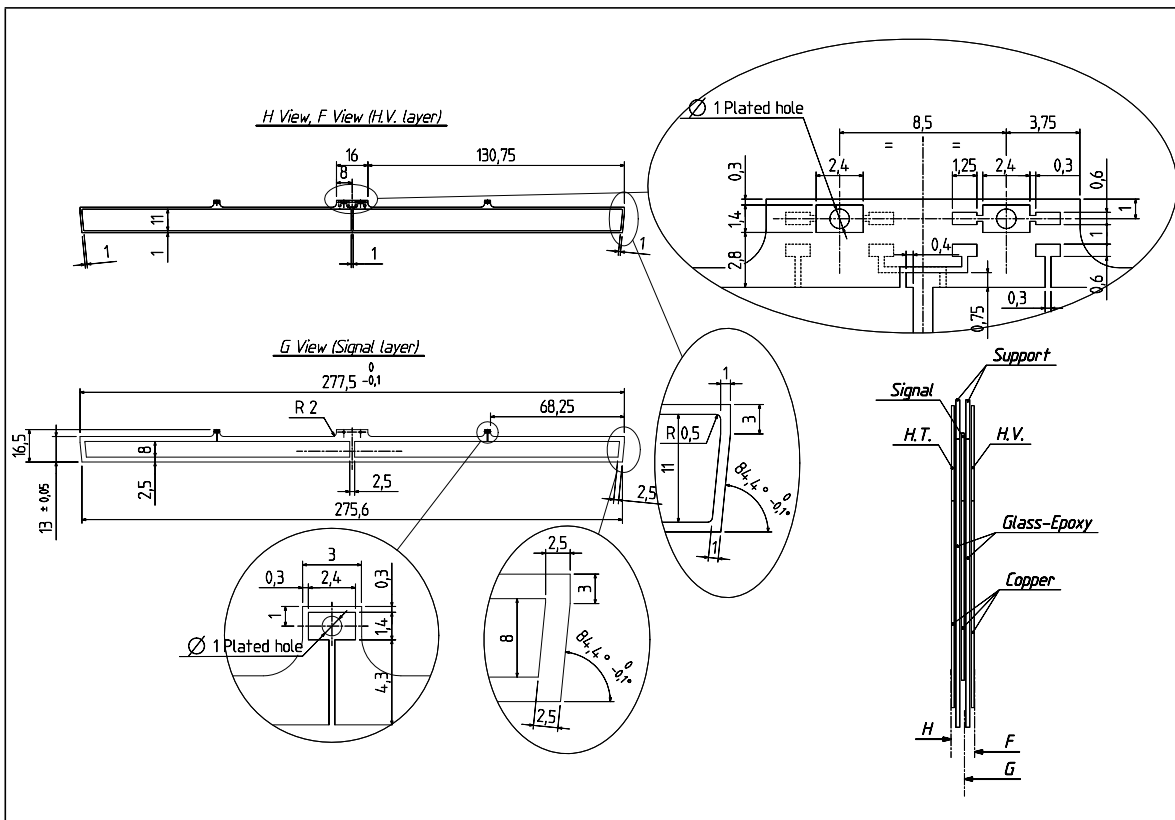
Because of the variation of their inclination angle, each kind of electrode comes in three different heights corresponding to modules of type 1, type 2 and types 3 to 8. With the envisaged spares included, the total number of electrodes per kind are 4050, 4650 and 40 000 for the three sizes, respectively. Small tabs located on the electrode upper edges offer the possibility to connect the signals, the ground, and the high voltage including some HV protection surface mounted resistors (1 MΩ) at the level of the electrodes themselves.

The electrode thickness tolerance is determined by the type of shims that will actually be used in the gluing jigs (see Section 6.5.2.3 below). With parallel shims, the length of a module is given by the overall shim-electrode stack thickness and a tolerance of 0.1 mm is put on the total thickness of 100 electrodes of each kind. On the other hand, with grooved shims, each electrode is required to fall within a tolerance of ±10 μm with respect to its nominal thickness. The preferred solution will be the least expensive configuration after tendering, within the technical specifications. The production of electrodes will come in three batches: one corresponding to the two presampler sectors needed to equip module 0, and two series production batches one year apart. Figure 6-26 shows the detailed drawings of the size 3 anodes.

6.5.2.3 Module production

As a result of an extensive prototyping phase, a gluing technique was finally selected for module production. The electrodes are first positioned in a jig by precision shims. Then, glass-epoxy plates covered with epoxy pre-impregnated foils are applied with a proper pressure on the top and bottom of the electrodes by means of tightening screws mounted on the jig. To symmetrize the mechanical structure, especially in view of reducing the deformations due to the thermal contraction, the glass-epoxy plates are coated when possible with prepreg foils on both faces. This is the case of the bottom plates and the central top ones. The pre-impregnated foils are 0.3 mm thick prior to polymerization and have a high epoxy impregnation density, to obtain the formation of glue menisci at the electrode edges that assure a good contact surface. Finally the modules undergo a polymerisation cycle that lasts approximately 16 hours in an automated autoclave with well-defined temperature ramps and plateaus. Thermal contraction and deformation tests were done in liquid nitrogen on the existing prototypes both in the x and y directions. We measured a shrinkage coefficient $\Delta L/L(293 \rightarrow 77 \, \mathrm{K})$ of 0.26±0.03%, and a sagitta around 0.2 mm.

The local connection of the ground lines, HV buses, and signal wires is performed right after the extraction of the module from its gluing jig. It is achieved by means of thin tinned wires that are first inserted through the copper-plated holes made on the electrode tabs and then soldered at each contact point. Two separate HV lines per pair of modules, each connected to the left or the right sides of the electrodes, will be used to prevent the full loss of a module in case of sparks.

Figure 6-26 Drawings of the size 3 anodes.
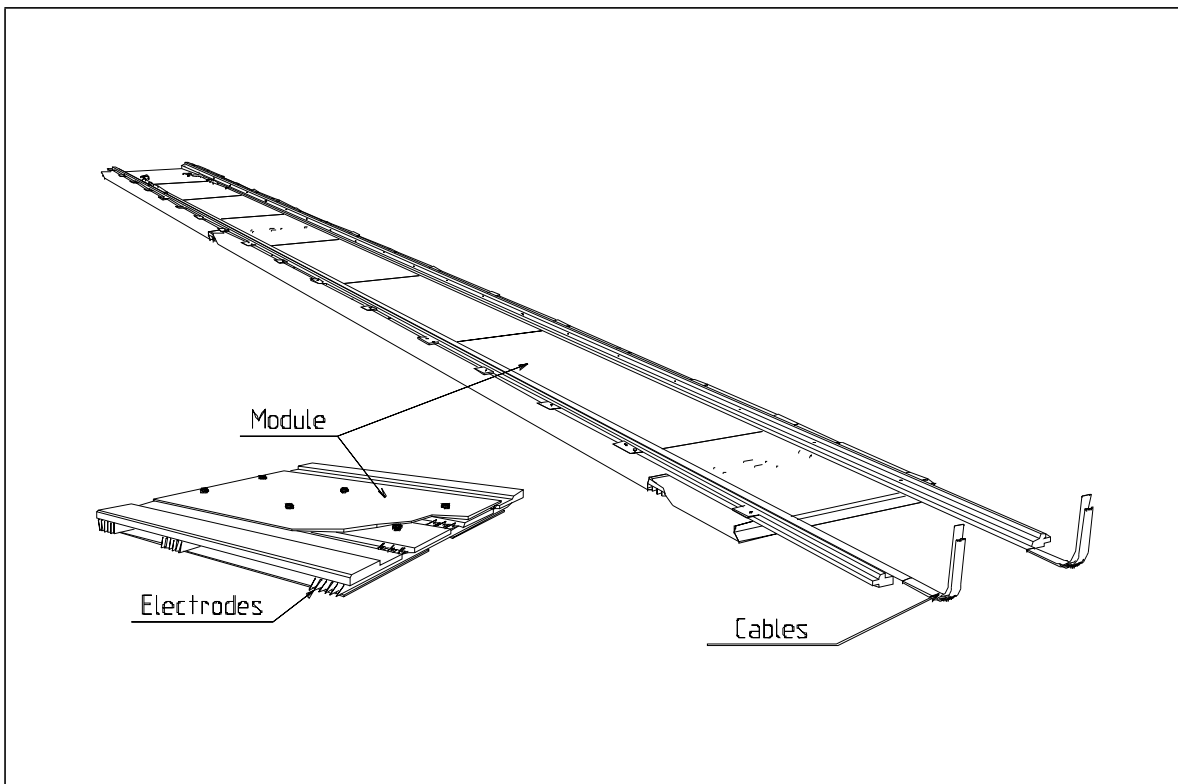
After completion, a module is cleaned by using high purity ethanol and placed in a protection bag filled with argon.

The module production including the connection soldering will be done by an industrial firm. The estimated cost corresponding to this operation was directly included in CORE at the beginning of the project. The tendering is under way. The delivery will be organized in four batches: one (16 modules) corresponding to the two sectors of module 0, two annual batches of 192 modules each, and a final one of 160 modules to complete the series production.

6.5.3 Presampler sectors and support structure

Figure 6-27 shows a perspective view of a presampler sector. Such an element is assembled by inserting eight modules with their mother boards soldered on their top in a thin glass-epoxy shell. This 0.4 mm thick shell acts as a protection and is made conductive on its lateral sides to collect the shower signals at the extremities of the electrodes and thereafter maximize the active coverage. Three long shell prototypes of different composition have already been received from the industry. Their tests revealed no major problems. Their measured thickness (0.38±0.01 mm) is well within our tolerances. The shell with its eight modules in place is then positioned in a guide that will give the sector its precise external geometry. Finally, two long longitudinal glass-epoxy bars are screwed in the lateral upper plates of the modules to secure the assembly.

At this stage the cables for the calibration pulses, HV distribution, and signals are laid down on top of the sector and soldered to the motherboards. The choice of soldering instead of connectors was dictated by the space constraints: 6.9 mm of radial space available for the cables and the motherboards. A connection test is performed immediately after soldering. The thermal

Figure 6-27 Perspective of a presampler sector.

shrinkage coefficients of a sector's parts are similar enough to avoid the opening of gaps between contiguous modules in the longitudinal direction. After cooling at the temperature of liquid argon, a sector will shrink by 8 mm in the longitudinal direction and 0.7 mm in ϕ. Each newly built sector is fully tested in a LN_2 cryostat before being placed in an argon-inerted protection vessel for storage.

As shown in Figure 6-vii, the sectors are mounted on G10 long rails which are screwed on the calorimeter internal rings. The rails are made of the same material as the one of the absorber bars in order to suppress the differential contraction stress. Contiguous sectors are mounted with a nominal gap of 0.4 mm at room temperature. When in liquid argon, this gap expands to 1.1 mm owing to the transverse thermal shrinkage of the sectors. Taking into account the thickness of the shells, there is 2 mm of inactive space between two adjacent sectors: a 0.7% loss. The sliding of sectors on their rails was checked on a full-length model of three sectors in horizontal and vertical position. The internal radius of the device is 1413.3 mm at 293 K and is not expected to change much (< 1 mm) at liquid argon temperature owing to the thermal stability of the calorimeter inner radius (see Section 6.6.2 below). A finite-element analysis of the thermo-mechanical behaviour of the sectors is under way, the first results of which confirm that there is no deformation of the presampler modules. In addition, they predict that the shells after thermal contraction will press slightly on the modules with a tiny force.

6.5.3.1 Cold electrical connections

As already stated, the electrical connections at the level of the presampler sectors will be soldered for reasons of compactness. The sectors will be delivered to CERN with all their electrical connections made and tested in liquid nitrogen. For a sector, two harnesses of 64 coaxial leads each are necessary to ensure the connection of the physics signals according to the following as-

signment: harness 1 to modules 1-4, harness 2 to modules 5-8 with 6 unused channels soldered to the sector ground.

To distribute the calibration signals, eight coaxial cables (one per module) are needed. They are individual cables, stripped and soldered at both extremities, with a connection at the large rapidity sector edge made to a small intermediate printed board equipped to receive low-profile calibration connectors of the same type as those of the calorimeter. The lengths of these cables are adjusted to provide a time distribution of the calibration signals close to the particle time-of-flight sequence.

The high voltage is supplied by eight coaxial Kapton cables per sector: two lines for each pair of contiguous modules with the left and the right sides of the anodes separately connected. The HV cable shields are soldered at one extremity to the ground of the motherboards and left unconnected at the other end. This provides us with a distributed capacitor for HF filtering.

Each sector is electrically insulated from its neighbours and the rest of the calorimeter. The ground of each sector is propagated to the cryostat Faraday cage via the output signal and the calibration cables. The cables lying on top of the sector motherboards are separated from the calorimeter connections by thin glass-epoxy protection plates as depicted in Figure 6-vii.

6.5.4 Summary of specifications

A summary of the presampler specifications is presented in Table 6-4.

6.6 Rings

6.6.1 External rings

The 1024 absorbers constituting one half-barrel calorimeter are screwed onto seven stainless-steel rings. The aim of these supporting rings is to give the necessary rigidity to the whole half-calorimeter and to define precisely its geometry. These rings stand on the cryostat rails.

One ring is made of 16 ring-pieces, $22.5°$ in ϕ, a ring-piece corresponding to one module of 64 absorbers. The 16 ring-pieces are screwed together to form a complete circle. The 16 ring-pieces are identical with an I shape beam except for the two ring-pieces at the level of the rail (Figure 6-28). The main dimensions of a ring-piece are: I shape height 100 mm, wing width 80 mm, wing thickness 12 mm, and web thickness 10 mm. The thickness of the two plates at both ends of a ring-piece is 15 mm. The holes in the web of the ring-piece allow the passage of cables and of cooling pipes. The dimensions have been chosen to give a tolerable deformation under the weight of the calorimeter, less than 4 mm. To minimize the deformation, a dowel pin is placed between two ring-pieces. To evaluate precisely the weakening due to the junction between two ring-pieces, loading tests have been performed with a straight I shape beam with the same cross-section as the ring-piece and with two straight beams linked like the ring-pieces. We observed a deformation 25% greater in the second case. This weakening effect is taken into account in the finite-element calculations.
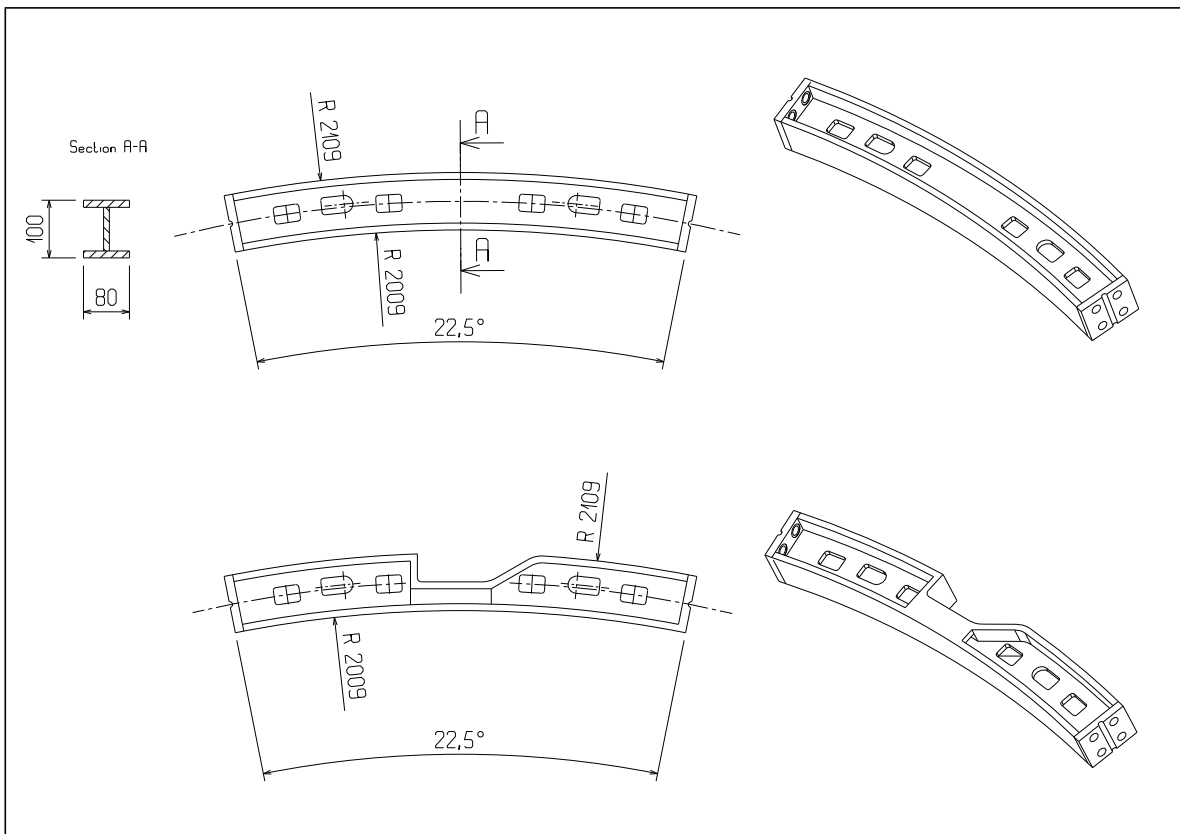
The rings are placed close to every $\eta = 0.2$ to ease the cabling of the electronics. The maximal weight supported by the ring at $\eta = 1.2$ is about 12 tons, the weight of a half-calorimeter being 55 tons. The I shape of the ring close to $\eta = 0$ has to be modified to give the necessary clearance for the middle flange of the cold outer wall of the barrel cryostat. As these rings are immersed in

Table 6-4 Presampler specifications

General features	full efficiency active thickness = 11 mm $\Delta\phi = 2\pi, \Delta\eta = 1.51$ HV = 2000 V liquid argon gap ~ 2 mm drift time ~ 400 ns detector capacitance = 160 pF -380 pF
Sectors	64 units (+6 spares) $\Delta\phi = 0.2, \Delta\eta = 1.51$ L = 3068 mm / l = 281 mm / h = 35mm (T = 293 K) L = 3060 mm / l = 280.3 mm / h = 34.9 mm (T = 89 K) $\Delta L/L(293\rightarrow89\ K) = 0.26\%$ 8 modules/sector weight = 20±1 kg/sector
Modules (see Table 6-3 for more details)	8 types of 64 units each - 512 in total (+ 48 spares) $\Delta\phi = 0.2, \Delta\eta = 0.2$ (except type 8; $\Delta\eta = 0.11$) $\Delta L/L(293\rightarrow89\ K) = 0.26\%$
Motherboards	1 unit/module 8 different types 5-layered printed circuits: ground, signals, ground, calib lines, ground FR4
Shells	64 units (+ 6 spares) L = 3068 mm / l = 281 mm / h = 21 mm (T = 293 K) L = 3060 mm / l = 280.3 mm / h = 20.9 mm (T = 89 K) thickness = 0.4 mm laterally conducting (grounded) made of glass-epoxy $\Delta L/L(293\rightarrow89\ K) = 0.26\%$
Sector assembly bars	2 types of 64 units each (+ 12 spares) made of FR4 $\Delta L/L(293\rightarrow89\ K) = 0.26\%$ L = 3057 mm (T = 293 K)
Support rails	same material as EM absorber bars 2 types of 64 units each L = 3057 mm (T = 293 K)
Electrical connections	122 signal cells/sector 16 signal cells/module (except type 8; 10 signal cells/module) 8 calibration coaxial lines/sector 8 HV coaxial lines/sector 7808 signal channels in total

liquid argon, they have to be in stainless steel. INOX 316LN has been chosen for its good characteristics at cold. Several techniques have been considered to build them: welded pieces, cast pieces or mass machining. The welded piece method with a suitable thermal stabilization has been retained.

To validate the method, a prototype of one ring has been ordered. Geometric measurements of the pieces are foreseen at each stage of the fabrication: after welding, after thermal stabilization, and after the final machining. The final machining includes the machining of the 22.5° angle of

Figure 6-28 Drawings of external rings.
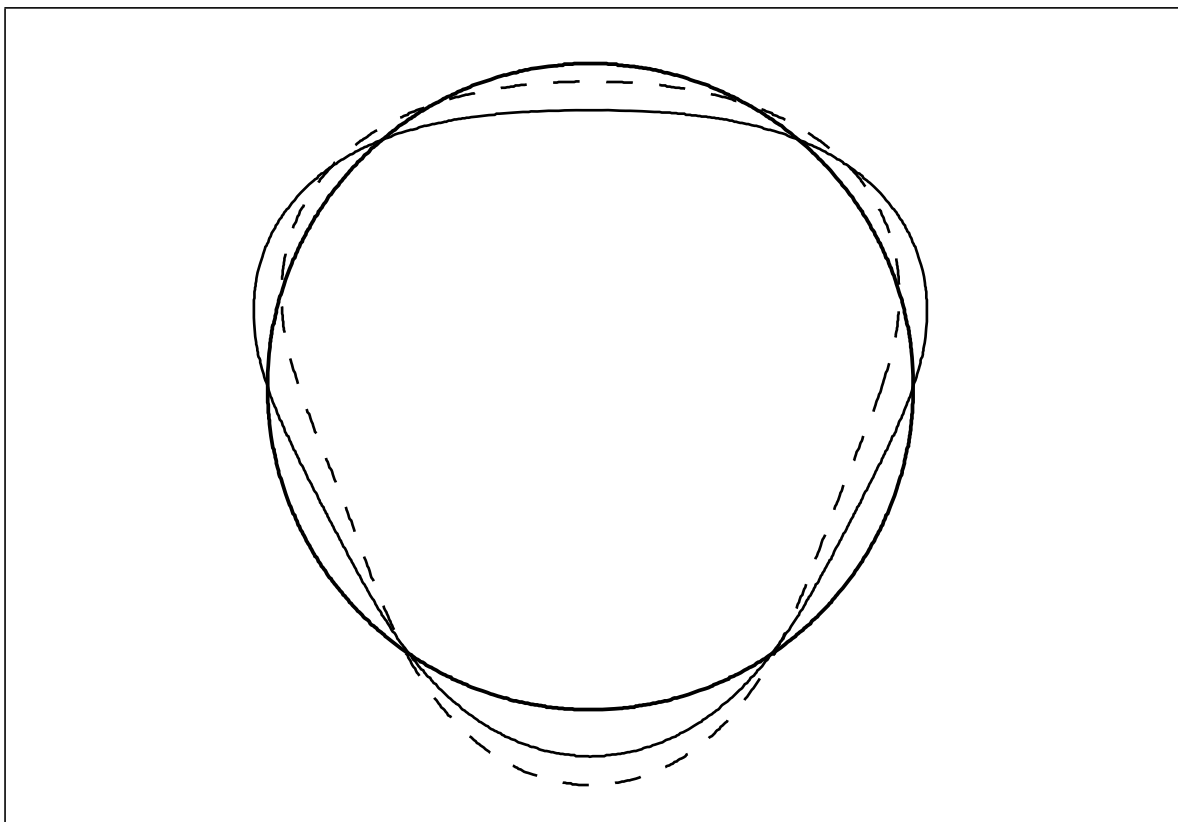
each ring-piece and the machining of the external and internal radius of the reconstituted ring. We aim to get an accuracy of 0.1 mm on the internal radius and 0.5 mm on the external radius.

For the assembly phase, the inner radius of the ring is the reference radius on which the external G10 bars of the 1024 absorbers are mounted. Special care has been taken to get a reference radius as close as possible to its true value in order to avoid any clearance between the external G10 bars.

A special jig to measure these radii and also to measure the deformation and the stresses under the weight of the calorimeter has been studied.

When the checks are finished, seven ring-pieces from the ring prototype will be re-used for the construction of module 0.

The ring has been modelled to perform finite-element (FE) calculations. Figure 6-29 shows the deformation of a ring under a weight of 12 tons and imposing no displacement in the horizontal plane of the ring where it rests on the cryostat rail. The maximal deformation for a continuous ring is 3.0 mm at the top and bottom. This maximal deformation becomes 3.5 mm when taking into account the weakening effect due to the junctions. At cold, apart for the normal thermal contraction of the ring, the differential contraction between the stainless steel of the ring and the aluminium of the rails imposes a deformation of 2 mm in the horizontal plane giving finally a maximal deformation of 5.0 mm at the bottom of the ring. Taking into account the higher Young modulus of the stainless steel at cold and the reduced weight of the calorimeter due to the density of the liquid argon (d = 1.4), the maximal deformation will be about 4.0 mm. Assuming that the accuracy of these calculations is 10%, this maximal deformation induces an uncertainty of 0.4 mm on the calorimeter radius, which will have to be recovered from the data. The stress in
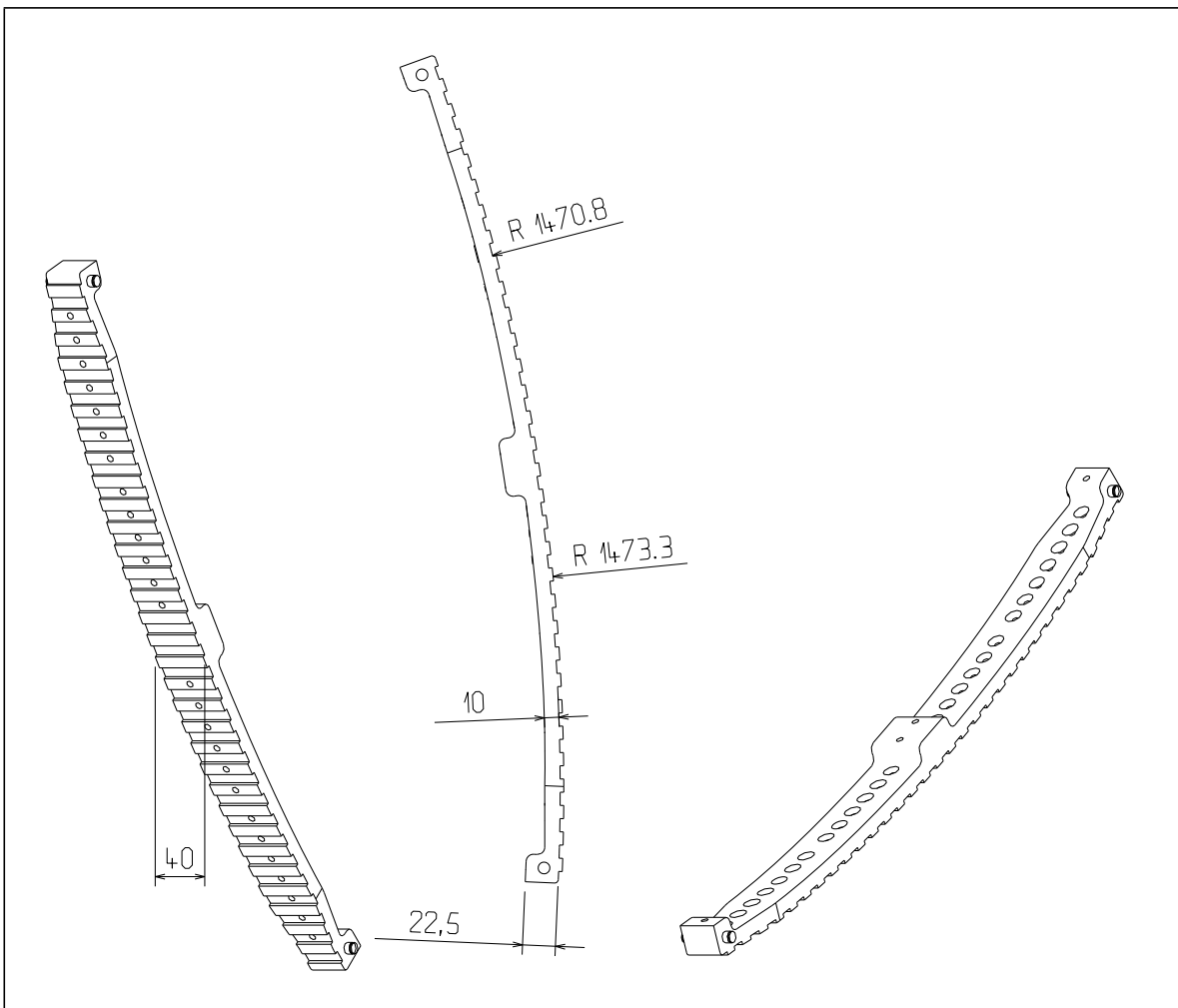
Figure 6-29 External ring deformation under weight. Continuous line: deformation assuming no horizontal displacement at the support level; the dashed line corresponds to a 2 mm displacement; the thick line shows the ring undeformed. Deformations are magnified by a factor of 100.

the screws at the level of the junctions have been evaluated with a FE model to be well below the elastic limit for the chosen screws.

6.6.2 Internal rings

The internal rings fulfil four functions. During the assembly phase they insure the mechanical rigidity of the module at the internal radius level. At cold they provide a small tension of the absorbers in such a way that all absorbers are in extension, even those which are at the bottom of the calorimeter. At cold, also, they index the absorbers so that the gaps appearing at cold are equally shared between absorber G10 bars. Finally the presampler is fixed on these rings.

The 8 rings are placed close to every $\eta = 0.2$ to ease the cabling of the electronics. They are made also of 16 ring-pieces, $22.5°$ in ϕ (Figure 6-30). These ring-pieces are 40 mm wide and 10 mm thick except at the level of the bumps where the thickness is 20 mm. The ring close to $\eta = 0$ has a width of 20 mm only. The bumps at the inner face allow the fixing of two sectors of the presampler. The space between the presampler and the rings, about 10 mm in radius except at the level of the bumps, allows the passage of the electronic cables connecting the motherboards to the patch panel fixed at the end of a module. The gear-wheel shape of the ring at its outer face allows the indexing of the absorbers. Every second absorber is screwed on this internal ring. The ring-pieces are made of composite material. Two stainless-steel axes are inserted at both ends to allow the junction of two ring-pieces with closing links.

Figure 6-30 Internal ring

As mentioned in Section 6.2.1.1, several considerations have led to the design of the internal rings and the internal absorber G10 bars. We first studied the possibility of not opening gaps at cold between these G10 bars. The contraction at cold of the stainless-steel ring is 5.5 mm and the contraction of a free absorber is 5.0 mm, hence the internal radius will shrink by 0.5 mm if no effort is applied on the absorbers. This would imply a thermal contraction of $3.4\ 10^{-4}$ in the $R\phi$ direction for the internal G10 bars. Prototype G10 bars have been made, trying to ensure the correct longitudinal contraction and the lowest possible transverse contraction. The transverse contraction achieved was $10\ 10^{-4}$, still too high to reach the closure condition. We then considered having the absorbers in extension to fulfil the closure condition: the internal radius must shrink by 1.5 mm instead of 0.5 mm. To get this additional 1.0 mm reduction, the internal rings have to pull the absorbers. Considering a 60 cm calorimeter slice, which corresponds to the ring supporting the largest effort, one is led to a force of about 40 kg per absorber and a force of about 6 tons on the ring. In practice it was found impossible to design a ring holding this force with a reasonable safety margin. A further disadvantage would have been important forces on the screws which link the absorbers to the rings, with the risk of G10 delamination.

We have chosen a solution where a small gap appears at cold between the internal G10 bars. With normal G10 bars one gets a gap of 0.024 mm. The gear-wheel shape of the inner ring at outer radius ensures a regular sharing of these gaps. To avoid the absorbers at the bottom of the calorimeter being in compression, the inner ring has to exert a force of about 17 kg on each ab-

sorber corresponding to a total shrinking of the internal calorimeter radius of 0.9 mm and a force inside the inner ring of 2.6 tons. This can be achieved with inner rings made of unidirectional G10. The exact composition will be fixed after measurements of the final absorber.

The tolerance on the teeth of the ring-gear has to allow the mounting of the module and to be as small as possible since this tolerance contributes directly to the gap variation. The target value is 15 microns.

Several modellings of a calorimeter slice have been done to confirm the above considerations and to understand in more detail the deformations and the stresses of the calorimeter due to the weight and the thermal contractions.

6.7 Ancillary equipment

6.7.1 Cooling circuits

As mentioned in Chapter 4, four cooling circuits are used in the barrel to control the temperature of the liquid, at the top and bottom of each half-barrel. Each cooling loop is a pipe of 20 mm diameter, with two runs along the half-barrel per module. The pipe is integrated with the module and runs through holes in the external rings. The connection of the pipe to the outside is made at the end of the cryostat.

6.7.2 Sensors

6.7.2.1 Position and strain sensors

Four position sensors (LVDT type) are located in the middle plane at $\phi = 0$, $\pi/2$, π, $3\pi/2$, at the outer radius of the barrel, to monitor the distance between the two half-barrels, during the insertion in the cryostat, and during cool-down (Figure 6-31).

Four strain sensors are installed on the external rings number 4 and 7 on each half-barrel, to monitor their deformation under loading during the installation and cool-down (Figure 6-32).

6.7.2.2 Temperature gauges

Six temperature gauges (Pt 100) equip each module (Figure 6-33), three at different z on the front face, three on the back face (hence 192 gauges for the whole barrel). They are connected by four wires to the temperature monitoring system.

6.7.2.3 Purity monitors

Nine purity monitors (see Chapter 12), are installed at the outer radius of the barrel calorimeter, three in the middle plane and three at each end (Figure 6-34).
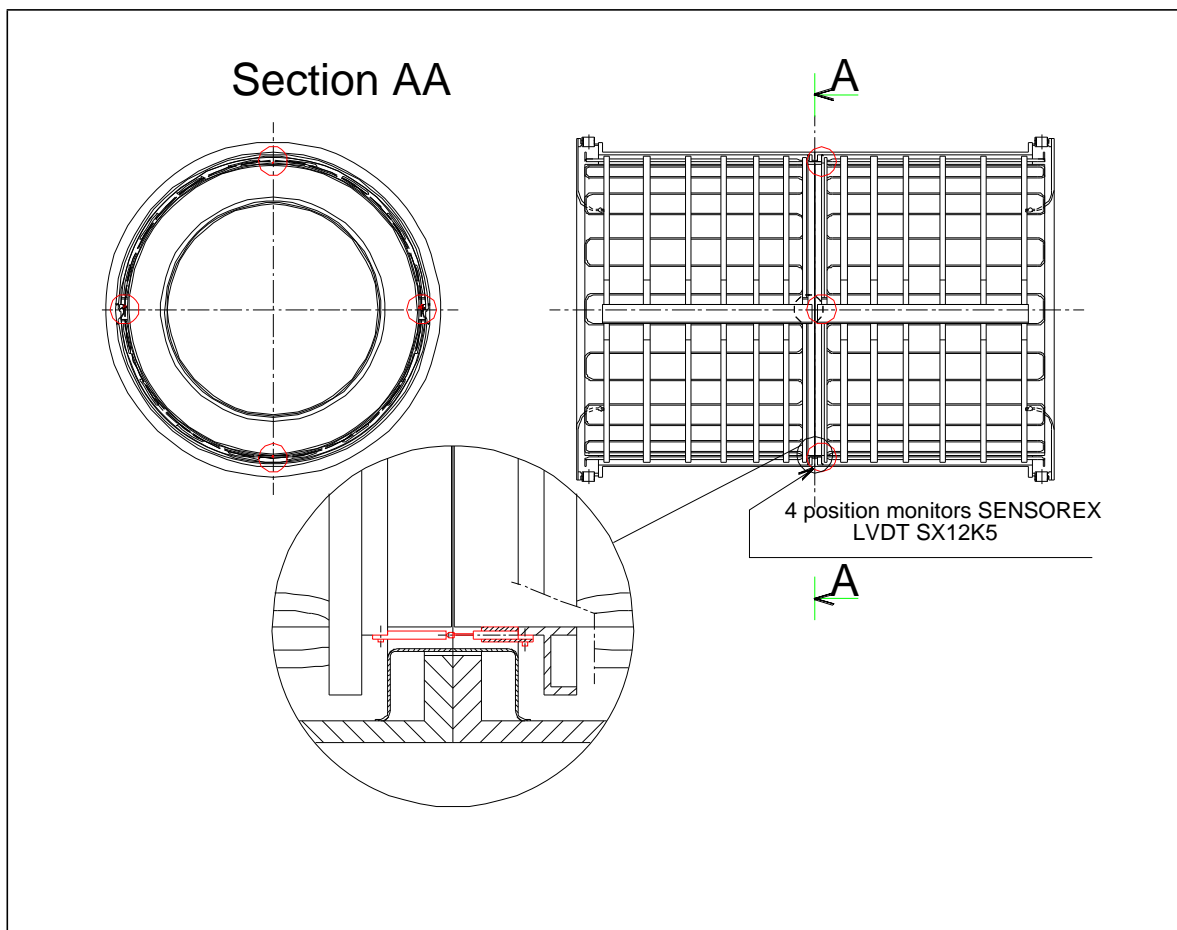
Figure 6-31 Position-monitor locations.
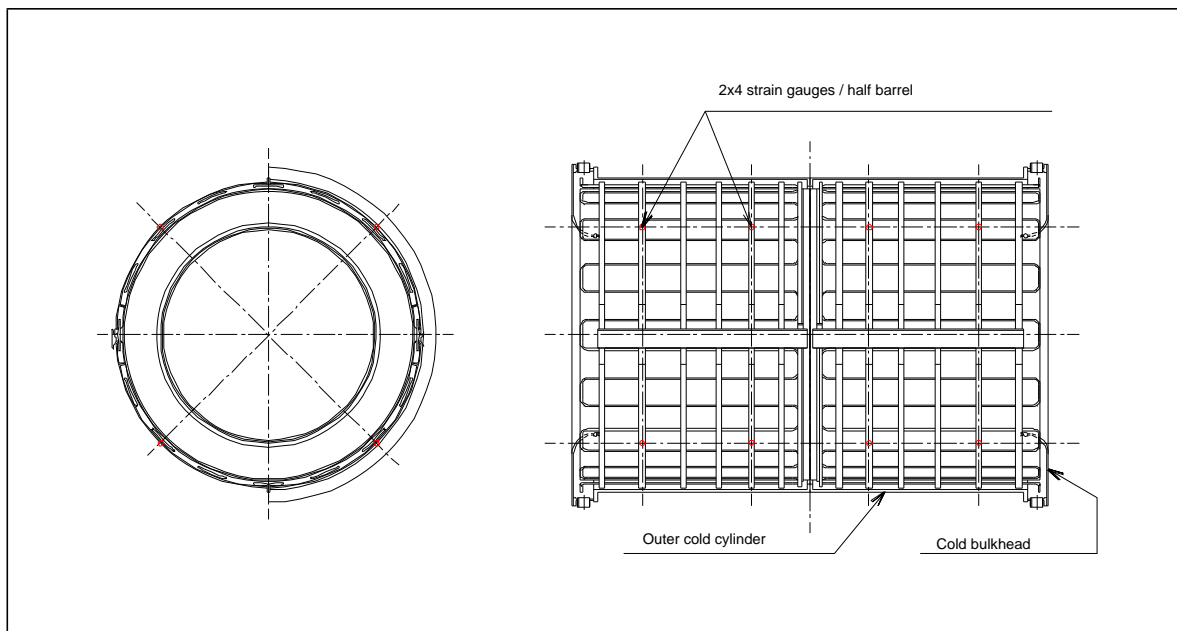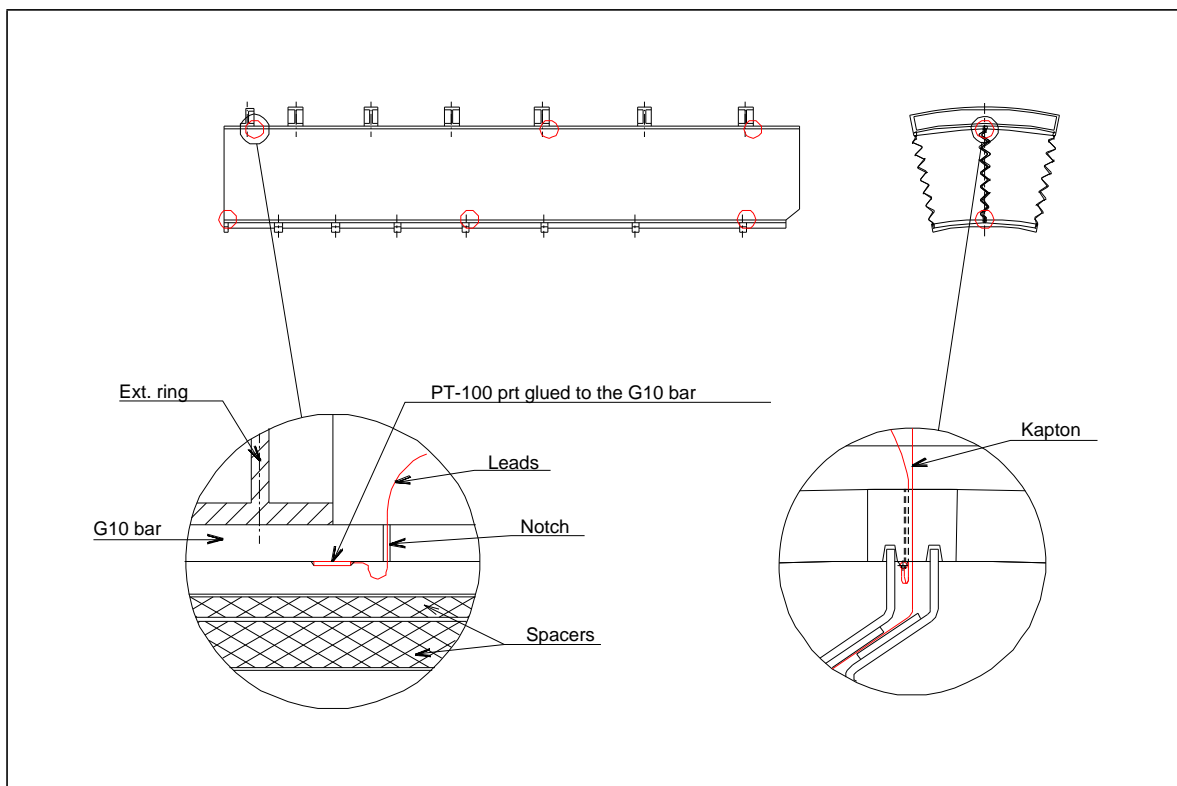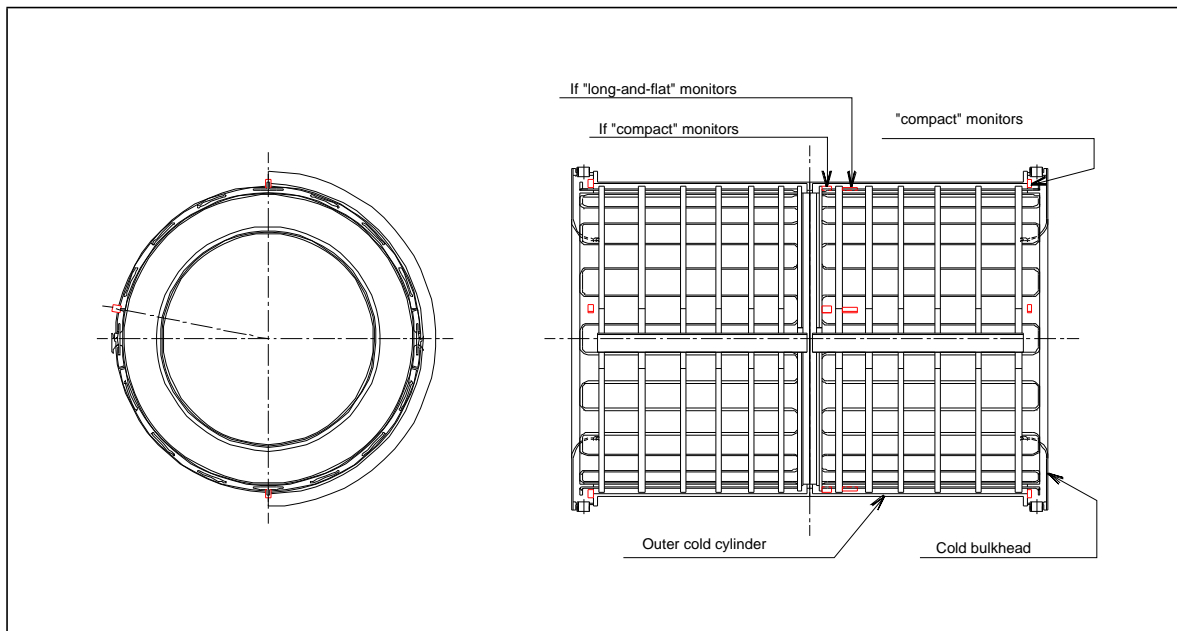
Figure 6-32 Strain-gauge locations.

Figure 6-33 Temperature-gauge locations.

Figure 6-34 Purity-monitor locations.

6.8 Assembly scenario and benches

6.8.1 Overview (Figure 6-35)

Starting from the elements described above, the two half-barrels must be assembled with the constraints of excellent geometry, electrical connectivity, high-voltage rigidity.

Each half-barrel is made of 16 modules which are independent to a large extent; the scheme adopted for one half-barrel is the following:

16 "module assembly backbones" are manufactured: these are very rigid structures in ordinary steel, which will be used to assemble and support modules throughout the process.

In parallel, the external rings are fabricated, leaving some extra material on the inner and outer faces. Each ring is made of 16 segments, with a very strong binding between them.

The backbones are mounted together vertically and assembled in a circle [Figure 6-35 a], and pads on the inner face are machined on a vertical lathe. The external rings are also assembled and their outer face is machined to the same diameter [b]. The rings are then mounted in the backbones circle, one ring segment facing one backbone.

The inner face of the rings is then machined to the diameter wanted for the outer G10 bars barrel (to ±0.5 mm) [c].

At this stage, reference measurements and marks are made: the angular position of ring segments is done to ±0.5 mm, and marks are machined to indicate the correct angular position every 22.5°, with an accuracy of ±0.1 mm. This mark will be used during the module assembly to position the absorber with respect to the ring segments.

Then the circle is disassembled, keeping the seven ring segments of a module fixed to the corresponding backbone. The backbone with the seven rings segments will then be the basis for assembling the module, using the angular mark as a reference.

The modules are assembled on the backbone and rings [d], as detailed in Section 6.8.2 below. The module is then equipped with its printed-circuit boards and cables up to the end patch-panel. This assembly takes place in a clean-room [e].

The full module is tested, first at ambient temperature, then in liquid argon (Section 6.9) [h]. All modules will be tested cold at laboratory test stations (except those which are brought to the beam-test). The tests check all electrical continuities and high-voltage performance.

The module leaves its backbone once during the assembly and test process [f,g]: it is transferred momentarily to a frame for cabling its back face and cold testing. This was made necessary by accessibility requirements during cabling, and to minimisze the size of the test cryostats (home-test and beam-test). After this the module is put back onto its backbone; careful checks of the geometry are done before and after this operation.

Once 16 modules are ready and tested, they are shipped to CERN for the final assembly (Section 6.10). In this phase, they are stood up vertically with their backbones [i], and the circle is reconstituted [j,k]. The ring segments are joined into complete rings and the backbones are joined together; hence the complete half-barrel is obtained, still with a very strong external structure which allows handling in good conditions before the insertion into the cryostat.
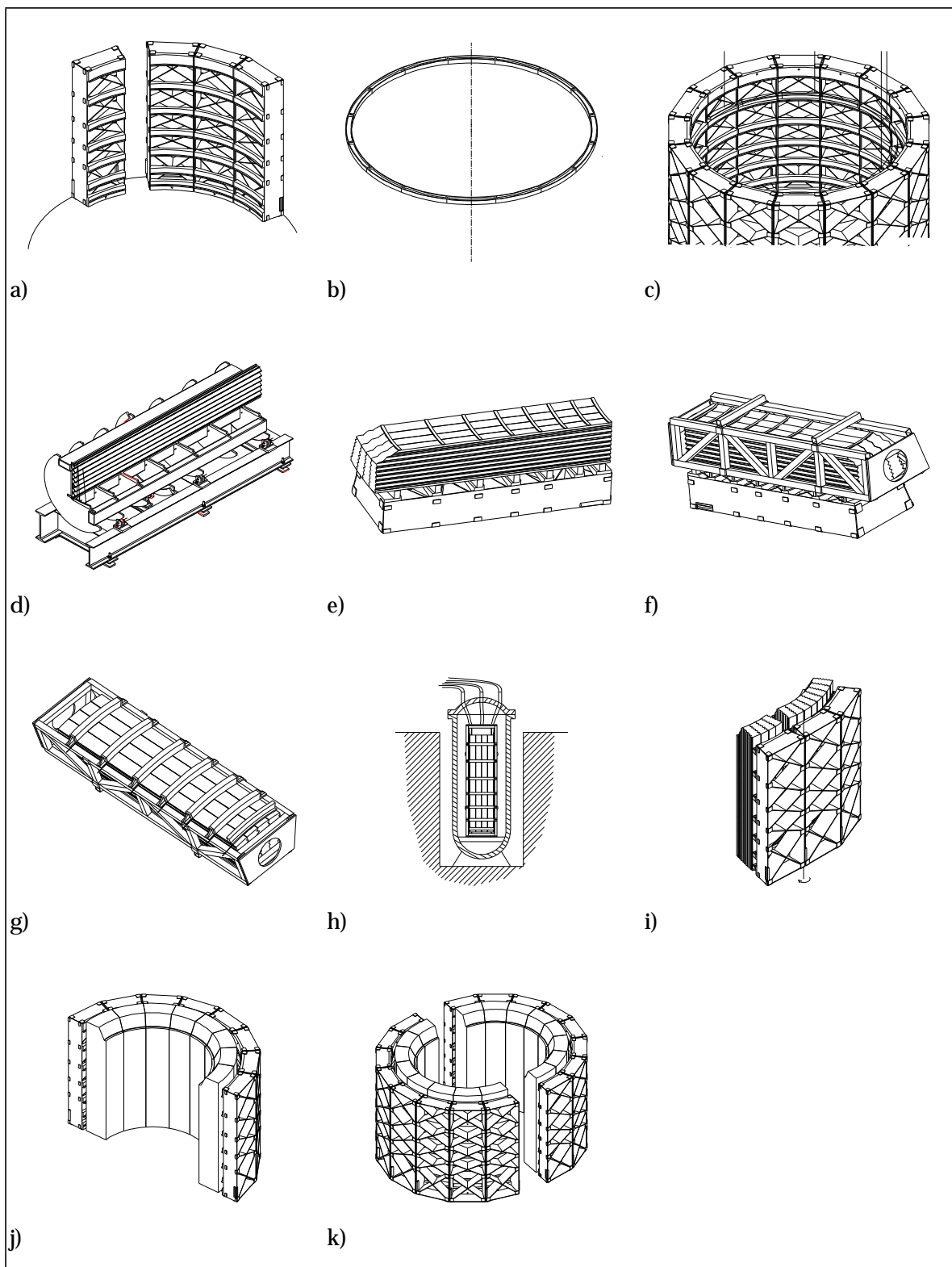
Figure 6-35 Scenario of the mechanical assembly (see text).

6.8.2 Module assembly and electrical tests
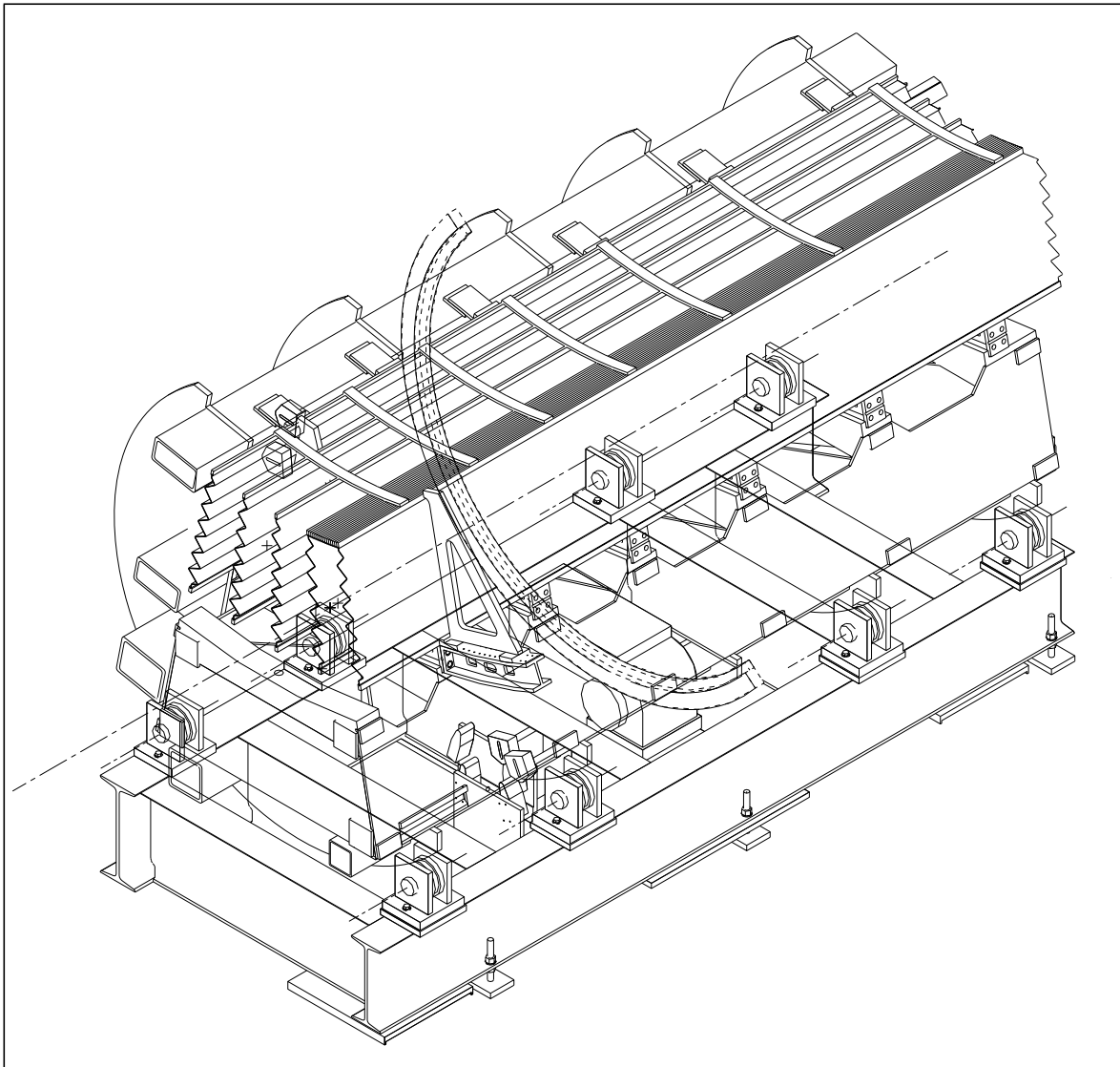
Figure 6-36 Module assembly jig

A module is a set of 64 absorbers and 64 electrodes. To protect and test the 64th electrode a 65th absorber is installed and will be removed only when two modules are assembled together. A module weighs about 3.3 tons.

To constitute the module assembly jig (Figure 6-36), the module assembly backbone where the ring-pieces have been installed at their final position is put on a complementary bench which allows a rotation of 90° of the module in construction. Other additional parts materialize the φ reference plan against which the first absorber has to be put.

The assembly sequence is as follows. The first absorber is installed against this reference plan with removable dowel pins and screwed on the outer ring-pieces. Then in a nearly horizontal or in horizontal position one installs successively one spacer, two half-electrodes, one spacer, and a new absorber. Two dowel pins fixed in the G10 bars are used to position in r and z each half-electrode. Some other dowel pins are used to pre-position the new absorber in r and z . To check the position of the new absorber, the module is set vertical to avoid distortions due to the

sagitta of the absorber in the horizontal position. The absorber is pressed against the preceding one with electrical jacks acting on the outer and inner G10 bars. The complete set of dowel pins is installed. The jacks are removed and the installation of the next set (spacer, half-electrodes, spacer absorber) can be done. A careful check of the geometry is done every 4 (8) absorbers: a temporary inner gear wheel ring-piece is used to fix the right position of the inner G10 bars. Shims may be installed between G10 bars if necessary. Then the external G10 bars are screwed on the external ring-pieces and the jacks are removed, the temporary inner ring-pieces maintaining the absorbers at the inner radius. The sequence is repeated for the next set of 4 (8) absorbers. The tolerances on the transversal dimensions (Rϕ) of the G10 bars being +0,-0.005 mm, the use of shims should allow a tolerance in the Rϕ position of +0,-0.05 mm for any absorber at the inner and outer radius. The tolerance in z of the G10 bars is 0.1 mm. The temporary inner ring-pieces are replaced by the final ones indexing the 64 absorbers at the end of the module assembly. A 65th absorber is installed after the 64th electrode.

To avoid any problem of dust, the assembly of a module will be done in a clean room (class 100 000). A last cleaning of the absorbers, the electrodes, and the spacers will be done before assembly.

During this assembly only high-voltage (HV) tests are performed, as the electrodes have already been tested. After installing one electrode, it is equipped with temporary connectors and cables to ground all signal output pins and to connect the HV input pins to the high voltage. These temporary connectors and cables will be removed only at the final cabling stage. With such a scheme one can test individually each electrode or any group (4,8,16,64) of electrodes, in the vertical position. These tests are interleaved with the mechanic assembly of the module.

The front face of the module is then fully cabled: summation and motherboards and cables between motherboards and the module patch panels are installed. These module patch panels are fixed at the end of module using holes in the inner and outer G10 bar ends. The boards equip exactly 64 electrodes. Then a temporary frame is bolted onto the outer ring-pieces using the holes in the ring-piece end-plates, and the module assembly backbone is removed without losing the position of the ring-pieces relative to each other. The inner ring-pieces are also fixed on this temporary frame. This removal greatly eases the cabling of the outer face of the module by giving a nearly free access to it. The module is rotated by 180° and the outer face of the module is cabled: installation of summation boards and motherboards, signal and HV cables from motherboards to module patch panel. The module patch panel is fixed on the ring-piece at largest z. The temporary frame is also used to carry the module from one place to another and to put it in the home or beam-test cryostats. Therefore this temporary frame will be made of stainless steel. Furthermore, to avoid problems due to even small thermal contraction differences between the temporary stand and the absorbers along the z direction, six out of seven outer and inner ring-pieces can move slightly in z with respect to this frame. The cabling will be done in a clean area; the cleanliness is less demanding than for the module assembly as all absorbers and electrodes are packed in a module.

After the test at cold (Section 6.9), the module assembly backbone is reinstalled and the temporary frame is removed and can be reused for a new module. This operation has to be done carefully as the seven ring-pieces have to re-find their initial position to allow the mounting of the half-calorimeter later on. The module assembly backbone is used to store the modules for up to three years. The modules will be stored in a controlled atmosphere.

The mechanical assembly of a module will last four to five weeks and the cabling of both calorimeter faces two weeks. With the cold test, the full sequence to produce a module will last 2.5 months. Therefore with three assembly sites and two cabling sites, the whole production will last three years.

6.9 Module qualification

6.9.1 Warm and cold tests

Only a few modules (six) will be fully scanned with an electron beam. So a complete test procedure has to be developed to qualify all calorimeter modules. As the electromagnetic calorimeter has only passive electronic components in the cold, the module is equivalent to a set of capacitors. The qualification procedure has to check the following items: continuity of the electric circuit and cabling errors; high-voltage holding; measurement of the cell capacity. Tests are planned during the assembly of sub-modules and modules and after the cabling of the whole module.

6.9.1.1 Tests during sub-module and module assembly

These tests are done in the clean room. As the different components of a module (electrodes, summation cards, motherboards and cables) are tested during the production, the aim is to detect any damage to the electrodes done during the sub-module assembly or any high-voltage problem linked to a cleanliness problem or a wrong position of the read-out circuit. After the assembly of a module, with a dedicated summation card and a temporary cabling, the resistor chain on the electrodes is checked to verify that high voltage is distributed everywhere. After this test, high voltage is raised and the current of the 64 cells is monitored. Discharge detection is also envisaged.

6.9.1.2 Qualification tests at ambient temperature

After full cabling of the module, the preceding tests are repeated using the final cabling. The capacity of each individual cell and the crosstalk with the neighbouring cells are measured. The aim is a relative measurement of the capacity of the order of 1%. The measurement of the cells capacity is a test of the quality of the mechanical assembly, of the whole cabling and of the calibration system.

6.9.1.3 Qualification tests in the cold

The same series of tests is done in liquid argon to eliminate problems possibly induced by the thermal contraction. The tests have to be done in liquid argon for the following two reasons: (a) liquid nitrogen has an electric rigidity greater than liquid argon so discharges appear in liquid nitrogen for a higher voltage than in liquid argon, and (b) the purity of liquid argon is monitored with alpha and beta sources so pollution coming from the module can be detected. A test cryostat will be installed at each assembly site, LAPP-Annecy and DAPNIA-Saclay. After tests in the cold, the module is put back on the backbone and packed, ready for final assembly of the barrel.

6.9.1.4 Description of the electronic chain

Each channel of the sub-module or of the module is connected to a multiplexer and only one channel at a time is analysed on a digital scope. Three crates are needed to read half the module through the multiplexer.

Electrical continuity

This is a fast 'yes or no' test. A low-frequency signal (50 Hz, 80 V) is generated and distributed with a temporary cabling or the high-voltage lines. The output signal must be above a given threshold if all the resistors which distribute the high voltage on the read-out electrodes are good. This threshold is sampling position dependent.

High-voltage test

The current of 64 cells is monitored to detect any high-voltage leakage. A discharge detection is also envisaged

Test-pulse measurement

Step pulses are sent on the calibration lines. The fit of the tested cell response gives the capacity of the cell linked to the rise time, and the value of the calibration resistance linked to the maximum amplitude of the signal. The neighbouring cells' response give a measurement of the crosstalk. This test is also a powerful way to find cabling errors. A full module can be tested in a few hours.

Through a GPIB bus, a PC commands the multiplexer and the pulse generator modules, reads the digital scope, controls the high voltage, and treats the data.

6.9.2 Home cold stations

6.9.2.1 Description of the 'home cryostat' (Figure 6-37)

A cryostat of affordable price is needed to test 16 modules in liquid argon on each assembly site. The best solution is a vertical vacuum insulated cryostat with a foam insulated lid in the argon gas. A nitrogen heat exchanger is used to cool down the module and to regulate the temperature in the cryostat. The module in its handling frame is suspended under the lid. All the services enter the cryostat through the lid: two feedthroughs for signal cables, one hole for high-voltage, test-pulse and slow-control cables, argon and nitrogen pipes and security valve. For the feedthroughs we may use two flanges as developed for the ATLAS cryostat.

Owing to the limited height under the crane, a special tooling is needed at LAPP to introduce the module in the cryostat. Two tanks are needed for the storage of the cryogenic fluids. A certified-purity argon is envisaged to permit several cycles with the same argon charge.
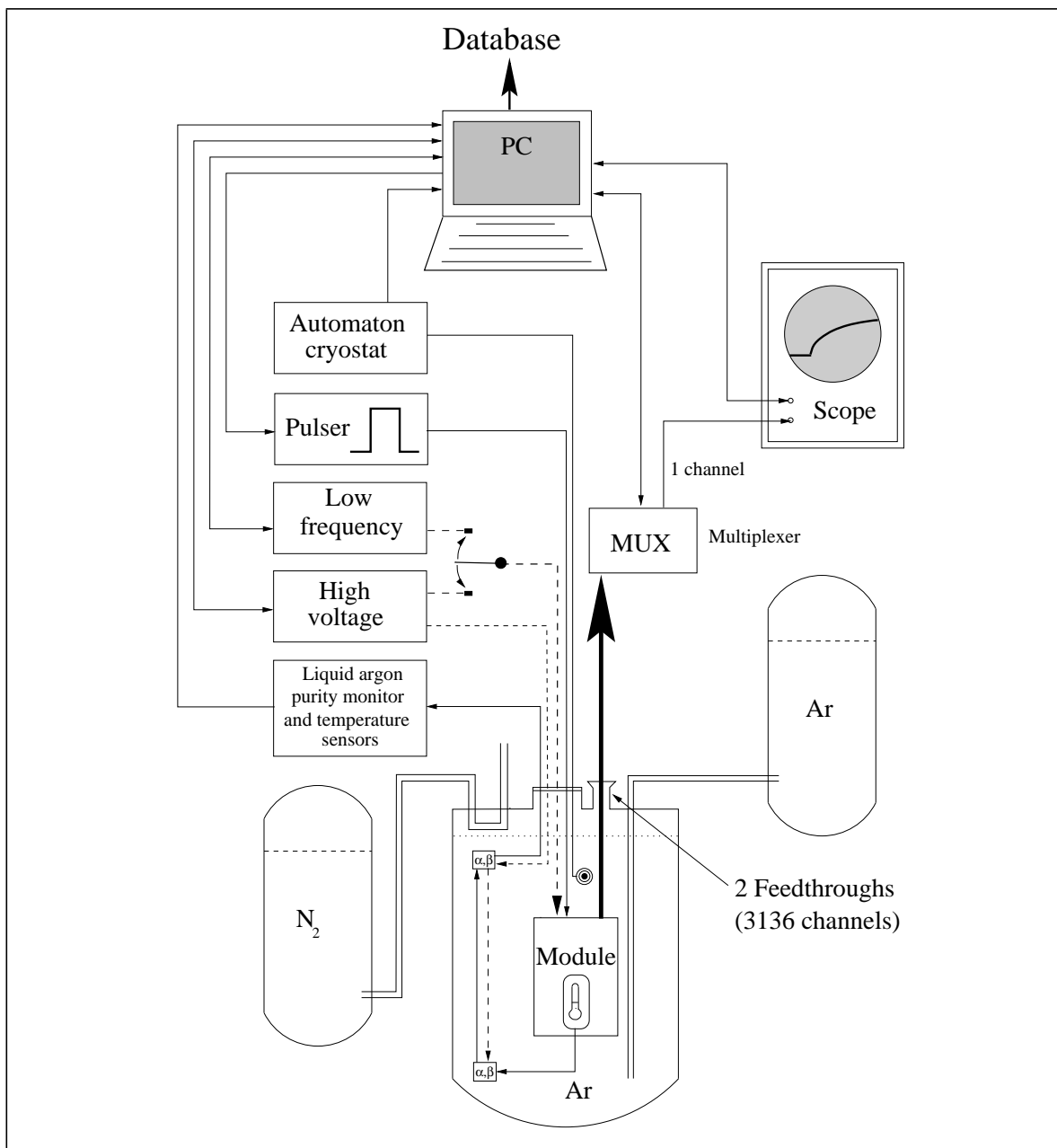
6.9.2.2 Description of cooling cycle

Cleaning

The cryostat is filled with helium gas and emptied two or three times, making a primary vacuum to eliminate air and water vapour. At the end of the last cycle a good primary vacuum is made to eliminate outgassing from the material of the module.

Cooling

The cryostat is filled with helium gas and cooled at a speed of 2 K per hour down to 120 K to minimize mechanical constraints in the absorbers introduced by the thermal gradient. At 120 K the helium is pumped and some liquid argon is introduced to finish the cooling between 120 K and liquid argon temperature.

Figure 6-37 Home test cryostat principle.

Tests   The cryostat is filled with liquid argon and the module is maintained in
                 liquid argon for 5 to 7 days during which the argon purity is monitored
                 and the above tests are regularly repeated.

Warming up   The cryostat is emptied and the temperature is raised at a speed of 2 K per
                 hour using warm nitrogen gas. To avoid water condensation in the module
                 the temperature in the cryostat is raised above the dew point before open-
                 ing the cryostat.

6.10 Barrel assembly and installation

6.10.1 Half-barrel assembly (Figure 6-35 j,k)

The half-barrel is assembled from modules in the vertical position, in a clean environment. A first module is set vertical and put on the assembly area where it is secured in place. The 65th (dummy) absorber is removed, and the spacer sheet is put in place. The second module, also vertical, is brought close by the crane with adjustable slings. The contact with the first module is done at the outer corner of the module backbones, which acts as a joint. Rotating the module all the fixtures are brought in contact, the bolts of the rings are put in place and tightened, starting by the central one (fourth in z), then the backbones are bolted together. This is repeated with other modules until 8 are assembled, making a semi-half-barrel. Capacitance measurements are performed to check the gap size between modules. The other semi-half-barrel is made the same way.

The cylinder of a half-barrel is made by bringing together the two semi-half-barrels. One is fixed to the ground, the other can slide on low-friction pads, and is moved by jacks. The rings and backbones are bolted. The internal ring segments are joined. The presampler modules are inserted by sliding them from the top, with a visual control of their clearance with respect to the calorimeter cables.

6.10.2 Half-barrel insertion into the cryostat (Figure 6-38 a to h).

The cylinder made with the backbones secured together makes a very rigid structure which is used to handle the half-barrel with small deformations. The backbones are calculated such that the maximum deformation of the whole structure in any position be less than 1 mm.
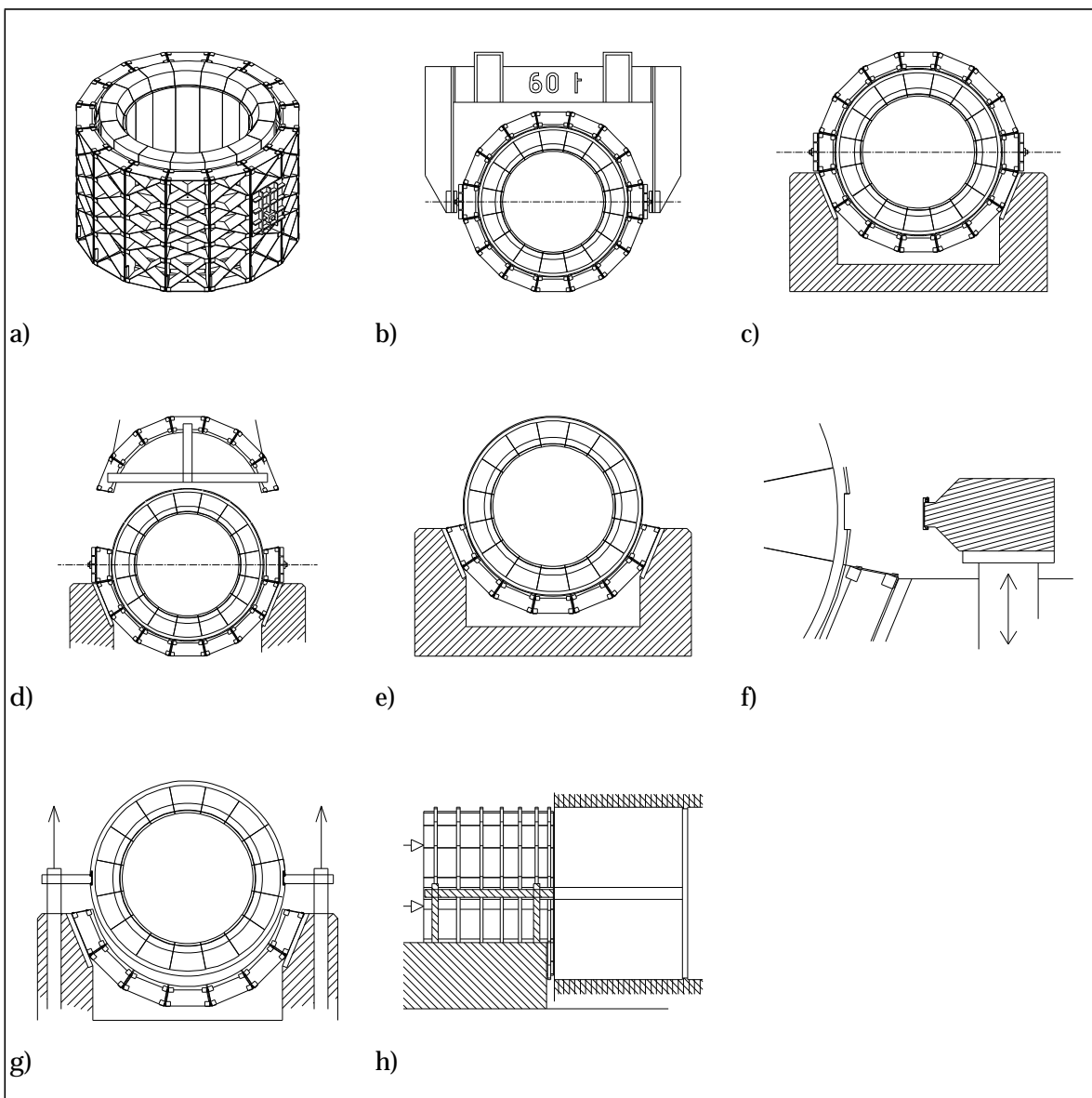
Two pivot nuts are mounted on the backbone structure [Figure 6-38 a]. The half-barrel is lifted by a crane (80 tons or 2×40 tons) [b], rotated to horizontal, then laid on the insertion cradle, just in front of the cryostat entrance [c]. At this stage the calorimeter weight is supported by the backbone structure, itself supported by the cradle.

The special ring at $\eta = 0$, which is in only two parts, is put in place.

The next step is to transfer the weight of the calorimeter to its final supports: the two sliding beams located on each side in the horizontal plane. The external rings are supported by these sliding beams, which in turn will be supported by the cryostat rails. In this way, the insertion of the calorimeter does not imply any gliding of the rings on the cryostat rails, which would tend to tear them away from the G10 bars. Instead, the rings do not move with respect to the beam, which slides on the cryostat rails (see Chapter 4).

Starting form the horizontal half-barrel with the full backbone structure, the seven top backbones are unbolted and removed (stiffening beams were put in place beforehand)[c]. The two backbones in the horizontal plane are removed [d]. The seven bottom backbones assembly is able to keep the calorimeter geometry at this stage. The sliding beams are brought onto the cradle and to their location in the ring notches. They are adjusted, and raised by jacks to progressively take the weight of the half-barrel [e]. The bottom backbones are disassembled. At this stage the half-barrel is supported by the sliding beams as in its final position.

The plane of the sliding beams is adjusted with the jacks to match exactly that of the cryostat rails [f,g]. The half-barrel is inserted into the cryostat by pushing on the sliding beams with other jacks [h].

Figure 6-38 Barrel assembly and installation.

The cryostat rails will have to be adjusted beforehand to centre the calorimeter in the clearance circle of the cryostat cold wall (10 mm minimum clearance at every point).

6.10.3 Calculation and preparations.

A calculation note is in preparation on all aspects of the barrel assembly: module handling, half-barrel rotation and insertion. It will also be the document for the safety approval of these operations. The note will be finalized by March 1997. The first results (behaviour of the back-bones) are reported in [6-3].

After the backbones and rings are machined and assembled as described above, tests will be made to qualify the geometry capability of the assembly process. The rings and backbones will be disassembled and set horizontal; dummy loads simulating the modules will be attached to

them; they will then be put vertical and reassembled exactly as foreseen for the final operation. Deformations will be surveyed during the whole test.

6.11 Schedule

A detailed schedule exists, which takes into account the resource availability in the participating institutes. A summary is shown in Figure 6-39 for the barrel calorimeter, and in Figure 6-40 for the barrel presampler; these are shown separately since they are mostly independent for the construction period.

6.12 Cost, resources, and task sharing

Detailed cost estimates are available and will be included in CORE 6.

6.12.1 Barrel EM calorimeter

The cost is summarized in Table 6-5, with the level of information for each large item, indicated by a letter. E stands for estimate based on previous experience or prototype, C stands for industry consultation, O for industry offer or ordered product.

Five laboratories are involved in the mechanics aspect: LAPP-Annecy, CERN, LAL-Orsay, LPN-HE-Paris, DAPNIA-Saclay. The financial and manpower resources of these laboratories cover the needs of this project. All the manpower is in-house or accounted for in the laboratories budget, with the exception of the absorber manufacture where 400 kCHF have been budgeted in CORE for extra manpower.

The responsibility for the design, construction and test of the connection boards for the barrel region rests with Brookhaven National Laboratory.

The responsibility for the procurement of the cold cables rests wih LAPP-Annecy and LAL-Orsay.

The institutes involved in the design and procurement of the read-out electrodes (EM barrel and end-cap) are: CERN, INFN, IN2P3, US[DOE+NSF], CEA-DAPNIA.

6.12.2 Presampler mechanics

The assembly and the tests of the presampler sectors (64 + 6 spares) will be shared by ISN Grenoble and KTH Stockholm. However, to minimize the logistic problems at the beginning only one construction chain (at Grenoble) will be settled for the pre-series phase. The second chain (at Stockholm) will come into service soon after completion of the tests of module 0.
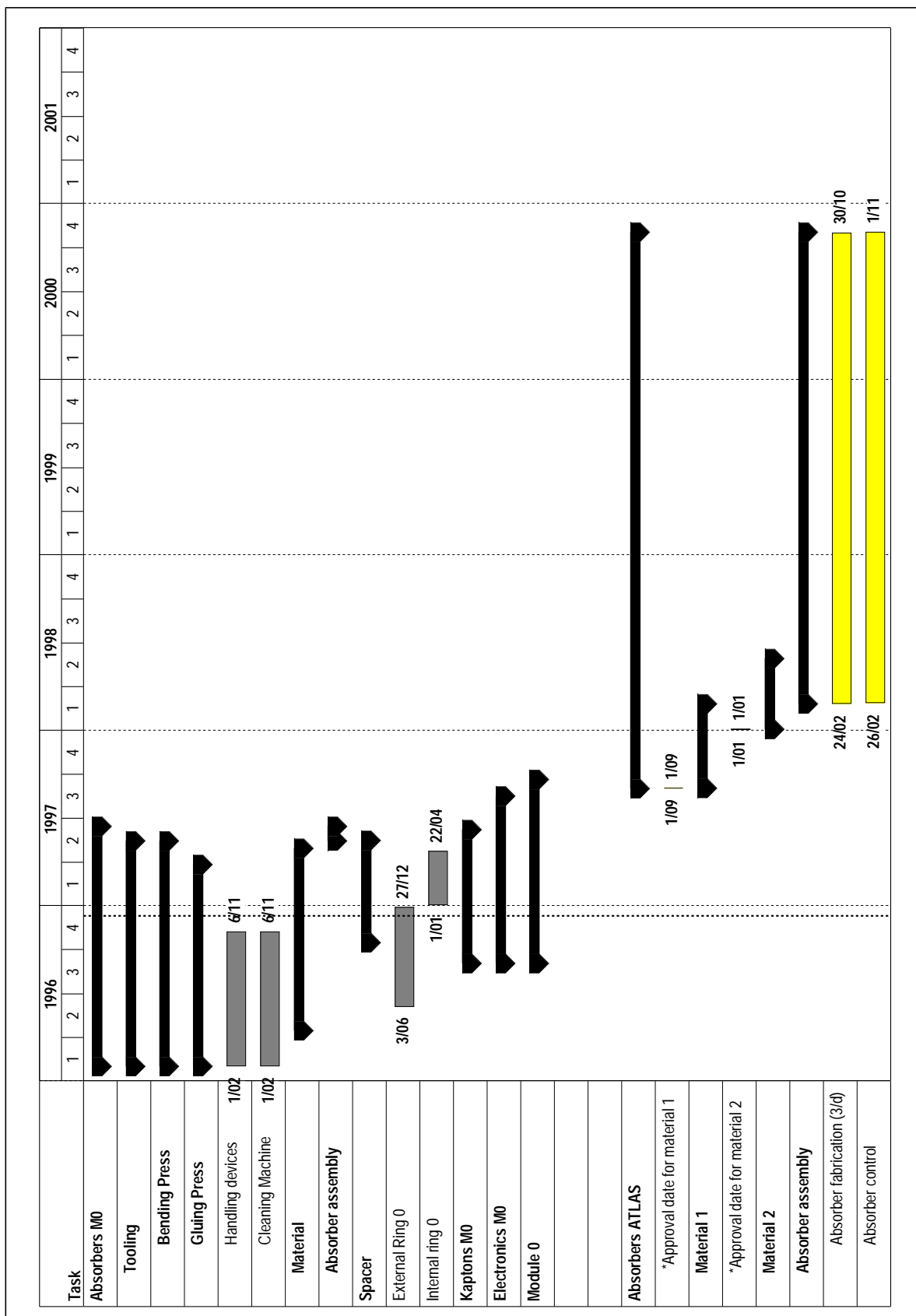
Figure 6-39 Schedule of the EM barrel calorimeter.
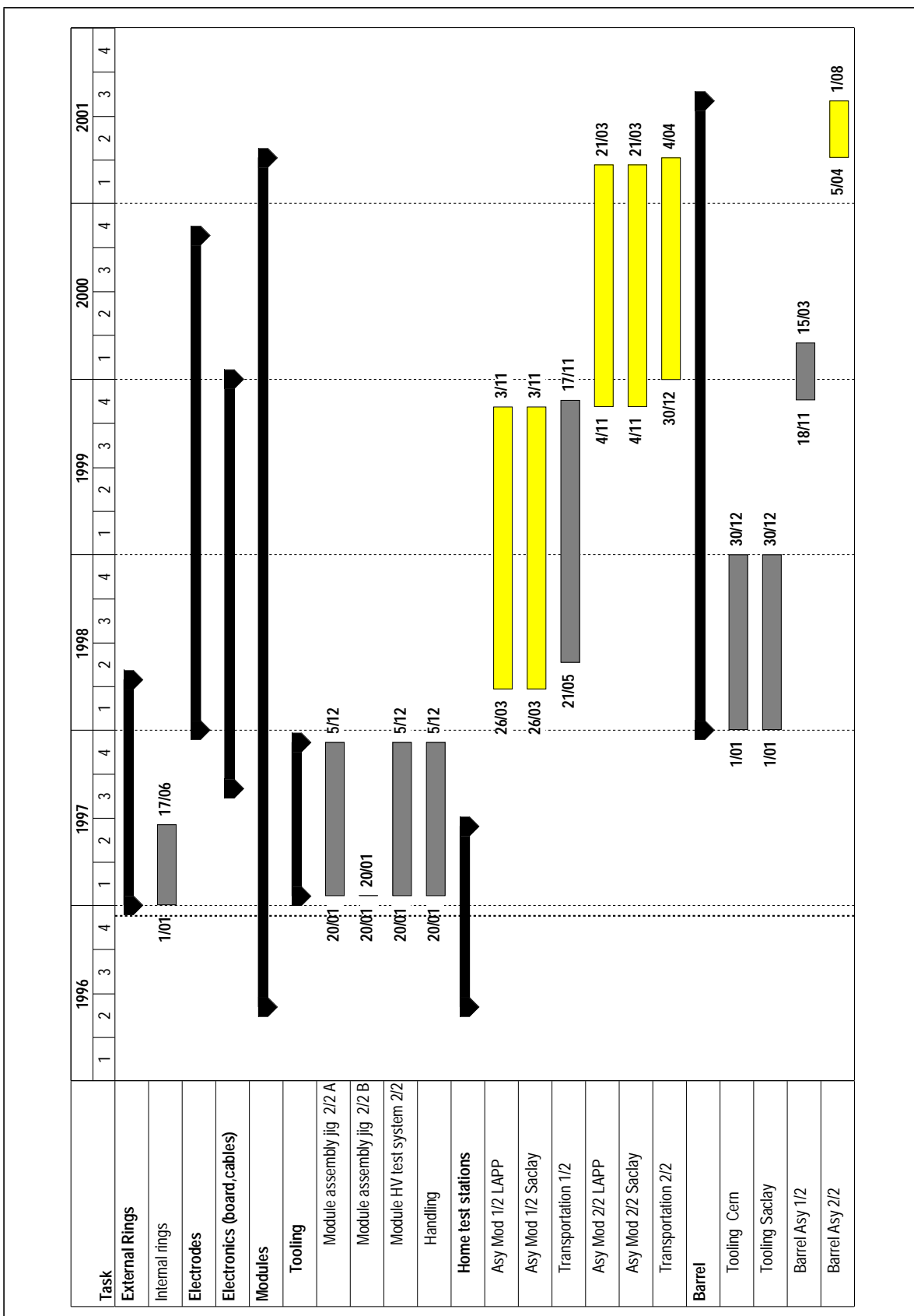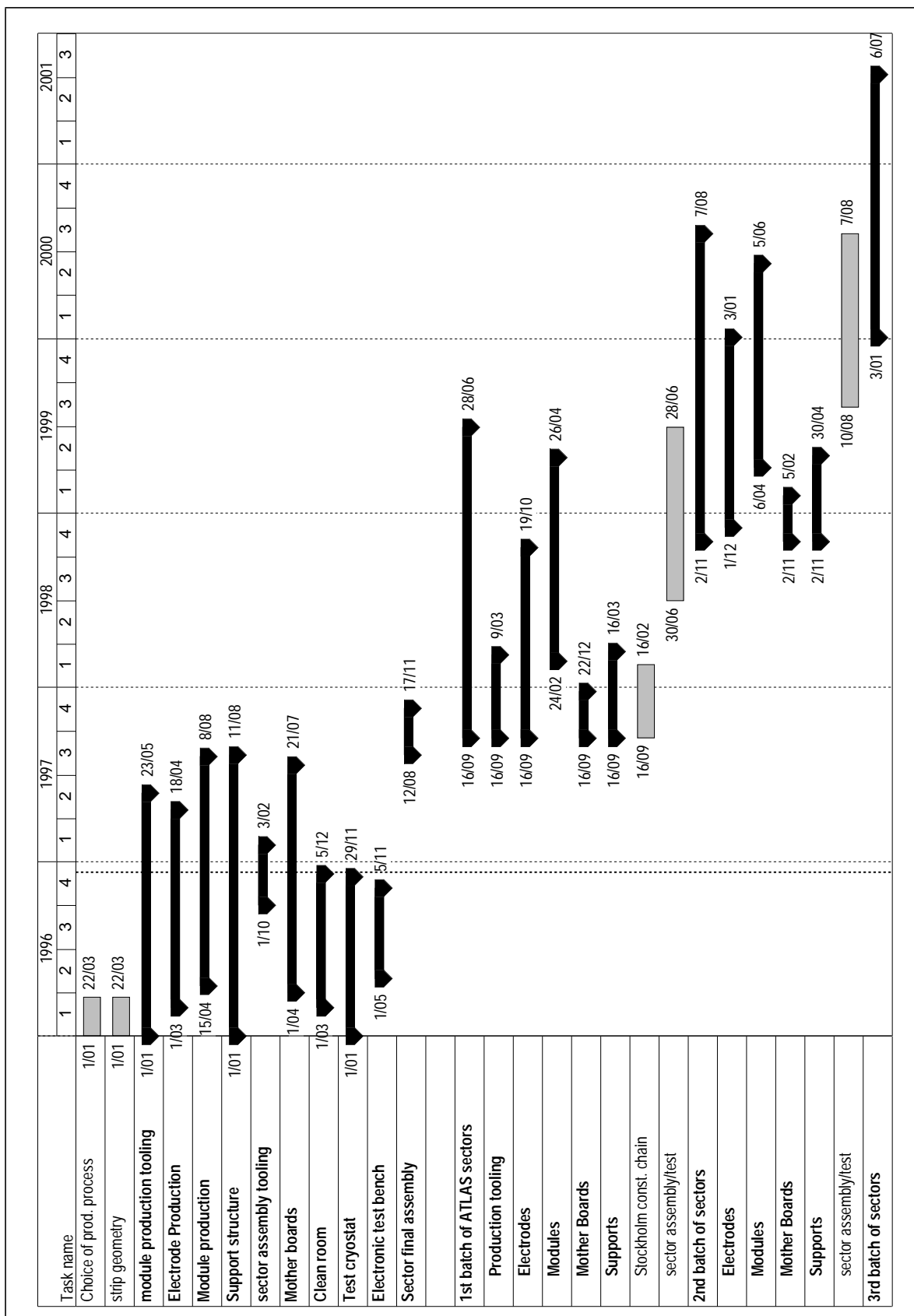
Figure 6-39 Schedule of the EM barrel calorimeter.

Table 6-5 Cost of the barrel E-M calorimeter.

	kCHF	Info
Mechanics		
Absorber sandwich materials	1430	O
Bars	1510	C
Absorber tooling	1719	O
Spacer and spacer tooling	390	C
Rings	1290	C
Backbone structure	450	E
Module assembly tools	950	E/C/O
Module test stations	1000	C
Barrel assembly tools (incl. transport)	280	E
TOTAL Mechanics	*9019*	
Connection boards	1230	E
Cold cables	1400	O
Read-out electrodes		
Tooling	650	E/C
Procurement	6050	O
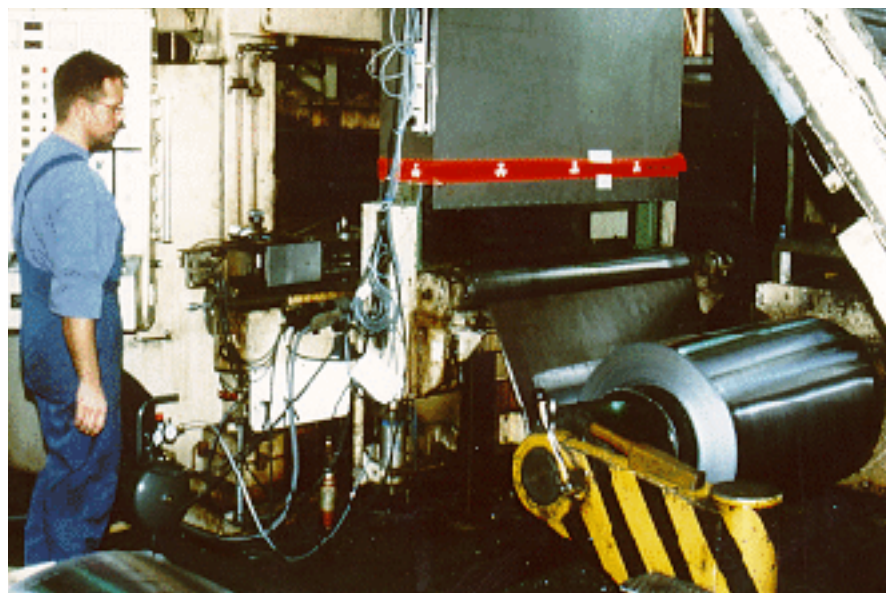
Figure 6-40 Schedule of the barrel presampler.

Table 6-6 Cost of the barrel presampler.

	kCHF	Info
Mechanics		
Integration tools	25	E
LN_2 test cryostats	75	E
Test benches	75	E
Assembly tools	47	E
Storage vessels	50	E
Jigs and shims	280	O
Electrodes	470	C
Module production	412	O
Shells and support bars	125	C
Support rails	32	C
TOTAL *Mechanics*	**1591**	
Connection boards	87	
Cold cables	109	

6.13 References
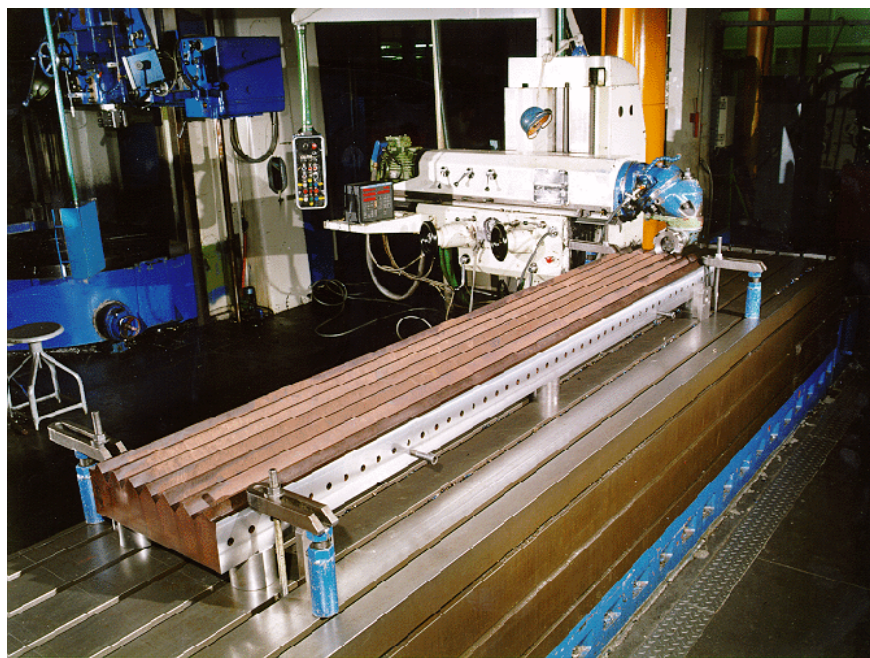
6-1   ATLAS Collaboration, Calorimeter performance Volume, CERN / LHCC 96-40, 1996.

6-2   G. Besnard et al., ATLAS LARG-NO-36 (1996).

6-3   F. Desages, Saclay note No. 6M5710C002 (1996).
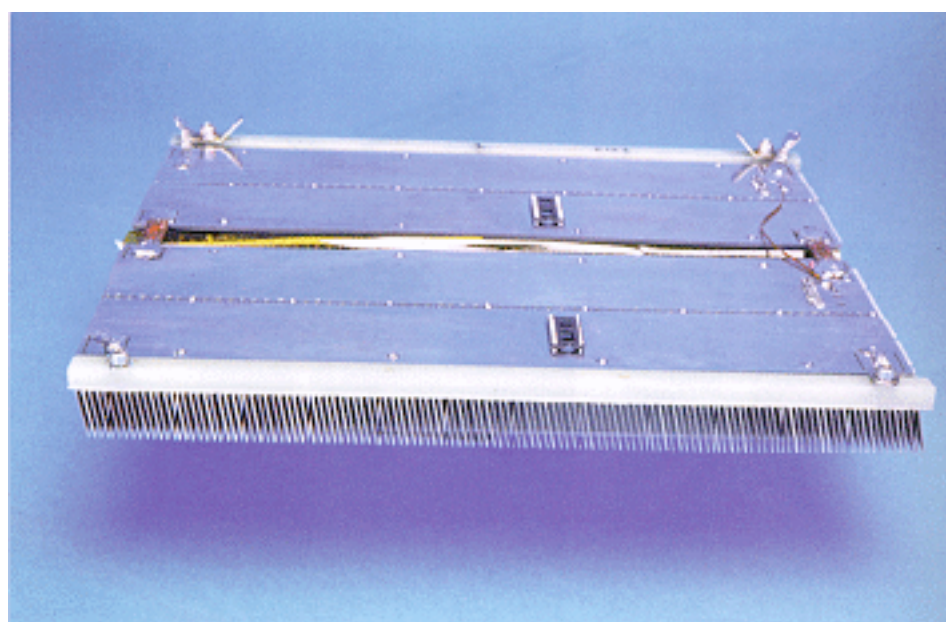
Figure 6-i Rolling of the lead for barrel and end-cap EM module 0, with the X-ray measurement system
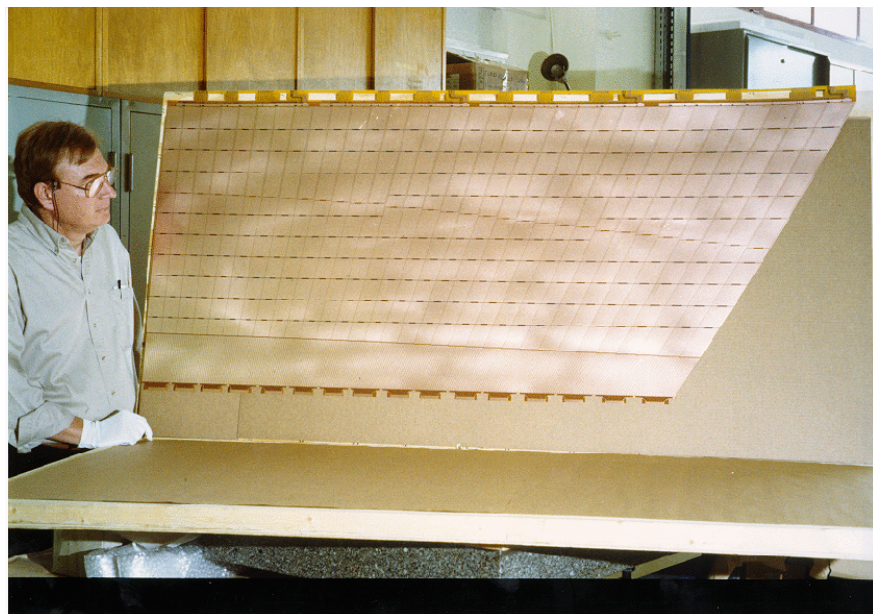
Figure 6-ii Tool for absorber sandwich preparation.
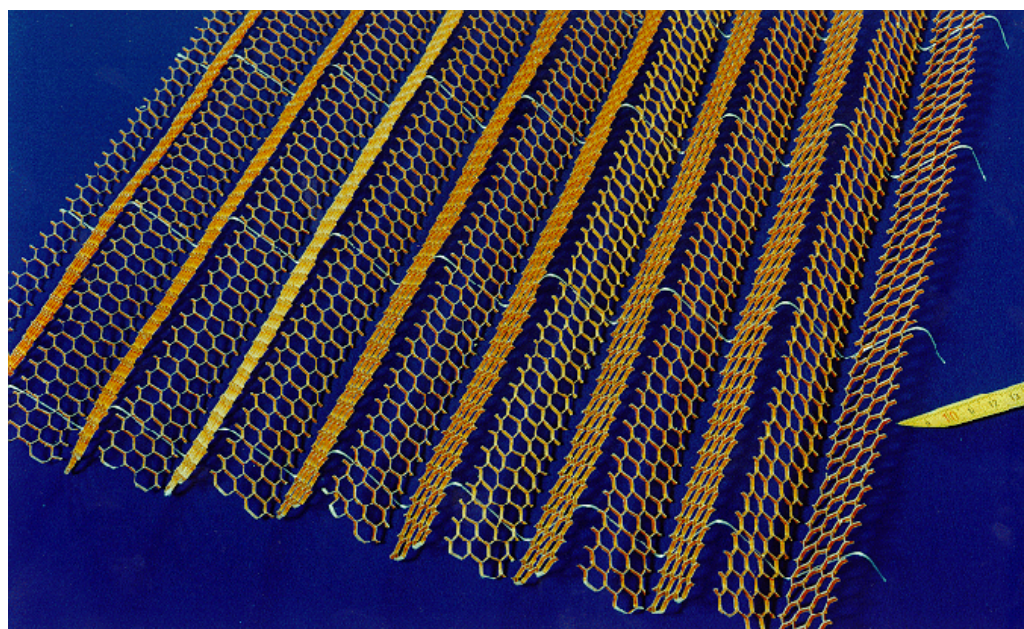
Figure 6-iii Matrix for the gluing press.
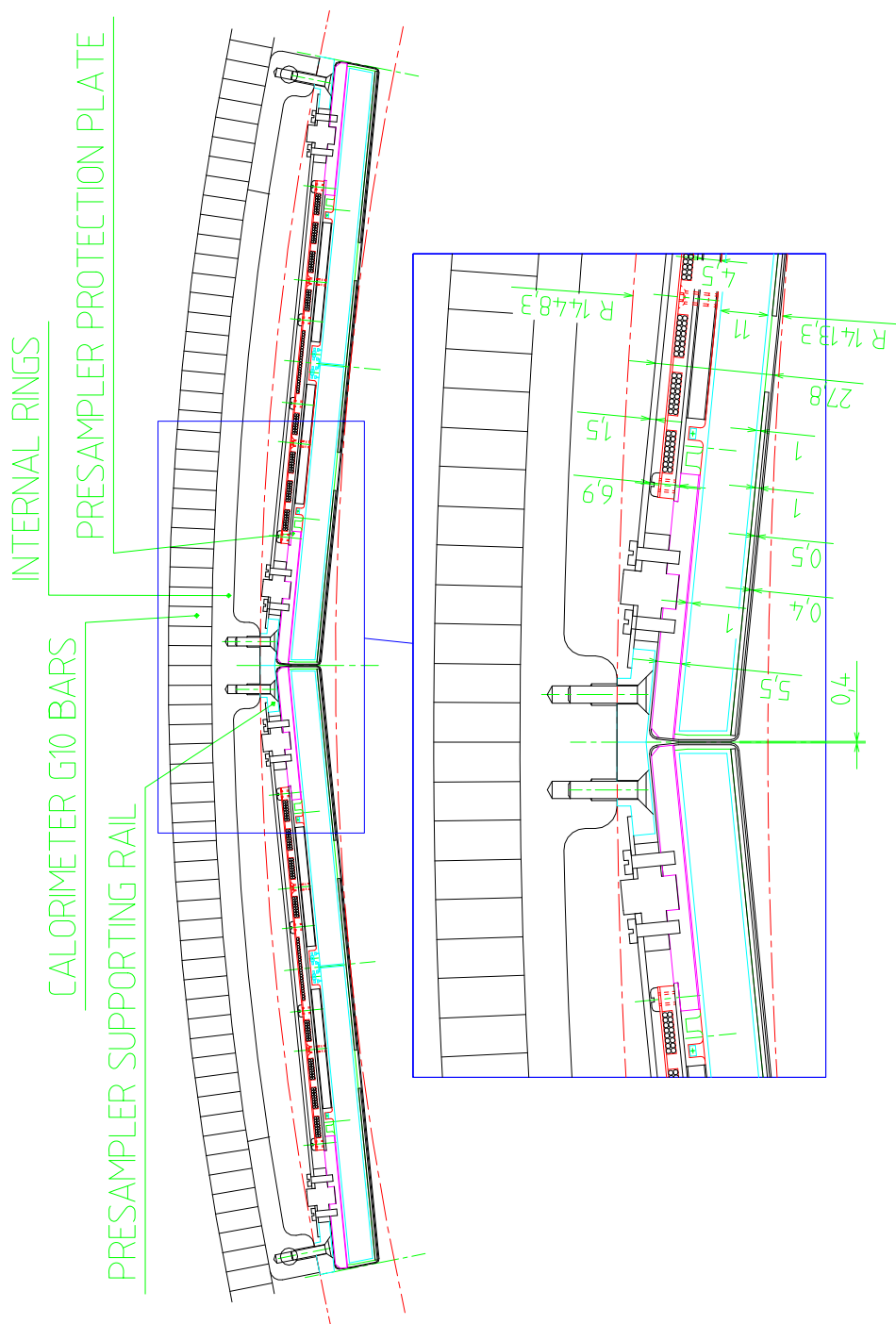
Figure 6-iv Presampler module, cabled.

Figure 6-v Prototype of a large-size read-out electrode.
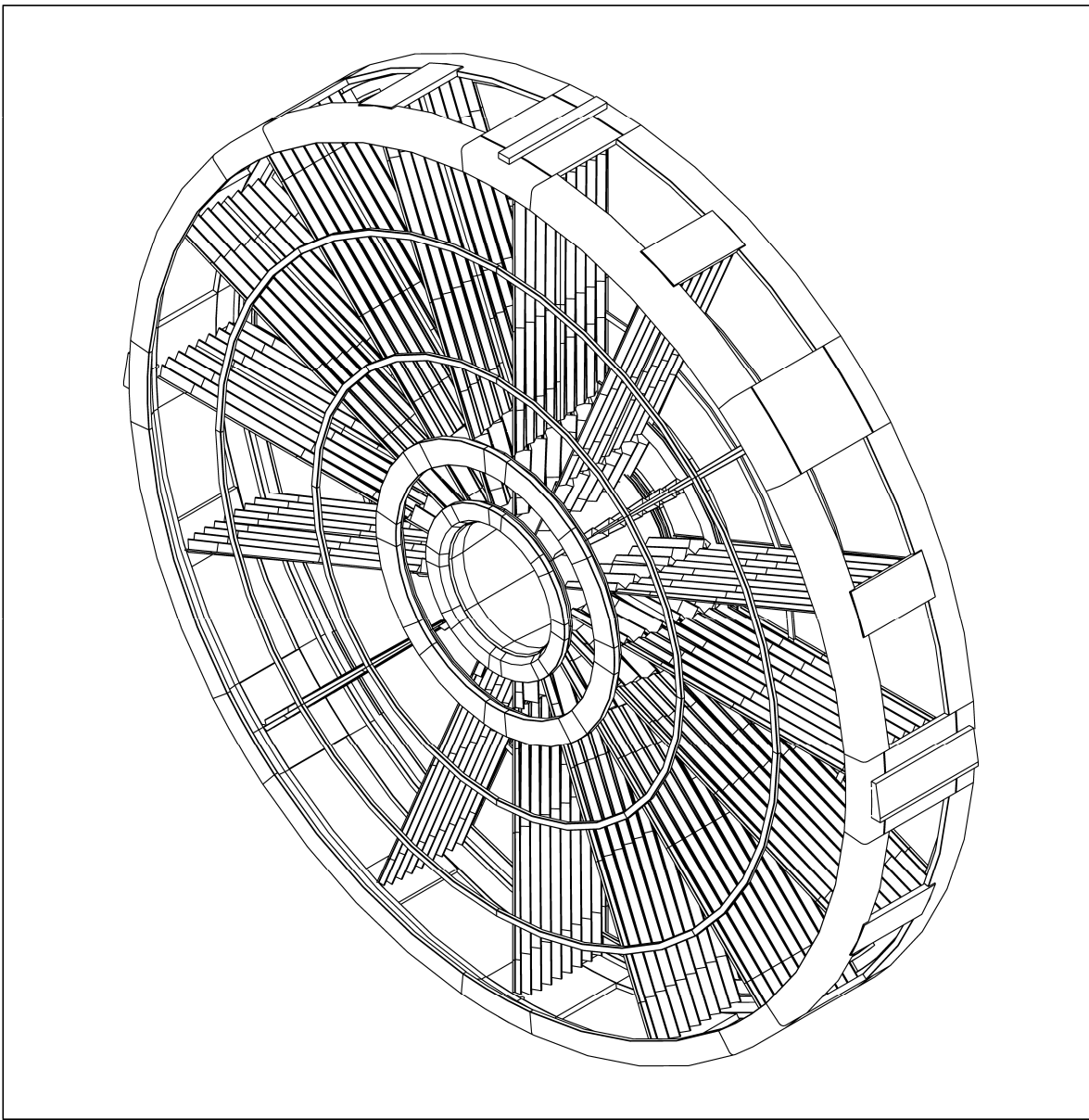
Figure 6-vi Prototype of a spacer sheet.

Figure 6-vii Section of the EM barrel calorimeter with two presampler modules suspended in front.

7 The electromagnetic end-cap calorimeter and presampler

7.1 Global engineering design
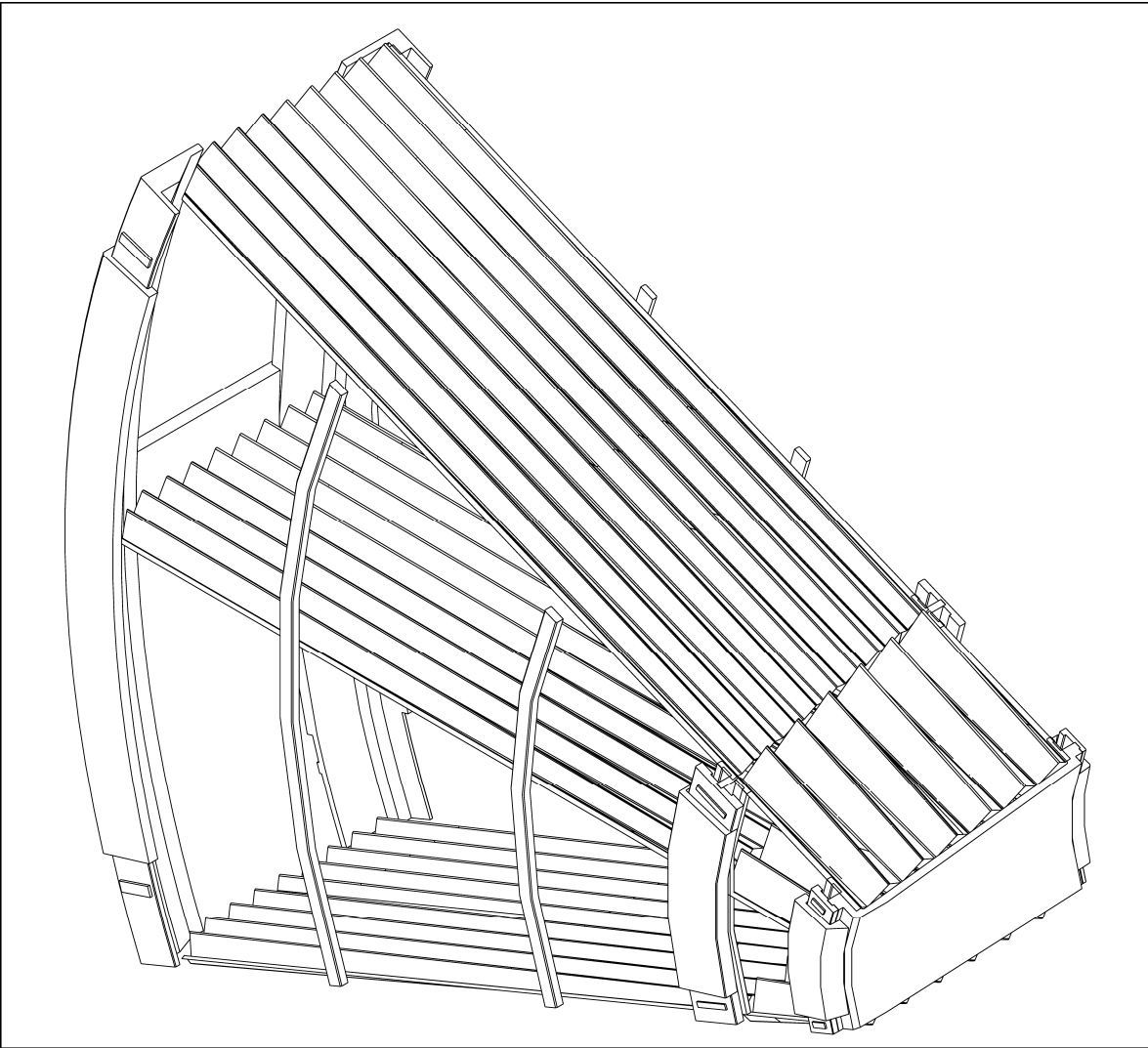
Figure 7-1 General view of an electromagnetic end-cap calorimeter, with only a few absorbers.

The end-cap calorimeters consist of accordion-shaped lead absorbers interleaved with electrodes, the gap being filled by liquid argon. As shown in Figure 7-i, each electromagnetic end-cap calorimeter appears, at room temperature, as a 632 mm thick wheel with an external radius of 2077 mm.

It is located inside the end-cap cryostat 3641 mm from the interaction point. It covers the pseudo-rapidity range $1.375 \leq |\eta| \leq 3.2$, for a full thickness ensured between 1.475 and 3.2. The nominal active volume, 510 mm deep, is limited externally by a cylinder with a radius of 2034 mm and internally by a cone with an aperture of 4.7°. This corresponds for the smaller radius to 302 mm with a front face positioned 3704 mm from the interaction point.

Each end-cap calorimeter is mechanically divided into eight wedge-shaped modules (Figure 7-2).

Figure 7-2 Schematic view of an electromagnetic end-cap module. Only 3 absorbers out of 96 (in the outer wheel) are represented.

In order to accommodate the accordion geometry in this region, the absorber plates are arranged radially like the spokes of a bicycle wheel and the accordion waves run parallel to the beam axis. To ensure a uniform response in ϕ, the combined thickness of liquid argon and absorber crossed by the particles must be independent of the azimuthal angle. As the liquid argon gap naturally increases with the radius it is necessary to adapt the wave height and thereby the folding angle, at each radius. The geometry described in the Technical Proposal tried to keep the lead-to-liquid-argon ratio constant everywhere. This led to a lead thickness varying as a function of the radius. It has been proven that it was possible to achieve, by machining, lead absorb-

ers with a variable thickness and a 10 µm accuracy. But clearly it seemed that it would be easier and cheaper to use lead plates of constant thickness. Another problem was the large variation range of the high voltage. This high-voltage variation with respect to the radius was needed to compensate for the signal change with the increasing gap. In the Technical Proposal design the maximum high-voltage value was too high (about 3.5 kV) to be safely implemented. Furthermore, because of the variation of the electric field in the opening liquid-argon gap, the constant sampling ratio concept did not guarantee the response uniformity of the calorimeter. For these reasons another design with constant-thickness absorbers was studied. The variation of the sampling fraction induced by the variation of the lead-to-liquid-argon ratio is partially compensated by the increase of the gap. So the variation range of the high voltage is smaller. The optimization of this concept, as well as the comparison of the performances of both geometries, are described in ATLAS internal notes [7-1]. The simulations exhibit the same level of the signal modulations in ϕ, namely less than 4% peak to peak in the region $1.6 \le |\eta| \le 3.0$, in both geometries. Concerning the energy resolution the results are also similar, with a sampling term around 7-8%. The main drawback of the constant-thickness design is the total depth of the detector, which is only 25 X_0 at low rapidity ($1.5 \le |\eta| \le 1.7$).

As explained before, the folding angle and the wave height must vary with the radius. However, for technical reasons the folding angle must be kept between about 60° and 120°. This limits the ratio of the external to internal radii of the absorbers to about three. So it is impossible to cover the pseudo-rapidity range with only one accordion structure. Thus, the end-cap calorimeter consists of two coaxial wheels. The boundary between these two wheels is projective and corresponds to $\eta = 2.5$. The corresponding crack is about 3 mm wide. The outer wheel contains 768 absorbers and 768 electrodes, while the inner wheel contains only 256 absorbers and 256 electrodes. Each absorber of the inner wheel is aligned with an absorber of the outer wheel.

At room temperature the absorbers are 578 mm wide in both wheels, about 1429 mm long in the outer wheel and about 319 mm long in the inner wheel. For both absorber types the folding angle ranges approximately from 60° at the external edge up to 120° at the internal edge. The lead thickness is 1.7 mm in the outer wheel and 2.2 mm in the inner wheel. As in the barrel, the converters are made of lead plates claded between two layers of 0.20 mm thick stainless steel. These layers are glued using a 0.15 mm thick glass-fibre prepreg adhesive. The weight of the absorbers is about 7.5 kg for the small ones and 26.0 kg for the large ones. The converters have nine waves in the outer and six waves in the inner wheel. The ϕ amplitude of the waves is $2\pi/256$ in the outer wheel and $2\pi/64$ in the inner wheel. Along the two straight edges of the folded absorbers, corresponding to the front and back sides of the end-cap calorimeter, two glass-epoxy bars are glued. These longitudinal bars are used to position the absorbers. Because of the high density of connectors, these bars are not in contact with each other and do not define directly the gap thickness. They are linked and indexed to the structure.

This structure is composed of six support rings: three on the front and three on the back. The total weight of the detector is supported mainly by two large external rings. In order to minimize the width of the crack between the wheels, the intermediate rings are designed to bind these wheels together. The wheels are not independent objects. While the intermediate front ring is made of a composite material, the five others are made of aluminium. The position of each absorber is precisely defined by pins inserted into centring holes drilled in both bars and support rings. Two lighter rings are added on each side of the outer wheel; they help to minimize the bar deformation and to control the gap thickness. On the external edge of the absorber (corresponding to the side of acute folds) a transverse bar is glued. This transverse bar minimizes the absorber sagitta. Those located in the crack between the two wheels are made of composite material in order to reduce the amount of dead material and to ensure an electrical insulation between the two wheels.

The read-out electrodes are centred between absorbers by honeycomb spacers. These electrodes consist of three layers of copper insulated by Kapton[1] polyimide sheets. The two external layers carry the high voltage used to drift the ionization electrons. Because of the fan geometry of the EM end-cap, the liquid-argon gap defined by absorbers and electrodes varies with the radius (or the pseudo-rapidity). It ranges from 1.5 mm up to 2.7 mm in the inner wheel and from 0.9 mm up to 2.7 mm in the outer wheel.

Projective read-out towers are defined by etching copper strips on the electrodes. In the outer wheel these strips are divided into three longitudinal compartments, while they are divided into only two compartments in the inner wheel, where the strip width is $\Delta\eta = 0.1$ and four adjacent electrodes are ganged together to give a $\Delta\phi = 2\pi/64 \cong 0.1$ segmentation. The first sampling is 24 X_0 deep. In the outer wheel, the width of the middle compartment (M) is $\Delta\eta = 0.025$ and three adjacent electrodes are ganged together to give a $\Delta\phi = 2\pi/256 \cong 0.025$ segmentation. The segmentation of the back compartment (B) is double in pseudo-rapidity, $\Delta\eta = 0.05$, and the same in azimuth. In the first longitudinal compartment (F) the strip width is $\Delta\eta = 0.025/8$ for $1.5 \le |\eta| \le 1.8$, $\Delta\eta = 0.025/6$ for $1.8 \le |\eta| \le 2.0$, $\Delta\eta = 0.025/4$ for $2.0 \le |\eta| \le 2.4$, and $\Delta\eta = 0.025$ for $2.4 \le |\eta| \le 2.5$. Everywhere in this first compartment twelve electrodes are summed in ϕ, giving a segmentation of $\Delta\phi = 0.1$. The frontier in depth between the first and second compartments corresponds to about 6 X_0 of material crossed in total (including material in front of the calorimeter), while the middle compartment ends after 24 X_0. The read-out cell granularity and the corresponding number of channels are given in Table 7-1 for the outer wheel and Table 7-2 for the inner wheel.

Table 7-1 Outer wheel: granularity, multiplicity and number of read-out channels (for one end-cap)

Region	Compartment	$\Delta\eta \times \Delta\phi$	η	ϕ	total
$1.375 \le |\eta| \le 1.50$	F	$0.025^a \times 0.1$	4	64	256
	M	0.025×0.025	4	256	1 024
$1.50 \le |\eta| \le 1.80$	F	$0.025/8 \times 0.1$	12×8	64	6 144
	M	0.025×0.025	12	256	3 072
	B	0.050×0.025	6	256	1 536
$1.80 \le |\eta| \le 2.00$	F	$0.025/6 \times 0.1$	8×6	64	3 072
	M	0.025×0.025	8	256	2 048
	B	0.050×0.025	4	256	1 024
$2.00 \le |\eta| \le 2.40$	F	$0.025/4 \times 0.1$	16×4	64	4 096
	M	0.025×0.025	16	256	4 096
	B	0.050×0.025	8	256	2 048
$2.40 \le |\eta| \le 2.50$	F	0.025×0.1	4	64	256
	M	0.025×0.025	4	256	1 024
	B	0.050×0.025	2	256	512
					30 208

a. The first cell covers $1.375 \le |\eta| \le 1.425$

---

1. Kapton is a trade mark of Dupont Corporation

Table 7-2 Inner wheel: granularity, multiplicity and number of read-out channels (for one end-cap)

Region	Compartment	$\Delta\eta \times \Delta\phi$	η	ϕ	total
$2.50 \leq \mid\eta\mid \leq 3.20$	M	0.1×0.1	7	64	448
	B	0.1×0.1	7	64	448
					896

In the outer wheel signals from the first compartment, and the middle compartment for $\eta \leq 1.5$, are routed to the front of the EM end-cap calorimeter, the other signals are routed to the back. In the inner wheel the signals of both compartments are routed to the back. The signals of adjacent electrodes are summed by printed circuit boards to give the ϕ granularity. These printed circuits, so-called motherboards, also provide the connections to the output cables and distribute the calibration signals. In some areas, because of the high density of signals to read-out, the motherboards are split into two boards, lying upon the other. Except for the $\eta \leq 1.5$ region, in both wheels the high voltage is supplied, from the back, to the edges of the motherboards. The high-voltage distribution allows seven different values, ranging from 0.9 kV up to 2.6 kV, in the outer wheel and two (1.5 kV and 2.5 kV) in the inner wheel [7-4].

The large amount of material (inner detector, cables and cryostat walls) in front of the electromagnetic end-cap calorimeter in the transition region with the barrel ($1.55 \leq \mid\eta\mid \leq 1.80$) degrades the energy resolution. In this region a 6 mm active liquid-argon presampler helps to recover the energy resolution. It is placed in front of the EM end-cap calorimeter in a notch machined in the cold wall of the cryostat.

7.2 Absorbers

7.2.1 General description

Extensive Monte-Carlo simulations have shown that the ATLAS liquid-argon EM end-cap calorimeter will provide the discovery potential needed for LHC physics if a constant term in the energy resolution below 0.7 % is achieved. This fact imposes very stringent criteria on the design and construction of the calorimeter. Critical items are the uniformity of passive and active calorimeter materials along the particle shower development direction, i.e. the uniformity of the lead thickness and the liquid-argon gap, respectively.

Simulations [7-5] have shown that Gaussian local lead-thickness non-uniformities of the order of 1% r.m.s. (i.e. $\approx 17\,\mu m$) will contribute to the constant term by an amount low enough not to put the above 0.7% in jeopardy. A similar result was obtained if the local non-uniformities were distributed uniformly around ±1.8% of the nominal value (i.e. $\approx 30\,\mu m$).
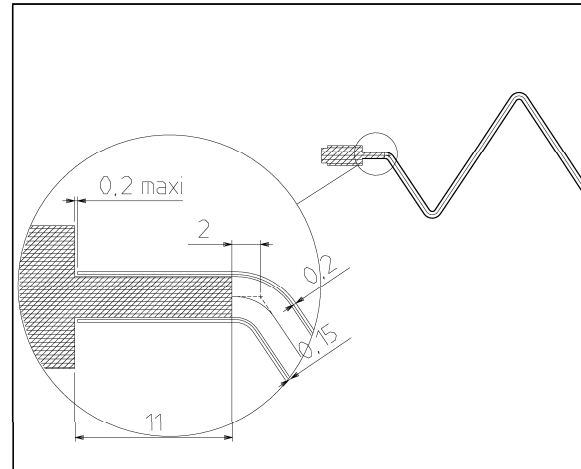
On the other hand, and also from physics considerations, local non-uniformities of the liquid-argon gap should be kept below 50 μm. This restriction constrains both the reproducibility of the geometry of the fabricated absorbers and of their relative positions, once inside the detector.

Lead being a soft material, it is not possible to maintain an accordion shape without reinforcement. This is provided by two skins of stainless steel, glued on both faces of lead plates by a layer of glass-fibre prepreg adhesive. In both wheels, the stainless-steel skins are 0.2 mm thick and the prepreg layers are 0.15 mm thick.
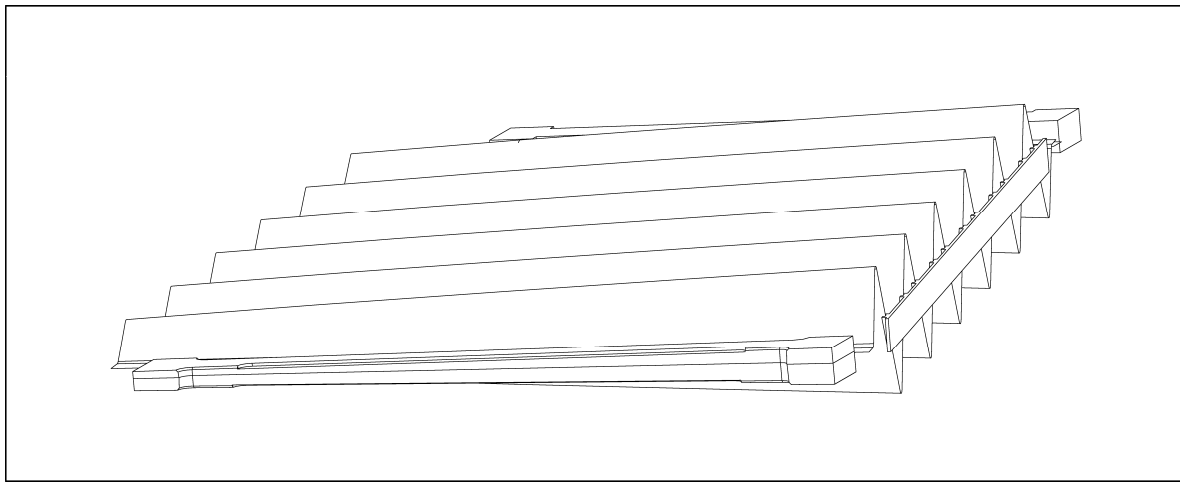
To link, with good accuracy, the absorbers to the structure, we use structural bars on both sides parallel to the waves. To ensure a good positioning and a stiff junction between absorbers and bars, the latter have a flat part, with the same thickness as lead, which is glued, during the absorber curing process, between the same stainless-steel foils, edge to edge with lead (Figure 7-3).

Figure 7-3 Cross-section of an absorber showing the gluing scheme of a longitudinal bar.

We also added a third transversal bar, at the level where folding angle is the sharpest. Its purpose is to minimize plane sagitta of the absorber, and to control thermal deformation of wave angles (Section 7.2.2).

Figures 7-4 and 7-5 show views of inner and outer wheel absorbers with their two longitudinal bars and their transverse bar. Table 7-3 gives the geometrical characteristics of the absorbers at liquid-argon temperature. In addition to their dimensions, the two types of absorber differ in terms of lead thickness, which is 2.2 mm in the inner wheel and 1.7 mm in the outer wheel.

Figure 7-4 Axonometric view of an inner-wheel absorber with its bars.

7.2.2 Shape of absorber elements at room temperature

The shape of absorbers is defined, from the simulation, at liquid-argon temperature. Then the shape at room temperature has to be determined to specify the dimensions of each individual

Figure 7-5 Axonometric view of an outer absorber with its bars.

Table 7-3 Geometrical characteristics of the absorbers at liquid-argon temperature

Parameters	Inner wheel	Outer wheel
Number of waves	6	9
Wave length	85 mm	56.67 mm
Lead thickness	2.2 mm	1.7 mm
Lead width	514 mm	514 mm
Width of the flat composite sides	11 mm	11 mm
Width of the bar body	20 mm	20 mm
Total width	576 mm	576 mm
Front-edge lead length	308 mm	1387 mm
Back-edge lead length	351 mm	1336 mm
Total weight	26.0 kg	7.5 kg

component (lead plates, stainless-steel sheets, prepreg sheets and bars). The procedure followed to compute the room temperature shape is based on measurements and computations.

Several tests, performed with RD3 prototype absorbers in liquid nitrogen, exhibited non-linear behaviour of the cured sandwich during cool-down operation. The measured thermal-shrinkage coefficient of an absorber is far from the average of the shrinkage coefficients of its components. These tests have also shown that the folding angle decreases with temperature. This variation depends on the nominal value of the folding angle: sharpest angles close more.

A finite element model of the prototype absorber, taking into account plasticity of lead, was developed with `ABAQUS` software [7-6]. It was adjusted to fit real measurements in liquid nitrogen. It was then extrapolated to describe the inner- and outer-wheel absorbers. The latter are described at liquid-argon temperature and their behaviour during an artificial warm-up is simulated. In this way we obtain the absorber shape at room temperature. Figure 7-ii illustrates the result of this modelling for small absorbers. The blue projection corresponds to the cold geometry and the red one to the room temperature shape. Thermal expansion is enhanced to make it visible. For example the front edge (bottom on the figure) length is 308.2 mm at cold and

309.1 mm at warm. The thermal expansion depends on the lead thickness. From this computation we obtain

α = 14.1 10^{-6} K^{-1} for large absorbers (1.7 mm of lead)

α = 14.3 10^{-6} K^{-1} for small absorbers (2.2 mm of lead)

The folding-angle variation explains the curved outline of the absorber at warm temperature. The sharpest angles (right on the figure) open more than the obtuse angles. This last phenomenon is "soft", as it concerns the "spring" characteristics of absorbers. It is easy to control with a transversal bar, made of a material with a thermal coefficient comparable with that of the aluminium of the structure. Figures 7-7 and 7-8 show the flat shape of lead plates for the inner and outer wheels, respectively. The precise geometry is defined by the position of each intersection point of bending lines with the outline. On these figures the notches made to accommodate the structure rings are also visible.

7.2.3 Lead plates

After a specific R&D programme, the severe thickness tolerances for thin lead plates of large area (≈ 1 m^2) were achieved either by means of standard surface machining or by rolling. For economic reasons we chose the rolling technique for the production of the lead plates. However, we found only one company[1] in Europe able to do it.

The lead production for the EM end-cap module 0 took place in October 1996 at the same time as the lead production for the EM barrel module 0. The same insitu quality control procedure described in Chapter 6, Section 6.2.2.2, was applied. The analysis of the thickness measurements taken at the factory gave similar satisfactory results as shown in Chapter 6, Figure 6.6. The raw material composition is also Pb 99.94 DIN 1719. The lead is delivered as rectangular plates $1504 \times 1005 \times 1.7$ mm^3 for the outer absorbers and $1504 \times 1005 \times 2.2$ mm^3 for the inner absorbers. In this last case three inner absorbers are cut from the same rectangular plate.

The rectangular lead plates are cut to the required absorber dimensions (Figures 7-7 and 7-8) by means of a computer controlled CO_2 laser beam (2 kW max. power). The accuracy

Figure 7-6 Lead thickness distribution in one plate.

of the beam position is $\approx \pm 100$ μm along distances of a few metres. The cut plates are then cleaned of lead oxide and other dust deposits by an automatic surface brushing machine (the brush is a Scotch-Brite with a 220 g equivalent roughness). The absorber curing has to be done not later than 24 hours after the lead cleaning to prevent new oxide formation which could jeopardize its bonding to the stainless steel sheets. The sticking capabilities of lead cleaned according to the above procedure were checked carefully during the R&D part of the project.

---

1. Röhr+Stolberg GmbH (Krefeld, Germany)
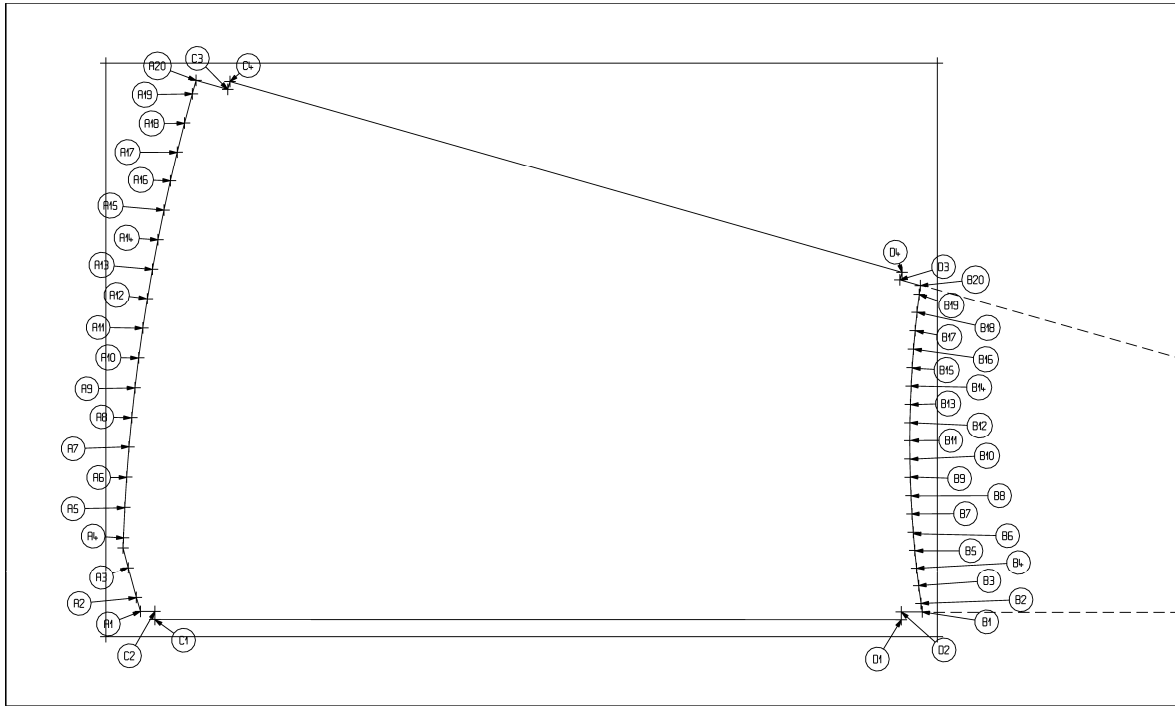
Figure 7-7 Room temperature lead-plate shape for inner absorbers. The precise geometry is defined by the labelled points, for which the coordinates are given to the manufacturer.

Quality control of the lead plates is done in three steps. Before the cutting of the rectangular plates, their thicknesses are mapped (50×50 mm^2 grid) in the home institute by a robotic set-up with an ultrasonic probe. First, this measurement helps to detect possible defects and to reject the corresponding plates. Then, for each absorber a computer file with the results of this thickness mapping is kept for the whole life-time of the experiment. Figure 7-6 shows the results of the mapping for one lead plate corresponding to a module 0 outer absorber. The thickness dispersion is less than 5 µm r.m.s. At the time of the thickness mapping, each absorber lead plate is given a serial number for back-tracking purposes. This number is written permanently on the lead.

On the other hand, the shape dimensions of the cut plates will be checked at the time of the absorber sandwich stacking by means of precision location pins. Finally, a careful optical inspection for scratches and other imperfections is also carried out at the time of the absorber stacking.

7.2.4 Stainless-steel sheets

The plates used for cladding the lead are made of stainless steel of the AISI-304-L (surface finished 9F) type. The manufacturer[1] guarantees a thickness tolerance of ± 6 µm. Its final shape in the absorber is the same as for lead except that the two lips running longitudinally at the two

Figure 7-8 Room temperature lead plate shape for outer absorbers. The precise geometry is defined by the labelled points, for which the coordinates are given to the manufacturer.

lateral extremes are 11 mm wider to accommodate the corresponding lips of the longitudinal bars. As for the lead, the cutting is done by a laser beam and the final dimensions of the cut plates are checked, by means of precision pins, at the time of the absorber sandwich stacking. After cutting, the stainless-steel sheets are degreased with FINOX[1], picked with NET-INOX and passivated with N 50.

7.2.5 Prepreg sheets

The material used for sticking the lead to its cladding stainless steel plates is a prepreg Brochier 1454 NC/50% /759 VIT.200[2], which consists of a resin-glass fibre cloth. It comes from the factory with a thin layer of light adhesive, properly protected, on its two surfaces. This material has been used in previous prototypes with satisfactory results [7-10]. The resin polymerizes at a temperature of approximately 120°. The prepreg is manually cut to the absorber dimensions with the help of a metal pattern plate. The dimensions of the cut prepreg sheets are checked, by means of precision pins, at the time of the absorber sandwich stacking.

---

1. Teledyne-Rodney Metals, France
1. FINOX, NET-INOX and N 50 are products from CHIMIDEROUIL, France
2. BROCHIER SA, filiale CIBA-GEIGY, France

7.2.6 Longitudinal bars

7.2.6.1 Requirements

Longitudinal bars are dedicated to the positioning of absorber in the structure. As already explained in Section 7.2.1 they are strongly fixed to the absorbers: a flat extension of the same thickness as lead is glued between the two stainless-steel sheets during the absorber curing process (Figure 7-11). The bars have to provide accurate geometrical references. Attachment to the structure is achieved by T-shaped heads. The relative positioning of adjacent absorbers is ensured by precise pins indexed to the structure itself (Section 7.5).

Another role of the longitudinal bars is to maintain the electrode connectors. For this purpose notches ($1.2\,\text{mm} \times 7\,\text{mm}$) have been made in the edges of bars, opposite to the flat side (Figure 7-12).

Material selected for production of these bars should be transparent to radiations to avoid masking the front face of the active part. It should be non-conductive to insulate the absorbers from each other. It must also be radiation hard, and should not pollute the argon by any emanation of electronegative elements.

The shrinkage coefficient of the longitudinal bars has to be adjusted to minimize the stresses induced during cool-down operation. Mechanical and thermal computations (Section 7.5.7) show that a mean thermal-expansion coefficient close to $15.5\ 10^{-6}\ °\text{C}^{-1}$ would be appropriate.

7.2.6.2 Material choice
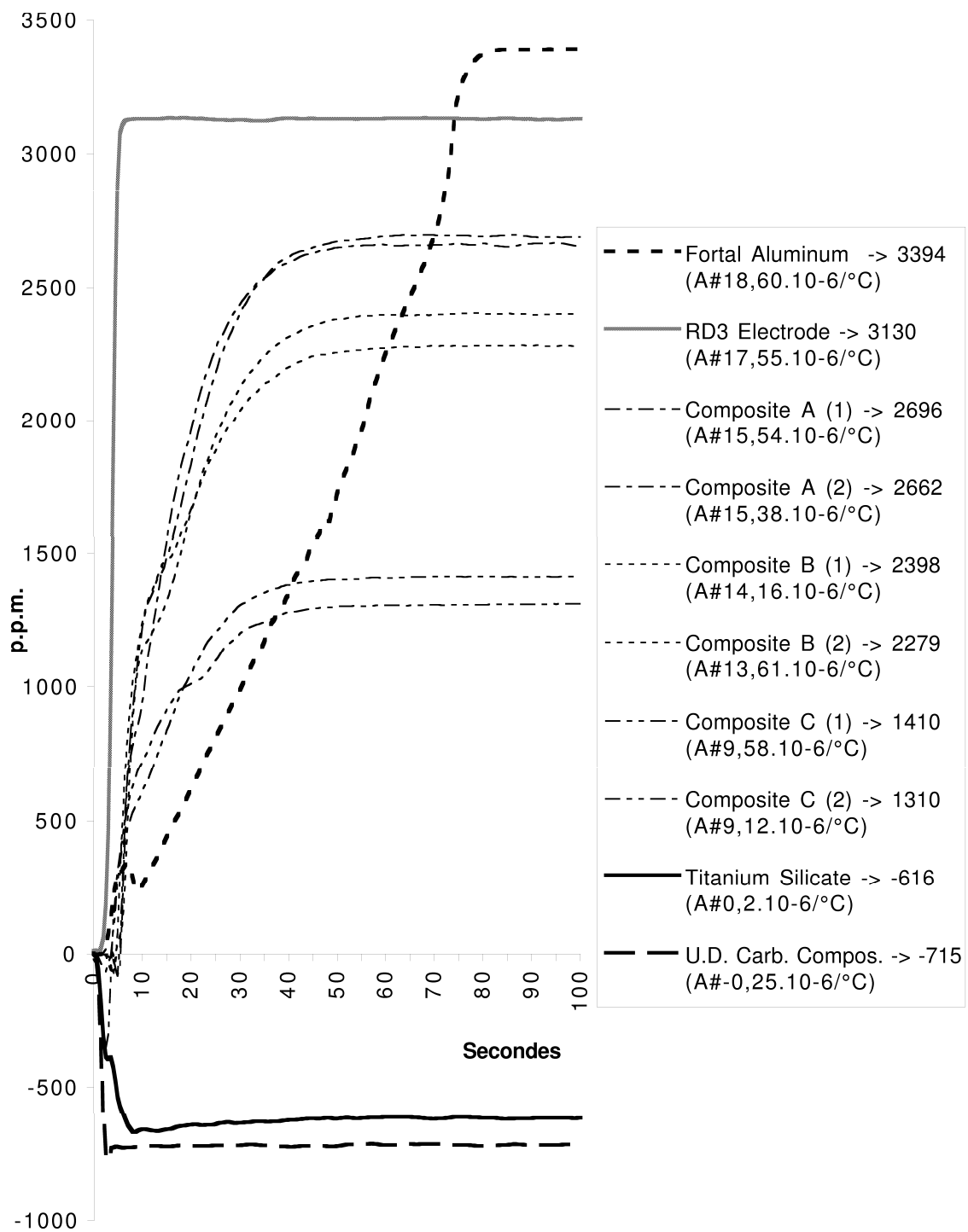
Requirements are very much in favour of glass-fibre composite materials. For nonpoisonous and radiation-hardness needs, we investigated the glass/epoxy family. We chose the resin (5052 CIBA) because it is free of solvent and has good thermal behaviour. Literature references and mechanical simulations gave some hints, but only real tests could confirm behaviour in cryogenic conditions. Therefore, shrinkage measurements were performed between room and liquid-nitrogen temperatures. Figure 7-9 shows some results. Titanium silicate and U.D. carbon composite are reference materials. Other curves correspond to materials foreseen for the detector construction:

- Fortal HR: aluminium alloy used for the structural rings;

- Glass-fibre epoxy composites with different fibre orientations;

- Read-out electrodes (material used in the prototypes).

The average (integrated between 20°C and −196°C) thermal-expansion coefficient for each material is measured after thermalization of the sample (on the plateau). When possible these coefficients were compared with the literature, and found to be in good agreement. The thermal-expansion coefficient of composite A (Figure 7-9) fulfils the requirement, and therefore was chosen for the bar production.

A sample of this material was irradiated in the SARA neutron beam, in liquid argon (Chapter 11, Section 11.4.). No signal loss was observed during the exposure (equivalent to $1.6\ 10^{14}$ neutrons/cm^2).

Schrinkage curves between 20°C and -196°C

Figure 7-9 Material shrinkage measurements between room and liquid-nitrogen temperatures.

7.2.6.3 Production process

The so-called Resin Transfer Moulding (RTM) process is well adapted to medium-size series. Resin is injected at low pressure into a mould (Figure 7-10); in this way the leakage requirements for the mould are less stringent, and therefore RTM is less expensive than for other techniques. First, the glass-fibre cloths are stacked in the mould; then the resin is injected.

The RTM process does not provide a shape precise enough for the absorber positioning. The reference are given by the faces of the T-shaped heads with respect to the flat extension. For that purpose these T-shaped heads are machined with a $\pm 40\,\mu m$ absolute accuracy. Then the indexing holes are drilled with a $\pm 10\,\mu m$ centring accuracy with respect to the median plane of the flat extension.
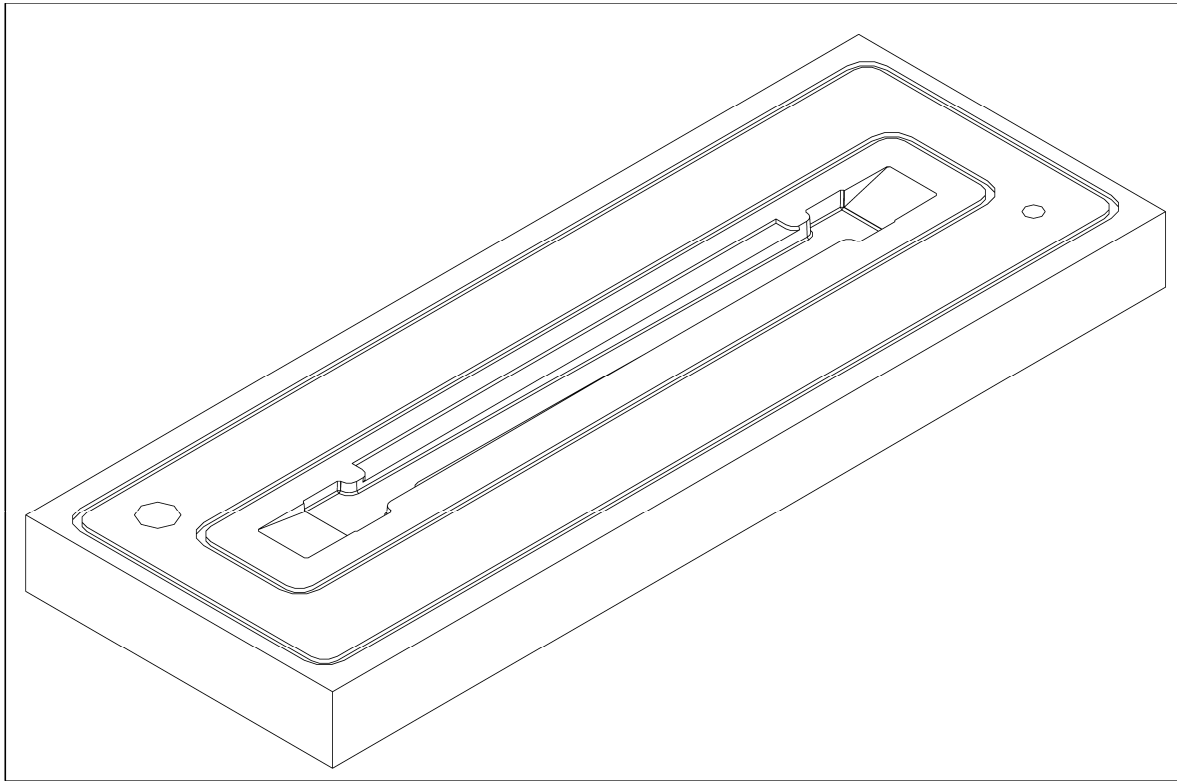
Figure 7-10 Injection mould for a longitudinal bar.

7.2.7 Transversal bars

Transversal bars (Figure 7-13) are dedicated to control the shrinkage of the absorbers in the direction perpendicular to the waves (Section 7.2.2). They also decrease the sagitta of the absorbers in the same direction. Only one transverval bar is needed per absorber. The bar is glued to the outer edge of the absorber, corresponding to the sharpest folding angles. In the $\eta = 2.5$ crack the thickness is small enough to accommodate the 3 mm
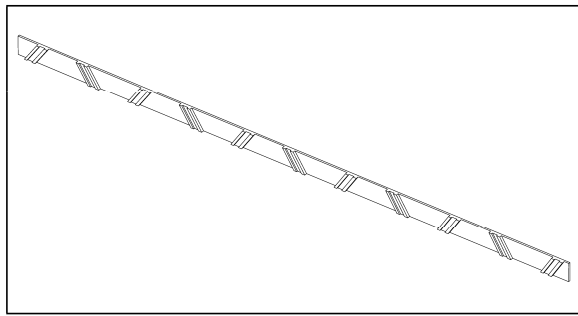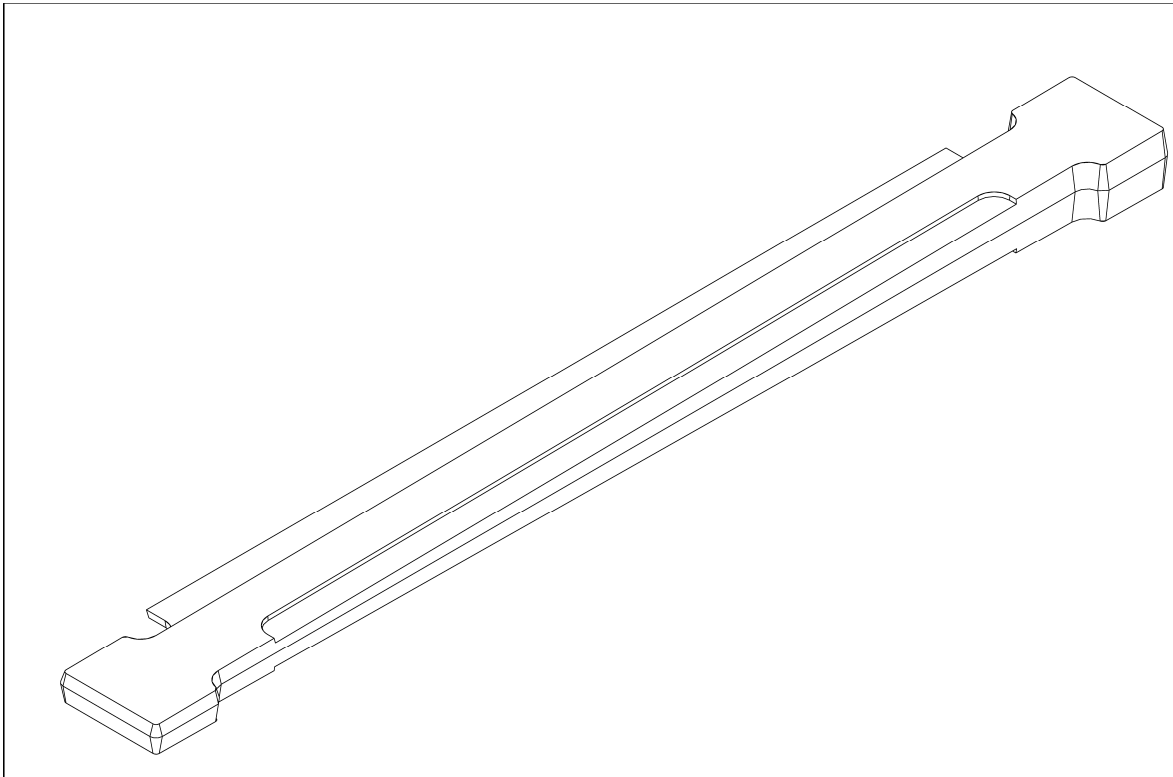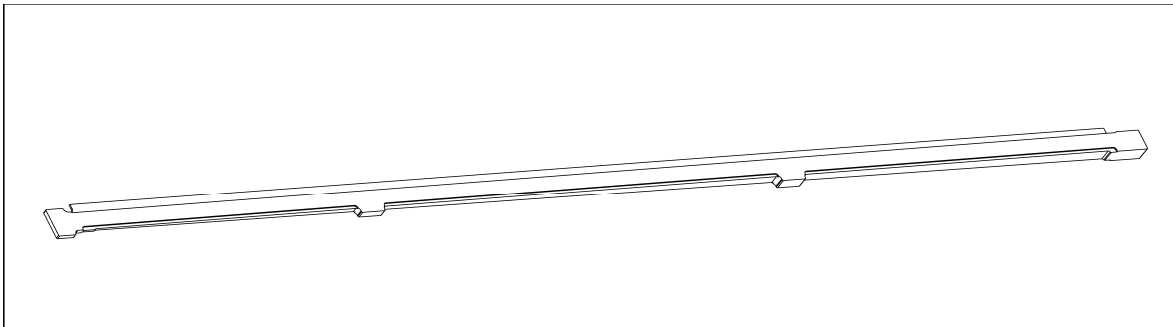
Figure 7-13 Transversal bar for inner absorbers.

Figure 7-11 Axonometric view of a bar for front-face edge of inner-wheel absorbers. Note the flat side, inserted in a sandwich (in place of lead) and the recess dedicated to electrode connectors.

Figure 7-12 Bar for front-face of outer-wheel absorbers. Humps are dedicated to indexing rings fixation. Total length is 1398 mm.

gap. In this region the transversal bars also ensure an electrical insulation between the two wheels.
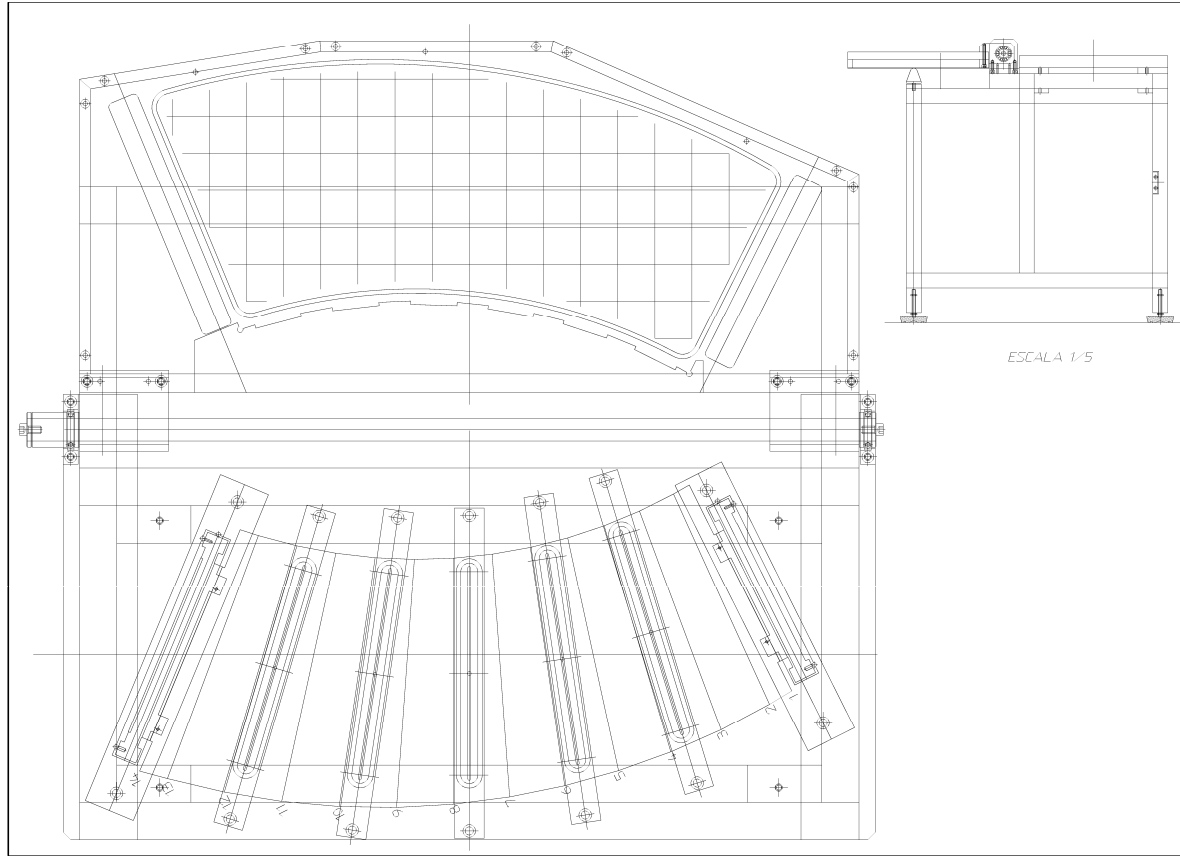
To ensure homogeneous shrinkage with respect to the structure, the thermal-expansion coefficient has to be close to the coefficient of the aluminium alloy used: $18.6 \ 10^{-6}°C^{-1}$. This can be achieved with a material like Ultran 2100 or Fortron 6165, loaded with a few glass fibres.

7.2.8 Sandwich stacking

The fabrication of one absorber consists of three steps: the stacking of the different plates (lead, stainless-steel and prepreg) and lateral bars to form a flat absorber sandwich; the bending of this sandwich to the required absorber geometry; and finally the curing of the prepreg to firmly

stick the lead to the stainless steel and bars as well as to provide the final shape, rigid enough, to the absorber.

Once the lead and stainless-steel plates and the prepreg sheets are cut and cleaned (lead and stainless steel), and the lateral bars machined and cleaned, a flat stainless-prepreg-lead-prepreg-stainless sandwich, with the two straight sides ended by the lateral bars, is formed by using the tool depicted in Figure 7-14. It consists of two flat tables; one is fixed permanently to the bench, and the other rotates around an axis running parallel to and located close to the inside straight side of the first plate. The system works like the opening and closing of a book wich has one of its covers permanently fixed to the desk.

Figure 7-14 Stacking table for small absorbers.

Both plates incorporate a vacuum system to hold the sandwich plates as well as a set of precision pins in order to guarantee accurately enough the relative position of the different components of the absorber. In addition, both plates have two grooves each to accommodate the two lateral bars and the two clamps (one per bar) which temporarily rigidly hold the bars and the sandwich together during the bending of the sandwich. The precision pins ensure a relative positioning between the lead plate and the bars of better than $\pm\,50\,\mu$m, as well as a relative positioning of the stainless-steel plates and the prepreg sheets with respect to the lead of better than $\pm\,100\,\mu$m.

The stacking procedure starts with the two jig plates (fixed and movable) in open position and with one stainless steel plate precisely located and held by vacuum on the fixed plate. Next, one prepreg sheet is positioned and held by vacuum on the movable plate. After having taken away its protection, the movable plate is rotated until it reaches the top of the fixed plate (closed position). At this point the vacuum in the movable plate is switched off, the prepreg sheet is stuck

to the stainless steel plate by the prepreg adhesive, and the movable plate is rotated back to its open position. The other protection on the prepreg is removed. Next, the lead plate is precisely positioned and held by vacuum on the movable plate, which is rotated and, when on top of the fixed plate, its vacuum is disconnected and the lead is stuck to the prepreg. After the rotation of the movable plate to its open position comes the precision positioning of the lateral bars (manual operation). The remaining sandwich components (one prepreg sheet and one stainless steel plate) are assembled following the same operations. Finally the clamps are firmly closed, the bars, therefore, becoming rigidly attached to the absorber. The vacuum systems for the movable or fixed plates are different. For the movable plate, the vacuum is provided by a vacuum pump which provides a high mass flow with a relatively low vacuum pressure, guaranteeing proper handling of the soft prepreg sheet. The vacuum system for the fixed plate, which is less critical, is provided by a conventional Venturi device.

Once the flat sandwich has been formed (lateral bars included), it is carefully transported to the bending press with a special trolley which also serves to feed the press with the absorber.

7.2.9 Absorber folding

The main purpose of bending the sandwich is to deform locally, into the plastic regime, the sandwich so as to form the top and valley curves of the absorber waves with high precision in the relative location wave-to-wave ($\pm 150\,\mu m$).

Given the two different types of absorber forming the end-cap EM calorimeter (inner and outer), two different presses are needed. In Figures 7-16, 7-17 and 7-18 the press corresponding to the inner absorber is depicted (both presses have similar designs). Its main components are: a) The main structure, designed according to strength requirements in order to support the stresses due to the applied load by the main (vertical) hydraulic cylinder and by the secondary (lateral) hydraulic cylinders. b) The jaw structure with the moving bending knives. Its main design requirement was to have enough rigidity to distribute uniformly along the knives the point-like load provided by the main hydraulic cylinder. c) The knives themselves

Figure 7-15 Example of knife profile.

which can slide (by means of rollers) over two hardened plates attached to the jaws structur. The movement of the knives are arcs around an axis perpendicular to the corresponding jaw (and hardened plates) plane. These circular paths (in contrast to the straight paths followed by the barrel press knives), and also the peculiar bending surface shape of the knives (Figure 7-15) are consequences of the variation of the folding angle along the absorber (see also Figure 7-18). The precise location of the knife rotation axis is determined by the absorber geometry. The knives are made of Alloy Steel Forging F1250, Spanish standard UNE (34CrMo4 DIN equivalent). They are provided with a precision location pin on the surface opposite to the absorber-shaped surface for fine positioning of the knives before bending. d) The positioning system of the knives (before bending) consists of two 'combs' (one each for the knives in the bottom and top jaws) with high precision notches on them which will define the precise location of the knife positioning pins.

Figure 7-16 Side views of the folding press for inner-wheel absorbers.

The two lateral hydraulic cylinders (and their corresponding force-transmitting structures) provide a lateral force at each end of the already bent absorber to compensate force transmission losses from the main hydraulic cylinder due to the complicated geometry of the absorber. From experience gained during the construction of previous accordion prototypes, the optimum vertical pressure was estimated to be around 400 kPa. These figures translate into vertical (lateral) hydraulic cylinders able to provide total forces of 9 and 30 tons (1 and 3 tons) for the inner- and outer-absorber presses, respectively.

The bending process starts with the jaws open and the knives prepositioned in their open configuration. Next, the knife positioning system slides the combs in until the knife positioning pins are trapped by the notches in the combs. One should note that this is probably the most critical operation of the bending process since the distance between the lines defined by the top and bottom knife waves will define the distances between the corresponding top and bottom wave lines in the folded and cured absorber. The presses are designed to give an accuracy on these distances between lines of $\pm 150\,\mu m$. Next, the flat sandwich is slid in between the jaws and is left lying on the top wave lines of the bottom-jaw knives. The sandwich is positioned with respect to the knives with the help of yet another three positioning pins located on the bottom-jaw lateral knife against which the corresponding lateral bar of the absorber will be manually pushed. The two absorber edges with the lateral bars are then firmly clamped to the two lateral knives by means of pneumatic actuators on these knives which provide a clamping force of approximately 80 N/cm.
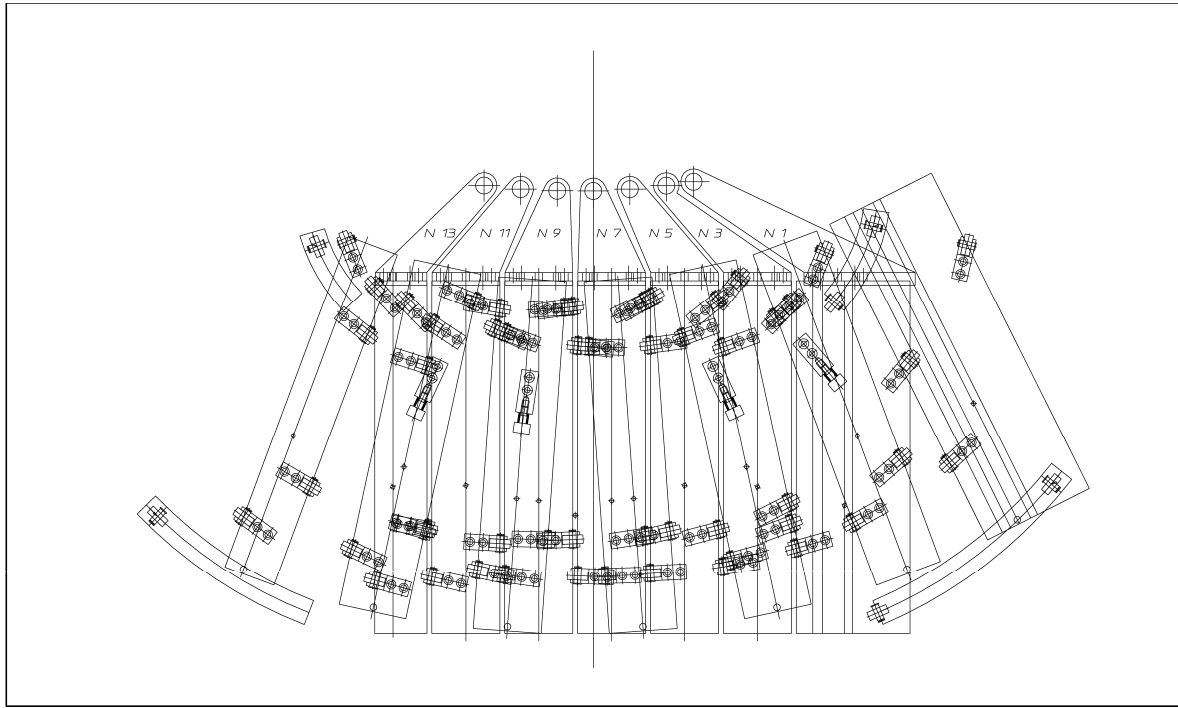
Figure 7-17 Top view of the folding press for inner-wheel absorbers.

The next operation is the closing of the jaws (by the force of the vertical hydraulic cylinder) up to the point where the sandwich gets a slight deformation (a peak-to-peak distance of ≈ 2 mm). The purpose of this prebending operation is to keep the knives held in their starting position by the absorber itself and therefore to allow the extraction of the knife positioning combs, as well as to produce a deformation zone in the absorbers, at the top of the knives, whose main function is to be used as a cam profile during the subsequent movement of the knives. Once the combs are out and the knives can roll "freely" around the rotation axis, the vertical cylinder applies its full force. The absorber ends being rigidly attached to the two lateral knives, and thanks to the kinematics of the knife movement, the sandwich gets deformed into approximately its final shape in this operation.

Next, the two lateral hydraulic cylinders push the knives against each other (the force of the vertical hydraulic cylinder is slightly increased during this operation to ensure perfect bending). Finally all the hydraulic cylinders are retracted to their rest position, the pneumatic clamping of the absorber to the lateral knives is relaxed and the bent absorber is extracted from the press by a simple extraction system also built into the press.

7.2.10 Absorber curing

The final step in the absorber fabrication is the polymerization of the prepreg inside the absorber. For this purpose, the absorber is sandwiched between two sub-moulds (the set of two

Figure 7-18 Top view of the folding press for inner-wheel absorbers, showing the knife rotation system. Positions of knives before and after bending are shown.

sub-moulds will thereafter be called a mould) shaped both with the final absorber geometry and machined with the precision defined at the beginning of this section. The mould is subject afterwards to the temperature-pressure cycle for the prepreg polymerization.

The gluing operation has two main outcomes: the prepreg polymerizes and the absorber assumes its final permanent shape at room temperature. Notice that once the prepreg is polymerized, the absorber becomes a single rigid body elastic enough to maintain the moulded shape along the handling, storage, transport and assembly operations.

Unlike the barrel case, the prepreg curing and absorber moulding will be done in an autoclave. An autoclave could be described as a closed room inside which any uniform pressure and temperature state can be obtained by a proper air treatment. In our case, the curing moulds containing the folded sandwiches will be placed inside the autoclave run following the required pressure-temperature cycle. The autoclave technique for curing accordion absorbers was successfully tested during the R&D phase of the project.

Also, unlike the barrel, and because of the space capabilities of modern Air-Industry autoclaves, the moulding/curing will be done in batches of 10 outer absorbers and four inner absorbers. This feature speeds up considerably the production process but introduces the necessity for even more careful manufacturing of each batch of outer and inner absorber moulds in order to guarantee the absorber-geometry reproducibility defined at the beginning of this chapter. This reproducibility will be extensively checked, and corrections to the moulds applied, if necessary, by detailed 3D mapping (with a tridimensional measuring machine) of the first absorbers coming from the different moulds.
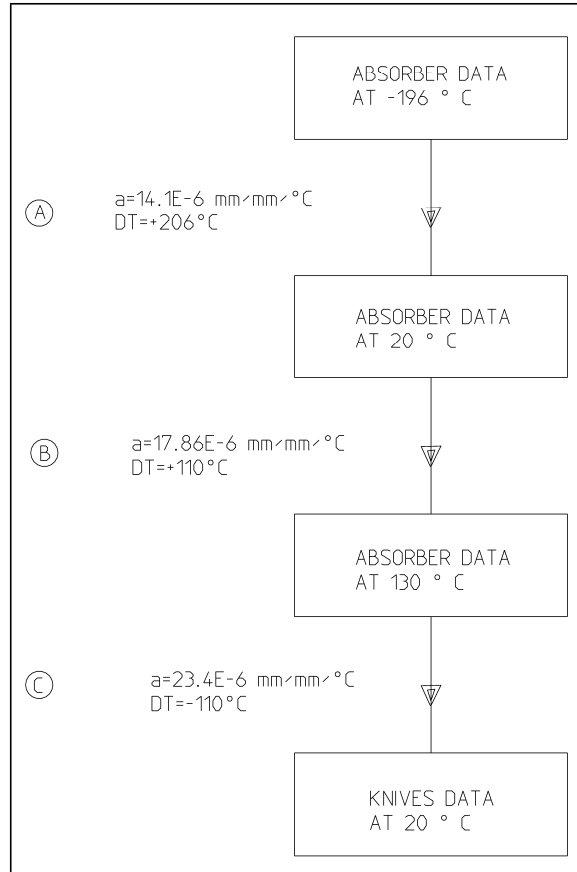
The raw material used for the moulds is aluminium (AL 6082T4) since this material is a good compromise between hardness and good mechanical machining properties. The geometrical shape of the mould surfaces at room temperature has been carefully determined by the thermal analysis outlined in Figure 7-19.

Before placing the folded absorber in the curing mould, the clamps firmly attaching the lateral bars to the absorber must be removed. Therefore the mould is provided with a bar positioning system consisting of three pins (per bar) precisely positioned with respect to the top and bottom lines of the absorber waves, and with a set of springs to push the bars against these pins, in order to prevent any misalignment of the bars during the moulding preparation. Another precision pin will fix the location of the absorber in the mould along the wave-line direction.

From the 3D measurements of the first absorbers produced with all the moulds, a real absorber geometry will be defined and used as a pattern for the rest of the production. The quality control of the produced absorbers will consist of an optical inspection for possible damage to the piece during production and a comparison of its geometry with that of the pattern.

Figure 7-19 Steps for calculating the knife shape.

For 90% of the absorbers this comparison will be coarse, namely the thickness of the absorber will be measured at six points of its contour (with a palmer or similar), its length and width (distance between the lateral bars) will each be measured at two predefined locations (with a long calibre or similar), and finally the wave-length of the accordion waves will also be measured at two predefined locations using a long custom calibre with the positioning tips replaced by special pieces made in the shape of the wave valley. If the quantities measured in the absorber do not differ more than an established amount from that in the pattern (40 µm for the thickness, 100 µm for the absorber width and wavelengths and 400 µm for the absorber length), the absorber will be accepted, otherwise it will be rejected.

For the remaining 10% of the absorbers, a complete 3D mapping will be carried out and thicknesses, lengths, widths and wavelengths extensively compared with those from the pattern. For each end-cap module produced at least one absorber cured in each mould will be measured in such an extensive way. The idea behind this procedure is to monitor the stability of the geometry of the moulds during production (and correct it if necessary).

7.2.11 Logistics

Absorber production will be performed mostly by Spanish industry. The absorber stacking, bending and curing will be done at Fibertecnic S.A. (Vitoria), a composite specialized aeronautics workshop. The necessary tools (stacking tables, presses, curing moulds, etc.) are being manufactured by Talleres Aratz S.A. (Vitoria), a medium-sized mechanics workshop specializing in high-precision prototyping. The laser-beam cutting of both the lead and stainless-steel, and the cleaning of the lead, will be performed by Mendiaraiz S.L. (Zumaya, Guipuzcoa), a workshop specializing in laser-beam cutting.

The foreseen production rate is one module (96 large absorbers and 32 small absorbers) every two months. The production chain will be as follows: The rolled lead (in rectangular plates) will be delivered at Madrid where it will be stored and its thickness mapped. In batches corresponding to one end-cap module, the rectangular lead plates will be shipped to Mendiaraiz S.L. where, after being cut to absorber dimensions, they will be temporarily stored. In batches of 10 large and four small (corresponding to an autoclave cycle) the lead plates will be cleaned and shipped to Fibertecnic S.A., where they will be processed within a ≈ 24-hour time interval. This operation will be repeated ten times per module.

All the stainless steel will be produced in one or two batches (to be decided) and shipped to Mendiaraiz S.L. for laser-beam cutting to the absorber dimensions. It will be shipped afterwards to Chimiderouil for cleaning and then to Fibertecnic S.A. for storage and processing.

The produced absorbers will be shipped, in batches corresponding to one end-cap module, alternatively to Marseille and Madrid for module assembly at the two institutes.

For each produced absorber, a file with information on the lead-plate number (given at the time of thickness mapping), the results of the thickness mapping, the temperature-pressure cycle in the autoclave, mould number, results of the quality control, dates of the different subprocesses in the production, etc. will be recorded.

7.3 Read-out electrodes

7.3.1 Introduction

The read-out electrodes are flexible printed circuit boards folded with the same geometry as absorbers, with which they are interleaved. They consist of three layers of copper, insulated by two Kapton polyimide sheets. The external copper layers are connected to the high voltage needed for drifting the ionization electrons in the liquid-argon gap. The induced current is collected by capacitive coupling on the inner copper layer.

In their principle the electromagnetic end-cap calorimeter electrodes are similar to the electrodes of the barrel. Material characteristics, electrode production and test procedures have already been described in Section 6.3. Here we will focus only on the aspects specific to the EM end-cap geometry: the electrode design and the bending machine.

7.3.2 Design

The capability to produce large electrodes allows the pseudo-rapidity range of the outer wheel ($1.4 \le |\eta| \le 2.5$) to be covered with only one board. Figure 7-20 shows the overall dimensions of

the outer-wheel electrode before bending: 956 mm × 1445 mm. The inner wheel needs a smaller board: 869 mm × 533 mm (Figure 7-21).

Projective towers are defined in η by etching copper strips on the three copper layers. The corresponding segmentation is described in Section 7.1 and summarized in Tables 7-1 and 7-2. In order to protect preamplifiers from accidental sparking, the strips of the external copper layers are longitudinally split into pads connected by a resistive coating. Figure 7-20 depicts the active high-voltage layer of an outer electrode. Due to their different η segmentations the three longitudinal compartments are clearly visible. The depth of each was optimized for π^0 rejection (first compartment) and shower containment (second sampling). The first sampling ends after 6 X_0 of material crossed, including the material in front of the calorimeter, while the second stops at 24 X_0. Figure 7-21 shows the high-voltage layer of an inner wheel electrode. It contains only two longitudinal samplings, the boundary being at 24 X_0.

In the outer wheel, signals from the first compartment are routed to the front face of the detector. Except for $1.375 \leq |\eta| \leq 1.50$, signals from both second and third compartments are routed to the back face. In the inner wheel, all the signals are read out on the back face.

Technical constraints limit the width of the useful area of kapton to about 950 mm out of a maximum of 1000 mm. For this reason the outer electrode extensions, allowing for the positioning with respect to the bars and for the signal routing, are cut without reducing the active region. The inner electrode does not need such an adjustment. A notch is made on each corner of both kinds of electrode, in order to make them fit within the rings of the mechanical structure.

The width of the connection strips of the second sampling of the outer electrode is set to 2.5 mm for the signal layer, and 3 mm for the high-voltage layer. This width is large enough to minimize the strip inductance (about 17 nH), and has a small effect on the third sampling active region.
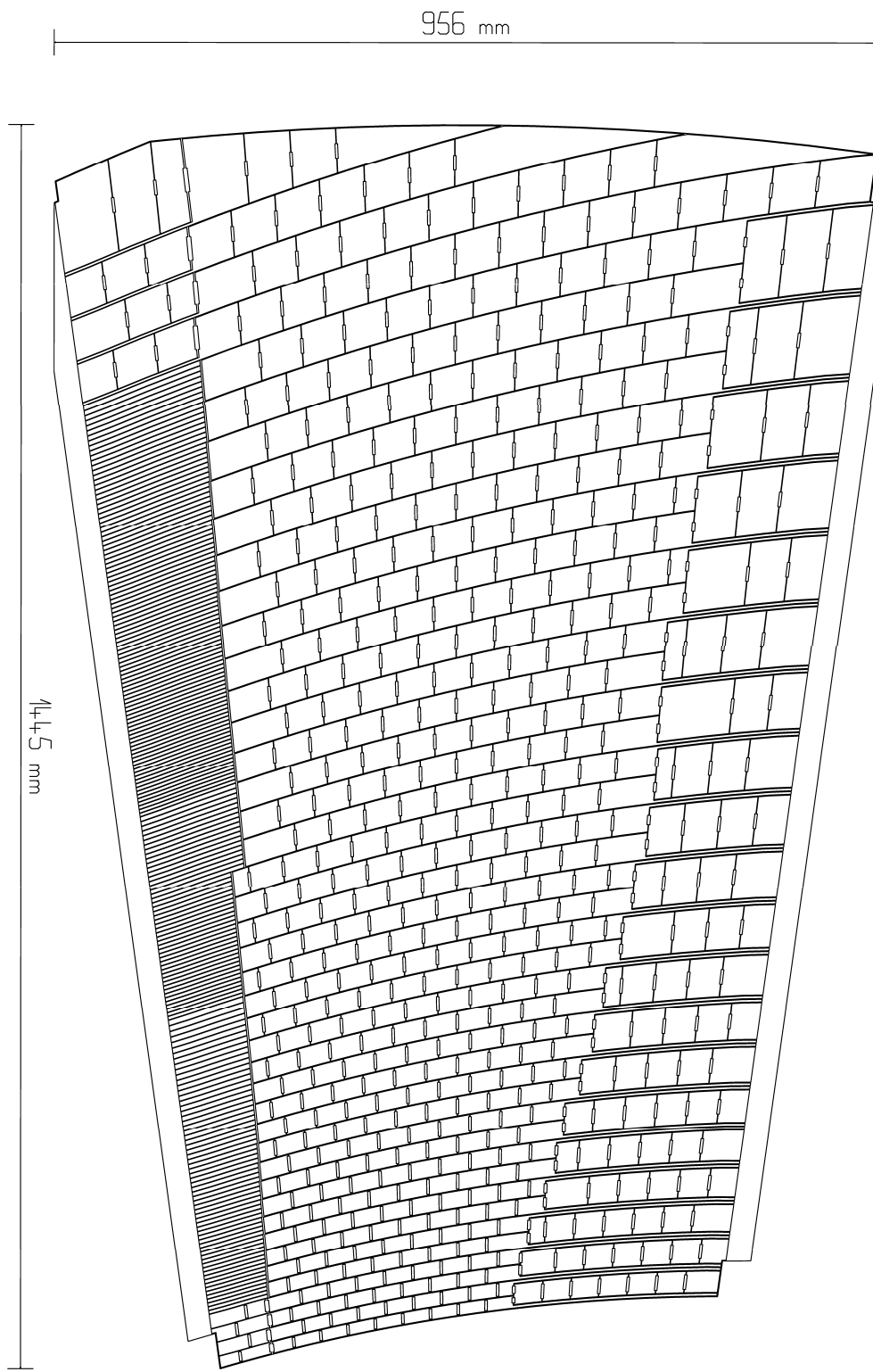
The resistive ink pads were optimized to minimize crosstalk between neighbouring channels (requiring high resistance values), and to minimize the high-voltage drop induced by the minimum bias pile-up events (requiring low resistance). A resistance value of 0.5 MΩ maintains a relative drift-velocity variation at the level of 10^{-3}.

Connectors are stapled on both flat edges of the outer electrodes and on the back only of the inner electrodes. As the signal layer is insulated by the two Kapton layers, cutouts are machined to make contacts on output and ground pads. Regions of the flat edges which are not used by connectors and ground distributions are strengthened with copper. This allows easier handling and precise hole-making, for indexing and fixing purposes.
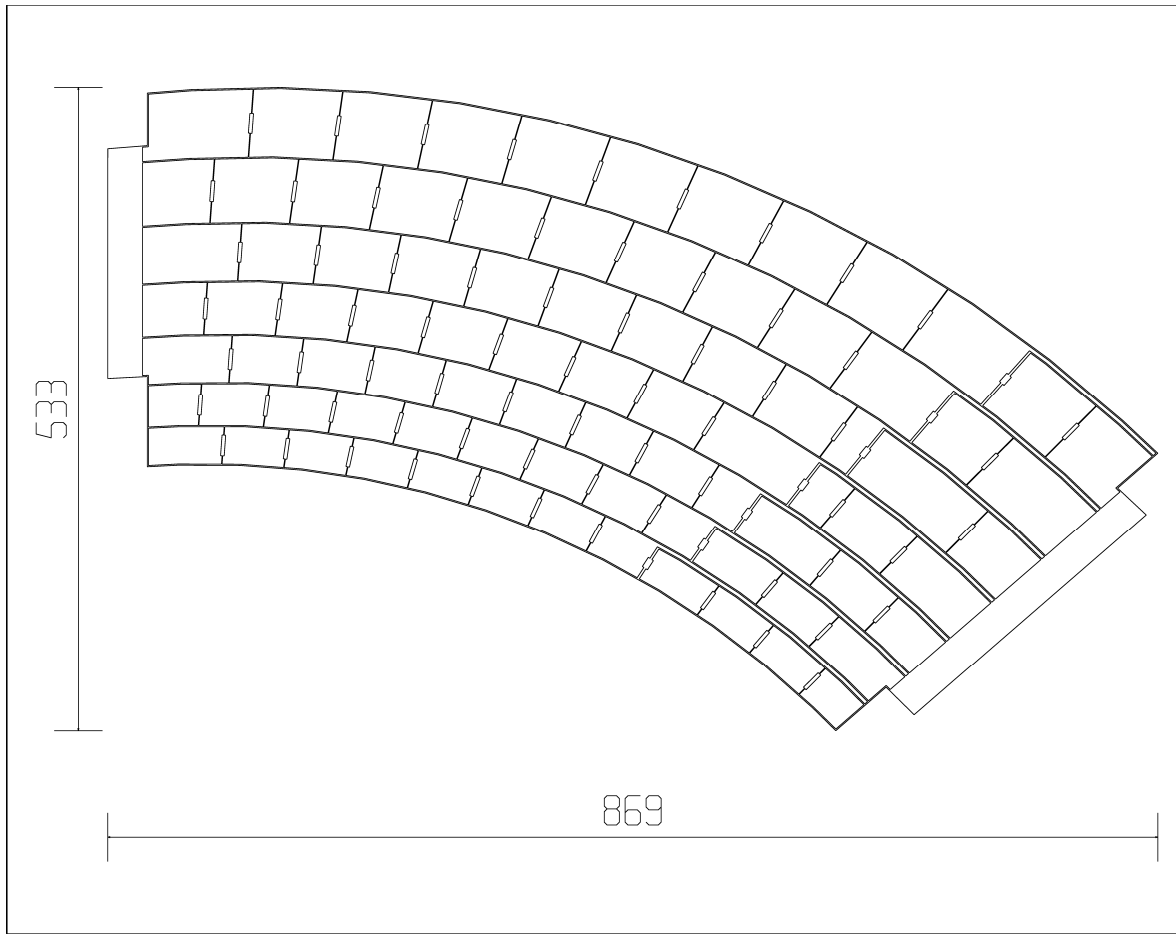
7.3.3 Bending press

The variable folding angle makes the bending of the end-cap electrodes rather complex: before bending, the folding lines are not parallel. The bending press has to fulfil the following requirements:

- Match the absorber geometry: the electrode shape is identical to the shape of the neutral fibre of the absorbers, implying the same variation of the folding angle, 3 mm and 3.25 mm curvature radius for the outer and inner electrodes respectively. As electrodes are centred between absorbers by honeycomb spacers the main constraint applies to the curvature radius. A folding angle close to its nominal value facilitates the module stacking procedure.

- Comply with the liquid-argon gap requirements: the folds have to be defined with an accuracy of 150 μm.

Figure 7-20 High-voltage layer of an electrode of the outer wheel. The signal routing strips and the connectors which are located on both front and back (i.e. left and right) extensions are not drawn here.

Figure 7-21 High-voltage layer of an electrode of the inner wheel.

- Avoid any damage to the electrodes, especially the resistive coating. Studies have shown that a bending knife sliding on the electrode surface induces strong stresses which may tear out some resistive ink pads.

A multi-knife bending press similar to the one used for the absorbers is not appropriate for the electrodes. The movement of the knives cannot be defined by the electrodes themselves as is the case for the absorbers. Therefore, such a machine would require a complex knife-steering system, which would be rather expensive. For this reason, the bending machine will probably consist in a single knife associated with a positioning table. Two precisely machined knives are needed, one for each electrode kind. The knife will push the electrode against an elastic support, such as a rubber tube or the table itself. This way the electrode fits the shape of the knife without any longitudinal stresses, and the fold is symmetrical with respect to the knife axis. This method, which avoids any sliding of the knife on the electrode, requires a precise positioning of each fold before bending. This could be achieved with two indexing holes per fold drilled in extra material added on both edges of each electrode. This extra material then has to be removed.

7.3.4 Interface with absorbers and bars
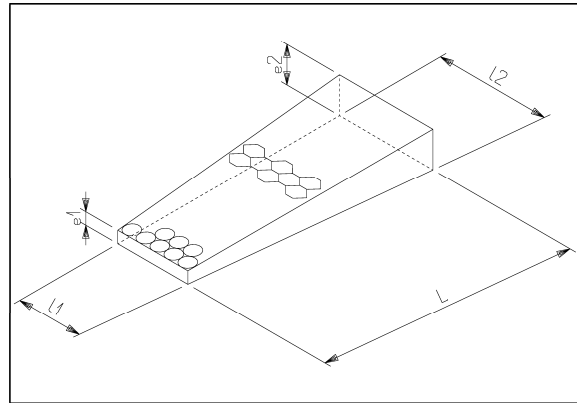
Electrodes in both wheels are indexed to the absorber in the vicinity of the $\eta = 2.5$ crack, so the differential thermal shrinkage of the electrode with respect to the absorber will not open this crack. A circular hole in the lower region (near $\eta = 2.5$) of the front extension of the big electrode is used to index the electrode to the absorber bar by means of a pin. Oblong holes in the upper

region of the same edge, and the lower region of the backward edge will allow safe shrinkage of the electrode in both directions. A symmetrical solution with respect to the $\eta = 2.5$ crack is applied for the indexing of each inner electrode.
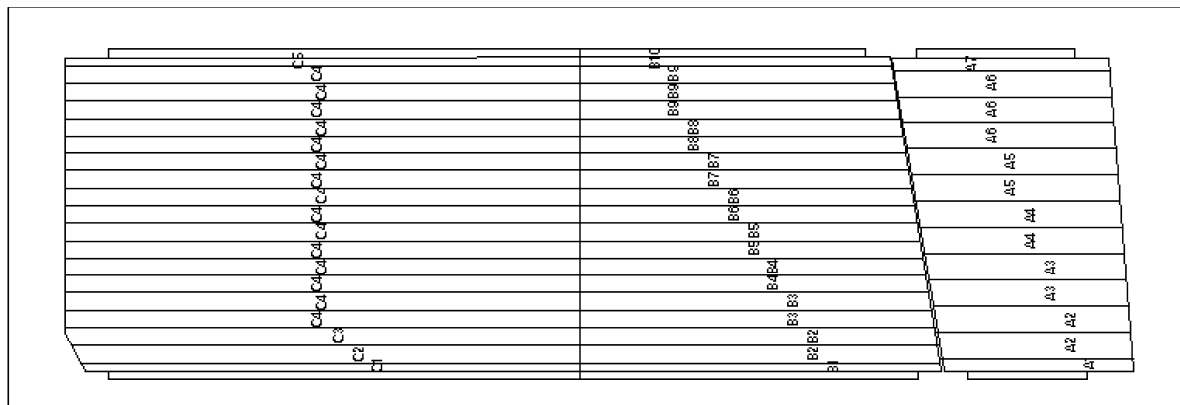
The absorber bars are designed to keep a constant gap between two adjacent bars along the η direction. This gap (0.8 mm for both wheels) leaves enough free space to avoid any friction of the electrodes on the bars during the thermal shrinkage. Notches (1.2 mm × 7 mm) are provided on these longitudinal bars for connectors. They keep these connectors in place when the motherboards are inserted.

7.3.5 Spacers

The spacers keep the electrodes centred between the absorbers. They consist of strips of honeycomb (NOMEX: paper impregnated with phenolic resin) laid in the flat parts of the accordion, on both sides of the electrodes. This material can be cut with linearly-variable thickness. In the outer wheel, in order to accommodate the nonlinearity (deviation up to 250 µm) of the liquid-argon gap variation, two strips are used to cover the overall length of the absorber (Figure 7-23). The deviation is then smaller than 40 µm. The width of the honeycomb strips varies according to the width of the corresponding flat sections. Figure 7-22 shows the parameters necessary

Figure 7-22 Shape of a honeycomb spacer strip.

to define the shape of each strip. Due to the projective geometry of the wheels, twenty-two different shapes of strip are needed (Figure 7-23). To reduce the machining cost they are grouped in three classes of same slope and same width variation. Inside a class the strips only differ in terms of the position of their extremities. The most stringent tolerance is given on the thickness: +0.0 mm and −0.1 mm.

Figure 7-23 Twenty-two different strips are needed in the EM end-cap. The three classes of strip (see text) are labelled A, B and C.

7.4 End-cap presampler

In spite of large efforts to optimize the geometry of both barrel and end-cap cryostats, the amount of dead material (inner detector, cables, cryostat walls, services, etc.) in front of the EM end-cap is equivalent to about 3-4 X_0 in the region $1.50 \leq |\eta| \leq 1.80$. This degrades the energy resolution of the calorimeter, resulting in a sampling term larger than 20% for electrons. Several attempts were made to recover the energy resolution by modifying the EM end-cap calorimeter design, but simulations ([7-8]) showed that an additional device is required. For this reason it was recently decided (September 1996) to include a presampler in the end-cap region covering $1.50 \leq |\eta| \leq 1.80$. The granularity of this device is the same as in the barrel region: $\Delta\eta \times \Delta\phi = 0.025 \times (2\pi/64)$. This segmentation corresponds to 768 channels per end-cap, compatible with the number of free connectors available in the end-cap feedthroughs.

A 5 mm active liquid argon layer would give a sufficient signal/noise ratio: the ionisation signal from electron showers after 3 X_0 of material corresponds to several tens of mips, while the expected noise level is only a few mips. Mechanical studies have shown that a 10 mm thick device can be housed in a notch in the cold wall of the end-cap cryostat (Chapter 5). The presampler is thus located at 3625 mm from the interaction point. The external radius of the active volume is 1700 mm, and the internal radius is 1232 mm.

As the end-cap presampler was proposed only recently, a complete design study is not available yet. Two options are considered. The base line option uses the same technique as in the barrel region. Electrodes, perpendicular to the front face of the EM end-cap calorimeter, are arranged in concentric layers around the beam axis. The electrodes are multi-layered glass-fiber-epoxy printed boards. The cathodes are copper-plated on both sides. The anodes contain three layers of copper. A positive high voltage is applied to the external layers, while the signal is read-out by capacitive coupling to the internal layer. The gap between the electrodes is kept to 2 mm everywhere, for a 2 kV high voltage supply. The electrodes are glued, using prepreg, onto glass-fibre-epoxy boards defining the front and back faces of the detector. The active part of the electrodes would be 6 mm high, while the total thickness of the presampler would be 10 mm including the cables. The η segmentation is obtained by ganging the appropriate number of anodes. Figure 7-24 indicates the number of elementary cells (4 mm wide) constituting each read-out cell. The constant gap between the electrodes does not allow to exactly match the $\Delta\eta = 0.025$ segmentation, but the discrepancy is always smaller than $\delta\eta = 0.001$. The presampler consists of 32 azimuthal sectors (Figure 7-24), with 117 electrodes per sector. Each sector is fixed directly on the cold wall of the cryostat. The crack between two modules is 2 mm

In the other option the active liquid argon layer ($4 \div 5$ mm) will be defined by three electrodes parallel to the front face of the EM end-cap calorimeter. The two external electrodes (cathodes) are made of single sided copper plated glass-fibre-epoxy boards. The structure of the anode is similar to the read-out electrodes of the EM calorimeters. The segmentation is achieved by etching the copper layers, in concentric strips.

Both options have to be studied in detail: energy deposit simulation, signal weighting, cell capacitance, noise, mechanics, etc. The choice will be made on the basis of the performances and the cost.
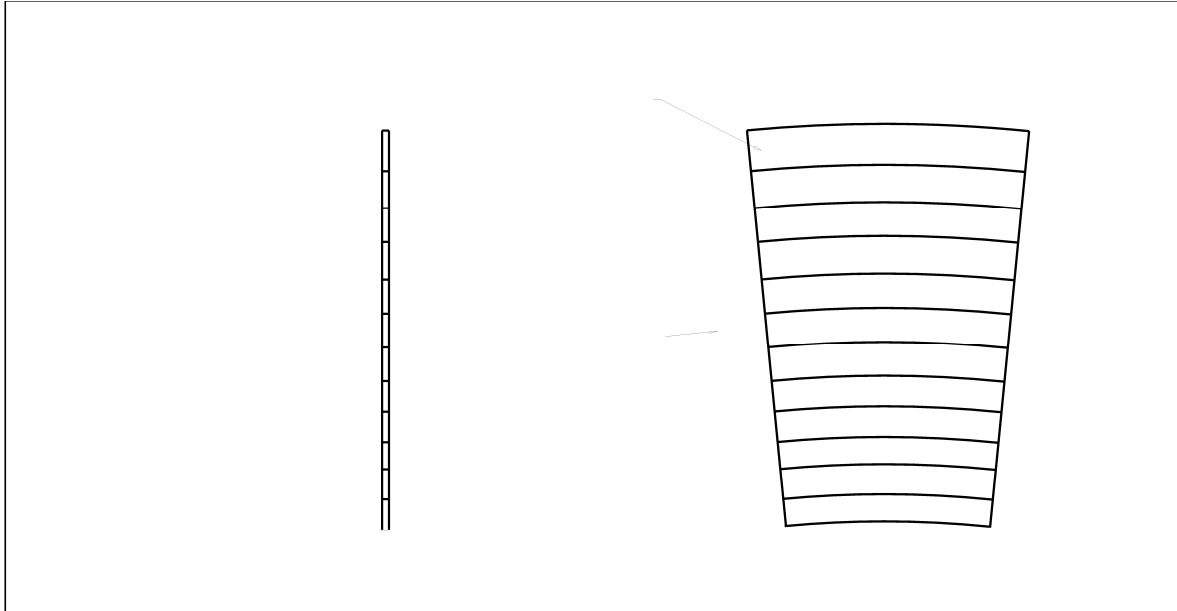
Figure 7-24 Schematic design of an end-cap presampler module.

7.5 Structure

7.5.1 Requirements

The main function of the structure is to hold the detector both outside and inside the cryostat, at temperatures ranging from room temperature down to liquid-argon temperature. This support function has to be provided not only for the detector as a whole but also for each module. The structure has also to guarantee the geometry and the position of the end-cap calorimeter with respect to the beams and the other subdetectors of ATLAS. Simulations have shown, for example, that the maximum deviation with respect to the ideal cylindrical shape must be smaller than 1.5 mm. For the energy resolution it is also essential to control the gap thickness everywhere in the calorimeter. To keep the constant term well below the target value (0.7%), the gap variation must be smaller than 50 μm. It is also mandatory that the structure does not introduce too much dead material, especially in front of the precision region (1.5 $\leq$ | η | $\leq$ 2.4).

Some of the other constraints on the structure come from the life cycle of the modules. The absorbers are connected to the structure, which should be therefore designed to ease absorber stacking during the module building process. The structure has to hold each module during the storage, handling and transport operations, as well as during the cold tests, and for some modules during the beam tests. As each end-cap calorimeter consists of two coaxial elements, the structure must bind these elements together with as small a crack as possible: the simulations were performed assuming a crack width of 3 mm. The shape of each module must be guaranteed during all the operations it will have to undergo until it is inserted in the full wheel.
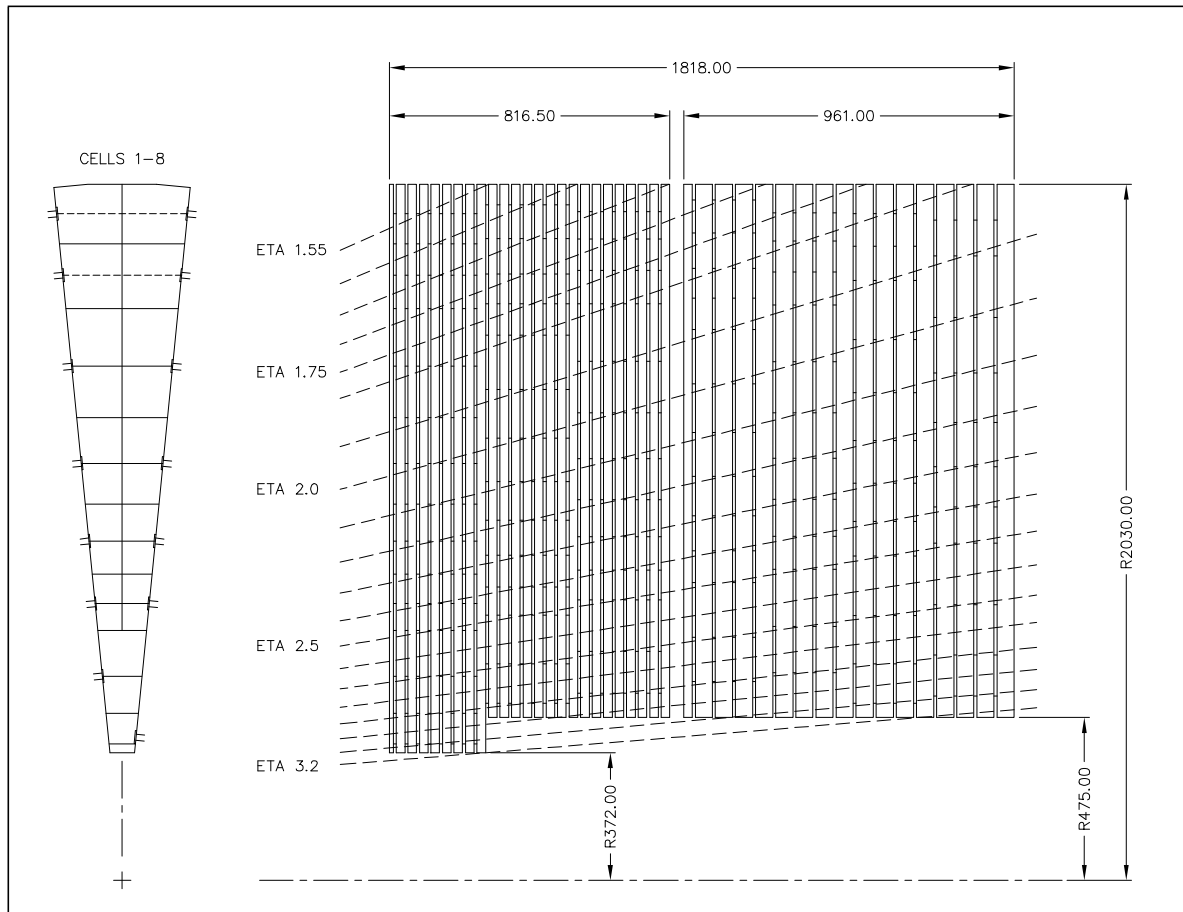
The structure will be used to form a full wheel made of eight modules. In order to achieve the largest flexibility during this phase these modules have to be identical. In the cryostat the detector is supported by two rails, to which the structure has to transfer the weight of the detector (about 24 tons). The corresponding parts, breaking the ϕ-symmetry of the detector, have to be independent of the modules. The wheel assembly will be made in a horizontal position. The wheel will be rotated in a vertical position to be inserted into the cryostat. During the cooling

Adobe's PostScript Language Reference Manual, 2nd Edition, section H.2.4
says your EPS file is not valid, as it calls setglobal

8 The hadronic end-cap calorimeter

8.1 Introduction

The hadronic end-cap calorimeter (HEC) is designed [8-1] to provide coverage for hadronic showers in the range $1.5 < \eta < 3.2$ (see Figure 8-1). The HEC detector elements are located in the

Figure 8-1 Schematic r-z and r-ϕ view of the hadronic end-cap calorimeter.
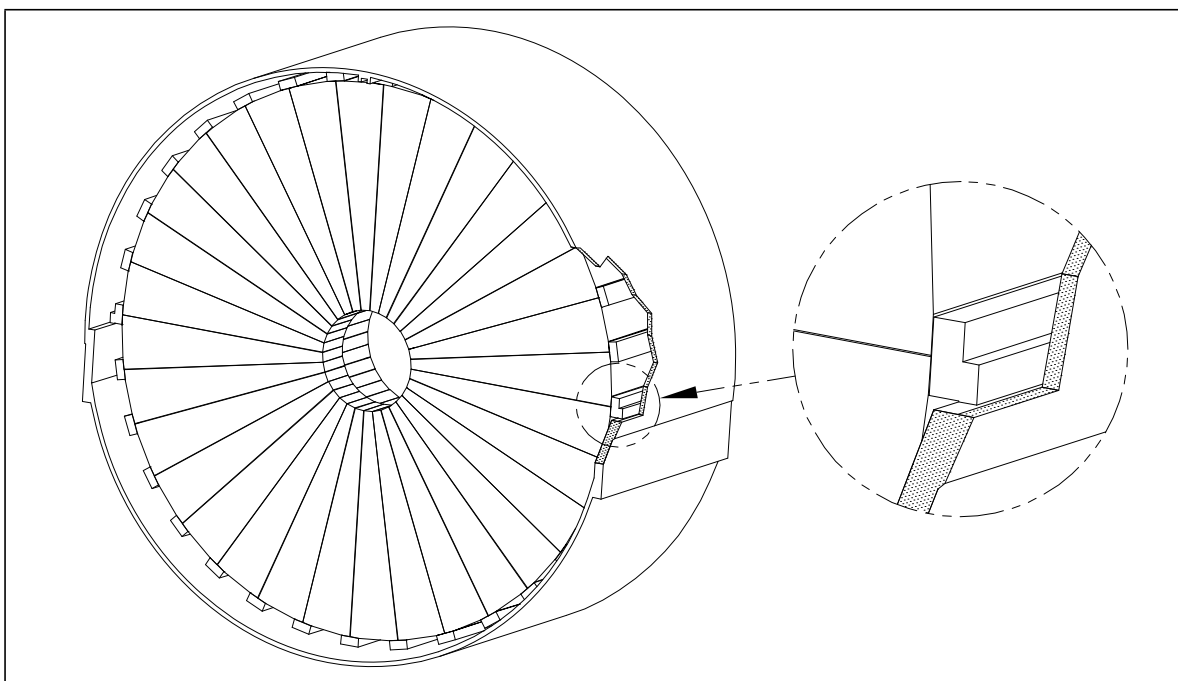
end-cap cryostats at either end of the ATLAS tracking volume. They share the cryostats with the EMEC and the FCAL detectors. The HEC sits behind the EMEC and is completely shadowed by it. The boundary between the HEC and the FCAL is on a cylinder of radius 0.475 m. Thus the η boundary between the two detectors varies as a function of z.

The HEC is a liquid argon (LAr) sampling calorimeter with copper-plate absorbers. This technology was selected as it allows a simple mechanical design to be produced that is radiation resistant and covers the required area in a cost-effective way. The gaps between the copper plates are instrumented with a read-out structure forming an electrostatic transformer (EST). This structure optimizes the signal-to-noise ratio while reducing the high-voltage requirement and ionization pile-up, and limiting the effect of failure modes such as high-voltage sparks and shorts [8-2]. The signals from the EST are amplified and summed employing the concept of "active pads": the signals from two consecutive pads are fed into a separate amplifier (based on

GaAs electronics) mounted on the outer radius of the HEC. The use of cryogenic GaAs preamplifiers provides the optimum signal-to-noise ratio for the HEC. An important aspect of the HEC is its ability to detect muons, and to measure any radiative energy loss.

8.2 Global engineering design

The HEC consists of four doughnut-shaped wheels, two in each end-cap cryostat (see Figure 8-2). The dimensions of the HEC detectors are provided in Table 8-1. The HEC modules

Figure 8-2 Three dimensional schematic view of the wheel and the rail system used to support the hadronic end-cap calorimeter.

Table 8-1 Locations and dimensions of the hadronic end-cap calorimeter.

Parameter	Value
Z position of front of HEC	4,262 mm
Z position of rear of HEC	6,120 mm
Outer radius of HEC	2,090 mm
Clearance between HEC and FCAL	10 mm
Outer radius of copper	2,030 mm
Inner radius of copper:	
Plates 1-9 front module	372 mm
All other plates	475 mm
Gap between copper of HEC1 and HEC2 wheels	40 mm
Clearance between HEC1 and HEC2 wheels	10 mm

sit on rails, shared with the EMEC, in the end-cap cryostat. Each wheel is made of 32 identical modules (see Figure 8-i). The dimensions for the HEC wheels are given in Table 8-2 .

Table 8-2 HEC wheel parameters.

Parameter	HEC1	HEC2
Number of wheels	2	2
Weight of wheels	67,300 kg	89,900 kg
Number of modules per wheel	32	32
Gap between modules in azimuth	2 mm	2 mm

Each module of the front wheel (HEC1) is made with twenty-four 8.5 mm inter-plate gaps read out in two read-out depths. The first depth is comprised of the front 8 gaps and the second of the rear 16 gaps. The front plate of the front module is a 12.5 mm copper plate and the remaining 24 plates are 25 mm copper. The rear wheel (HEC2) modules are each made with sixteen 8.5 mm gaps read out into a single read-out segment. The front plate of the rear module is a 25 mm copper plate and the remaining 16 plates are 50 mm copper. All plates are machined to meet the required flatness and thickness tolerances. The parameters for the modules are provided in Table 8-3 and a cutaway schematic of the module structure is provided in Figure 8-ii.

The structural strength of the front and rear modules is maintained by seven 12 mm and 16 mm stainless steel tie rods, respectively, that pass through the plates and are bolted down with a tension such that the minimum pressure holding the plates together is equivalent to three times the weight of the module. Annular spacers on the tie rods maintain the 8.5 mm gaps. In the front modules these spacers have a 17 mm outside diameter, and in the rear modules a 23 mm outside diameter. All of the plates are "quarter-hard copper" to maintain the structural strength of the HEC1. That is, they have been cold rolled and had their thickness reduced in the process by 10.9% [8-3]. This cold-rolled hardened copper has a yield strength of about 205 MPa (about three times that of hot-rolled copper), and is easier to machine and less prone to damage in handling than softer hot-rolled copper. This allows us to distribute the tension in the tie rods plus the weight of the module on the spacers bearing on the copper in the front(rear) modules without exceeding 2/3 of the yield strength of the material. The slight increase in the spacer diameter in the rear module is to allow enough force to be applied on a minimum three spacers to flatten the stiffer 50 mm copper plates.

Each of the boards of the read-out structure in the inter-plate gap has seven holes that encompass the tie rods and spacers (see Figure 8-3).Thus the position of the read-out structure is fixed by the location of the tie rods. The components are punched with oval holes to allow for expansion of these elements relative to the copper during cool-down. The orientation of the oval holes (see Figure 8-3) is such that the most central rods on the plate define the radial position of the foil while the other rods define the ϕ-orientation of the foil. The extent of the length of the ovals is set by the relative thermal-expansion coefficient between the copper and the adjacent board, the maximum temperature difference during cool down (estimated to be about 2˚K), the mechanical tolerances, and the maximum distance between the slots. These dimensions are summarized in Table 8-4.

The space between the boards is maintained using a honeycomb sheet, which is also captured by the seven tie rods.
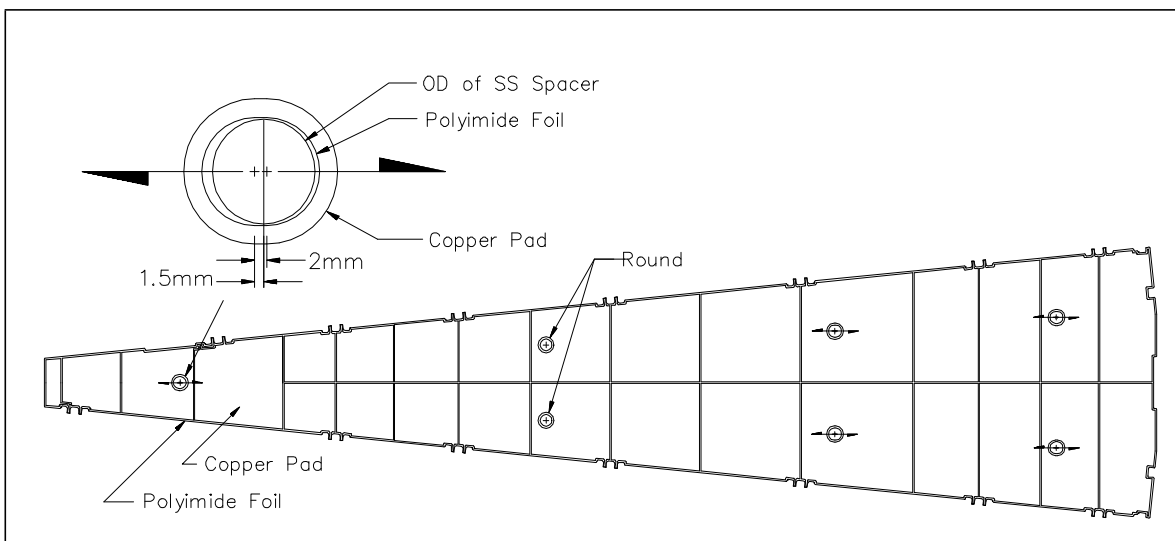
The individual modules are self-contained with their own preamplifiers and high-voltage lines. The GaAs preamplifiers and summing networks are located at the outer radius of the modules.

Table 8-3 Module parameters.

Parameter	Front modules	Rear modules
Number of copper plates	25	17
Thickness of first plates in module	12.5 mm	25.0 mm
Thickness of standard plates in module	25.0 mm	50.0 mm
Weight of standard plates	90 kg	180 kg
Number of tie rods per module	7	7
Tie rod diameter	12 mm	16 mm
Outside diameter of spacers for 8.5 mm read-out gaps	17 mm	23 mm
Module weight	2103 kg	2811 kg
Distance from copper plate to copper plate	8.500 mm	8.500 mm
Argon gaps	1.954 mm	1.954 mm
Honeycomb thickness	1.774 mm	1.774 mm
Thickness of PAD and EST boards	0.685 mm	0.685 mm
Number of read-out gaps	8+16 = 24	16
Number of read-out segments	2	1
Number of read-out towers	24+23 = 47	22
Number of preamplifier boards	3	2
Number of preamplifier chips	42	28
Number of read-out channels	24+24 = 48	24
Number of low-voltage lines	12	8
Number of calibration distribution boards	1	1
Number of calibration lines	28	16
Number of high-voltage lines	4+4 = 8	4

The signals from pairs of electrodes are transmitted through 50 Ω lines on the side of the module to the preamplifiers [8-4]. Examples of the type of notches on the side of each module that will house the signal and high-voltage wiring can be seen in the photograph of the HEC prototype module shown in Figure 8-i.

The modules are to be stacked in laboratories in Canada, Germany and Russia, warm tested on site and shipped to CERN for cold testing and subsequent assembly into wheels. Modules will be stacked and assembled under 10,000 particles per cubic foot clean-room conditions. Each module is light and robust enough to be transported by conventional means. Experience with our recent full prototype has shown that modules survived shipping by road and through sea ports in a conventional crate without shock absorbers. For series modules, shipping will be by container in shock-absorbing frames. Stringent capacitance tests carried out at CERN upon receipt are foreseen to monitor any changes resulting from shipping.

Figure 8-3 Profile of a typical read-out board, showing the oval holes in the board.

Table 8-4 Slot dimensions used in electrodes.

Module Length (mm)	Front module		Rear module	
	radial	azimuthal	radial	azimuthal
Spacer	17.0	17.0	23	23
Inner single slot	19.5	17.5	25.5	23.5
Inner double slot	17.5	17.5	23.5	25.5
Middle double slot	19.5	17.5	25.5	23.5
Outer double slot	19.5	17.5	25.5	23.5
Percentage dead area	0.4%		0.8%	

The following testing procedures are being considered and the feasibility investigated. One in eight modules will be tested in liquid argon in the beam at CERN. The remaining modules will be cooled in liquid nitrogen or argon, and have their tower capacitance values and high-voltage capability checked. The structural integrities of the individual modules and of the wheel have been studied in detail. Extensive engineering design effort has been applied to produce an inexpensive conservative design that meets the physics requirements.

8.3 Copper absorbers

8.3.1 Geometry and material

The copper plates are designed in two radial sizes. The first nine plates of the modules of HEC1, which do not encompass the FCAL, are larger than all other plates. The plates will be cut and finished in machine shops in Canada and Russia. The Canadians will use a numerically controlled milling machine, while the Russians will use conventional milling machines. All plates have notches on both sides for wiring. To keep machining costs to a minimum, the module is designed to have a minimum number of signal-cable notches, all with the same width. For this

reason each notch carries the signal lines from two sets of radially adjacent electrodes. Seven different copper-plate profiles are required.

Each plate has seven holes in it to accommodate the tie rods. The material of the plate is quarter-hard copper. In order to limit the possibility of producing copper slivers when attaching fasteners to the copper plates, threaded bolt holes are equipped with stainless-steel threaded inserts at all mechanical fastening locations.

8.3.2 Tolerances

The plate thickness tolerance is 0.050 mm, the flatness tolerance is 0.5 mm for the 25 mm plates and 0.25 mm for the stiffer 50 mm plates. The plate thickness and flatness tolerances are those that are obtained when a rolled plate is faced using a milling machine. The plate thickness tolerance comes from the engineering requirement that the stack height variations are small enough for the outer inter-module clamping bar to be installed. This tolerance gives rise to a variation in sampling frequency (number of samplings per interaction length) with an r.m.s. of 0.1% from each plate. For the set of plates that make up a read-out segment, the sampling frequency variation will be reduced by an amount that will depend on how correlated the plate thicknesses are with respect to each other. Clearly, if they are not correlated, the variation will be reduced by the square root of the number of plates in the depth under consideration; if they are fully correlated the sampling frequency variation will still have an r.m.s. of 0.1%. The actual situation will lie between these two extremes, and the sampling frequency variation will be below an r.m.s. of 0.1%. The sampling frequency is also affected by density variations that will depend on the composition of the copper in each batch of plates. The density of the copper obtained in North American industry is warranted by the supplier to be between 8.89 and 8.94 g/cm^3. This indicates that density variation is a similar source of sampling frequency variation as the plate thickness machining tolerances. The density will be the same for each melt, and one melt provides enough copper for about four modules. Thus, the density will be fully correlated between adjacent plates in most cases, and so will be monitored, along with the yield strength, for each copper plate shipment. The energy resolution of the calorimeter is required to have a constant term of less than 1%, and thus the plate thickness and density tolerances will not add significantly to the constant term.

The tightest constraints on the machining tolerances of the copper plates arise from the requirement to form a wheel with 2 mm inter-module gaps. By utilizing shims during the stacking process to align the copper plates within a module, the tolerance requirements on the plates have been relaxed enough to allow them to be manufactured on mills without numerical control.

8.3.3 Tooling and fabrication

Each copper plate weighs about 90 kg for the 25 mm plates and 180 kg for the 50 mm plates, and must be handled using a crane. To facilitate this operation two small dimples (about 1 cm in diameter and 0.5 cm deep) are machined on both inter-module plane edges of the plates. The plates can then be lifted in the horizontal orientation using two clamps that fit into the dimples. In this way the plate can be handled easily and safely during all operations: cleaning, inspection and stacking.

Rolled copper plates are purchased from the rolling mill in rough cut pie-shaped pieces that are machined into single plates. At the plate production facility the plate is faced on one side, removing the minimum of material. The plates and mill bed are then carefully cleaned, to ensure

no chips are present that can become embedded in the plates. After careful inspection of the cleaned surfaces, the plates are rotated and faced to the correct thickness, profiled, and featured. The stainless steel thread inserts are installed and checked for ease of bolt insertion and inspected for metal slivers.

8.3.4 Quality assurance

At the machining centre, the plate is cleaned, deburred, and tested in a go/no-go gauge for dimensional tolerances. This gauge checks the thickness, the flatness, the location of the holes for the tie rods, and the transverse plate dimensions. The plates are then cleaned and labelled on the side at the outer radius and packed for shipping. The labelling will include the plate serial number, copper shipment batch number, orientation and site of manufacture. For ease of handling two plates are shipped per crate, and the crates reused. The boxes will be marked with the plate stack layer number.

Upon receipt at the stacking location, each plate is first checked for mechanical tolerances. All edges are inspected for slivers. The cleanliness is inspected. If required the plate is further cleaned. The surface quality of each plate is checked by applying a high voltage between it and a reference plate. This is mainly to check for material embedded in the surface. The plate is weighed to check for any plate-to-plate density variations. The plate is then stored in the clean room ready for stacking.
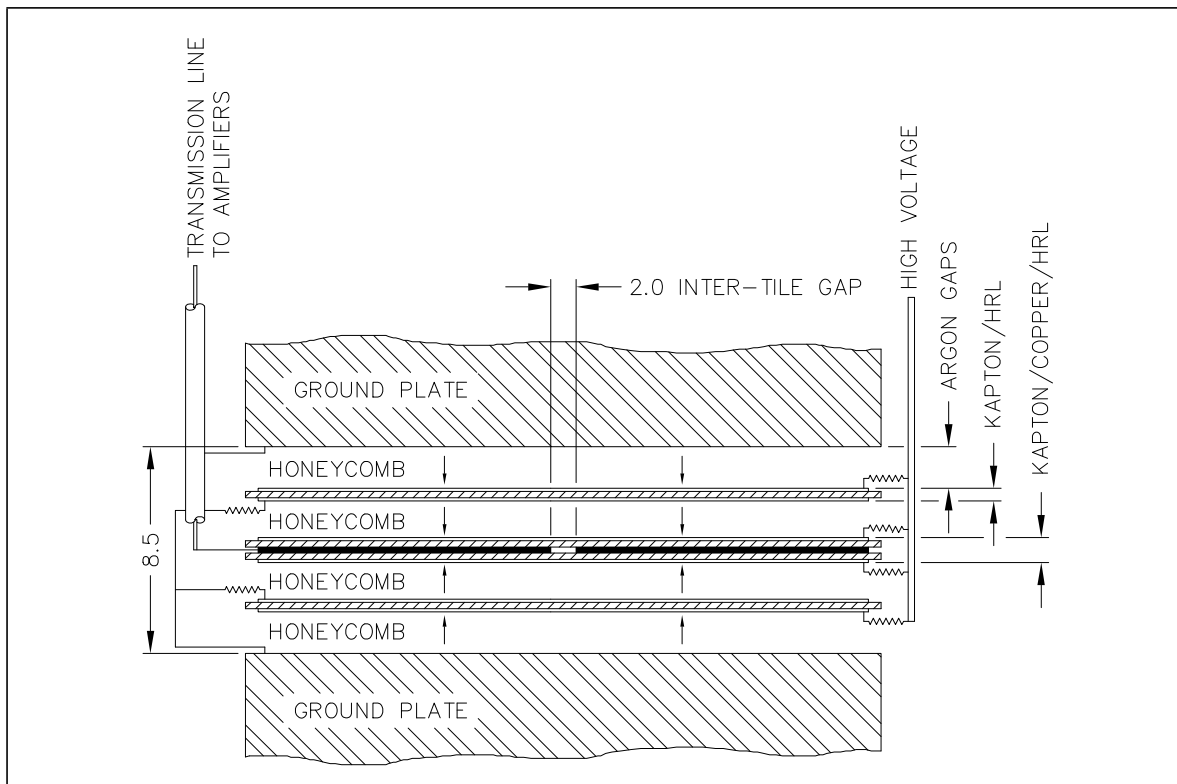
8.4 Read-out electrodes

8.4.1 Design considerations

The three boards in the 8.5 mm inter-plate gap (see Figure 8-4) are of two types: a central board that contains the read-out electrode pads (hereinafter referred to as the PAD board) and two boards that are part of the EST (referred to as EST boards). Each EST board is made of a layer of insulator sandwiched between two high resistive layers (HRL) [8-5]. The HRL material has a nominal resistivity of 0.5 MΩ/square on the side facing the PAD board and 1 MΩ/square on the side facing the copper absorber [8-6], [8-7]. The PAD board is made of 35 μm thick copper read-out electrode (see Figure 8-5 and Figure 8-6) sandwiched between two insulators. This is then covered on both outside faces with HRLs with a resistivity of 0.5 MΩ/square. The PAD board, together with the EST boards, completes the electrostatic transformer structure. The HRL resistivities are chosen to equalize the voltage drop across their surfaces due to the ionisation current. The higher resistivity of the layers facing the copper compensates for the lower resistance of the copper.

To arrive at a practical engineering design the following criteria were established:
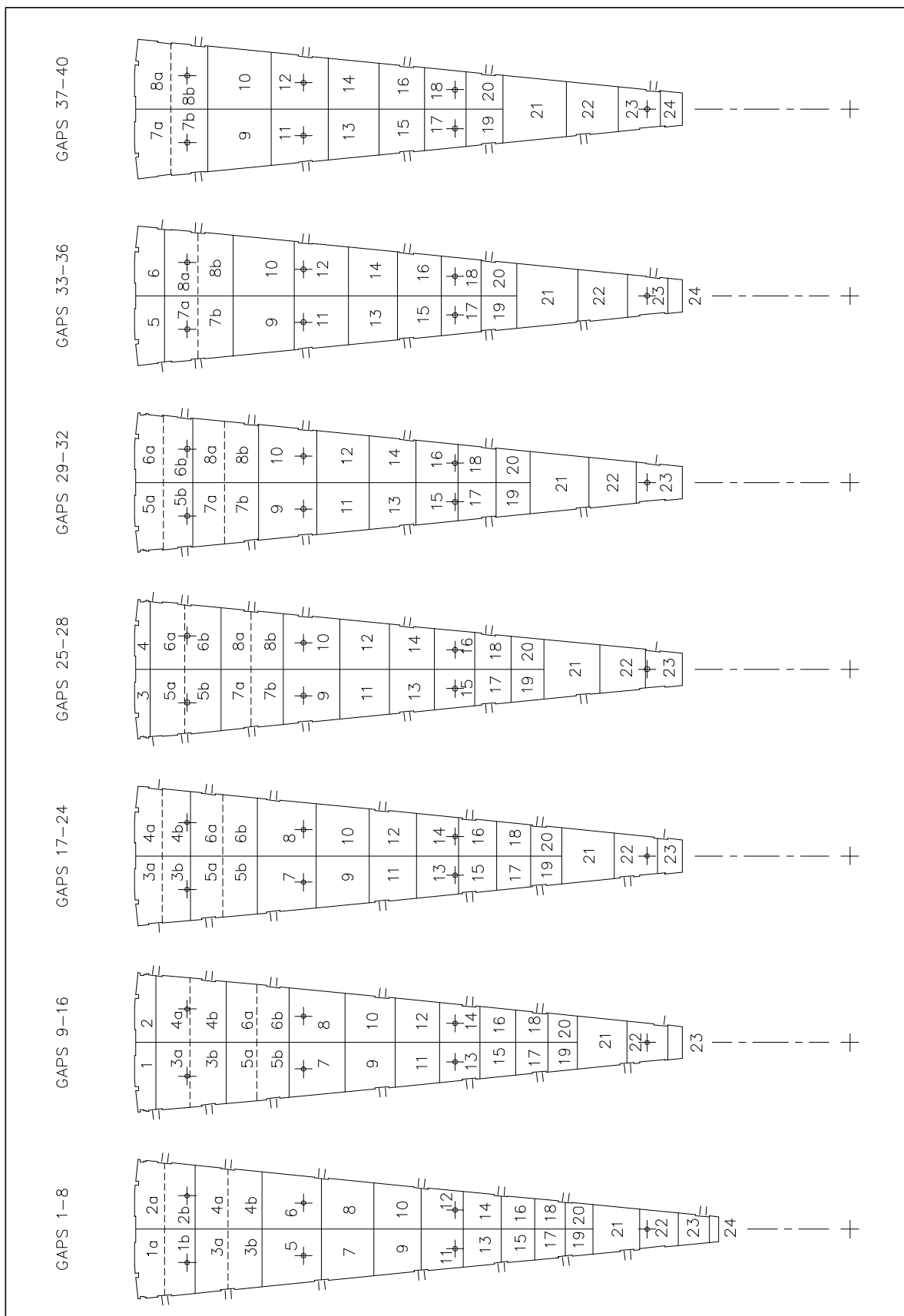
- Every board is symmetric in structure to prevent curling during cool down.

- Standard industrially available materials will be used.

- Polyimide (PI) will be used as the main insulator.

- Between any high voltage and ground potential at least two independent layers of insulator will be used. This severely limits the possibility that a problem area in one insulator will align with that in another, causing a short circuit.
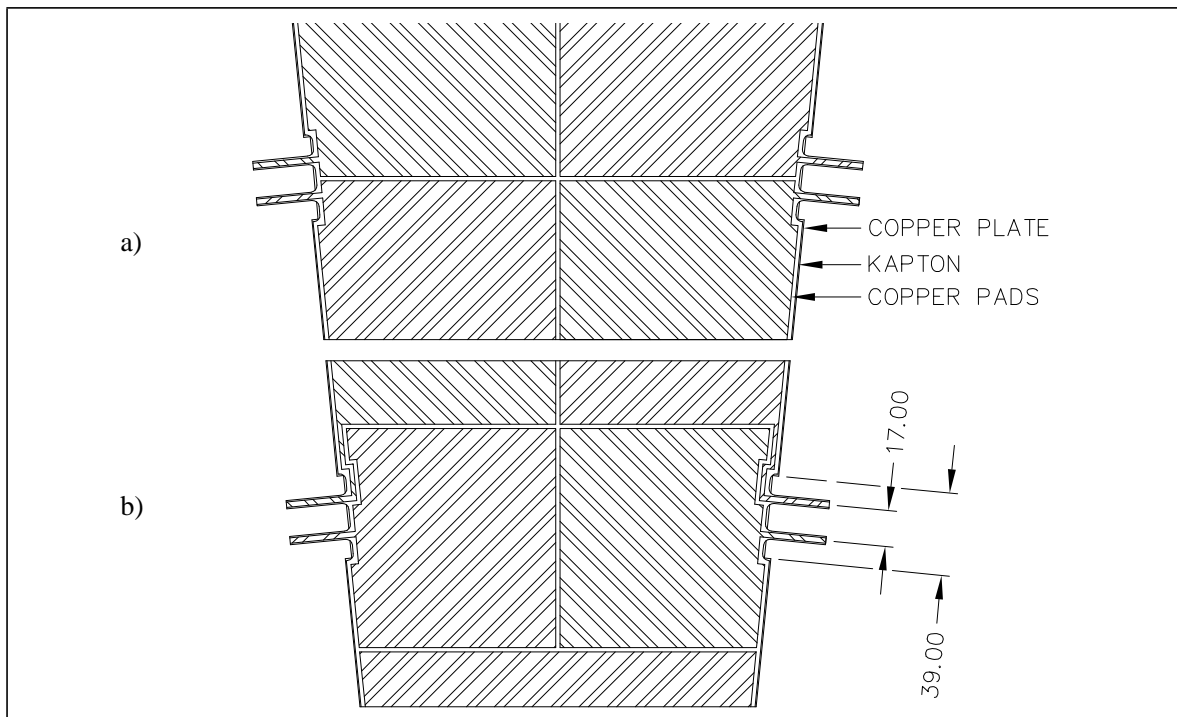
Figure 8-4 Schematic of the arrangement of the read-out structure in the 8.5 mm inter-plate gap.

- The maximum electric-field strength along the insulating surface between any two conducting surfaces at different potential must be 1000 V/mm.

- The field strength between two conducting surfaces through the insulating layer must be at most 20 V / μm.

- The nominal operating voltage is 2000 V, with a maximum of 2500 V.

- Signal and high-voltage connections must be easily disconnectable to facilitate stacking and (if necessary) unstacking of modules.

- No soldering on the assembled module.

- The resistivity of the HRL must be within ± 50% of the nominal value (0.5/1 MΩ/square).

- The conduction through the resistive surface must not decrease the signal by more than 0.3%.

- The copper of the PAD board must be able to withstand flexing during handling without developing cracks.

- The difference in the thermal-expansion coefficient between the copper and the electrode structure shall not exceed 10^{-5} K^{-1}.

Because Russian and Western industry have different standard PI thicknesses, glues, and copper clad-etching technologies, it is not possible to manufacture the same product in each country without exchanging materials. Purchasing non-standard thicknesses would increase costs drastically and potentially lower quality. It may be envisaged for mass production. However for module 0 this will not be necessary as two mildly different technologies for creating the HRL will be used that conform to the above specification and to the criterion that liquid argon gaps will have about the same size in both designs. These two technologies are carbon-loaded PI

Figure 8-5 Drawing of the seven PAD board electrode structures. Note that electrodes labelled a and b, and separated by dashed lines, are summed in the cold and read out as single towers.
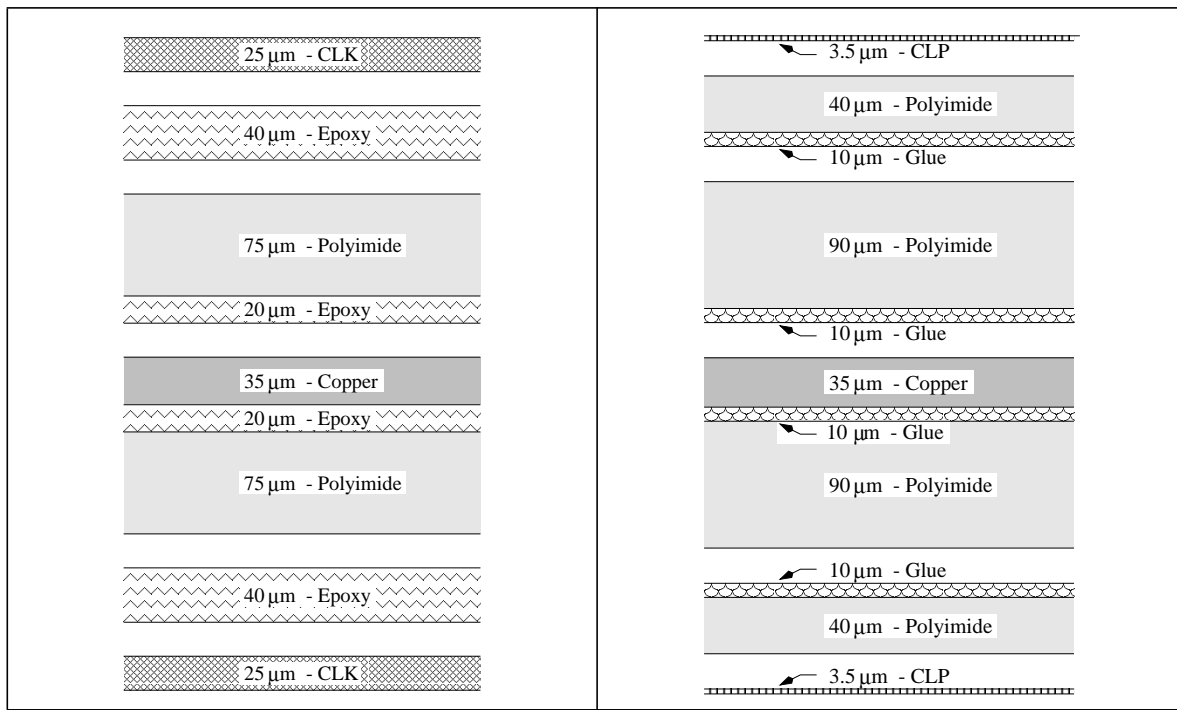
Figure 8-6 Drawing of a detail of the conceptual design of the electrode structures. The upper part a) shows the electrode arrangement when the slot is centred on the inter-electrode gap, while the lower plot b) shows the traces on the electrodes when the notch is not aligned with the inter-electrode gap.

glued onto the insulating PI (technology CLK), and carbon-loaded paint applied to the insulating PI (technology CLP). Both are being developed for module 0, as the carbon loaded PI has not been tested in a full module, while the painting procedure requires further development to make it suitable for series production. The cross-sections with suggested thickness through the PAD boards for the two technologies are shown in Figure 8-7 and Figure 8-8 for technologies CLK and CLP, respectively. For the EST boards the cross-sections are shown in Figure 8-9 and Figure 8-10. For series production either the resistive paint or carbon-loaded PI technology will be used. The thicknesses of the other components will also be finalized when this decision is made. This is especially important as each wheel of the HEC will be a combination of European and Canadian modules.
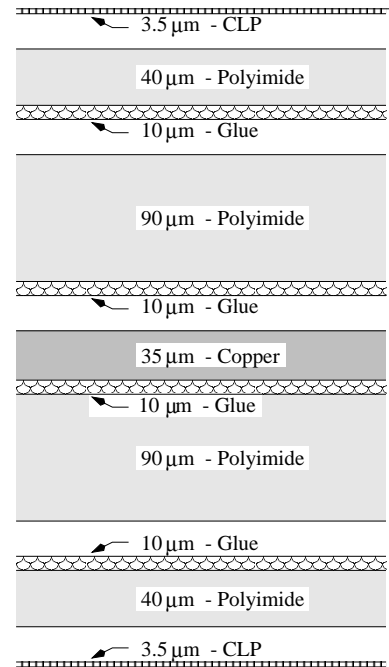
8.4.2 Technology CLK: fabrication

The PAD boards and EST boards are made of only four primary components, namely PI, epoxy glue, annealed copper, and carbon-loaded PI. Figure 8-7 and Figure 8-9 show the structure of the PAD boards and EST boards, along with the premanufactured composite sheet materials used in the assembly. As there are several types of epoxy and PI, and to simplify product qualification, all of these materials except the carbon-loaded PI are purchased from a single supplier.
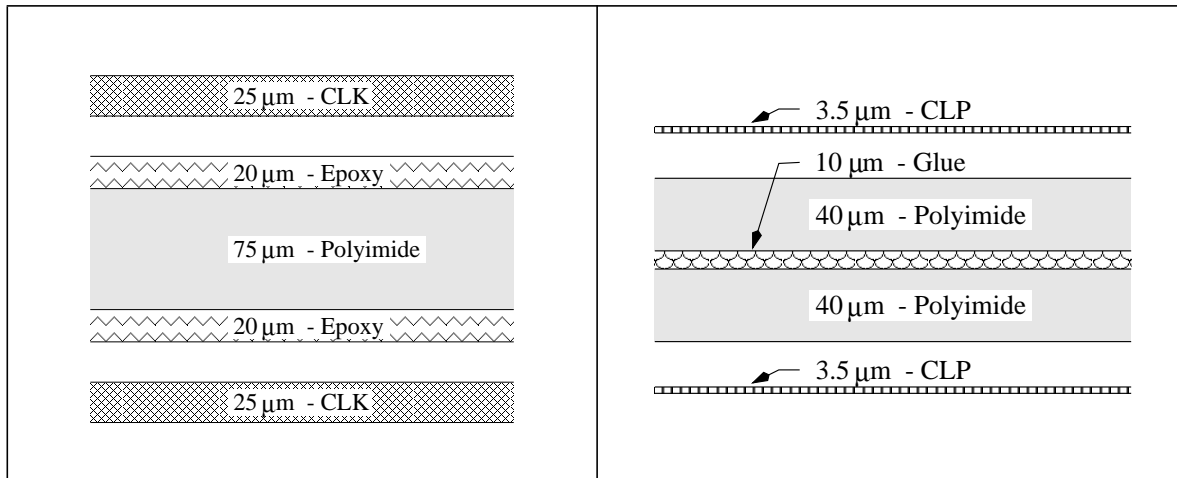
The carbon-loaded PI is a product used extensively in satellites to protect sensitive electronics. The satellite requirements are for a resistivity within plus or minus two orders of magnitude. The manufacturer (see Ref. [8-8]) has recently improved the process and is able to provide us with a product that varies 30% in resistivity, well within our tolerance of 50%. The product is purchased in 25 μm thickness and has mechanical properties similar to PI. The volume resistivi-
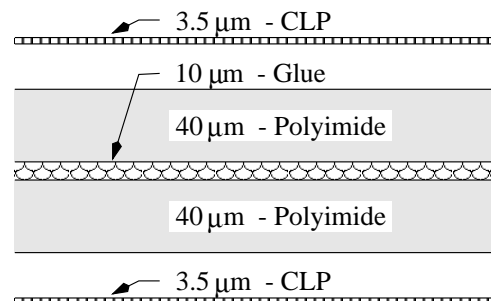
Figure 8-7   Cross-section with proposed thickness, PAD board technology CLK.

Figure 8-8   Cross-section with proposed thickness, PAD board technology CLP.

Figure 8-9   Cross-section with proposed thickness, EST board technology CLK.
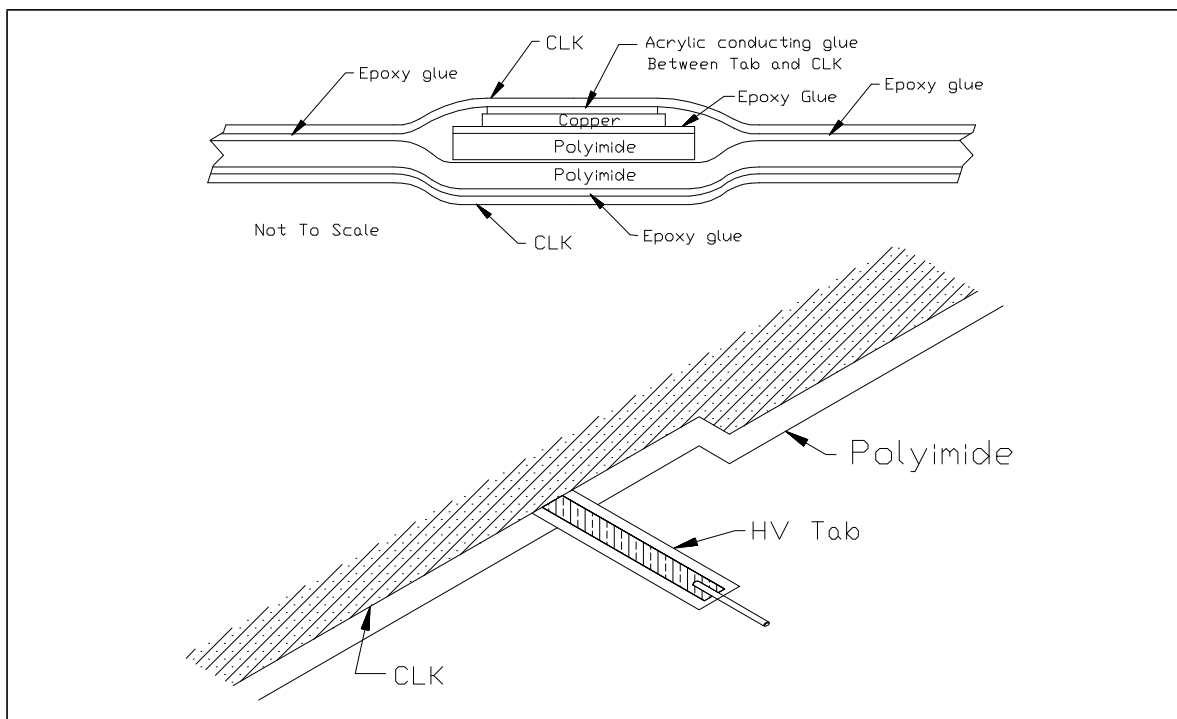
Figure 8-10   Cross-section with proposed thickness, EST board technology CLP.

ty of the material is about 24 kΩ mm, which gives rise to a small resistance in series with the capacitance of the gap. This resistance decreases the signal by less than 0.3%.

The high-voltage and ground connections to the resistive PI are made by inserting a small copper-clad PI tab between the resistive PI and the first glue layer (see Figure 8-11).

A small sheet of conductive acrylic glue is placed between the tab and the resistive PI. While the connection does not depend on this conductive glue, it does provide a conservatively engineered solution.

Figure 8-11 Sketch of the high-voltage connection. A pin is soldered to the HV tab to connect to the HV strip line connector (see Figure 8-17).

The production of the PAD boards begins by etching the copper of the copper/epoxy/PI sandwich with the read-out electrode design. The copper/epoxy/PI material is purchased in 500 mm wide rolls. Particular attention is paid to cleaning the boards after etching. If not removed, residual copper and chemicals will become sandwiched in the final PAD board and can lead to deterioration of its electrical stand-off properties.

Each of the six layers that make up the PAD board is first cut approximately to size. Temporary reference holes are punched using the same punch in all six layers. These reference holes are external to the final product, and also external to the press, thus facilitating assembly. In the case of the etched copper/epoxy/PI sandwich, these reference holes are matched to alignment marks etched in the copper, thus providing the required alignment between the etched read-out electrodes and the temporary reference holes. The carbon-loaded PI is then cut to its final shape using a steel-rule die. The reference holes for this sheet are punched into temporary tabs that can be removed after the gluing process. The six-layer sandwich is then assembled in a press, with the relative alignment of the layers set by dowels in the press that pass through the temporary reference holes. The press is then activated to 20 bar and placed in an oven at 180°C for two hours. Once cooled, the glued board is put in a jig using dowels through the temporary reference holes and the final outline is cut. The gold-plated signal and high-voltage pins are then soldered in place. The flux is removed by brushing the joints with alcohol. The boards are visually inspected for the cleanliness and quality of the solder joints.

The EST board is made using the same reference holes, punch (for the carbon-loaded PI), press and oven as the PAD board. Only the final cutting jig is of a different shape, and then only because this board has no signal tabs.

The high-voltage connections are made and inspected in the same way as for the PAD board.

8.4.3 Technology CLP: fabrication

The PAD boards and EST boards are made of four components, namely PI, polyurethane glue, annealed copper, and the liquid solution for making the HRL. Figure 8-8 and Figure 8-10 show the structure of the PAD boards and EST boards, along with the premanufactured composite sheet materials used in the assembly.

As there are several types of polyurethane glue and PI, and in order to simplify product qualification, these materials, except for the liquid solution for the HRL, are purchased from a single supplier. A high resistive coating compound was developed [8-9] as a special material to paint the external surfaces of calorimeter electrodes. It was used to produce the HRL in two of the four modules produced as part of the prototype module production and was tested in the beam. This production demonstrated that a resistivity variation of ±30% can easily be obtained. As for the carbon-loaded PI production the resistivity acceptance window for production will be 30%: well within the engineering requirement of 50%. The thickness of this high resistive paint is about 3.5 μm and the bulk resistivity of the high resistive layer is about 3.5 Ω mm.

The high-voltage connection to the high resistive layer is made by a connection, to be developed, that connects from the high resistive coating to the high-voltage strip line connector. A design similar to that used in technology CLK will be employed.

The production of the EST and PAD boards closely follows the procedure described in the previous section. The main differences are that the reference holes are internal to the board, and the HRL is applied after gluing.

The high resistive coating process is carried out using a computer operated two-coordinate spraying machine in a clean area. The board is first fixed on a special plate using the reference holes. The mask for the borders of the high resistive coating is placed on the plate and fixed with dowels. Through this process the required alignment between the mask, the etched copper, and the edge of the board is obtained. The plate with board and mask is positioned in the two-coordinate spraying device. After spraying and drying the board is turned over, and the other side of the board is covered with coating by the same method.

8.4.4 Tolerances (technologies CLK and CLP)

The tolerances on the boards arise from the need to provide good high-voltage stand-off on all surfaces. As the maximum operating voltage is assumed to be 2,500 V, we require 2.5 mm along all surfaces between high voltage and ground. This criterion comes into play at two places for the PAD and EST boards. The first is at the seven inner tie rods, where a nominal stand-off of 3 mm is supplied. The second is at the outer edge of the boards where a nominal stand-off of 2.5 mm is supplied.

There are three distinct failure modes that must be considered:

- Breakdown from HRL to grounds (at the tie rods and signal strip lines).
- Breakdown from HRL to HRL on the opposite side of the same sheet around the edge of the sheet.
- Breakdown from HRL to copper electrodes on the same sheet (through a failed glue joint or around the edge of the sheet to the HRL).

From the prototype we know that the tolerance on the etching of the copper on the PI is ± 0.3 mm. The steel-rule punch for cutting the surrounds of the boards has a tolerance of ± 0.3 mm. The mask for the CLP and the punch for the CLK both have a tolerance of ±0.3 mm. The punch

that punches the seven tie-rod holes can be adjusted to ± 0.2 mm. Thus the minimum distance from the etched copper to the edge of the board at the tie rods is 3 mm, minus 0.3 mm for the etching tolerance and minus 0.2 mm for the punching tolerance, giving 2.5 mm. This will be inspected. Around the perimeter the minimum distance from the copper electrode to the edge of the PI is 2.5 mm, minus 0.3 mm for the etching and minus 0.3 mm for the cutting, giving 1.9 mm. This is not easy to inspect as the copper is not easily visible. However, the distance to the edge of the CLP or CLK is also 1.9 mm, giving a total of 3.8 mm between high voltage and ground. This is considerably more than the required 2.5 mm, but in view of the difficulty of inspection is reasonable. Around the perimeter the minimum distance from the HRL to the edge of the board is 2.5 mm, minus 0.3 mm for the HRL size tolerance and minus 0.3 mm for the board cutting, giving 1.9 mm. However the same minimum distance is available on the reverse side, giving a total stand-off distance of 3.8 mm. This will be inspected.

8.4.5 Quality assurance

The first quality-assurance test on the PAD and EST boards is a visual inspection of the board edges to check for any tears. Lengthening of tears during cool down and operation can lead to short circuits between HRLs. To minimize this failure mode any boards with even minor tears are rejected. During this inspection any boards with less than 2.5 mm of insulator surface between high voltage and ground are rejected. The PAD and EST boards are electrically tested [8-10].

The surfaces are then visually checked for embedded particles. Any such particles are removed. The boards are then tested to check that there are no serious corona points on their surfaces. This is done by forming a sandwich of a metal plate, a honeycomb spacing mat, PAD or EST board, honeycomb and metal plate. With the metal plates at ground the HRLs are raised to 2,500V and the voltage applied until the current drops below 50 nA. This corona test is applied again during stacking and can be omitted at this stage if the failure rate experienced is low.

8.4.6 Storage

The storage of the boards requires a low-dust and low-humidity environment. In order not to damage the boards by introducing metal filings, they are stored between high-quality paper. This paper also facilitates the handling of the boards. For low humidity and cleanliness the boards are stored in the clean room. For ease of handling an arrangement of 14 drawers is provided, with each drawer containing one of the seven different types of PAD or EST boards.

8.5 Honeycomb spacing mats

Honeycomb spacing mats maintain the gaps between the PAD and EST boards. The nominal thickness of the honeycomb is 1,774 μm with a tolerance of 150μm. This thickness is calculated taking into account the nominal gap (1,954 μm), minus the thickness tolerance on the honeycomb (150 μm), plus the amount of give in the honeycomb due to its spongy nature (37 μm), minus 1/4 the thickness tolerance of the PIs (42 μm), minus half the maximum deflection of the copper due to lack of flatness (25 μm). The honeycomb arrives cut to thickness in rectangular sheets from which two pie-shaped sheets can be cut. The honeycomb is first measured for thickness tolerance, then cut to the required shape using a steel-rule die cutter, and then baked in an oven to remove moisture. Each honeycomb is then placed between two metal plates and checked for high-voltage stand-off at 2,500 V. To pass this test the honeycomb must pass less

than 3 nA. If the failure rate is low, this high-voltage test can be omitted, as the test is repeated during stacking of the module. The honeycomb spacing mats are stored in the clean room until required for stacking.

8.6 Module construction

8.6.1 Stresses in the modules

As discussed earlier the structural strength of the front modules is maintained by seven 12 mm stainless-steel tie rods that pass through the plates and are bolted down with a tension such that the minimum pressure holding the plates together is equivalent to three times the weight of the module. This arrangement gives 78 MPa on the front-module tie rods. At the root of the threads of the bolts that tighten the rods this stress increases to 125 MPa. There are stainless-steel spacers on the tie rods, that maintain the 8.5 mm inter-plate gap. In the front modules these spacers have a 17 mm outside diameter. The tension in the tie rods plus the weight of the module is distributed on the 17 mm diameter spacers bearing on the copper in the front modules over a nominal area of 114 mm^2. This gives a nominal pressure of 103 MPa bearing on the surface of the 25 mm thick copper, which, allowing for tolerances and chamfering, is still below 2/3 of the yield strength of the material (205 MPa).

The rear modules have stiffer plates so the engineering solution is slightly different. The total force required to flatten all the plates in a module in which the plates are in the most unfavourable orientation has been calculated to be about 30,000 N. This situation is rather unlikely and if encountered could be corrected by inserting special-thickness spacers. If the rods and spacers were designed to take this force their size would seriously compromise the active area of the calorimeter. Hence the rods and spacers have been designed to take half this force, so that in most situations the plates can be flattened by simply tightening the rods to their specified torque, but in situations where the plates' lack of flatness is highly anticorrelated between adjacent plates in the module, custom-size spacers will be used. Table 8-5 lists the parameters of the front- and rear-module tie rods.

Table 8-5 Parameters of the module tie rods and spacers.
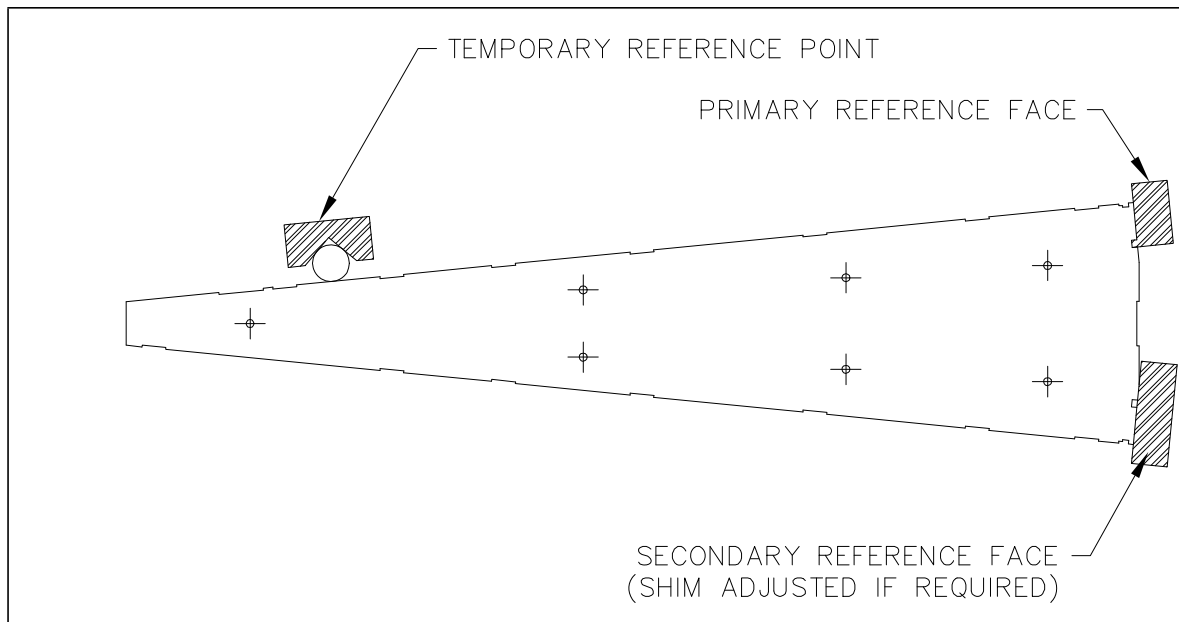
Module	Front module	Rear module
Tie rod diameter	12 mm	16 mm
Tie rod stress	78 MPa	79 MPa
Tie rod thread root stress	125 MPa	118 MPa
8.5 mm gap spacer outside diameter	17 mm	23 mm
Maximum stress on the copper by the spacer	138 MPa	138 MPa

Thus the modules are stiff structures that are able to tolerate horizontal acceleration of up to about 0.75 g without any internal slippage. In the vertical direction they can withstand additional forces up to 1.5 g before any indentation of the copper plates at the spacer location occurs. Forces during shipping will be monitored to check these accelerations are not exceeded.

8.6.2 Module stacking and testing at the production site

The HEC modules are stacked in a 10,000 particle per cubic foot clean room, with special attention given to the number of larger dust particles present, as these can cause serious problems in production. The clean room is regularly tested to check compliance with the low-dust specification. In addition the clean room is air conditioned and heated (if required) to keep the relative humidity below 45% so that the current draw in the module gaps at nominal high voltage is not too high. These conditions will allow current draws which are due to imperfections to be detected at the few nA level.

Shims are used during the stacking process to align the plates within a module. The concept is to manufacture modules with two reference faces at the outer radius onto which the inter-module clamping bars are bolted. Clamping bars are connected to these faces when the modules are manufactured. During all subsequent operations the forces are such that the individual copper plates of the module do not move with respect to each other. The procedure to create these two reference faces is as follows: The module is stacked using as reference one stainless steel inter-module clamping bar which is notched into the copper, and one temporary reference face near the toe of the module (see Figure 8-12). Once a layer is stacked, the bar defining the tempo-

Figure 8-12 The copper plate, showing the two reference faces and the temporary reference face used during stacking

rary reference face is removed. The plate at the second stainless steel inter-module clamping-bar location is now shimmed at the two bolt locations to better than [+0 µm –25 µm], and the clamping bar bolted in place. The temporary reference face is now returned and the movement of the copper plates measured at that location. If relative movements of more than 0.3 mm occur then the plate will be shimmed again so as to be within this tolerance. The mechanical lever between the reference clamping bar bolting surface and the copper at the temporary reference face of the module is such as to provide a movement amplification of about a factor of four. Hence shimming to the nearest 25µm should easily allow alignment to 0.2 mm. After all the plates of the module are thus adequately aligned, the tie rods are tightened to a tension such that the minimum pressure between any two adjacent plates is equivalent to three times gravity. This pressure is sufficient to hold the copper plates in place without any slippage during subsequent operations. The tolerance in the width of the plates at the outer radius of the module is taken up

by adjusting the inter-module gap at the outer radius. The tolerance in the average length of the plates of a module is taken up, during module construction, at the outer radius by shimming the stainless-steel connecting bar. The tolerance in the length of the individual plates of the module is taken up, at the time of wheel assembly, at the inner radius by a slight ϕ movement of the inner tie bars. The tolerance in the angles of the various faces is taken up, at the time of wheel assembly, by shimming and by flexing the inner and outer connecting elements.

Module production starts by placing the rearmost plate of the module on the stacking table with the seven tie rods inserted. The stainless steel spacers are placed over the tie rods and a honeycomb spacing mat is placed on the plate. This is followed by an EST board, a honeycomb mat, a PAD board, a honeycomb mat, an EST board, and finally a honeycomb mat. The components, especially the honeycomb, have their positions carefully adjusted so they do not extend over the edge of the copper plate. Finally the next copper plate is added on top. The alignment procedure outlined in the previous paragraph is now carried out. Upon completion the alignment of the top copper plate is checked.

Having thus completed the layer, the tabs of the PAD boards are connected to a circuit board and they are all temporarily grounded to the copper. The high voltage and ground are now connected to each HRL in the final voltage configuration. The high voltage is raised to 2,500 V and the layer is accepted when the current drawn is less than 30 nA. The lowest-current short circuit draws a few microamps, so this current is a safe indication that the gaps have no short circuits. To check for shorts between the high-voltage planes of a PAD board, high voltage is applied to one HRL plane with the other two planes (electrode and HRL) grounded. The integrity of the high-voltage connections to the HRL is checked by measuring the resistance between the two connections. In the event of a layer not passing the tests, the layer will be restacked with new electrode components. Once a layer is completed the stacking of the next layer commences, following the same procedures as the first layer. Upon completion of all the layers of the module the tie rods are tightened. The nuts on the tie rods are tightened to a predefined torque, thus producing the required tension in the rods. The torque is checked.

A slight variation on this procedure is required for the rear modules because of their considerably stiffer plates. When the plates are received at the stacking site and the flatness is measured, this information is analysed for all the plates of the module. If the non-flatness of the plate conspires so as to require custom spacers, the size and location of these custom spacers will be determined prior to stacking. These spacers will then be inserted as required as stacking proceeds.
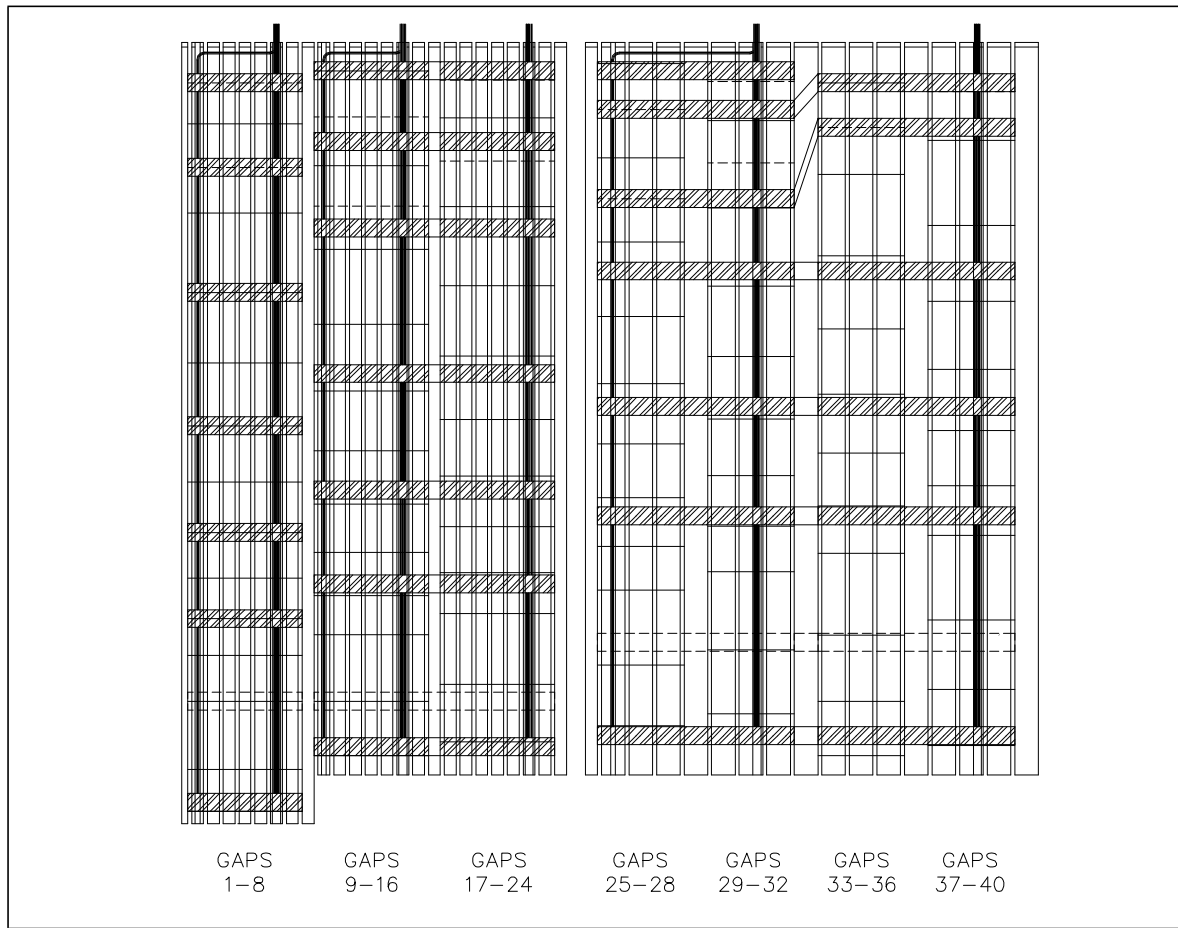
At this stage the final module tests are undertaken. The final physical dimensions of the stack are checked by a go/no-go gauge similar to the one that will be used on arrival at CERN. While the capacitance measurement will monitor the gap dimensions, the average plate thickness will be monitored by measuring the height of the module. The module is then wired for high voltage and left for about three weeks at 2500 V to check that all boards have good long-term high-voltage stand-off.

Next the calibration and signal cables are connected as discussed in the next section. All HRLs are now grounded and the capacitance of each read-out cell measured, to check that all the connections are made correctly and no cables are damaged. The connection of the calibration lines to each electrode pair is checked by measuring the resistance between the calibration line and each amplifier line. The continuity of the ground is checked by measuring the resistance to ground for each ground line at the amplifier. Then the read-out electrodes are grounded and the HRLs brought up to voltage (2000 V), and left at voltage until the current draw is below 100 nA. Finally, before packaging and mounting on the module shipping frame, the high-voltage channels are all grounded and a final capacitance measurement is made of each read-out cell with a meter that measures both series resistivity and capacitance. This measurement is the reference measurement for the detector and checks most electrical aspects.

8.7 Signal, high-voltage connections and cold cables

The cabling concept for the HEC is determined by the locations of the signal feedthroughs allocated to the HEC. These feedthroughs are at the centres of the four quadrants of the wheel (i.e. at about 45, 135, 225, and 315 degrees) and so the wiring is designed to be symmetric about the feedthrough in each quadrant. A detailed description of the cabling system is give in [8-11].

The signal, high-voltage and calibration cables for each module are housed on the side of the module. The arrangement of the signal and calibration cables is shown in Figure 8-13. These ca-

GAPS 1−8   GAPS 9−16   GAPS 17−24   GAPS 25−28   GAPS 29−32   GAPS 33−36   GAPS 37−40

Figure 8-13 Drawing of the side of a module showing the signal and calibration cables. The calibration cables are radially fed in on the front plate of each read-out segment. The signal cables are routed radially outwards along the plate in front of the second to last gap in each eight gap segment. The signal and calibration lines are transmitted in the z direction across the module on PI strip lines in the 39 mm wide (double dashed) notches, where connection is made to each gap's electrode.

bles are protected by being in notches that are 3 mm deep and 39 mm wide. The high-voltage cables are protected in notches that are 3 mm deep and 73 mm wide.

The 50 Ω signal cables are attached to strip line connectors that carry the signals from the copper electrodes which form radially adjacent pairs of eight gap read-out subsegments. These cables bring the signals from the strip line connectors to the preamplifier boards at the outer radius of each module. Here the signals are summed to read-out towers. In the read-out arrangement (read-out channel) each line corresponds to a fixed η-bin.

The calibration system calibrates the preamplifiers by feeding pulses in at the electrode level. This injection at the electrode is required to make the system insensitive to changes in preamplifier input impedance due to radiation. The design goal of the calibration system is to achieve an accuracy of ±0.5%. The calibration signal is fed to a single resistor (5 kΩ) for each pair of electrodes through a 50 Ω line. This line feeds all electrodes in an eight or sixteen LAr gap read-out segment through a set of these resistors. The calibration line is terminated by these resistors in conjunction with an additional resistor to ground that provides proper termination of the calibration cable. There are 28 independent calibration lines per front module and 14 per rear module.

8.7.1 Preamplifier motherboard

The GaAs preamplifier and summing chips (see Chapter 10) are located on the preamplifier and summing motherboards which are mounted on the back of the modules. They slide into guiding frames fixed to the copper structure. The motherboards have signal inputs from the read-out cells and signal outputs corresponding to read-out towers which are routed via the quadrant cabling towards the signal feedthroughs.

Three types of motherboard are used: Type A is specific for the first read-out segment, it carries 14 chips. Type B and C together serve both the second and the third read-out segments. Type B carries 12 chips and type C 16 chips. Type B handles the low-η region and type C the high-η one. Figure 8-14 shows a schematic drawing of a motherboard of type A. As shown, the input
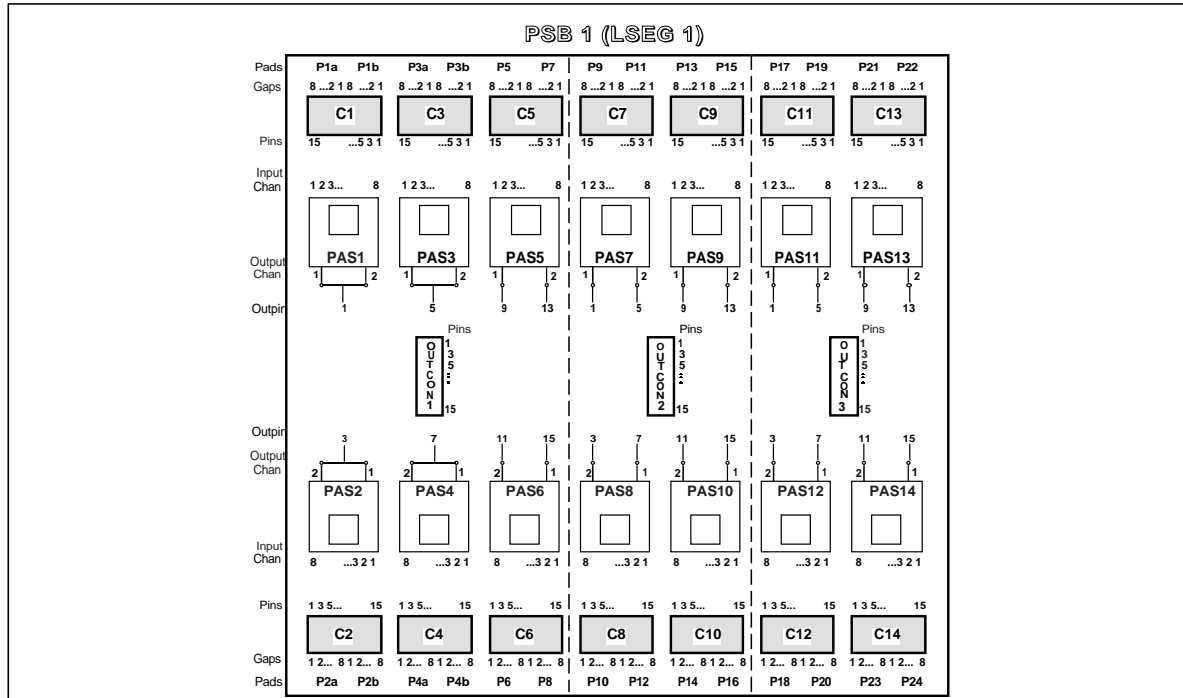
Figure 8-14 Schematic view of a preamplifier motherboard of type A.

connectors and the preamplifier chips are arranged in two identical rows on either side of the board serving the signal lines arriving from the two sides of the module.
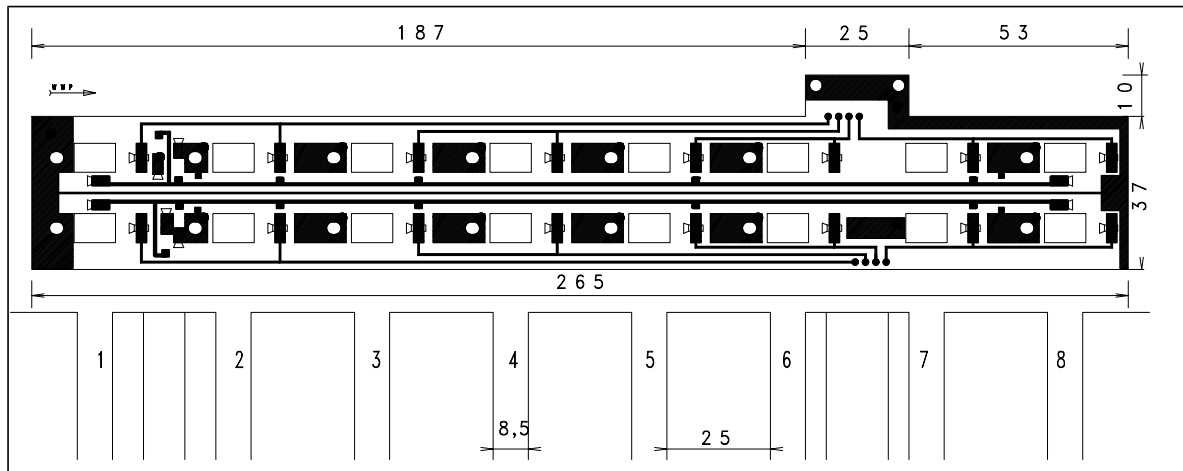
The cables from pairs of read-out cells arrive at 16-pole connectors grouped for summing to read-out towers in the preamplifier chips. There is one 16-pole connector per preamplifier chip.

The output connectors as well as the connections for three supply voltages and ground are arranged in the centre of the motherboard. There are different numbers of output lines from each motherboard grouped into output connectors of eight lines each. Type A has three output connectors for the 24 read-out channels of the first segment. Type B has a full connector of eight and one connector carrying two lines. Type C has a full connector and a connector filled with six lines. The two partially filled connectors are grouped into one full connector of eight at the level of the "patch panel" in front of the feedthroughs.

The width of each motherboard is 230 mm. Because of the different number of preamplifier chips the lengths of the boards are different: type A 260 mm, type B 230 mm and type C 290 mm. The outer radius of the front module is therefore densely covered with three types of boards, one of each kind. There are two boards at the outer radius of the rear module. Four low-voltage lines feed each motherboard. Redundancy in the low-voltage system is under study.

8.7.2 Signal Lines

Each individual copper electrode must be connected through a 50 Ω line to the signal amplifier. A small tab (with a soldered pin) connected to each electrode is passed through a hole in the signal strip line connector and attached to a special socket on the strip line (see Figure 8-15). The
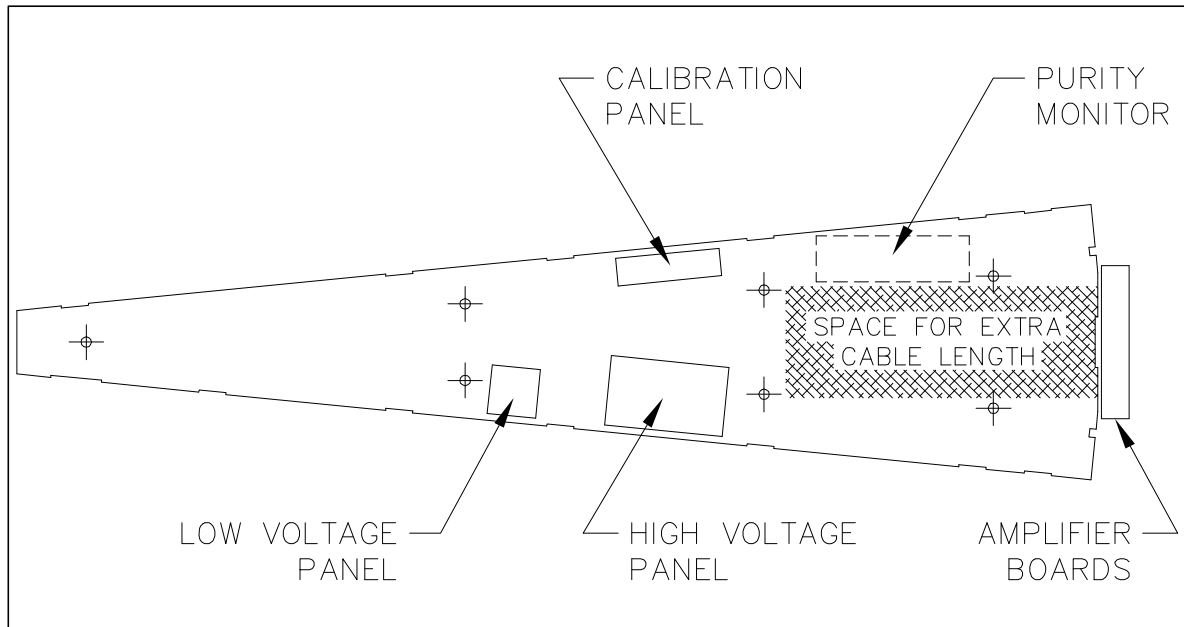
Figure 8-15 Layout of the signal strip line connector. The back plane serves as ground bus. All connecting surfaces are gold plated.

face of the strip line that is against the copper plates acts as the ground plane for the strip line. All conducting surfaces are gold plated. The signals from longitudinal pairs of electrodes are summed locally and carried along the strip line via a trace. For each set of eight read-out gaps, a strip line carries the signals from a pair of radially adjacent read-out sub-segments, so there are eight signal traces on each strip line (four from each sub-segment). A 50 Ω cable is soldered to the end of each trace and passes along a slot in one of the copper plates (see Figure 8-13) to a motherboard at the outer radius of the module. The side of the strip line connector facing away from the module (i.e. with the traces and electrode connection tabs) is insulated from the next module in the wheel with an insulating sheet placed in the inter-module gap prior to wheel assembly.

Each set of eight read-out gaps in a module is served by 14 signal strip line connectors (seven per side, see Figure 8-13), except for the rearmost eight gaps in the rear module which only have 12 strip line connectors (six per side). Thus, there are 42 strip line connectors in each front module with eight signal cables attached to each connector, and 26 connectors in each rear module. These signal cables pass through slots in the copper plates to the motherboards at the outer radius of the module. After the signals have passed through the preamplifiers, they are summed into read-out towers with each tower in the first read-out depth composed of the signals from four (or eight for the split electrodes, see Figure 8-5) signal cables and each tower in the second and third read-out depths composed of the signals from eight (or 16) signal cables. Thus, there are 47 (24 in the first read-out segment, 23 in the second) read-out towers in each front module and 22 read-out towers in each rear module.

The signals are passed to the back plane of the module through signal output cables which are attached to the motherboards via connectors that can hold up to eight cables. Each of these cables carries the signal from one read-out tower, and so there are seven connectors for the front module and four connectors for the rear module. These output cables, which must all be the same length, are routed on top of each other to the back plane of the module, regrouped within the quadrant and routed in groups of 64 lines to the feedthrough. Since the cabling is done symmetrically for each quadrant, we have reserved some space at the back plane of each module for storing the unused extra cable length. This space is only required after turning the wheel into the vertical position, and so we foresee the use of the centre region of the back plane, which is normally blocked prior to this operation by the transportation frame. Figure 8-16 shows sche-

Figure 8-16 Schematic view of the back plane of a module. Shown is the space allocated for individual boards (calibration, high voltage and low voltage) and for additional extra cable length. Also note the two notches for the high voltage strip line connector: the first being the wide notch near the inner tie rod, and the second being under the amplifier board.

matically the space allocation at the back plane of a module.

The signal cabling of the module will be done immediately after finishing stacking and the long high-voltage test of the module. At this time there is free access to the sides of the module, where the strip line connectors are placed, as well as to the outer radius of the module.

8.7.3 Calibration lines

In order to have the calibration signal match the real signal as closely as possible, the calibration pulse is fed in at the level of the electrodes. The calibration lines deliver the calibration signals to pairs of electrodes using traces at the centre of the strip line connector (see Figure 8-15). At most, 32 electrodes are calibrated with a single generator.

The cabling for the calibration lines is symmetric about the feedthrough in each quadrant. The calibration cables run from the feedthrough to a small calibration distribution board at the back plane of each module (see Figure 8-16). This cabling is installed only after turning the wheel into the vertical position. The cable lengths must again be equal, and so a dedicated region at the back plane of the module will be used to store extra cable.

The calibration input cables are routed from the board on the back plane to the outer radius of the wheel, then under the motherboards, and finally along slots in the copper plates to the front of the strip line connector in the first and third read-out segments. The first and second read-out segments are connected via jumpers.

The space reserved on either side of each motherboard accommodates up to 28 cables. The signal strip line connectors have one (third read-out segment) or two (first and second read-out segment) calibration traces which are connected to separate calibration cables. A set of 5 kΩ resistors connects each trace to the corresponding signal lines on the connector (see Figure 8-15), providing the means to input the calibration signal directly to the signal lines. In the second and third read-out segments where the read-out towers are formed from longitudinal pairs of strip line connectors, the calibration signal is carried to the rear strip line connector via a jumper. Introducing the calibration signals at the front of the read-out sections simulates the time evolution of a real particle shower in the calorimeter.

The concept of the connection of the calibration generator to groups of electrodes is shown in Chapter 10, Table 10-7, and is discussed in detail in a technical note [8-11]. The rationale for this scheme arises from the different allowed saturation levels of the amplifiers and summing networks in the different longitudinal read-out segments. As can be seen from the table, each calibration generator nominally feeds 24 electrodes in the front module and 32 electrodes in the rear module. The realisation of this concept produces a calibration scheme that requires 28(14) calibration generators in the front(rear) module. The calibration lines from individual generators are attached to the board at the back plane of the module using connectors that can hold up to eight lines. Thus, there will be four connectors for the calibration lines from the front module, and two connectors for the calibration lines from the rear module.

The calibration scheme does not use independent generators for radially adjacent electrodes in the third read-out segment, and hence precludes the crosstalk measurement for these electrodes. However, similar measurements with the prototype module yield typical values for this crosstalk at the level of 1%. Since this level is so small, the chosen technique seems to be adequate.
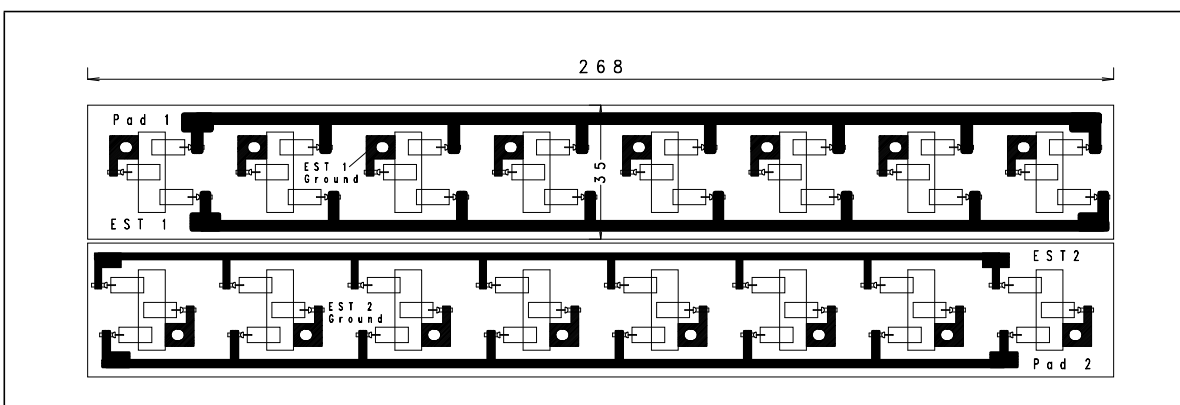
The connection of the cables between the strip line connectors and the board at the back plane will be done immediately after the stacking of the module. In order to mount this board in the horizontal position (with the transport frame mounted) the board must be close to the side of the module. The input connector at the level of this board for the calibration lines is as close as possible to the side of the module allowing easy connection in all test situations: after stacking or transportation, following the wheel assembly in the horizontal position on the wheel assembly table, after rotating the wheel, and during and after insertion into the cryostat.

8.7.4 High-voltage lines

The connection of the high voltage and ground to the PAD and EST boards is done following the strip line connector technique. For each read-out depth of 8 or 16 LAr gaps, four independent high-voltage lines feed the four high voltage potentials (one for each EST board and two for each PAD board in the read-out gap). Each EST board also requires a ground connection. For safety, and to limit current due to pile-up, two high-voltage connections are used for each plane: one near the inner radius of the board on the side of the module, and one on the outer cylindrical surface of the module. The location of the notches for the strip line connector can be seen in Figure 8-16.

The high-voltage planes in each read-out gap are symmetric around the copper electrode plane, with two high voltage planes separated by a ground plane on each side of the electrode (see Figure 8-4). Thus, two high voltage strip line connectors, identical but rotated 180° from each other, are used in each high voltage notch in the copper plates. The ground connections are made with screws mounted to the copper plates (see Figure 8-17) and situated along the centre line of the strip line connector. On either side of the ground connections run the two high voltage lines supplying voltage to the two sets of high voltage planes in the eight gaps.

The high voltage and ground connections to the strip line connector are done via tabs with small pins soldered to them, similar to the ones used to connect the electrode pads to the signal strip line connector. These tabs are insulated on one side to prevent contact with the copper

Figure 8-17   Layout of the high voltage strip line connector (for two sets of high voltage and one ground line). Two connectors, with the second one rotated by 180 degrees, are used to serve the four high voltage and two ground connections required per LAr gap.

plates. The tabs are passed through holes in the strip line connector and then bent in alternating directions and the pins plugged into sockets on the strip line. The non-insulated faces of the tabs are covered, as in the case of the signal lines, with an insulating sheet placed in the inter-module gap prior to wheel assembly.

These tabs are 6 mm wide, and the guard zone between the traces on the strip line is 2 mm, so the width of the strip line connectors must be at least 35 mm. Thus, the notch in the copper plates must be at least 70 mm to hold the two high-voltage strip line connectors. In addition, all high-voltage lines for a module are guided to a high-voltage distribution board at the back plane of the module through these same notches. This means that, with up to eight high-voltage lines in each notch as well as the strip line connectors, the total width of each high-voltage notch must be 73 mm. Because each high-voltage line splits into two lines (one at the inner radius and one at the outer radius of the module), space has been foreseen for guiding up to eight

high-voltage lines from the inner radius to the outer radius region at the back plane of the module. The final connection from the high-voltage distribution board to the relevant feedthrough (one for the whole wheel) is of varying length, depending on the module position within the wheel, and must be added after insertion of the wheel into the cryostat.

As in the case of the signal strip line connector, the high-voltage cables are soldered to the strip line connector prior to mounting the connector onto the module. After module assembly, these lines are connected to the high-voltage distribution board mounted at the back plane of the module. This board is mounted and accessible while the module is in the stacking position (i.e. horizontal copper plates), and so must be close to the side of the module. The high-voltage connections on the distribution board on the back plane of the module are arranged to facilitate checking the resistance between the two connections to each HRL.

8.7.5 Low-voltage lines

The low-voltage lines supplying power to the preamplifiers (four lines per motherboard) are attached with connectors at the motherboard. They are routed to the back plane of the module in a similar manner to the high-voltage lines, passing on either side of the motherboards. At the back plane, they are connected to a low-voltage distribution board, which again must be close to the side of the modules to facilitate access in the stacking position. The lines between this board and the feedthrough are attached with connectors. With up to 12 input and output lines on each board, we foresee a space of about $7 \, \text{cm} \times 7 \, \text{cm}$.
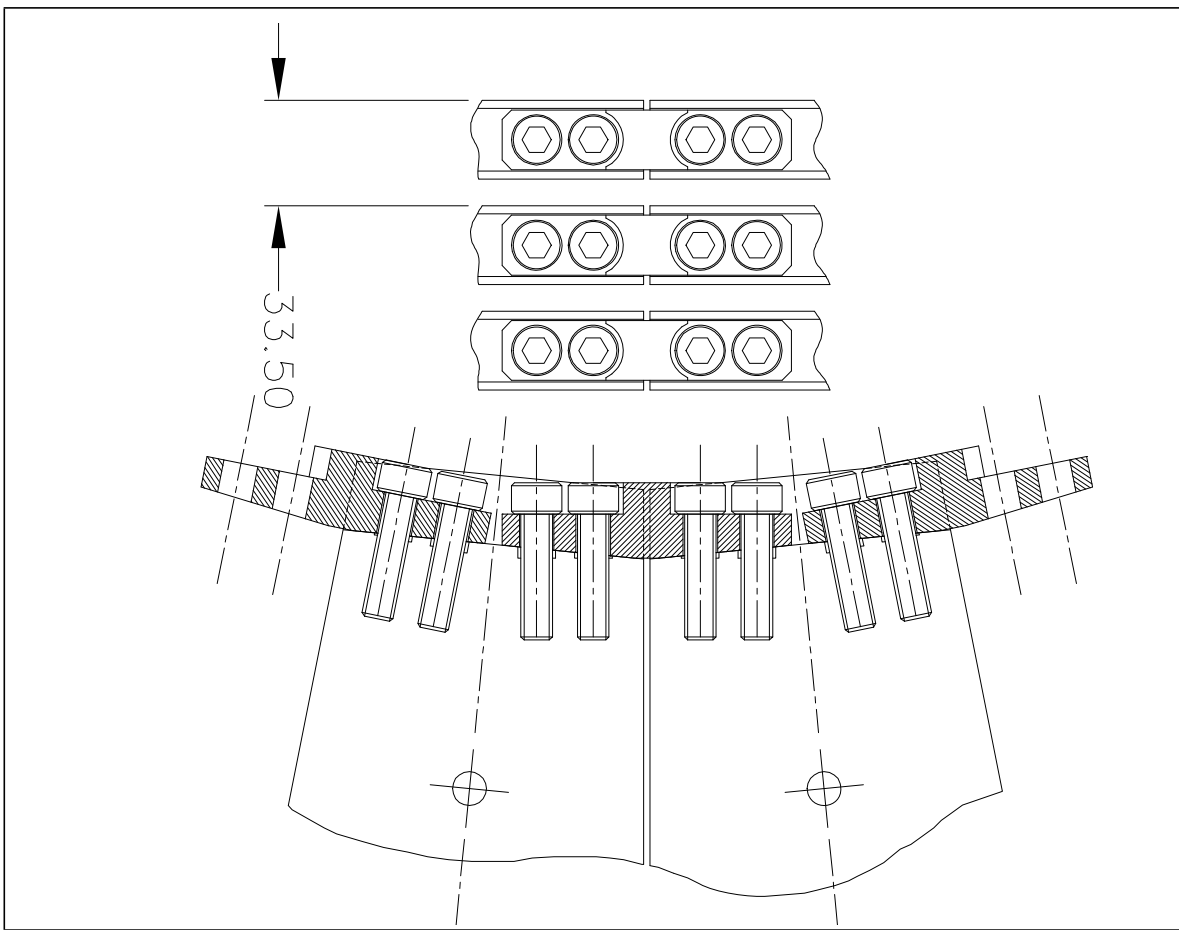
The variation of the length of the low-voltage lines is not a critical issue. However, it is desirable to maintain a standard voltage drop along the cable for all low-voltage lines. Therefore, we require them to be the same length. The low-voltage cabling is again symmetric for each quadrant, and so space is allocated at the back plane of each module for the extra cable length. Again, these cables will be connected after turning the wheel into the vertical position. Therefore, some of the space occupied by the module/wheel support structure in the horizontal position can be used for storing the extra cable.

8.8 Wheel structure

8.8.1 Inter-module connecting items and wheel support

The modules are bolted together at both the inner and outer radius by stainless-steel connecting pieces bolted to every plate. At the inner radius these are individual tie bars (see Figure 8-18). At the outer radius these are solid pieces that span the entire depth of the module and tie the two reference surfaces together (see Figure 8-19). They are referred to as inter-module clamping bars. The routing of the signal and calibration cables from the side of the module, through this inter-module clamping bar, to the preamplifier circuit-board location is shown in Figure 8-20. At the location of the rails in the cryostat the inter-module clamping bar is replaced by a slider that fulfils both the functions of the inter-module clamping bar and slider (see Figure 8-21). The inter-module clamping bars will be shimmed to accommodate the length tolerance of the copper plates (±0.2 mm).

The geometry of the wheel with the engineering tolerances of the individual plates has been studied. This study shows how these tolerances translate into misalignments and deformation of the components (especially the inter-module clamping bar and inner tie bars) of the wheel.
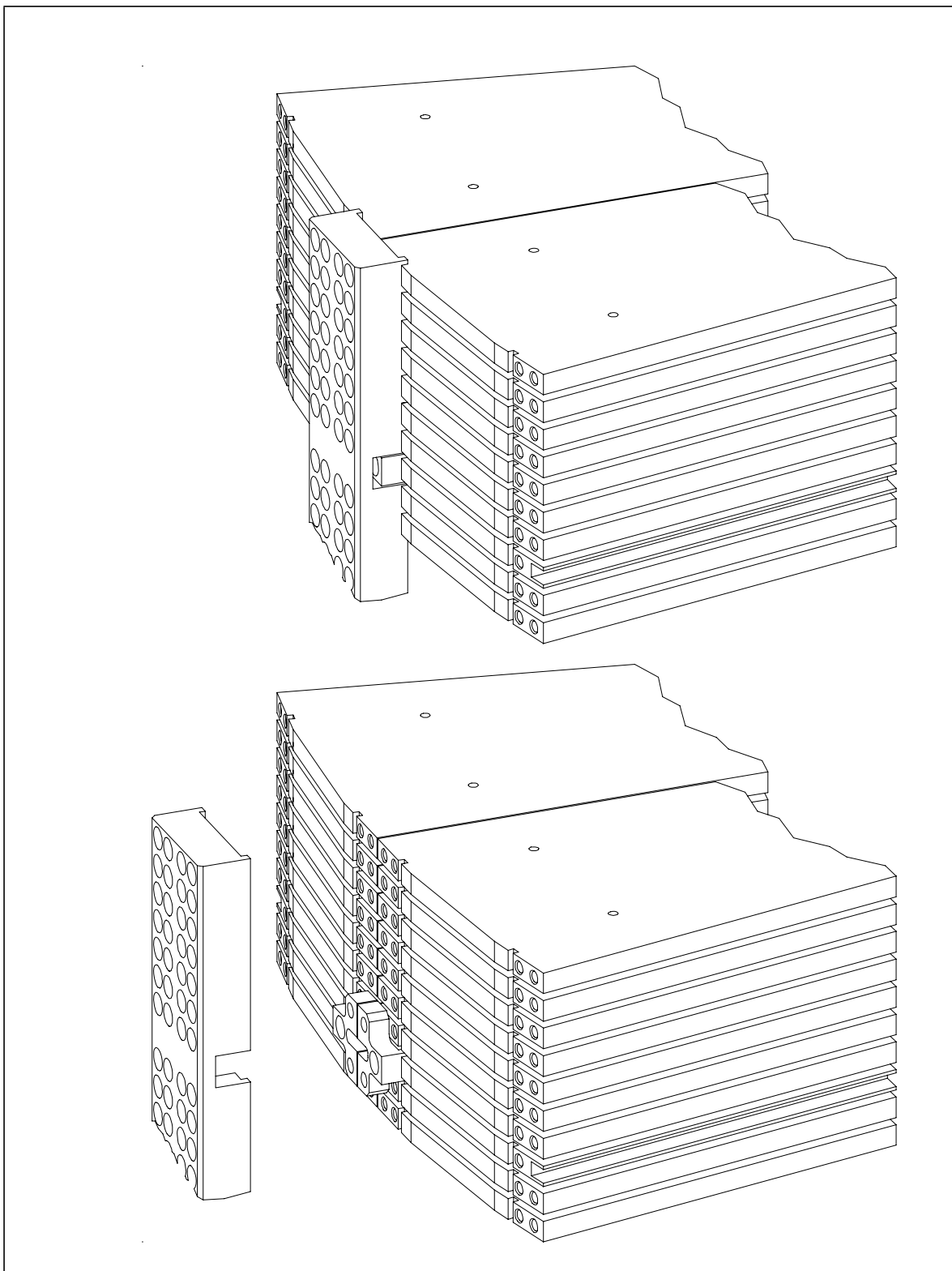
Figure 8-18 Details of the inner tie-bar region.
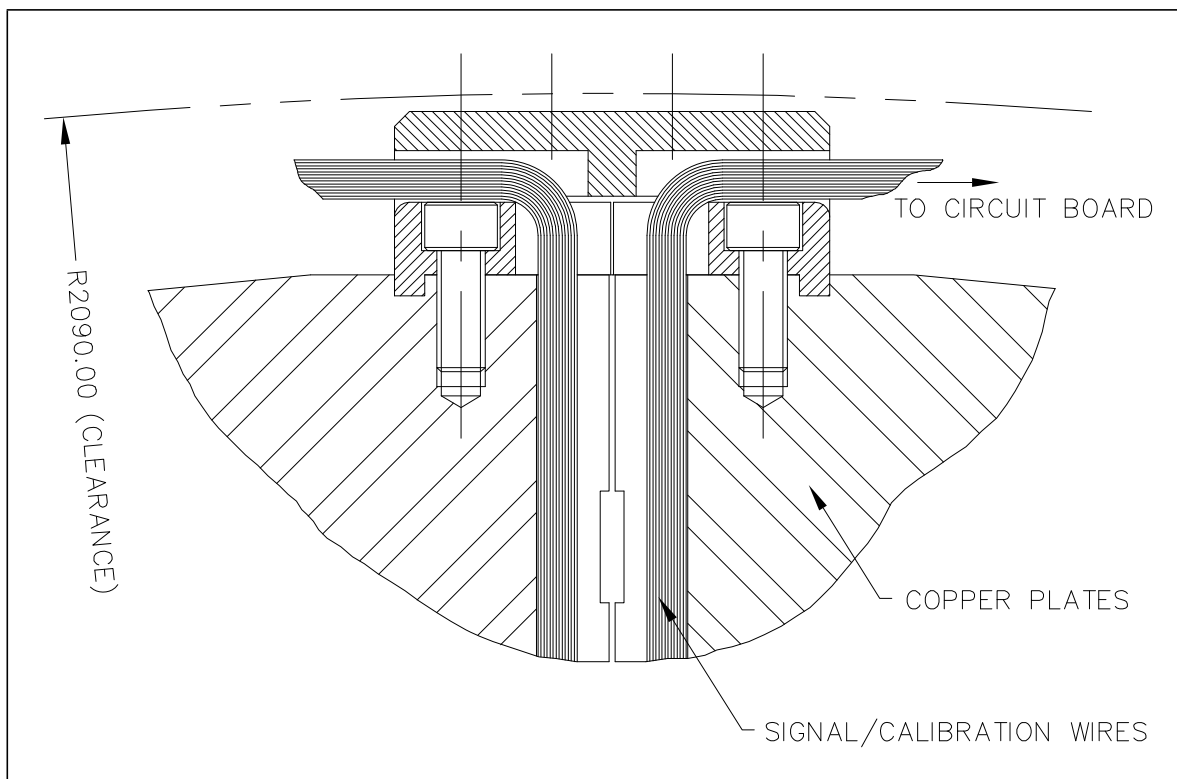
For this study 10,000 hypothetical wheels were constructed of plates of randomly chosen dimensions within the allowed engineering tolerances (i.e. the nominal size randomized using a uniform distribution for the tolerances). Three effects of the tolerances were studied: the change in the inner and outer radius of the wheel from the nominal, the variation in the inter-module gaps at the inner and outer radius, and the flexing angle required in the inner tie bars and inter-module clamping bar. Table 8-6 shows the results of this analysis. It must be remembered that this analysis assumes a random variation in the plate sizes: any systematic tolerance variations can give rise to significantly larger effects. The angle of flex of the outer inter-module clamping bar is too large to be taken up by flexing this rather solid bar. It must be shimmed to the nearest 25 μm. Once shimmed the forces required to flex the clamping bar to conform to the geometry are small compared with the force constraining each plate, and the tensile stresses along the clamping bar due to the flexing are an order of magnitude less than the yield strength of stainless steel.

8.8.2 Deformation and stresses in the wheel structure
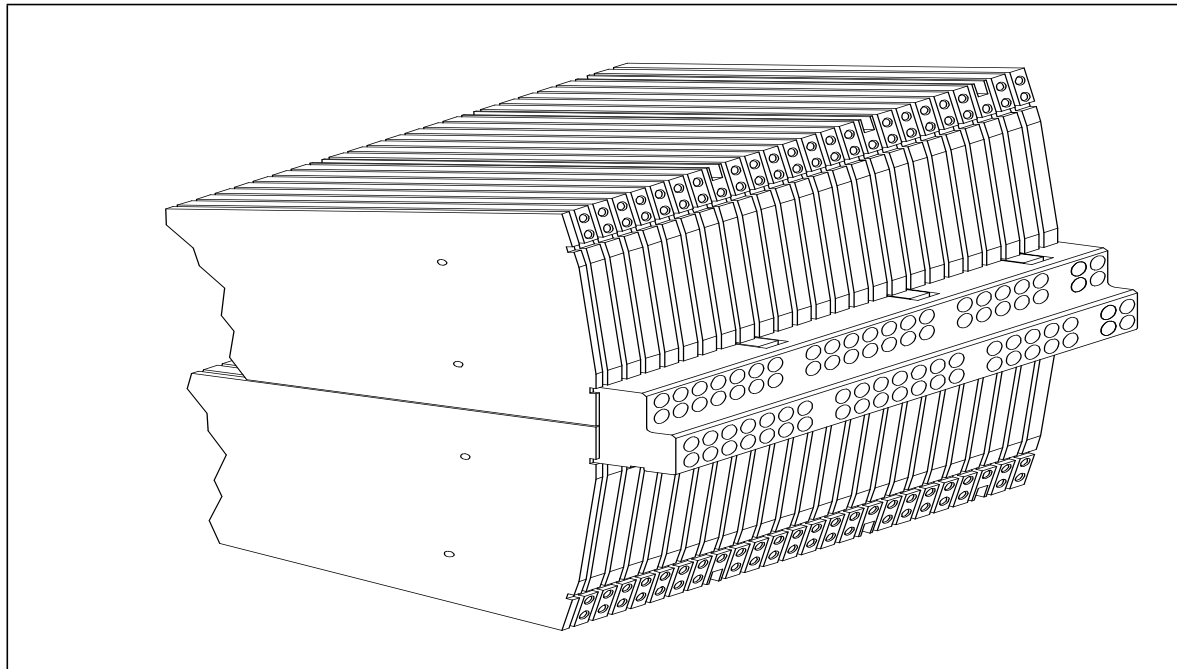
The wheel structure has been studied in detail using the ANSYS code [8-12]. The finite element analysis model is shown in Figure 8-22, the y-z plane of symmetry allowing one half of the structure to be used in the modelling. The vertical constraint is supplied by rigid support points under the slider rail. Symmetry constraints are applied to the inner and outer tie bars at the symmetry plane locations. The bolted joints are modelled as beam elements, held rigid in the region where there is thread engagement, but free to bend in the region between the bolt head and

Figure 8-19 Three-dimensional view of the inter-module clamping bar. The top figure shows the clamping bar in place. The bottom figure shows the module with the clamping bar removed, thus revealing the special inter-plate clamping bars at the location where the signal and calibration cables are routed to the preamplifier boards which will subsequently be installed between the two inter-module clamping bars.

Figure 8-20 Cross-section of the inter-module clamping bar at the location where the signal and calibration cables pass through this bar.
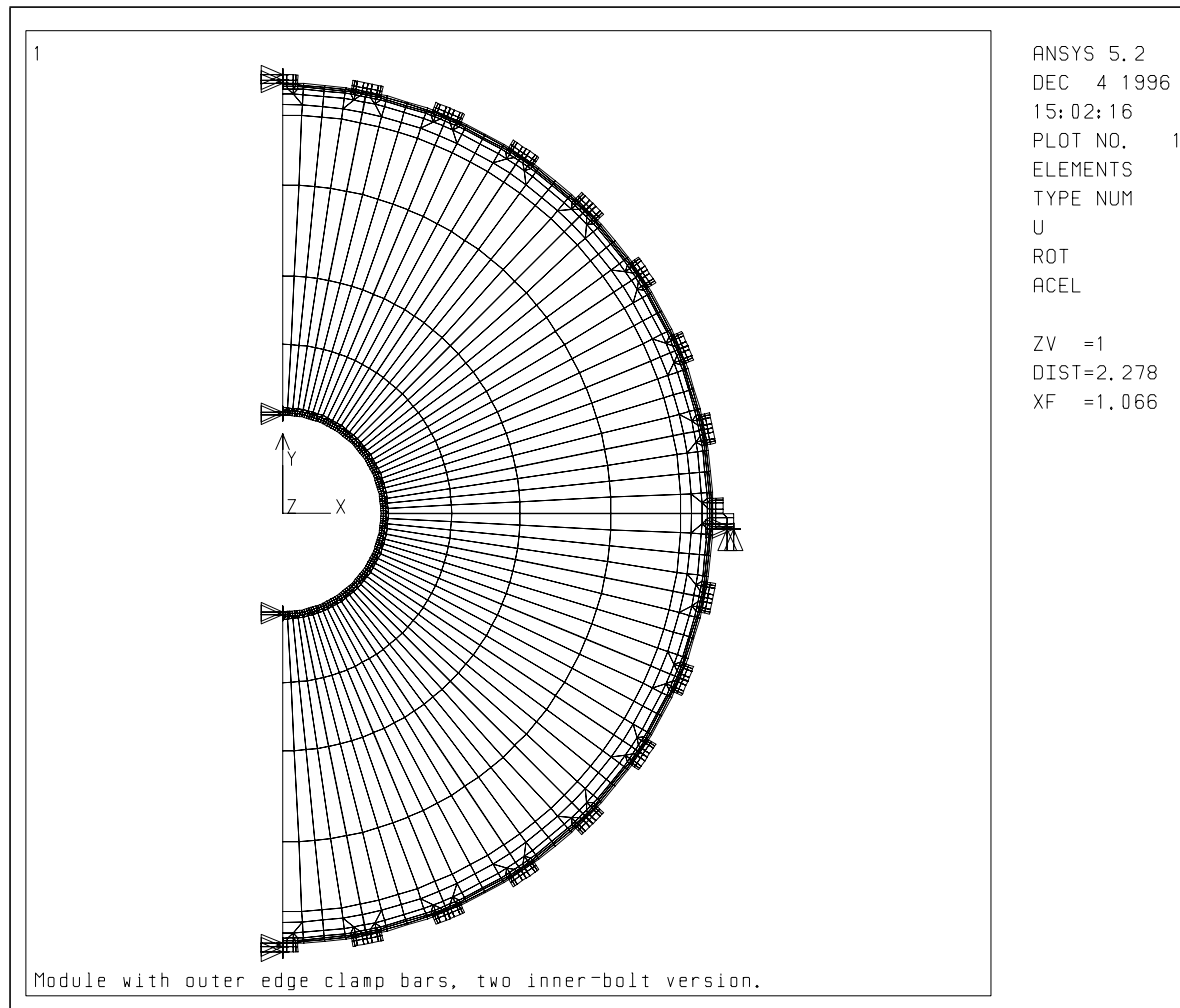
Figure 8-21 Three-dimensional view of the slider.

first thread engagement. An initial strain is applied to the bolts to give the required clamping force and a friction coefficient used to realize sliding resistance. Motion of the clamped surfaces relative to each other is controlled and recorded by contact elements at the clamped surfaces. Thus the frictional forces are reduced as the clamping force falls, and become zero at any point

Table 8-6 Possible misalignments and deformations due to tolerances.
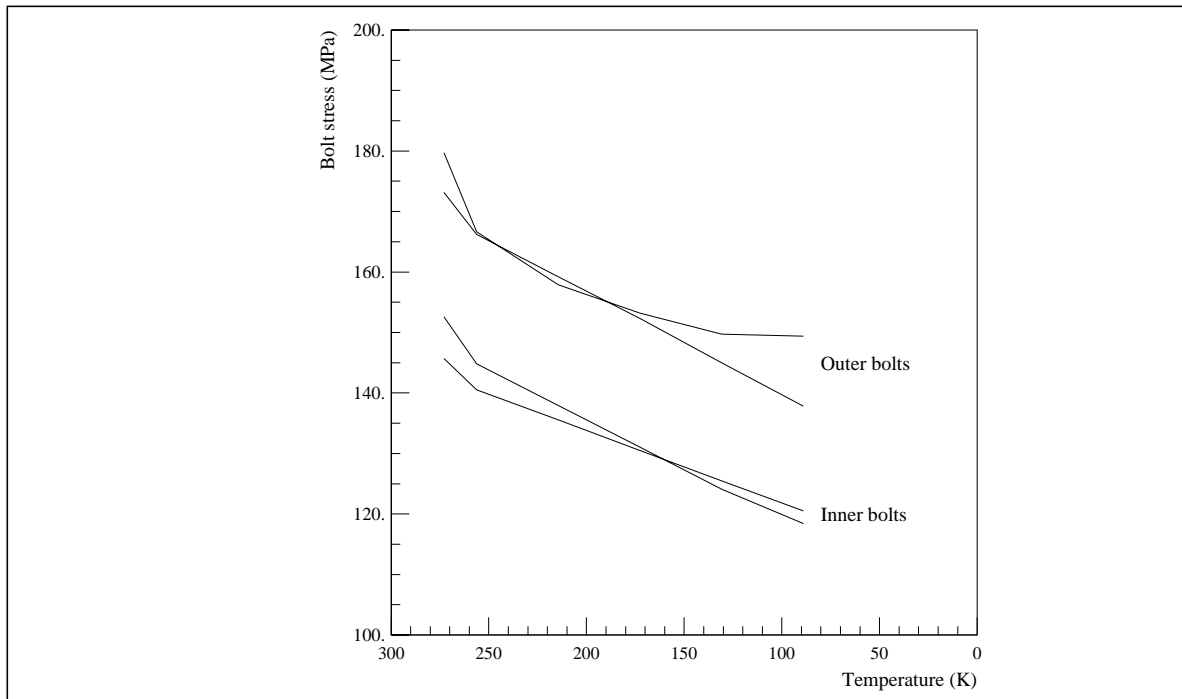
Parameter	Mean	r.m.s.
Outer radius of wheel	2030 mm	0.12 mm
Inner radius of wheel	372 mm	0.19 mm
Inter-module gap at inner radius	2.00 mm	0.036 mm
Inter-module gap at outer radius	2.00 mm	0.037 mm
Angle at inner tie bar	2.945 radians	0.0041 radians
Angle at outer inter-module clamping bar	3.142 radians	0.0029 radians

Figure 8-22 The finite element analysis model.

where separation occurs. The model would not generate reaction force if the circumference of a clearance bolt hole were to come into contact with a bolt, that is the bolts may not act as pins in shear: this scenario has not been seen in any analysis so far. To examine the way in which the structure might "fail" (by excessive deformation), the gravity loading, modelled by vertical upward acceleration, was increased in steps until a finite element analysis solution was not found (at about 4.5 g).

When the temperature of the structure is reduced to liquid argon temperature, there are two main effects. The first is the overall contraction of the structure from the room-temperature state, shown in Figure a to the LAr-temperature state, shown in Figure b. The support rails will be surface treated to provide a low-friction environment to allow the structure to slip laterally at the support points to accommodate the contraction. The position of the structure inside the cryostat is determined by guides located at the 12 o'clock position within the cryostat. The second effect of the cooling is caused by the differential contraction (2.2×10^{-4}) of the stainless-steel components relative to the copper plates. The clamping force of the various bolts will be reduced by about 20% because of this effect (see Figure 8-23), which poses no threat to the stabili-
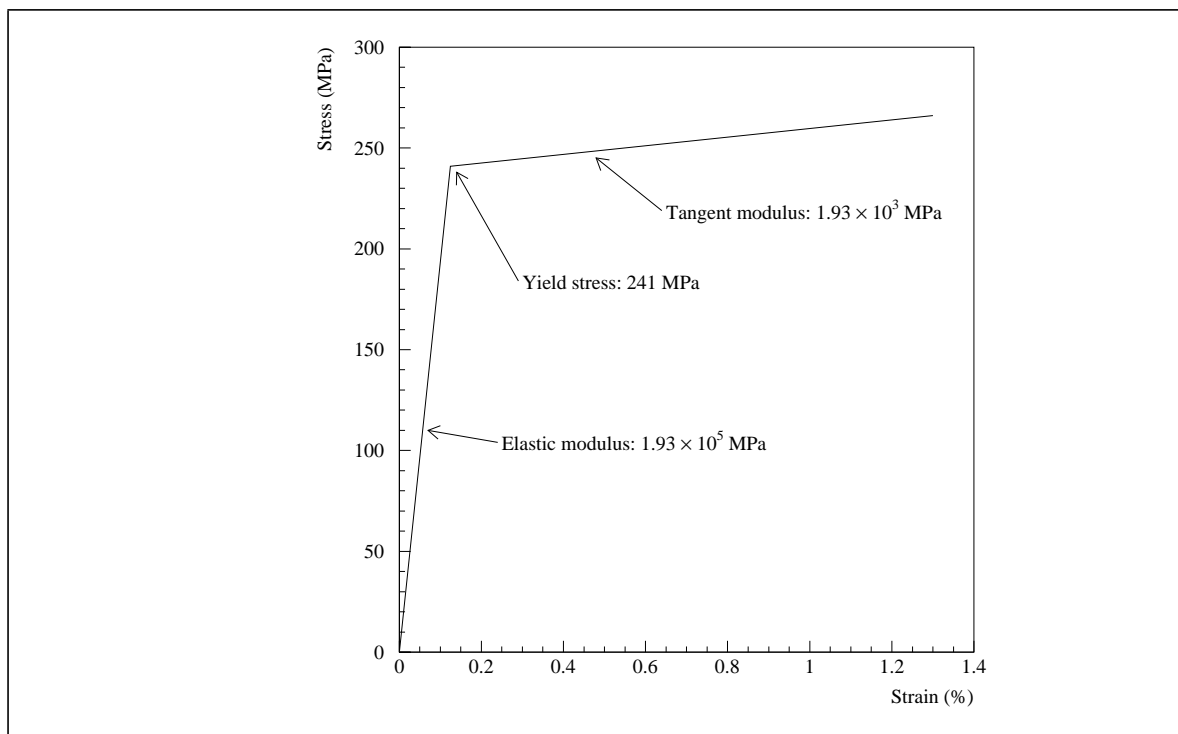
Figure 8-23 Typical change in bolt stress (and hence clamping load) due to cooling from 298K to 89K. The two separate lines show examples of bolts within the respective groups.

ty of the structure.

Figure 8-iva shows the Von Mises stresses and the (greatly exaggerated) deformation in the structure at 4g at the vertical support location. The inter-module clamping bar "key" does not come clear of the slot in the copper as shown in the exaggerated picture, but moves as far as allowed by the clearance spaces (0.25 mm) until it contacts the solid copper surface: the radial separation varies between zero and about 70 μm, which reduces frictional restraint and allows the latter slipping to occur. Figure 8-ivb shows the similarly exaggerated situation at the inner bolted joints under the 4 g load. The elastic/plastic behaviour of the stainless-steel bolt material is characterized by a bilinear stress/strain function as shown in Figure 8-24.

To examine the behaviour of the structure subjected to overload, a cyclic load of one to four times gravity was applied. Figure 8-25a shows the vertical deflection of the structure under such conditions: there is some irreversible plasticity in a few bolts and sliding at the copper plate/inter-plate clamping-bar interface at the support locations. The "sagging" which is thus produced is determined by the peak overload, but the structure returns to an elastic regime at modest loads. The plastic straining which occurs in the most highly stressed inner tie bar and
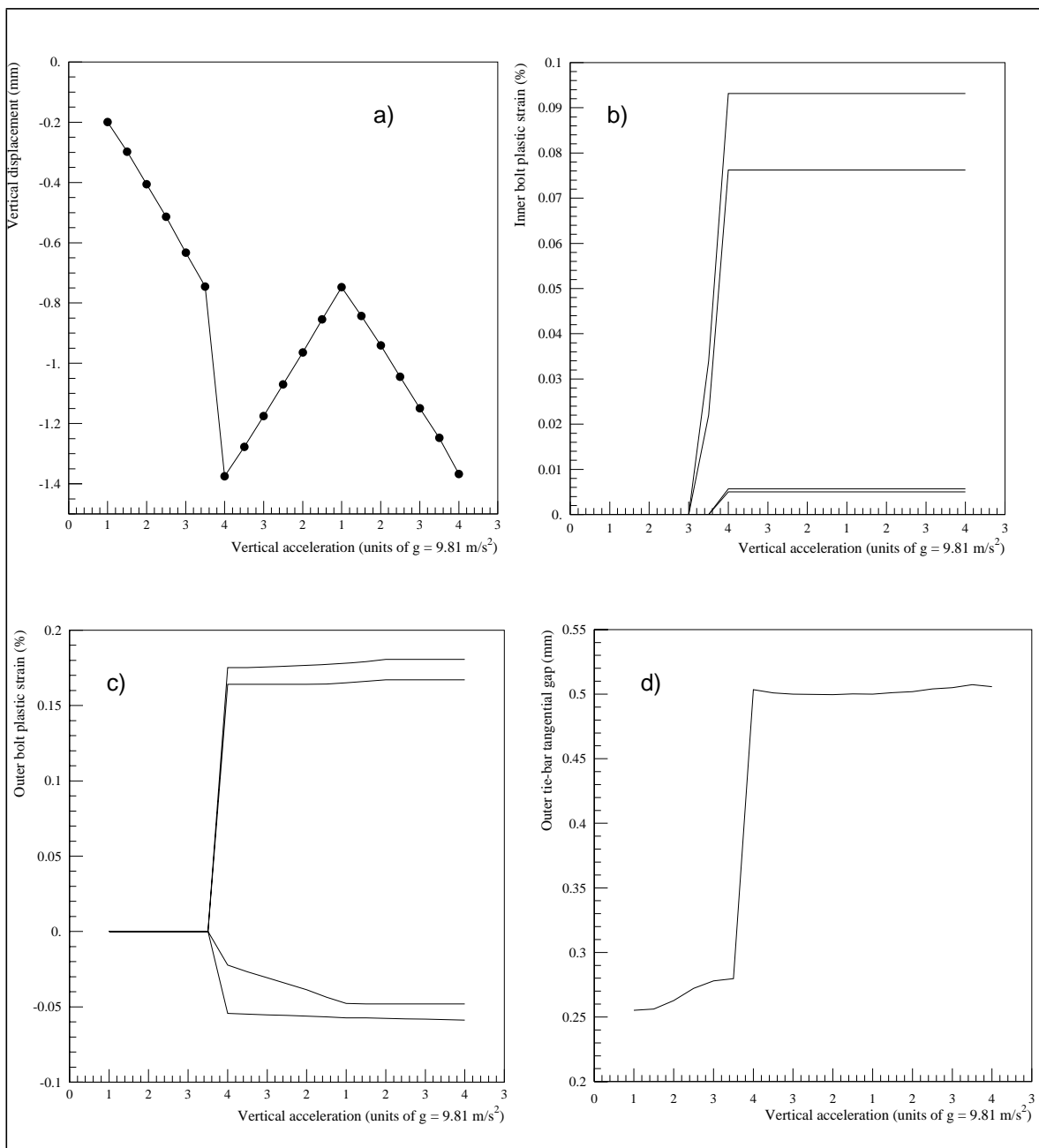
Figure 8-24 The bilinear stress versus strain function used to characterize the elastic and plastic behaviour of the stainless-steel bolt material.

inter-module clamping-bar bolts is shown in Figure 8-25 b and c. The sliding of the tie bar at the support position is shown in Figure 8-25d.

The conclusion of this finite element study is that the HEC wheel structure is strong enough to withstand the maximum likely forces that the structure will be subjected to during installation. We note that with crane use, even in emergency situations, additional g forces are below 1 g even when placing heavy objects on hard surfaces. By building a device that nominally withstands 3 g forces, and even under severe conditions is unlikely to exceed 2 g, we have allowed a certain engineering safety margin to allow such effects as differences in coefficients of friction from those assumed. The device that lifts the wheel and places it on the rails has yet to be designed, but these studies show there are no severe design constraints. In addition, the normal sag of the wheel is 0.2 mm if subjected to less than 3 g and 0.8 mm if subjected to forces up to 4 g.
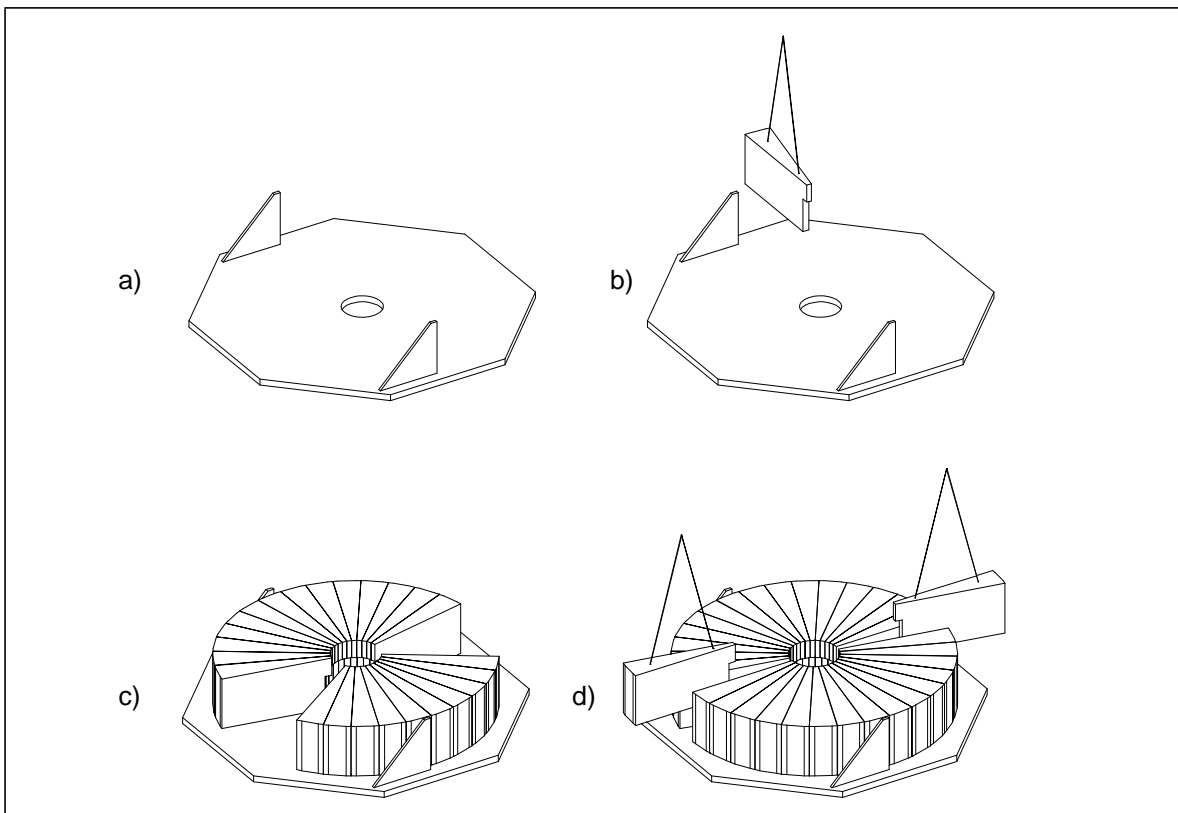
8.9 Wheel assembly

After warm and cold acceptance testing, the modules are assembled into wheels at CERN. Figure 8-26 and Figure 8-27 outline the major steps for the wheel assembly. The modules arrive on shipping frames that also serve as the interface between the modules and the wheel assembly table. The wheel assembly table is a flat table with two rails protruding from it, that are in the same position relative to the wheel as the rails in the cryostat. In addition the table has the ability to insert an alignment keyway at the same location (top of the wheel) that it is in the cryostat. The primary alignment is with reference to the machined table. The tightest clearance requirement for the HEC is that between the forward calorimeter and the HEC. For that reason the important function is to transfer the alignment from the rails (that define the vertical location of the wheel) and the keyway at the top of the wheel (that defines the sideways location of

Figure 8-25 Effect of a cyclically applied 4 g load on the HEC: a) vertical deformation; b) and c) the plastic straining that occurs in the four most highly stressed inner and outer tie-bar bolts, respectively; and d) the movement of the tie bar at the support position relative to one copper plate of the module at that location. The joint deforms elastically up to 3.5 g, then moves to the limit allowed by the notches in the copper plate.
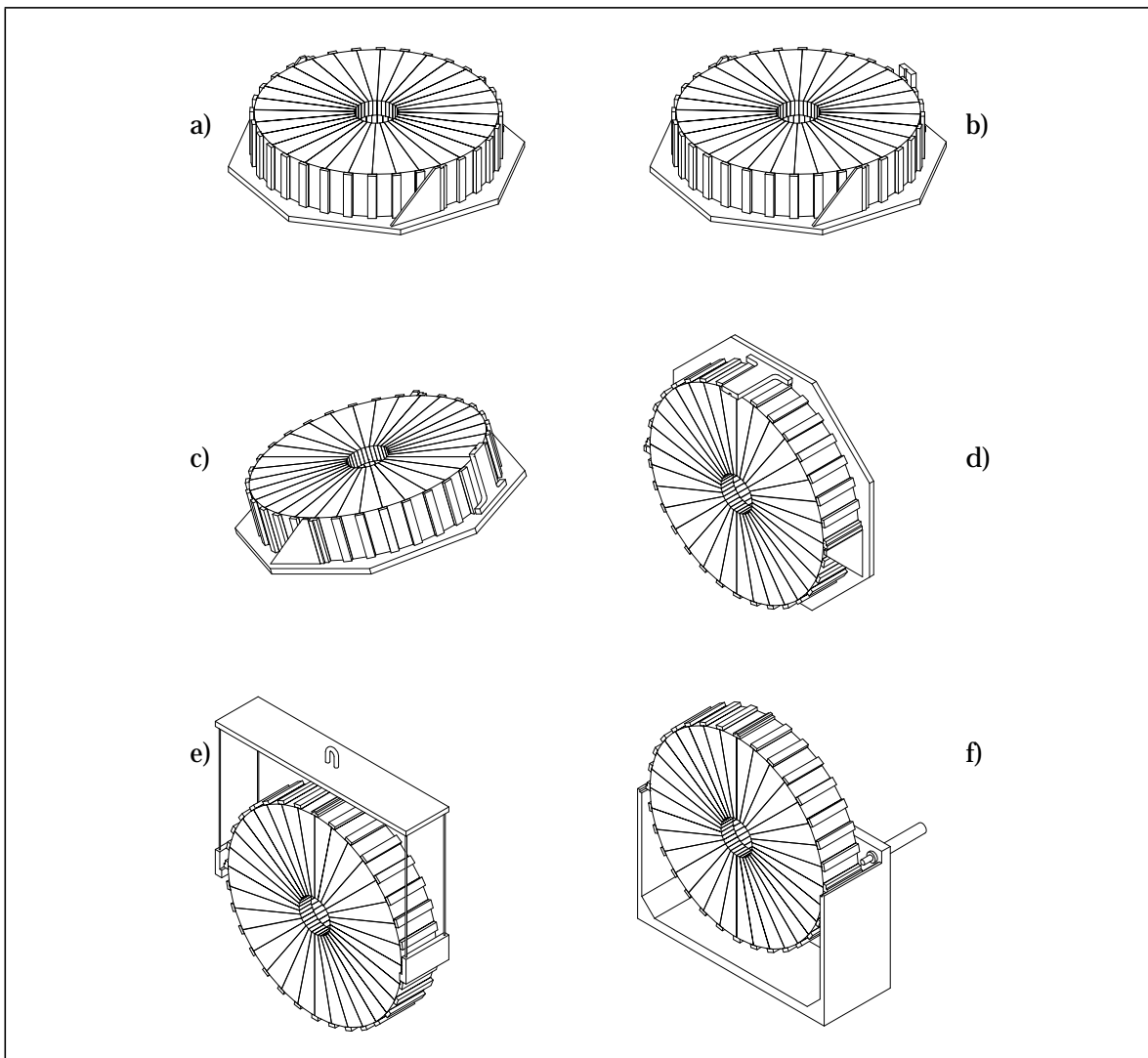
the wheel) to the inner diameter. The keyway guide is shown in Figure 8-28. Because the inner radius is the tightest clearance, the reference point used on the module while constructing the wheel is the tie rod at the innermost radius. The engineering concept for the method of constructing the wheel is to adjust for any module-to-module radial-dimension differences at the outer radius by shimming, and to accommodate individual plate-length differences between the modules at the inner tie bars. In addition any angular tolerances between bolting faces are designed to be accommodated by flexing the relevant tie bar. The tolerance on the radial dimension of the stack at the inner and outer radius is to be accommodated by adjusting the inter-module gap. This is possible because tolerances on the dimensions of the plates of the

Figure 8-26 Schematic of the initial steps in the wheel assembly, a) shows the stacking table with the support rails, b) shows the initial step of placing the first module at the rail position, subsequently a module will be placed at the azimuthal and radial opposite rail position, c) shows the continued stacking, where the wheel has been built in a symmetric way from the initial two modules at the rails, d) shows the final modules at the top and bottom of the wheel being inserted.

modules are at the 0.2 mm level. The notch in the copper plate is designed to accommodate at least 0.4 mm of movement.

The wheel assembly starts at the rail and as each module is set on the table its position is adjusted so that it is at the correct inter-module (ϕ) location, and the bolt faces shimmed until it can be bolted to the adjacent module. By obtaining the correct average ϕ position at this stage, the possibility that the final module will not fit due to accumulation of tolerances, is eliminated. By starting at the rails the final modules to be inserted will be at the top and bottom of the wheel. The base of the tie rod at the innermost radius is seated on one of 32 reference locations that serve to align the centre on the wheel with respect to the rails. Before bringing the modules together the inter-module insulating foil is inserted. Once the module is in the desired location the inner tie bars are bolted in place with a low torque such that no plate can be displaced in the module relative to its neighbours. Next the inter-module clamping bar at the outer radius is bolted in place. Again, to prevent subjecting any plate to forces that might cause a plate to move within a stack, this is initially done with a low torque on the bolts. At this low torque all the bolt joints must become fully seated. If they do not, shims will be added to facilitate seating. Once all the bolt joints are fully seated the inner and outer bolts are tightened to their final torque. The module is then tested along with its neighbour for high voltage, resistivity and capacitance (at about 500 kHz) to check no damage has occurred to the module. The assembly proceeds until the final module is in place. All the bolts in the wheel are then tested to check they have the correct torque. The alignment is recorded. Final high voltage tests in this orientation are undertaken.

Figure 8-27 Schematic of the final steps in the wheel assembly. Figure a) shows the completed wheel with the inter-module clamping bars bolted in place, b) shows the keyway guide installed, c) shows the wheel being rotated into its final orientation, d) shows the wheel rotated into its final orientation, e) shows the wheel being lifted ready to go to the cradle for insertion into the cryostat, f) shows the wheel in the insertion cradle.

Next the table is rotated until the wheel is in its final orientation: sitting with its weight supported on the rails of the table. The capacitance, resistance, and high-voltage measurements are repeated to check for any failures. The wheel dimensions are measured and the sag due to gravity ascertained. The temperature, strain, and position monitors are now installed. Strain gauges are installed on the front, middle, and rear of each support slider, and also at these same depths on the horizontal alignment guide at the top and bottom of the wheel. These will mainly be used to monitor strains in these items during insertion. As the front and rear plates have significantly more area exposed to the cool gas during cool down than the inner plates of the stack, they will cool slightly faster than the inner plates. While we have calculated the maximum temperature difference between adjacent plates due to this effect to be 2 K, monitoring would be prudent. Hence we propose to install a set of temperature probes at various positions of each wheel. 16 modules of each wheel will be equipped with three probes each. Position monitors that sense alignment marks on the rails and alignment guide are mounted on the front of each module. The wheel is now ready to be craned into the cradle, where final wheel cabling will be applied, and from which it will be inserted into the cryostat.
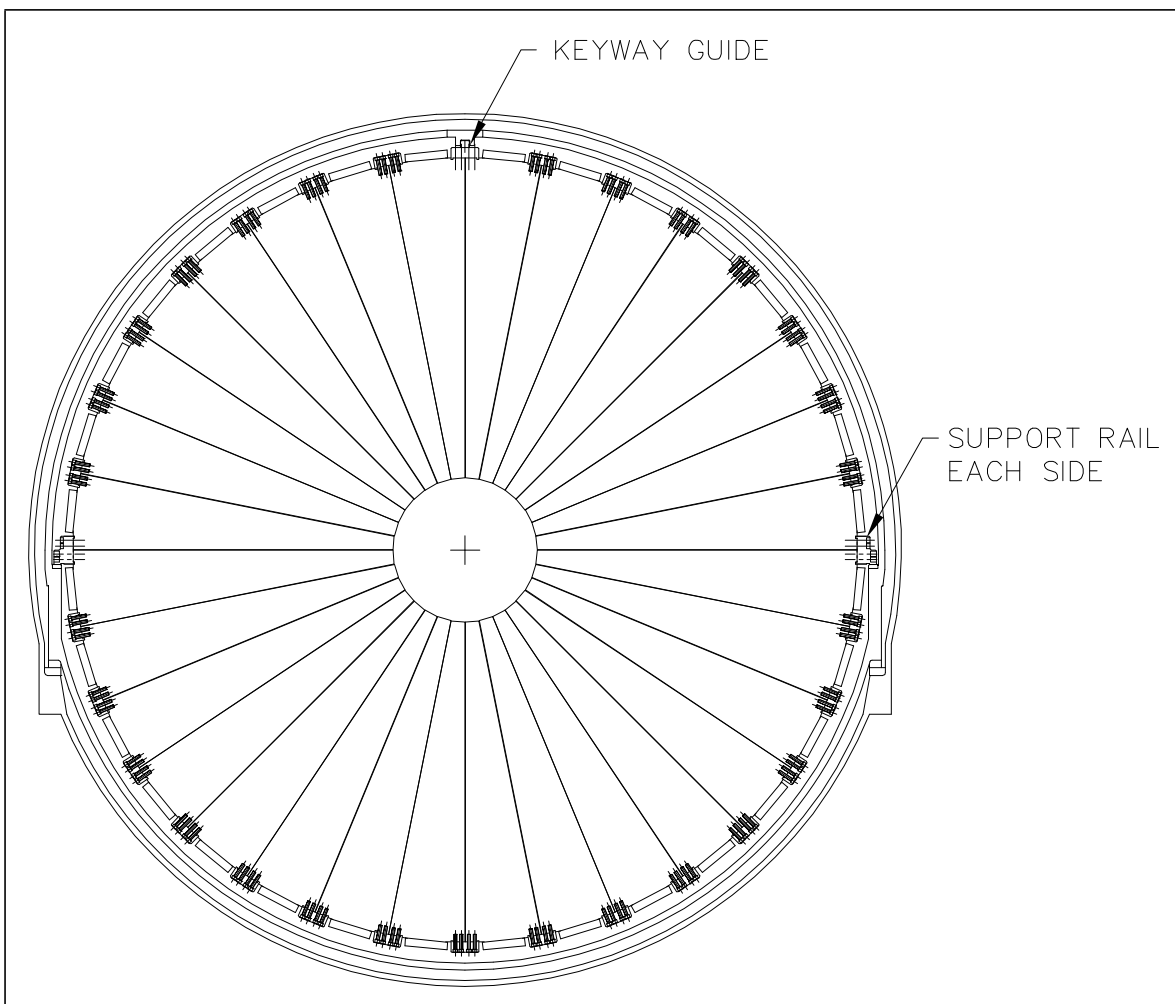
Figure 8-28 R-f view of the wheel showing rails and keyway.

8.10 Qualification

8.10.1 Test of materials for radiation hardness and LAr pollution

All materials must be selected to withstand the radiation levels that we anticipate will occur in the HEC (see Chapter 11). They must also be shown not to contaminate the liquid argon at this radiation level. Initial tests of all materials have been undertaken to ensure that suitable materials are being used at the design stage. This has been done by preparing a small cell that contains all the components that are expected to be used in the HEC. A combined radiation/purity test will be carried out with this cell in a neutron and gamma beam.

The module 0 materials will be tested at radiation levels that exceed the anticipated LHC radiation levels for 10 years of operation by another factor of 10, namely 600 kGy and 3×10^{16} neutrons cm^{-2}. This will both ensure radiation hardness of the materials and check that there are no effects whereby materials which are themselves suitable, are unsuitable in combination.

8.10.2 Results on radiation hardness of PI electrodes

Various samples of electrodes expected to be used in the LAr hadronic end-cap calorimeter were exposed to a high fluence of fast neutrons and to high γ doses. Before and after the irradiation, mechanical tests were performed. Glued films were subjected to a so-called "peeling test". A force was applied to a strip of 3 mm width, and the critical value to tear off the strip was measured. For the electrodes used in the hadronic end-cap calorimeter, a value of 0.2 N is required in the design specifications.

In Table 8-7 the critical values measured are presented for different samples of the EST electrodes. A 20 μm epoxy-acrilate-rubber composition was used to glue two layers of PI and copper or two PI layers together. Different pieces of the same sample were tested before and after irradiation. The range of the measured critical values are given in Table 8-7. Some variations of the values can be attributed to the non-industrial gluing procedure. Within the rather large uncertainties no degradation due to radiation damage is observed. The same conclusion can be drawn from tests of PI+copper and from polyethylene-tereftalat-copper (PT) samples glued by means of polyurethane, and from EST electrodes prepared by gluing the layers with acrylic adhesive .

Table 8-7 Results of the peeling tests for different types of glue.

Type of glue	Irradiated sample	Peeling force before irradiation	Peeling force after irradiation	Neutron fluence and γ dose
Epoxy	PI + copper	1.6 - 2.5	1.6 - 2.7	7.0×10^{14} n cm^{-2} 4 kGy
	PI + PI	0.6 - 1.5	1.1 - 1.5	
	PI + copper+ PI	1.0 - 1.2	0.9 - 1.0	
Polyurethane	PI + copper	1.5 - 1.7	1.5 - 2.1	1.8×10^{15} n cm^{-2} 20 kGy
	PT + copper	2.2 - 2.4	1.3 - 2.4	
Acrylic	PI + PI	5.1 - 7.1	4.9 - 6.8	1.8×10^{15} n cm^{-2} 20 kGy
	PI + copper	1.5 - 1.7	1.5 - 2.1	

In addition to the peeling tests, the radiation hardness of high resistive coating foils was investigated [8-13] at a neutron fluence level of 9.9×10^{14} n cm^{-2}. No visible change in the foil resistivity was measured after the irradiation. Recently, an irradiation study of CLK was performed at a neutron fluence level of 4.5×10^{15} n cm^{-2} and a γ dose of 150 kGy. Preliminary results show no changes of the CLK resistivity.

8.10.3 Warm test stations at CERN

Upon receipt at CERN, the modules will be retested for high-voltage stability, and capacitances will be remeasured. The height of the module will be remeasured, the module weighed, and the dimensions checked in a go/no-go gauge. By weighing the module with an accuracy of 0.25% the systematic effect of density on sampling frequency will be monitored. Measurements will be closely compared with the identical measurements made at the stacking sites prior to shipping. The two measurements of high-voltage current draw, and capacitance will be made at each

stage of the subsequent production tasks at CERN: after cold testing, before being assembled into the wheel, when the wheel is completed, after wheel rotation into final orientation, before the wheel is pushed into the cryostat, and finally after the wheel is located in the cryostat. Independent tests of the preamplifiers will also be made at these stages.

8.10.4 Installation of preamplifier boards on modules at CERN

Once warm tested the modules will have their preamplifiers added. This is done prior to cold testing so that the amplifiers can be cold tested for both the modules that will be beam tested and those that are only cold tested. The amplifiers will be tested and the calibration network exercised to check the system is functional.

8.10.5 Cold testing of modules at CERN

The following testing procedures are being considered and the feasibility investigated.

One eighth of all modules will be beam tested at CERN. For this purpose four modules will be tested in each beam test so as to enable hadronic showers to be contained. As we have 128 modules in our two end-caps this will require four beam tests. One test will be conducted each year starting 1998. These tests will be undertaken in the HEC cryostat in the H6 beam line.

Those modules not scheduled for beam tests will be cold tested in the HEC cryostat. Six modules can be introduced into the cryostat for testing, so, allowing for some loads to be less than six modules, a total of 20 tests will be required. Spread over four years, with each test taking three weeks (including one week for cool down, and one for warm up), this will use 15 weeks per year, which should leave adequate time for other tests in the cryostat. The above times for cool-down and warm-up are the fastest the module will experience and are used to calculate the maximum temperature difference between the copper and the PIs during cool down. Once cold, the modules will be tested for high-voltage integrity and the amplifiers and calibration system checked. It is considered to test the early-series modules in various orientations to establish that any module can be used in any position in the wheel. Once the modules have warmed up to room temperature, the capacitance and continuity will be measured again to check the warming up has not damaged any connections. The high voltage will be tested again, and also the resistance between the two high-voltage tabs on each HRL.

8.11 Tooling and process for installation in the cryostat

The mechanical installation in the cryostat follows closely the EMEC installation procedure using the same tooling (wheel assembly table, wheel lifting bar, and wheel insertion assembly). First the EM module is installed in the cryostat. After HEC1 has been assembled and rotated into its final orientation, the wheel is lifted off the wheel assembly table using a custom-made lifting bar. It is then lowered onto the rails, from which it will be pushed into the cryostat. At this point access is provided to the backside of the wheel to apply the quadrant cabling. The wheel is electrically tested and carefully checked for mechanical deformation. Calibration, low-voltage and high-voltage cables from the distribution boards, and signal cables from the preamplifiers are connected to the modules and routed to the rear of the module where they are temporarily stored. The cables and amplifiers are tested. The calibration system is operated to establish that the system is fully operational. Wheel installation in the cryostat then commences, with the wheel being pushed into the cryostat using jacks attached to the rails pushing on the

module sliders that sit on the rails. Once the wheel is in place, and has been rechecked electrically and for deformation, the temporarily stored cables are released and attached to the cryostat wall and the ends stored outside the cryostat. Once completed this allows the same procedure to be followed for HEC2.

8.12 Cost

Table 8-8 shows the material costs for the HEC project, displaying that 88% of the cost are in the

Table 8-8 Material costs (kCHF) of the HEC project.

HEC wheel mechanics	
Copper absorber	5,797
PAD and EST boards	1,500
Honeycomb spacing mats	131
Stainless steel components	935
Shipping	343
Installation fixtures	192
Module assembly	123
Module test at CERN	156
Wheel assembly at CERN	495
Module 0 and special modules	766
Total wheel mechanics	10,436
HEC wheel electronics	
Preamplifier system	675
Signal distribution system	399
Low voltage distribution system	33
High voltage distribution system	117
Calibration distribution system	52
Module 0 electronics	146
Total wheel electronics	1,422
Total HEC	11,858

mechanics and 12% in the cold electronics. 49% of the cost are in the procurement and machining of the copper plates. The spending profile starts in 1997 peaks in 1999/2000 and drops considerably in 2002. There are no production costs in 2003 and thereafter. PAD and EST board production is the next biggest expenditure at about 13% of the materials budget. The stainless steel components are 8%, the module and wheel assembly costs are 7%, with the remaining taken up with miscellaneous items such as shipping.

The manpower requirement is spread mainly over the years 1998 to 2001 when production will be underway. As might be expected, the biggest user of manpower is module stacking at, with the production of PI boards, module testing at CERN and wheel assembly requiring considerable amounts of manpower.

8.13 Schedule for production, testing, transport, final assembly at CERN, and installation in the pit.

The schedule of the main production of the modules is shown in Figure 8-29. This shows the series module production starting in September 1997, with the tooling and design for production. Module stacking starts in April 1998. Acceptance testing of modules at CERN starts in the spring of 1999.

Figure 8-30 shows the schedule of the wheel assembly and insertion. Wheel assembly of end-cap C starts in September 2000, when the stacking table is first available, and is completed by April 2001 in time for the beginning of wheel insertion into the cryostat at that time. The final module arrives at CERN in the late spring of 2002. The wheel assembly of end-cap A starts in February 2002 and is completed in time for insertion in the cryostat in December 2002.

8.14 Responsibilities

The construction of the HEC wheels is a joint effort of six groups from Canada (Alberta, British Columbia, Carleton/CRPP, Montreal, TRIUMF, Victoria), four groups from Germany (Heidelberg, Mainz, MPI Munich, Wuppertal), three groups from Russia (JINR, Moscow FIAN, Protvino), and one group (Kosice) from Slovakia.

The mechanical design is the responsibility of TRIUMF, whereas the electronic and cabling design is the responsibility of MPI Munich.
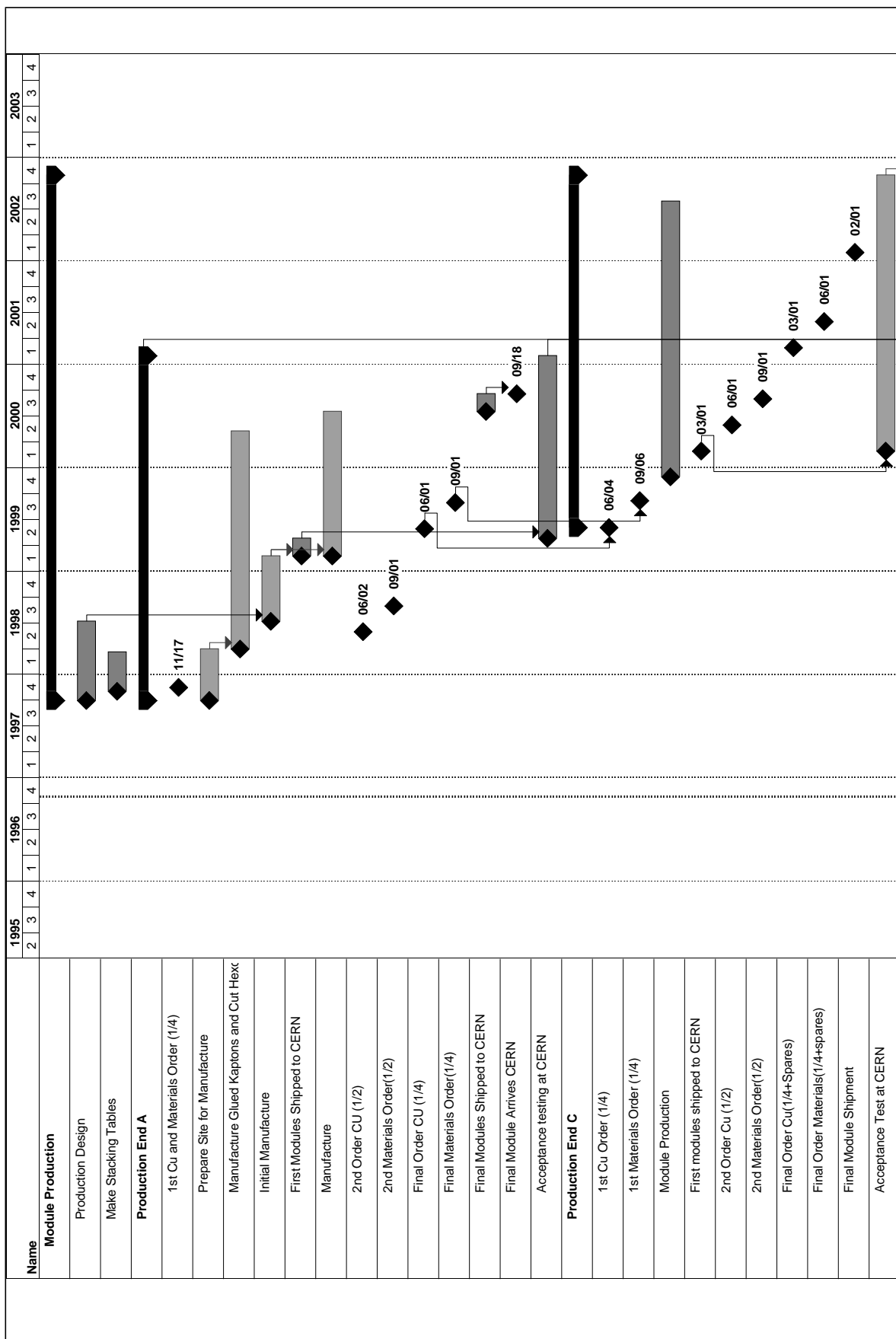
The copper absorber structure and the stainless-steel fixing components will be produced by Canada, JINR and Protvino. Canada, Moscow FIAN and Mainz will supply the read-out structure. The cold amplifier electronics together with the low voltage system will be delivered by MPI Munich. The signal cabling as well as the high-voltage distribution and cabling will be shared by Canada, MPI Munich and Wuppertal. Canada, Kosice and Mainz will be responsible for the calibration distribution and cabling system.

The parts will be delivered to five places where modules will be assembled: CRPP, JINR, MPI Munich, Protvino and TRIUMF. The cold testing of modules will be done in the HEC cryostat in the H6 beamline at CERN. It will be the responsibility of the institutions assembling modules to perform these tests. These institutions will assemble the wheels and insert them in the cryostat as well.

The overall project is jointly coordinated by TRIUMF and MPI Munich.

8.15 References

8-1   T. Hodges et al., ATLAS Internal Note CAL-060, 1994.

Figure 8-29 Schedule of Module Production
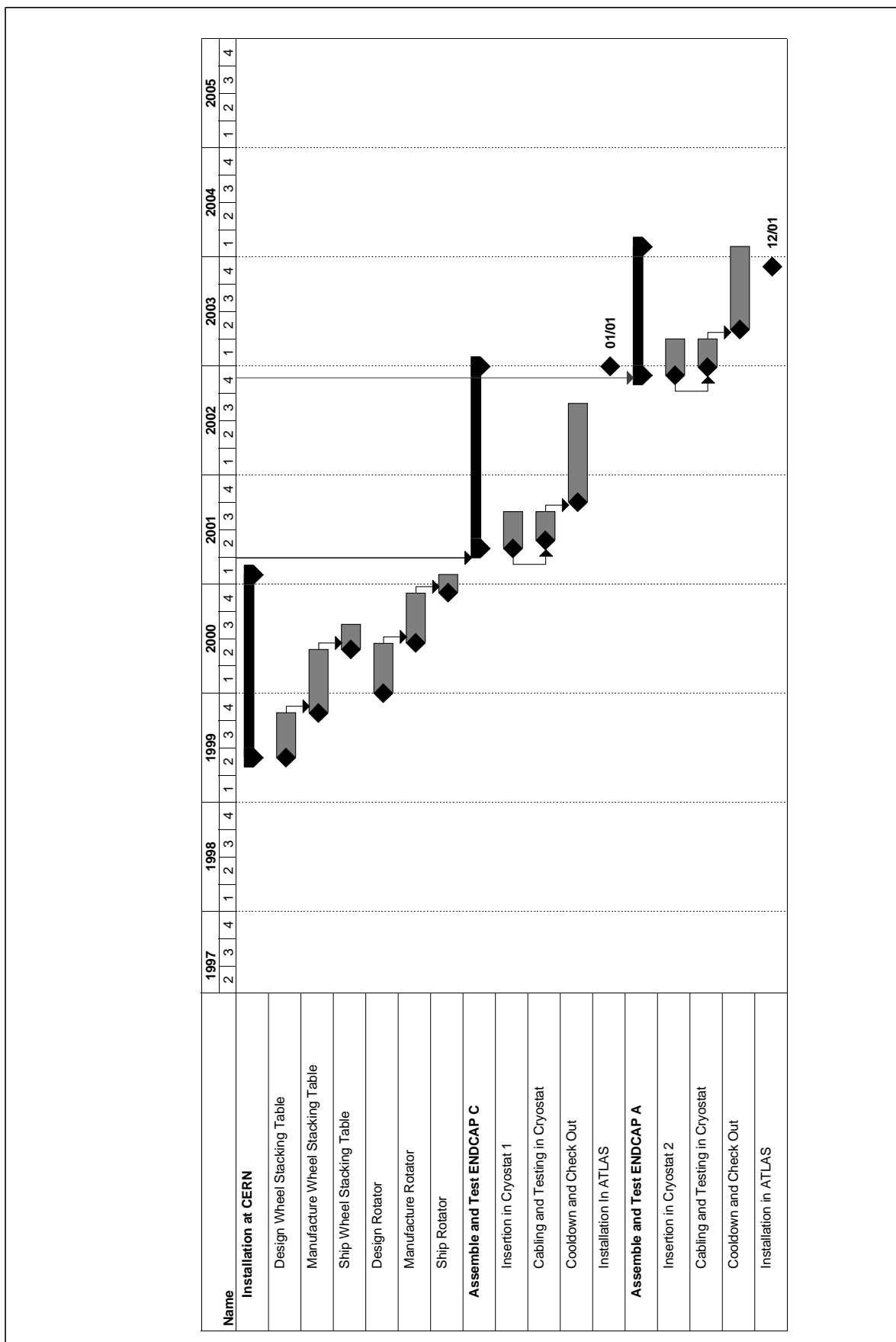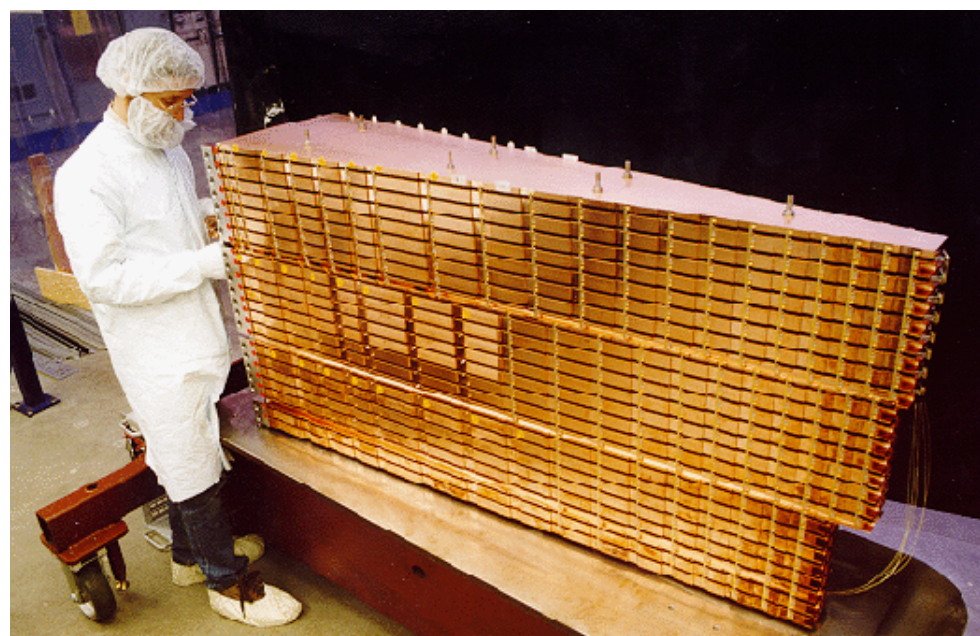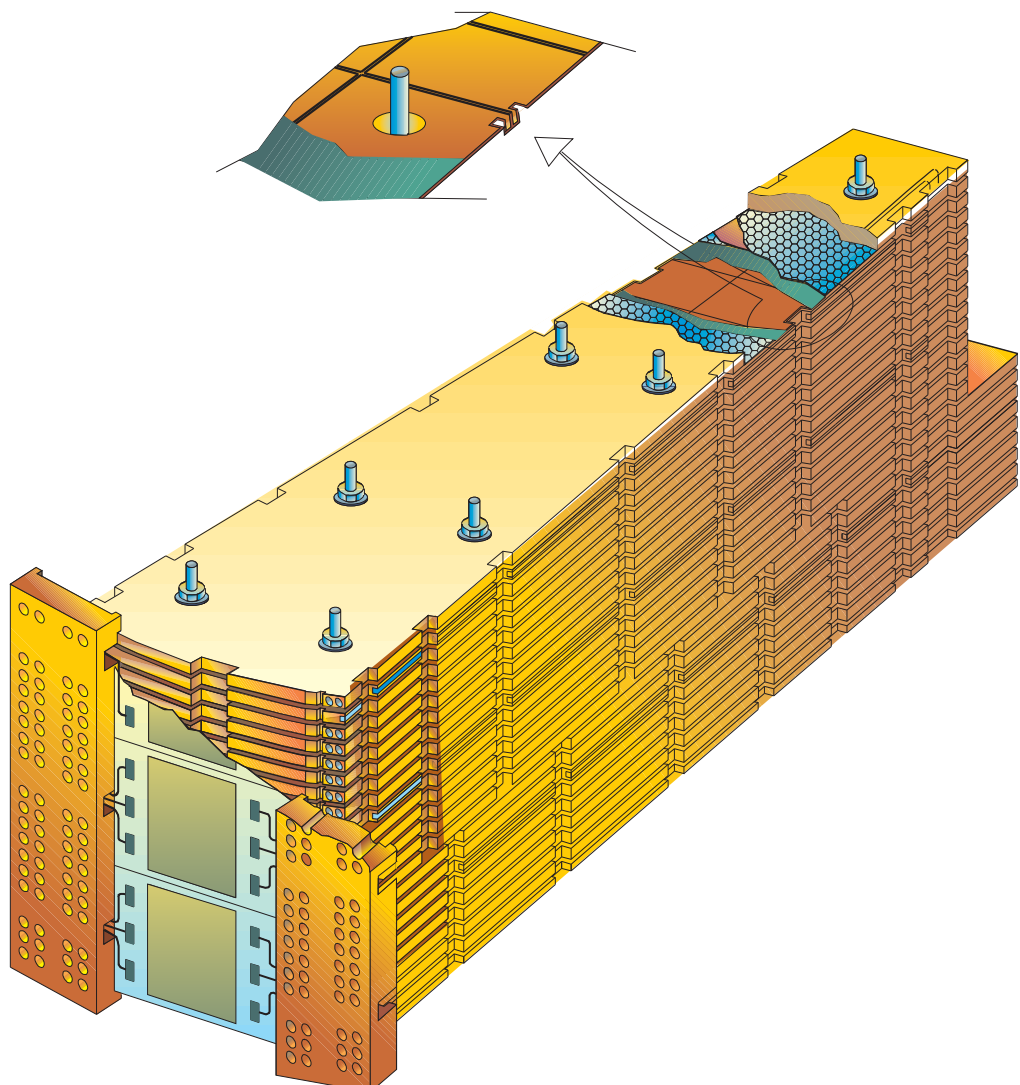
Figure 8-30 Schedule of Wheel Assembly and Insertion in Cryostat

8-2   P.M. Mockett, ATLAS CAL-033, January 1996.

8-3   American Society for Metals, Metals Handbook, 10th edition, vol. 1, American Society for Metals, Metals Park, Ohio, 1990.

8-4   H.P. Wellisch, W. Roberts, C.J. Oram, ATLAS Internal Note LARG-026, r 1995.

8-5   H. Brettel, D. Kalkbrenner, P. Schacht, ATLAS Internal Note LARG-046, 1996.

8-6   H.P. Wellisch, W. Roberts, C.J. Oram, ATLAS LARG-NO-024, September 1995.

8-7   M.S. Levitsky, A. A. Minaenko, ATLAS Internal NoteLARG-050, 1994.

8-8   XC Kapton produced by DuPont, High Performance Films Division.

8-9   This product was developed by Electro-Carbon Institute, Moscow Division.

8-10   H.P. Wellisch, C. J. Oram, Proposal for quality control in the ATLAS end-cap hadronic calorimeter, ATLAS note in preparation.

8-11   H. Laskus, H. Oberlack, P. Schacht, cabling scheme for the hadronic end-cap calorimeter, ATLAS LARG-NO in preparation, December 1996.

8-12   ANSYS v5.2, Swanson Analysis System Inc, Houston, PA, USA.

8-13   ATLAS HEC Note-014, Minutes of the workshop at the Ringberg castle, Ringberg, 30.08-2.09.1995.
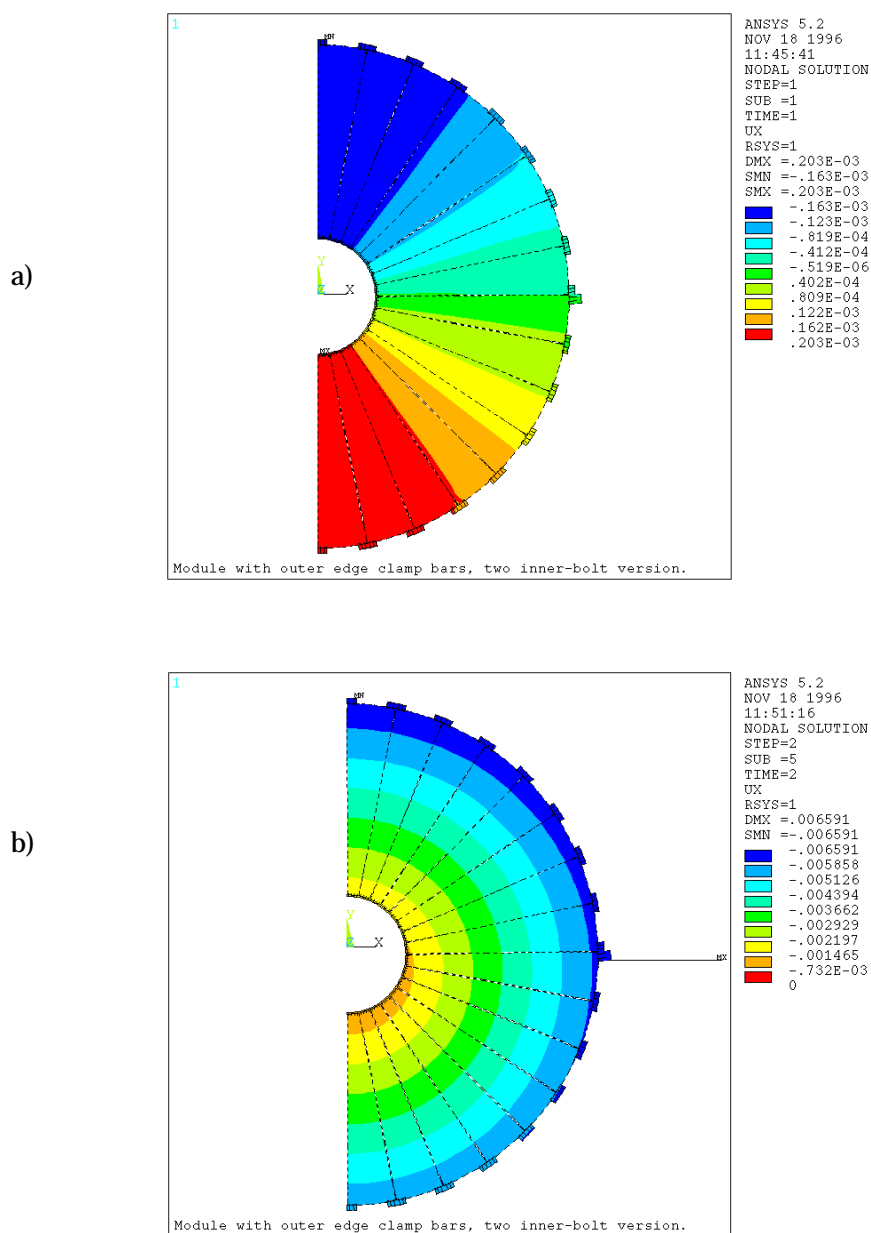
Figure 8-i Photograph of the prototype during construction prior to signal cabling. Note the notches on the side of the module that will house the signal cables.
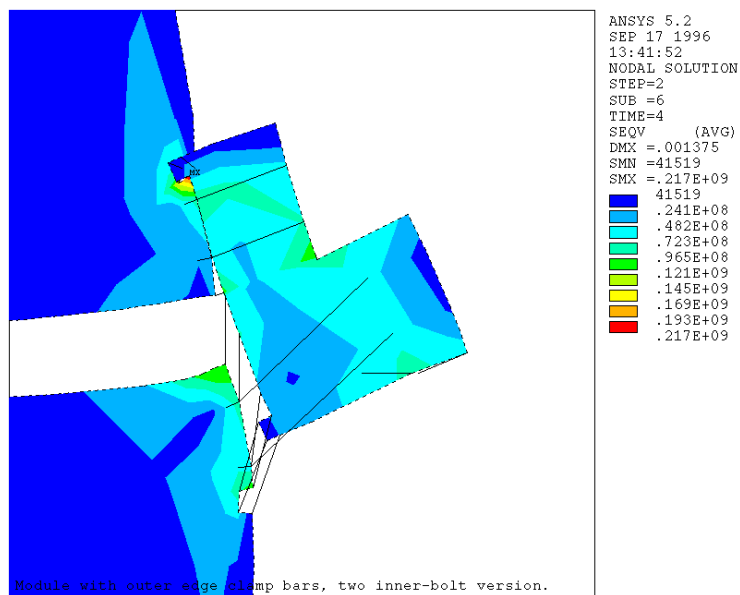
Figure 8-ii Artist's impression of a module, with cutaway showing the read-out structure.
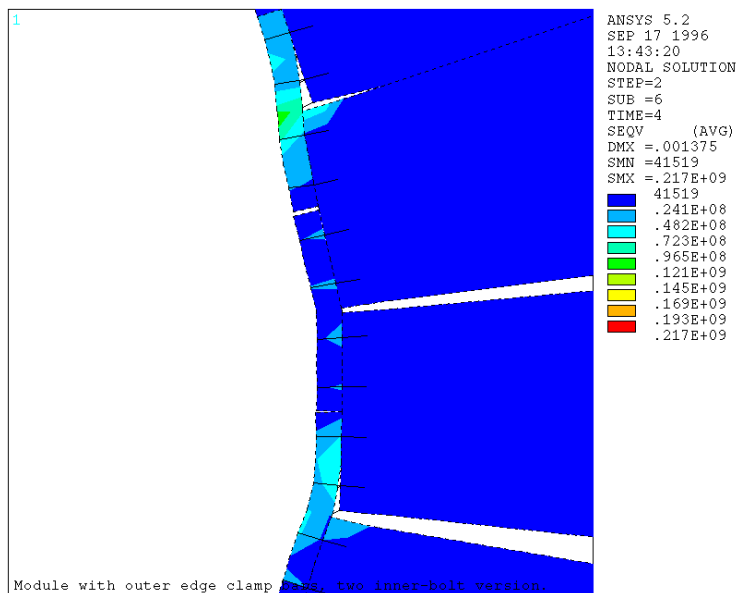
Figure 8-iii Stress analysis of the HEC: Plots a) and b) show the radial distorsion of the structure due to a) a normal gravity load at room temperature and b) due to gravity and cooling from 298K to 89K. Note that the thermal movements are much larger than those due to gravity.

a)

b)
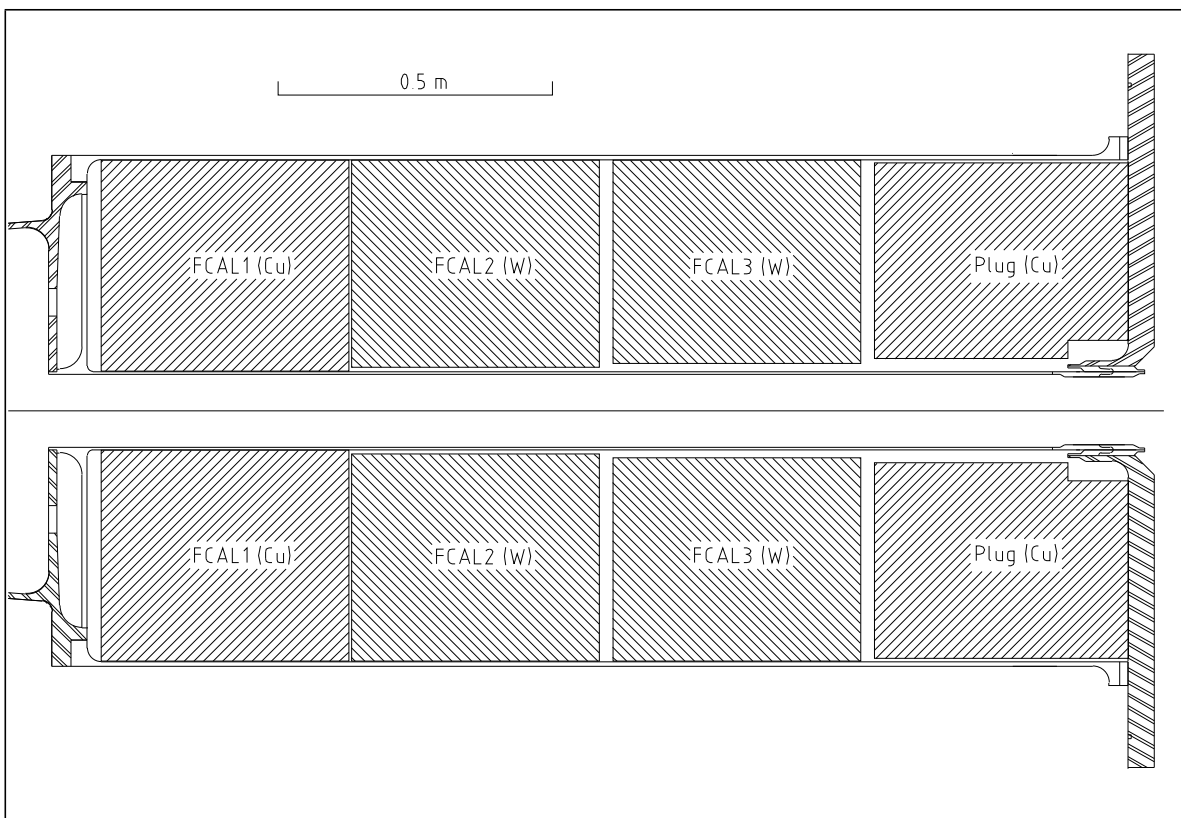
Figure 8-iv Stress analysis of the HEC: The Von Mises Stresses (in Pascals) and the (greatly exaggerated) deformation (the actual maximum deformation is given in each figure caption as DMX in units of metres) under 4 g load are shown for a) the slider where the wheel is supported and b) at the inner bolted joints.

9 The Forward calorimeter

9.1 Engineering overview

The ATLAS Forward calorimeter or FCAL, (see Figure 9-1) provides electromagnetic and hadronic calorimetry coverage in the range $3.2 < |\eta| < 4.9$ and has been previously described [9-1]. The FCAL is a liquid argon ionization device integrated into the end-cap cryostat [9-2][9-3][9-4] so as to minimize the effects of the transition in the region $|\eta| \sim 3.2$ [9-5]. The three modules of the FCAL are positioned within the forward tube structure of the end-cap cryostat. A fourth module, a passive shielding plug, is also contained within the forward tube.

Figure 9-1 The ATLAS FCAL (vertical section along the beam line axis, particles incident from the left).

Due to its location, the FCAL is subjected to radiation dose rates up to 10^6 Gy yr^{-1} and a neutron flux (kinetic energy > 100 keV) up to 10^9 cm^{-2} s^{-1} [9-6][9-7]. With these conditions in mind, the FCAL has been designed using the following guidelines:

- mechanical simplicity with short materials list

- radiation damage resistant materials

- high-Z materials

- high average density

- maximum projective thickness (along projective rays from the interaction point)

- minimum number of projective thin spots.

The FCAL is composed of three modules; the electromagnetic (FCAL1) and two hadronic modules (FCAL2 and FCAL3). The FCAL1 module is of copper composition and the hadronic modules of tungsten and sintered tungsten alloy. All three modules have the same nominal outer dimensions (450 mm in z, 455 mm outer radius) and have a centered beam hole of different radius for each module. Structurally, the FCAL modules are quite simple, consisting of single absorber matrix bodies carrying an array of tube electrodes in holes in the matrix bodies. Mechanical stress considerations are, therefore, largely reduced to questions of tube electrode integrity near module bearing points. The modules are supported by contact between their outer circumferences and the inner surface of the cryostat's forward tube.

A summary of FCAL dimensions is given in Table 9-1.

Table 9-1 FCAL dimension summary.

Dimension	Unit	FCAL1	FCAL2	FCAL3
Module outer radius (warm)	mm	456.4	456.4	456.4
Module outer radius (cold)		455	455	455
Module inner radius	mm	72	79	86
Module length (warm)	mm	451.5	451.5	451.5
Module length (cold)		450	450	450
Module front face (warm, cryostat open)	mm	4677.5	5134	5610.5
Module front face (warm, cryostat closed)		4662.5	5119	5595.5
Module front face (cold)		4668.5	5123	5597.5
Module rear face (warm, cryostat open)	mm	5129	5585.5	6062
Module rear face (warm, cryostat closed)		5114	5570.5	6047
Module rear face (cold)		5120	5573	6047.5
Pseudorapidity of front face inner (outer) edge	η	4.87 (3.02)	4.87 (3.12)	4.87 (3.20)
Pseudorapidity of rear face inner (outer) edge	η	4.96 (3.12)	4.95 (3.20)	4.95 (3.28)
Tube-to-tube spacing	mm	7.5	8.179	9.0
Gap centerline diameter	mm	5.00	5.125	6.00
Gap thickness	mm	0.250	0.375	0.400
Number of tubes		12 000	10 000	8 000
Absorber material		Copper	Tungsten	Tungsten
Module mass	ton	2.3	4.1	4.0

The basic electrode cell used in the FCAL is a tubular electrode with the tube axis parallel to the beam line. The electrode is composed of a rod held within a tube to form an exceptionally thin cylindrical shell liquid argon gap between them. Unit cell dimensions have been optimized for physics performance [9-8]. The tube electrode signals are summed at the module face to form read-out cells. Cell signals are carried on miniature (~1 mm diameter) polyimide-copper coaxial cables which run rearward in cable troughs on the module outer surfaces. These cables then emerge from the forward tube via notches in the rear face of the forward tube.

A shielding plug is located behind the FCAL modules in the forward tube. This shielding plug acts to provide shielding for the most forward muon chambers and is not instrumented.

Each of the FCAL modules is assembled at the institution responsible for them, tested and then transported to CERN. In the final assembly process, the modules are cabled and inserted into the forward tube. One of the finished FCAL assemblies will be calibrated in the H6 test beam. Each FCAL is then installed in its end-cap cryostat.

The FCAL is designed to detect jets with an E_T resolution of $\sigma(E_T)/E_T < 10\%$ for $E_T > 100$ GeV. This requires the FCAL energy resolution to be $\sigma(E)/E < 7\%$ and the jet angle resolution to be $\sigma(\theta)/\theta < 7\%$ typically. At the highest $|\eta|$, it is the angular resolution which dominates. A summary of FCAL physical parameters is presented in Table 9-2.

Table 9-2 FCAL physical parameters.

Parameter	FCAL1	FCAL2	FCAL3	FCAL Total
dE/dx Sampling Fraction (%)	1.49	1.36	1.68	
dE/dx Sampling frequency (cm^{-1})	0.59	0.36	0.34	
Depth (X_0)	29	92	91	212
Depth (λ)	2.6	3.5	3.4	9.5
Drift time (ns)	50	75	100	
Q/E (mip) (ke$^-$/GeV)	297	272	337	
i_{max}/E (mip) (μA/GeV)	1.9	1.2	1.1	
Potential across gap (Volts)	250	375	500	
Electrode capacitance (pF)	379	276	227	

9.1.1 Positive ion buildup

The argon gaps in the FCAL are quite thin (250 μm in the FCAL1 module) to avoid degradation of the signal at high luminosity from positive ion buildup. The prediction [9-9] for the onset of this effect depends on the ion drift speed which is not accurately known. Instead we will compare to measurements. Results reported in Chapter 2 show that up to an energy density of 5×10^6 GeV/cm^2/s the effect is smaller than 1% for 2 mm gaps. From the minimum bias energy distribution (see Chapter 1) one estimates a flux of electromagnetic energy on the front face of FCAL1 of about 130×10^6 GeV/cm^2/s at $\eta = 4.5$. Taking into account a factor 64 due to the use of 250 μm gaps in place of 2 mm gaps, a safety margin of a factor 2 results.

9.2 The FCAL1 module

9.2.1 Introduction

The FCAL1 module is composed of a cylindrical copper absorber matrix holding approximately 12,000 tube electrodes in a hexagonal-axis array. Module dimensions are 450 mm in z, 455 mm outer radius and 72 mm inner radius (cold dimensions). The FCAL1 module rests in the end-cap cryostat forward tube with its front face (nearest the interaction point) at z = 4668 mm.
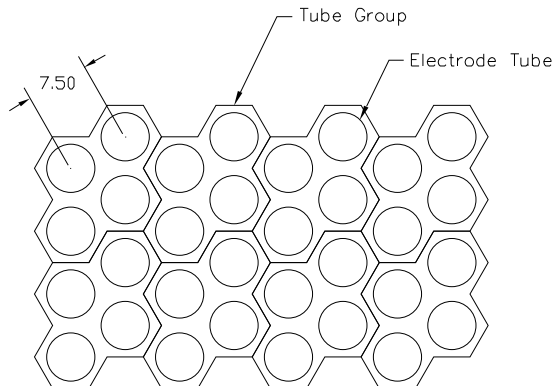
The tube electrodes are made of copper. The space between the rod and tube forms a cylindrical shell liquid argon gap of 250 μm thickness and 5 mm diameter. The electrodes are set on 7.5 mm centers. The tube electrodes are electrically connected at one end of the mod-

Figure 9-2 FCAL1 Tube Groups

ule in roughly rectangular groups of four (see Figure 9-2). All tube groups cover the same area measured in x-y (13×15 mm^2) so that the η–φ coverage varies with η. Each tube group is connected via one coaxial cable to one warm preamplifier. Signal read-out is done at the front face with striplines routed radially to the module outer edge where they turn rearward and are then connected to coaxial cables which run rearward in cable troughs cut in the module outer surface.

9.2.2 The electrodes.
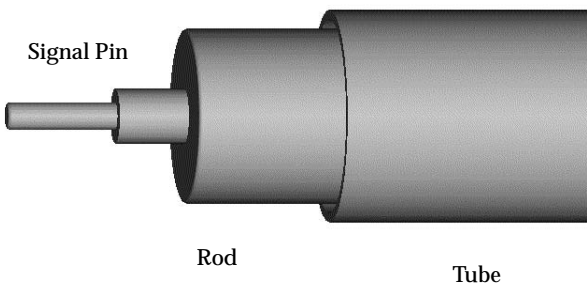
9.2.2.1 Electrode overview

The electrodes consist of a rod (with a signal pin inserted in one end) inside an outer tube such that there is a cylindrical shell gap of liquid argon between the two (see Figure 9-3). Centring of the rod in the tube is done by means of a polyimide-coated quartz fibre wound onto the rod (prior to insertion in the tube) in a single helical pattern. The choice of the fibre material is driven by radiation dam-

Figure 9-3 Tube electrode (exploded view).

age considerations only and does not indicate the use of any light-carrying capability of the fibre.

It is important to note that the electrode rods taken as a whole represent roughly half the mass of the module and therefore play an important part in the absorption characteristics of the module.

Table 9-3 FCAL1 module dimensions.

Item	units	value	plus tol	minus tol
Tube-to-tube spacing	mm	7.500	0.025	0.025
LAr gap thickness	mm	0.250	0.013	0
Centre of gap diameter	mm	5.000	0.013	0
Tube outer diameter	mm	5.750	0	0.025
Tube inner diameter	mm	5.250	0.025	0
Tube length	mm	447.65	0.250	0.250
Rod diameter	mm	4.750	0	0.005
Rod length	mm	447.4	0.250	0.250
End-plate hole diameter	mm	5.750	0.025	0
Absorber plate hole diameter	mm	5.850	0.025	0.025
Rod & tube straightness (sagitta)	mm		0.5	0

9.2.2.2 Rods

The rod material is hardened copper. The rods are centreless-ground to achieve the tolerance [9-10] and surface finish necessary for control of the electric field in the gap and to avoid sparking in it. One end of the rod is drilled with a 1 mm diameter by 6 mm deep hole to accept a push-in signal pin (Mill-Max #5601). The signal pins are inserted manually and maintain their grip and electrical connection by means of a spring pin end and barbs in the pin shaft. The rods are inspected with a "go/no go" gauge to verify the tolerance limits (see Table 9-3 for dimensions and tolerances). The length is similarly inspected with a "go/no go" gauge.

9.2.2.3 Tubes

The tubes are custom drawn from UNS alloy C12200 copper to the necessary dimensions. The tube ends are cut square and de-burred. The tubes are vapour-degreased by the vendor. Upon receipt of the order the tubes are inspected with a set of precision rod gauges (see Table 9-3 for dimensions and tolerances). Each tube must allow the "go" gauge to slide completely through it and must not allow the "no go" gauge to enter either end. Length is similarly inspected with a "go/no go" gauge.

9.2.2.4 Fibre & gap

The fibre which holds the rods in the centre of the tubes and allows the liquid argon gap to form symmetrically is a polyimide-coated quartz fibre of 240 μm diameter (PolyMicro Technologies # FHP200220240 or equivalent). The fibre is helical-wound with four turns per rod length. To prevent unwinding, the fibre ends are caught between retaining washer sets.

9.2.3 The matrix, end-plates, signal grounds

9.2.3.1 Matrix overview

The copper absorber matrix is composed of nine 50 mm (nominal) thick copper plates stacked in the z direction. Each plate has the hole pattern drilled in it to accommodate the tube electrodes. Absorber plates are joined by means of dowel pins and through rods near the outer periphery.

Absorber and end plates are purchased as 2 inch (50.8 mm) thick plate. After fly-cutting, the plate thickness is 49.78 ±0.1 mm. Crudely, a stack of nine plates gives 448.02 ±0.9 mm. The rather large stack-up error will be reduced by custom fly-cutting the ninth plate to give a tolerance of ±0.1 mm. The 451.5 mm warm module length given in Table 9-1 is actually an envelope including the retainer pins on the rear module face (but not the signal pins on the front face). The pins and washers total 3.5 mm in length.

The absorber plates are positioned with respect to each other by one INOX dowel pin and one INOX rolled spring pin per plate pair joining. This combination assures repeatability of justification of the plates for the various assemblies that are required. Fourteen INOX through rods fastened with circlips and tensioned with spring washers are used to hold the absorber matrix assembly together prior to tube insertion and swaging.

The outer circumference of the absorber matrix is shaped with 32 longitudinal cable troughs occupying a total of half the outer surface area. There are two grooves parallel to the beam axis in the uppermost boss between the cable troughs. These grooves, 3 mm wide by 4 mm deep by 20 mm apart, are for securing a polyimide sheet wrapping during the Final Assembly procedure.

9.2.3.2 Absorber plate design

Figure 9-4 shows a face view of one quarter of an absorber plate. The plate is nominally 50 mm thick. Seven absorber plates and two end-plates are required for one FCAL1 module matrix body. Matrix absorber plates are made from copper (UNS alloy 18700 [1% Pb for machinability].) The tube hole pattern is such that each tube centre is unambiguously contained within one quadrant of the FCAL, as defined by two diameter lines drawn at right angles.
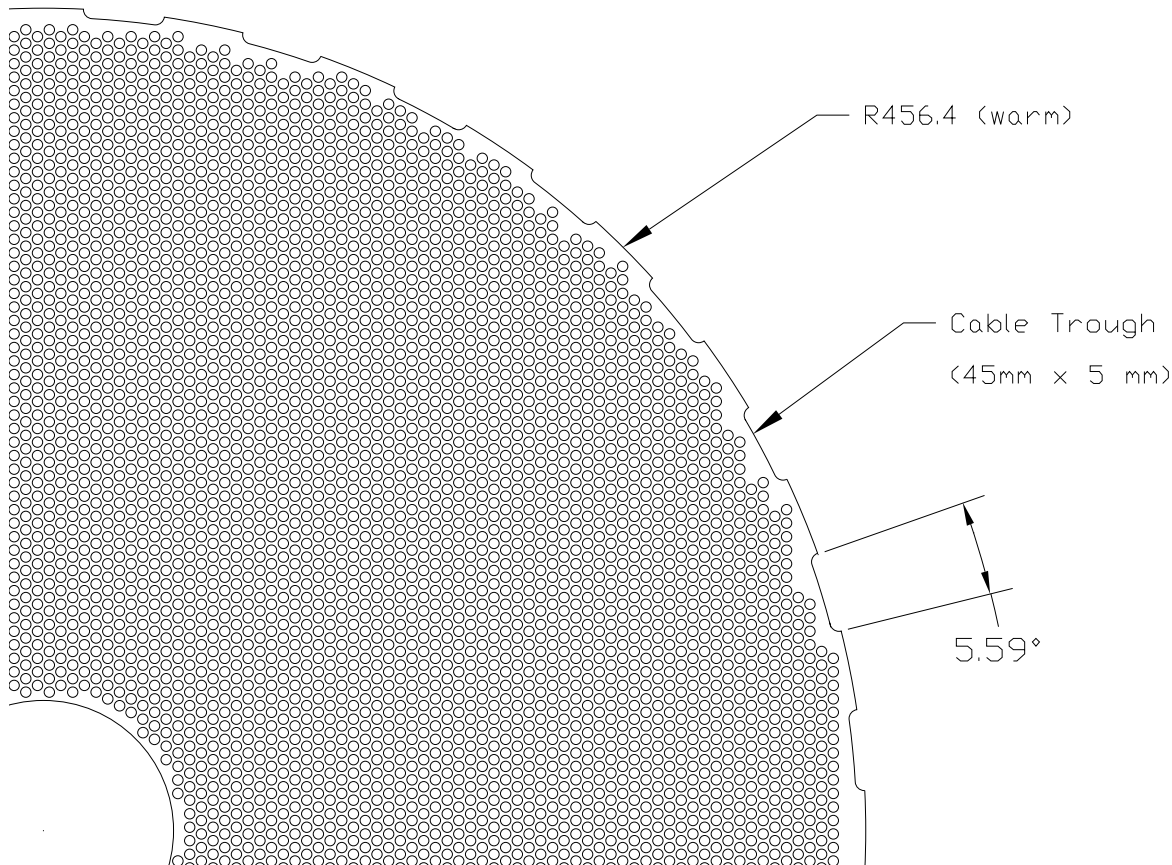
9.2.3.3 End-plate design

The end-plate design is very similar to the absorber plate design but with the following changes:

- tube holes are slightly smaller for a closer fit (one end only)
- addition of a swaging groove in each tube hole (one end only)
- addition of ground pin hole array on exterior face
- addition of module locating screw holes on outer circumference (one end only).

9.2.3.4 Fabrication and assembly

The copper plates are purchased as 91.5 cm (36 in.) square × 50.8 mm (2 in.) thick plates. The round plate profile (with the cable troughs and bosses) and the beam hole is then cut from the

Figure 9-4 FCAL1 absorber plate (quadrant view).

square plate by wire-EDM process, leaving precision surfaces (interior and exterior circumferences) which have no further need of machining. Each plate face is then fly cut to achieve the necessary thickness and flatness tolerance.
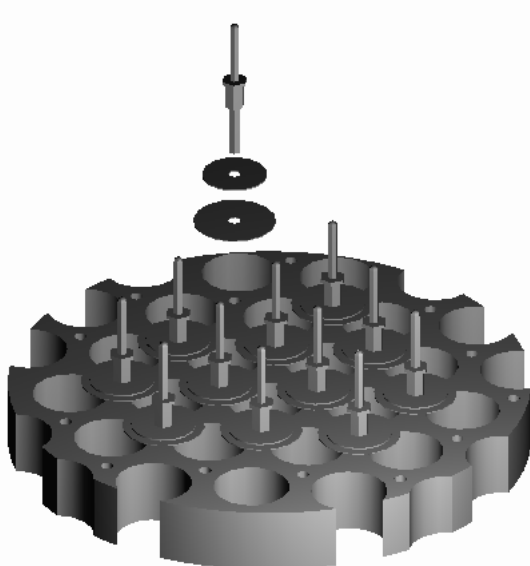
The tube hole pattern for each plate is centre-drilled using a Computer Numerical Controlled (CNC) machining center for accurate hole locating and then drilled to 5 mm diameter. Matrix end-plates are also drilled with a pattern of 1 mm holes to allow for the insertion of ground and retention pins. Once all the plates for a matrix are drilled, they are assembled with dowel pins in the final stacking order and gun-reamed to the finished hole size of 5.85 mm. This drilling process is designed to improve the straightness of the finished matrix holes over that resulting from a purely gun-drilling process.

The matrix is then disassembled and each plate is thoroughly cleaned. Re-assembly of the matrix then occurs in a clean room assembly area.

9.2.3.5 Ground pins and retainers

At the signal cable end of the module, an array of push-in signal pins anchored in holes in the matrix end-plate provides electrical grounds for the signal cables and to guard against movement of the electrode rods out of the end of the tubes. In addition, this feature retains the end of the electrode fibres to prevent them from unwinding. The pins are inserted through a polyimide washer (for electrical isolation) and an INOX washer (for strength) (Figure 9-5).

At the other end of the module, a similar array of pins cut off at the pin shoulder act solely as retainers for the rods and the fibre.

9.2.3.6 Interconnect boards

An array of interconnect boards at the front face of the module provides the electrical connections to form four-tube groups or cells. In addi-

Figure 9-5   End-plate ground pin and retainer assembly.

tion the signal cables are soldered to the appropriate interconnect boards. The interconnect boards are of glueless copper-clad polyimide construction (50 μm polyimide, 35 μm copper) with Mill-Max sockets (part #0285) inserted into board holes and then soldered in place.

9.2.4 Module assembly

9.2.4.1 Clean room and cleaning procedures

A clean room is required for module assembly that provides adequate floor space and clean conditions. It is estimated that 50 m^2 of floor space should be adequate. The modules will be assembled in succession, so space is required for one assembly area only. In accordance with the procedures listed in this document, the modules will be assembled part by part on their respective module carriers, thus avoiding the necessity of an overhead crane capable of lifting the complete modules. A 1 ton crane or hoist is still required for the movement of individual end plates. The assembly area must also be such that the finished modules can be removed (attached to their carriers) for shipment.

Class 2 clean room conditions (~10^5 particles ft^{-3}) are thought to be adequate.

Cleaning procedures for all module components will follow ATLAS LAr guidelines and be based on the prior experience with other experiments having LAr detectors, e.g. H1. Once components have been cleaned they will be packaged in protective plastic bags and not removed except in the assembly clean room.

9.2.4.2 Module carrier

The module carriers serve several functions including support of the modules during assembly, shipment, and FCAL final assembly. Prior to module assembly, each matrix body is placed on a

module carrier and fixed in position. The module carrier acts to hold the matrix during assembly and subsequent shipping (for which both are placed in an appropriate shipping container). It is also used during the FCAL final assembly operation.

The carrier must have the following:

- Carrying capacity of ~2 tons.
- Angular fixation capability for modules.
- Swivelled casters to allow the carrier to be moved in the assembly area.
- Capacity for steel casters (two of which are grooved) for use on final assembly track.
- Hand operated hydraulic jacks for height adjustment during final assembly.
- Removable sealing containment for shipment.

9.2.4.3 Tube swaging

Electrical contact between each copper tube and the signal end-plate is ensured by swaging each tube to a groove cut in the end-plate tube hole near the outer surface of the signal end -plate (see Figure 9-8). Swaging is done with a manual tool. The tube interior is cleaned and visually inspected after the swaging operation. Further details of the swaging design and process can be found in Section 9.3.3.

9.2.4.4 Fibre winding and rod insertion

After all the tubes have been inserted into the matrix and all the swaging completed, rod insertion begins. Each rod has a signal pin pushed into the hole at the signal end. A temporary rubber clamp is then pushed over the pin and the fibre end secured in the slit in the clamp. The fibre is then helically wound down the rod with four turns in all. The rod is then inserted into the tube, signal end first from the rear (non-signal) end of the matrix. Once the rod is fully inserted, the rubber clamp is removed from the signal pin. Retainer assemblies are pushed into the hole at the rear end after all the associated rods are in place. Signal end ground pin retainer assemblies are then also pushed into the end-plate holes at the signal end. The fibre is then trimmed to protrude 2 mm beyond the retainer washers.

9.2.4.5 In-line electrical testing

After each rod is inserted into its tube, a set of electrical tests are conducted to verify the tube gap quality. In order that these tests be repeatable and accurate, the liquid argon gaps must be filled with a dry dust-free gas rather than ambient air. Nitrogen gas is introduced into the gaps by holding a 6 mm rubber hose against the rear (or ground) end of the module over the rod in question. This causes nitrogen to blow through the gap and out the front face end of the gap. Each tube gap has a volume of 1.77 cm^3 so several complete turnovers of the contained gas can be done in a brief time using a reasonably low gas flow rate (several litre/sec).

Next, a continuity check is carried out on the electrode to detect any contact between the tube and the rod. Then, a capacitance measurement of the electrode is made using a hand-held capacitance meter. This test verifies that the tube and rod are adequately coaxial. Finally, a high voltage stand-off test is done to detect the presence of any shorting contamination in the electrode. All tests are done on a "go-no go" basis with each test having an established threshold(s) for passing. Test results are recorded for each electrode. Electrode assemblies failing any of

these tests are then disassembled, cleaned, and redone. Ground and retainer pins can be extracted by hand without damage to the pin hole. A new pin must be used during re-assembly.

9.2.4.6 Complete module electrical testing

After each module is assembled, the above-mentioned capacitance and high-voltage tests are conducted on tube groups. One end of the module is bagged, and bottled dust-free nitrogen gas is then introduced into the bag which causes the gas to flow through the module argon gaps. All the results are recorded, including the leakage current under the HV load. Tube groups which fail these tests are investigated tube by tube and the unsatisfactory electrode assembly is disassembled, cleaned and redone. Ground and retainer pins can be extracted by hand without damage to the pin hole. A new pin must be used during re-assembly.
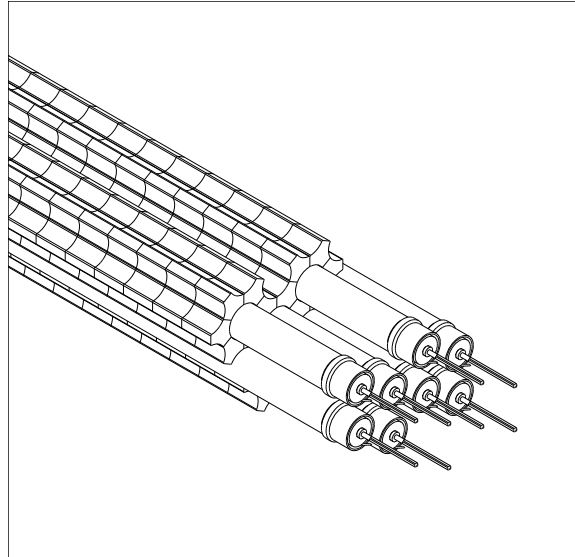
9.2.5 Shipping preparation

Once the modules are completely assembled and all the electrical inspection tests are complete, the modules are prepared for shipping. Both the front and rear face of the modules are covered with a thin (13 μm) polythene film and then a 25 mm thick piece of soft, dust-free foam is applied to each face. The crating that is then constructed on the module carriers presses the foam to the module faces, protecting the module, and helping to retain the rods and pins during accelerations associated with shipment.

9.3 The hadronic modules

The adoption of a high density tungsten absorber for the hadronic modules of the FCAL allows the design criteria to be met by a device small enough to make the integrated design feasible. In essence the absorber and structure of the hadronic modules are identical to the electromagnetic modules; but the detailed building of the structure is very different. The electrode structure is identical to the electromagnetic modules, except that the electrode rods are pure tungsten. The bulk of the absorber matrix is built up of small sintered tungsten alloy slugs.

An FCAL hadronic module consists of two precision drilled 25 mm thick (nominal) copper end plates with the ends of the copper tubes of the electrodes attached to them. With ~10,000 (8,000 for FCAL3) tubes arranged in a hexagonal pattern, this structure provides the mechanical integrity of the device. The electrode rods are inserted in the tubes in a manner identical to the electromagnetic modules;

Figure 9-6 A cut-away view showing how the absorber matrix of the hadronic modules is composed of tubular electrodes embedded in a matrix of small tungsten slugs.

and the absorber matrix is built up from layers of small sintered tungsten slugs, layered between the tubes. The tungsten absorber matrix between the tubes is not part of the load bearing structure.

9.3.1 Structural analysis

The design of a device weighing approximately 4 tons and having an average density of ~15 g cm^{-3} raises questions of mechanical and structural integrity. The design of the hadronic modules is a highly modular one, with the structural characteristics of each tube and rod set largely independent of all others.

The basic structural unit of the hadronic modules is that of the tube electrode. Each electrode assembly, supported at its two ends by the module end plates, carries its own weight and that of two rows of the sintered tungsten slugs that form the absorber matrix. In detail, the copper electrode tube carries the slug weight (190 g) via its exterior and has the weight of the tungsten rod (153 g) in its interior. The addition of the tube mass (~18 g) yields a total unit mass of 361 g. This load is uniformly distributed along the electrode which is a member of 400 mm length (subtracting the 25 mm length at each end which is held inside a hole in the end plate) supported at both ends. The electrode consists of a rod and tube combination which can share loading, if needed, through forces exerted on the quartz fibre which separates them. The study of the FCAL2 maquette (see section 9.3.2) shows negligible sag of the electrodes after construction.

With the load of the tungsten slugs and rods transferred to the end plates, the remaining questions pertain to the ability of the end plates to support this load without excessive deformation. The normal FCAL2 and FCAL3 module support surfaces experience a contact pressure on the order of 4 MPa. During Final Assembly, the modules are temporarily supported on the beam hole surface, resulting in contact pressures roughly 10 times higher. This is to be compared to yield strength of ~250 MPa for the material in question. Clearly, a large safety factor is present.

The remaining question, then, is that of the exact electrode placements near the bearing surfaces. Excessive loading which might cause permanent electrode deformation must be avoided. To be more precise, the question is whether a particular electrode in the regular pattern (near the module bearing surfaces) should be included in the module or left out. The electrode pattern itself, i.e. centre-to-centre spacing and angle, will not be modified. Finite element analysis is being undertaken to determine the electrode placements near support surfaces.
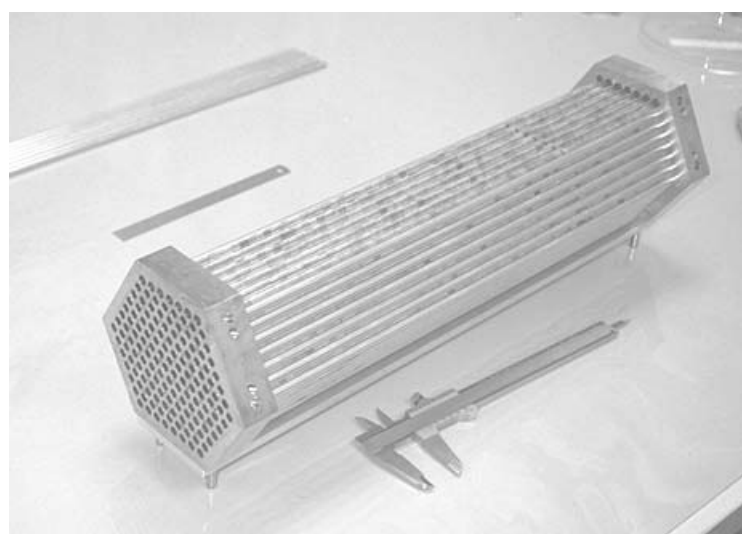
9.3.2 The tungsten absorber matrix

Tungsten is difficult to form and machine, so innovative construction technologies must be used for the hadronic modules. Pure tungsten is too refactory and expensive to work with, so the hadronic modules are constructed from small sintered tungsten slugs. Sintered tungsten is formed from tungsten powder and other binder metals; in our case Ni and Fe. With relatively modest heating, this powder mixture can be used to form complex and comparatively easily machinable parts.

The absorber matrix of the hadronic modules is formed by inserting 6.22 mm long sintered tungsten slugs between the copper electrode tubes. An exploded view of this structure is shown in Figure 9-6. The slugs are pre-formed before sintering to be of the appropriate shape to fit into the hexagonal matrix. The length of the slug is constrained by the ability of industrial suppliers to maintain the required tolerance on the straightness of the pieces. The slugs must be precisely shaped so that all gaps are small. The result is a very dense radiation-hard calorimeter with a very small sampling fraction and no dead space.

An engineering maquette [9-11] has been produced (see Figure 9-i, Figure 9-ii) in order to verify the feasibility of this structure, and also to confirm the ability of manufacturers to produce the tungsten components. In addition to providing the first information on the various components, the maquette has facilitated the development of the tooling necessary for the module-0 construction. The device shown in Figure 9-7 is essentially a laterally reduced FCAL2 module; apart from the lateral extent, it incorporated all the proposed features of the final design. The FCAL2

Figure 9-7 The engineering maquette, before the installation of the electrode rods.

electrodes are grouped in read-out cells of six, so the maquette was constructed to accommodate 108 sensitive electrodes; corresponding to 18 read-out cells. The number of copper tubes, tungsten rods, and tungsten slugs was large enough to allow us to have a good statistical sampling of the manufactured components.

9.3.3 End-plates

The maquette allowed us to test and develop the swaging technique of attaching the copper tubes to the end-plates. The end plates in the maquette are 25 mm thick copper plates, with holes for the copper electrode tubes. In the swaging process the copper tubes are radially deformed where they pass through the end plates. This radial deformation into a groove in the end-plates locks the tubes into place. This method was chosen after extensive tests of both swaging and various welding techniques. Swaging was found to be faster, cleaner, and more reproducible. In order to carry out, it is necessary to machine an internal groove to a depth of $300\,\mu m$ inside each hole. Figure 9-8 shows the ma-

Figure 9-8 A close-up view of an end-plate, showing the grooves necessary for the swaging operation and the ground pin holes.

chined grooves inside the end-plate holes. To ensure good electrical and mechanical contact, these grooves must be precisely cut to the correct depth.

A lot of production experience was gained when machining the maquette end-plates. Rapid tool wear was experienced from the softness and work hardening of the pure copper. The use of

pure copper makes it difficult to maintain the required precision on the holes and grooves. The final design will use a copper-lead alloy rather than pure copper.

9.3.4 The Copper electrode tubes

The copper tubes form the outer element of the electrode structure, and must be of high quality. We require an absence of internal defects; that the tubes are seamless, straight, and produced to high precision. Also, to maximise the amount of tungsten absorber, the tube walls must be as thin as is consistent with economical assembly. The tube specifications are a length of 450 ± 0.5 mm, and outer diameter 6.00 ± 0.02 mm, and an inner diameter of 5.50 ± 0.01 mm. These specifications yield a tube wall thickness of 0.25 mm. Our measurements of the tubes supplied for the maquette are given in Table 9-4.

Table 9-4 Dimensions of copper tubes supplied for maquette.

	Tube Length	Outer Diameter	Inner Diameter
Specified	450.00 ± 0.5 mm	6.00 ± 0.02 mm	5.50 ± 0.01 mm
Supplied	450.09 ± 0.10 mm	6.015 ± 0.005 mm	5.474 ± 0.006 mm

9.3.5 Tungsten slugs

The sintered tungsten slugs used in the maquette constituted the first sample of slugs produced. They were obtained from the Mitech corporation. The slugs were produced by sintering a mixture of 97% W powder, 2% Ni and 1% Fe; the Ni and Fe acted as binding metals. The powdered material was mixed with an organic binder and pressed into "greenform" slugs. These greenform slugs are approximately 20% larger than the specified dimensions of the final parts. The slugs were then fired at the melting temperature of the binding metals, causing the parts to shrink as the metal flowed between the W granules. The resulting sintered tungsten slugs have a density of 18.5 g cm^{-3}; for comparison, industrially

Figure 9-9 Sintered tungsten slugs as obtained for the engineering maquette.

"pure" tungsten has a density of 19 g cm^{-3}. The shape of the tungsten slugs can be seen in Figure 9-6, and Figure 9-9 shows a photograph of the slugs used to construct the maquette.

The ability of the manufacturer to produce the small tungsten slugs to the required tolerance is the largest uncertainty in the entire design of the hadronic modules. The production of the slugs for the maquette was the first test of this process; it has given us confidence that the process is practical. Except for a small number of outlyers, the manufacturer was able to meet the length requirements. In fact, they were able to produce a large sample of slugs with a length fluctuation of 78 μm r.m.s. deviation, which is much better than the 200 μm tolerance specified.

Table 9-5 Lengths and masses of tungsten slugs supplied for maquette.

	Slug length (mm)	Slug mass (g)
Specified	6.15 ±0.20	
Supplied	6.180 ±0.078	1.484±0.027

The variation in the lateral profile size of the slugs was checked by passing a sample of 10% of them through a gauge that we had constructed. It was found from this that the company met the tolerance on the maximum size. To check the variation of the minimum lateral dimensions, the masses of a sample of slugs were determined. We measured the density of a sample of slugs, and found it to be 18.5 g cm^{-3}, as specified. This and the measurement of the slug lengths and masses, allowed us to determine that they are very close to the specified nominal lateral dimensions. The characteristics of the slugs supplied for the maquette construction are shown in Table 9-5.

9.3.6 The tungsten rods

For the engineering maquette, tungsten rods with two different surface finishes were ordered from Schwarzkopf Technologies. One sample of rods was produced according to their "standard" grind finish. A second sample was produced by passing the standard finish rods through a "fine" grinding procedure. We checked that the dimensions of the rods were in agreement with the specified dimensions and tolerances. These measurements indicated that the process of fine grinding the rods produced a sample with a worse dimensional spread than the standard finish sample; although the spread was still within acceptable limits. This is an interesting result in that it will allow us to specify the less expensive standard grind in the future.

Table 9-6 Characteristics of tungsten rods supplied for maquette construction.

	Rod Length (mm)	Rod Diameter (mm)	Rod Mass (g)
Specified	450 ±0.50	4.750±0.010	
Supplied	449.95±0.460	4.748 ±0.004	153.39±0.28

The characteristics of the rods supplied for the maquette construction are shown in Table 9-6.

In summary, the production of the maquette was a very valuable exercise. It tested the manufacturing capabilities of our suppliers and has shown where there is need for improvement. It also provided assembly experience on which to base the design of the production tooling. Most important, the experience proved that the design of the tungsten hadronic forward calorimeter modules is sound.

9.3.7 Hadronic module assembly process

The procedure for assembling the hadronic modules is shown schematically in Figure 9-10. The two machined end plates will be mounted in a two-part jig. One part will be a fixture on the assembly area floor, to provide alignment with the rod insertion system, whilst a second part will be detachable, and will provide a means of shipping and storing the finished modules. The whole jig will maintain the separation and parallelism of the plates during assembly of the slugs and tubes. The outer layer of the module will be formed copper pieces attached to the end plates. These pieces will be applied to the module in strips as the tube assembly level rises.

The first layer of copper tubes will be installed, and their ends swaged to the end-plates. As a tube is swaged it slightly contracts in length. If the end-plates are not maintained at a fixed separation, they are drawn together as the tubes are swaged. The result would be a bowed and distorted end-plate. To prevent this from occurring, dismountable stiffeners will be placed between the plates during the stacking operation, and inserted and removed as needed.

A layer of tungsten slugs will then be laid down using a vibratory feeder, then the next layer of tubes will be inserted and swaged in place. This simple procedure will be continued up until the mid-plane, at the centre of the beam aperture. Surrounding the beam tube there will be a single piece of formed sintered tungsten which makes up the inner face of the calorimeter. This piece will be installed, and then the layer by layer stacking will continue up to the top.

After the tungsten matrix has been completely stacked, the tungsten electrode rods will be installed. To facilitate this operation, we require a simple machine which will insert the rod while rotating it so as to take up the quartz fibre at the correct pitch. This machine will be mounted in an indexing frame which will position the rod to be inserted accurately in front of the tube into which it will go. The quartz fibre will be clamped to the end of the rod, and fed from a reel mounted beside it. Rods will be placed in a ready hopper within reach and will be inserted in groups of three, so that a fibre retention washer can be placed to prevent the fibre unwinding and failing to maintain the gap.

The final assembly task is the placement of cover plates on the front face, and read-out boards at the rear face of the module. The final read-out boards will not be assembled until they arrive at CERN, to protect the read-out cables. However, after assembly individual tubes will be measured for breakdown potential and capacitance in dry nitrogen or argon gas. The assembly of a module requires a modest quality (Class 2) clean room (~10^5 particles ft^{-3}).

After assembly of a module, it will undergo electrical tests at the assembly site. These tests will comprise measurement of the capacitance and electrical resistance of the electrode structures. For these tests to be meaningful they would have to be carried out in an atmosphere of dry nitrogen. The cost estimate includes a test chamber for this purpose. When a module has been tested successfully in this fashion, it will be dispatched to CERN.

9.4 Shielding plug
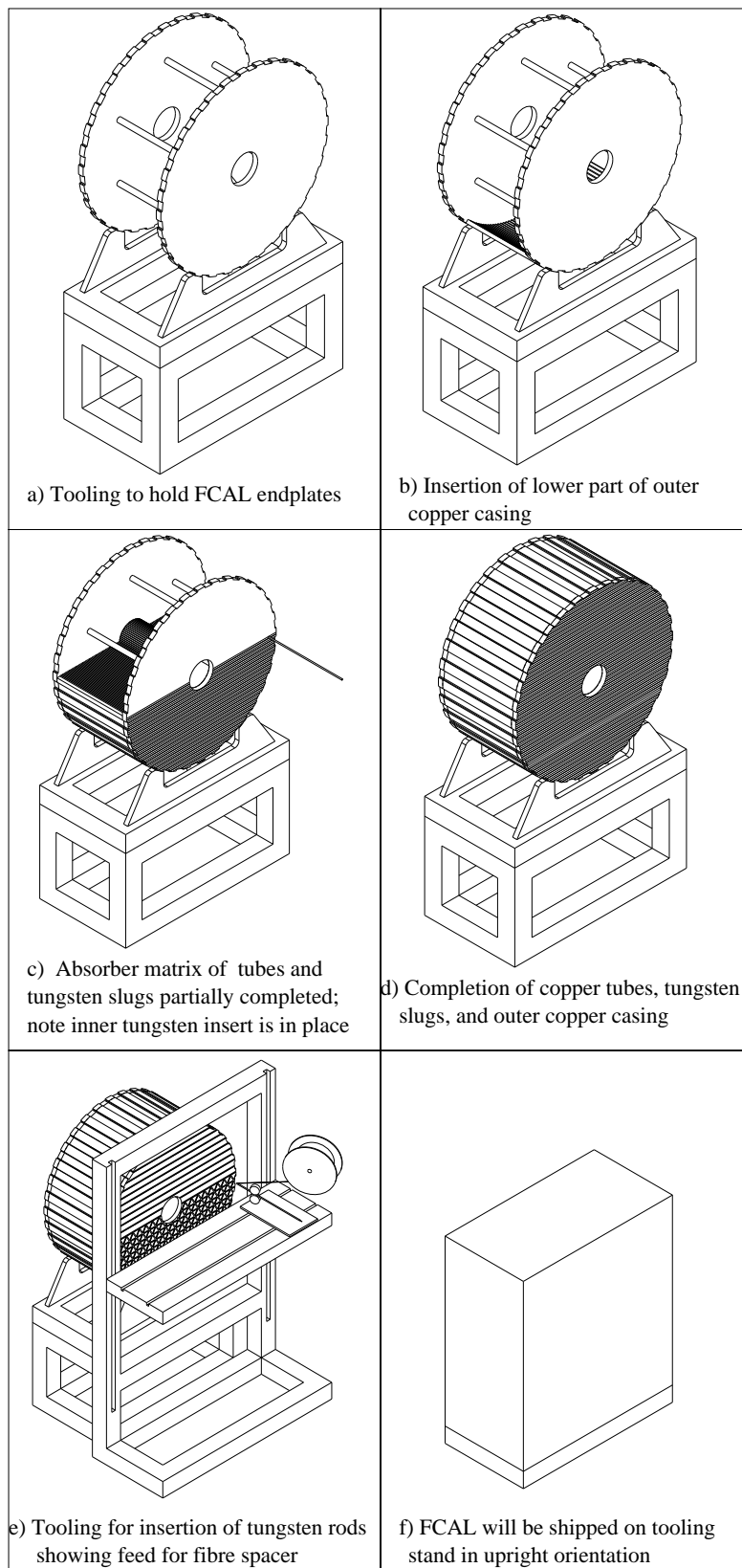
The shielding plug which is located at the rear of the FCAL in the cryostat forward tube is of copper construction and has the same outer radius dimensions and features (including cable troughs) as the FCAL modules. It is not considered a part of the FCAL and is mentioned here for explanatory purposes because it is included in the FCAL final assembly process.

9.5 Inner and outer edges of modules

9.5.1 Inner edge

9.5.1.1 Dimensions

The design of the inner radius edge of each module is guided by the desire to reduce secondary sources of particle "spray". Therefore the module inner surfaces are kept as close as reasonably

a) Tooling to hold FCAL endplates

b) Insertion of lower part of outer copper casing

c) Absorber matrix of tubes and tungsten slugs partially completed; note inner tungsten insert is in place

d) Completion of copper tubes, tungsten slugs, and outer copper casing

e) Tooling for insertion of tungsten rods showing feed for fibre spacer

f) FCAL will be shipped on tooling stand in upright orientation

Figure 9-10 The assembly procedure for constructing a hadronic FCAL module.

possible to a cone of η = 4.9. Each module's inner radius surface is cylindrical rather than conical due to the necessity of keeping the tube electrodes oriented parallel to the beam axis. A conical inner surface would result in an uninstrumented region at the inner edge.

The inner radii of the FCAL modules are chosen such that a η = 4.9 ray intersects each module's inner surface at its midpoint in z. Thus, the inner radius is 72 (79,85) mm for the FCAL1 (FCAL2, FCAL3) module. A similar consideration is followed for the shielding plug, yielding an inner radius of 95 mm (in front of the bellows pocket at the rear face of the plug.)

9.5.1.2 Tube pattern fitting

Clearly, any regular tiling pattern for tube groups will cease to work cleanly near the round beam hole boundary. When fitting the tube group pattern in this region, partial groups of at least half the standard group tube count are allowed. In addition, there must be at least 1 mm wall thickness between the hole in the end-plate for any tube and the beam hole. There are mechanical considerations arising from the FCAL assembly process, during which each module must be supported by a mandrel passing through the module's beam hole. The rather small contact patch between the mandrel and the module's beam hole surface results in a large pressure load in this region. Finite element analysis (FEA) is being undertaken to determine how closely tubes may be placed to this boundary.

Owing to the special attention required in data analysis for special tube groups, their number is kept as small as possible. This consideration is balanced by the desire to fit a maximum number of tubes in each module.

9.5.2 Outer edge

9.5.2.1 Dimensions

All modules have the same outer radius of 456.4 mm (warm) so that they fit as closely as is feasible into the cryostat forward tube. The forward tube has an inner radius of 457.3 mm (warm) giving an assembly clearance of 0.9 mm in radius. This clearance reduces to 0.5 mm when the cryostat has been cooled to liquid argon temperature. The tolerance specification for both pieces will be such that it protects this clearance.

9.5.2.2 Tube pattern fitting

Generally, the same considerations as for the inner edge case apply to the outer edge. In addition, the module weight is supported by contact of the bosses between the cable pockets with the inner surface of the cryostat forward tube. The high stresses near the lower support bosses result in some tubes not being placed in these areas although they might physically fit. Ongoing FEA study is being carried out to determine where the tubes should be placed at the outer edges.

9.5.2.3 Cable troughs

The outer radius surface of each module has 32 cable pockets running longitudinally. The cable troughs in the FCAL1 and FCAL2 modules carry only the signal cables from the FCAL1 mod-

ule, while the FCAL3 cable troughs carry the cables from both the FCAL1 and the FCAL2 modules.

In the FCAL1 and FCAL2 module case, the cable troughs are approximately 45 mm $\times$ 5 mm, therefore having an area of approximately 225 mm^2. A maximum of 100 cables (1 mm diameter each) occupy each trough, having a total area of ~87 mm^2. The extra trough area allows for reasonable packing density and space for the cable to stripline tab transition. For the FCAL3 module, the cable troughs must carry the FCAL1 cables and the FCAL2 cables, so an increase in the trough depth to 10 mm is required on four troughs per quadrant

9.6 FCAL cabling harness

9.6.1 Cable harness design

The FCAL cold cable harness (also known in the Orsay terminology as "A" cables) consists of 56 separate cable bundles (32 FCAL1, 16 FCAL2, 8 FCAL3) each having 64 miniature polyimid coaxial cables terminated at one end with a 100 pin Micro-D female connector. [Please note that the numbers used here refer to the cable harness of one FCAL only, not to the sum of both ends.] The connector pins are used as follows: 64 pins for signals, 32 for grounds, 4 unused. Thus two coaxial cables share one ground pin in the connector. The other ends of the cables are manually soldered to polyimide stripline tabs which are, in turn, soldered to the appropriate interconnect board at the module face.

The mechanical design of the FCAL and its surroundings leaves little room for the cable passage and therefore, the cable lengths must be quite precise to fit into the allocated space. To achieve this, the cable bundles are prepared on a jig which models the FCAL modules and their support tube.

9.7 Fabrication

The bundle making jig consists of 5 mm thick aluminium plates profiled to match the end-plate profile (cable troughs and bosses) and which have a small number of ground pin holes identical to the module end-plates. These ground pins are sufficient to allow the interconnect boards to be attached in their appropriate places. The jig plates are then held parallel with the correct separation between them to model the real FCAL. A connector block plate is also mounted in the correct orientation and a mock-up of the cryostat tube end with the cable-passing notches is also used.

Each cable's connector is plugged onto the connector block and the cable is routed through the end of the forward tube to the correct module face. The interconnect boards serviced by the cable are placed in position, the stripline tab is positioned and soldered to the interconnect and routed into its cable trough, and the cable cut to the correct length, its end dressed and then soldered to the tab end. Before dismounting, the cable and its interconnect boards are carefully marked with a unique identification code.

Cable harnesses are then cleaned to remove soldering residues.

9.8 Final assembly of FCAL

Final assembly refers to the procedures involved in mounting the individual modules into the forward tube to form a complete FCAL. They start with the shipment of modules to the FCAL assembly area at CERN. Mounting of the finished FCAL in the end-cap cryostat is covered under Installation.

9.8.1 Transport and receiving

Modules will be shipped directly to the ATLAS Liquid Argon assembly area in the CERN West Area. There the exterior crating will be removed prior to introduction to the clean area. Exterior crating is wooden, while the interior crating will be steel and plastics. The interior crate is also cleaned before introduction to the clean area.

9.8.2 Clean room assembly facility

A clean assembly area of approximately 100 m^2 will be provided by CERN in the West Area.

9.8.3 Module inspection and testing

Modules are shipped directly from their respective assembly sites to the FCAL assembly area at CERN. There, they are unpacked in a clean environment and inspected for damage in shipment. The full set of individual module completion electrical tests are carried out on each module and the results checked against previous results obtained at the assembly site.

9.8.4 Assembly stand

An FCAL assembly stand is used to place the modules in correct orientation to each other for cabling and mounting in the cryostat forward tube. This stand consists of a mandrel which passes through the beam hole of each module and can be supported at both ends on a floor mounted rail system. The floor mounted rails consist of two parallel rails 5 m long and approximately 1 m apart. The module carriers, the shielding plug carrier, the forward tube carriers, and the supports for the mandrel are supported by the rails and can be rolled along them and locked into place. The module carriers can also be adjusted in height to allow the alignment of the modules necessary for insertion of the mandrel.
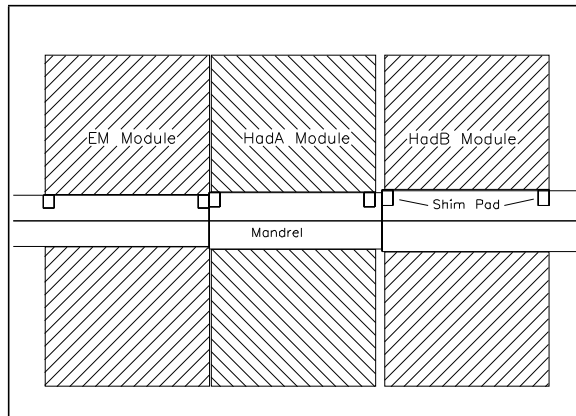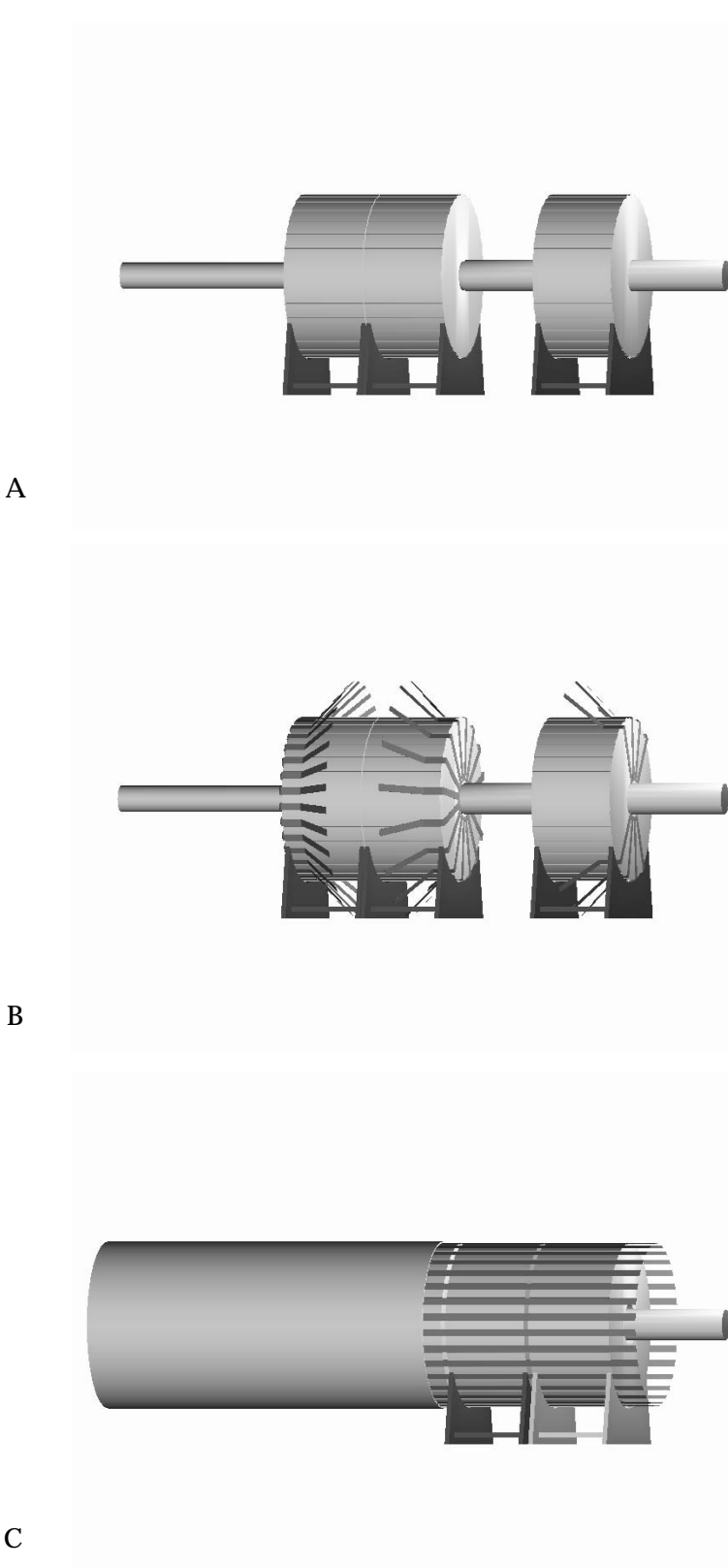
Figure 9-11 Assembly mandrel (showing shim pads).

At each section of the mandrel (corresponding to one FCAL module), the mandrel is 2 mm smaller in radius than the module inner bore. A 2 mm thick shim pad is epoxied to the top third of the circumference of the mandrel at the position of each module end plate (see Figure 9-11).

Figure 9-12 FCAL final assembly procedure.

This mandrel design allows adequate clearance to the mandrel for the assembly operation but also allows good contact for the support of the modules.

9.8.5 Assembly and cabling procedure

1. The three FCAL modules (on their respective carriers) are placed on the rails. The FCAL1 and FCAL2 modules are placed with their final 5 mm separation and the FCAL3 module is placed at its final 25 mm separation from FCAL2. The mandrel is inserted through the beam holes and supported on its end supports. (see panel A of Figure 9-12.) The module carriers are lowered, leaving the modules supported by the mandrel only. The misalignment of the modules caused by sagging of the mandrel under its load is measured. The module carriers are raised to support the modules, removing the load from the mandrel. The FCAL3 module is moved to a 500 mm separation from FCAL2 to allow room for the cabling operation. Shims are placed between the shim pads and the modules for the FCAL1 and FCAL2 modules such that the modules will be in alignment when supported by the mandrel only.

2. The cable harnesses for all three modules are installed on the appropriate module faces and then each harness is held in place by a temporary strap around the outer circumference of its module. (see panel B of Figure 9-12.) Electrical tests of continuity, capacitance, leakage current, and HV stand-off are conducted.

3. The FCAL3 module is then moved to its final separation from FCAL2 of 25 mm, and the necessary alignment shims are placed between the shim pads and the FCAL3 inner bore. The plug (on its carrier) is mounted on the rail. The cable harness retaining straps are then removed, the cable bundles routed in the module cable troughs, and the cable harness retaining straps remounted.

4. The mandrel support at the FCAL1 module end is removed, the cryostat Forward Tube is moved onto the mandrel, placed on its carrier, and the mandrel end is then resupported. The FCAL1 module carrier is dismantled from under the module, leaving the module supported on the mandrel. The cable retaining straps are removed and a polyimide wrap is applied and secured into place to protect the cables and act as a dust-free skid plate during assembly. The forward tube is then carefully moved over the FCAL1 module. This process is repeated with the remaining modules. (see panel C of Figure 9-12.)

5. When the tube has been moved to its final location over the modules, the locating pins are inserted through the tube wall into the module end plates. The forward tube carrier is then raised to support the FCAL and the mandrel is removed. The cables are placed in the routing notches of the tube end and the rear cold wall cover plate is attached to the tube end.

   - The second FCAL to be assembled is subjected to a calibration beam test in the H6 beam line in the North Hall at this stage of assembly

6. The "cone and cold tube" portion of the end-cap cryostat forward structure is assembled to the forward tube. The cold tube is inserted through the module beam holes. The bolts at the front end of the forward tube, securing it to the cone portion are fastened. The INOX seal weld at the rear cold bellows is then made. The FCAL is then covered by a plastic bag and the weld is helium leak-tested using a hand-held "sniffer".

7. The assembled FCAL is then subjected to electrical tests for continuity, capacitance, leakage current, and HV stand-off. A temporary plastic bag cover is applied for protection from dust and the cable end connectors are protected in plastic bags.

9.8.6 FCAL stand

The finished FCAL can then be moved to the FCAL stand to await installation in the end-cap cryostat. The stand supports the FCAL in a horizontal position and incorporates shrouding to guard the environment of the FCAL. It is such that the FCAL can be lifted onto and off of the stand using the tooling required for mounting the FCAL in the end-cap cryostat, see Chapter 14 for further details.

9.9 Quality control

All FCAL design and production activities will be carried out in accordance with a quality assurance plan which will meet all standards set by the ATLAS quality assurance plan [9-12].

9.10 Cold cabling

9.10.1 Cable routing at Forward tube end

Cold cables are routed longitudinally in the cable troughs on the outer surface of the FCAL modules and the shielding plug. Upon reaching the rear of the forward tube, they pass through the notches in the rear face of the forward tube and curve back towards the IP. The connectors on the cold cables then plug onto the appropriate patch panel. There are 64 64-signal cables from the FCAL1 module assigned two per cable trough for all 32 troughs. There are 32 64-signal cables from the FCAL2 module assigned two per cable trough for alternating troughs. There are 16 64-signal cables from the FCAL3 module assigned two per cable trough in two of the troughs per quadrant that are not used for the FCAL2 cables. This results in each cable trough having either two or four 64-signal cables.

9.10.2 HV patch panels

The patch panel serves both as an inter-connect point to facilitate the assembly of the FCAL and as a distribution point for the high voltages for the FCAL. An array of 64-signal patch panels is mounted on the rear face of the HEC. The panels are mounted in 32 stacks, each stack having the correct number of panels for the cables reaching it from the modules (see Figure 9-13). The signals leave the patch panels on the "pigtails" attached to the feedthroughs.
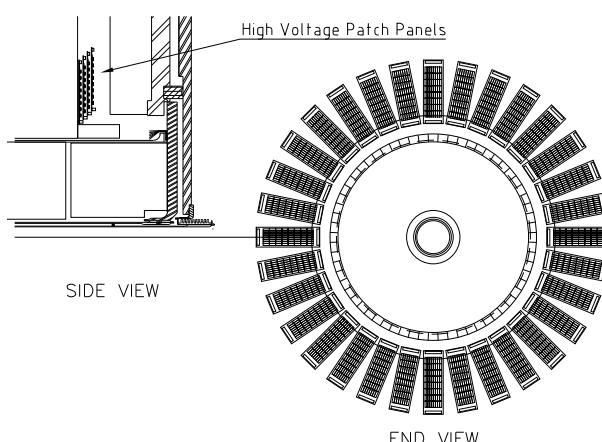
Figure 9-13 Physical layout of HV patch panels.

9.10.3 Pigtails

The pigtails are considered part of the feedthroughs for design and procurement purposes but are described here for continuity's sake. Each pigtail is a 64-signal cable connecting the interior

(liquid) cold side of the feedthrough pins to the patch panel. The patch panel end of the pigtail is terminated with a 100 pin MicroD connector. All of the pigtails are connected to the feedthrough during assembly of the feedthrough body. The pigtail connections to the patch panel are made and tested during FCAL Installation. Strain reliefs for the pigtails are then attached to the rear face of the HEC by means of previously drilled holes.

9.10.4 Feedthrough utilization

The FCAL uses one feedthrough for each quadrant. The allocation of feedthroughs has the FCAL assigned the two feedthroughs at the top of the cryostat and the two at the bottom. Within each of these feedthroughs, there are 15 pairs of 64pin connectors. Each pair of 64-pin connectors services one Front End Board (FEB). Per quadrant the FCAL uses eight FEBs for the FCAL1, four for FCAL2, and two for FCAL3 for a total of 14 connector pairs.

9.11 Heating and cooling the FCAL, LAr flow

The FCAL is heated by two mechanisms:

- by energy deposition from showers initiated by particles generated by minimum bias collisions at the interaction point.

- by ohmic heating from the ionization currents flowing through the liquid argon in the electrode gaps. In this case, the power is delivered by the HV power supplies.

For an optimal forward calorimeter, the latter case is significantly outweighed by the former, which is on the order of 45 Watts per FCAL at a luminosity of 10^{34} cm^{-2} s^{-1}. Whilst more energy is emitted in hadronic showers than in electromagnetic showers, the EM showers are more localized and therefore present the dominant source of point heating. Calculations [9-13] show that shower-induced heating results in less than a 0.15 K temperature rise at the hottest point. The superior thermal conductivity of copper over brass is seen to be an important point in the choice of the module materials.

Heating of the FCAL region is also caused by direct heat leakage through the cryostat inner tube walls. All sources of heat are dealt with by allowing convective liquid argon flow through flow holes in the cryostat forward tube at the top and bottom. These holes are located in z such that they fall between the various FCAL modules. Furthermore, by alternating the flow holes at the gaps between modules, a convective flow of liquid argon along the axis of the tube gaps is accomplished.

9.12 Radiation damage considerations

For minimum bias events electromagnetic shower maximum is the point of highest ionizing dose, of order 10^6 Gy yr^{-1} at highest rapidity. At this location in the FCAL1 module the only materials are copper, polyimide clad quartz fibre, and liquid argon. The effects of ionizing the liquid argon drive our electrode design and are treated elsewhere [9-9]. Copper easily withstands much higher doses than the LHC can deliver. Quartz and polyimide have been tested at CERN [9-14] up to 10^8 Gy. Polyimide begins to show damage between 10^7 and 10^8 Gy, somewhat above the worst location in the FCAL after ten years of operation at full luminosity at the LHC.

The Hadronic shower maximum occurs near the rear of the FCAL1 module. To avoid this region the read-out of the FCAL1 module is located on the front face and the read-out of the FCAL2 module on the rear face. The FCAL2 module includes the materials tungsten and tungsten alloy. The only additional materials on the faces between the FCAL1 and FCAL2 modules are copper pins, copper washers, and polyimide washers. Activation is a serious concern in this region [9-15][9-16]. For instance, due to its short half-life (~ 2 hours), the amount of ^{41}Ar in the FCAL builds up to a constant level of ~ 2 GBq. This fast decay time indicates that emergency venting of activated argon gas is acceptable.

At the read-out ends of the modules, the only additional materials are polyimide interconnect boards and solder. Coaxial cables with polyimide dielectric and insulation are on the outer periphery of the modules.

There is a very limited number of materials in the FCAL and each of them is very radiation resistant. Furthermore each is deemed *safe* for use in liquid argon by extensive prior experience. What is still not known is whether any of these materials might not be *safe* after extensive exposure to radiation. ATLAS has established a program to study poisoning of argon after exposure to radiation. Each of the materials in the FCAL list will be tested throughout this program.

9.13 FCAL project schedule

9.13.1 Schedule overview

The FCAL schedule as presented in Figure 9-14 and 9-15 is constrained mainly by the delivery dates for the finished FCALs to the end-cap assembly processes. These dates are, in turn constrained by the scheduling of the downhole installation of the various LAr cryostats. Any change in the overall ATLAS or LHC schedules would result, in turn, in changes to the FCAL schedule. The FCAL schedule has been drawn to maximize the use of the available FCAL group manpower.

9.14 Maintenance

The ATLAS FCAL has been designed using a zero-maintenance approach. This is due to the extreme difficulty of accessing the FCAL modules because of their location within the end-cap cryostat and the cryostat's location within ATLAS. For the FCAL, it has been assumed that any access into the end-cap cryostat would require the cryostat to be lifted to the surface and opened in a surface clean room. This is made necessary by the requirement to remove the FCAL entirely in order to remove the cryostat cold end wall. With this in mind, it is understood that access to the FCAL will only be possible in the most extreme of circumstances.

Repair or replacement of the FCAL front-end electronics is possible during an access involving a retraction of the end-cap toroids.

9.14.1 Failure scenarios

Due to the difficulty of accessing the liquid argon detectors (including the FCAL) for repair or replacement of detector elements, the threshold for the number of bad channels which will imply such an access has to be quite high. It is therefore planned to be able to operate ATLAS for
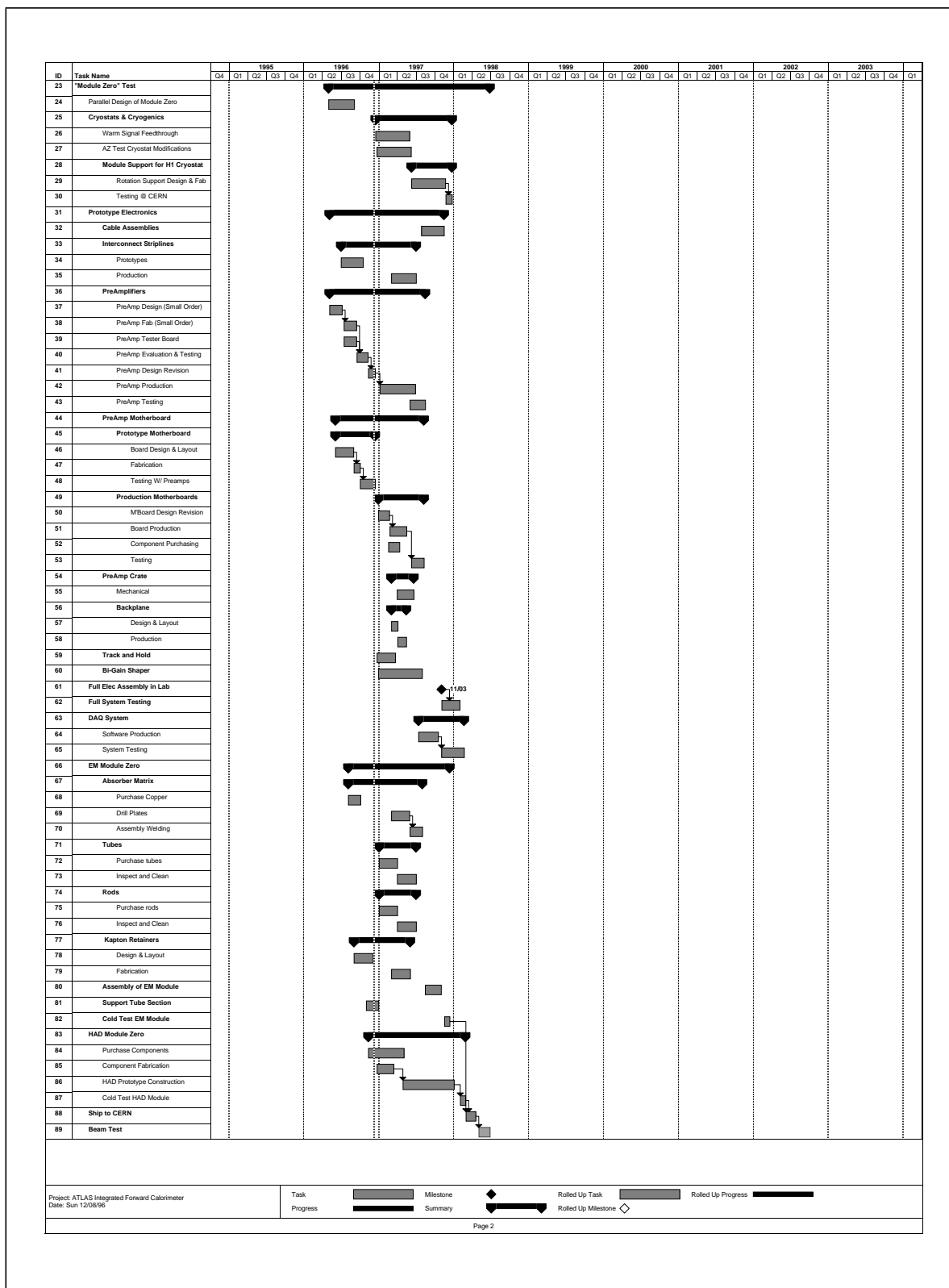
Figure 9-14 FCAL project schedule - part 1.

an extended period of time with some bad channels. It is thus necessary to evaluate the effect upon performance that various failure scenarios might have.
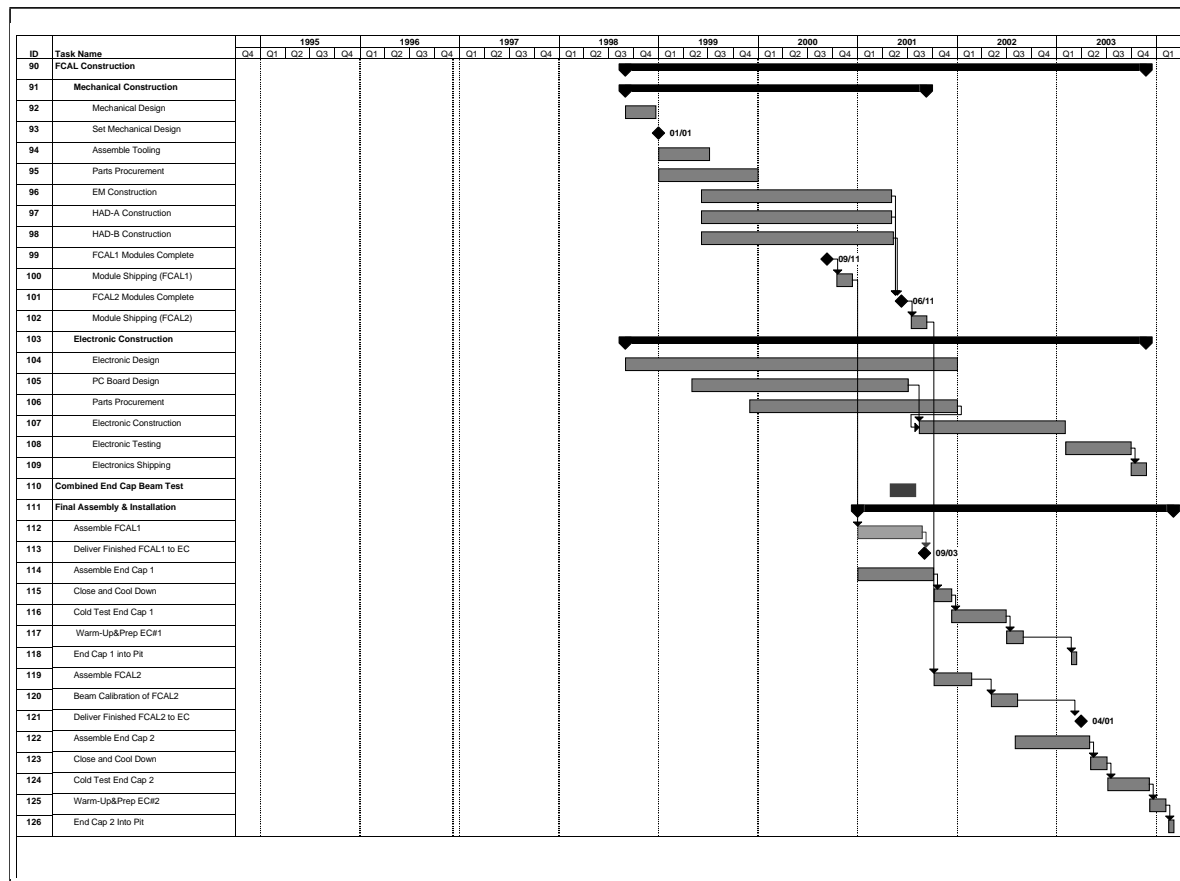
Figure 9-15 FCAL project schedule - part 2.

The tube electrodes themselves are quite robust to sparks. However the more likely failure of protection resistors and blocking capacitors could lead to dead channels. To reduce the probability of such failures we employ two series and two parallel resistors (capacitors) where logically one resistor (capacitor) is called for. While the final components have yet to be chosen we intend to specify break-down potentials well in excess above the modest high voltages in the FCAL (see Table 9-2). The components are relatively small compared to those for more conventional liquid argon calorimeters with potentials of the order 2 kV.

9.14.2 Solenoid magnet quench

If the solenoid magnet were to quench then the rapidly changing magnetic field would induce eddy currents, particularly in the copper FCAL1 module. These eddy currents in the non-uniform fringe field of the solenoid would then lead to a force on the FCAL pulling it towards the interaction point. The maximum value of this force on the FCAL1 module is 204 N which amounts to a g-force of 0.01, a small value likely below the earth-quake limit. The Ohmic heating due to these eddy currents is about 100 Joules in the FCAL1 module. The specific heat of copper at 84 K is about 0.05 Cal K^{-1} g^{-1} so the module heats up by about 2 x 10^{-4} K, a negligible amount compared to other sources.

9.15 Cost and Responsibilties

The responsibilty for fabricating the FCAL rests with four institutions: the University of Arizona, Tucson (AZ), the University of British Columbia, Vancouver (BC), Carleton University/Center for Research in Particle Physics, Ottawa (CRPP), and Institute for Theoretical and Experimental Physics, Moscow (ITEP). FCAL electronics (not treated in this chapter) are the responsibility of AZ with ITEP playing a role yet to be defined.

The FCAL mechanics are divided as follows:

- FCAL1 - AZ
- FCAL2 & FCAL3 - BC, CRPP (ITEP providing the tungsten electrode rods)
- FCAL system assembly and installation - AZ, BC, CRPP, and ITEP.

More detail on the sharing of responsibilities can be found in Chapter 14.

FCAL costs are summarised in Table 9-7.
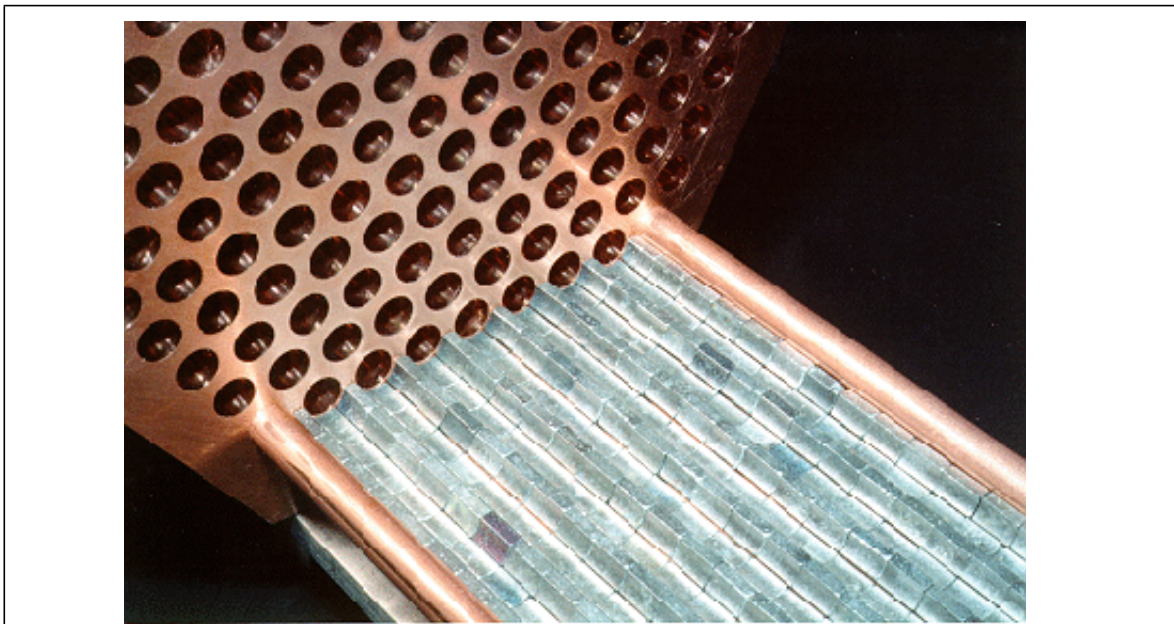
Table 9-7 Summary of FCAL costs.

FCAL Mechanics Item	Cost (KCHF)
FCAL1 matrix	217
FCAL1 electrodes	175
FCAL2 matrix	462
FCAL2 electrodes (excluding tungsten rods)	20
FCAL2 tungsten rods	423
FCAL 3 matrix	422
FCAL3 electrodes (excluding tungsten rods)	20
FCAL3 tungsten rods	445
FCAL1,2,3 interconnects	120
FCAL design	28
FCAL tooling	177
FCAL assembly	264
FCAL installation	150
FCAL prototypes	173
FCAL cold electronics	200
FCAL Total	**3296**

9.16 References

9-1   The ATLAS collaboration, Technical Proposal, CERN/LHCC/94-43 (1994).

9-2   J. Rutherfoord, L. Shaver, and M. Shupe, ATLAS Internal Note CAL-035, 1994.

9-3   J. Rutherfoord et al., ATLAS Internal Note CAL-055, 1994.

9-4   J. Dowell et al.., ATLAS Internal Note GEN-007, 1994.

9-5   M. Shupe and J. Rutherfoord, ATLAS Internal Note CAL-036, 1994; M.Shupe, , ATLAS Internal Note CAL-037, 1994.

9-6   M. Shupe, ATLAS Internal Note GEN-011, 1994.

9-7   G .Battistoni, A. Ferrari, and P.R. Sala, ATLAS Internal Note, GEN-010, 1994.

9-8   P. Loch, ATLAS Internal Note LARG-039, 1996.

9-9   J. Rutherfoord, *Ion Loading in Liquid Ionization Calorimeters*, GEM TN-91-27, 25 October 1991; J.Rutherfoord, *Testing for Effects of Ion Loading in Liquid Ionization Calorimeters*, GEM TN-93-410, 18 May 1993.

9-10   J. Rutherfoord, ATLAS Internal Note LARG-020, 1995.

9-11   J.K.Mayer, et al., ATLAS Internal Note LARG-057, 1996.

9-12   The ATLAS collaboration, *Quality Processes Management Manual*, CERN/QAP/500 (1996)

9-13   J. Rutherfoord, ATLAS Internal Note CAL-056, 1994.

9-14   P.Beynel, P. Maier, and H. Schonbacher, *Compilation of Radiation Damage Test Data*, CERN 82-10, 1982

9-15   Laurie Waters and William B. Wilson, *LAHET/MCNP/CINDER'90,* ATLAS Internal Note CAL-047, 1994.

9-16   A. Ferrari, et al., "New Results on Activation in the Calorimeter", ATLAS Internal Note in preparation.

Figure 9-i One end of the enginnering maquette showing a layer of tungsten slugs on top of copper tubes. The next layer of tubes is ready to be inserted. This method of alternating the slugs and tubes is repeated from bottom to top until the matrix is completely stacked.

Figure 9-ii The engineering maquette at a stage of partial completion. The copper end-plates, and the copper electrodes tubes are clearly vivible. The next layer of tungsten slugs (foregrounds) is ready to be layed.

10 Liquid argon electronics

10.1 Introduction and overview

Experimentation at the LHC sets new demands on calorimeter read-out electronics. The very high energy and large luminosity of the collider call for a large number of high-speed, large dynamic range read-out channels which have to be carefully synchronized. In addition, the system has to satisfy many other constraints while meeting the required performance specifications:

– the read-out electronics needs to fit into the overall detector structure; in particular into the available space, which has important consequences for our requirements on radiation hardness, reliability, power, and cooling.

– the read-out electronics will be built by teams from several institutions; strong and efficient collaborations will have to be built.

– the cost of the read-out electronics must stay within strict specified limits.

Since the writing of the Technical Proposal [10-1], a great deal of work has been done to define this electronics system, and a number of important technical decisions have been made. Throughout this process a few general guiding principles have been followed, which have important implications on the final system such as:

– simplicity in the design, which brings increased reliability and cost reduction;

– homogeneity of the design for all LARG calorimeters, which minimizes design effort, standardizes hardware and facilitates maintenance;

– accessibility to the electronics (limited, in some cases), to allow for repair, which should give a higher reliability, a serious concern for a system of this size;

– modularity of the read-out system, which will allow different teams to work in parallel as well as the possibility for piecewise upgrades.

This section reviews the requirements of the read-out electronics and detector characteristics, and it also discusses briefly the general architecture and the basic building blocks; it closes with a few remarks on organizational issues.

10.1.1 Requirements

As detailed in Section 10.2, the electronics system has to read out several subdetectors (presampler, EM calorimeters, hadronic end-cap and forward calorimeters) for a total of ~ 190 000 channels. These detectors deliver on their electrodes a triangular-shaped current signal with a fast rise time (a few ns), decreasing to zero at the end of the drift time of ionization electrons in liquid argon (~ 450 ns). For the FCAL, since the argon gap is smaller, the pulse duration is shorter (~ 50 ns). The amplitude of the current varies from one subdetector to another (see tables in Section 10.2). A value of 2.8 μA/GeV is typical for the EM accordion calorimeters. This signal is delivered on the detector impedance which, to a very good approximation, is a pure capacitance from as low as 20 pF to as high as 3 nF (see Section 10.2).

The main requirements for the read-out electronics can be summarized as:

– The energy to be measured in a single read-out cell can be as large as ~ 3 TeV [10-2]. On the low end, energy deposits arising from multiple interactions in a single crossing pro-

duces a distribution in deposited energy whose mean and width is ~ 50 MeV. This distribution can be described statistically and is given the name "pile-up noise" [10-3]. Thus the dynamic range to be covered is at least 16 bits. We require that degradation introduced by the read-out system be minimal; the EM calorimeters are the more demanding in this respect.

– The LARG EM calorimeters measure energy with a relative resolution of ~ $10\%/\sqrt{E}$, reaching a lower limit at high energy set by various imperfections of ~ 0.5%. The read-out electronics should not degrade this performance except for unavoidable electronics noise which contributes significantly only at low energy. In particular, to maintain a small constant term in the energy resolution, the read-out system should be calibrated to better than 0.25% over the whole energy range.

– The energy of an electromagnetic cluster or of a jet is the sum of the energy measured in many cells (~ 100 to ~ 1 000). Coherent noise over many cells should be kept to a minimum. More specifically the amount of coherent noise per cell should be less than 5% of the level of incoherent noise.

– The read-out system should sample the signals at 40 MHz and introduce no additional dead time; to this end a pipeline with a depth of at least 2.5 μs should be provided; in addition a large enough derandomizing buffer and a fast enough read-out should allow for a maximum Level-1 trigger rate of up to 75 kHz.

– Cells should be summed in trigger towers $\Delta\eta \times \Delta\phi = 0.1 \times 0.1$ and the result sent out to the Level-1 processor. The required precision for the analog trigger sums is 5%.

– A fair fraction of this electronics will be located in an area with limited access. High reliability is thus a concern. In addition, although radiation levels at that location are not very large ($10^{12}n/cm^2/yr$; 20 Gy/yr; 10^{10} ionizing particles/cm^2/yr; see chapter 11), this electronics has to be radiation tolerant.

– The large number of channels (~ 190 000) involved requires development of a system with low power consumption and low cost.

The following sections provide more details on these requirements and show how we plan to meet these challenges.

10.1.2 Read-out architecture

Signals from the detectors are processed by various stages before being delivered to the DAQ system. Figure 10-1 shows the logical flow of information as well as the basic elements of the system: preamplifiers, shapers, pipeline memory, digitization, and digital filtering. The data are then sent to the Level-2 buffers.

The harsh environment in the vicinity of the detector (a limited space with poor accessibility in a non-negligible radiation field) suggests a solution with remote electronics. On the other hand, the large signal dynamic range and the requirement of a very low level of coherent noise favours a solution with at least the preamplifiers 'on' the detector. In addition, practical considerations concerning the size of the cable plant needed to extract the information indicate the need for multiplexing the data in any 'off-detector' solution. Detailed consideration of all of these points leads us to the read-out architecture sketched in Figure 10-1, which is common to all the LARG calorimeters.

Much of the digital electronics: control, digital filtering, and Level-2 buffering, is located off the detector, in a control room. This limits digital activity close to sensitive analog electronics to the

absolute minimum. The off-detector electronics will use standard non radiation-hard techniques. It will be easily accessible, and can be delivered relatively late, i.e., the latest available technology can be used. It will also be more easily upgradable.

The sensitive analog electronics is housed 'on-detector', in a front-end crate attached to the cold to warm feedthroughs, in the crack between the barrel and end-cap calorimeters and at the rear of the end-caps (see Figure 10-2). This crate is positioned on top of the warm feedthrough flange, effectively becoming an extension of the cryostat Faraday cage. This should efficiently shield the LARG read-out electronics against external electromagnetic radiation. Indeed, as explained in Section 10.4.4, this crate is carefully designed to minimize pick-up noise which might be coherent over many channels. In addition, this keeps the warm part of the signal and calibration cables to a minimum length and therefore minimizes the associated attenuation and noise.

The very limited space puts constraints on the packaging of the electronics and on the power dissipation and cooling. In addition, radiation levels in this area, although not very large, call for radiation tolerant-electronics. To access these front-end crates, the end-caps will have to be recessed by a couple of metres.

The front-end crate (FEC) contains the following types of boards:
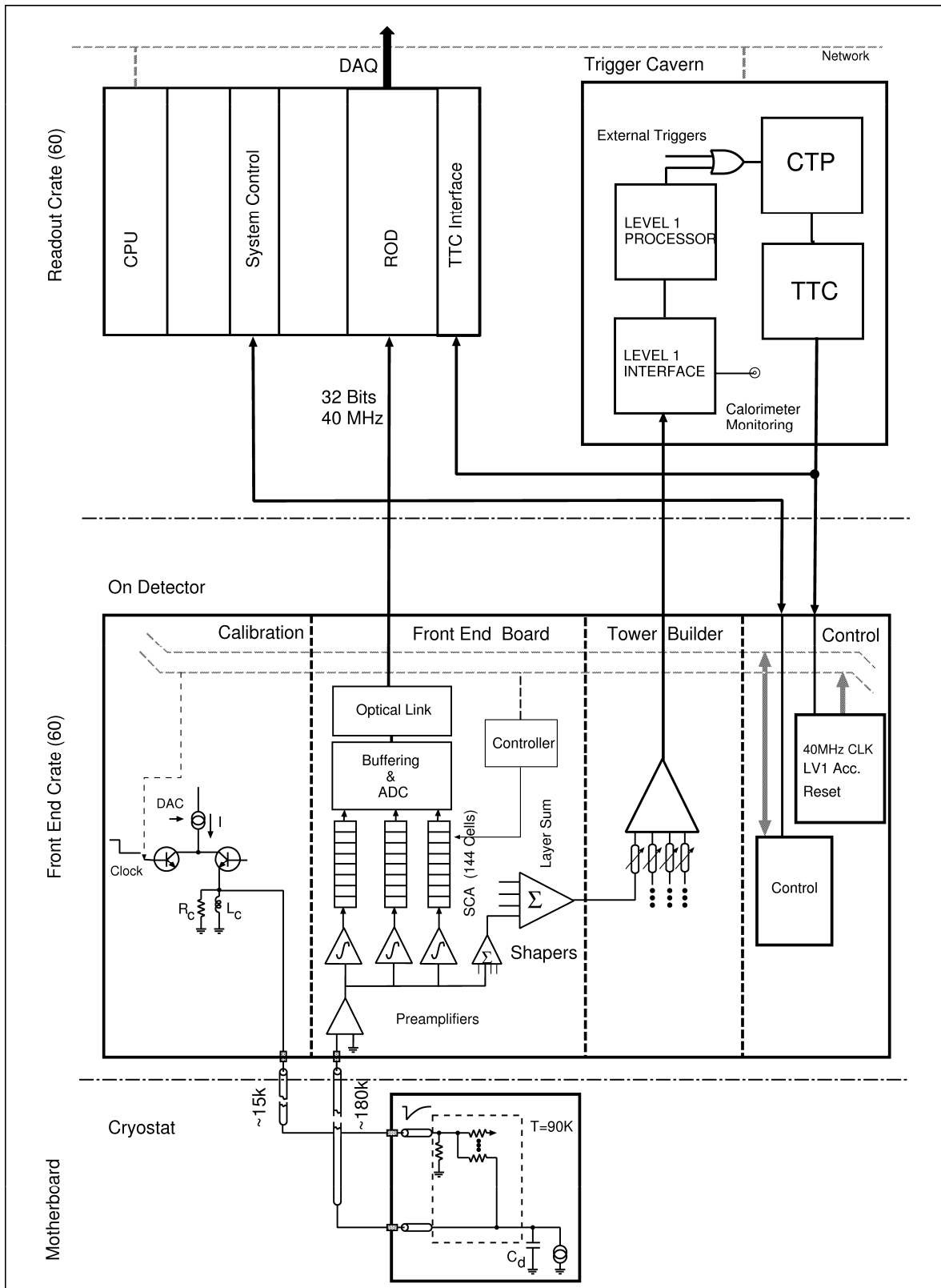
– Calibration boards with precision pulsers;

– Front-end boards (FEBs) which

- amplify and shape the analog signals,

- sum the calorimeter cells by trigger tower within each depth layer, and prepare the input signals for the tower builder board,

- store the signals in an analog memory waiting for the decision by the first level of triggering,

- digitize the selected pulses, and

- transmit on optical fibres the multiplexed digital results.

– Tower Builder Boards (TBBs) to perform the final level of analog summation to form trigger tower signals and to transmit the analog signals to the Level-1 cavern for digitization and processing by the Level-1 trigger processor.

– Control boards to receive and distribute the 40 MHz clock, the Level-1 accept signal, as well as other fast synchronous signals, and to receive and distribute control information to configure and control the various boards in the crate.

– Monitoring boards to read out various monitors.

10.1.3 The front-end system

Figure 10-1 shows schematically the front-end crate with the various boards and links to the rest of the electronics. The monitoring boards are not shown in this drawing, nor are they discussed in this section; their function is covered briefly in Section 10.6.2 below and in more detail in Chapter 12.

10.1.3.1 Calibration pulsers

In order to render the constant term in the energy resolution as small as possible, the aim is to calibrate the read-out electronics of the EM calorimeters to a precision better than 0.25%. Pre-

Figure 10-1 Block diagram of the read-out electronics. In the drawing warm preamplifiers are located on the front-end board which is the case for the EM and FCAL calorimeters. For the hadronic end-cap calorimeter, the preamplifiers are located in the liquid argon.
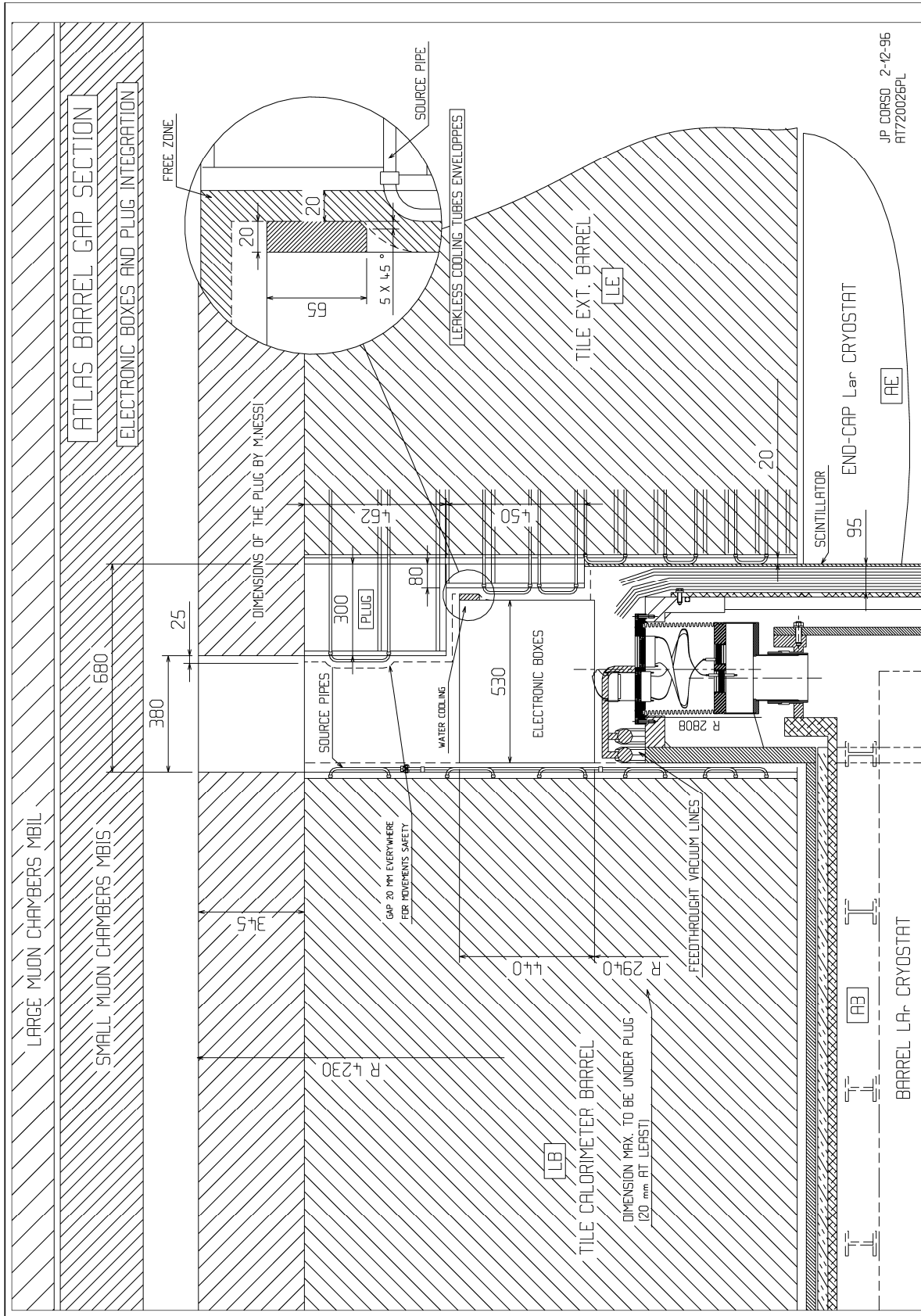
Figure 10-2 Drawing of a front-end crate in the crack between the barrel and end-cap calorimeters.

cisely known current pulses are injected as close as possible to the read-out electrodes through high-precision resistors located in the cold, to simulate energy deposits in the calorimeters.

Two techniques have been investigated and tested in the beam. Either a precise DC current is switched locally in the cold, or, a pulse is formed in the warm close to the feedthroughs and sent on 50 Ω cold transmission lines to the precision resistors. Similar performances have been obtained with the two schemes. The technique with warm pulsers has been selected, since in this scheme the only components which would be inaccessible would be the precision resistors.

As detailed in Section 10.3, the pulser system covers the whole dynamic range and allows for a measurement of cross-talk between channels. Experience in the test beam with the RD3 2 metres prototype [10-4] revealed several systematics effects at the per cent level. They are being carefully studied and there is good hope to meet the ATLAS goal. The timing of the calibration pulses is set to reproduce the timing of physics signals, taking into account the variation of time of flight.

10.1.3.2 Preamplifiers

Preamplifiers must amplify the detector signal to be above the noise level of downstream stages and thus should be the only contributor to the electronics noise. They have to accept the whole signal dynamic range ($\geq$ 16 bits) and have a high speed, requiring them to have a low input impedance.

The high radiation levels in the EM end-cap calorimeters led us to develop warm preamplifiers coupled to the detector through transmission lines [10-5]. This permits the preamplifiers to be located remotely, in the front-end crate, where there is a reduced radiation field. This technique was successfully tested in the beam by the RD3 Collaboration. As explained below in Section 10.4.1, to minimize any coherent noise pick-up at the preamplifier input, these circuits are carefully enclosed in a Faraday cage.

Precision energy measurement requires minimal dead material in front of the calorimeter. Warm preamplifiers are ideal in this respect as there are neither electronic circuits in the cold nor the hardware needed to cool them. Therefore this option was selected for the presampler and the strip section of the barrel calorimeter.

Cold preamplifiers amplify the detector signal right at the electrode, reducing the sensitivity of pick-up noise on the transmission line. The low input impedance of this circuit also lowers the cross-talk [10-6]. Measurements in beams have shown that cold GaAs preamplifiers have superior noise performances, with noise a factor of ~ 1.4 lower than for warm preamplifiers. However, when the irreducible pile-up noise is taken into account, the slight remaining advantage for cold preamplifiers (~ 10%) is judged insufficient to outweigh the increased risk of a solution where preamplifiers in the cold would have been inaccessible.

Thus all EM calorimeters are read out using the same technique: warm preamplifiers coupled to the detector through transmission lines. Depending on the cell capacitance, the cable impedance is either 50 Ω (presampler and strip layers) or 25 Ω (middle and back sections). The high speed silicon bipolar transistors used in these preamplifiers should provide adequate radiation hardness [10-7].

The mechanical structure of the hadronic end-cap (HEC) – parallel absorber plates with electrodes forming an electrostatic transformer structure – is very different from that of the electromagnetic part, and the ganging in depth of the cells is not as natural as in an accordion structure [10-8]. In each gap, 50 Ω transmission lines running radially bring signals to cold preamplifiers

located at the periphery of the calorimeter at a radius of ~ 2 m. The radiation field in this area is manageable. There is no need to read out individual gaps so, signals are summed locally in groups of four or eight, and only the sum is sent out of the cryostat. As explained in Section 10.4.1.3, a GaAs chip containing eight preamplifiers and two summing amplifiers/drivers has been developed for this purpose. Such an active summation scheme also helps in matching the detector capacitance to the preamplifier thereby reducing electronics noise.

No presently available electronics can survive the intense radiation flux received by the Forward Calorimeter (FCAL), so remote preamplifiers coupled by transmission lines are mandatory. Bipolar transistors with their well-controlled transconductance ensure a good matching of the line impedance. Thus, the same warm preamplifiers as for the EM calorimeters are used in FCAL with 25 Ω cables (cell capacitance is ~ 1.5 nF).

10.1.3.3 Shaping amplifiers

Shapers are the input to the sampling stage, and one of their functions is to limit the system bandwidth to match the 40 MHz sampling frequency. In addition, to minimize baseline shift, a bipolar CR-RC^2 prefilter is adopted. The shaping time constant is not critical, as downstream digital processing can effectively modify it (within limits), which is an advantage since the optimum shaping time is luminosity-dependent. In order to maximize the range of luminosities over which the digital filtering functions optimally, a value of the hardware shaping time which minimizes the total noise (electronics $\oplus$ pile-up) at nominal luminosity is selected (see Section 10.4.2.1).

Precision calorimetry requires very good calibration of the electronics response. Experience has shown that this is best achieved in linear systems. However, it is not possible to handle without degradation the 16-bit dynamic range of the input signal on a single gain scale. Multiple ranges, each with a linear response can be used to extend the dynamic range. As explained below, a 12-bit pipeline and digitizing system is used. Two such systems could be used to span the entire range, but there is essentially no margin for unanticipated coherent noise. To be on the safe side, we have chosen a system with three ranges. Thus for each input, the shaper produces three output signals with gains approximately in the ratio 1/10/100; each gain has a dynamic range better than 12 bits. The resulting quantization error is negligible and this provides some immunity against coherent noise which would enter the system downstream of the shaper output. As detailed in Section 10.4.3.3 several other measures are implemented to keep coherent noise under control.

The shaping amplifiers will be built as integrated circuits using a bipolar technology, which should provide adequate radiation hardness. There will be four shaper circuits (three gains each) in one integrated circuit. In addition the integrated circuit will contain a linear mixer, which will provide a first stage of analog summing for the trigger.

10.1.3.4 Analog pipeline/ADC

Signals from the shaper outputs are sampled at 40 MHz and the results stored in an analog memory chip during the latency of the first-level trigger (2.5 µs maximum). The phase of the sampling clock is adjusted so that one sample is near the peak of the pulse (± 2 ns, see Section 10.4.3.2). To minimize digital noise pick-up, the number of clock phases on the front-end board is kept to a minimum. The cabling detailed in Section 10.2 has been carefully arranged to ensure that each front-end board treats only cells from the same layer, whose pulse shapes are approximately constant. There can be significant variations in pulse shape between layers, owing to large differences in both cell capacitances and cable lengths.

Upon receipt of a trigger accept signal (75 kHz maximum average value) typically five samples around the peak of the pulse originating at the triggered crossing are extracted and multiplexed to a 12-bit ADC for digitization. One ADC digitizes the signals from eight calorimeter cells. The same gain is used for all samples in order to minimize systematic effects due to small differences in pulse shapes of the different gain channels. The results are sent off-detector through digital optical links.

The analog pipeline is 144 cells deep, giving, in addition to the 100 cells needed to cover the trigger latency, enough memory to store seven events with five samples each. The dead time due to the finite size of this derandomizing buffer is very small, less than 0.5%.

Results obtained in test beams with this kind of electronics, convincingly demonstrate that the required performances are achievable. A first attempt at producing a radiation hard chip has been done using the DMILL technology and the results are very encouraging [10-9]. Evidence that commercial bipolar ADCs can resist the expected level of radiation has also been reported [10-10].

A fully digital solution, in which a fast-gain selector circuit chooses the suitable range and feeds the signal to a 40 MHz ADC, has also been studied [10-11]. The gain bits and the digitization results are stored in a digital memory similar to the one developed by the FERMI Collaboration[10-12]. With presently available technologies, the power requirements of such a solution far exceed that of the architecture we have selected (by more than 1 W/channel). The relevance of this figure arises from the large number of channels in the system. Every additional watt in the front-end circuits translates into 300 kW of supplied AC power and into 30 m^3/h of cooling water required to flow through the crates. However, technology may improve, so, depending on the progress made on our baseline option, we might review the situation in two years.

10.1.3.5 Level-1 sums

The trigger towers in the ATLAS calorimeters are divided in electromagnetic and hadronic sections, with a transverse size $\Delta\eta \times \Delta\phi = 0.1 \times 2\pi/32$ (extending to $\Delta\eta \times \Delta\phi = 0.2 \times 2\pi/32$ for rapidities above 2.5). Inside a trigger tower (TT), all samplings in depth are summed together. In each trigger tower, there are a total of between 3 (HEC) and 60 (barrel EM) read-out cells (see Section 10.2).

Transverse energy is the important quantity for the first level trigger and the signal delivered should be proportional to E_T with saturation at or above 250 GeV. The precision is limited to ~5%. The noise level is another important parameter as it impacts both the capability to tag the bunch crossing for low energy cells in triggered events and the threshold that can be set on towers which should contain zero energy. The summation tree should degrade as little as possible the limit set by the preamplifier electronics noise.

An analog summation scheme has been adopted. The four channels in a shaper chip are first summed together and the signal shaped and amplified to minimize the effect of downstream noise. Cells from the same layer in depth are cabled to the same FEB; the summed signals from the shapers are summed again in a plug-in 'layer sum board' which adapts to the varying number of channels per trigger tower and drives the layer sum signal to the Tower Builder board (TBB) located in the same crate. Up to that point, inside a trigger tower, signal shapes and gains are uniform enough ($\leq$ 3%)to be summed together without any adjustment. Summing in depth is done in the TBB, where provision is made for gain, shape, and timing adjustment between the various layers in depth. This board also drives the output signals to the Level-1 cavern on individually shielded twisted-pair cables. If state-of-the-art analog optical links reach the required performance with respect to dynamic range, linearity, stability, and cost, they will also

be considered. The signal is received in the Level-1 cavern, where an η-dependent gain factor is applied to bring all signals to a common transverse energy scale, to within $\pm 10\%$. They are then fed into the trigger processor (where a last calibration in E_T is applied) and also made available to a waveform monitoring station. This will be useful as a diagnostic tool for problem channels, for detecting possible pick-up, and for measuring system parameters such as the noise autocorrelation function.

10.1.3.6 Low-voltage power, cooling, grounding

Quite a substantial amount of power (~ 250 kW) is needed to supply the large number of electronics channels in the front-end system. None of this power should be transferred to the surrounding detectors and water cooling is mandatory. The baseline is to use the 'leakless water cooling' system as developed at CERN for the L3 experiment.

The distribution of this large amount of power has to be done carefully. Each front-end crate will have its own low voltage power supplies. These supplies will be 'isolated'. Strict control of ground loops will be observed, and there will be only one location allowed where connection to ground is made. The cryostats with all their cryogenic lines and services will be electrically insulated.

10.1.4 Off-detector electronics

For reasons connected with the construction schedule for the experiment, the front-end electronics has received considerably more attention than the electronics which will reside off the detector. We anticipate that by carrying out detailed development of this part of the system at a later date we will be able to take advantage of improvements in digital technology. We discuss here mainly the required functionalities, which are rather well understood.

10.1.4.1 Trigger clock and control system

In the Level-1 cavern, 50 metres away from the detector, as mentioned above, signals from trigger towers are received and delivered to the calorimeter Level-1 trigger processor, which is also located in this cavern. The central trigger processor (CTP) will deliver not only physics triggers but also calibration signals and triggers. These signals, together with the 40 MHz clock and other synchronous commands, are transported to the front-end crates and to the read-out crates described below by the TTC system (timing trigger and control) developed in the RD12 project [10-13].

To ease the timing in of the system, fibres distributing the clock will be cut to length and/or their transit time measured, and programmable delay lines in calibration boards will be preset to reproduce the timing of physics signals. These adjustments will be checked and refined by analysing real shower pulses. To benefit from the excellent intrinsic time resolution of the detector (50 ps at high energy), clock jitter should be kept as low as possible (< 100 ps).

10.1.4.2 Read-out driver system

To each front-end crate is associated a read-out driver crate (ROC). The pair front-end crate – read-out driver crate is the smallest module of the calorimeter read-out electronics. The read-out driver crate contains:

> – a CPU connected to the network to control this subassembly;

> – a communication module to configure or down-load parameters into the various boards of the front-end crate or to read back registers;

> – Read Out Driver (ROD) modules, which receive raw data from the FEBs and produce the corresponding energy, time, and some form of data quality measure, sending the result to the DAQ, i.e. to the Read Out Buffer (ROB) modules.

Fast unidirectional, 1 Gbit/s optical links connect the FEBs to the RODs. A slower but bidirectional link connects the communication modules in the front-end and ROD crates.

As explained in Section 10.4.3, a frame of typically five samples centered around the bunch crossing of interest is sent down the link to the ROD module for digital processing. This is accomplished using the well established method of optimal filtering [10-14]. In practice one obtains a weight for each sample which results in the minimum error on the energy subject to the constraint that the pulse can be moved in time without affecting the result, to first order. Any loss in energy resolution due to small phase jitter between the pulse and the clock is minimized. The weights are chosen to minimize the total noise (electronics $\oplus$ pile-up) for the current value of the luminosity, and the quality of the waveform can be checked to detect events subject to large out-of-time signal overlaps.

The available computing power in these modules will also be used to monitor every channel. Examples include checking for drift in the phase of the clock with respect to the particle signal, histogramming energy spectra, and the preprocessing and histogramming of data during calibration runs.

10.1.4.3 High-voltage system

In order to create a drift field of ~ 1kV/mm, a DC potential of ~ 2 kV (as low as 250 V for the electromagnetic FCAL) is applied to the read-out electrode. Each module will be HV tested in the cold (LAr) at least once. Furthermore, a low HV test will be made before assembling modules in wheels or cylinders (see chapter 14). However, a short in one of the argon gaps could develop with time, requiring that the high voltage be reduced or even switched off. To limit the impact of such an event, the two sides of an electrode are powered by independent HV supplies, permitting the correct response to be recovered by appropriate weighting. In addition, the detector is subdivided into zones which are independent from the high voltage point of view. Altogether, including purity monitoring probes there are ~ 3600 independent high-voltage lines entering the cryostats. Each of these lines needs to be powered separately, and the individual DC currents will be monitored. In addition to checking for correct detector behaviour, a measurement of DC current should provide a relative measure of the luminosity in the machine together with a test of the uniformity of the calorimeters.

10.1.5 Organization of the work

Intense R&D activity with many tests in the beam has led to the definition of the read-out chain described in this document. Now, we will have to move from the R&D to a construction phase.

The activity of the LARG electronics teams will have to be organized accordingly. Given the size and complexity of the project, rather strict rules will have to be followed:

– For each part, detailed specifications will have to be written down. The present TDR is a first step in that direction and provides the general guidelines. These documents will be approved by the electronics conveners and the people in charge of the construction of the corresponding parts.

– For each important item, design review meetings will be held to check the design and to compare results obtained on prototypes against specifications. They will help in setting up milestones before we embark on mass production. Such meetings have already been held on preamplifiers.

– Coherent noise can be very detrimental to the detector performance. In order to keep this kind of noise at an acceptable level, rather strict rules concerning the decoupling of lines entering the cryostat, links to the outside world, and cabling of power supplies will be defined. They will have to be obeyed.

– A policy of systematic tests will be enforced. This includes: test of radiation resistance, cold testing of every part which will go in the cold with a particular attention to cold preamplifiers, burn-in of components and of full boards. Time has been reserved in the schedule for these important activities. An essential element in this testing policy is the 'module 0' exercise. As mentioned above, we plan to build in the coming two years a representative fraction of the LARG read-out electronics. This will no doubt provide very valuable information.

The main responsibility for the construction of the read-out electronics will be with the institutes in charge of various parts. A well-defined sharing agreement is under way. Important first steps in that direction are reported in the extended PBS at the end of this document. The responsibility for the coordination of this activity rests with the project leader and the electronics conveners. They must verify the consistency of the various parts in the read-out chain, and they must handle all the interface problems with the other parts of LARG, a good example being the protection against ground loops. They are members of the LARG steering group. An electronics steering committee is helping them to monitor progress, detect problems and to propose solutions. In this committee, members from the TILE and TRIG/DAQ communities are helping to ensure that the system we are building is compatible with the rest of ATLAS.

10.2 Structure of the calorimeters

The design of a read-out electronics depends strongly on the characteristics of the detector to read out. This chapter tries to answer questions like: What does the signal look like? What is its intensity and temporal shape? What is the source impedance? How many channels have to be read-out? In addition some attention is paid to seemingly trivial matters such as cabling, which can have a profound impact on the organization of the read-out.

10.2.1 Detector granularity

Several criteria, energy resolution, position and pointing resolution, isolation, cost, etc., have been used to optimize the longitudinal and transverse granularity of the various LARG calorimeters [10-15]. The basic EM cell has a transverse size $\Delta\eta \times \Delta\phi = 0.025 \times 0.025$ which becomes 0.1×0.1 in the hadronic end-cap.

Granularity of trigger towers

Calorimeter cells are grouped in trigger towers whose granularity is shown in Table 10-1. In the overlap region between the barrel and end-cap, the barrel EM will provide a tower covering $1.4 < |\eta| \leq 1.47$ with only partial longitudinal containment of the EM shower. The end-cap EM will provide another tower covering $1.4 < |\eta| < 1.5$ with the complementary containment. In the central region, the transverse granularity is the same as the one chosen for the hadronic tile calorimeter. The exact number of bins in rapidity for the FCAL is still being optimized.

Table 10-1 Trigger granularity of the calorimeter as function of η

Calorimeter	η	$\Delta\eta$	$\Delta\phi$	No. of Channels
EM barrel	$0 < |\eta| < 1.4$	0.1	$2\pi/64$	1792
EM barrel	$1.4 < |\eta| < 1.47$	0.07	$2\pi/64$	64
EM end-cap	$1.4 < |\eta| < 2.5$	0.1	$2\pi/64$	1408
EM end-cap	$2.5 < |\eta| < 3.1$	0.2	$2\pi/32$	192
EM end-cap	$3.1 < |\eta| < 3.2$	0.1	$2\pi/32$	64
HEC	$1.5 < |\eta| < 2.5$	0.1	$2\pi/64$	1280
HEC	$2.5 < |\eta| < 3.1$	0.2	$2\pi/32$	192
HEC	$3.1 < |\eta| < 3.2$	0.1	$2\pi/32$	64
FCAL	$3.2 < |\eta| < 4.9$	1.7	$2\pi/32$	64
TOTAL				5120

Granularity of the EM barrel

The barrel EM calorimeter is split into two halves, each covering a rapidity range of $|\eta| < \sim 1.5$ with fine granularity up to $|\eta| < 1.4$. In azimuth, each half-barrel is made of 16 modules, each with an azimuthal width of 1 trigger tower. In rapidity, each module consists of 15 trigger towers. In depth, the calorimeter has effectively four layers: presampler, strips (with high granularity), middle, and back layers. Inside of a trigger tower, for $|\eta| < 1.4$, the detector granularity is illustrated in Figure 10-3. At the end of the barrel ($|\eta| > 1.4$) the structure of a trigger tower is different (see Figure 10-3). Table 10-2 summarizes the number of active channels in the calorimeter.

Granularity of EM end-cap

Each EM end-cap consists of two coaxial wheels covering the rapidity range 1.4-2.5 and 2.5-3.2. The wheels are divided into eight modules, each of them with 15 trigger towers in the η direction (11 from 1.4 to 2.5 with a granularity of 0.1 and four from 2.5 to 3.2). In depth, the calorimeter has 2 to 3 layers depending on rapidity. A presampler covers the region $1.5<|\eta|< 1.8$. Figure 10-4 defines the detector granularity (varying with rapidity) inside of a trigger tower.

Granularity of hadronic end-cap

Each of the two hadronic end-cap calorimeters, in the forward and backward region of the detector, consists of two wheels, which together cover the rapidity range between 1.5 and 3.2. The detector granularity varies with rapidity as shown in Figure 10-5. More information can be found in chapter 8.

Table 10-2 Number of active channels in the LARG calorimeters.
The number of read-out channels in the forward calorimeter is still being optimized.
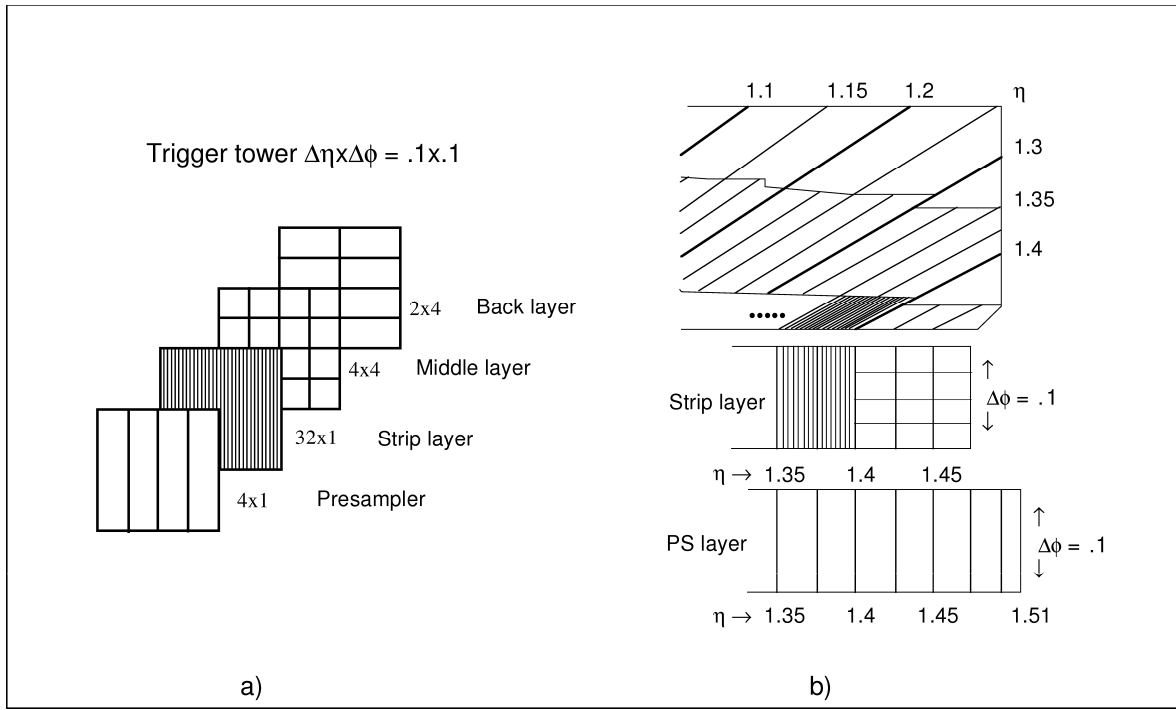
Calorimeter	Layer	No. of Channels	Total
EM Barrel	Presampler	7 808	
	Strips	57 344	
	Middle	28 672	
	Back	14 336	
	Barrel End	2 048	
Total			110 208
EM end-cap	Presampler	1 536	
	Strips	27 136	
	Middle	21 888	
	Back	13 184	
Total			63 744
HEC	Front	1 536	
	Middle	1 472	
	Back	1 408	
Total			4 416
FCAL	1	6 088	
	2	3 456	
	3	1 744	
Total			11 288
TOTAL			189 656

Granularity of the forward calorimeter

Each forward calorimeter consists of three wheels, one behind the other (FCAL1, 2, 3). Each wheel is structured in tubes and rods parallel to the beam axis inside a metal matrix (see Chapter 9).These all have coverage up to η = 4.9.The low-rapidity edge of each calorimeter starts where the hadronic calorimeter coverage ends. Adjacent tube electrodes are ganged together in parallel so that the total cell capacitance is about 1.5 nF. In the FCAL1 module four tubes are ganged together to form a read-out channel. Figure 10-6 shows the granularity of read-out and trigger cells in the forward calorimeter. An option where channels would be summed in the cold using transformers is seriously being considered (see Section 10.4.1.4). This would reduce the number of read-out channels by about a factor of two.

10.2.2 Signal characteristics

After the passage of ionizing radiation produced in the shower, electrons and positive ions drift in the liquid argon gap. The electrical current produced is a triangular waveform with a rise time of the order of a few nanoseconds followed by a linear decay for the duration of the elec-

Figure 10-3 a) Granularity of a trigger tower of the EM barrel ($|\eta| < 1.4$). There are 64 such towers in azimuth and 2 x 14 in η. b) Granularity at the end of the barrel (r-η and η–ϕ views). For rapidity between 1.3 and 1.4, the structure of the trigger tower is standard, except for the missing cell in the back layer. For rapidity above 1.4 there are five cells in the PS and four cells in the calorimeter: three in the front and one in the middle. All of these are read out from the front face of the calorimeter. The ϕ granularity of these four calorimeter cells is $2\pi/256$.

tron drift time t_{dr}. The peak current I_0 is proportional to the deposited energy. This current is delivered on the cell impedance which for the characteristic read-out time can be described as a pure capacitance.

EM calorimeters
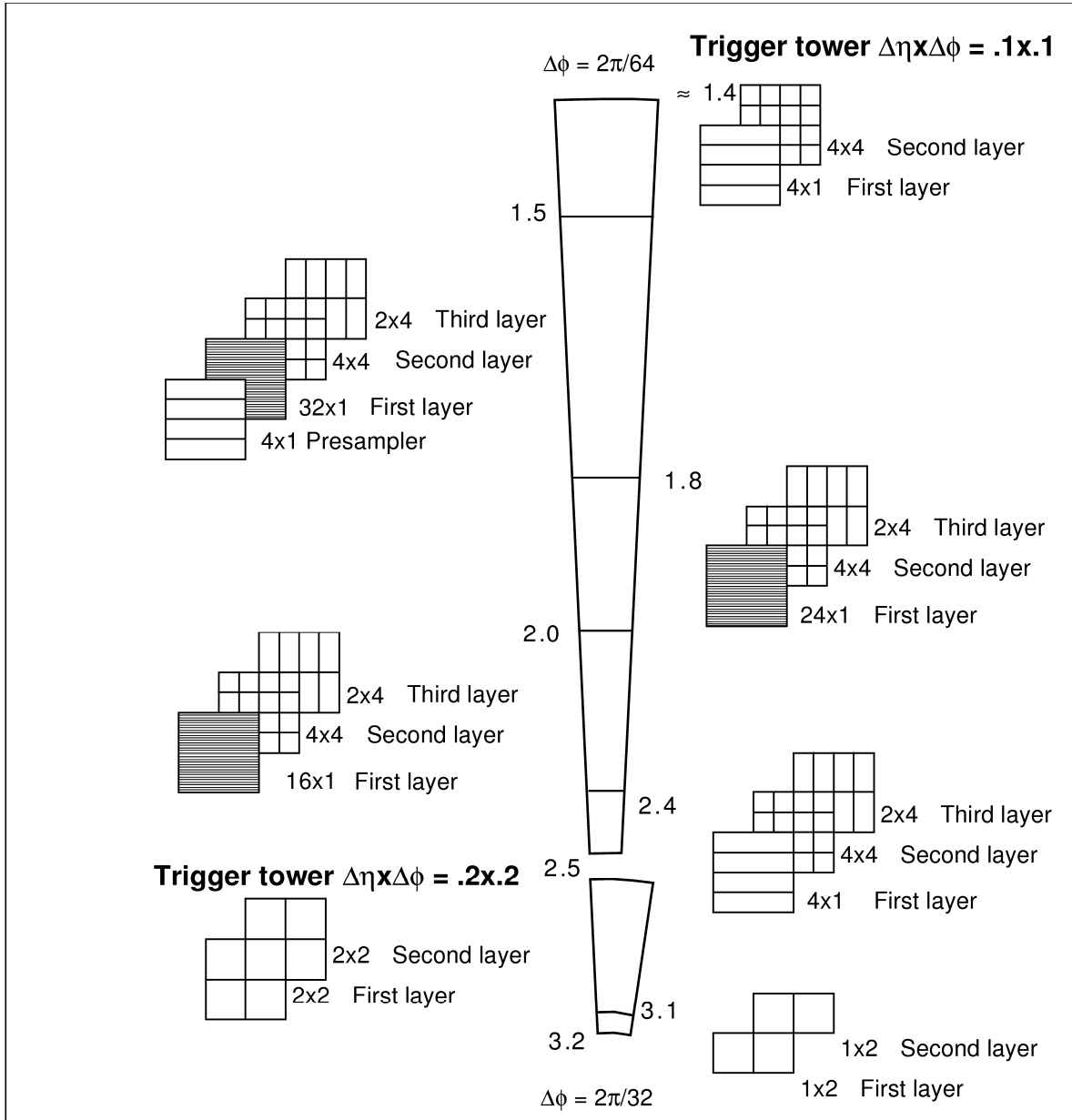
Table 10-3 and Figures 10-7 and 10-8 give the values of these quantities for the EM calorimeters. In the barrel, the change in lead thickness at $|\eta| = 0.8$ is reflected in the discontinuity of the peak current and of the capacitance curve. The transition to the EM end-cap is also clearly visible. In the EM end-cap, the argon gap and the cell area are continuously varying with rapidity. Discontinuities in that region result from a change in the granularity of the strip layer and from the transition from the outer to the inner wheel.

Hadronic calorimeter

The architecture of the HEC read-out described in Chapter 8 and in Section 10.4.1.3 is such that signals from two consecutive pads are fed into a separate amplifier which is located nearby at the circumference of the calorimeter wheel inside the liquid argon. The amplified signals of a certain number (8 or 16) of pads in subsequent read-out planes are actively summed at the same location. These summed signals form the longitudinal read-out channel. Table 10-4 gives the parameters of the signal input into these preamplifiers.

Forward calorimeter
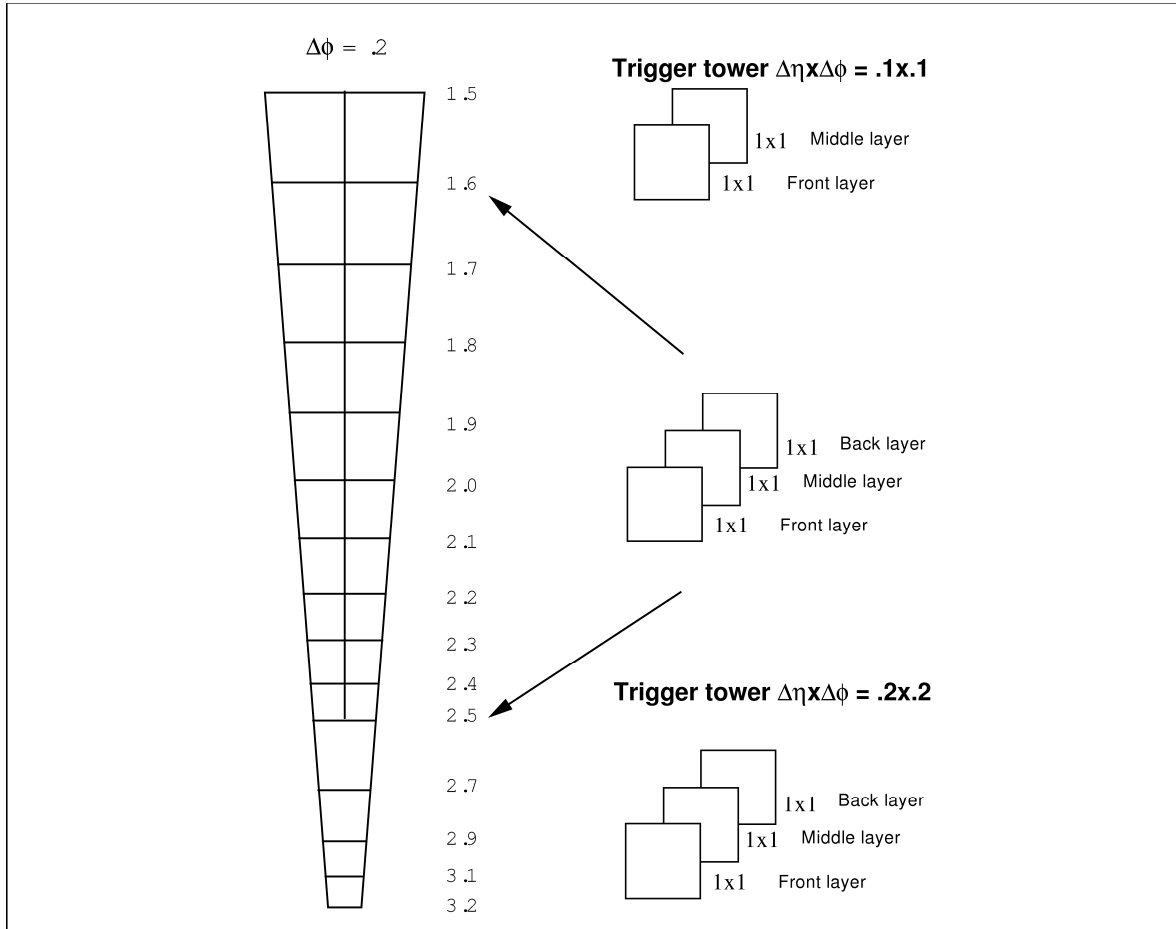
As can be seen in Table 10-5, the signal in the forward calorimeter is much shorter than in the other calorimeters owing to the small liquid argon gap used to minimize space charge effects. The mechanical design leads to a rather uniform capacitance.

Figure 10-4 Granularity of a trigger tower in the EM end-cap calorimeter. This pattern repeats itself in azimuth. Note the change of trigger tower granularity above 2.5 in rapidity.

10.2.3 System interconnections

The interconnections between electrodes and motherboards attached to the detectors are described in each of the previous detector chapters. From there, signals have to be routed to the read-out electronics housed in front-end crates. In the reverse direction, calibration pulses are sent from calibration boards in the front-end crates to the motherboards for distribution to calorimeter cells. The following reviews the basic elements of this interconnection, describes the mapping of the detector onto electronics modules and gives some information on the selected cables and connectors.

Figure 10-5 Granularity of a trigger tower in the HEC calorimeter. This pattern repeats itself in azimuth. Note the change of trigger tower granularity above 2.5 in rapidity. Due to the interface with FCAL, in the middle layer the highest rapidity cell does not exist.
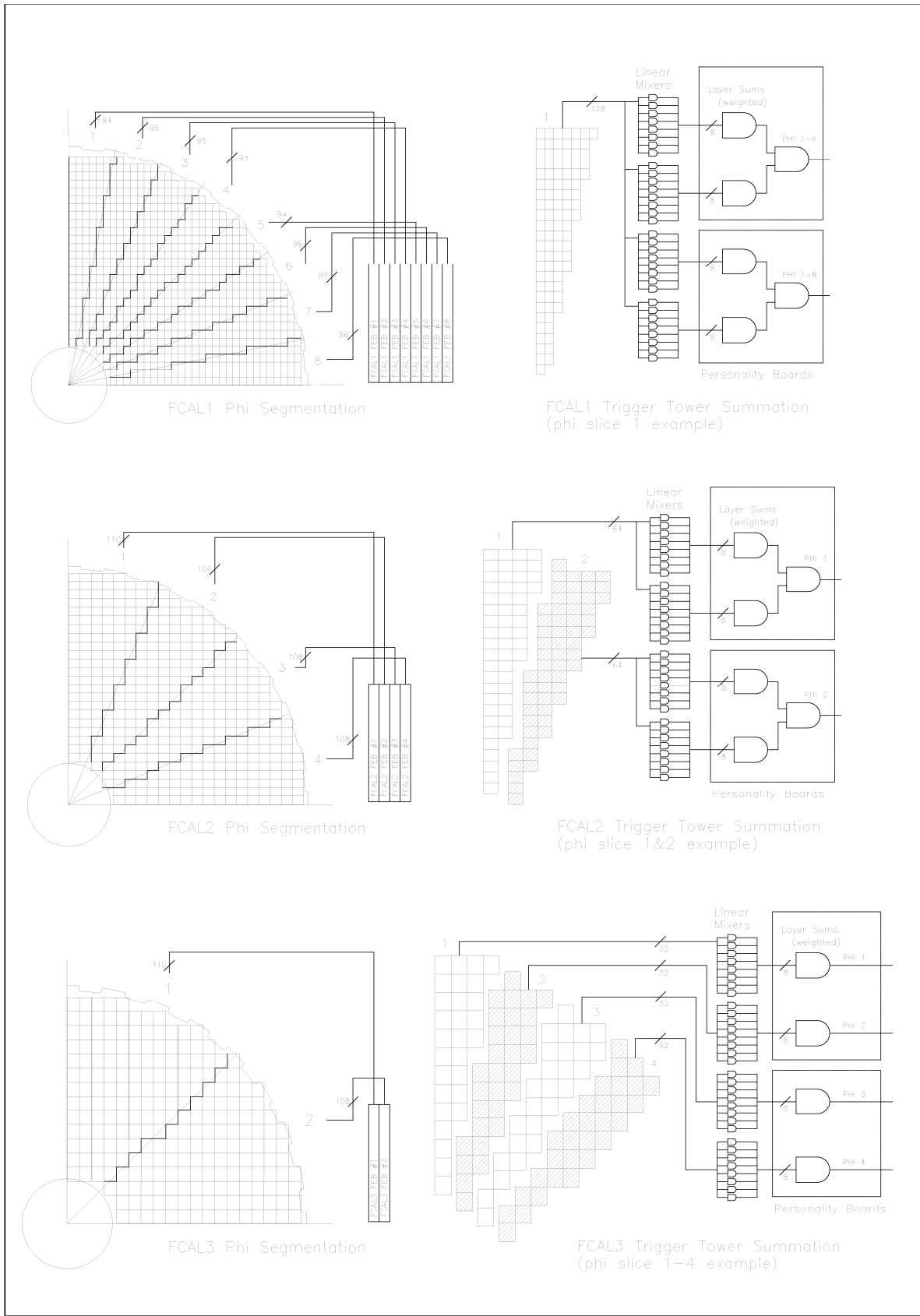
10.2.3.1 Components

In Figure 10-9 we show schematically the cable interconnections for the EM calorimeter signals and calibration lines. The cables from the motherboards to the read-out electronics box have four segments:

1. cold cable, from the motherboard to the patch panel that is attached to the calorimeter module;

2. pigtails, that go from the patch panel to the cold flange of the feedthrough;

3. vacuum cables, that connect the cold to the warm flange of the feedthrough; and

4. flat cables from the warm flange to the electronics box, which are described with the front-end crates in Section 10.4.4.

The schematic diagram for the HEC is identical but in addition, coaxial cables carry the signal from the pads to cold preamplifiers located on the motherboards, as described in Chapter 8.
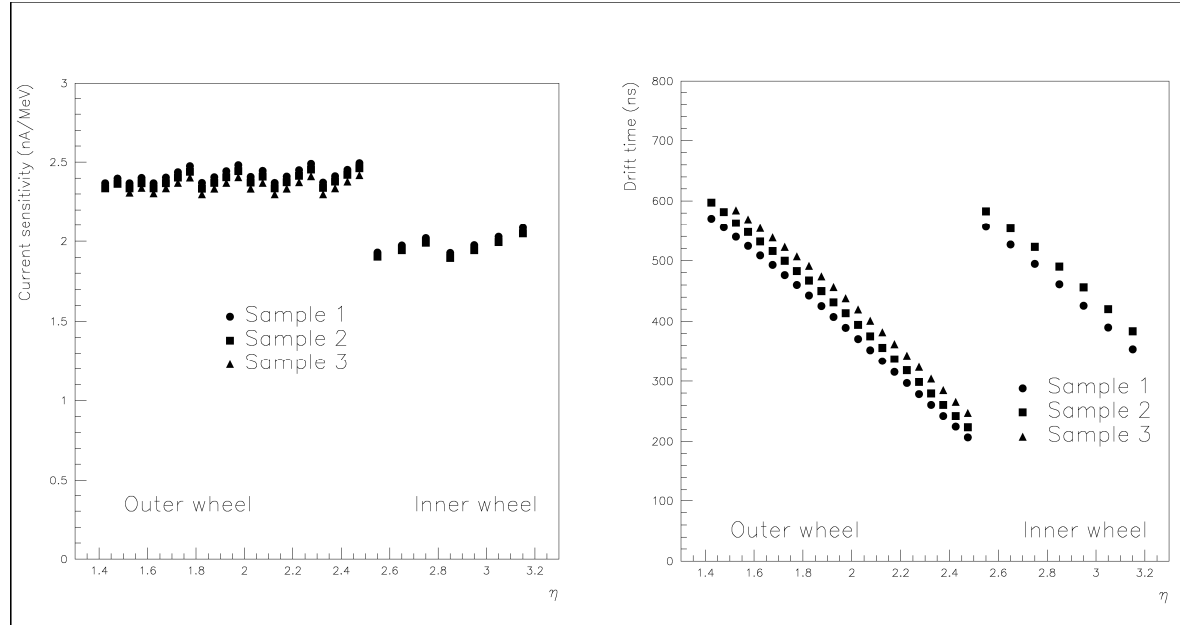
As described in detail in Chapters 4 and 5, identical feedthroughs are distributed in ϕ on both the barrel and end-cap cryostats to transmit signals to the front-end crates. There are 32 feedthroughs on each side of the barrel cryostat. In each of the end-cap cryostats, 20

Figure 10-6 Granularity of read-out and trigger cells in the forward calorimeter.
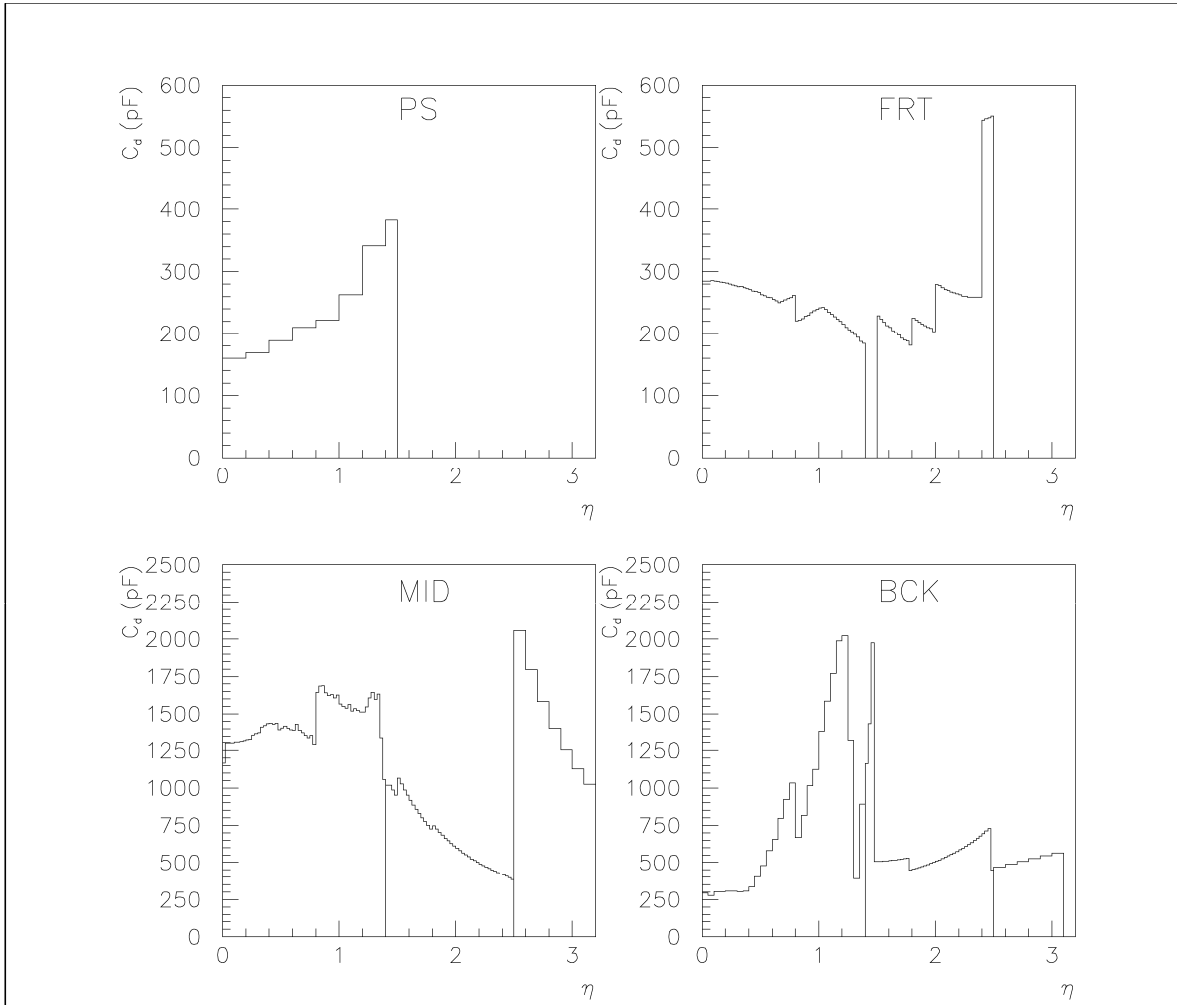
Table 10-3 Drift time (t_{dr}), conversion factor from the deposited energy in a layer to current (I_0/E), maximum current expected in one cell (Imax) and the detector capacitance Cd for all sections of the EM calorimeters. The design of presampler for the EM end-cap is not yet final.

Calorimeter	Layer	t_{dr} (ns)	I0/E (μA/GeV)	Imax (mA)	Cd (pF)
Barrel centre $0<|\eta|<0.8$	Presampler	420	0.9-0.7	0.1	160 − 220
	Strips	450	2.7	0.2 − 0.3	250
	Middle	450	2.7	4.5 − 6	1300
	Back	450	2.7	1.5 − 3	300 − 1000
Barrel edge $0.8<|\eta|<1.5$	Presampler	420	0.85	0.1	220 − 400
	Strips	450	3.1	0.3 − 0.4	220
	Middle	450	3.1	6 − 9	1600
	Back	450	3.1	3 − 4.5	650 − 2000
End-cap	Presampler				
Outer wheel $1.4<|\eta|<2.5$	Strips	600 − 250	2.4	0.3	250
	Middle	600 − 250	2.4	7.5	1000 − 400
	Back	600 − 250	2.4	5	2000 − 500
End-cap Inner wheel $2.5<|\eta|<3.2$	Middle	600 − 400	1.9	8	2000 − 1000
	Back	600 − 400	1.9	4	500 − 600

Figure 10-7 Current sensitivity (left) and drift time (right) in the EM end-cap as a function of rapidity.

feedthroughs serve the EM end-cap and presampler, four are needed for the hadronic end-cap, and four for the forward calorimeter (see Figure 10-10).

Figure 10-8 Cell capacitances of the EM calorimeters as a function of rapidity, including the cross-talk capacitance to the neighbours (particularly sizeable in the strips) and a contribution of 50pF from the summing boards and motherboards.

A feedthrough flange has 30 connectors with 64 pins each, giving a total of 1920 pins. These connectors are organized in two columns (A and B) of 15 connectors each (see Figure 10-11). One pin is used per calorimeter cell or calibration line so one connector serves up to 64 channels. As described in more detail in Section 10.3 and Section 10.4.3, a front-end board can read-out up to 128 channels and a calibration board can pulse up to 64 lines.

10.2.3.2 Detector mapping

Several constraints define the mapping of the detector onto read-out modules.

– Two connectors in line on a feedthrough flange (i.e. 3A and 3B) are connected to the same front-end board to ease cabling between the warm flange and the front-end crate. This helps in reducing the space needed by this connection.

– Signals read out by the same front-end board should be roughly in time to minimize the number of sampling clocks on these boards and to allow for a simple analog summation for the formation of the Level-1 signal. In the EM calorimeters, signals from different lay-

Table 10-4 Detector and signal characteristics for the HEC, separately for a read-out cell (preamplifier) and for a read-out channel (summing stage). The |η| bins correspond to four read-out sections. Here C_d is the detector capacitance of a read-out cell, l is the cable length between the read-out cell and the preamplifier, $<C_{tot}>$ is the average capacitance of a read-out channel without the cable capacitance, I_0/E is the conversion of deposited energy to current, I_{max} is the maximum current of the triangular waveform expected in a read-out cell or in a read-out channel.

| Longitudinal sampling	read-out cell				read-out channel	
	C_d (pF)	l (cm)	I_0/E (µA/GeV)	I_{max} (mA)	$<C_{tot}>$ (nF)	I_{max} (mA)
$1.7 < |\eta| < 2.0$						
Front	217 – 340	76 – 115	0.32	0.18	1.08	0.48
Middle	191 – 342	44 – 121	0.32	0.18	2.59	0.92
Back	192 – 399	46 – 130	0.16	0.05	3.55	0.23
$2.0 < |\eta| < 2.3$						
Front	113 – 174	102 – 135	0.32	0.16	0.56	0.51
Middle	128 – 220	100 – 145	0.32	0.16	1.34	0.77
Back	162 – 321	80 – 152	0.16	0.05	1.83	0.19
$2.3 < |\eta| < 2.6$						
Front	74 – 91	140 – 154	0.32	0.16	0.30	0.55
Middle	84 – 116	131 – 170	0.32	0.15	0.71	0.67
Back	106 – 169	136 – 178	0.16	0.04	0.97	0.11
$2.6 < |\eta| < 2.9$						
Front	147 – 223	160 – 177	0.32	0.20	0.59	0.65
Middle	166 – 282	160 – 201	0.32	0.18	1.41	0.85
Back	210 – 411	156 – 210	0.16	0.06	1.92	0.25

Table 10-5 Drift time (t_{dr}), conversion factor from the deposited energy in each module to current (I_0/E), maximum current expected in one cell (Imax) and the detector capacitance C_d for all sections of the forward calorimeters.

Module	t_{dr} (ns)	I_0/E (µA/GeV)	I_{max} (mA)	C_d (pF)
FCAL1	50	1.9	6	1500
FCAL2	75	1.2	2	1600
FCAL3	100	1.1	1	1700
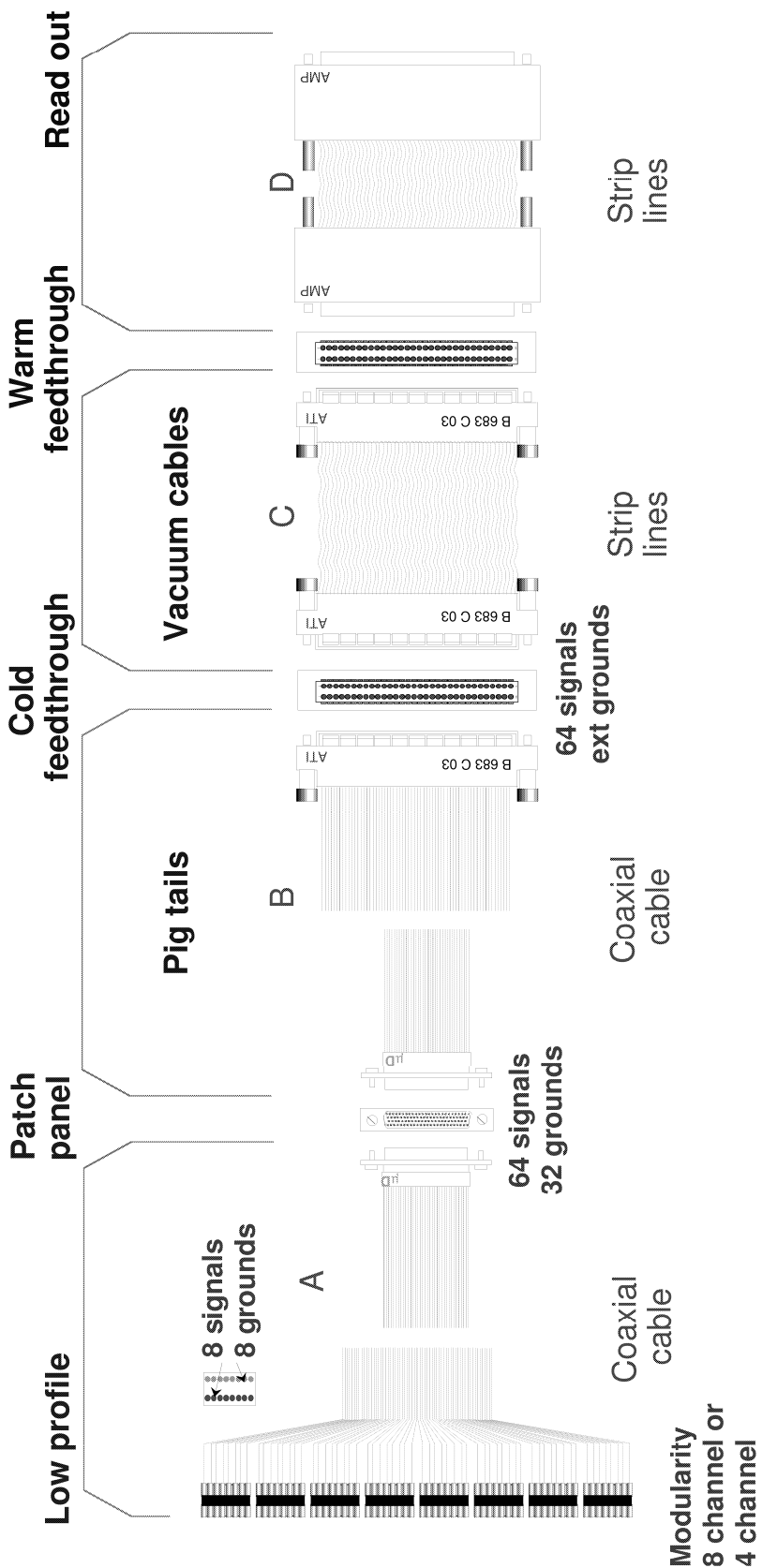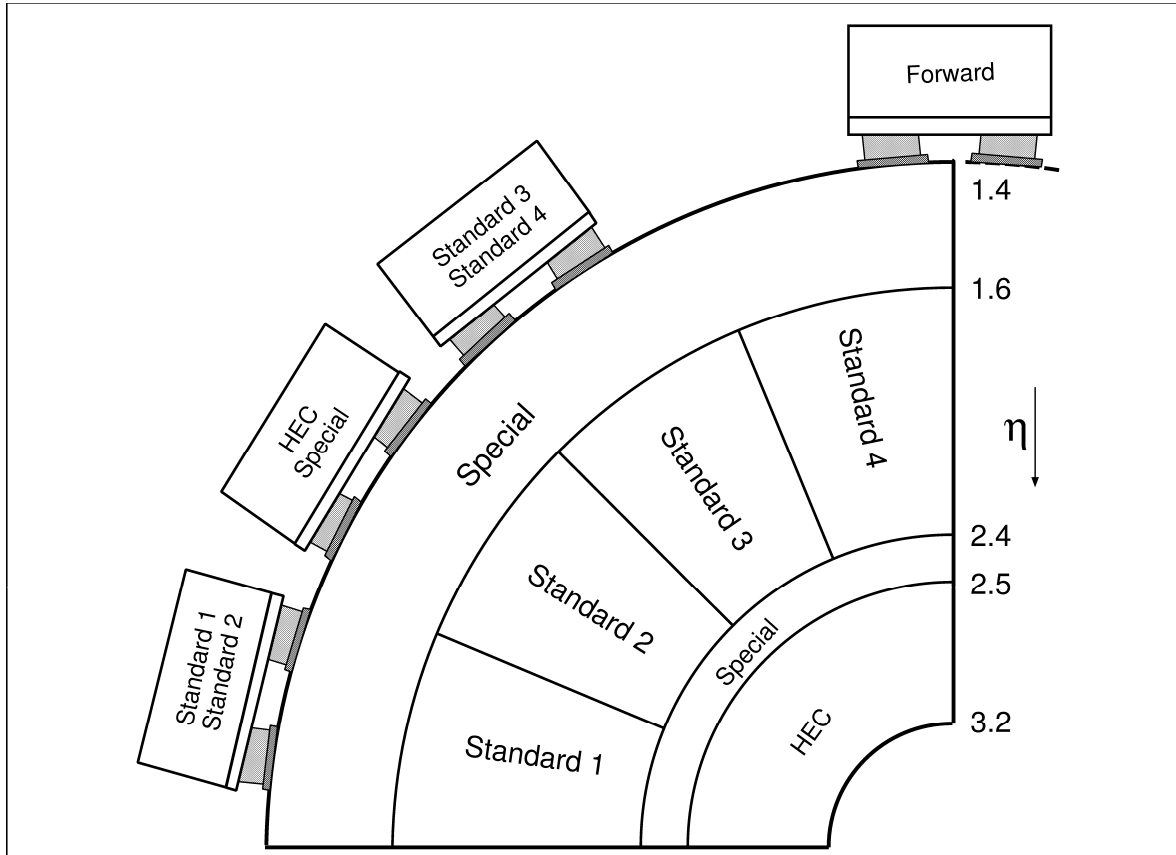
Figure 10-9 Schematic diagram of the cable interconnections.

Figure 10-10   Feedthrough allocation diagram of the end-cap calorimeters showing for the EM calorimeter each division and its corresponding feedthrough. The EM inner wheel and the HEC share a common feedthrough.

ers have different shapes (see Section 10.4.2) and the peaks of the pulses are not aligned. Signals from different layers are routed to different pairs of connectors.

– There is not much space to store cable loops in the cryostat, and in most cases cables are cut to length. To maintain the equal timing requirement, cells close to each other which have similar cable lengths are brought to the same connector.

– To minimize cross-talk, lines with potentially large signals (in particular the calibration lines) are kept far away from low-level ones.

– Cable crossing should be avoided to minimize the risk of error and a solution as uniform as possible should be found.

– To help in the control and management of the calibration, front-end boards and the corresponding calibration boards should be housed in the same crate.
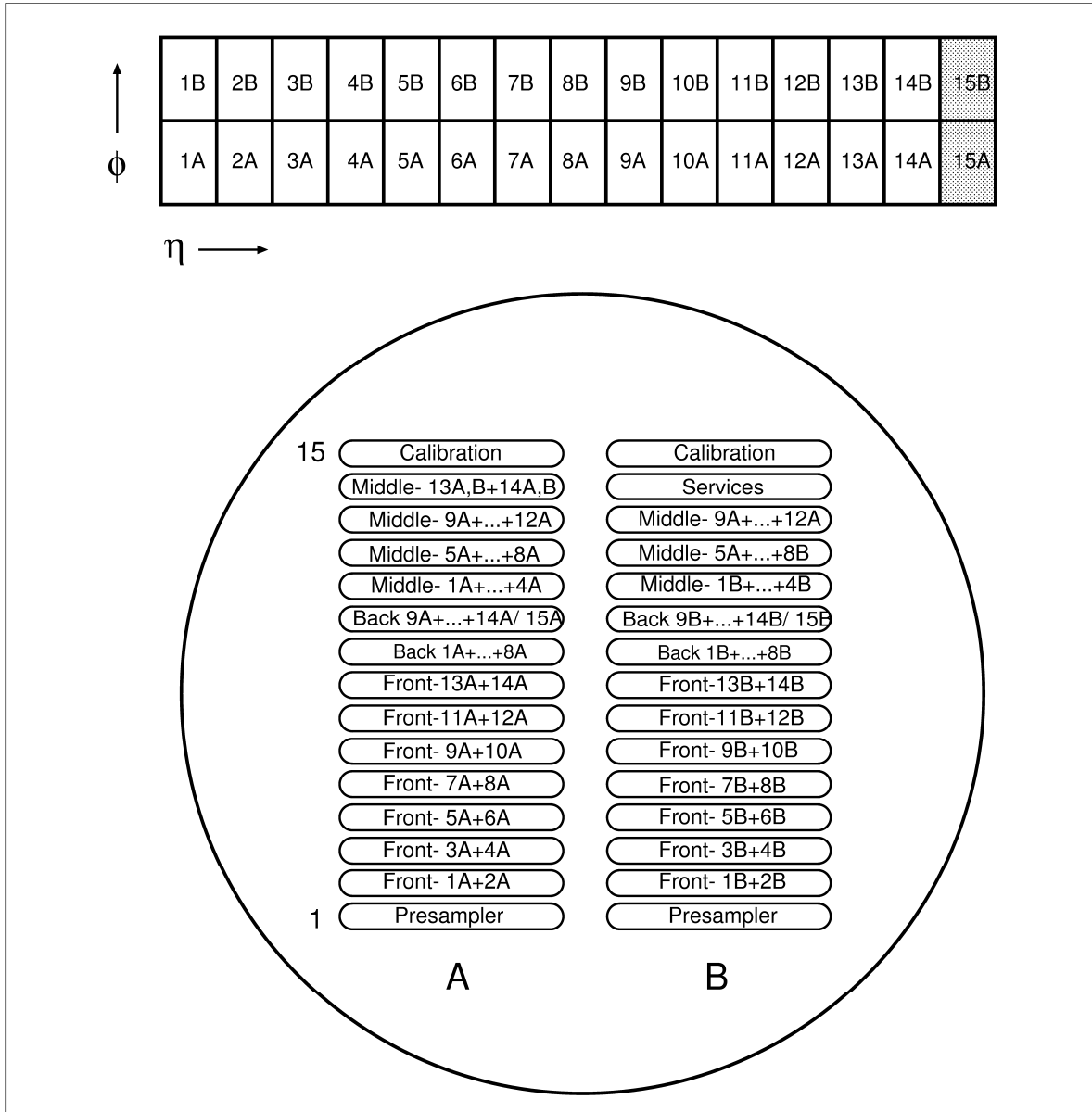
These considerations lead to the mapping shown in Figures 10-12, 10-13 and 10-14.

EM barrel

The EM barrel cabling is quite uniform. All 64 barrel feedthroughs have an identical cabling. Figure 10-11 shows the connectors reserved for calibration lines or monitoring equipment.

EM end-cap

The situation of the EM end-cap is a bit more complex. As shown in Figure 10-10, the cabling is by quadrant. The region $1.6 < |\eta| < 2.4$ is cabled to so-called 'standard' feedthroughs. Signals

Figure 10-11 Top: numbering scheme of trigger tower in half a module. Bottom: sketch of a feedthrough flange showing the 30 connectors (64 pins each) with their numbering and their allocation to a trigger tower.

from the 'small' wheel share the same feedthrough as the hadronic end-cap. The rest of the EM end-cap cables go to the so-called 'special' feedthrough.
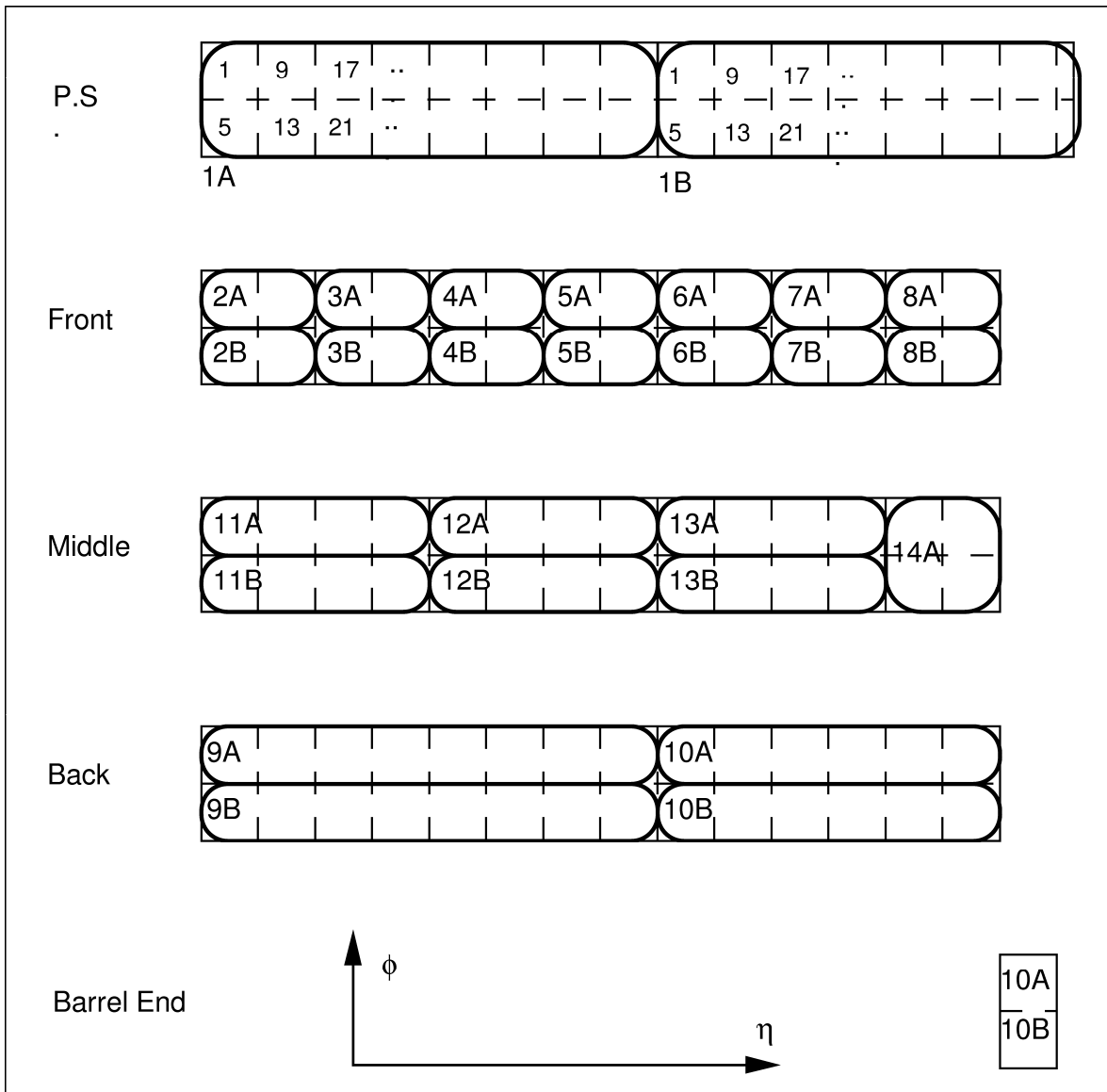
Hadronic end-cap
In the HEC, the cabling is also by quadrant. Unlike the EM calorimeters, to ease the summation for Level-1 (only three cells need to be added), all layers in depth go to the same connector. Signals are brought in time by adjusting the length of the signal cables (cf. Figure 10-14).

FCAL
The cabling of the forward calorimeter is sketched in Figure 10-6.

Organization of the front-end crates
One crate serves two feedthroughs but there is no crossing of cables between feedthroughs and front-end boards. The mechanical construction of the crate is discussed in Section 10.4.4. It is

Figure 10-12 Mapping of each layer of the barrel EM on feedthrough connectors. Each square represents a trigger tower. Adjacent squares are neighbouring trigger towers in ϕ (vertical) and η (horizontal). Groups of trigger towers sharing a common feedthrough connector are labelled by the connector number. For the presampler the feedthrough connector pin number of the first cell of each trigger tower is also indicated.
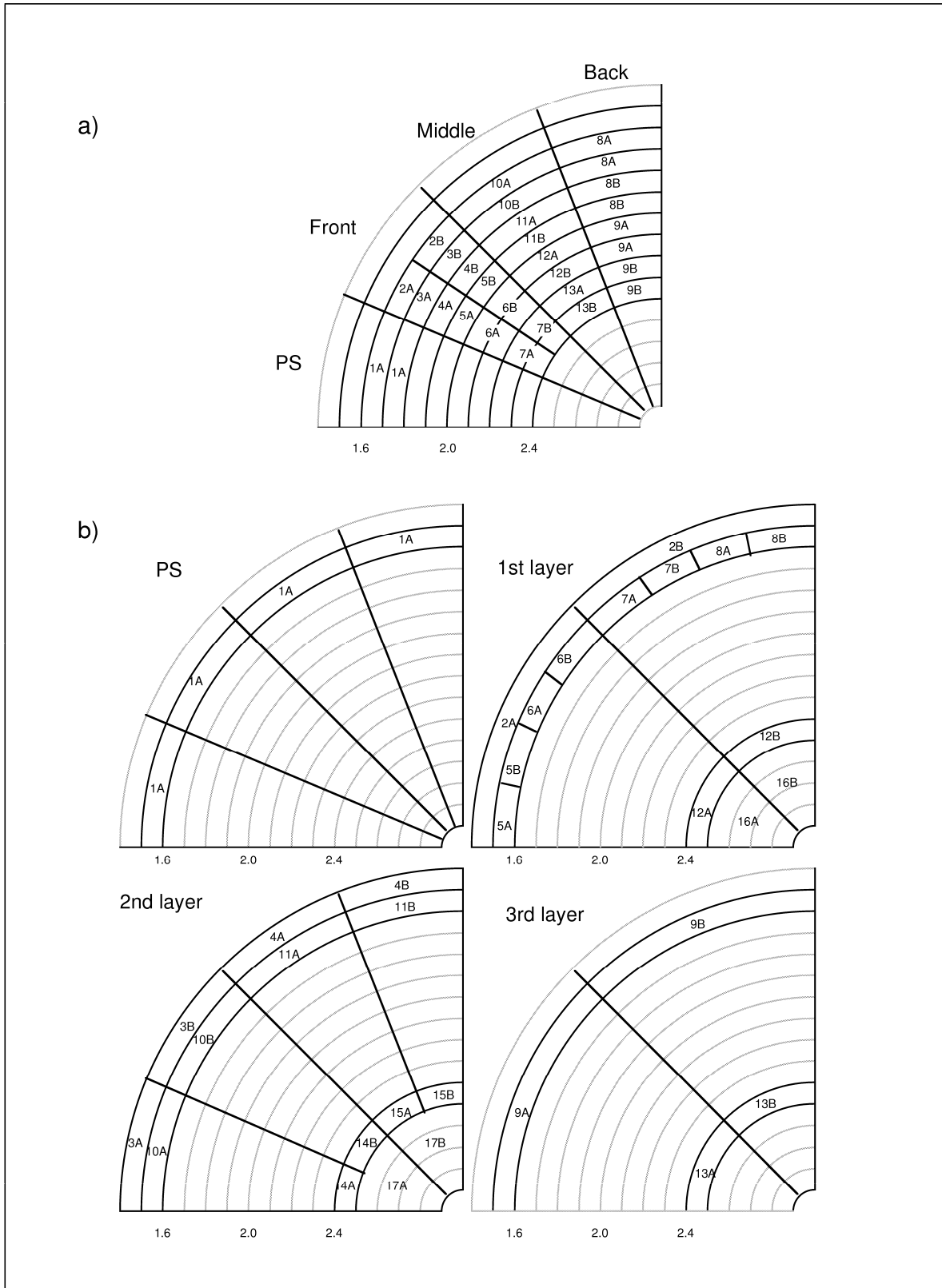
proposed to populate each crate with 38 modules. The location of circuit boards by their function in the crates is shown in Figure 10-15.

10.2.3.3 Cold cables: requirements
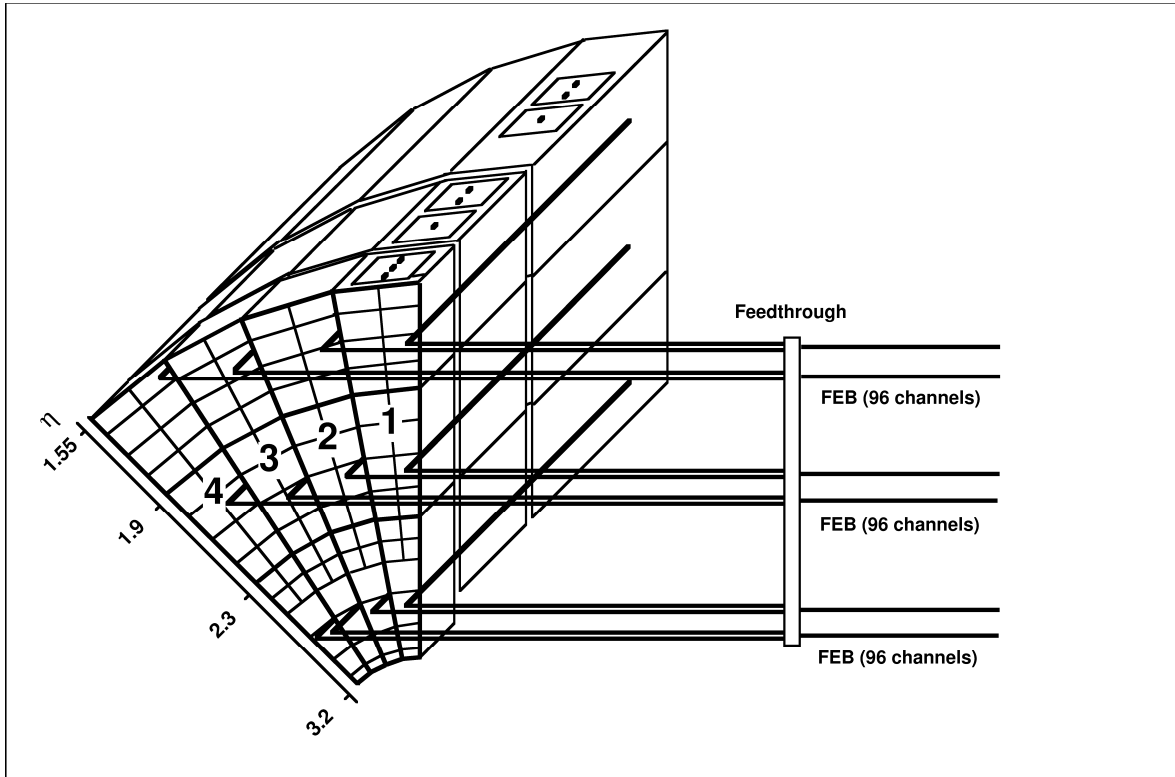
The cables and connectors transporting the detector and calibration signals must satisfy the following requirements:

Impedance

As explained in Section 10.4.1, the different capacitances of the various longitudinal layers of the calorimeters (Tables 10-3 to 10-5) lead to different optimum values for the cable impedance. The presampler, strips and hadronic end-cap are read with 50 Ω cables, whereas the middle and back sections of the EM calorimeter and the forward calorimeter are read with 25 Ω cables. The

Figure 10-13 Mapping of each layer of the EM end-cap on a feedthrough connector. a) Cabling for a standard feedthrough, which covers an azimuthal sector of width 22.5°. The rapidity boundaries of trigger towers are indicated by the circular arcs. Groups of trigger towers sharing a common feedthrough connector are labelled by the connector number. Although the connector allocation is identical for all feedthroughs, the drawing shows the assignment for a different depth layer for each crate. b) Cabling for the special feedthrough, which covers particular rapidity intervals for the entire quadrant. The rapidity boundaries of the trigger towers serviced by this feedthrough are indicated by heavy circular arcs. Groups of trigger towers sharing a common feedthrough connector are labelled by the connector number.

Figure 10-14 Mapping of the hadronic end-cap on a feedthrough connector. All depth layers share the same connector.

calibration signals are transmitted on 50 Ω cables. The accuracy to which the cable impedance can be specified is ±5%.

Dimensions
To minimize dead material, in particular in front of the calorimeter, the cable outer diameter should be around 1 mm.

Attenuation
The cable attenuation is an important parameter for the calibration accuracy. It also affects the noise performance of the warm preamplifiers. It should be less than 10% for 5 m, which translates into 0.25 dB/m at 10 MHz and at room temperature.

Cross-talk
The design requires that the cross-talk of the full chain for nearest neighbours is less than 1% and less than 0.1% for distant channels, which is a very stringent specification for connectors.
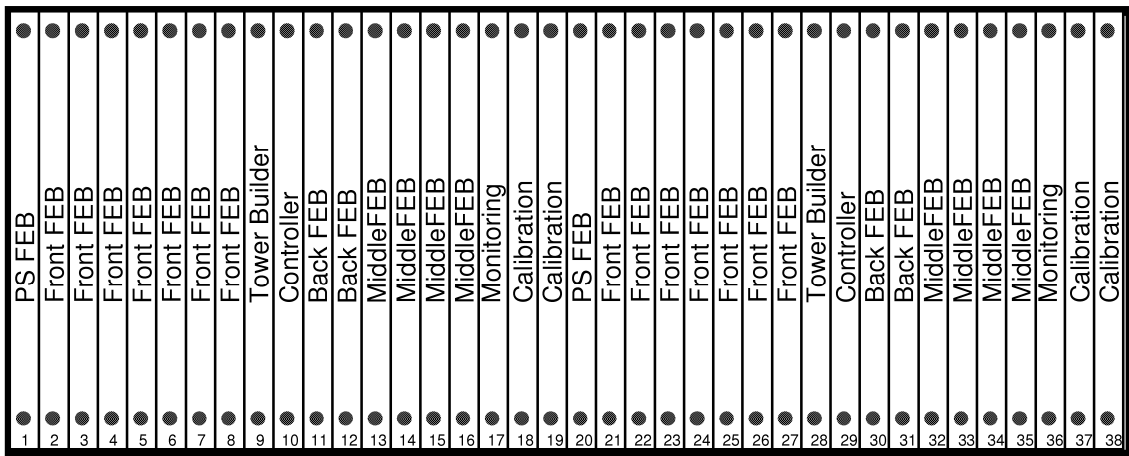
Environment
The cold cables and connectors should withstand the maximum levels of radiation (1 MGy in the forward calorimeter) without degradation or pollution of the liquid argon.
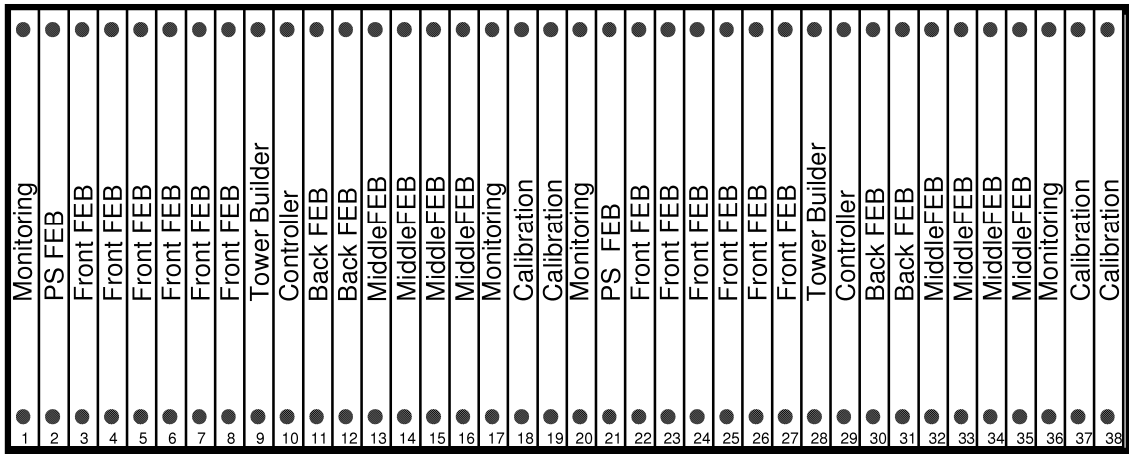
10.2.3.4 Cold cables and connectors: proposed solution

The cables used in the liquid have already been chosen and are being manufactured: mini-coaxial cables made out of pure polyimid by the AXON [10-16] company will be used. These cables have been tested to meet the requirements listed above, particularly those concerning radiation

Barrel Crate

PS FEB	Front FEB	Front FEB	Front FEB	Front FEB	Front FEB	Front FEB	Front FEB	Tower Builder	Controller	Back FEB	Back FEB	MiddleFEB	MiddleFEB	MiddleFEB	MiddleFEB	Monitoring	Calibration	Calibration	PS FEB	Front FEB	Front FEB	Front FEB	Front FEB	Front FEB	Front FEB	Front FEB	Tower Builder	Controller	Back FEB	Back FEB	MiddleFEB	MiddleFEB	MiddleFEB	MiddleFEB	Monitoring	Calibration	Calibration
1	2	3	4	5	6	7	8	9	10	11	12	13	14	15	16	17	18	19	20	21	22	23	24	25	26	27	28	29	30	31	32	33	34	35	36	37	38

EMEC "standard" Crate

Monitoring	PS FEB	Front FEB	Front FEB	Front FEB	Front FEB	Front FEB	Front FEB	Tower Builder	Controller	Back FEB	Back FEB	MiddleFEB	MiddleFEB	MiddleFEB	MiddleFEB	Monitoring	Calibration	Calibration	Monitoring	PS FEB	Front FEB	Front FEB	Front FEB	Front FEB	Front FEB	Front FEB	Tower Builder	Controller	Back FEB	Back FEB	MiddleFEB	MiddleFEB	MiddleFEB	MiddleFEB	Monitoring	Calibration	Calibration
1	2	3	4	5	6	7	8	9	10	11	12	13	14	15	16	17	18	19	20	21	22	23	24	25	26	27	28	29	30	31	32	33	34	35	36	37	38

EMEC + HEC Crate

PS FEB	Front FEB	Middle FEB	Middle FEB	Front FEB	Front FEB	Front FEB	Front FEB	Tower Builder	Controller	Back FEB	Middle FEB	MiddleFEB	Front FEB	Back FEB	Tower Builder	Middle FEB	Middle FEB	small wheel FEB	Tower Builder	small wheel FEB	Monitoring	Calibration	Calibration	Controller	FEB	Tower Driver	FEB	FEB	Tower Driver	FEB	FEB	Tower Driver	FEB	LV supplies	LV supplies	Calibration	Calibration
1	2	3	4	5	6	7	8	9	10	11	12	13	14	15	16	17	18	19	20	21	22	23	24	25	26	27	28	29	30	31	32	33	34	35	36	37	38

Figure 10-15 Location of circuit boards by their function in the crates for the barrel, EM end-cap, and HEC.

hardness and argon purity. The geometry of these cables together with electrical measurements are summarized in Table 10-6.
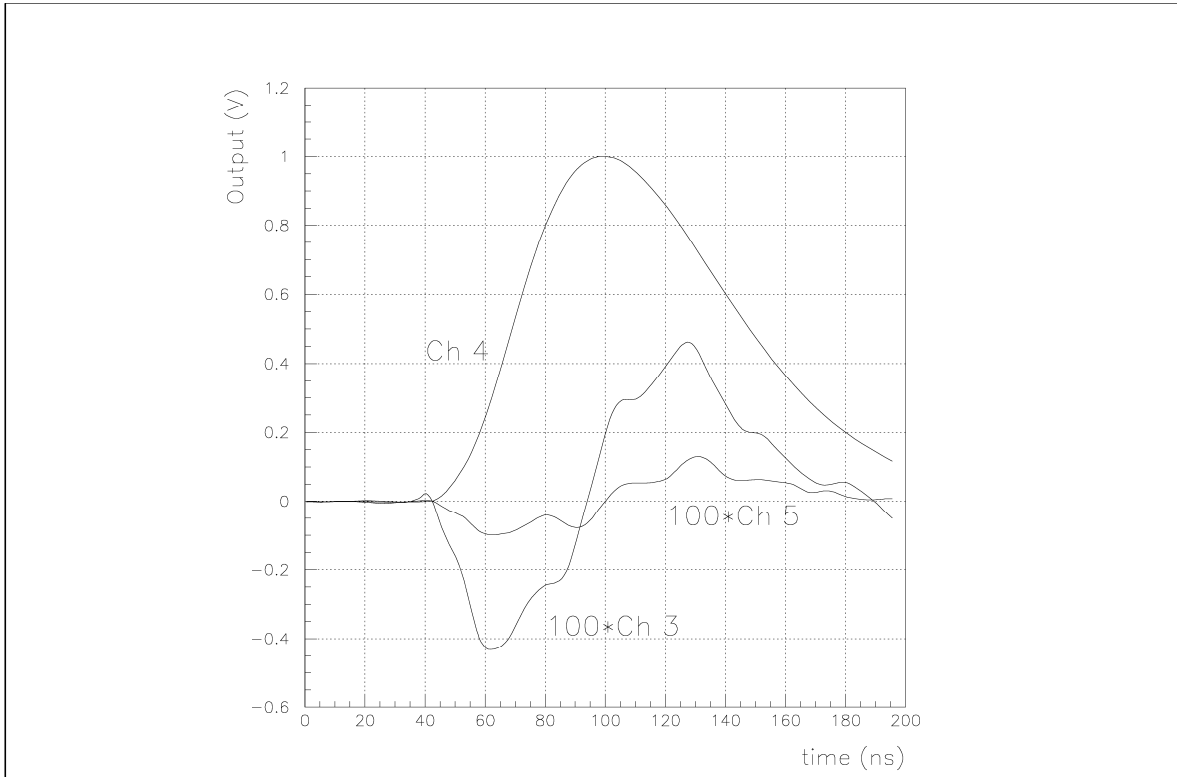
Table 10-6 Geometrical dimensions and measured electrical properties of the selected cold cables

Cable	25 Ω	50 Ω		
Wire gauge (AWG)	28-07	32-01		
Inner conductor diameter	0.381 mm	0.203 mm	CuAg	
Dielectric diameter	0.8 mm	0.8 mm	polyimid	
Braid cross section area	0.15 mm2	0.15 mm2	CuAg	
Ext. sheath diameter	1.2 mm	1.2 mm	polyimid	
Characteristic impedance	26 Ω	49 Ω	90 K	
Propagation delay	6.1 ns/m	6.1 ns/m	90 K	
	6.5 ns/m	6.5 ns/m	300 K	
Attenuation at $t_P(\Delta)$ = 40 ns		-0.55%/m	90 K	
		-1.3%/m	300 K	
Shielding efficiency at 10 MHz	42 dB	48 dB	300 K	

The connectors used in the liquid have also been chosen and are displayed in Figure 10-9. They have been carefully selected to meet the performance and reliability requirements. The materials used in the cable and connectors (Kapton and epoxy) have been scrutinized for radiation hardness.

On the motherboards, low profile connectors with eight signal channels and eight ground connections are used to minimize the height (to 5 mm) and thus the amount of dead liquid in front of the EM calorimeters. The cables are soldered to gold-plated brass pins and then potted in epoxy to ensure robustness. They run along the module in bunches of 64 channels, called 'harnesses', up to the edge, where they are attached to a 100 pin μD connector on a patch panel. These connectors have four rows of 25 pins at a pitch of 1.27 mm, allowing the patch panel to be very compact. There are 64 signal and 32 ground connections, so that two channels share the same ground. As can be seen in Figure 10-16, this is the dominant source of cross-talk, up to 0.4% peak. However, these would be neighbouring channels in the detector, for which the cross-talk requirement is less stringent. The pins are gold-plated and the male pin is twisted to have the best contact quality. These connectors have been used for 10 years in military applications requiring high reliability. Here again, the cables are potted to relieve the crimps from mechanical stress. All the harnesses will be cut to the proper length, in order to avoid any cable loops and dead space.

The cables from the patch panel to the feedthrough, called pigtails, are similar with the mating male μD connector on one side and a custom connector to fit on the feedthrough, manufactured by ATI. It uses 64 pins in a double row of 2.54 mm pitch to feed the signals, while the ground return is carried by a surrounding copper-beryllium spring. In order to keep the cross-talk within the specified limits, all the connections inside the connectors must be low inductance. The cross-talk of the whole chain is currently under measurement, but each piece has been measured separately and found to meet the specifications.

Figure 10-16 Cross-talk measurement of the μD connector. For the measurement a triangle signal simulating the calorimeter pulse is injected into one channel. The figure shows the shaped output signal, Channel 4, and the shaped output signals of its immediate neighbours, Channel 3 and Channel 5. The level of cross-talk observed in Channels 3 and 5 (magnified by a factor of 100) are 0.4% and below 0.1%, respectively. Channel 3 shares the ground return with Channel 4.

The cables used inside the feedthrough are polyimid striplines, especially designed to minimize the heat transfer into the cryostat. As the feedthroughs all need to be identical, their characteristic impedance has been set to 35 Ω as a compromise between 25 and 50 Ω. As they are short (30 cm), the impedance mismatch has been checked and found to be tolerable. These striplines contain 32 channels with 150 μm wide traces at a pitch of 0.8 mm. The ground return is 300 μm wide on one side only and the dielectric thickness is 40 μm. The distant cross-talk has been measured to be less than 0.05%. The connectors are almost identical to the ATI connectors described above, except that they are adapted to connect to striplines.

10.3 The calibration system

One of the important advantages of liquid argon calorimetry is the stability and uniformity of the ionization signal. To exploit this advantage, it is necessary to provide a very precise system to calibrate the electronics chain. Because of the very high energies attained at the LHC, the constant term in the resolution function must be kept small, in order to guarantee good energy resolution over the entire range. Part of this constant term stems from the accuracy with which the electronics chain is calibrated. For instance, non-uniformity of the calibration pulse amplitude affects directly the measurement of high-energy electromagnetic showers; imperfections of the electronics are propagated to the constant term of the jet energy resolution. Our aim is to limit the contribution from the constant term due to the calibration system to less than 0.25% for the EM calorimeters, less than 1% for HEC and less than 2% for FCAL. More detailed information than the description given here can be found in [10-17] and [10-18].

10.3.1 Requirements

Dynamic range

The dynamic range of the calibration system has to match the maximal current in the preamplifiers listed in Tables 10-3, 10-4 and 10-5 in Section 10.2 (up to 10 mA in the EM calorimeters). At the low end of the energy scale, the system must permit one to understand the response of the calorimeter down to the energy deposition of a minimum ionizing particle.

Linearity

The calibration system should cover the whole dynamic range in one linear scale. This will allow one to intercalibrate the three gains of the shaper. The integral nonlinearity of the pulser signal should be less than 0.1% for each of the three gains of the shaper to permit an accurate correction of the nonlinearities in the whole electronics chain.

Pulse Shape

As the charge is not totally integrated, the signal shape should be as close as possible to the real signal. The rise time should be fast (less than a few nanoseconds) and the decay time should be close to the drift time of the signal induced by incident particles (which are called "physics" signals hereafter).

Timing

The relative timing between the calibration and the physics pulses has to be adjusted in order to provide the best accuracy with the minimum number of calibration parameters. To minimize any effect of jitter, the alignment should be kept within ± 1 ns (cf. Section 10.3.2.3).

Environment

The calibration elements should tolerate without any degradation, radiation fluxes shown in Chapter 11. There is also a magnetic field of a few tens of gauss in the cracks [10-19]. The signal pattern distribution must permit the study of cross-talk. The rate has to be larger than ~ 1kHz and the design of the board should allow the taking of calibration events during the physics run for monitoring.

10.3.2 Description of the calibration system

The simplicity of the ionization mechanism in liquid argon calorimeters allows one to compute *a priori* the gain factors, i.e., the ratio of the ionization current to the incident particle energy. The gain factor is a property of the calorimeter and in principle needs to be determined only once for a given geometry. This factor is calculated on the basis of detailed knowledge of the signal produced by the particle shower. Although simulations permit the evaluation of the calorimeter response with a certain accuracy, the actual gain factors will be extracted from test beam measurements.

The ability to evaluate the gain factors is particularly important in face of varying detector geometry, such as the change of the absorber thickness (from 1.8 mm to 1.2 mm) in the EM barrel at $\eta = 0.8$. With proper gain factors, even in transition regions the energy measurement will be uniform. These factors can also take into account the presence of material in front of the calorimeters.

The same remarks apply to the hadronic calorimeter. In both cases detailed maps of the energy response will be measured in the test beam on actual ATLAS modules and the calibration system will ensure the transfer of the calibration to ATLAS.

The proposed electronics calibration system is uniform to 0.25% in a slice of $\Delta\eta = 0.2$ for the EM calorimeter. Variations in the amplitude of the calibration pulses arise mainly from differences in the attenuation in the cables that transport the calibration signals. These are measurable and will be taken into account. The system will also maintain synchronism between the calibration and physics signals at ± 1 ns over the entire calorimeter.

In addition, the calibration will be independently checked *in situ* either using Z decays into a pair of electrons [10-20] or E/p matching with an inclusive single electron sample for the EM calorimeters [10-20] and either γ-jet or Z-jet events [10-21] for the hadronic part.

10.3.2.1 Principle of the calibration

The principle of the calibration method, which is common to all the LAr calorimeters (EM, HEC and FCAL) is illustrated in Figure 10-17. A voltage pulse, which simulates the physics signal, is applied across an injection resistor R_{inj} in the cold, directly on the electrodes (except for the FCAL where the radiation levels make it too risky). The decay time is determined by the pulser circuit. There are important advantages in using a resistor for calibration rather than the traditional capacitor: it is easy and inexpensive to obtain 0.1% precision; it shows little sensitivity to stray capacitance; and it is robust and radiation hard. A calibration current of 10 mA can be achieved by sending a 5V pulse into $R_{inj} = 500\ \Omega$. At fast shaping and relatively high detector capacitance, the parallel noise generated by R_{inj} is almost negligible [10-22]. Smaller currents are obtained by increasing R_{inj}, with a practical limit around 5 kΩ, due to parasitic stray capacitance. To obtain the required accuracy, it is essential to form the pulse right on the electrodes, in order that the path for calibration signals be as close as possible to the path for physics signals. The main difficulty of this calibration method is to distribute the voltage pulse uniformly throughout the calorimeter. To reduce the number of cables, the pulse is distributed locally to channels with little or no cross-talk in the detector. However, these channels must be in close proximity, since the calibration signals must remain isochronous with the arrival of particles. It is also important that all the elements in the calibration path be as uniform as possible, in the range of 0.1%. Among those, the cables that transport the signals to the EM motherboards are of major concern and are discussed in detail below.

10.3.2.2 Pulse generator

The fast pulse is made by interrupting a precise DC current I_p that flows in an inductor L. A command pulse is applied to the base of Q2 which diverts I_P to ground, cutting off transistor Q1 (Figure 10-17). The magnetic energy stored in the inductor produces a voltage across the parallel combination of the cable of characteristic impedance R_C and a termination resistor R_0 of the same value. This yields a current in the resistor of the form

$$V(t) = -\frac{R_0}{2}I_p e^{-t/\tau_{exp}} \qquad \text{with} \qquad \tau_{exp} = \frac{L}{2R_0} \qquad \qquad 10\text{-}1$$

Because of the small DC resistance of the inductance, the power dissipation is low, since the collector of Q1 operates close to 0 V. It is therefore possible to generate pulses up to -5 V from a single +6 V power supply. This also results in negligible power dissipated in the terminating resistor, ensuring long term stability. Moreover, the resistance of the inductor has no influence on the pulse amplitude. It generates an offset of $V_0 = R_L I_P$, which is removed by the AC coupling at the preamplifier input. It should nevertheless be kept small to minimize the power dissipated in the inductor so as not to alter its inductance.

11 Radiation levels, radiation tests, qualification of materials

11.1 Radiation map

11.1.1 General framework

The dominant source of radiation in the calorimeter is, by far, particles produced in proton-proton collisions at the interaction point. Whilst most of the collision products are absorbed in the calorimeters, depositing relatively large amounts of energy, particles from backsplash and shower tails will affect the inner tracking, and the muon spectrometer, respectively. The background in the tracking system has been taken into consideration when optimizing the longitudinal position of the forward calorimeter inside the end-cap cryostats. The total active depth of the hadronic calorimeters has been driven by a compromise between cost and calorimetric performance. In most of the solid angle, the thickness chosen is not enough to shield efficiently the muon chambers sitting immediately behind. This is why passive shielding has been added (see Chapter 1,Fig 1.8). Protecting the barrel muon chambers was also a driving element when trying to fill as much as possible with the "intermediate Tile calorimeter" the space remaining beyond the front-end crates in the barrel to end-cap gap [1-2]. The optimization of the experiment in terms of radiation levels was carried out using detailed simulations of proton-proton collisions (with DTUJET [11-1]), followed by transport and showering of secondary particles using FLUKA [11-2]. In this code the transport of low-energy neutrons is carried down to thermal energies, taking into account the temperature of the liquid argon in the detector. This is important for calculating the activation of materials, and in particular the amount of ^{41}Ar produced.

11.1.2 Radiation levels

The results presented correspond to a one-year run at standard high luminosity ($\int$Ldt $= 10^{41}$cm^{-2}). The neutron fluence (see Figure 11-i) corresponds to neutrons above 100 keV, weighted using standard coefficients for silicon in order to obtain the "1 MeV" equivalent. The dose (Figure 11-ii) integrates all photons down to 30 keV. It is worth noticing that the worst place of calorimeter electronics (the barrel to end-cap gap for warm front-end electronics, and the periphery of hadronic end-cap wheels for cold preamps) receive less than or about 10^{12} neutrons/cm^2 and 20 Gy per year.

11.1.3 Activation

11.1.3.1 Activation of Ar

The concentration of ^{41}Ar in the liquid at "equilibrium" during high luminosity running was calculated as discussed above shortly, taking into account the ^{41}Ar life time (6560 s) and the capture cross-section of neutrons in the various materials of the detector. The resulting activity is given in Table 11-1.

Whilst most of the energy is deposited in the forward calorimeter (FCAL), this detector contributes only a small part of the total ^{41}Ar activity. This results from several facts: tungsten has a

Table 11-1 ^{41}Ar activity in the calorimeter (GBq)

Half life (s)	Decay	Barrel	EMEC	HEC	FCAL1	FCAL2 + 3
6560	β$^-$	49	98	11	1.1	0.5

high absorption cross-section for thermal neutrons and the sampling fraction of the FCAL is small.

11.1.3.2 Activation of other materials

As an illustrative figure, the activity of dominant isotopes, 7 days after the end of a 100 days high luminosity running, is given in Table 11-2. This table was produced considering only the dominant materials of the calorimeter (by weight). The presence of some impurities (like Cobalt), even in small quantities, could change significantly the content of Table 11-2. Further results, including the dose rate close to the detector will be discussed in a forthcoming note [11-3]

Table 11-2 Calorimeter bulk material activation (in GBq) after 10^7 s of irradiation and 7 days of cool-down

	Barrel	EMEC	HEC	FCAL1	FCAL2 + 3
Dominant isotope	^{55}Fe	^{201}Tl	^{58}Co	^{58}Co	^{185}W
Activity	2.1	9.7	6.5	19	600

11.2 Facilities for irradiation studies

11.2.1 Dubna facilities for radiation hardness tests

The Join Institute for Nuclear Research (JINR) has good facilities for radiation-hardness tests. There are two reactors which are sources of fast neutrons and photons, and a powerful ^{137}Cs γ-source.

The Frank Laboratory of Neutron Physics has two fast neutron high flux periodic pulsed reactors, IBR-30 and IBR-2. The reactors operate in the regime of periodic, short power pulsations with a high average power rating. The power pulses are generated by external modulation of the reactivity, for example, by periodic motion of some component of the reactor which affects the reactivity. A short duration state of superprompt criticality is achieved periodically, during which the power increases and decreases rapidly. The reactors are highly subcritical and power is low between pulses.

11.2.1.1 Reactor IBR-2

The majority of the radiation hardness tests at Dubna were performed with the IBR-2 reactor. Some general characteristics of the reactor IBR-2 are listed in Table 11-3 [11-1]. The reactor is surrounded by two concrete rings of biological shields, each 2.5 m thick. The 3 m inner corridor between the shielding walls is intended for the location of various pieces of equipment to be irradiated. The experimental hall is directly outside the concrete shield. It also serves as an area for the assembly of reflectors, water moderator, etc., installed on roll-away shielded trolleys.

Table 11-3 General characteristics of the IBR-2 reactor

Average thermal capacity	2 MW
Working frequency	5 Hz
Peak power in pulse	1500 MW
Critical mass	100 kg PuO_2
Half-width of fast neutron pulse	220 μs
Flux density of neutrons (E > 0.01 MeV) in central channel (time average)	$3.0 \; 10^{14}$ n cm^{-2}s^{-1}

There are 14 horizontal channels for the extraction of neutron beams, some of which are accessible for radiation tests. The channels are equipped with communication lines for signal cables and cryogenics. The geometrical cross sections of these channels are typically 10x40 cm in the vertical and horizontal directions. The neutron fluxes vary between a few 10^8 n cm^{-2}s^{-1} and a few 10^{12} n cm^{-2}s^{-1} depending on the shielding. The shape of the fast neutron kinetic energy spectra is rather similar for various channels. The average value is about 1 MeV. In addition to neutrons, γ radiation is produced in the nuclear reactions with maximal dose rates up to 10 Gy.s^{-1}. The ratio between the neutron flux and the γ dose can be varied by several orders of magnitude by using appropriate beam filters and absorbers. A pneumatic system is also available for transport of the material to be tested into and from the irradiation zones [11-2].

An irradiation facility has been developed at beam line no.3 for radiation-hardness tests of electronics and materials to be used for building the ATLAS detector. The channel has a geometrical acceptance of 20x40 cm^2 and a fast neutron flux density value around 10^{10} n cm^{-2}s^{-1}.

11.2.1.2 Reactor IBR-30

The IBR-30 reactor was used to perform the photon irradiation of the latest prototypes of GaAs preamplifiers and various samples of different materials.

The IBR-30 has the same operational principle as the IBR-2. The half-width of the fast neutron pulse is about 4 μs and the fast neutron flux is 10^{11} n cm^{-2}s^{-1} near the reactor moderator surface. The reactor geometry allows a larger suppression of the neutron background compared with the IBR-2 reactor. In particular, equipment was protected from the back against rescattered neutrons. The fluence of fast neutrons is attenuated by a combination of a paraffine moderator and a cadmium absorber, where neutrons are absorbed in an n-γ reaction. The photon average energy is estimated to be about 1.5-2.0 MeV and the γ dose rate is measured to be 0.3 kGy.h^{-1}.
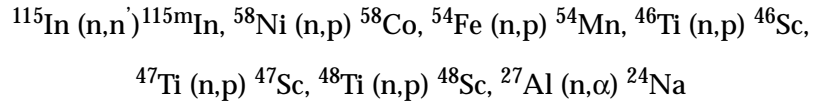
11.2.1.3 γ-source

A ^{137}Cs source was used earlier for the radiation-hardness tests of the GaAs electronics and calibration of the TLD-700 γ dosimeters.

The γ source irradiates a cylindrical hole 15 cm in diameter and 30 cm high. The hole has four special slits on a circle at symmetrical positions. The γ rates in the hole were modified by putting sources of ^{137}Cs isotopes of different activity (20-1800 Ci) in front of each slit. Topology and γ dose rates in the hole have been measured in a special run. It was found that the γ dose is constant along the horizontal level but varies by 10% along the vertical axis in the frame. The average maximal dose rate in the irradiated zone was measured to be 1.8±0.3 kGy.h^{-1}. The γ quanta produced have an energy of 661.7 keV.

11.2.1.4 Particle fluences and dose rates at Dubna

The standard method of threshold detector activation was used to measure the kinetic energy spectrum and the absolute value of the neutron fluence at the IBR-2 reactor. The spectrum was reconstructed by applying the unfolding procedure to the yield measurements of the following reactions:

$$^{115}\text{In (n,n}')^{115m}\text{In, } ^{58}\text{Ni (n,p) } ^{58}\text{Co, } ^{54}\text{Fe (n,p) } ^{54}\text{Mn, } ^{46}\text{Ti (n,p) } ^{46}\text{Sc,}$$

$$^{47}\text{Ti (n,p) } ^{47}\text{Sc, } ^{48}\text{Ti (n,p) } ^{48}\text{Sc, } ^{27}\text{Al (n,}\alpha\text{) } ^{24}\text{Na}$$

The threshold values for these reactions range between 0.4 and 6 MeV. The yields were determined from the measurements of the induced γ activity by means of a GeLi detector. Based on the experimental values of $\int \phi(E)\sigma(E)dE$ and known dependences for the cross sections $\sigma(E)$ [11-4], the shape of the $\phi(E)$ spectra was reconstructed and the total fast neutron flux was calculated. The accuracy of the values does not exceed 10 to 15%.

Fast neutrons kinetic energy spectra are shown on Figure 11-1 for two irradiation set-ups. The average kinetic energy right after the lead filter was found to be 1.5 MeV and the flux in the energy interval 0.4-11 MeV was $9.5 \cdot 10^9 \text{ n cm}^{-2}\text{s}^{-1}$. For the n/γ converter, the flux was measured to be $4.0 \cdot 10^8 \text{ n cm}^{-2}\text{s}^{-1}$ and the average energy value was equal to 2.1 MeV.

Because of the high energy thresholds of the above-mentioned dosimeters, the measurement below 0.4 MeV was not performed. It was found via Monte-Carlo calculations [11-5] that the resonance neutron spectrum in the interval 0.1-0.4 MeV is proportional to ~1/E. The total flux of these neutrons was estimated by comparing with the experimental data for fast neutrons at E~0.4 MeV. It turned out that, after the lead filter, neutrons within the energy range 0.1-0.4 MeV contributed to the calculated fast neutron flux for $\approx$ 30%.

Figure 11-1 The kinetic energy spectra of the neutrons from the IBR-2 reactor.

In order to compare the results of different radiation-hardness tests, the fluence values are expressed in effective values for neutrons with an equivalent energy of 1 MeV. The corresponding fluence $\phi_{\text{eff}}(1 \text{ MeV})$ is defined as:

$$\phi_{\text{eff}}(1\text{MeV}) = \int_{E_{\text{min}}}^{E_{\text{max}}} \phi(E)\frac{D(E)}{D(1\text{MeV})}dE$$

where $\phi(E)$ is the measured neutron fluence and D(E) is the energy-dependent neutron kerma-factor[1]. Using the kerma-factor values for GaAs [11-6], the effective neutron fluence after the lead filter inside the cryostat filled with liquid nitrogen was obtained for the irradiation of the GaAs preamplifiers: $\phi_{\text{eff}}(1\text{MeV(GaAs)}) = 8.9\times10^9\text{ ncm}^{-2}\text{s}^{-1}$.

---

1. kerma: kinetic energy released in matter.

The IBR-30 reactor was used to perform the photon irradiation of GaAs preamplifiers for the hadronic end-caps. The γ energy spectra of IBR-2 and IBR-30 reactors are similar and consist of three different components:

- nuclear reactions prompt photons emitted during the reactor bursts,

- delayed photons emitted from nuclear decay in between bursts,

- photons from the Cd(n-γ) reaction in the (n/γ) converter.

The energy spectra of primary and delayed photons have been measured previously [11-7] at IBR-30. Folding all components together, the average photon energy was found to be in the range between 1.5 and 2.0 MeV. The γ dose rate was measured to be 0.3 kGy.h^{-1} with an underlying neutron flux of 0.7 10^{12} n cm^{-2}h^{-1}.

11.2.2 SARA neutron facility at Grenoble for radiation-hardness tests

11.2.2.1 The SARA neutron facility

SARA (Système Accélérateur Rhône–Alpes) is a heavy-ion accelerator mainly devoted to nuclear physics studies. The SARA facility is jointly run by the Institut des Sciences Nucléaires of Grenoble and the Institut de Physique Nucléaire in Lyon, under the join authority of the IN2P3-CNRS and the Université Joseph Fourier (France). A full description of the facility and its performances can be found in [11-8]. The neutron facility is installed at SARA in one of the extremities of its beam lines (**H** experimental area) allowing irradiation studies both at room and cryogenic temperatures. It permits the exposure of various types of detectors, readout electronics and mechanical parts to high fluences of neutrons. The cryogenic conditions are provided by a liquid argon cryostat. Intense sources of neutrons are produced by charged-particle-induced nuclear reactions, particularly between projectiles of hydrogen isotopes (^{2}H, ^{3}H) and targets of higher elements. Compared with other sources, they have the advantage of providing higher fluxes and therefore are convenient for radiation damage studies. At the extremity of the **H** beam line there is a neutron source consisting of a 3 mm thick beryllium target, 35 mm in diameter. A steady 7 µA beam of 20 MeV deuterons, when incident on the Be disk, produces a high neutron flux by stripping reactions. The beam power (140 W) released in the Be target is removed by a flow of cooling water that is placed in thermal contact with the source through a brazed copper ring. At full beam power, the highest temperature on the target does not exceed 40°C. At the design level, some precautions have been taken to maintain the Be disk electrically insulated, thus permitting on–line monitoring of the beam current that stops in it. Because of the emission of secondary electrons off the beryllium, the beam current as seen by the target is approximately 20% higher than the real one. In order to ease the tuning and positioning of the beam on the target with a radiation–robust system, a carbon ring, segmented into 4 separate sectors independently read out in current, was fixed a few centimetres upstream. It then defines the permitted external diameter (25 mm) in which the beam is focused. The liquid argon cryostat consists of a cylindrical cryogenic vessel 30 cm in diameter, with a 5 cm thick external thermal insulation. The vessel walls are made of aluminium in order to minimize the neutron activation, and consequently to ease its handling after exposures (see Figure 11-iii). It can contain up to 10 l of liquid argon obtained by circulating pressurized liquid nitrogen through an internal heat exchanger. The cryostat is installed as close to the Be target as possible, thus reaching a minimal irradiation distance of 10 cm. Some feedthroughs allow the exposed electronic circuits to be biased, their output pulses to be read out and optical fibres used in opto–electronic tests to be inserted. A data acquisition station is installed on the roof of the facility and is safely accessible even during full power irradiations. 40 BNC and 10 SHV cables housed in a copper

sleeve to protect them from external electromagnetic noise, allow high sensitivity measurements of the exposed circuits to be performed on site.

11.2.2.2 Fluences and doses at SARA
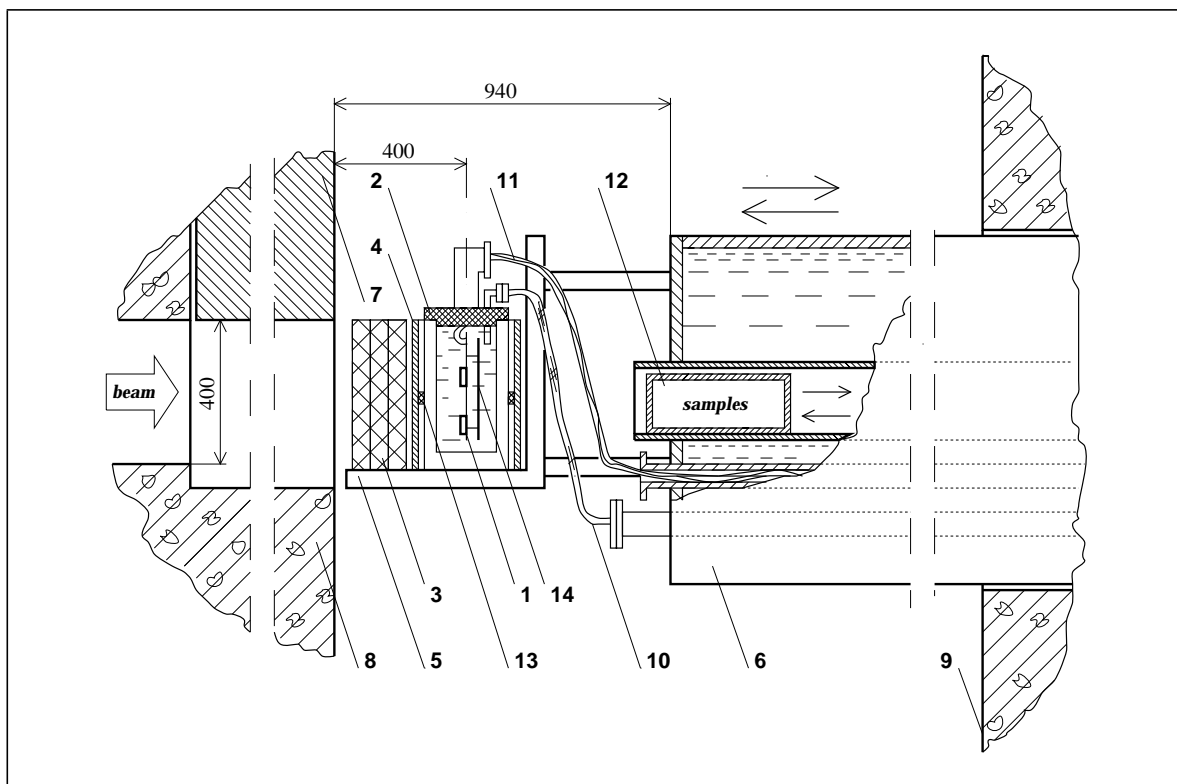
The D+Be neutron source, as all other fast neutron sources, is contaminated with photon radiation. A dosimetric characterization of the SARA facility was performed prior to the radiation-damage studies. Alanine, ^{6}LiF and ^{7}LiF dosimeters were used to determine the neutron and photon doses, and to measure the total absorbed dose angular distribution. The neutron flux at 0° (i.e. in the beam direction) was found to be equivalent to 4.8 10^7 (± 15%) neutrons (nA)$^{-1}$Sr^{-1}s^{-1}. The higher part of the energy spectrum was derived from the time of flight (TOF) recording on a NE213 detector. The lower part, down to 100 keV, was measured using the same TOF technique applied on a fission detector consisting of a ^{235}U plate mounted a few millimetres in front of a silicon diode housed in an evacuated vessel of reduced size. This fraction represents 15% of the neutron yield measured by the NE213 scintillator. Neutrons were detected by the fission products on the junction. The neutron efficiency is directly proportional to the fission cross section, which is very well known in this energy region. The detector was located 70 cm downstream of the Be target to allow 100 keV neutrons to cover this distance in less than a burst period (280 ns). The TOF resolution was 2 ns. The neutron energy spectrum shows a mean energy of 6 MeV. The neutron and gamma components of the mixed radiation field give rise respectively to 78 ± 2% and 22 ± 2% of the total air kerma [11-9]. The photon contamination is found to be equivalent to 1.20 Gyh^{-1}µA^{-1} air–kerma rate for a neutron fluence rate of 6.67 10^{10} n cm^{-2}h^{-1}µA^{-1} at a distance of 50 cm from the neutron source. In practice, a mean neutron fluence up to 2.0 10^{14} cm^{-2} can be obtained in about two days, over an area 8×8 cm^2 and 8 cm in depth.

11.3 Experimental set-ups

11.3.1 Experimental set-up at the Dubna reactors

The radiation-hardness tests of GaAs electronics (kept at cryogenic temperature) and materials (so far at the room temperature) of the ATLAS Liquid Argon hadronic end-cap calorimeter have been carried out at the fast-pulsed neutron reactors IBR-2 and IBR-30 at Dubna [11-1]. The experimental set-up developed at IBR-2 is presented schematically in Figure 11-2.

During the experiment with GaAs preamplifiers, the cryostat was installed on a movable shielding platform. For the irradiation, the support frame was positioned in the ring corridor between the reactor shields at a distance of 10 cm from the beam shutter. During the experiment the cryostat was filled remotely with liquid nitrogen using special cryogenic lines. Additional tubes are available for signal cables and for the delivery of various material samples to the irradiation zone. The neutron and gamma dosimeters were mounted temporarily around the cryostat for dose rates monitoring. Furthermore, a wide nickel foil covering the back of the motherboard with the electronic chips was kept in the cryostat during the whole irradiation period. It was used as a fast neutron flux monitor via the activation reaction ^{58}Ni (n,p) ^{58}Co. The induced activity of the nickel foil was also used to measure the homogeneity of the neutron fluence. It was found that the neutron fluence is homogeneous within ± 5% over the area of 20×10 cm^2 (the size of the motherboard).

Figure 11-2 Schematic layout of the experimental setup: (1) Motherboard with the electronics; (2) Cryostat; (3) Beam filter; (4) Boron carbide layer; (5) Support frame; (6) Movable shielding platform; (7) Beam shutter; (8) Inner and (9) Outer reactor shields; (10) Cryogenic lines; (11) Measurement cables; (12) Tube for the transport of samples; (13) Neutron and γ dosimeters; (14) Nickel foil.

During samples irradiation, the facility allows simultaneous irradiation of other samples to be performed. For this purpose, a special container of 13 cm diameter and 80 cm maximal length was installed behind the cryostat through a special slightly-curved tube inside the platform.

To address the radiation hardness questions, the electronics and materials were exposed to high doses of neutrons and photons. A 5 cm thick lead filter was installed in front of the cryostat to suppress the γ radiation during irradiation with neutrons. For the γ irradiation, this filter was replaced by the (n/γ) converter consisting of a paraffine moderator interleaved with cadmium foils. Activation of the equipment by thermal neutrons was reduced with a 5 mm thick layer of boron carbide (B_4C) surrounding the cryostat.

11.3.2 Experimental setup at SARA
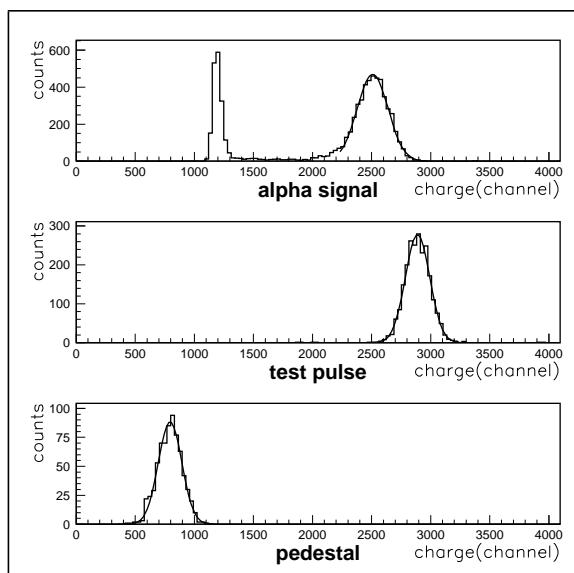
Five litres of liquid argon in the cryostat were sufficient to cover the samples of materials to be tested. The samples were immersed together with an alpha cell whose function is to monitor the purity evolution during irradiation. It is assumed that the pollution rate is a surface more than a volume effect. Therefore the relevant parameter will be the total area of the samples normalized to the liquid volume. In order to measure the pollution more easily, this normalized area was made larger than in the calorimeter itself, by a factor sometimes greater than ten. The samples are irradiated with measured fluences up to 2×10^{14} n cm^{-2}. The alpha cell consists of two metallic disks separated by a liquid argon gap of 0.8 mm. A ^{241}Am source was deposited on the cathode. The anode signal is read by a charge preamplifier which is located outside the cryostat in a region exposed to smaller neutron fluences. The output of the charge preamplifier is further processed by a CR-RC filter with a 100 ns time constant, and

Figure 11-3 Charge spectra before irradiation: the smooth lines are the result of a gaussian fit. In the top figure, the peak on the left is the noise, cut with the threshold.

is finally digitized by a 12-bit charge ADC with a 100 ns gate centered on the maximum of the filter output. The value of the filter time constant was optimized to reduce the pile-up noise arising from the ^{41}Ar beta-activity during irradiation. A calibration pulse with a proper shape is injected at the input of the preamp to fully monitor the gain stability of the read-out chain. The pedestal of the chain is determined by randomly triggering the acquisition which is done by a PC equipped with a GPIB board. The collected charge in the α-cell is measured at several electric field values ranging from 5 to around 20 kV/cm. Three sets of data are collected on the same analog channel, from the charge preamplifier to the ADC: the α signal, the pedestal (enhanced on purpose) and the calibration signal. An example of the raw data is shown in Figure 11-3.

After pedestal subtraction and calibration, the charge signals before and after irradiation are compared. The attenuation factor is related to the pollution through the expression:

$$\frac{Q_{after}}{Q_{before}} = \frac{\lambda}{d}(1 - \exp(-d/\lambda))$$

where λ is the charge carrier absorption length and d is the gap width of the α-cell. In the case of oxygen pollution, λ has been shown [11-10] to be best fitted with:

$$\lambda(cm) = (0.14 \pm 0.03) \frac{E(kVcm^{-1})}{\rho(ppm)}$$

Great care is taken to fill the cryostat with very clean argon. Then, the relative charge is measured several times over a few days to make sure that everything is stable, at one or two field values. Eventually, its dependence on the field is recorded. It will be the zero-pollution reference. After the irradiation has started, it is measured again regularly at the same field values to observe the evolution of the pollution. At this stage, the charge spectrum exhibits a stronger and stronger contribution from β-signals mostly due to the activation of argon: $n+^{40}Ar \rightarrow {}^{41}Ar \rightarrow {}^{41}K+\beta^-$. After the irradiation, the evolution is checked again and once the β⁻ rate has gone very low, a new field curve is recorded again. The charge, as collected in the α-cell during a particular run, is displayed in Figure 11-4.
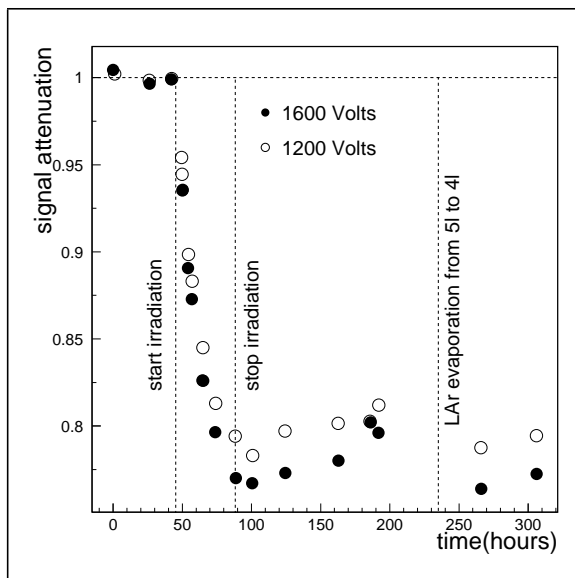

Figure 11-4 Evolution of the charge signal during the prepreg run.

11.4 Results

11.4.1 Purity
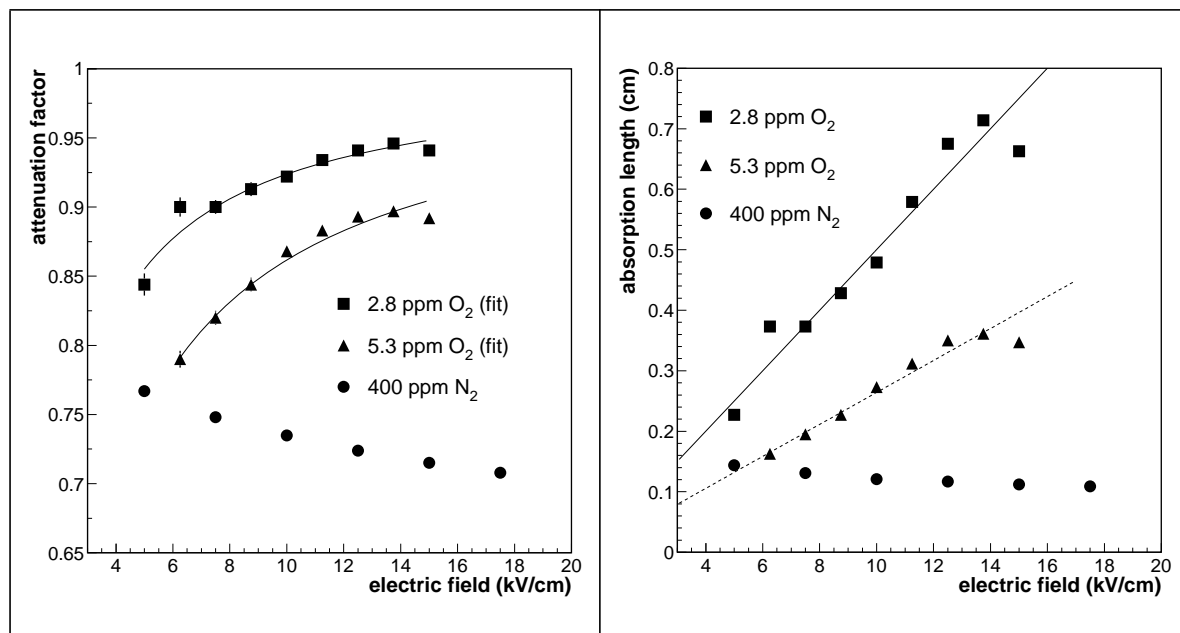
#### 11.4.1.1 Purity study results at SARA

1. Oxygen and nitrogen tests
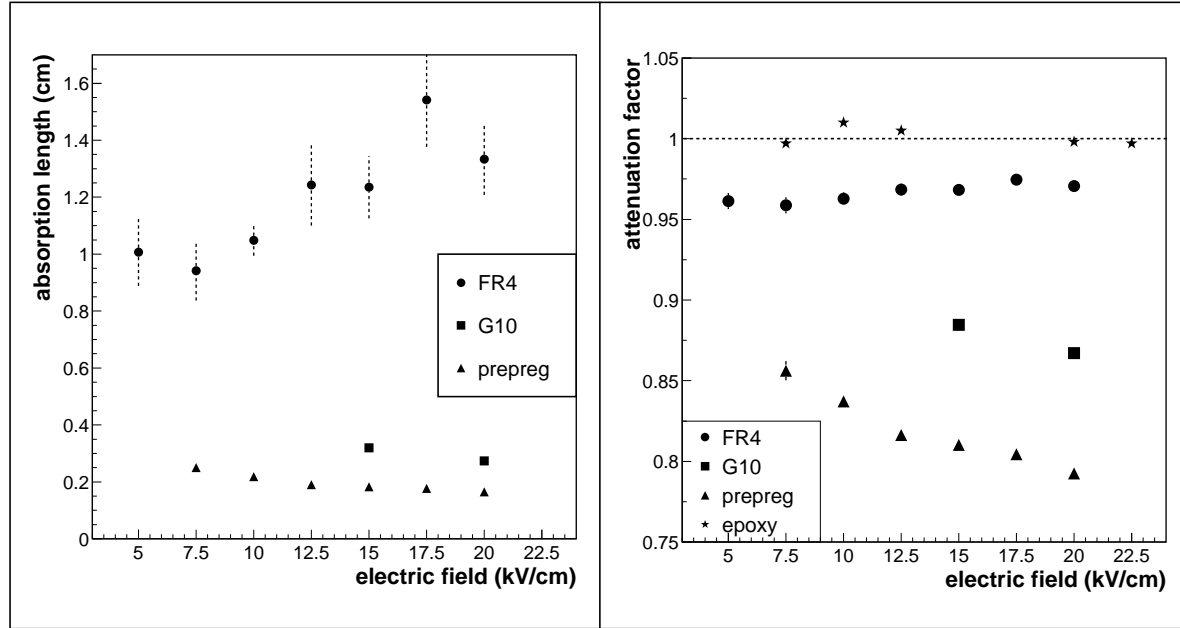
The whole set-up was tested by introducing known contaminants into the cryostat and the attenuation of the charge signal was determined each time [11-11]. They were oxygen (about 3 and 6 ppm) and nitrogen (about 400 ppm). A few hours were necessary each time to reach an equilibrium. The results are shown in Figure 11-5 and Figure 11-6. If the oxygen data are well fitted using the relations of reference [11-10], the nitrogen data were rather a surprise, as the first idea that comes to mind is that the absorption length should increase when the electric field is increased.

The nitrogen pollution of liquid argon has been studied before [11-10] [11-12], but not in the same range of field or concentration. Furthermore, the variation of the absorption length as seen here in the presence of nitrogen could not be evidenced then. In fact, this behaviour is not unique and was explained many years ago [11-13] [11-14]. The absorption length λ is related to the attachment rate of the drifting electrons k_s: $\lambda = v_{drift}/k_s[S]$, where v_{drift} is the electron mean drift velocity and [S] is the impurity concentration. The attachment rate on O_2, N_2O and SF_6 in liquid argon was studied by Bakale et al. [11-13]. It can be seen that N_2O is a much stronger absorber than oxygen, and that contrary to oxygen, the attachment rate increases with the field. There is no universal law about the variation of the absorption length versus the electric field, it depends on the nature of the impurity. If one extrapolates the O_2 k_s curve of [11-13] to a field of 10 kV/cm and one uses the 2.8 ppm derived from the fit, the calculated absorption length value is as measured in this test [11-11], within the extrapolation errors.

2. Results for various materials

Figure 11-5 Signal loss due to oxygen and nitrogen impurities. The curves are the result of a fit according to equation 1.

Figure 11-6 Absorption length of charge carriers in liquid argon with oxygen and nitrogen impurities. The lines are drawn according to equation 2.

The materials that have been irradiated so far are FR4, G10 (von Roll Isola 64220 and 64060), prepreg (CTMI 5512-1383-1808-50/110) and epoxy Ciba-Geigy 5052. Although neither the fluences nor the normalised areas were identical during these four runs, the results [11-11] are summarized on Figure 11-7 and Figure 11-8.

Figure 11-7 Absorption length of charge carriers in liquid argon after irradiation. The error bars are purely statistical.

Figure 11-8 Signal loss caused by impurities released after irradiation. The error bars are purely statistical.

The very first observation which can be made is that the main contaminant released into the liquid is not oxygen, and at this point nothing can tell us about its nature. At the end of some of the runs, part of the liquid argon was evaporated into a bottle and sent off for chromatography analysis. Traces of oxygen and nitrogen were identified but in no case compatible with the observed attenuation. One may have noticed in Figure 11-4 that, when evaporating, the impurity level in the remaining liquid seems to concentrate accordingly. The very last litre of liquid was recovered once and analysed, but although impurities were more abundant, they could not explain the absorption length data.

An attempt was made to normalize all our data at a field value of 10 kV/cm as in ATLAS, for a fluence equal to $1.6 \, 10^{14}$ n.cm^{-2} and a value of the normalised sample area equal to 70 m^2/m^3 liquid argon, in order to compare the pollution rates coming from the various materials tested so far. The results are shown in Table 11-4. The quoted uncertainties are estimates. They nevertheless indicate that the comparison of the attenuation factors is meaningful.

Table 11-4 Alpha-signal loss after irradiation. Data are normalized to a fluence of $1.6 \, 10^{14}$ neutrons/cm^2 and to a ratio (open area of samples/liquid argon volume) equal to 70 m^{-1}.

Material	Signal loss (%)
Epoxy	0 ± 1
FR4	4 ± 1
G10	8 ± 2
Prepreg	15 ± 3

We suspected that the contamination probably might come from halogens, but it must be pointed out that FR4, which contains bromine whereas G10 does not, gives the most encouraging results after the epoxy 5052. The prepreg tested contains 4% chlorine and so far it has not been possible to make a test with a lower percentage product.

3. Signal loss in the e.m. calorimeter from pollution measurements

The signal loss expected in the e.m. calorimeter for a given amount of pollution can be derived from the data above obtained at SARA.

The output signal of the alpha cell, used to monitor the purity evolution during irradiation with fluences up to $2 \, 10^{14}$ n cm^{-2}, is calculated [11-15] as the inverse Laplace transform:
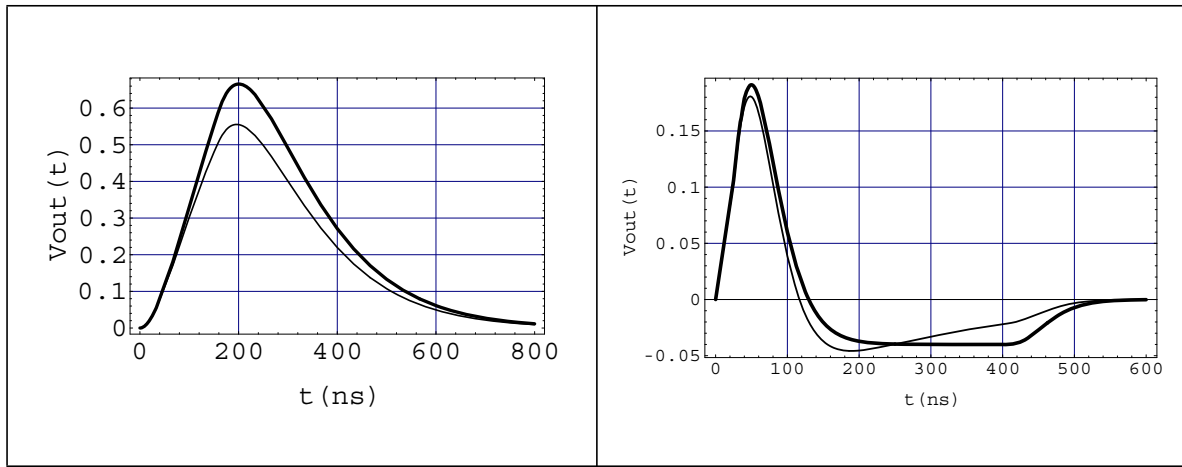
$$v_{out}(t) = L^{-1}(v_{out}(s)) = L^{-1}\left(V_0 \frac{1 - \exp\left(-(st_d + \frac{d}{\lambda})\right)}{st_d + \frac{d}{\lambda}} \frac{\tau_{sh}}{(1 + s\tau_{sh})^2}\right)$$

where t_d is the drift time. d and λ are the gap width of the alpha cell and the absorption length of electrons drifting in the liquid argon gap, respectively. t_{sh} is the time constant of the CR-RC filter and $V_0 = Q/C_f$. Figure 11-9 shows the result obtained in our configuration: d=0.8 mm, τ_{sh}=100 ns, t_d=160 ns (E=1 kV/mm), with two different values of the absorption length. The resulting shape is in very good agreement with the one measured. By evaluating the signal loss
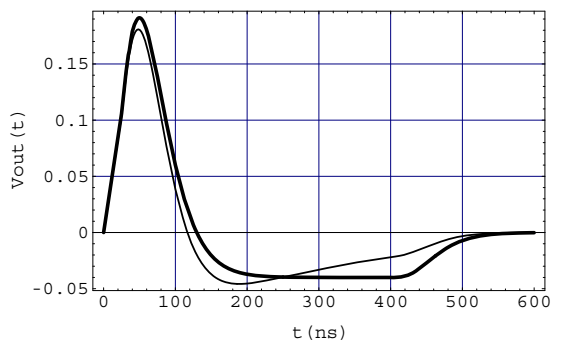
through the ratio $v_{out}^{max}(\lambda)/v_{out}^{max}(\lambda=\infty)$, it was realized that this lengthy procedure is equivalent with a good precision to using the simple expression [11-15]:

$$\frac{v_{out}^{max}(\lambda)}{v_{out}^{max}(\lambda = \infty)} = \frac{\lambda}{d}\left(1 - \exp-(\frac{d}{\lambda})\right)$$

In other words, the read-out chain almost behaves as a charge integrator as the above expression is in principle only valid when the total charge is collected, and this simplified expression will be used to extract the absorption length for a given signal attenuation.


Figure 11-9 Output signal of the alpha cell with $\lambda = \infty$ (bold curve) and $\lambda = 2.18$ mm (light curve).
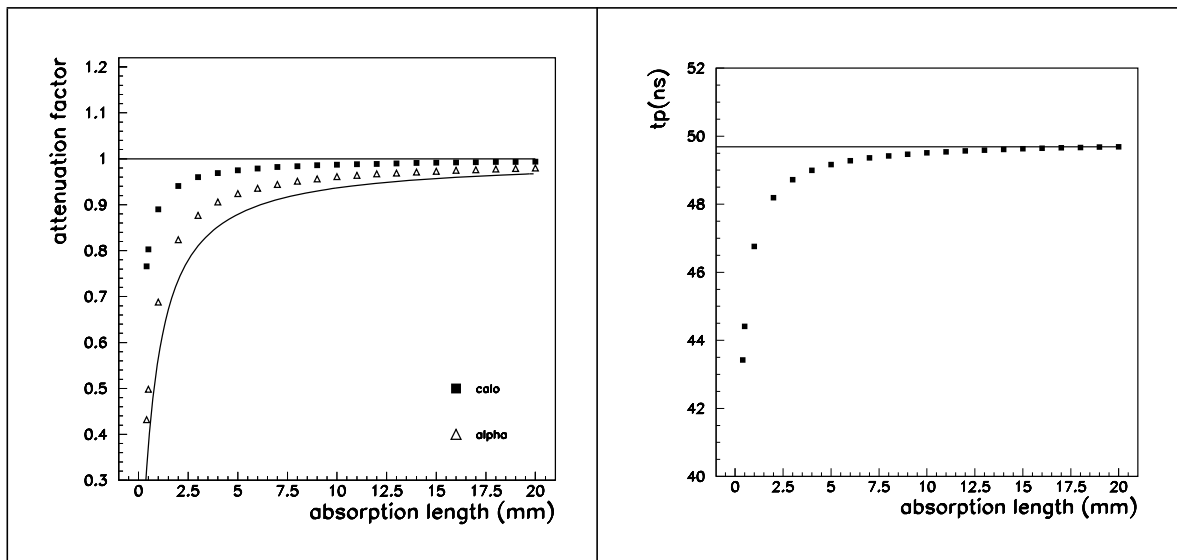
Figure 11-10 Output signal of the calorimeter with fast analog electronics for $\lambda = \infty$ (bold curve) and $\lambda = 2.18$ mm (light curve).
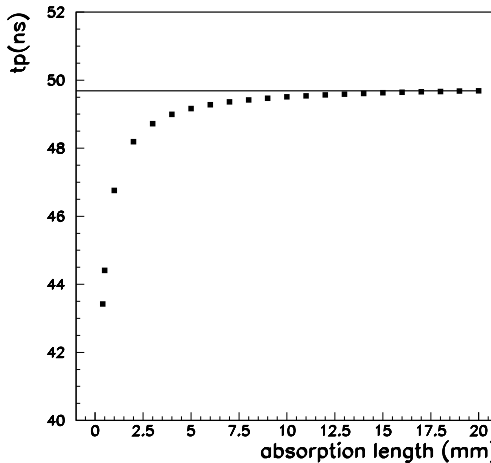
The signal $v_{out}(t)$ in the case of an electromagnetic shower in the calorimeter can also be calculated in the same way. Two extreme examples are presented in Figure 11-10 for $\lambda=\infty$ and 2.18 mm. Apart from a signal drop one may also note that a polluted pulse features both a slightly faster peaking time and a modified shape of its trailer.

The extrapolated signal drop of the calorimeter results from the calculation [11-15] of the ratio $v_{max}^{out}(\lambda(1 kV/mm))/v_{max}^{out}(\lambda=\infty)$ with the proper parameters corresponding to the calorimeter configuration: d=2 mm, τ_{0T}=22 ns (440 pF, 50 Ω), τ_{sh}=16 ns, t_d=400 ns, E=1 kV/mm. For the case of FR4 plates covered with prepreg foils [11-11], the attenuation of the calorimeter signal is 5.4% while it was measured to be 16.5% at 1 kV/mm with the alpha cell. Indeed this approach is only valid under the hypothesis in which there is no dilution nor any concentration of the pollution in the ATLAS cryostat with respect to what was obtained in the test cryostat, and for which the amount of tested material per litre of liquid is roughly the same in both situations. Knowing the presampler mechanical structure, we are entitled to say that the latter condition is far too pessimistic for the FR4/prepreg test. There was more than 20 times more FR4/prepreg per litre of liquid argon in this pollution test than in the ATLAS cryostat. This leads to an absorption length which for the e.m. calorimeter should be bigger than 44 mm. Figure 11-11 shows that if the attenuation length exceeds 20 mm, its effect on the calorimeter signal may be neglected.

A slight change in the peaking time (Figure 11-12) of the calorimeter signal together with a modification of the after-pulse shape may also be caused by pollution of the liquid. When con-

Figure 11-11 Attenuation of v_{out}^{max} as a function of the absorption length with the following parameters t_d = 400 (160) ns, τ_{0T} = 22 ns, τ_{sh} = 16 (100) ns, d = 2 mm (0.8 mm) for the calorimeter (alpha cell). The calorimeter signal attenuation curve with $\tau_{sh} > t_d$ is also shown.

Figure 11-12 Peaking time (0-100%) of the calorimeter output signal as a function of the absorption length for t_d = 400 ns, τ_{0T} = 22 ns, τ_{sh} = 16 ns and d = 2 mm.

sidering the proper amount of polluting material, the present data suggest that the induced signal drop should remain below 1% after 10 years of operation.

11.4.1.2 Mass-spectrometry analysis at Dubna

The main goal of the mass-spectrometry analysis is to estimate the pollution of liquid argon caused by the outgassing of materials immersed in the cryostat in between the copper plates of the hadronic end-cap calorimeter. These results complete the measurements of argon pollution performed at cryogenic temperature.

The samples of EST electrodes with high resistive coating sprayed with graphite and HEXCELL spacers of epoxy type were exposed to an integrated neutron fluence of $1.0 \; 10^{15} \, n \, cm^{-2}$. The samples were put into the vacuum container in order of being pumped out to high vacuum. The amount of material was the same as in one half of the liquid argon gap in hadronic end-caps. The composition of the residual gas was measured before and after irradiation using a mass-spectrometer MX-7304 which permits a scan of a broad region of atomic mass, and allows to measure the corresponding partial pressures. The irradiation and measurements were performed at room temperature and the estimate could therefore be considered as an upper limit for the pollution level value. No significant changes were found for the majority of the residual gas components before and after irradiation, but a noticeable oxygen outgassing was found in the container after irradiation.

To make a quantitative estimate of the liquid argon pollution, it was assumed that the whole amount of oxygen found in the container resulted from the irradiation. Relating the measured mass of desorpted oxygen to the amount of liquid argon contained in one half of the liquid argon gap, a figure of $3.5 \; 10^{-3}$ ppm was obtained. If the leakage of the oxygen is constant during the whole period of the experiment, after 10 years a pollution of 0.05 ppm can be expected. This meets the requirement of 1 ppm as an acceptable value of the liquid argon pollution.

Thus, the first mass-spectrometry analysis indicates a good radiation hardness of the EST electrodes with high resistive coating and HEXCELL spacers, in terms of liquid argon pollution.

In conclusion, the measurements reported here, and their extrapolation to the ATLAS situation, indicate that, after ten years of high luminosity running, and even without exchange nor purification of the liquid, no alarming effect due to pollution induced by neutron irradiation should happen. The efforts reported here will be pursued in such a way as to cover the full list of calorimeter materials.

11.4.2 Results on radiation hardness of electrodes (kapton) at Dubna

Various samples of electrodes expected to be used in the LAr hadronic end-cap calorimeter were exposed to high fast neutron fluence values and γ doses. Before and after irradiation, mechanical tests were performed. The glued films were expected to satisfy the "peeling test". The strain was applied to a strip 3 mm wide, and the loading value sufficient to tear off the strip was measured. Standard technology requires the threshold loading to be not less than 1 N. Actually, for the electrodes used in the hadronic end-cap calorimeter, the value of 0.2-0.3 N seems to be acceptable.

In Table 11-5, the loading values for different samples of EST electrodes are presented. The values of the neutron fluence quoted below correspond to effective fluences of 1 MeV Si equivalent. The glue used to stick the kapton (polyimide - PI) and copper (Cu) or two kapton layers together was an epoxy-acrilate-rubber composition 20 μm thick. Different pieces of the same sample were tested before and after irradiation. The ranges of the threshold loading values are presented in the Table. Some heterogeneity of the loading values is explained with a non-industrial procedure of gluing, but no degradation due to radiation damage is observed. The same conclusion was drawn from the tests of PI+Cu and PT(polyethylene-tereftalat)+Cu samples glued by means of polyurethane and EST electrodes prepared by gluing the layers with acrylic adhesive.

**Table 11-5** Results of the peeling tests for different types of glue.
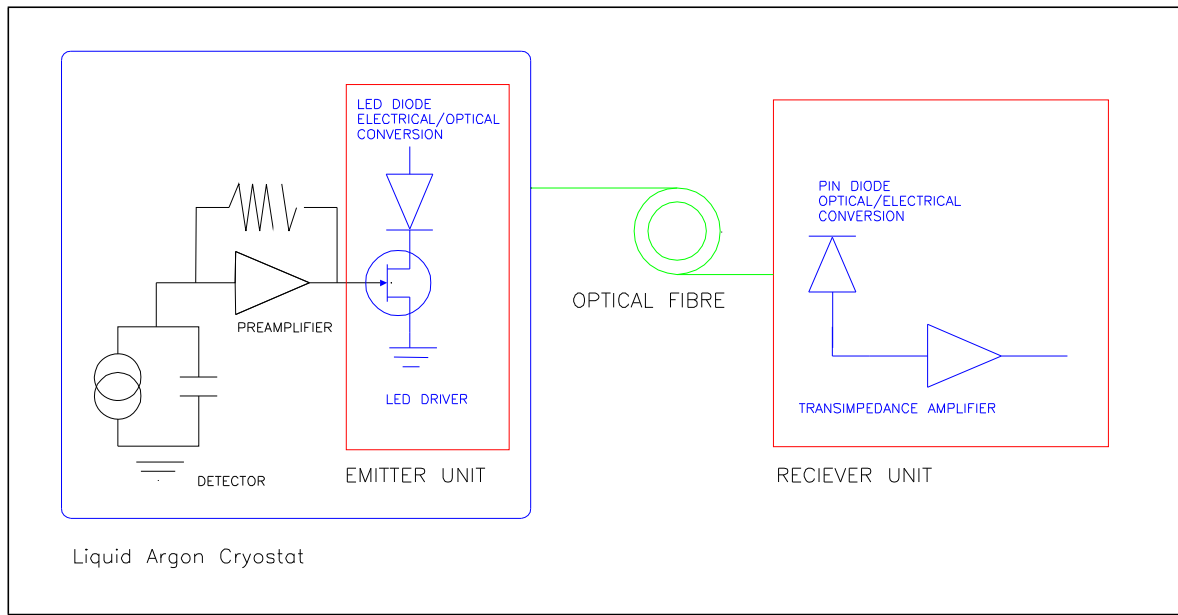
Type of glue	Irradiated sample	Loading value before	Loading value after	Neutron fluence and γ dose
Epoxy	PI + Cu	1.6 - 2.5	1.6 - 2.7	$7.0\ 10^{14}$ n cm^{-2}
	PI + PI	0.6 - 1.5	1.1 - 1.5	4 kGy
	PI + Cu + PI	1.0 - 1.2	0.9 - 1.0	
Polyurethane	PI + Cu	1.5 - 1.7	1.5 - 2.1	$1.8\ 10^{15}$ n cm^{-2}
	PT + Cu	2.2 - 2.4	1.3 - 2.4	20 kGy
Acrylic	PI + PI	5.1 - 7.1	4.9 - 6.8	$1.8\ 10^{14}$ n cm^{-2}
	PI + Cu	1.5 - 1.7	1.5 - 2.1	20 kGy

In addition to the peeling tests, the radiation hardness of HRC (high resistive coating) foils was investigated [11-16] at the neutron fluence level of $9.9\ 10^{14}$ n cm^{-2}. The foil resistivity was measured before and after irradiation and no visible change of this value was detected. The latest run of IBR-2 in October 1996 was devoted to the study of the new type of HRC (carbon loaded Kapton) at the neutron fluence level of $4.5\ 10^{15}$ n cm^{-2} and the γ dose of 150 kGy. Preliminary results show no changes to the foil resistivity.

11.4.3 Results on radiation hardness of optical links at SARA
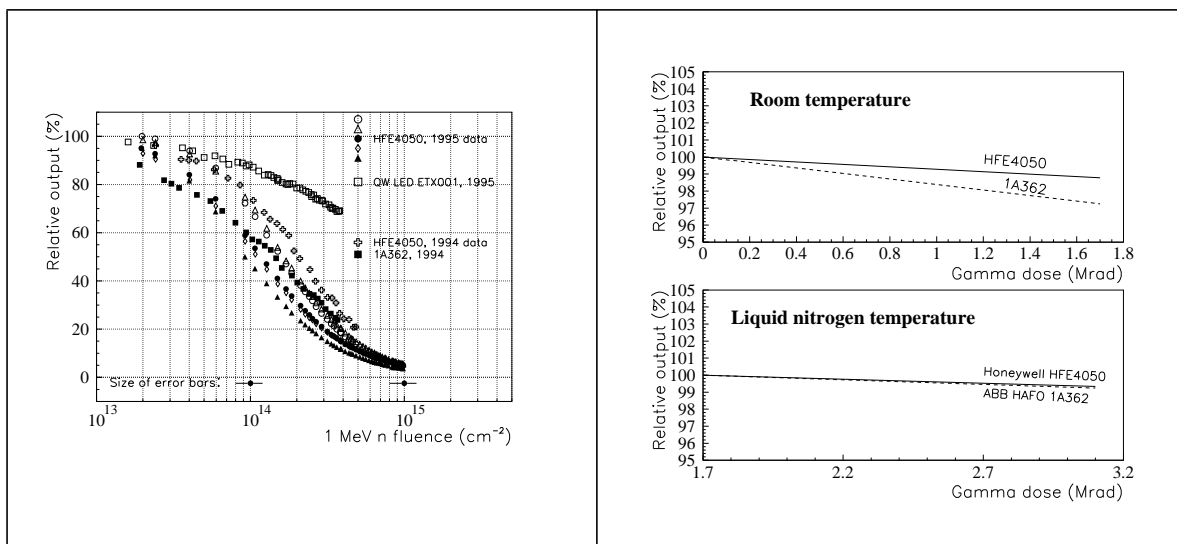
The effect of neutron radiation on light emitters and optical fibres at cryogenic temperatures (90 K) has been investigated at SARA [11-17] as part of the development of an analogue optical link, intended for use in future high-energy physics experiments. The LEDs were also exposed to a ^{60}Co γ radiation dose of 3 MRad. High radiance GaAs LEDs, quantum-well LEDs, quantum-well laser diodes and optical fibres have been exposed to neutron radiation reaching fluences of 10^{15} n cm^{-2}. A low-cost analogue optical link [11-18] (consisting of a driver, an emitter, an optical fibre, and a PIN photodiode followed by a transimpedance amplifier) has been developed for use in the ATLAS experiment. In the first phase of the project the link was intended to transfer signals from the preshower detector [11-19] to outside the ATLAS liquid argon (LAr) cryostat. Consequently, the emitting part of the link (driver, emitter and ~10 m of fibre) would operate at LAr temperatures (90 K) and would need to resist radiation levels of about 10^{14} (1 MeV) n cm^{-2} and 1 MRad of gamma radiation accumulated over 10 years. Other requirements for the analogue optical link include: dynamic range ≥ 11 bits, resolution 8 bits, non-linearity $\leq 2\%$, and bandwidth ≥ 50 MHz.

During irradiation the devices were contained in the test cryostat at SARA and all measurements were performed at liquid argon temperature unless otherwise stated. All devices were DC biased: ~10 mA for the light emitting diodes (LED) and ~4 mA for the laser diodes (LD). Current pulses were presented to one emitter at a time. The resulting light signals were transferred through optical fibres to remote receivers (Figure 11-13). The irradiations were performed over a period of 3-4 days. The results reported in Figure 11-14 show that commercial GaAs LEDs can withstand neutron radiation of 10^{14} (1 MeV) n cm^{-2} with a light output degradation of less than 50%. A dose of ~3 Mrad causes a ~3% loss of light output as shown in Figure 11-15
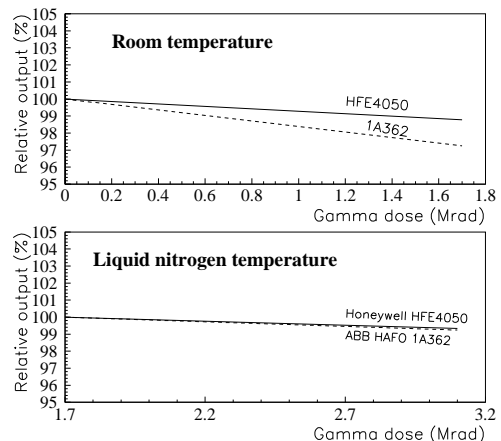

Figure 11-13 Schematics of the cold optical link intended for use with the ATLAS liquid argon preshower detector.
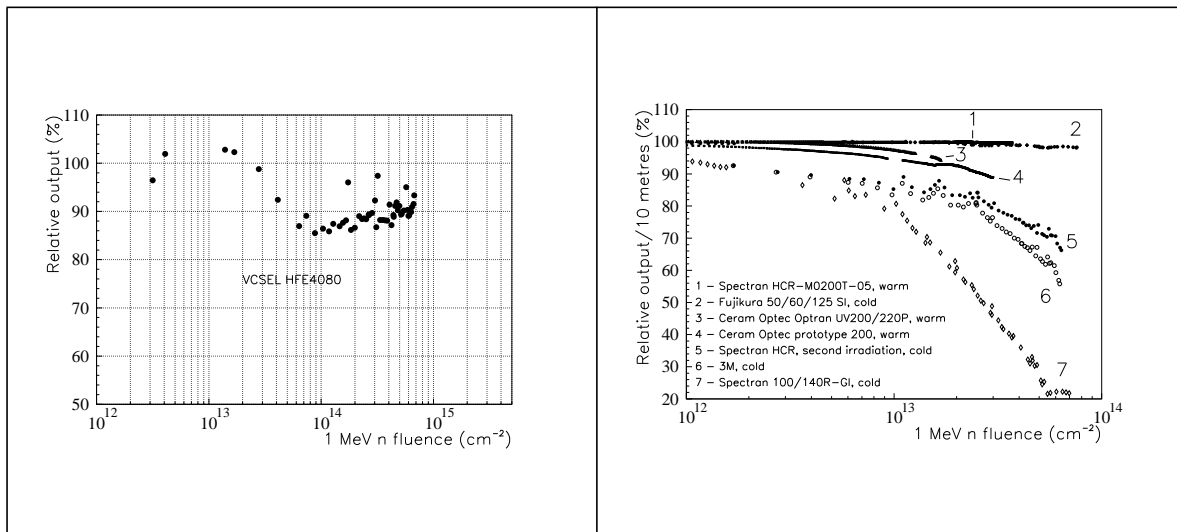
Quantum well LEDs and LDs were more neutron resistant than the GaAs LEDs. The high initial light output and low degradation of <15% after ~10^{14} (1 MeV) n cm^{-2} make QW devices suitable for analogue and digital links. Vertical cavity surface-emitting laser diodes (VCSEL) give excellent performance [11-20] and when exposed to neutron radiation the HFE 4080[1] showed a 15%
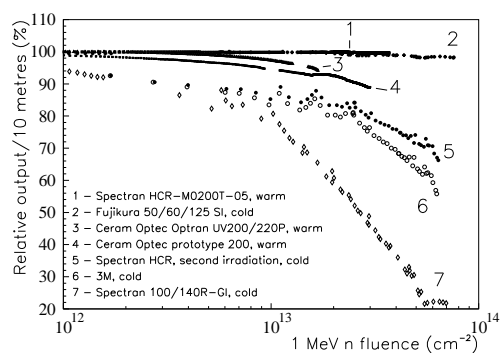
Figure 11-14 LED output as function of received neutron fluence.

Figure 11-15 The relative GaAs LED's light output as a function of received gamma dose from a ^{60}Co source at room temperatures (top) and cryogenic temperatures (bottom). The cold irradiation followed the irradiation at room temperature. The dose on the x-axis is the total accumulated dose.

Figure 11-16 VCSEL light output in liquid argon as function of received neutron fluence.

Figure 11-17 Relative transmission of optical fibres as a function of received neutron fluence.

loss after 10^{14} (1 MeV) n cm^{-2} but then no increased damage was observed up to the maximum fluence 8 10^{14} (1 MeV) n cm^{-2} as seen in Figure 11-16.

This VCSEL design is not optimized for liquid argon temperature and was biased at 15 mA. It showed good radiation hardness and looks very promising for future use in high radiation environments. A VCSEL array under development will be subjected to future tests. Several optical fibres, Figure 11-17, met the requirements for radiation hardness for use in the LHC.

---

1. Manufactured by Honeywell.

11.5 Future plans

11.5.1 Radiation tests at Dubna in 1997

The radiation-hardness study of different materials to be immersed in the end-cap cryostat of the ATLAS detector will continue in 1997.

The prototype of the GaAs preamplifier designed for "module 0" of the hadronic calorimeter will be irradiated both by neutrons and photons in the near future up to a high radiation dose (fluence of $5 \; 10^{14} \; \mathrm{n \; cm^{-2}}$ and γ dose of about 50 kGy). In addition, different connectors, HV and signal cables will also be exposed to higher doses. Thus, all the elements of the read-out chain of the HEC will be tested with respect to radiation damage.

The choice of coating for the read-out electrode has not yet been finalized and the irradiation of different materials (including kapton) will continue.

The mass-spectrometric analysis provides results on the actual composition of material outgassing caused by irradiation. This study will be continued under better conditions with respect to pressure control and spectrometer sensitivity. The data on the gaseous phase composition will complete the results of the "cold" tests to be performed in 1997. The liquid argon cryostat and corresponding systems have been built and the laboratory tests (such as the calibration of the ionizing chamber by oxygen probes, etc.) will start at the end of 1996.

11.5.2 Radiation tests at SARA in 1997

A few more irradiation tests have been scheduled in 1997. The program may go on for another year but it is very likely that the SARA neutron facility will close down in 1999. The materials to be irradiated in the cryostat will be some prepreg without halogen, pieces of the presampler protection shell, cables and kaptons to be used in the EM barrel and end-caps. An effort will be made to try and identify the polluting agents. Finally, 0T preamplifiers shall be exposed at room temperature.
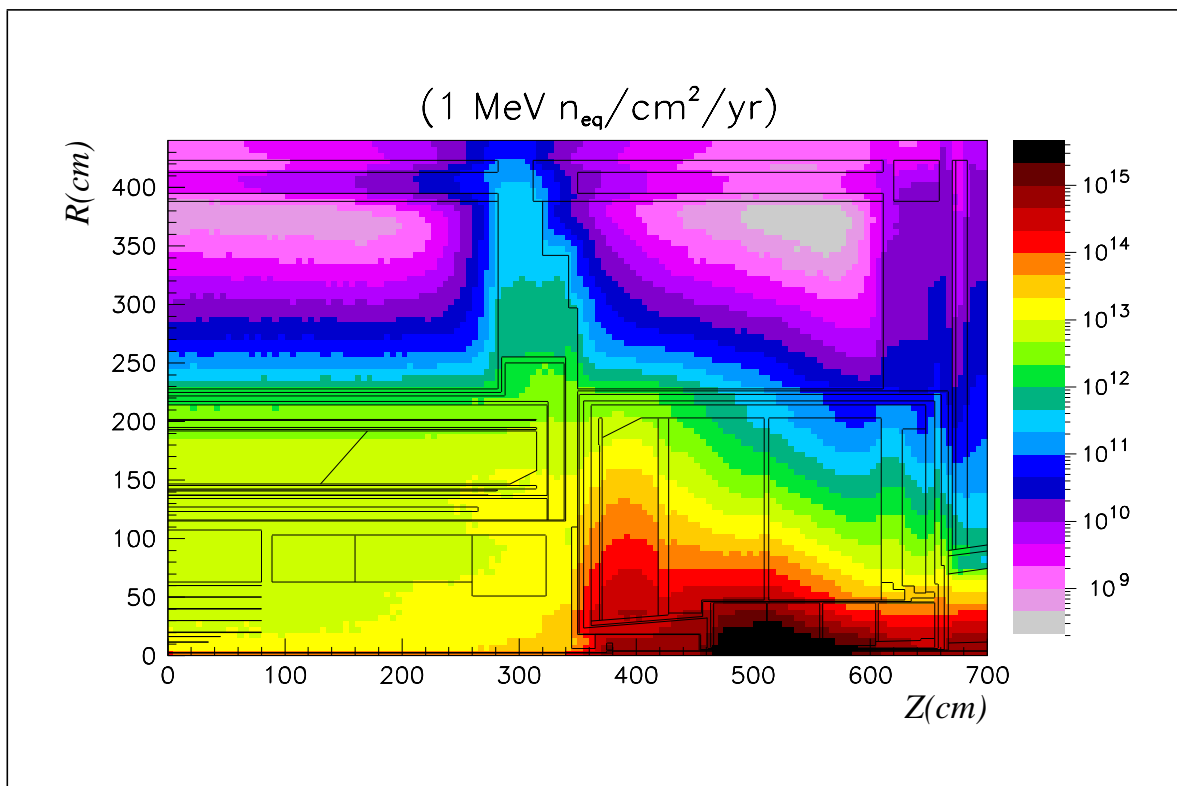
11.5.3 Future radiation tests at CERN

Further test will be performed at CERN in the coming years with components of the electromagnetic, hadronic and forward calorimeters. The future tests will help to select the material (kapton, glues,...) leading to minimal amount of impurities. These future irradiation studies will take place at a new irradiation zone to be built at the CERN-PS. This project takes place within the reorganization of the CERN-PS East Hall needed to fulfil the needs of the LHC experiments in terms of test beams. In particular, an area will be dedicated to ATLAS irradiation studies. This area will be created behind the newly approved DIRAC experiment at the end of the new T8 beam line. The building of this new zone will start in September 1997 and will be completed for October 1998. This new irradiation zone will provide an operational volume of $4 \times 4 \times 4 \; \mathrm{m^3}$ capable of accommodating the installation and operation of a 10 litres liquid argon cryostat put behind the production target and so allowing liquid argon purity studies under irradiation. The cryostat with its contents will be exposed to a shower-like environment provided by the interaction of 24 GeV protons with a lead target. A lead target with a diameter of 20 cm and a length of 60 cm will produce 300 neutrons per incoming proton. Considering a proton flux of $2 \; 10^{11}$ per spill, a uniform flux of $6 \; 10^{13}$ neutrons per spill (every 14.4 s) is expected over an area of about 300 $\mathrm{cm^2}$ which gives a net neutron flux of $2 \; 10^{11}$ neutrons per $\mathrm{cm^2}$ per spill leading in a few days
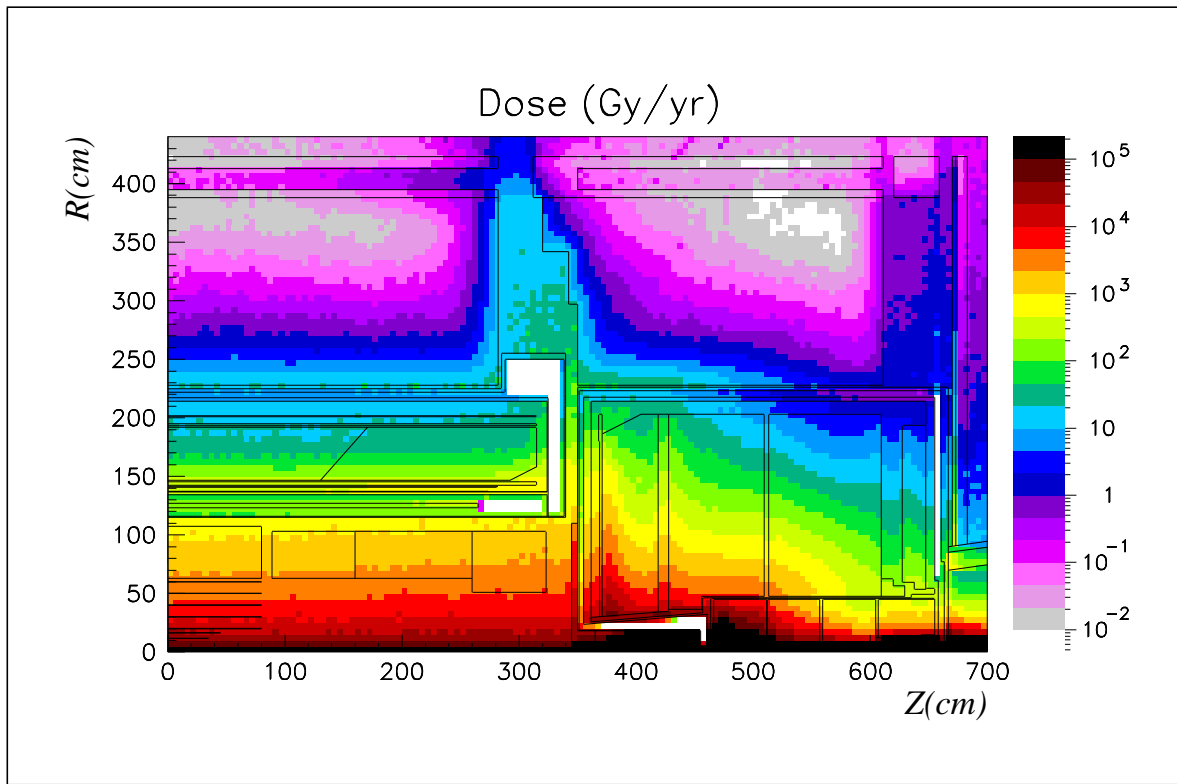
to fluences typical of those borne over a period of 10 years by the end-cap and forward calorimeters. These neutrons will span a wide energy range, with the maximum production around 1-2 MeV.

11.6 References
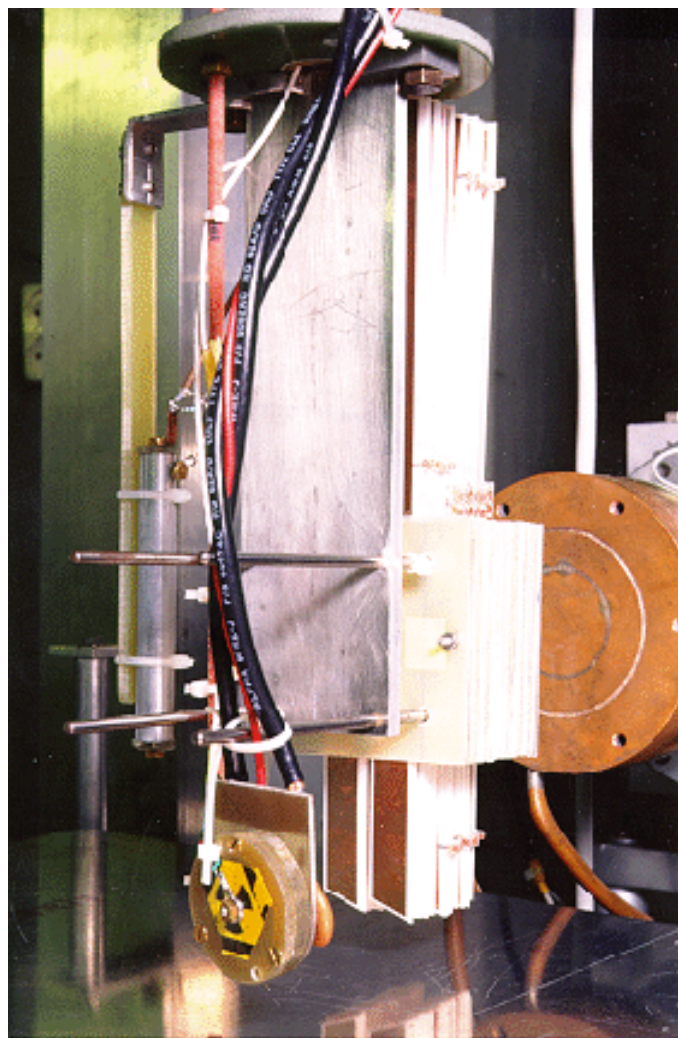
11-1   E. Shabalin, Fast Pulsed and Burst Reactors, Pergamon Press Ltd., (Oxford 1979).

11-2   V. Nikolaev et al., in Proc. Int. Workshop "Analysis", D4-88-256, 25-26 June, Dubna, 1985.

11-3   ATLAS Internal Note LARG, to appear in 1997.

11-4   V. McLane, C.L. Dunford and. P.F. Rose, Neutron Cross Section, Vol.2, Academic Press Inc., (1988).

11-5   V.F. Peresedov, A.D. Rogov, JINR Rapid Communication, 1-[75]-96, Dubna (1996) 69.

11-6   A.M. Ougouag et al., IEEE Trans. Nucl. Sci. **NS-37** (1990) 2219.

11-7   V.A. Khitrov and Pack Hong-Cher, JINR Internal Report, Dubna (1974).

11-8   J. Collot et al., Nuclear Instruments and Methods A 350 (1994) 525.

11-9   Elena León Florián and Claude Leroy, Nuclear Science Journal, Vol. 31, No 5, (1994) 380.

11-10   W. Hofmann et al., Nucl. Instr. and Meth. 135 (1976) 151

11-11   Ph. Martin, Pollution of liquid argon due to neutron radiation, ATLAS LARG note-no-52 1996.

11-12   S. D. Biller et al., Nucl. Instr. and Meth. A276 (1989) 144.

11-13   G. Bakale, U. Sowada and W. F. Schmidt, J. Phys. Chem. 80 (1976) 2556

11-14   L. G. Christophorou, Electron-molecule interactions and their applications (Academic Press, 1984).

11-15   J. Collot, Ph. Martin and A. Belymam, ATLAS Internal NoteLARG-056, 1996.

11-16   ATLAS HEC Note - 014, Minutes of the Workshop at the Ringberg castle, Ringberg, 30.08 - 2.09.1995

11-17   J. Söderqvist et al., Radiation Hardness Evaluation of an Analogue Optical Link for Operation at Cryogenic Temperatures, submitted to IEEE, 1996.

11-18   S. Tisserant, Proc. 5th Int. Conf. Calorimetry in HEP, BNL (1994)449-454, L.O. Eek, Int. Europhysics Conf. on HEP, Brussels 1995, World Scientific

11-19   The RD3 collaboration: B. Aubert et al. Nucl. Instr. and Methods A330(1993)405. The RD3 collaboration: D. Gingrich et al., Construction and test of a fine-grained liquid argon preshower prototype, PREPRINT CERN-PPE 96-123, also accepted for publication in NIM

11-20   Proc. SPIE, Vol. 2398, p.65-93.

11-21   Kubasta, et al., ATLAS Internal Note, TECH-No-016, CERN, 1995.

Figure 11-i 1 MeV neutron fluence in the calorimeter and vicinity, integrated over a standard high luminosity year (10^{41} cm^{-2}).


Figure 11-ii Yearly integrated dose (photons above 30 keV), for a standard high luminosity year.

Figure 11-iii The neutron irradiation facility of Grenoble. The photograph shows, prior to closing the cryostat, the a-cell (bottom), some FR4/Prepreg/Electrode samples and the copper cooling plate of the Be target.

12 Monitoring

12.1 Overview

Four main areas in the ATLAS liquid argon calorimetry have been identified which need close monitoring. They are the purity of the liquid argon itself, the temperature inside the different cryostats, the strain put on the inner mechanical structures and the relative positions of the different detector components. The last two items are mainly important during cool-down plus filling and warm-up plus emptying of the cryostats. Although stresses on the cryostat and the detector components during these phases have been calculated, close monitoring is of utmost importance for the safe operation of the experiment. The temperature measurements are of the same importance during the cool-down and warm-up phases but also under normal running conditions. They allow the safe operation of the cooling system to be controlled. In addition, the response of the liquid argon calorimeters depends on the temperature and varies roughly by ~2% per degree Kelvin. Purity monitoring is in a somewhat different class. Although not required for the safe operation of the experiment, high purity of the liquid argon is essential to obtain good quality data. Impurities have to be kept below the ppm level otherwise the signal becomes strongly dependent on the amount of pollution and deteriorates fast.

Another important item is the slow control for the liquid argon calorimeters. All the sensors described above plus a non-negligible number of different additional parameters such as high and low voltages have to be monitored and evaluated. Since there are many other areas in the ATLAS experiment concerning slow control, the development of the slow control will follow as much as possible standardized procedures. Since it is rather too early for exact technical specifications, only the general baseline approach will be discussed here.

12.2 The purity monitoring system

12.2.1 Introduction

The signal of drifting electrons in liquid argon detectors is decreased by initial and column recombination and by the attachment of electrons to electronegative molecules like O_2, called "impurities" [12-1], [12-2]. An estimation of the O_2-equivalent concentration of impurities p has been shown to be possible [12-3]. While the mean recombination rate is constant for a fixed electric field and geometry, the electron lifetime has to be monitored since a possible change affects the resolution of the calorimeter.

Because of the short shaping time of the calorimeter electronics the measured response is rather insensitive to impurities. As shown in [12-4], for shaping times around 40 ns impurities up to $\approx$ 1 ppm O_2 -equivalent can be tolerated. Nevertheless the purity has to be monitored with special devices highly sensitive to changes in the electron lifetime τ, in order to ensure stable running conditions.

Two different types of purity measuring devices will be implemented in ATLAS: the so-called α- or β-chambers and the so-called laser chamber. The laser chamber has the advantage of measuring directly and simultaneously the electron lifetime and the drift velocity as opposed to the α- and β-chambers which only allow a relative determination of the electron lifetime. Therefore the laser chamber provides the calibration for the source based chambers.

The purity monitoring concept for the three liquid argon cryostats of ATLAS foresees the installation of several basic monitors, which are combinations of α- and β-chambers, inside the cryostats close to the calorimeters, and one laser chamber in contact with the liquid argon of each cryostat.

A moveable purity measuring system using the same probes has been designed [12-5]. It may be used to examine samples of liquid argon for impurities.

12.2.2 The basic monitor

12.2.2.1 Principle of the α and β-chambers

Figure 12-1 and Figure 12-2 show a schematic view of both ionization chambers.
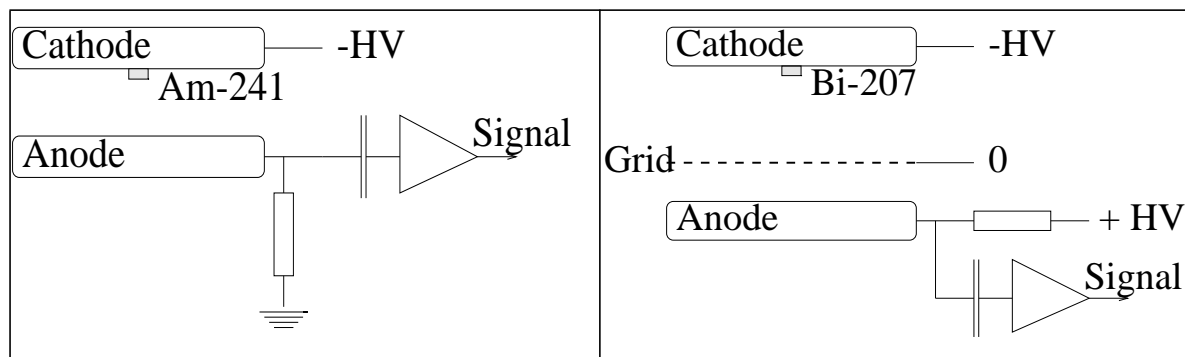
Figure 12-1 Schematic view of the α-chamber.   **Figure 12-2** Schematic view of the β-chamber.
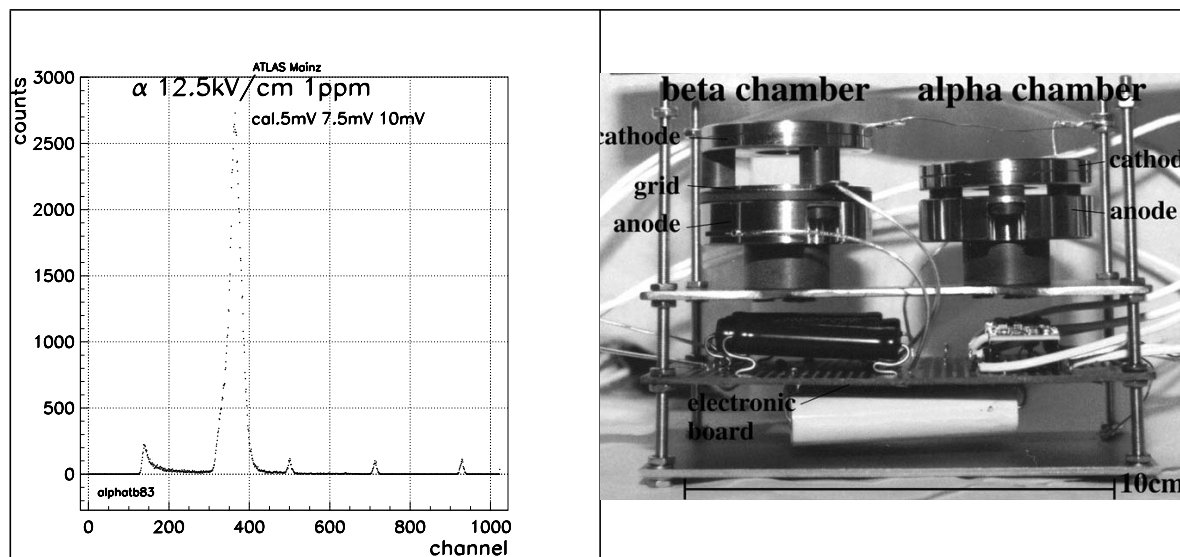
In the α-chamber, strongly ionizing α-particles from an ^{241}Am source produce electron ion pairs in the liquid argon within approximately 200 μm in front of the cathode. The quasi-pointlike electron charge drifting in the electric field $\vec{E}$ induces a signal on the anode which is converted into a voltage signal by a charge sensitive preamplifier. A typical spectrum for the α-chamber is shown in Figure 12-3.

The β-chamber exploits the fixed energy of the conversion electrons from a ^{207}Bi source mounted on the cathode to produce an approximately 3 mm long track of electron ion pairs. The electrons drift towards the anode passing a Frisch grid which electrically shields the anode from the first gap. Electrons in the second gap induce a signal on the anode which again is converted to a voltage signal by a charge sensitive preamplifier.

Both chambers allow to monitor the changes in the mean free path length for the absorption of conduction electrons by impurities in liquid argon and thus the stability of the liquid argon purity.

12.2.2.2 Mechanics of the basic monitor

The basic monitor consists of one α- and one β-chamber together with a board for HV blocking resistors and two preamplifiers as shown in the prototype's picture (Figure 12-4). The chambers are made of stainless steel and polyimide [12-6]. Everything is mounted on a solid stainless-steel plate. The entire assembly is mechanically shielded by a case of perforated stain-

Figure 12-3 Spectrum of the prototype α-chamber. The low noise at a level of approximately 1 mV is a precondition to directly trigger on the typical signal output of a few mV in the case of the α-chamber.

Figure 12-4 Photograph of a basic monitor prototype.

less-steel sheets. For the complete basic monitor two alternative outer envelopes have been defined, the dimensions of which are given in Table 12-1.

Table 12-1 Basic monitor envelopes.

	Name	Height x width x length
Basic monitor type A	'compact'	90 x 65 x 120 mm^3
Basic monitor type B	'flat and long'	40 x 65 x 220 mm^3
Laser chamber		80 x 100 x 130 mm^3

12.2.2.3 Cables

For the basic monitor the electrical connections listed in Table 12-2 are necessary. In the future the signal lines may become differentially driven lines.

Table 12-2 Number of cables.

Purpose	Type	Basic monitor α-chamber	β-chamber	Total	Laser chamber
HV up to 3kV	HV	1	2	3	3
Preamp supply (-6V, 0V, +12V)	coax	3	3	6	3
Signal	coax	1	1	2	1
Calibration pulses	coax	1	1	2	1

12.2.3 The laser-chamber monitor

12.2.3.1 Principle of the laser chamber

Figure 12-5 shows a schematic view and Figure 12-6 a picture of the laser chamber. Pulses of UV-laser light brought onto the gold-coated cathode by a quartz fibre produce photoelectrons at the cathode. As the electrons drift through the electric field towards the anode they pass two Frisch grids: the cathode and the anode grid. These grids shield the middle drift space electrostatically from the anode and the cathode, which are connected to the same charge sensitive preamplifier by a decoupling capacitor each. The four electrodes define an increasing electric field since the field ratio at the Frisch grids has to be adjusted to allow for optimal transparency [12-7].
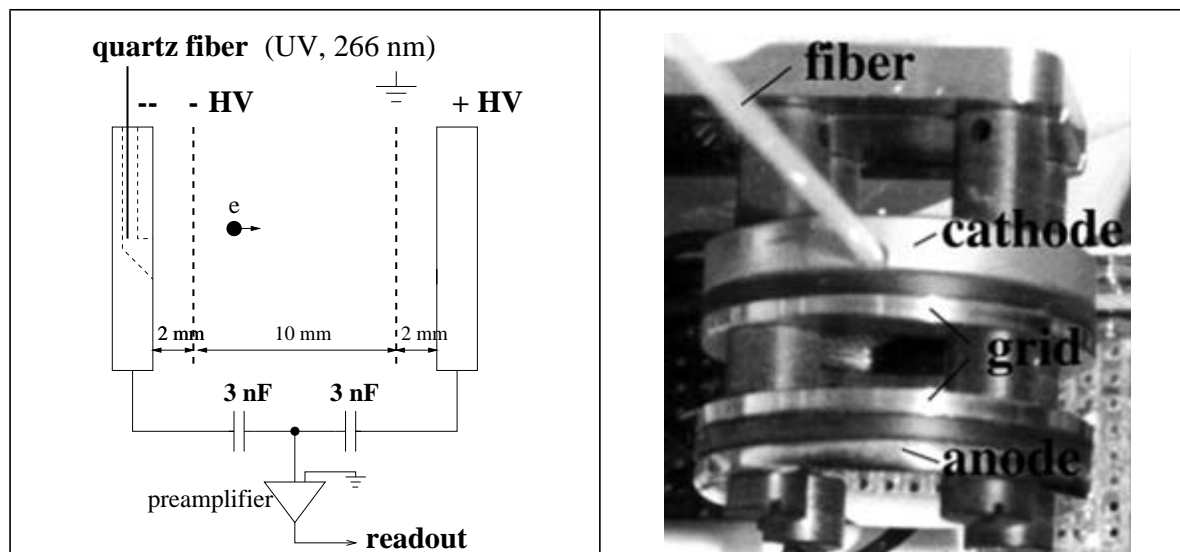

**Figure 12-5** Schematic view of the laser chamber.

**Figure 12-6** Photograph of the laser chamber prototype.
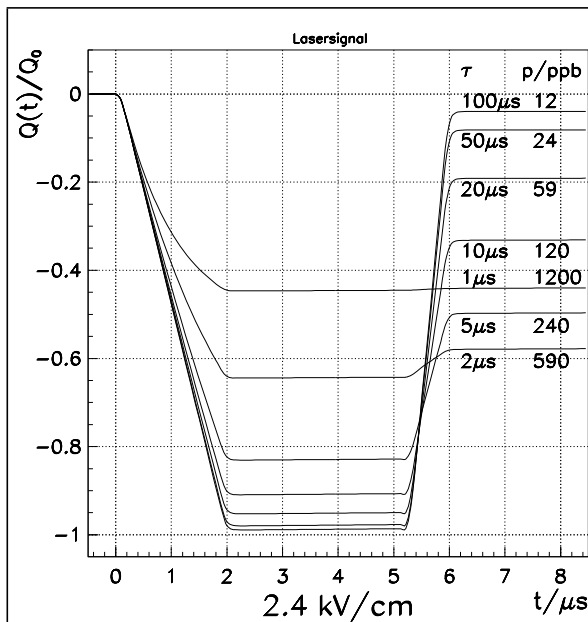
Figure 12-7 shows the ideal output signal of the laser chamber and its variation for different electron lifetimes. The electron lifetime can be extracted from the signal shape. A typical pulse of the laser chamber as measured in a test set-up is shown in Figure 12-8 .

#### 12.2.3.2 Mechanics of the laser chamber
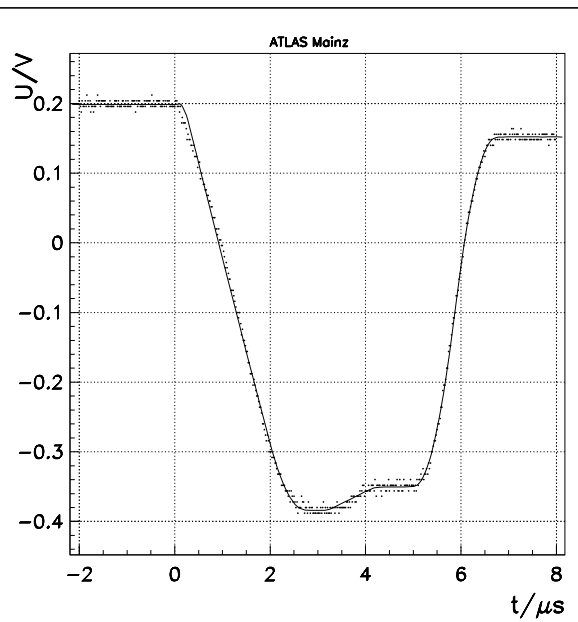
The laser-chamber monitor consists of the chamber made from stainless steel and polyimide, one board for the HV-blocking resistors, and the preamplifier board. The components are mounted into a perforated metal box for mechanical protection. The maximum outer envelope is defined in Table 12-1.

12.2.3.3 Cables

The electrical connections for one laser chamber are listed in Table 12-2. In the future the signal lines may become differentially driven lines. In addition a quartz fibre for the UV-light is needed.

Figure 12-7 Laser chamber signal for different electron lifetimes as an example given for the geometry and field as used for poisoning studies. The corresponding concentrations of impurities in oxygen equivalents are given.

Figure 12-8 Typical pulse of the laser chamber prototype with an overlay of the fitted function $\tau \approx 30\ \mu s$.

12.2.4 Distribution of monitors in the cryostats

12.2.4.1 General considerations

The placement of the liquid argon purity monitors in the cryostats is guided by the need to monitor the liquid argon purity close to the different calorimeters, by the wish to cover the entire cryostat and by the amount of available space. Since the basic monitors (with the exception of the basic monitors in the FCAL region) will be equipped with cold preamplifiers they will be placed on or close to the outer radius of the different calorimeter wheels in order to suffer less from radiation.

In addition there will be one laser chamber per cryostat to measure the absolute electron lifetime in the liquid argon. It serves for an initial calibration of the basic monitors. Since the laser chambers require an additional feedthrough for the UV-light fibre, they will be placed further out in the liquid argon expansion system. Possible noise induced by the laser is uncritical since the laser-chamber data will only be taken when it is considered necessary.

The numbers of cables and feedthrough connectors needed for the liquid argon purity system are given separately for the barrel and the end-cap cryostats. For the low voltage and signal connectors 64 pins per connector (two rows of 32) are assumed (Chapter 10).

The numbers of FT-connections needed for the HV and LV correspond to the number of cables. In order to avoid cross-talk the signal pins will be shielded from each other by low voltage pins placed in between. For the calibration lines a similar scheme is foreseen. The signal lines may become differentially driven lines and therefore two pins per signal line are reserved.
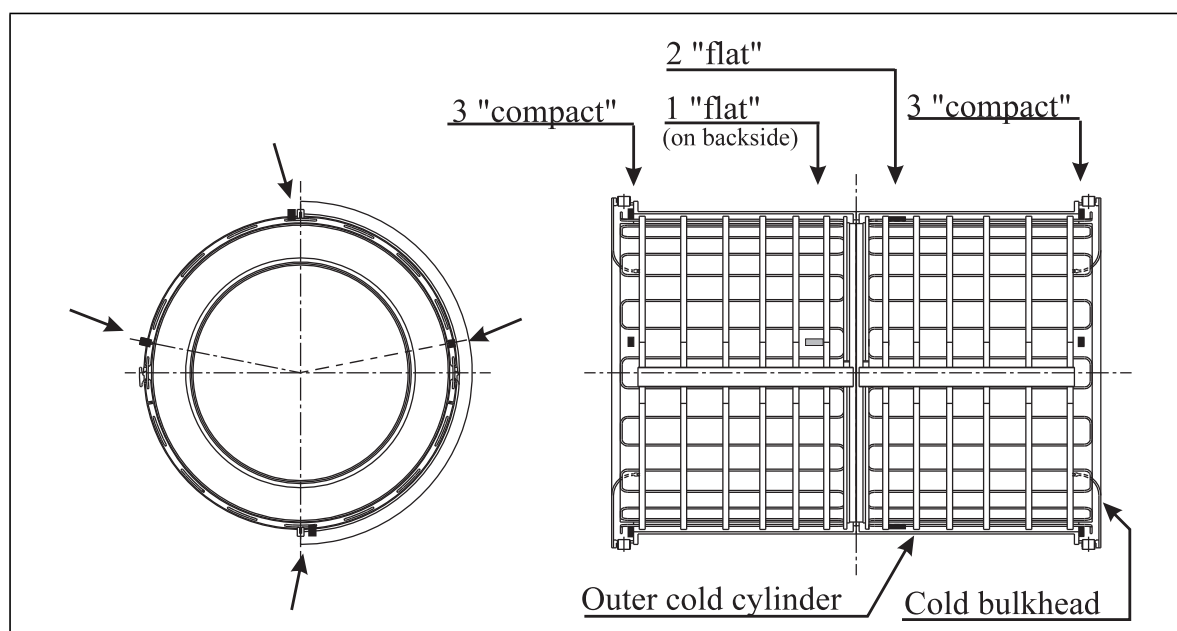
The feedthrough pins for the signal lines and the calibration lines of different basic monitors in one cryostat should be grouped on one or more connector(s) separated by type.

The operating HV will be 2.5 kV, therefore the HV-feedthroughs should allow for up to 3 kV.

Spare lines will be put into the cryostats to avoid the loss of a monitor due to broken cables.

12.2.4.2 Barrel cryostat

The entire barrel cryostat will be equipped with nine basic monitors of type B as shown in Figure 12-9. They will be located at three positions in z (at both ends and in the middle of the cryostat) on the outer circumference of the barrel EM calorimeter at three different heights. The three monitors placed on half height are put on alternate sides in z. Two of the three monitors at $z \approx 0$ will be mounted on one half barrel, the third on the other.

Figure 12-9 Locations of the basic monitors inside the barrel cryostat. This longitudinal placement is repeated three times at the top, middle and bottom of the cryostat. In total there are nine basic monitors.

Table 12-3 summarizes the number of lines for a half barrel / barrel. The number of connectors needed is given per half barrel allowing for five basic monitors. Per half barrel one connector (+1 reserved for the separation of signal and calibration lines) and 15 HV lines are needed.
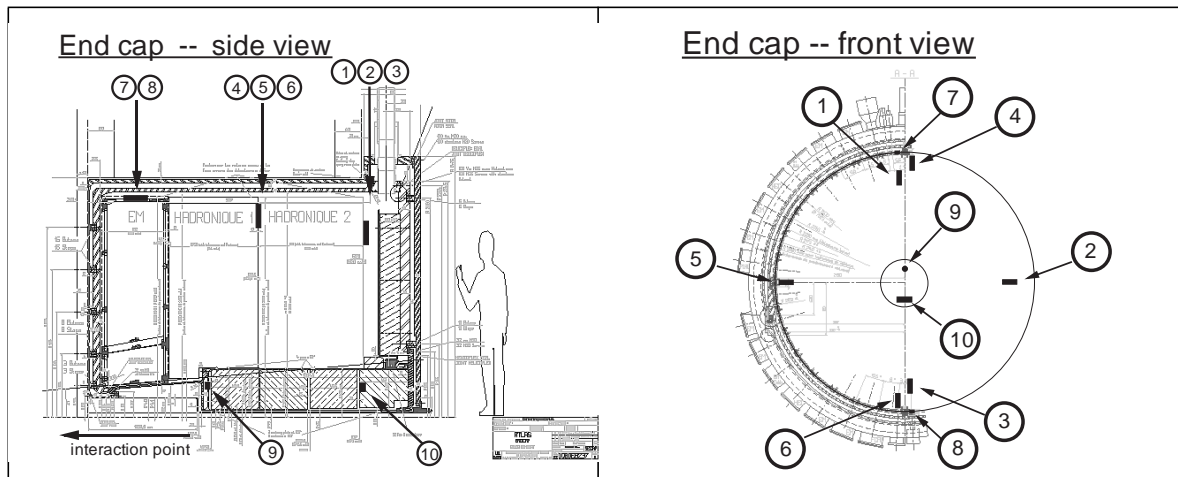
Table 12-3 Number of lines, pins and connectors for the barrel.

Type	No. of lines	No. of pins	Connectors	
	per half barrel	per half barrel	per half barrel	full barrel
Signal	10	10 + 10		
Calibration	10	10	1 + 1	2 + 2
Low voltage	30	30		
HV	15	-	-	-

12.2.4.3 End-cap cryostats
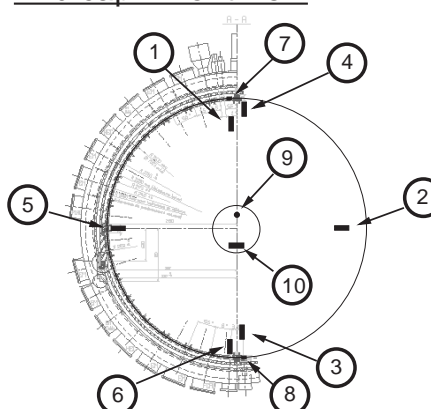
Per end-cap there will be 10 basic monitors of which eight will be equipped with cold electronics. They will be distributed on or close to the outer radius of the electromagnetic (EMEC) and hadronic end-cap calorimeters (HEC) in three positions in z and at three different heights.
As shown in Figure 12-10 and Figure 12-11 two probes (No. 7 and 8) of the geometric type B will be at the top and bottom on the outer circumference of the EMEC. They are mounted into the outer frame of the EMEC modules, thus taking up a minimum of the limited space between the calorimeter and the cryostat wall.

Figure 12-10 Location of the basic monitors inside the end-cap cryostat (side view).

Figure 12-11 Locations of the basic monitors inside the end-cap cryostat (front view).

Another three basic monitors (No. 4, 5 and 6) will be placed on three different heights between the first and second wheels of the HEC. They are partially embedded into a pocket machined into the last copper plate of the first wheel since there is not sufficient space on the outer circumference of the HEC modules. These pockets will be located close to the outer circumference of the HEC modules.

On the back of the calorimeter three basic monitors (No. 1, 2 and 3) of type B will be mounted onto the last copper plate of the second HEC wheel close ($\approx$ 20 cm inwards) to the outer circumference of the absorber plates. They will again be placed at the top (No. 1), half height (No. 2) and bottom (No. 3).

Two special monitors with remote electronics are situated in the vicinity of the forward calorimeter (FCAL). One basic monitor of type B (No. 10) is placed into a liquid-argon-filled pocket cut in the absorber behind the FCAL.

In front of the FCAL (No. 9) a single alpha cell will be put into a pocket of the cryostat wall filled with liquid argon. This pocket will use a cylindrical tube reaching into the evacuated space in front of the FCAL as shown in Figure 12-12.

The number of connectors needed is summarized per end-cap (one side) in Table 12-4. For one end-cap two connectors (plus one reserved for the separation of the signal and calibration lines) and 30 HV lines are needed.
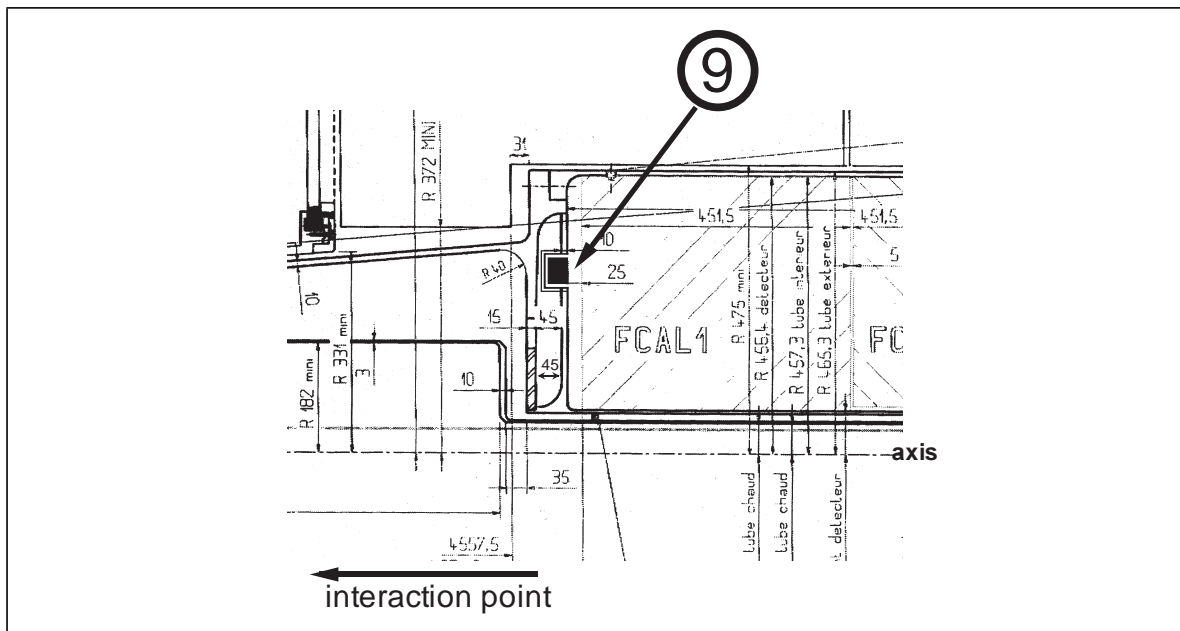
Figure 12-12 Location of the basic monitor in front of the FCAL.

Table 12-4 Number of lines, pins and connectors for one end-cap

Type	Total number of lines	Total number of pins	Connectors for one EC
Signal	20	20 + 20	
Calibration	20	20	2 + 2
Low voltage	60	60	
HV	30	—	—

12.2.4.4 Placement of the laser chambers

For each cryostat one laser-chamber monitor is placed inside the liquid argon expansion vessel. There will be warm feedthroughs for its supplies and signal lines (cf. Table 12-2) as well as for the quartz fibre.

12.2.5 Front-end electronics

12.2.5.1 Basic monitor

A charge-sensitive cold preamplifier is used to integrate the collected charge into an output voltage signal. On the warm front-end side the signal of each chamber needs to be shaped and a trigger has to be extracted from the signal itself. The shaped pulses then have to be recorded for subsequent analysis.

12.2.5.2 Laser-chamber monitor

A charge sensitive preamplifier in the liquid argon converts the collected charge into an output voltage signal. The signal of the preamplifier's output needs to be recorded for each laser trigger individually. An FADC is required to sample the waveform.

12.3 The temperature monitoring system

12.3.1 Introduction

The temperature monitoring system will allow temperatures in the cryostats during their cool-down and warm-up to be checked in order to prevent too large mechanical deformations of a detector component caused by too large temperature gradients. During normal running periods the temperature monitoring system is necessary for the control of the liquid argon cooling system and allows possible temperature gradients to be measured.

The temperature measurement system consists of the following parts:

- temperature sensors, distributed inside the cryostat in such a way that their distance is small enough to guarantee a sufficiently precise temperature map;
- cable branches arranged inside the cryostat;
- front-end electronics arranged directly on the cryostat;
- second-level electronics located in the control room.

12.3.2 The temperature gradients in the cryostat

Exact calculations of the temperature map are difficult since most of the heat exchanges will take place by convection, and the characteristics of the medium are not well defined due to the large number of cables, fixtures, etc.

In general there are several heat sources in the cryostat: the cryostat walls (axial symmetry), the suspension clips of the internal cryostat parts, the electrical cables and the ionizing radiation of the beam. The heat produced by these sources is taken away with liquid nitrogen heat exchangers.

12.3.3 The temperature sensors

The most important requirements for the temperature sensors are:

- lasting stability (the period without dismantling and recalibration assumed is of the order of 10 years);
- lowest possible susceptibility to minimize the influence of the magnetic field and ionizing- radiation background;
- high sensitivity in the range 70-90 K;
- acceptable dimensions and costs (altogether there are about 600 sensors).

To meet these requirements, it is proposed to apply platinum resistance thermometers (PRTs), series PT-100[1]. The main parameters of these resistors are 100 Ω at 273 K, and about 20 Ω at 77 K, with a sensitivity of about 0.4 Ω/ K. The sensor is a ceramic cylinder with 1.5 mm diameter and 12 mm length. To connect the thermometer, four-wire bifilar cable[2] will be used.

12.3.4 Distribution of sensors in the cryostat

In the barrel calorimeter six temperature probes per supermodule will be installed, three on the front and three on the back of the modules. Altogether there will be 192 probes with four read-out wires each. The EMEC will use 48 probes. In the HEC 96 probes will be distributed such that 16 modules of each wheel will be equipped with three probes each. The FCAL will use 12 temperature probes.

12.3.5 Front-end electronics

For the resistance measurements a special self-balancing DC resistance bridge has been developed, as shown in Figure 12-13. One read-out module will serve 32 thermometers.

12.4 Strain and position monitoring

12.4.1 Requirements

Measurements of strains and positions are mainly needed during cool-down operations. Differences between the materials used for the cryostat and calorimeter (in terms of shrinkage coefficients, thermal conductivities, Young moduli, etc.) could be destructive at some level. For example, the high conductivity, combined with a high shrinkage coefficient and a relatively small mass, could cause the inner cryostat vessel to shrink faster than the calorimeter and possibly damage some cables on the outer diameter. Other differences between materials used during the calorimeter construction (aluminium for the structure, steel/prepreg /lead /prepreg/ /steel sandwich for the absorbers, etc.) have been optimized whenever possible. Nevertheless, it is safer to ensure that stresses are of the same order of magnitude as predicted by finite element models. Also, the overall shape of the calorimeter (cylindricity, verticality, etc.) is of interest for the calibration. Online control is also useful to detect a possible long-term weakness of the structure or plastic flow of the lead.

12.4.2 Stress measurements

Stress is usually measured by the use of resistive gauges. These devices are made of an alloy (generally nickel-chrome for cryogenic applications) deposited on a small Kapton fold, which is then glued on the surface to be analysed. To avoid a local temperature increase, and vaporization when in liquid argon, the power needed for the read-out of the gauges should be small and their resistivity should be high enough. A typical value for calibrated gauges is 350 Ω. A schematic diagram of a gauge is shown in Figure 12-14.

---

1. Lake Shore Cryotronics, type PT-103.
2. Lake Shore Cryotronics, type WQT-36.
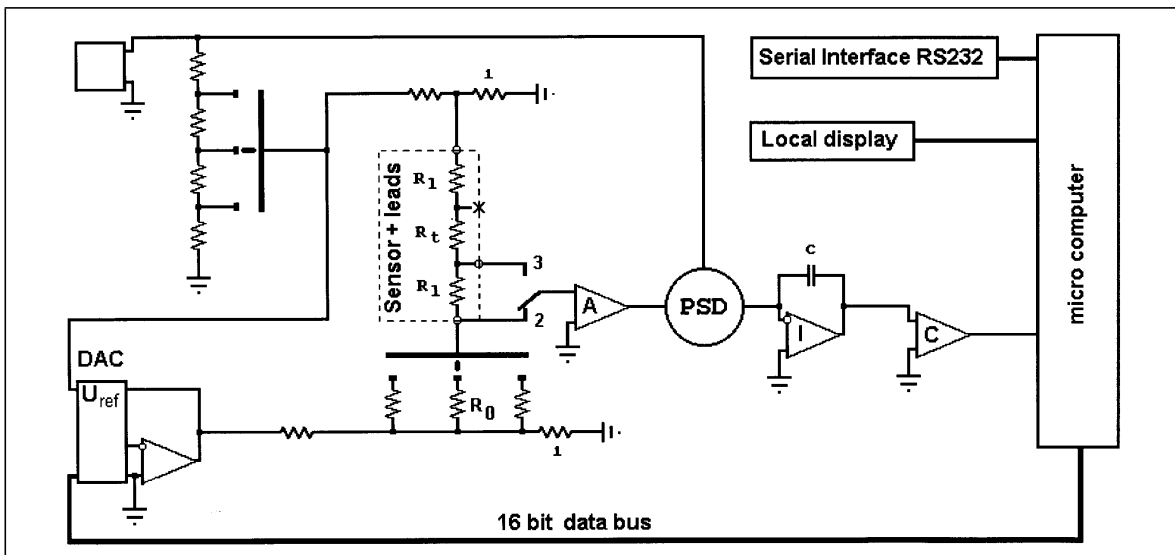
Figure 12-13 Simplified block diagram of the self-balancing AC/DC resistance bridge.
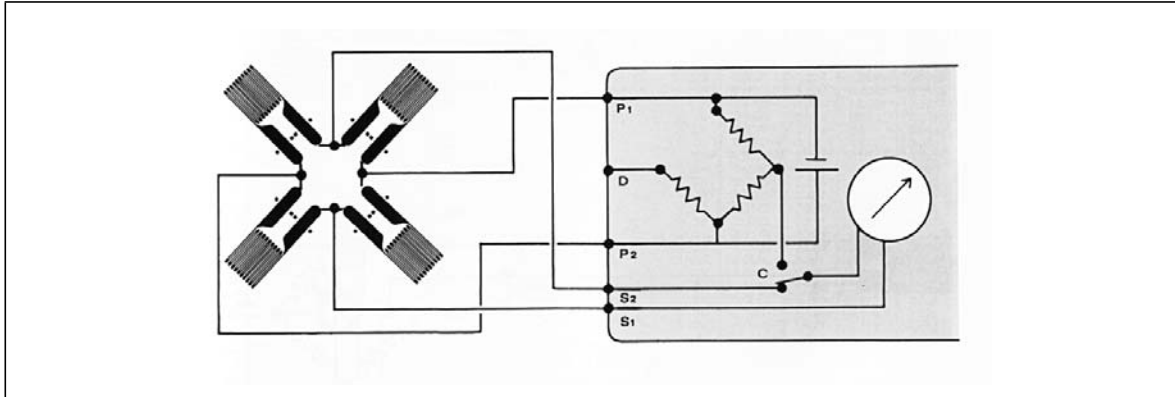

Figure 12-14 A typical gauge scheme.

Magnetic fields can alter the quality of the measurements significantly. To avoid this, some gauges should be composed of two similar elements, glued one above the other, in opposite directions to cancel induced currents. Radiation can also alter the measurements by changing the resistivity. Half or full bridges are less sensitive to this kind of variation, as they are compensated.

12.4.3 Position measurements

Position measurements are required to control the calorimeter centricity with respect to the cryostat inner vessel, and the position of the front face. The range of distances to be measured is of the order of 10 mm, with an accuracy of measurement better than 0.2 mm at room temperature and at liquid argon temperature of -186 °C. For prototype tests, cryogenic LVDTs (Linear Variable Differential Transformers) have been tested and calibrated, taking into account the coil shrinkage, but also the plunger shrinkage. A typical circuit for the LVDT is shown in Figure 12-15 and a calibration in Figure 12-16.
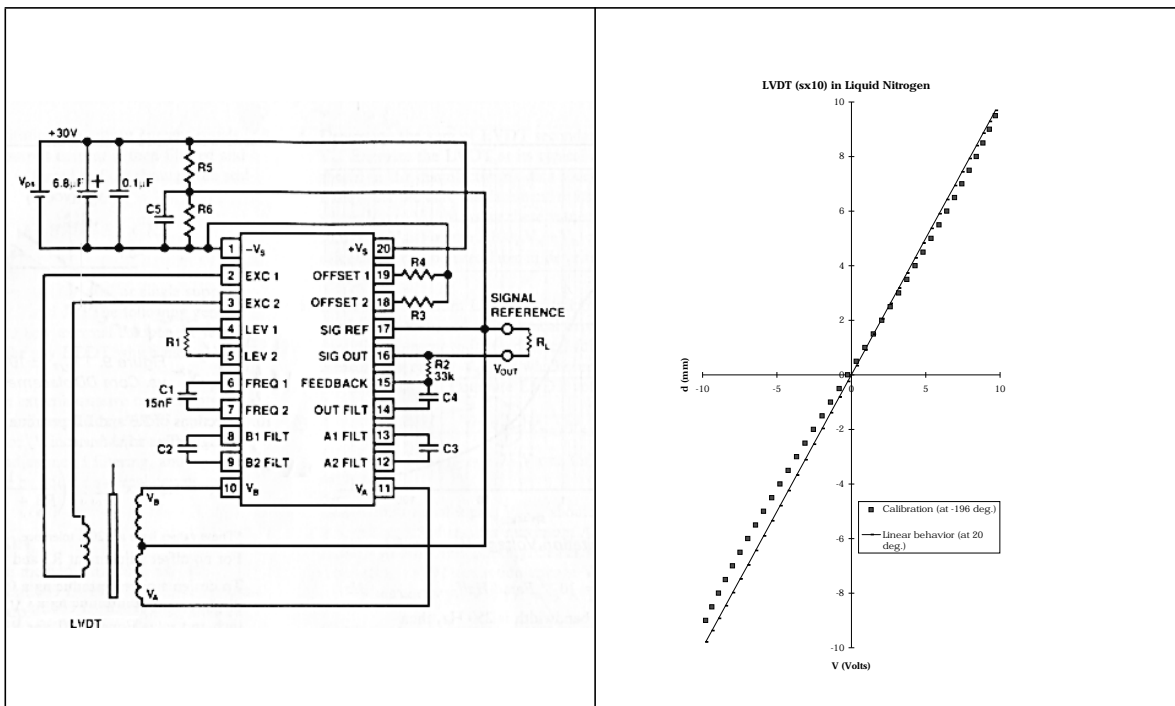
Figure 12-15 LVDT scheme.

Figure 12-16 Calibration of LVDT.

12.4.4 Number of sensors required

For the barrel calorimeter there will be four strain gauges mounted on rings four and seven of each half barrel (see Chapter 6). Altogether there are 16 strain gauges. Position monitors will be mounted at four locations (z = 0, ϕ = 0°, 90°, 180° and 270°). Forty strain gauges and eight position monitors will be installed in the EMEC at the locations given in Table 12-5. Figure 12-17 shows as an example the deflection of the front outer ring of the EMEC (see Chapter 7) amplified by a factor of 300. The hadronic end-cap calorimeter will be equipped with 24 strain gauges in total per end-cap. They will be located on each foot and each key at the top and bottom of each wheel in three positions: front, middle and rear. Position monitors will be mounted

Figure 12-17 Amplified deflection of front outer ring.

on the front and rear of each foot and key. Therefore there will be 16 position monitors in total per end-cap. In total there will be 64 strain gauges and 24 position monitors in each end-cap. They will be mainly used for cold tests. Only some of them will be connected using four wires, the LVDTs using five wires.

Table 12-5 Locations of strain gauges and position monitors in the EMEC.

Strain gauges	Quantity
Front outer ring	6
Back outer ring	6
Front intermediate ring	6
Back intermediate ring	2
Front inner ring	2
Back inner ring	2
Stretchers (rails and guides)	4
Rails (load)	4
Bars (front face)	8
Position monitors	
Front outer ring (parallel to z)	4
Back outer ring (+x,-x,+y,-y)	4

12.5 The slow control

12.5.1 Introduction

The detector control subsystem for the liquid argon calorimeters is used for the operation and monitoring of the detectors. It is one of several parts of the ATLAS detector control system (DCS) [12-8] and is mainly concerned with the

- monitoring of the detector mechanics (position and stress sensors),
- monitoring and diagnosis of subdetector conditions, (temperature and purity probes),
- monitoring, diagnosis and control of functional parameters, (high and low voltages, status signals)
- monitoring of safety relevant parameters.

In the following sections the first two points will be discussed.

12.5.2 General structure

The signal lines of position sensors, stress sensors, temperature probes and purity probes will be separated in the cryostats so that they can be connected to different feedthroughs. Each feedthrough has one connector of 64 pins assigned to monitoring purposes (see Figure 10.4, Chapter 4).

In order to keep the noise to a minimum, the signals have to be amplified, conditioned or possibly digitized at a location as close as possible to the feedthroughs, requiring radiation-tolerant electronics in a limited space. Two slots per front end crate (FEC), which is housed in a Faraday

cage and serves two feedthroughs, have therefore been reserved for this purpose (see Chapter 10, Section 10.2.3).

From the front-end crate the signals will be transmitted to the local control system (LCS), a standardized system for all ATLAS subdetectors. The crates for the LCS will be located in the cavern close to the calorimeters where radiation levels are low enough for commercial electronics to be used. The information from the LCS will be collected by server workstations and accessed by operator workstations (WS).

12.5.3 Sensors and probes

Table 12-6 summarizes the numbers of sensors in the barrel, EMEC, HEC and FCAL. The corresponding numbers of feedthroughs for the barrel and the two end-caps that are used for the sensor signal lines are also listed (No. of FT).

Table 12-6 Summary of number of sensors.

| Probe type | Barrel | | EMEC | HEC | FCAL | |
	No.of probes	No. of FT	No. of probes	No. of probes	No. of probes	No. of FT
Position sensor	8	2	2 x 8	2 x 16		2 x 2
Stress sensor	32	2	2 x 40	2 x 24		2 x 4
Calorimeter temperature	192	12	2 x 48	2 x 96	2 x 12	2 x 10
Cryostat temperature	32	2			2x32	2 x 2
Purity	9	2(4)	2 x 2	2 x 6	2 x 2	2 x 2 (2 x 4)

The number of cables needed per sensor is summarized in Table 12-3 and Table 12-4.

For the absolute measurement of the electron lifetime, one precision purity probe per cryostat (laser chamber, see Section 12.2.3) is foreseen which will be read out independently of the other probes.

We envisage that position and stress sensors will be read out mainly during installation and cool-down. Temperature will be monitored every few minutes while the purity will have to be checked every few hours.

12.5.4 Front-end board electronics

The conditioning of the sensor signals as well as the distribution of low voltage and calibration lines will be done on service boards (SB's) installed in the FECs. We foresee four different types of read-out boards for slow control purposes as listed in Table 12-6. The minimum number of boards needed corresponds to the associated number of feedthroughs, which is also listed in Table 12-6.

To guarantee that the slow-control signals can be monitored independently of the read-out, separate low-power lines are foreseen for the slow control SBs. If necessary, these will be connected

to an uninterruptable power supply. For the same reason the baseline option does *not* foresee the use of the data bus for the slow control read-out.

The main purpose of the slow control SBs is to amplify and condition the signals so that they can be transmitted to the LCS crates located in the cavern close to the calorimeter. Here commercial electronics will be used to digitize the signals whenever possible and an interface to DCS will be provided. A custom solution will be chosen for the liquid argon purity monitoring which requires a triggering mechanism and the shaping of the signals before digitization.

Should radiation-hard field-bus electronics become available, digitization could already take place in the FEC. A commercial field-bus protocol would then be used to transmit the data to the LCS crate.

12.6 Costs

The total costs of the liquid argon monitoring system has been estimated to be in the order of 780 kCHF.

12.7 References

12-1   G. Bakale, U. Sowada, W.F. Schmidt, J. Phys. Chem 80, (1976) 2556.

12-2   C. Brassard, Nucl. Instrum. Methods 162 (1979) 29.

12-3   W. Hofman et al., Nucl. Instrum. Methods 135 (1976) 151.

12-4   M. Adams et al., ATLAS LARG-053, (1996).

12-5   M. Adams et al., ATLAS LARG-Note in preparation

12-6   F. Hölldorfer, Diploma thesis in preparation, University of Mainz.

12-7   O. Bunemann et al., Canadian Journal of Research, Vol. 27, Sec. A, (1949).

12-8   ATLAS Detector Control System, User Requirements Document, draft 00, 25.9.95.

13 Test beam activity

The ATLAS calorimeters consist of a large number of modules: 32 for the EM barrel, 16 for the EM end-caps (EMEC), 128 for the hadronic end-caps (HEC) and 6 for the forward. Before starting the massive production of these modules, extensive tests of the so-called module 0's will take place in order to validate the full production chain. These first tests are scheduled in 1997/1998 and will be followed by qualification tests of the production modules.

13.1 General description of the liquid argon test beam areas

In this chapter we first briefly describe the test beam environment at the North Area of CERN for the different LAr subdetectors. In a second part we discuss the main modifications we have to carry out in the zones in order to start routine tests during the fall of 1997.

13.1.1 H6/H8 beam line characteristics

The H6 and H8 beam lines in the EHN1 experimental area provide both secondary and tertiary electron, pion and muon beams. The energy is limited to 300 GeV for H8 and to 200 GeV for H6 for standard running conditions. The H6 beam always runs at the polarity of the H8 beam and typically up to 50% of the momentum chosen for H8. The main advantage of operating in the tertiary mode is the ease of changing the beam momentum. Momenta from 10 to 150 GeV for a secondary setting of 200 GeV can be selected by the user simply by loading the corresponding beam files. The drawback is a loss in intensity.

Separation of electrons from hadrons is achieved by the synchrotron radiation energy loss in a serie of magnets followed by collimation of the hadrons. At 200 GeV, the separation is 16 mm at a distance of ~ 350 m.

The beam intensity is controlled by three collimators. It ranges from a few 10^4 p.p.s at 200 GeV (secondary) to a few 10^2 p.p.s at 10 GeV (tertiary). The momentum resolution is given by a set of two collimators and is of the order of $\Delta p/p = 0.3\%$ for a standard setting of the collimators.

13.1.2 Liquid argon specific equipment

Figure 13-i shows the general layout for both beam lines in mid 1997. The tests of the LAr subdetectors will take place in the H8 beam line (stand-alone barrel tests in H8B and common ATLAS run in H8A) and in the H6 beam line (for all the end-cap (EC) subdetectors). Figure 13-ii shows the layout in H8A for the combined ATLAS run. This specific run, scheduled for 1999, will be described later in more detail (see Section 13.5.1).

The major modifications we plan to do on both beam lines are as follows:

- Common cryogenic area: This completely new installation (common to the three test areas) is described in detail in Section 13.3. It will be located between the H8A and H8B areas (see Figure 13-i), protected from the beam in such a way that access will always be possible. The preparation of this zone has already begun. The layout for the cryo-lines which run along the floor from the common area to the detectors has yet to be finalized. Related to this system are the LN_2 and LAr tanks which we plan to install outside the Hall on a new platform on the Jura side. The construction of this platform will be finished early 1997, at the latest, in parallel with the installation of the pipes from the platform to the

common area, via the technical gallery. The overall installation will be ready for summer 1997.

- <u>Barrel H8B area and its clean room</u>: The position of the barrel cryostat is behind the dump in the H8B zone. To operate this large cryostat and to rotate it in both directions, a platform from the former UA2 collaboration will be used. This platform will be modified to allow full excursion in η and ϕ. The projectivity in η is obtained by two independent movements: a translation along the rails and a rotation of the platform itself. The correlation of these two movements makes smooth continuous data-taking, with no stops in between two different positions in η, more complicated. In ϕ, the rotation maintains the projectivity. The table will be ready for installation by the end of february 1997. The preparation of the floor (rails extension,...), and the enlargement of the zone is scheduled for the beginning of 1997. The clean area, which is close to the cryostat, is not yet fully designed. This area will be equipped with a crane to rotate the modules before insertion into the cryostat.

- <u>Barrel setup in front of the Tile calorimeter</u>: For the combined ATLAS run which is currently scheduled for 1999, the Barrel cryostat will be moved from H8B to H8A and put in front of the Tile calorimeter. A special extension of the existing Tile platform has to be designed. Owing to some space limitations and to non-projectivity in ϕ for the EM module when rotating the Tile table in ϕ, the scan will be limited to one single value in ϕ. In order to supply both the LN_2 and the LAr, the cryo-lines will run from the common cryogenic area to H8A. Since the distances are similar to the ones of the stand-alone position, we would use the same cryo-lines. The cool down and filling operations will be done in the final beam position. The transfer and installation of the cryostat from H8B to H8A is a delicate operation which will take at least one month (install new platform, move the cryostat, connect to the fluids...). For this reason, such a combined test should be scheduled at the very beginning of the beam period in April.

- <u>The end-cap region on H6 and the common clean room</u>: The EM end-cap (EMEC) and the hadronic end-cap (HEC) modules will be tested, respectively, in the modified NA31 cryostat [13-1] which will be moved to the H6B area, and in the H1 cryostat. Both subdetectors will share the same clean area for assembly and tests. The design of this area will start soon, in order to have this area ready for June 1997. The modifications to be made on both cryostats are described in the next sections. The preparation of both the beam and the garage positions for the NA31 cryostat began right after the heavy-ion period. The installation of the rails and of the rotation point for the η movement will be done immediately thereafter.

- <u>The control rooms</u>: The ATLAS control rooms in the North Area will be completely redistributed and made consistent with the safety rules. This operation has already started and will be finished early in 1997. The LAr community took this opportunity to reorganize the distribution of the LAr huts in order to have them located close to the corresponding detectors. Such a solution facilitates the sharing of some common equipment and will also help the setting up of the combined EC runs. The EMEC and HEC huts will be close together (HNA 451 and 455/7), facing the H6B and H6C areas and the Barrel control room will go to HNA468 (see Figure 13-i), near the H8B zone.

13.2 Barrel and end-cap cryostats

13.2.1 Barrel cryostat

The cryostat for the test/calibration of the barrel modules, the "barrel test cryostat", is made of two aluminium vessels, with a similar ovoid shape. The outside dimensions are: length about 5 m, height about 1.9 m, and 1.3 m wide at the bottom. The outer vessel (the vacuum vessel) is 40 mm thick; the inner vessel (the cold liquid argon containment vessel) is 50 mm thick. On the beam path in front of the calorimeter modules, a smaller thickness is implemented (respectively 30 and 40 mm). The ovoid shape is justified by the requirement that the dimensions from the back side of the calorimeter module to the outer vessel be as close as possible to the final ATLAS design. This will allow the calibration of the hadron response of the combined electromagnetic and hadronic ATLAS calorimeter. For technical reasons it is not possible to obey the same requirement on the front face of the calorimeter; the front wall is thus similar in shape to the back wall. To avoid a large amount of dead material (essentially LAr) in front of the detector, an argon excluder (Rohacell) will be inserted between the cold wall and the calorimeter front face. The cold vessel is computed to sustain a maximum working pressure of 2.3 bars (relative). Taking into account the hydrostatic pressure to the top of the full mechanical assembly, this corresponds to an opening of the safety valve at 1.7 bars (relative), with wide opening at 1.9 bars (relative) [13-2].

Simulation has shown that the mechanical strains are maximum at the bottom part of the cryostat. Therefore, the lower part of the cryostat is made by machining a massive aluminium plate. Afterwards, the upper part is soldered after proper bending. Finally, the cryostat is fixed on a frame to allow the positioning on the movable platform. On this frame is also mounted a cradle dedicated to support the expansion vessel and valve system on top of the cryostat.

Above the cryostat, the expansion vessel, with a LAr level 2 metres above the beam, is equipped with the main LN2 cooling loop. It is used to guarantee the pressure of the LAr bath. Inside the cold vessel another LN2 cooling loop will be used for the control of the LAr temperature close to the calorimeter module. The combined use of the two LN2 cooling loops will offer the opportunity to select various working points on the temperature vs pressure curve and to get experience with an accurate temperature measurement and regulation.

The cold signal feedthroughs which will be used for the test activity, are identical to the one used in ATLAS (see Chapter 4). They will be mounted on the side of the test cryostat at a position with respect to the modules which reproduces the ATLAS design. As a consequence, the cabling of the module, i.e. the cables from the motherboards to the feedtroughs, will be the final one. No cables will be removed from the modules after the calibration. For practical reasons, the mounting of the signal feedthroughs on the body of the cryostat vessels is done with stainless-steel flanges bolted on the aluminium vessel. The HV warm feedthrough is mounted on the expansion vessel above the cryostat body.

Figure 13-iii is a cross section of the barrel cryostat in the region of the three feedthroughs. It shows the module (and the argon excluder just in front), the insertion table and the rails, the massive aluminium plate and the frame. Just above the calorimeter is the LN_2 cooling loop and the expansion vessel. Figure 13-iv shows the cryogenic scheme corresponding to the cryostat. Its functioning will be described later (see Section 13.3). Finally Figure 13-1 shows a longitudinal view of the cryostat, with its internal and external dimensions as well as an exploded view of the different components. Shown in this figure is also the "reference module" built out of parts of the former "2 m barrel prototype "(see Chapter 2). It sits at the back end of the cryostat and will be used for normalisation purposes.
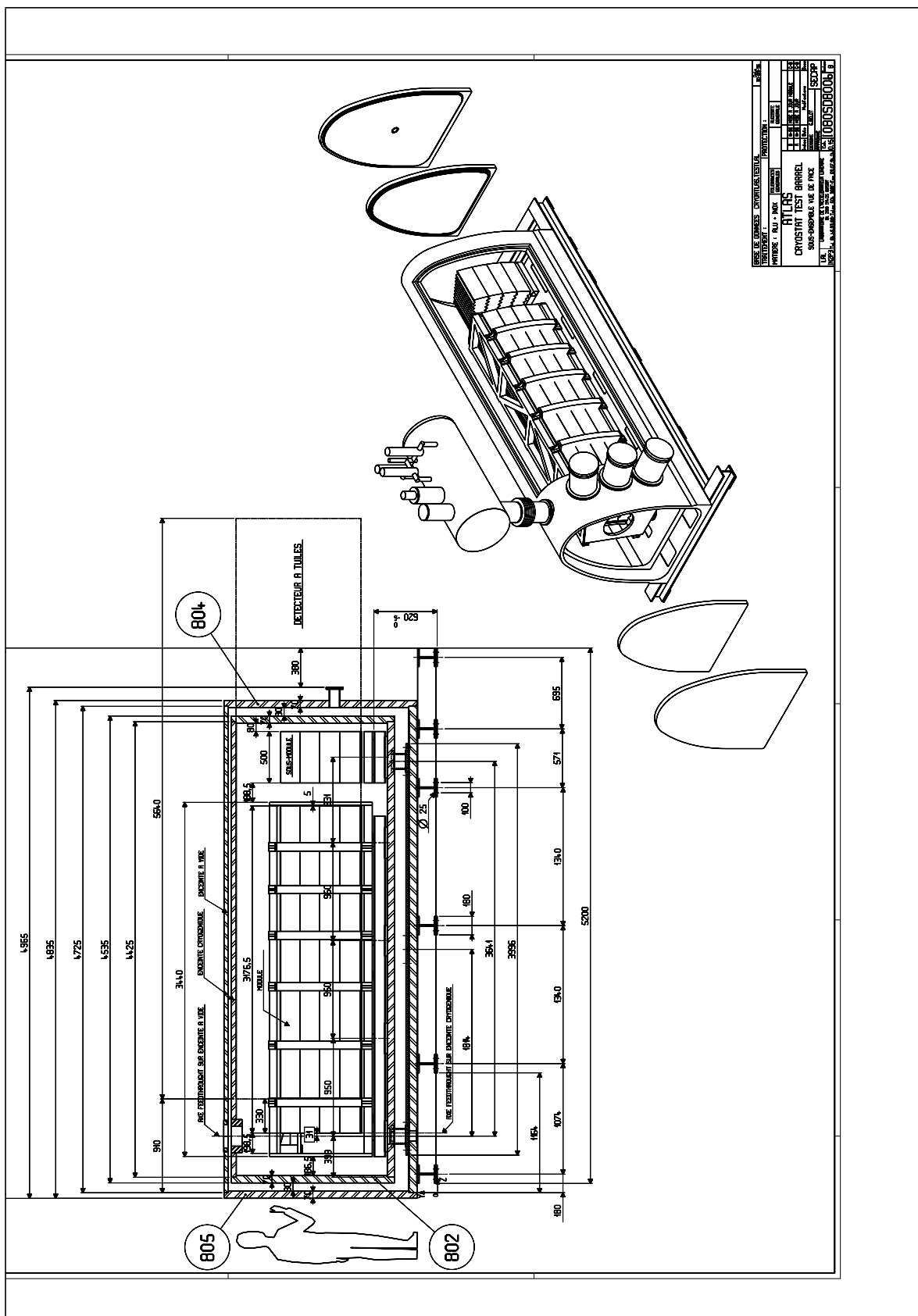
Figure 13-1 Longitudinal view of the barrel test beam cryostat.

The cold vessel is supported on the vacuum vessel by four tubular structures (epoxy/ glass fibre/ stainless steel), the total heat loss across is computed to be 20 W. Heat loss across the cold vessel is computed to be 200 W, a low value thanks to the superinsulation between the cold vessel and the vacuum vessel. The heat loss across the signal feedthroughs is computed to be 50 W.

The calorimeter modules ready for calibration are bolted on two I-shaped stainless-steel pieces, and are introduced/extracted by moving on sliding blocks: eight in the cryostat, eight outside on a table in the clean area.

13.2.2 Cryostats for the end-cap detector tests

13.2.2.1 Description and modification of the NA31 cryostat

The NA31 cryostat, somewhat modified, will be used to extensively test module 0 and one quarter of the production modules of the EMEC calorimeter.

The NA31 cryostat [13-1] is composed of an inner (liquid argon) vessel, an outer (vacuum) vessel, two large front and back flanges and a cover plate. The inner stainless-steel vessel is sealed to the outer one by means of an O-ring. The warm cover plate, which supports the calorimeter, seals the liquid-argon vessel without any vacuum insulation. The necessary feedthroughs for signal, HV and liquid transfer pass through the cover plate. The outward pressures on the liquid-argon vessel are transferred to the beam windows by means of truncated G10 cones.

The dimensions of the internal liquid-argon vessel are: 0.75 m along the beam, 2.80 m in the transverse direction and 3.7 m in height. The total material in front of the active part of the calorimeter amounts to 0.90 radiation lengths. Finally, the thermal loss of the cryostat is about 1500 W, divided into: 50% due to solid conduction, 25% due to radiation, and 25% to convection and transfer losses.
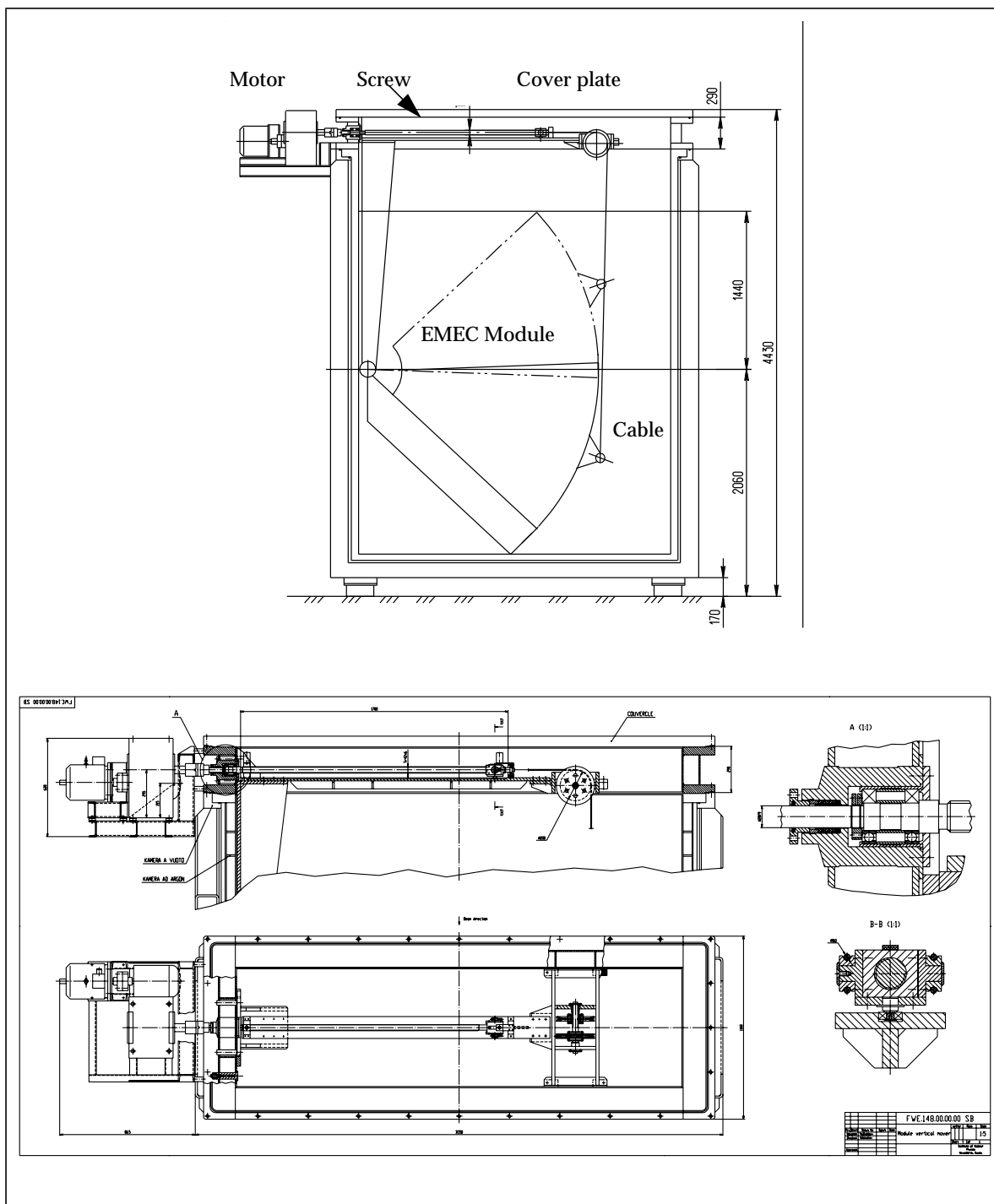
After an agreement signed between the Laboratory of Pisa (INFN) and the ATLAS management, which gave us the free use of the cryostat over the full test period, the collaboration decided to modify the NA31 cryostat in order to adapt it to our needs.

After successful safety tests (pressure, vacuum and cryogenic), made during the summer 1996, the following modifications will be made:

• Mechanics
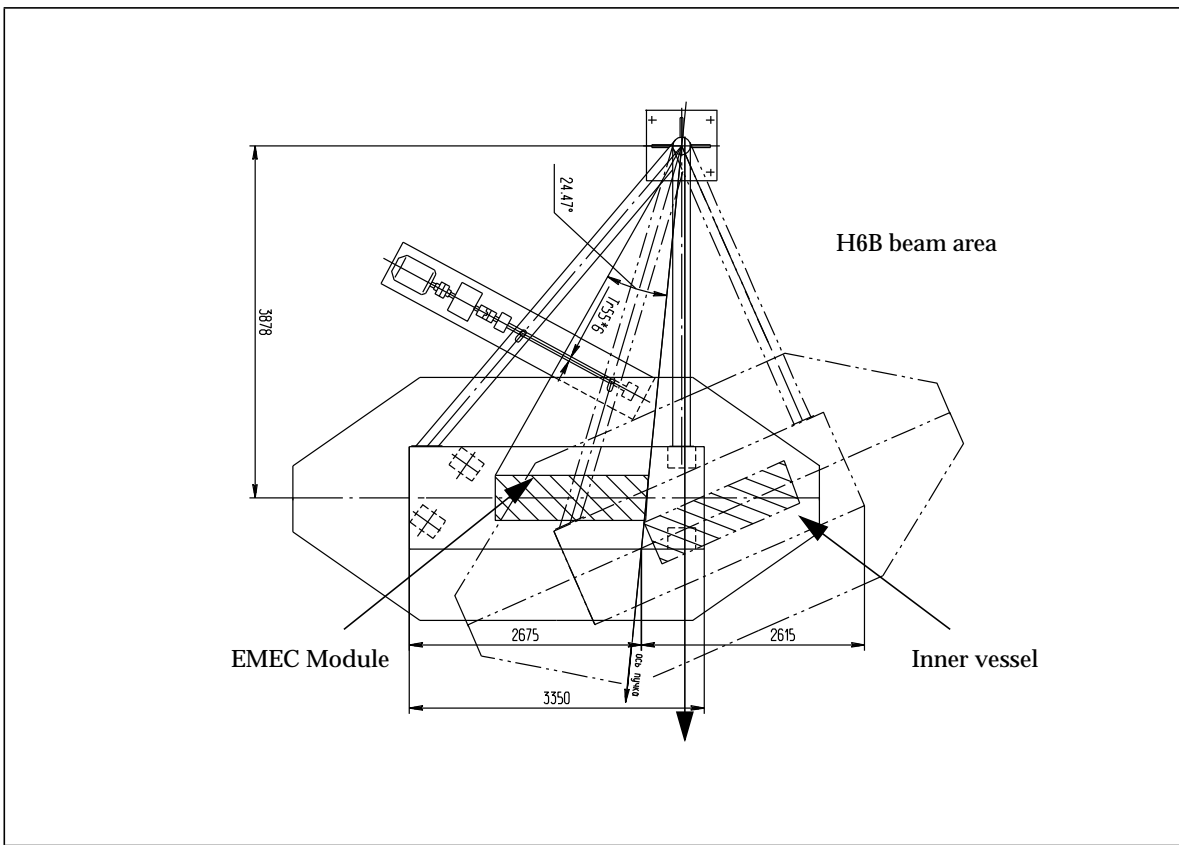
The internal dimensions of the cryostat are well adapted to the size of the EM end-cap module (essentially in z, along the beam direction). In order to allow movement of the module inside the cryostat (scan in ϕ), the mechanical structure will be modified. This will be done by means of an intermediate structure, located just below the cover plate. It will hold the internal movement structure (motor, screw and lifting cable). The material to be used is stainless-steel. Some experience with moving devices in the cold was already gained in the past when testing the EM end-cap prototype (see section 2.2). Detailed drawings of the structure are available and welding samples (in the critical region of the corners) have been sent to the CERN Safety (TIS) division for inspection. Figure 13-2 shows the vertical scan possibilities inside the cryostat. This intermediate structure, which is 29 cm in height, also supports a platform on which the module will be fixed. A full vertical scan of the module (45°) will then be possible.

In the NA31 experiment, this cryostat was operating at fixed position (beam pipe going through it). To scan the module over the full η region (1.375 to 3.2), a set-up similar to the one used in

Figure 13-2 View of the internal vertical displacement mechanism. The intermediate structure will hold the lifting device and the support for the EM module. The lower part of the figure shows in more details the intermediate structure with the motor, the screw and the driving-wheel.

RD3, with rails, rollers, and a fixed rotation point will be built. The main limitation with the NA31 cryostat is the space left under it for the rollers and the rails (only 17 cm) in order to have the beam well centred. To stabilize the cryostat during the rotation phase, it is foreseen to fix two I beams between the top of the cryostat and the rotation point. Figure 13-3 shows the horizontal scan possibilities on the H6 beam line. The hatched rectangle corresponds to the module

Figure 13-3 Top view of the modified NA31 cryostat and of the lateral excursion for a full scan in η of the EM end-cap modules.

inside the cryostat and the octagonal structure to the platform where the electronic boxes will be located.

To move the cryostat from the beam position to the garage position and vice versa, we propose to use the crane. Some studies have yet to be done (local stress calculations on the intermediate structure at the level of the four fixation points) to fully validate this procedure.

- Cryogenics

To comply with the new cryogenic installation and with the control scheme (see 13.3), the NA31 cryostat will be modified. The liquid-argon filling and emptying of the cryostat will be done by means of a cryogenic pump connected to the bottom of the cryostat.

We are presently studying how to pass a pipe through the internal and external vessels with low enough thermal losses. The design of the cryogenic scheme as well as the specifications of the vacuum pumps has also recently begun.

13.2.2.2 Modifications on the H1 cryostat

The HEC cryostat platform in the experimental zone has turned out to be too small to meet all the requirements imposed by the various tests. In particular the availability of a clean room area close to the cryostat has turned out to be rather crucial: Prior to placing the full set of modules into the cryostat a detailed check-out of all components including the electronics is essential.

Therefore we plan to enlarge the present platform to allow for a new cryogenic control system, for temperature and LAr purity monitoring as well as for the HV control system which has to be replaced completely. This requires a space increase of the platform of typically 2 m x 4 m. The clean area, shared in common with the EMEC community, will be designed soon. It will be ready for operation during spring 1997.

Finally the feedthroughs have to be adapted to the ATLAS design as well.

13.3 Cryogenic installation and control

13.3.1 Common cryogenics

The common cryogenic installation is designed to be used to simultaneously supply the liquids (LN_2 and LAr) to the three cryostats: EM barrel, EM end-cap and HEC.

To operate the three test cryostats a common cryogenic facility is proposed. It will allow cool down, filling with liquid argon, normal operation, emptying and heating to ambient temperatures and, if necessary, purification of liquid argon. These functions can be done in parallel. The various components of this cryogenic system are shown in Figure 13-4 and Figure 13-5 and listed in the following together with the major characteristics:

13.3.1.1 Liquid nitrogen system

- LN_2 dewar: minimum liquid fill quantity 30 m^3, operating pressure < 4 bars, equipped with pressurization system

- LN_2 transfer line: length 70 m, specific thermal losses < 3W/m

- LN_2 phase separator: volume 3 m^3, operation pressure < 4 bar

- LN_2 distribution valve box

- three LN_2 transfer lines connecting to the cryostats, lengths ranging from 25 m to 50 m.

13.3.1.2 Liquid argon system

- LAr dewar: liquid fill quantity approximately 25 m^3, operating pressure < 3 bar, equipped with a LN_2 cooled argon recondenser and with a pressurization system

- LAr transfer line: length 70 m, specific thermal losses < 3 W/m

- LAr distribution box: it is equipped with a phase separator having its own LN_2 argon subcooler and a cold centrifugal pump (pump speed 2000 l/h of LAr, maximum pressure head 4 bar)

- LAr purifier

- three independent LAr transfer lines connecting the distribution box to the cryostats, lengths 25 m to 50 m.

For reasons of safety and access for refilling by truck, the two large-capacity dewars (LAr, LN$_2$) are installed outside the EHN1 hall. The transfer of liquids to the experimental area is done via the two 70 m long vacuum insulated transfer lines.

Figure 13-4 shows a general outline of the hall with the location of the different components. Figure 13-5 shows the different flow schemes from the external dewars to the detectors, including the two recondensers (LN$_2$ and LAr), the purification system and the pump (see arrows). This scheme will allow very large flexibility in the use of the three separate cryostats. Provision is made to run with the three cryostats simultaneously.

13.3.2 Functioning

13.3.2.1 Standard running conditions

- Cool-down of a calorimeter module is done by conductive/convective heat transfer using a LN$_2$ cooled heat exchanger inside the cryostat. During the cool-down, the volume of the cryostat will be filled with gaseous argon (GAr).

- Filling is carried out via the LAr distribution box. The LAr withdrawn from the dewar is pumped into the cryostat by means of the centrifugal pump at a rate of 2000 l/h. The design of the LAr distribution box permits operational choices which are discussed at the end of this chapter.
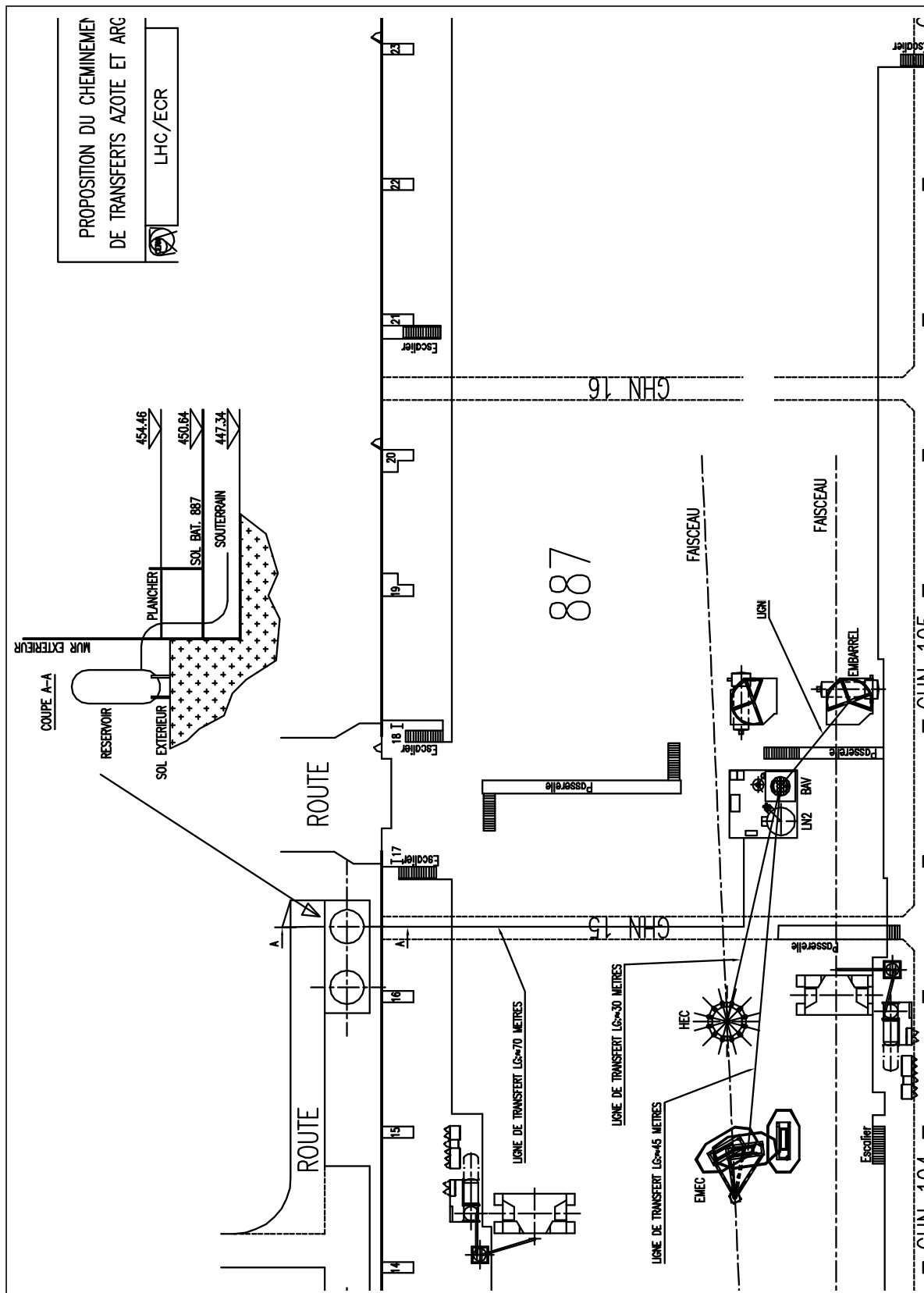
During cool-down, filling and normal operation liquid nitrogen is supplied to the heat exchanger with minimum vapour content. This is achieved with the intermediate N$_2$ phase separator from which only liquid is withdrawn and distributed via the LN$_2$ valve box.

- Emptying is started by slightly pressurizing the respective cryostat to get a small flow of LAr to the suction of the centrifugal pump. The pump will provide the required pressure head to complete emptying in a few hours.

- Purification of argon is done in the liquid phase with a cartridge of Oxysorb housed in an independent cryostat. The cartridge can be replaced if necessary.
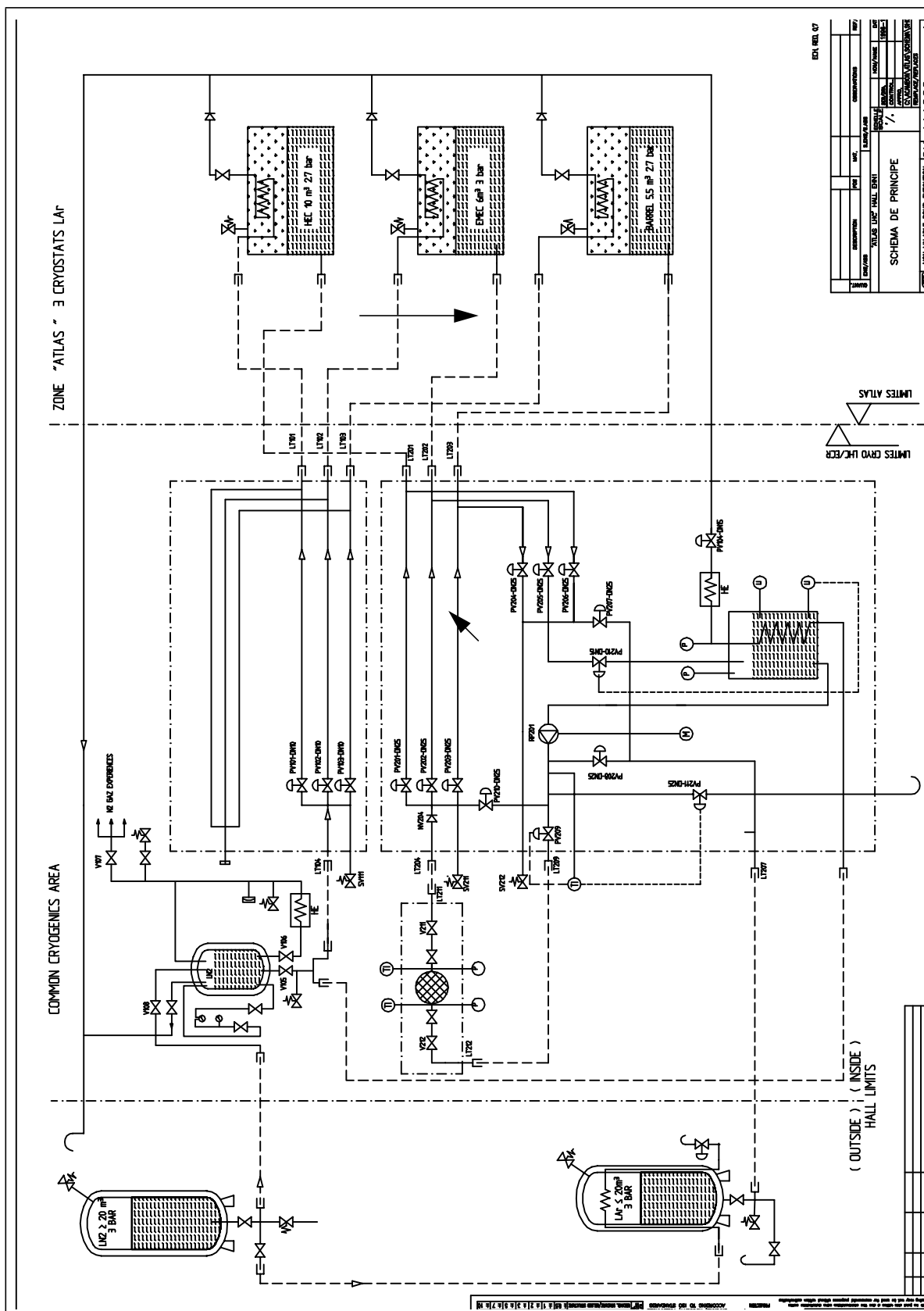
13.3.2.2 Design features of the LAr distribution box

The liquid argon distribution box contains the centrifugal pump which is a vital element for the functioning of the cryogenic system. At the suction side of this pump a phase separator of 0.2 m^3 volume allows the separation of liquid from the gas phase (a part of the liquid transfer is vaporized due to thermal losses in the rather long transfer lines). This gas is either partially vented to atmosphere or recondensed by a LN$_2$ cooled heat exchanger. This heat exchanger also allows a slight subcooling of the liquid phase, hence, further minimizing the risk of cavitation of the LAr centrifugal pump.

The design also permits flexibility in operation. While emptying a cryostat the LAr can be brought back to the large capacity dewar or be used to directly fill a second cryostat. In parallel, all or part of the flow can be purified during this operation phase.

Figure 13-4 Layout of the cryo-lines in the North Area, from the external tanks to the different LAr subdetectors.

Figure 13-5 Schematic view of the common cryogenic installation in the North Area. The dotted line, close to the cryostats, shows the limit between the common cryogenic installation and the detector local one.

13.3.3 Control and monitoring

13.3.3.1 Cryogenic scheme description

The control of the common cryogenic installation as well as of the three separate test-beam cryostats, aims on the one hand to avoid the presence of bubbles and on the other hand to reach a good homogeneity of the temperature in order to maintain a ΔT lower than 0.6° K.

Below we describe in some detail the operating conditions for the Barrel cryostat. Similar running conditions will also apply to the HEC and EMEC cryostats.

To satisfy the requirement of homogeneity, the liquid argon bath is maintained below its boiling point inside the cold vessel of the cryostat by means of a LN_2 cooling loop. The liquid argon bath is pressurized with a column of liquid on top of the cryostat. With this expansion vessel, the hydrostatic pressure obtained at the level of the detector will be 1.62 bar, which corresponds to a saturation temperature of 92° K.

The expansion vessel will be maintained at a constant pressure (1.25 bar) using an internal loop acting as an heat exchanger (condenser). It will also let the level of the liquid be maintained constant inside the cryostat.

To compensate for small leaks it is foreseen to supply argon gas from a separate gas distribution panel. This separate gas circuit will also be used when pre-cooling the cryostat (pre-cooling heat exchanger).

The three heat exchangers will be supplied with boiling LN_2 in order to have a uniform heat distribution along the exchanger. The LN_2 will be maintained at a temperature of approximately 87° K (corresponding to a pressure of 2.7 bar).

Figure 13-iv shows a simplified cryogenic scheme of the Barrel cryostat. It shows on the left side the LN_2 supply line with the three heat exchangers (one being inside the expansion vessel), the separate argon gas line used for rinsing and pre-cooling with the corresponding valves (FV059), as well as the LAr supply pipe on the right with its valves (FV255). All the valves and probes will be controlled or monitored using a centralized control system (see next section).

13.3.3.2 Automatic control system

The cryogenic processes that will be used in the Test Beam area by the three different cryostats will be very similar, if not identical. Such uniformity is desired, not only to standardize hardware and software but also to minimize the manpower for the operation and maintenance of the cryogenic installations and the controllers over a period of many years.

The automatic control system has to manage the cryogenic processes of the three cryostats (EMB, HEC, EMEC) as well as of the common cryogenic installation (see Section 13.3.1). The different components (valve control, probes, ...), located on different devices (the three cryostats, the valve box and the dewars) will be read out centrally. The data are then centralized and processed by means of a commercial controller (C370 from CEGELEC).

Figure 13-6 shows the logic diagram of the control system, with the different components (temperature, electrovalve and I/O modules) located on the different subsystems and linked together with the local network (FIP) as well as four Personal Computers (PCs), one in the common area and one per control room.
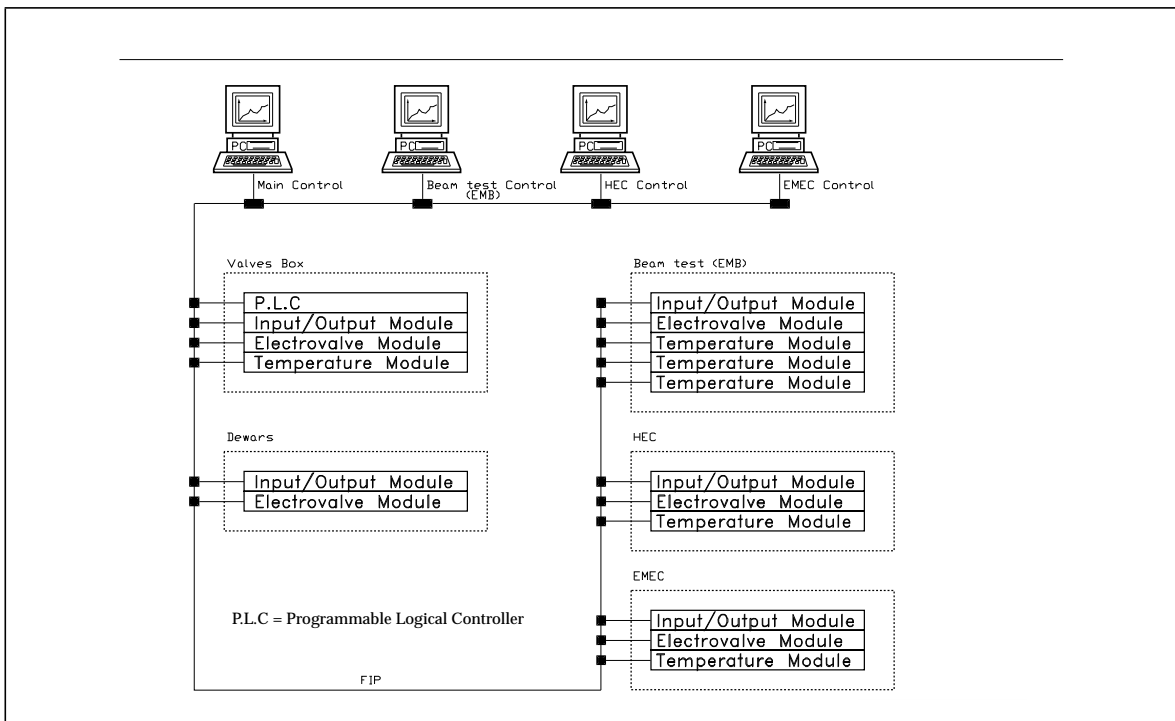
Figure 13-6 Logic diagram of the general common cryogenic system.

The display of the status of each of the cryostats as well as the attached commands can be visualized and operated by means of the Supervisor ('mimic display'). The overall control of the installation will be possible only from the central computer in the common area. Some local commands as well as the display of all the information will also be available on a PC, located in the control room of each subdetector.

Moreover, a more general control system will be installed inside the common cryogenic area, near the valve box (see Section 13.3.1) to give to the person with overall operation and maintenance responsibility, a global view of the installation and the possibility to set/modify the main parameters.

On the one hand, all these elements will be connected via a local network (FIP) and on the other hand, all control and command parameters can be accessed via Ethernet or simply by using the telephone line. Some critical data, like pressure and temperature, are then available and can be recorded. Nevertheless, and in order to visualize information using the standard display, a PC is desirable.

13.4 Installation plans, schedules, and beam time requests

13.4.1 Electromagnetic barrel
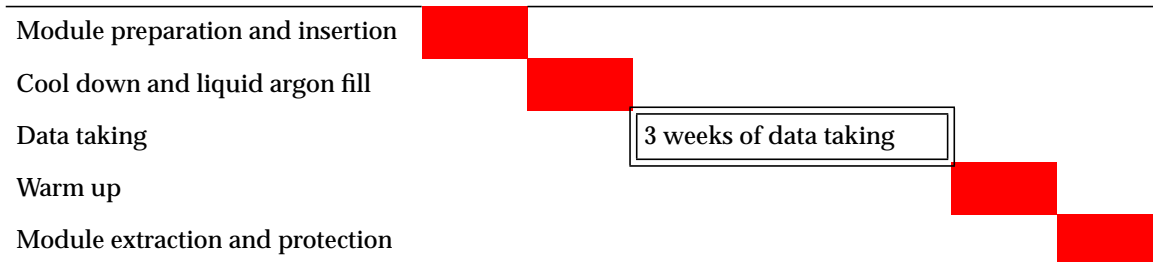
Module 0 will be thoroughly calibrated, first late in 1997 and extensively in 1998. Then only a fraction of the production modules will go through a full calibration procedure into a test beam. The main purpose of the calibration runs is to establish the uniformity of response within a module, and to verify the module to module reproducibility to typically 0.5% or better.

The modules are transported inside a protection frame from the different assembly sites to the EHN1 hall where they will be tested. Moreover, they will be mounted onto a backbone and rings as explained in Section 6.8. The backbone has to be dismounted in order to insert the module inside the test beam cryostat for the test and calibration procedures.

If most of the time, between the assembly and the final mounting into the ATLAS barrel cryostat, the lead plates of a module are positioned vertically in order to avoid any sagging, we have to rotate the modules after removal of the backbone to a horizontal position for the beam tests. A sequence of operations which will be performed in the clean area (a dust-free space in the garage position) has been worked out in order to minimize the mechanical constraints. The reverse operations will be done after the end of the calibration period, the module being mounted onto the backbone, stored vertically in the protection frame and shipped to the final assembly area in the West Hall at CERN.

The time needed for an extensive test of Module 0 (896 cells in the middle sampling) will be long. We plan a first run by the end of 1997, a technical run at the beginning of 1998, and finally a full scan in mid-1998. The time needed to test the production modules, during the series construction and assembly phase, will be limited to one run period per module. During these routine tests we plan to do a full η scan over a limited number of ϕ positions. Taking into account the time needed to move the calorimeter, to check the quality of the data, and to perform from time to time some calibration runs, this would correspond to ten days of fully efficient data taking at one energy. An energy scan on a few points will also be performed. The total time estimate, including preparation and dismounting, to test one given module is shown in Table 13-1.

Table 13-1 Time estimate for the test of a module (one black box corresponds to one week)

Module preparation and insertion	
Cool down and liquid argon fill	
Data taking	3 weeks of data taking
Warm up	
Module extraction and protection	

With a beam available over six months, we can expect a maximum of three useful periods per year.

13.4.2 Electromagnetic end-cap

The 16 modules of the EM end-cap will be tested in the cold. Only four to five modules will go to the beam to be calibrated using electron beams of different energies in the H6 beam line. The platforms (see Figure 13-2 and Figure 13-3), allow for a full scan of the module in the two η and ϕ directions.

13.4.2.1 Handling of the modules and insertion into the cryostat

To install the different modules inside the modified NA31 cryostat in a safe and clean way, the following scenario has been worked out. The module will arrive wrapped up from the assembly line. Once in the North Area, the spatula (see Chapter 7) will be attached at 90° to the support platform used for the internal movement inside the cryostat. The device is then rotated by 90° using the rotator available in the North Area. After having removed the spatula, the module is transported inside the clean area on a special table, located under the NA31 support frame. The

cryostat cover plate is then put into position, the screw mounted and the module cabled to the feedthroughs. The cover plate and the attached module are then moved onto the cryostat located in the garage position. This operation will be done using the crane. After having bolted the cover plate, made the vacuum tests and cooled down, the cryostat is moved to the beam line where we start filling with LAr.

13.4.2.2 Installation and beam schedules

- Installation work for 1997

In order to have a first test of module 0 in September 1997, the primary deadlines for the cryostat and cryogenic installations are the following:
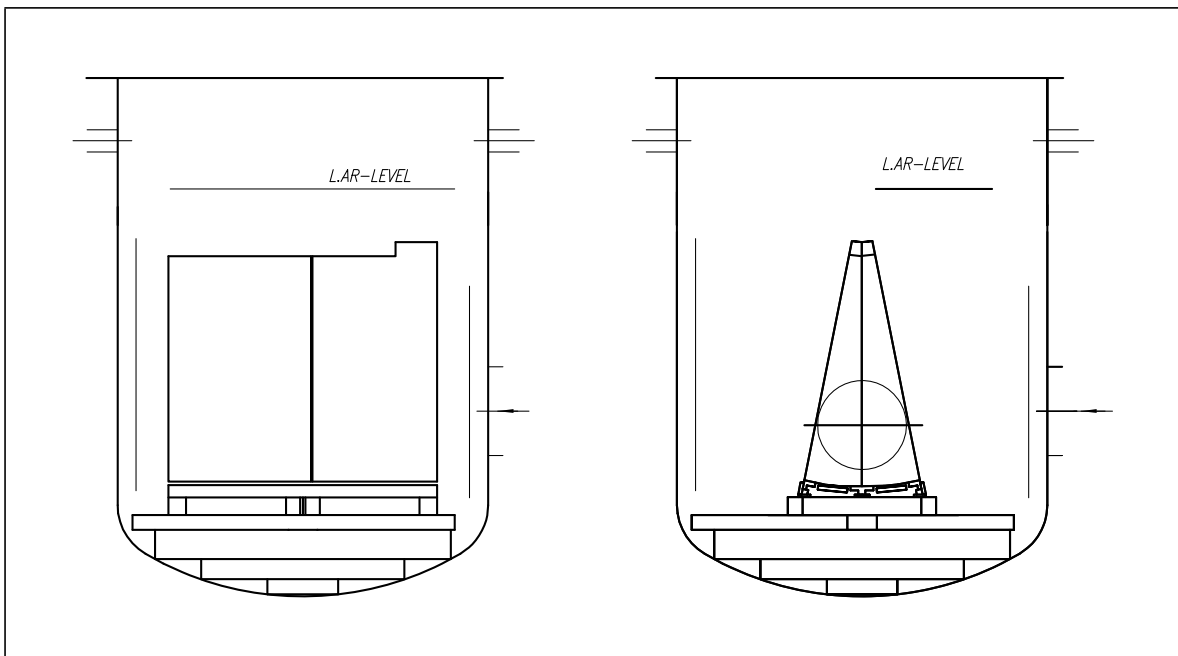
- design, fabrication and shipping of the external and internal platforms: October 1996 to May 1997

- mechanical modifications on cryostat, H6B area preparation, clean area: January to March 1997

- installation of the platforms and tests (pressure test, cold tests and automatic movement control): June 1997

- Feedthroughs (signal and HV), electronics (see Chapter 10) and DAQ: June to July 1997

- Cryogenics and control: June 1997

- Time estimates for run preparation and run

A first estimate of the time needed for all the operations mentioned in Section 13.4.2.1 is typically two weeks. Similarly two weeks are needed to warm up and extract the module, which then will be moved to the West Hall for the final assembly. To scan all the cells in the two η and ϕ directions with an electron beam of 200 GeV and to have an energy scan from 10 to 200 GeV on a few positions, a beam time of three weeks is needed.

The total time needed to test one module is of the order of seven weeks. This is similar to the estimates made for the barrel tests (see Table 13-1). Given the actual planning of the SPS proton periods, it seems possible to test at maximum three modules, corresponding to a total of nine weeks of beam time, as mentioned in Table 13-2 for 1999. For 1998, we plan only two periods for an extensive check of Module 0.

13.4.3 Hadronic end-cap

All HEC modules have to pass a cold test after the final assembly. One-eighth of them will be tested in the H6 beam at CERN, using electrons, pions and muons in the energy range $10 < E < 200$ GeV. Figure 13-7 shows the longitudinal and lateral view of the planned test set-up. The impact point can be varied in a scan range of $\pm$ 30 cm in the horizontal and vertical direction, respectively, by the appropriate movement of the cryostat or vertical bending of the beam. For Module 0 tests we foresee a set-up corresponding to $|\eta| = 1.8$ in the final ATLAS detector, including an exact matching of the impact point. In reality it turns out that in this position the energy measurement of hadrons is heavily affected by leakage. Because the main goal of the beam tests of the production modules is the quality control of modules produced, high sensitiv-

Figure 13-7 Lateral and longitudinal view of the set-up for the stand alone HEC test.

ity to energy resolution and calibration is an important issue. Therefore it is planned to do these tests in a horizontal position, thus minimizing any leakage effects in the energy reconstruction.

The main goals of these stand-alone HEC tests are:

- to obtain the calibration constants for electrons and pions for a predefined grid of impact points and energies. Any variation in the production process beyond tolerances will finally manifest itself in deviations from the expected calibration constants.

- to obtain the energy resolution at the various impact points and energies. Also here any hardware deficiencies will show up immediately.

- The variation of these results will yield a first estimate of systematic effects in this part of the detector. These systematic effects should be kept in mind when comparing experimental data with Monte Carlo data.

Testing four modules at a time will thus require four beam tests with typically four weeks running time per test period. The beam tests will be spread uniformly during the production phase. Our present best estimate is summarized in Table 13-2.

13.4.4 Forward calorimeter

The Forward Calorimeter Group plans to test one quarter of a copper (FCAL1) module followed by one quarter of a tungsten module (FCAL2) in May of 1998. These tests shall use the H1 cryostat in the H6 beam line. The primary goal of this test is to measure the response of the FCAL to electrons and, for the first time, contained pions. Energy linearity, energy resolution, and position resolution as a function of energy, angle, and upstream material will be determined. Final mechanical design concepts will be used in the construction of these modules in order to gain practical experience ahead of construction of the full FCAL modules. These quarter modules will be reused in the combined test in 2001.

For this test four weeks of running are requested, separated into two periods of two weeks each with a break of less than two weeks. In the first period the FCAL2 module will be exposed to electrons and pions. The second period is intended for the full test of both modules.

In 2002 one full FCAL will be exposed in the H6 beam, again in the H1 cryostat. The three FCAL modules will be mounted in their support tube, but the cone ahead of the support tube will not be attached so that the assembly can fit in the cryostat. Absolute calibration constants for electrons and pions will be determined in the low-energy regime.

13.5 Combined runs

13.5.1 Electromagnetic and hadronic barrel calorimeters

- At the SPS

A common run with both the liquid argon and tile calorimeters is scheduled. This common activity is mostly meant as a calibration with hadrons for the full ATLAS calorimetry.

The test beam cryostat with a module inside is taken with the crane from the garage position in the H8B area and put in front of the Tile calorimeter in the H8A area (see Figure 13-ii). It is mandatory that the cooling down be undertaken after the cryostat is in position and reconnected to the cryo-lines. Since the installation and the cooling-down operation will take approximately one month, the common ATLAS run should be scheduled at the beginning of the proton period in April. Our present schedule for this run is the year 1999 (see Table 13-2).

Figure 13-ii shows the two combined LAr and Tile calorimeters as they will be mounted on the common platform, the cryostat being mounted in front of the Tile calorimeter. Owing to some space limitations, the scan in η is somewhat limited at small values, starting at $\theta = 5°$ (which corresponds to $\eta = 0.09$). At higher values, the scan will be possible up to $49°$, i.e. up to the end of the module.

In ϕ, no scan will be possible since the two calorimeters do not have the same rotation point due to a different geometry between them compared to the ATLAS setup. Since a platform with two independent movable tables is far too expensive, the complete η scan will be done at a fixed ϕ position only. In other words the beam time spent as a common run is not sufficient for an extensive and complete calibration of the calorimeter module as in the case of a stand-alone calibration run.

- At the PS

Experience gained by the UA2 and CDF collaborations shows that the Monte Carlo simulation of the calorimeter response to very low energy hadrons is not satisfactory. Therefore a low-energy calibration run with beam will be necessary before the LHC is operational. A possible inter-calibration run at the PS, down to energies below 1 GeV, is under discussion. The consequences of moving the equipment (cryostat and cryogenics) from the North Area to the PS have not yet been considered, either in terms of manpower, or in terms of cost. Such a run, if proven feasible, could take place around 2000/2001 right at the beginning of the proton period.

13.5.2 End-cap combined runs
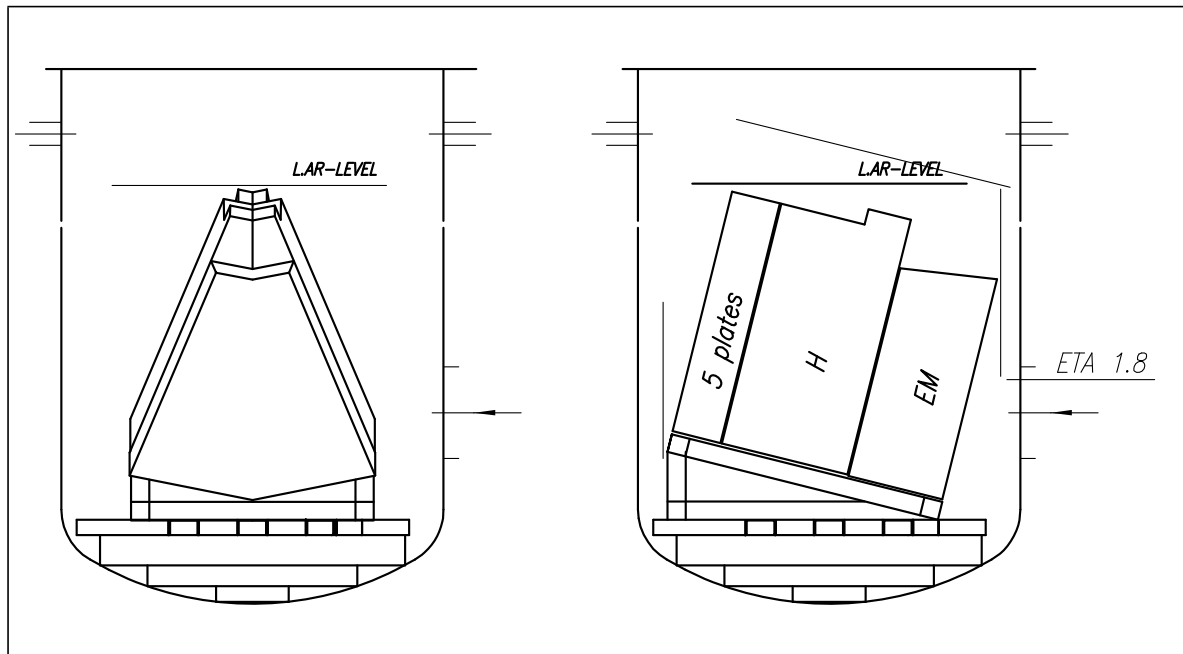
The individual beam tests of the electromagnetic, hadronic, and forward calorimeters provide an important assessment of the production quality and a stand-alone calibration of these calorimeters with regard to electrons and pions. On the other hand, calibration constants for electrons, pions, and jets are required for the global end-cap calorimeter. Therefore combined beam tests are planned with the following goals:

- to obtain intercalibration constants for electrons and pions in the energy range accessible in test beams. A detailed comparison with MC simulation opens the possibility to extrapolate via MC to jets at high energies.

- to study in detail the transition regions between different calorimeters. This is particularly important to gain precision on the determination of missing energy and to understand the jet tagging efficiency in the high $|\eta|$ region.

For practical reasons all tests are planned to be carried out using the cryostat for the hadronic calorimeter tests in the H6 beam line at CERN. This causes some spatial and operational limitations which have to be faced. On the other hand, they do not prevent us from achieving the goals mentioned above. A scan region of ± 30 cm in the horizontal or vertical direction, respectively, can be covered by appropriate movement of the cryostat or vertical bending of the beam respectively. In detail we envisage the following two combined test set-ups described below.

13.5.2.1 Combined test of electromagnetic and hadronic calorimeters

Figure 13-8 shows the longitudinal and lateral view of a combined test of the electromagnetic
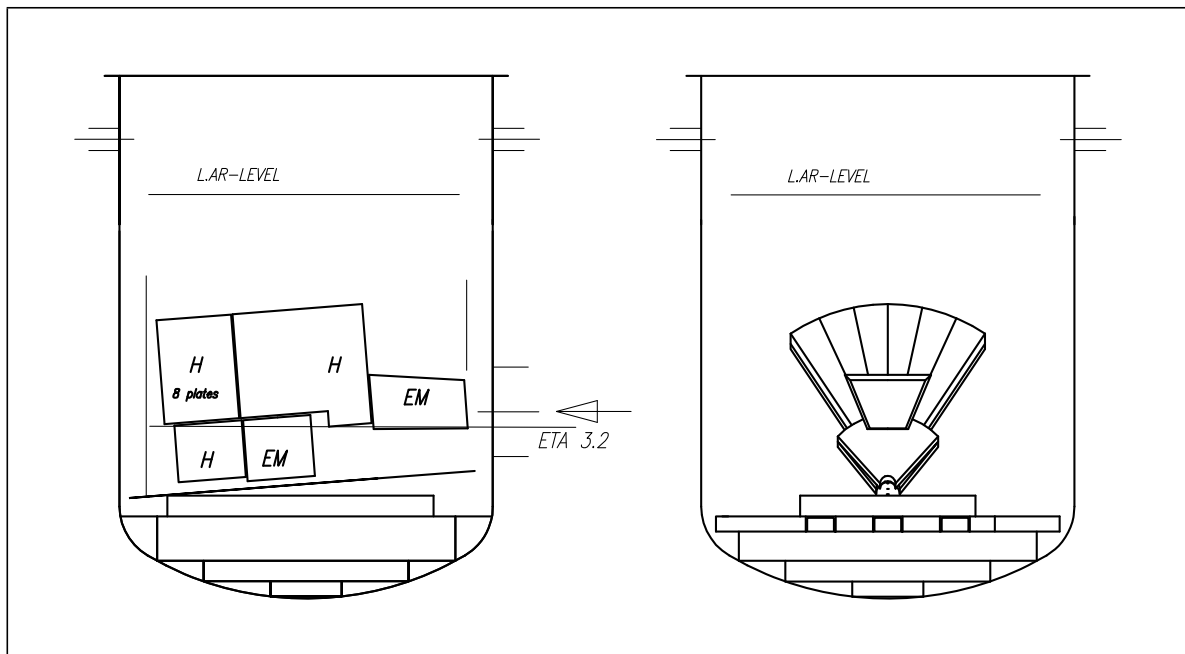
Figure 13-8 Lateral and longitudinal view of the set-up for a combined test of the electromagnetic and hadronic calorimeter.

and hadronic calorimeter in the region of $\eta \sim 1.8$. In ϕ a section of $1/8$ of the outer electromagnetic calorimeter wheel is combined with four full-size modules (each $1/32$ of a full wheel) of the first wheel of the hadronic calorimeter. For the second hadronic wheel the spatial limitations

do not allow the use of the standard size hadronic modules. The central region only can be equipped with two special modules with reduced longitudinal extension: 5 copper plates rather than 16. Given the lower energy regime in the test beam, the longitudinal leakage of hadronic showers should still be at an acceptable level.

13.5.2.2 Combined test of electromagnetic, hadronic, and forward calorimeters

Figure 13-9 shows the longitudinal and lateral view of a combined test of the electromagnetic, hadronic, and forward calorimeters in the region of $\eta \sim 3.2$. In ϕ a section of 1/8 of the inner wheel of the electromagnetic calorimeter is combined with 1/4 of the electromagnetic and 1/4 of the first hadronic section of the forward calorimeter. The forward calorimeter modules, i.e.

Figure 13-9   Longitudinal and lateral view of the set-up for a combined test of the electromagnetic, hadronic and forward calorimeters.

the copper and the first tungsten section (FCAL1 and FCAL2), will be used prior to the combined run, in the module 0 test run of the forward calorimeter (1998). To have a reasonable lateral acceptance for hadronic showers, six modules of the hadronic calorimeter have to be installed. Again, for the second wheel, only half the normal longitudinal extension (eight copper plates) is feasible. As a consequence of the larger coverage in ϕ, all modules have to be of a reduced size in R. In conclusion, this test requires 12 special hadronic modules. Owing to the large effort required, the test is not scheduled before 2001.

A further test of the combined performance of all the calorimeters in the end-cap region is envisaged in the X5 beam line, when a full end-cap is assembled (see Chapter 14). Detailed feasibility studies have still to be done.

13.6 Summary of test beam requirements

The intensive tests of the different module 0's as well as the quality control and the calibration of the production modules will require an important amount of beam on both the H8 and H6 beam lines. Our present estimate is summarized in the Table 13-2 for the years 1997 to 2002.

We also mention in this table the combined runs we plan to have in order to inter-calibrate the LAr barrel calorimeter and the Tile calorimeter, both using high-energy (300 GeV on H8) and, possibly, low-energy (below 1 GeV at the PS) pion beams.

The total number of weeks the LAr community requests is very high in the years 1999 to 2001. Obviously data-taking will go in parallel on at least two different beam lines at a time. This will be a very important effort for the groups involved.

If on top of the LAr request we add the beam time needed by the other ATLAS subdetectors also running their validation tests on H8, the H8 beam time request from ATLAS, in terms of main user of the beam line, amounts to values per year close to 30 weeks between 1998 and 2000. This is higher than the actual running time of the SPS with protons. Consequently, even if the H8 beam line is fully attributed to ATLAS, beam sharing will produce shortening of the initial requests. On H6, the situation is by far better, with a peak of 20 weeks in 1999 and 2000.

Table 13-2 H8 and H6 beam request for the next six years (units are weeks)
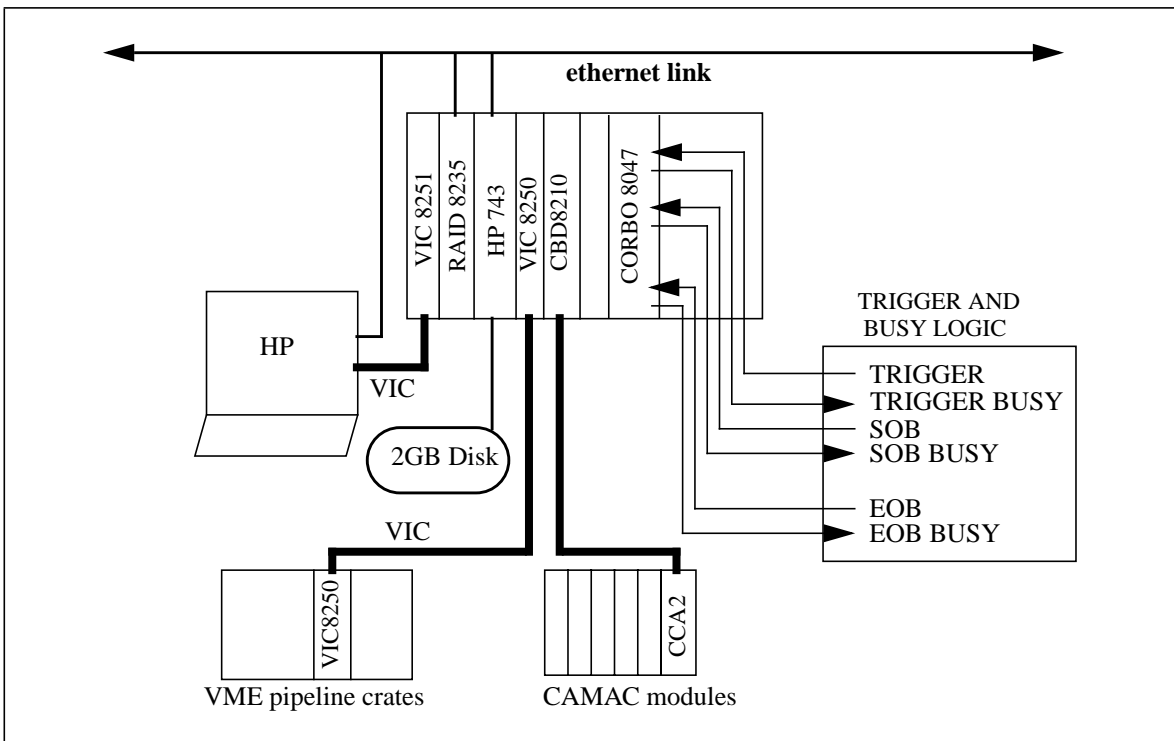
Beam line / Detector	1997	1998	1999	2000	2001	2002
SPS H8 / Barrel	3	7	7	7/4	4	
H8 / Common ATLAS run			6			
PS / Calo. intercalib.				0/6	6/0	
SPS H6 / EM end-cap	3	7	9	6	6	
H6 / HEC	6	6	6	3		
H6 / FCAL1,2		4				8
H6 / Combined runs			4	4	8	
Total	12	24	32	20/23	24/18	8

13.7 The test beam data-acquisition system

The data-acquisition system which we will use during the forthcoming years for the test of the calorimeter modules is based on the RD13 developments [13-3] and adapted to the specific needs of the test beam and of the LAr calorimeters.

The basic hardware configuration is presented in Figure 13-10. There are three processors, one workstation (HP), and two VME processor modules.

The user interface, the run control related processes (run control, database selection and updating) and the monitoring tasks run on the workstation. The local controller and the readout, sampler and calibration processes run on one of the VME processors, and on the other runs the

Figure 13-10 Testbeam DAQ configuration.

processes related to the remote data recording. The readout from the pipeline VME crates is implemented through a VICbus.

The run control system is able to work either in stand-alone mode (LAr detector alone) or in combined mode receiving data from several detectors at the same time [13-4]. It is based on commercially available tools for message handling (ISIS) and a database management system (QUID). The configuration data are stored in three databases (software components database, detector parameter and run control database, and hardware configuration database). The run control system is composed of three modules (processes), one is the main DAQ users control interface (Motif based) and the others are two processes interconnected in a hierarchical master slave configuration (global run controller and data flow protocol controller). A detailed description of the three modules mentioned can be found elsewhere [13-3].

The readout hardware is based on VME modules. At the initialization stage the run and detector parameters are read from the database. The readout process is based on a finite state machine (FSM) assuming a detector readout which takes place on an event-by-event basis. After each trigger the corresponding event is built and other specific actions are performed. In calibration mode data are taken outside the beam and after each event-building the conditions for the next calibration trigger are prepared (DAC values, delays, pulsers, etc.).

During the different calibration tasks (Pedestal, Test Pulse, Beam chambers), all the events are monitored. The tasks produce histograms which can be viewed using a Histogram Presenter integrated in the system, and special calibration files.

The recording of the data is done using a remote mode. It uses the central data recording (CDR) system provided by CN/PDP group [13-5]. CDR is on top of a Client-Server mechanism which fetches the run files locally written on the local disk of the DAQ and sends them over the Ethernet via the TCP/IP protocol to the staging machine in CN where files are copied to tape streams (mainly on DLT tapes).

Finally, a process running on a VME readout processor controls the cryostat horizontal and vertical displacements. It uses the RS232 port on the VME readout processor module to communicate with the state machine which controls electrical gears to move the cryostat.

This scalable system can also easily be adapted to any further development done by the ATLAS DAQ group and eventually makes the testing of new components of the final DAQ system possible.

This data acquisition system has been successfully tested during two data-taking periods in 1996 when running on H8 both in a stand-alone and in a combined mode. In the future this system will be used to read out the EM barrel, the EMEC and the HEC detectors. Most of the hardware has already been purchased and the system will be installed and tested before July 1997.

13.8 Cost and PBS

13.8.1 Present cost estimates

Table 13-3 summarizes our present knowledge of the cost for the installation of the three LAr test beam areas in the North EHN1 hall. It has been subdivided into four sections; one per detector and one for the common cryogenic installation. Detailed information on the sharing between institutes will not be mentioned here.

Table 13-3 Cost summary for the test beam activity

ITEM	Main topics	Cost (kCHF)
H8 Barrel cryostat	Cryostat and its equipment	700
	On detector cryogenic equipment and control	83
	Clean area (including crane)	100
	Feedthroughs (signal and HV)	243
	TOTAL	1126
H6 EM end-cap cryostat	Mechanics, including both platforms	105
	NA31 cryostat modifications	30
	On detector cryogenic equipment and control	105
	Clean area	35
	Feedthroughs [signal (warm) and HV]	60
	TOTAL	335
H6 HEC and FCAL	Mechanics: Insertion structure and platform extension	40
	On detector cryogenic equipment and control	105
	Clean area	40
	Feedthrough	20
	TOTAL	205
COMMON Cryogenics	Civil engineering	30
	Cryo-lines	50
	Cryogenic pump and valve box	160
	Cryogenic control: automaton part	65
	Purification system	30
	TOTAL	335

No precise estimates have been made yet for the additional cost due to the common ATLAS runs. Part of this will come from the extension of the existing Tile platform to support the LAr Barrel cryostat, part from the installation on both sites, at the SPS and the PS. This additional cost will be mainly covered by the ATLAS General Test Beam budget. Similarly, no estimate has been done for the test in X5. On the other hand, no additional costs are actually foreseen for the combined end-cap tests which are scheduled over the years 1999-2002.

13.8.2 Product breakdown structure (PBS) for the test beam activity

Since the Test Beam is not part of the general detector PBS (see Chapter 16), the PBS and Extended PBS for all the activities related to the test beam is given in Figure 13-11 and in Table 13-4.
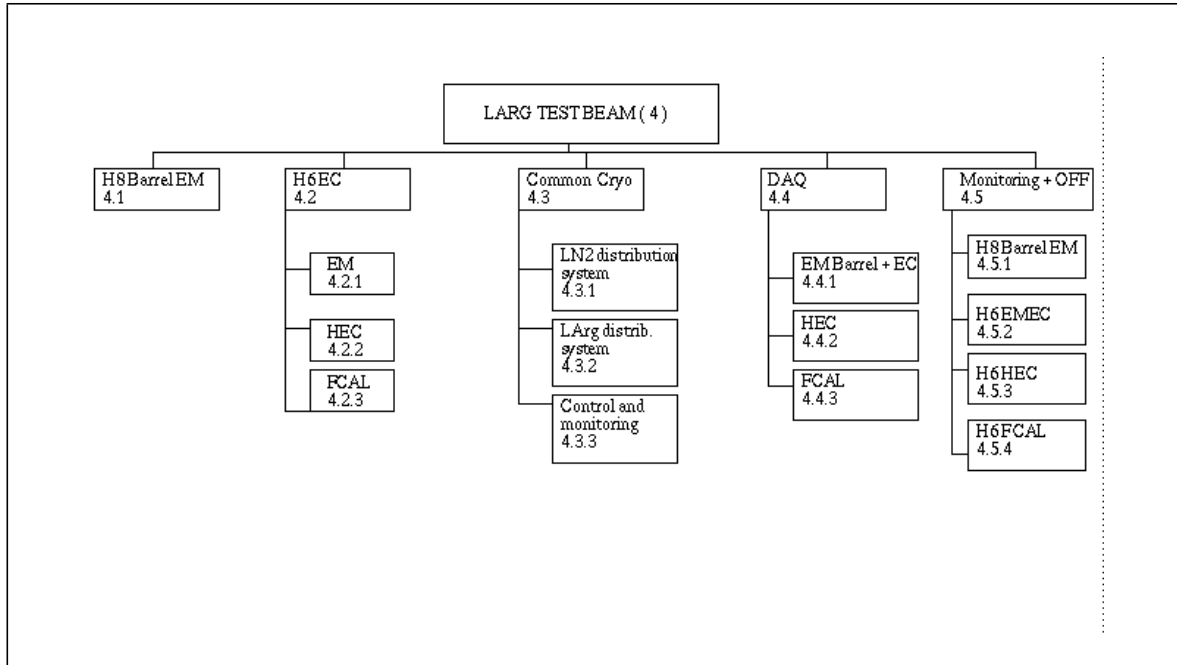
Figure 13-11 PBS relative to the Testbeam activity.

13.9 References

13-1   H. Burkhardt et al., CERN-EP/87-166.

13-2   G. Bellot et al., Cryostat group, "Dossier de conception: Cryostat Test Barrel", Note LAL-SECAP 96-163.

13-3   RD13 Collaboration, Status Report of a Scalable Data Taking System at a Testbeam for LHC, CERN/LHCC 95-47, 1995.

13-4   The Data Acquisition System of the ATLAS Combined Testbeam in April 1996, ATLAS Note DAQ-NO-058, 1996.

13-5   Central Data Recording, RD13 Note 160, 1995.

Table 13-4 Test beam extended product breakdown structure

4. LAr Test Beam PBS number and PBS item	List of related items	Responsible institute
4.1 <u>H8 Barrel</u>		
4.1.1 Mechanics		
4.1.1.1 Platform	Design and Fabrication Preparation of the H8B zone	Dubna/CERN CERN/CEA-Saclay
4.1.1.2 Insertion and extraction tools	Design and Fabrication	Dubna/CEA-Saclay
4.1.1.3 Table for combined runs	Design Fabrication	CERN (SL) CERN (SL)
4.1.1.4 Barracks	Modification and reinstallation	CERN
4.1.2 Cryostat		
4.1.2.1 Vessel	Design and test Installation Auxiliary equipment Procurement	LAL-Orsay LAL-Orsay LAL-Orsay/CERN IN2P3
4.1.2.2 Argon excluder		CERN
4.1.2.3 Expansion vessel	Design, fabrication and installation	CEA-Saclay/LAL-Orsay
4.1.3 Cryogenics		
4.1.3.1 Cryolines and valves	Procurement of valves Design, test and installation Maintenance	CEA-Saclay/.. CERN/LAL-Orsay/CEA-Saclay LAL-Orsay
4.1.3.2 Control system	Design Installation, test, maintenance Operation	CEA-Saclay CEA-Saclay LAL-Orsay
4.1.3.3 Monitoring probes	Temperature Purity	
4.1.4 Feedthroughs		
4.1.4.1 Cold signal FT's and pedestal	Design and fabrication Installation Pig tails procurement	BNL/Canada BNL LAL-Orsay
4.1.4.2 HV FT's		LAL-Orsay
4.1.5 Clean room	Design, procurement, installation	CEA-Saclay
4.1.6 Trigger and beam monitoring		LAL-Orsay/CERN

Table 13-4 Test beam extended product breakdown structure

4. LAr Test Beam PBS number and PBS item	List of related items	Responsible institute
4.2 H6 end-cap		
4.2.1 Electromagnetic end-cap		
4.2.1.1 Mechanics		
4.2.1.1.1 Platforms	Internal and external movement Control and monitoring of the movement	Novosibirsk/CERN CPPM - Marseille
4.2.1.1.2 Cryostat	Modifications of the NA31 cryo- stat H6B area preparation and instal- lation	CERN/CPPM CERN/Novosibirsk
4.2.1.1.3 Overturning tool		CPPM/Novosibirsk
4.2.1.2 Cryogenics		
4.2.1.2.1 Cryolines and valves	Procurement of valves Design Installation Maintenance	CEA-Saclay/.. CERN/CPPM/CEA-Saclay CERN/CPPM/Madrid LAL-Orsay
4.2.1.2.2 Control system	Design Installation, test and mainte- nance Operation	CEA-Saclay/CPPM CEA-Saclay LAL-Orsay
4.2.1.2.3 Monitoring probes	Temperature Purity	
4.2.1.3 Feedthroughs	Principle design of warm signal FT and adaptation HV FT Installation and tests	BNL/Canada CPPM/Madrid
4.2.1.4 Clean room	Drawings, installation	CERN (SL)
4.2.1.5 Trigger and beam moni- toring		CPPM/CERN
4.2.2 Hadronic end-cap		
4.2.2.1 Mechanics	Installation and cabling	Canada/MPI/Dubna
4.2.2.2 Cryostat		MPI
4.2.2.3 Cryogenics		
4.2.2.3.1 Cryolines and valves	Procurement of valves Design Installation and maintenance	CEA-Saclay/.. CERN/CEA-Saclay MPI/CEA-Saclay
4.2.2.3.2 Temperature probes		Dubna
4.2.2.3.3 Purity probes		Mainz

Table 13-4 Test beam extended product breakdown structure
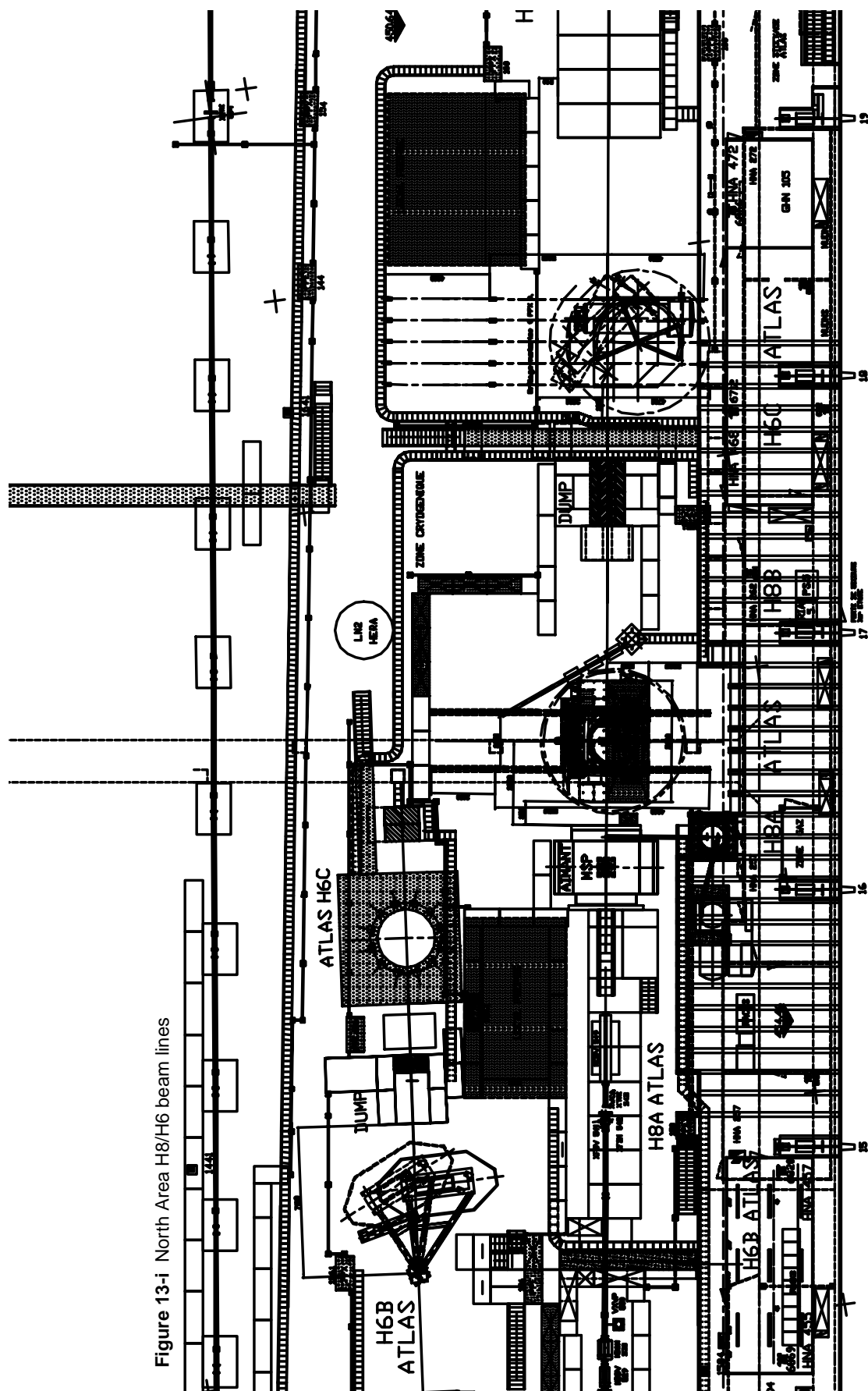
4. LAr Test Beam PBS number and PBS item	List of related items	Responsible institute
4.2.2.4 Trigger and beam monitoring	Calorimeter trigger MWPC Scintillators counters and fast logic	Heidelberg Dubna Protvino/Canada
4.2.2.5 Electronics		
4.2.2.5.1 High voltages		Wuppertal
4.2.2.5.2 Preamplifiers		MPI
4.2.2.5.3 Shapers		Dubna
4.2.2.5.4 ADCs		MPI
4.2.2.5.5 Calibration boards		Kosice/Mainz
4.2.2.6 Clean room	Drawings, installation	CERN(SL)
4.2.3 <u>Forward calorimeter</u>		
4.2.3.1 Cabling		Arizona/UBC
4.2.3.2 Cryostat		Arizona/UBC
4.2.3.2.1 Feedthrough		Arizona/UBC
4.2.3.2.2 Module support		Arizona/UBC
4.2.3.3 Cryogenics		Arizona/UBC
4.2.3.4 Trigger and beam monitoring	Fast trigger, beam scintillators, MWPCs and leakage calorimeter	Arizona/Toronto
4.2.3.5 Electronics		Arizona/UBC
4.2.3.5.1 HV		Arizona/UBC
4.2.3.5.2 Preamplifiers		Arizona/UBC
4.2.3.5.3 Shapers		Arizona/UBC
4.2.3.5.4 ADCs		Arizona/UBC
4.2.3.5.5 Calibration system		Arizona/UBC
4.3 <u>H8/H6 Common cryogenic system</u>		
4.3.1 LN$_2$ distribution system		
4.3.1.1 LN$_2$ external dewar		CERN (LHC)
4.3.1.2 LN$_2$ transfer lines	Design study, installation and test	CERN (LHC)
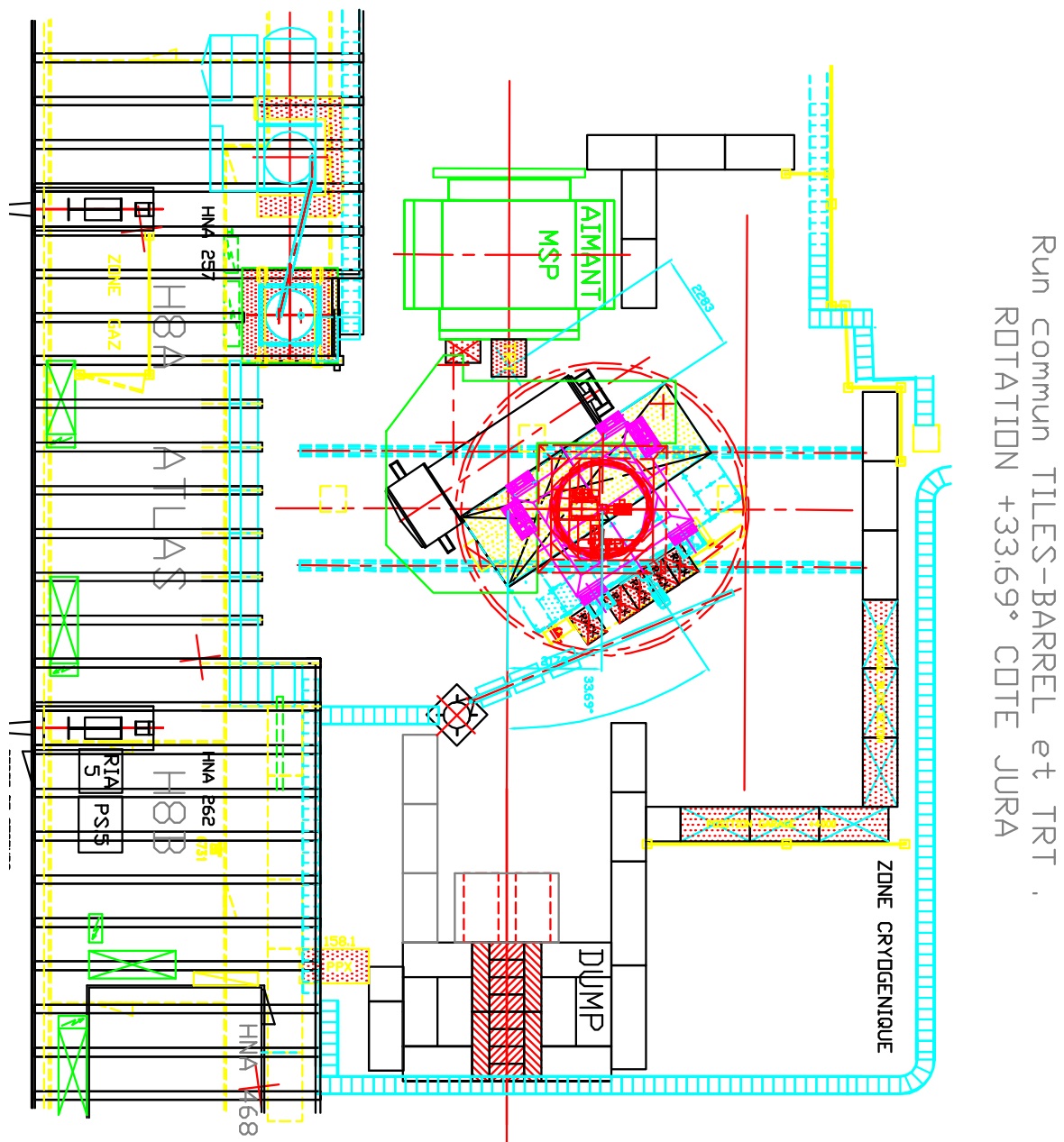
Table 13-4 Test beam extended product breakdown structure

4. LAr Test Beam PBS number and PBS item	List of related items	Responsible institute
4.3.1.3 LN$_2$ phase separator	Design study, modifications, installation and test	CERN (LHC)
4.3.1.4 LN$_2$ distribution valve box	Design study, modifications, installation and test	CERN (LHC)
4.3.1.5 LN$_2$ distribution lines	Design study Layout and connection to cryostats	CERN (LHC) LAL/CERN/CEA-Saclay
4.3.2 LAr distribution system		
4.3.2.1 LAr external Dewar		CERN (LHC)
4.3.2.2 LAr transfer lines	Design study, installation and test	CERN (LHC)
4.3.2.3 LAr distribution box	Design study Fabrication Installation and test Pump LAr purifier	CERN (LHC) CERN (LHC) via NIKHEF CERN (LHC) via NIKHEF CERN (LHC) CERN
4.3.2.4 LAr distribution lines	Design study Layout and connection to cryostats	CERN (LHC) LAL/CERN/CEA-Saclay
4.3.3 Control and monitoring system		
4.3.3.1 LAr and LN$_2$ distribution scheme	Design Instrumentation	CEA-Saclay CEA-Saclay
4.3.3.2 Control and monitoring system (automate)	Design study Installation	CEA-Saclay CEA-Saclay
4.3.3.3 Purity probes		Mainz
4.4 <u>Data Acquisition System</u>		
4.4.1 EM barrel and end-cap	Installation and test	CPPM/CERN/IN2P3
	Maintenance	CPPM/Novosibirsk
4.4.1 Hadronic end-cap	Installation and test	CPPM/Canada/MPI
	Maintenance	MPI/Dubna
4.4.3 Forward calorimeter	-Installation, test and maintenance	Arizona
	Programming	Montreal
4.5 Online monitoring and Offline		

Table 13-4 Test beam extended product breakdown structure

4. LAr Test Beam PBS number and PBS item	List of related items	Responsible institute
4.5.1 EM barrel		
4.5.1.1 Online		Annecy/..
4.5.1.2 Offline	Tools definition and preparation	Annecy/LAL-Orsay/...
4.5.2 EM end-cap		
4.5.2.1 Online		CPPM/Madrid
4.5.2.2 Offline	Tools definition and preparation	CPPM/Madrid
4.5.3 Hadronic end-cap		
4.5.3.1 Online		Canada
4.5.3.2 Offline	Tools definition and preparation	Canada/MPI/Dubna/ Kosice
4.5.4 Forward calorimeter		
4.5.4.1 Online		Arizona
4.5.4.2 Offline	Tools definition and preparation	UBC/Carleton/ Toronto/ Arizona

Figure 13-i North Area H8/H6 beam lines

Figure 13-ii LAr and tiles layout for the common run.
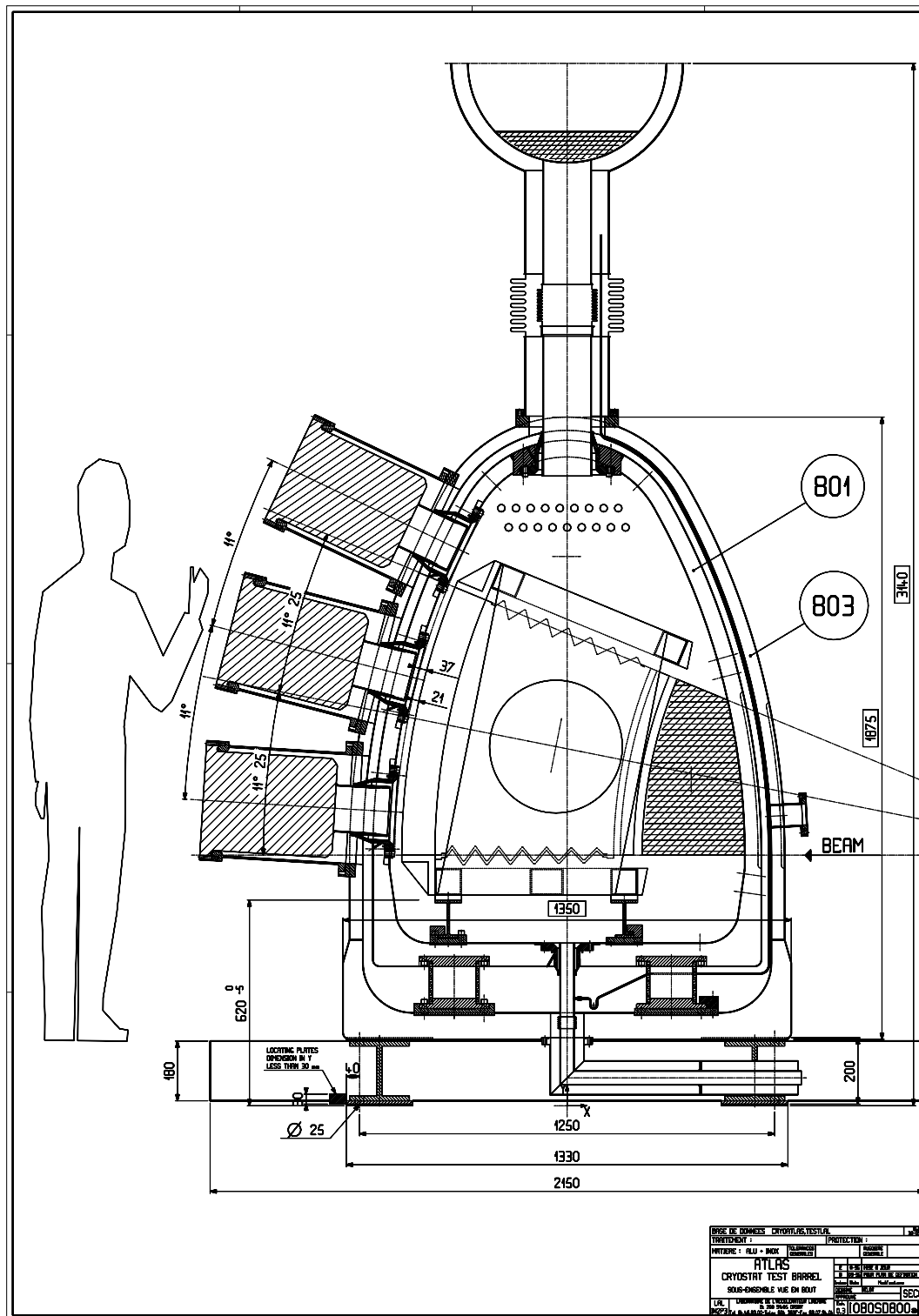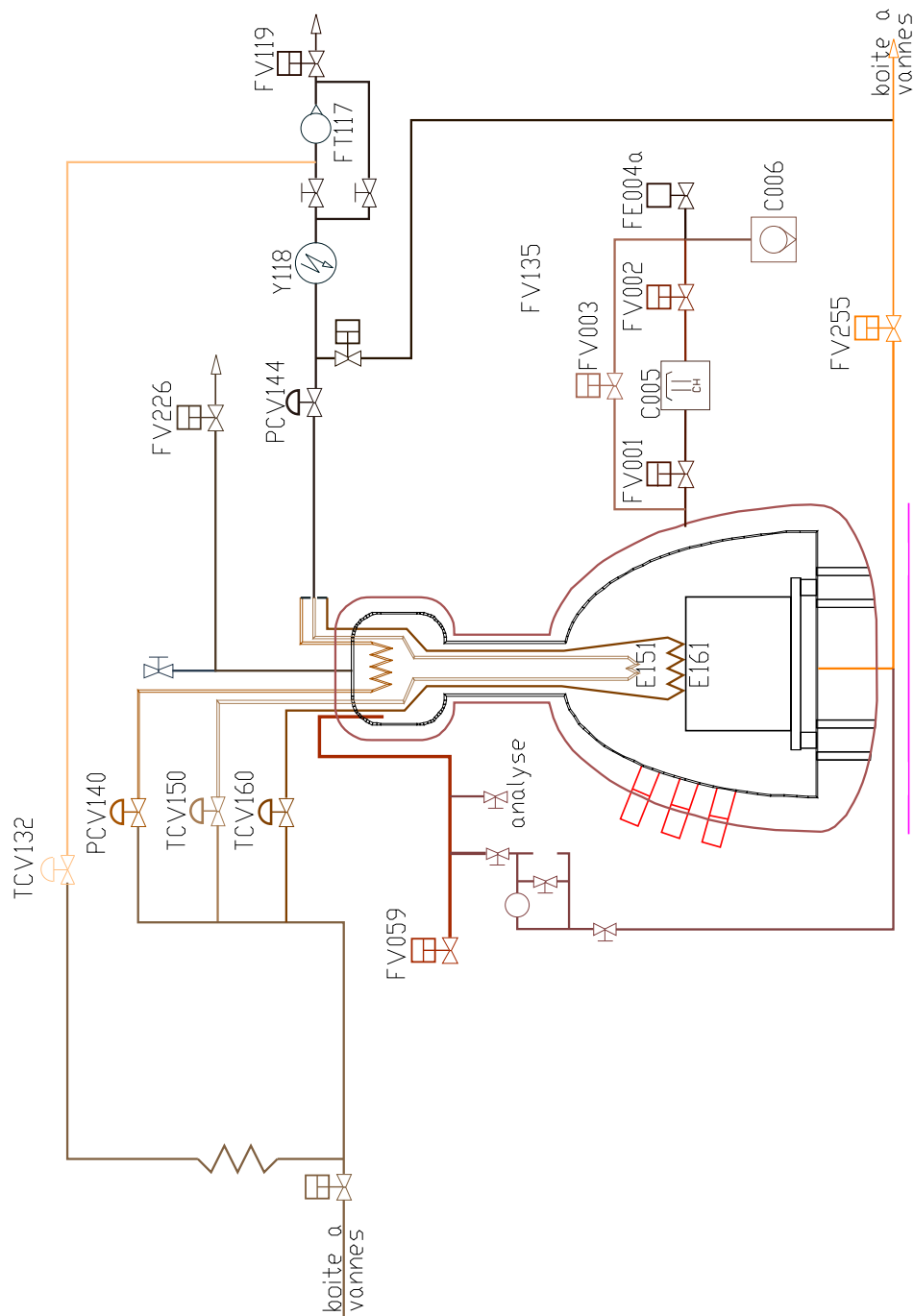
Figure 13-iii Transverse view of the barrel test beam cryostat.

Figure 13-iv Cryogenic scheme of the barrel cryostat.

14 The final assembly and cold tests in the West Area

The overall strategy of ATLAS is to concentrate all the assembly of the magnets and of the liquid argon final detectors and cryostats in the CERN West Area. Such activities require that the full hall be dedicated to this assembly and tests, to the exception of the X5/X7 beam areas.

14.1 Global description of the area

14.1.1 Spatial arrangement in the hall

The final assembly of the cylinders of the barrel calorimeter and of the wheels of the end-cap detectors should be performed in the close vicinity of the cryostats. Effectively the detectors should be directly integrated in the vessels as soon as they are ready. In addition the cylinders of the barrel cannot be transported without endangering their mechanical stability. As a conclusion, the final assembly of the detectors, the integration in the three cryostats, and the warm and cold tests of the full systems should take place in a unique area. Also, a single cryogenics system is foreseen for all of the three cold tests, which then have to be performed serially. The scenario is to share the West Area with the assembly of the magnets and thereby limit the size and corresponding costs of the new surface buildings at the LHC experimental point 1.

In order to liberate the necessary free space for such an assembly, the ATLAS experiment did not request any long-term use of the X5/X7 beams, and adapted its test beam strategy to the existing beams in the North Area, H6 and H8 [14-1]. For other reasons the CERN management decided to maintain the operation of the X5/X7 beams and to possibly upgrade their maximal energy. It was stated in the mentioned document that, if the X5/X7 beams should be maintained, ATLAS could consider asking for limited periods of beam time.

Keeping the X5/X7 beam lines alive of course diminishes the available floor space dedicated to assembly. The space is already smaller than originally foreseen. Further reduction of the space allocated to the general assembly and tests area of the LAr detectors would certainly be problematic. The necessary space for the LAr activities has been estimated as 2150 m^2.

The general layout is shown in Figure 14-1. Space has been reserved for:

- the barrel cryostat and the two half-cylinders of the calorimeter assembled vertically, on each side of the cryostat

- the two end-cap cryostats along with the space for the integration tooling and the assembly of the EM and hadronic wheels

- the solenoid

- the forward calorimeter

- some limited storage space.

The cryostats should be close to the cryogenics. More detailed plans should be issued for the overall arrangement of the cryostats and detectors taking into account the future arrangement of the cryogenics, the crane coverage, and the location of the doors.

14.1.2 General requirements

The assembly of the LAr detectors in their cryostats, the requirements for cleanliness, cold tests, and the large size of the objects impose several specific requirements on the assembly area. These are described below and are in addition to the need for services (cryogenics, power, compressed air, and cooling water).

Cranes:

The front wheel of the hadronic calorimeter weighs 68 tons and the back wheel 85 tons, not including the supporting table and the lifting tooling. That requires at least the full capacity of the 40 tons and of the 60 tons cranes available in the area. It would then be necessary to couple both cranes in order to lift these objects. The transport of the four hadronic calorimeter wheels will be done only once. A special derogation by CERN-TIS to exceed the load limit by 10% should be requested. It is therefore highly desirable that the total weight of the objects be less than 110 tons.

The height under the hooks of the cranes should be at least 8 m.

Clean areas:

The overall final assembly of the detectors and the cryostats should be done in a very clean area, such as a clean room of the class 10,000-100,000 [14-2]. This is a very large installation, given the size of the objects, cryostats and detectors, and the extensive use of overhead travelling cranes.

The best arrangement would consist of two large tents, one would protect the area for the assembly of the cylinders within the barrel, the other tent would protect the area for the assembly of the wheels within the end-caps. Inside these tents, overhead travelling cranes of 6 tons capacity will be needed. These cranes should be able to carry modules or sectors of wheels. For the barrel, the two cylinders will be assembled close to the cryostat, so the clean area could include the two cylinders as well as the cryostat. For the end-caps, the best would be to envisage the same set-up, including wheels, supporting frame and cryostat in the same clean area. In the latter case the use of the large 40 and 60 tons cranes would require that the ceiling of the area be provisionally removed and that the full modules be protected.

Access to the hall:
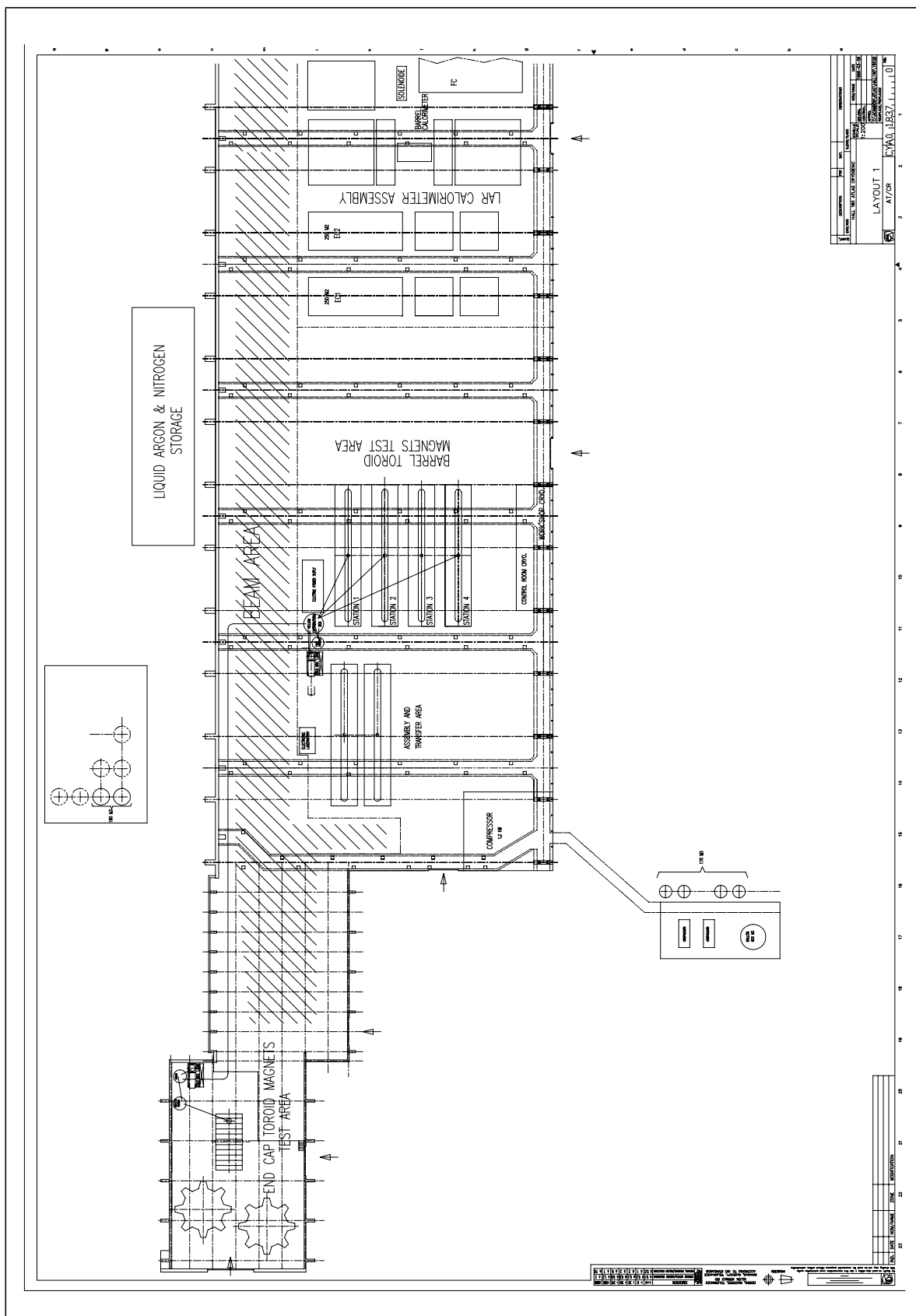
The diameter of the cryostats is at least 5.8 m. The present doors of the assembly hall are too small, being 5.7 x 5.9 m and should be enlarged. The vertical clearance has to be sufficient to allow, when going out of the building, for the additional height of the trailer, the bus bars of the solenoid, the HV feedthrough chimney and the pedestal bases of the electronics crates.

The final disposition of the elements inside the hall should take into account the geographical arrangement of the doors, along with the access for the transport trailers.

Availability of the hall:

The hall needs to be available well before the final assembly of the detectors for the reception of the cryostat vessels, their testing, and subsequent welding of the feedthroughs. It is also our intention to assemble the first half-cylinder of the electromagnetic barrel calorimeter as soon as enough modules are ready and tested.

The hall needs to be ready at the very beginning of the year 2000. As half a year is necessary for the emptying of this hall and for its modifications, all other activities should stop around mid 1999.

Figure 14-1 View of the CERN West Assembly Hall.

14.2 Assembly of the barrel system

The final assembly of the barrel calorimeter inside the cryostat is described in Chapter 6.

14.3 Assembly of the end-caps

The cryostat is delivered to CERN on its supporting frame. The cryostat-structure set is designed so as to be placed on a trailer and driven inside the hall where the final assembly will take place.

In its delivery state, the cryostat includes all the elements mentioned in the PBS (see Chapter 5), namely all the items corresponding to the non-equipped cryostat. The structure is complete and assembled and all passages on the warm and cold vessels, at the locations of the feedthroughs, are closed with dummy plugs in order to protect the cryostat internally from all dust coming from the transport. At this stage, all cold joints are replaced by elastomer joints.

14.3.1 Opening of the cryostat

The weld at the bellows of the inner central warm tube is cut open. The flange bolts are then unscrewed and the warm tube removed from the front.

The rear warm cover is removed and stocked on its support.

The removal of the forward calorimeter structure is performed as follows:

- remove the two limiting half-stops which maintain the front warm cover
- remove the nuts making the link between the structure of the FCAL and the front cold cover
- unscrew the link between the FCAL back cover and the cryostat back cold cover
- remove the FCAL structure with the help of the FCAL integration tube and the crane and place it on its support structure.

The cold cover is then removed and all plugs at the locations of the feedthroughs are dismounted.

14.3.2 Assembly of the electrical feedthroughs

Before the integration of the detectors inside the cryostats, it is necessary to finish the assembly of the cryostats themselves by mounting all feedthroughs, signal and high-voltage ones. This operation consists first in screwing the feedthroughs on the flanges of the warm vessel and then, from the inside of the cold vessel, welding them (stainless-steel welding) on the cold vessel.

When all feedthroughs are assembled, the cover of the cold vessel is put back in place as well as the FCAL structure in order to get the pressure vessel vacuum tight. Elastomer seals are used. The vacuum tightness of the cold vessel is helium tested to check all welds.

At this stage, the pressure vessel should be tested under the maximal required pressure using most probably inert gas. So, all safety measurements around the cryostats should be in place for

the pressure test. This operation will be carried out in collaboration with the CERN-TIS Division.

The FCAL structure and the cold vessel cover are then disassembled to allow the insertion and fixing of the detector parts.

14.3.3 Integration of detectors

The first operation is the assembly of the presampler detector on the front of the cold vessel and the fixing of its own cabling harness along the cylindrical cold wall of the cryostat.

The signal feedthroughs are delivered with the interfacing sections of cables (called pigtail cables) already connected.These will be further connected to the detector cables mounted on patch panels.

The EM and the two hadronic wheels can then be integrated inside the cryostat (see Figure 14-2). This assembly follows the same procedure for the three detectors, namely:

- position the detector on the support structure located in the front of the open cryostat. The cryostat rails are connected to the rails of this frame by extension pieces

- the detector is pushed inside the cryostat up to its position using jacks. It is then fixed from its back on the rails at its precisely defined position

- fix the cabling harnesses along the walls of the cryostat and the end connectors. These will have already been pre-connected on the patch panels

- install the protections for the cables.

When the three detectors are installed inside a cryostat, the pigtail cables are connected to the detector patch panels.

The copper plug is assembled on the cold vessel cover and the Cu plug/cover set is bolted on the cold vessel, using a helicoflex joint. Through the central hole of the cold cover, the extremities of the FCAL pigtail cables are extracted and provisionally fixed outside the cryostat during the FCAL installation.

At this stage, the three FCAL detectors will have already been mounted in the forward tube. The rest of the structure is then assembled as well as the back cover. The central tube is welded (stainless-steel welding).

The FCAL structure as a whole, including the detectors and the plug, is assembled in the central part of the cryostat. The tightening of the screws on the back cover of the cryostat generates the necessary pre-stress of the cold vessel. The FCAL structure is finally bolted to the front cover of the cryostat.

The last operation is to assemble the warm cover, the central warm tube, and weld it (stainless-steel welding) to ensure the vacuum tightness of the warm vessel. The end-cap is then ready to be tested.

14.3.4 Integration tooling

The list of the specific tooling for the full integration of the detectors in the cryostat is:

- supporting frame of the cryostat

- supporting frame to store the EM, hadronic 1 and 2 wheels

- lifting beam for the cryostat

- lifting beams for the detector wheels

- supporting frame for the detectors, prior to integration in the cryostat

- extensions of the rails

- storage frames for the cold and warm covers

- lifting beam for the warm cover

- FCAL tube for its integration

- supporting frame for the FCAL

- lifting beam for the FCAL

- supporting tube for the FCAL, needed for its integration in the cryostat.
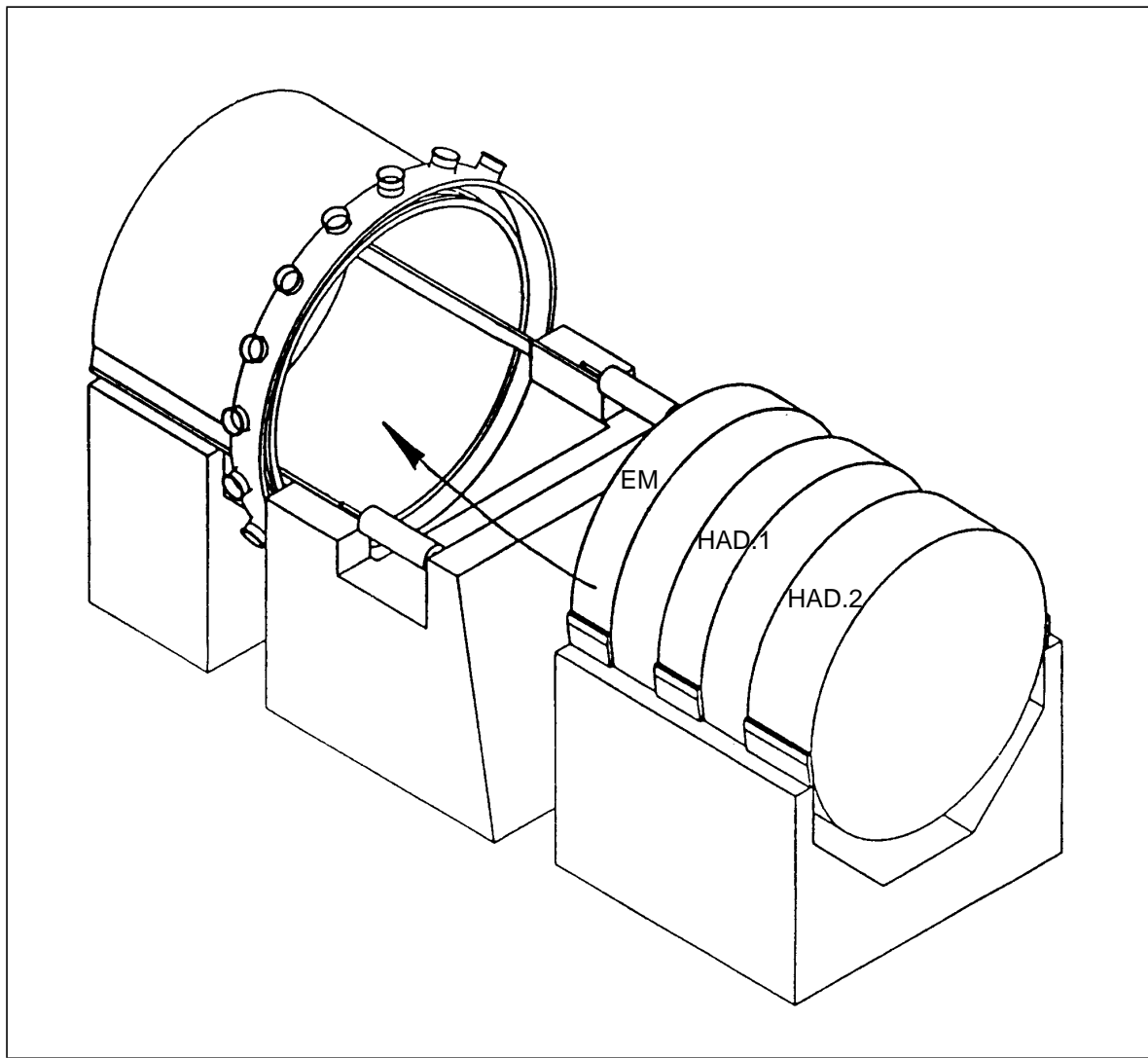
Figure 14-2 Principle of the integration of the end-cap detectors in the cryostat.

14.4 The cryogenics system

In order to perform the cold tests, the cryostats will be cooled, filled with LAr, and subcooled at 89.3 K, at a pressure of 1.25 bars, as in the normal future operations. As the space inside the ATLAS detector is insufficient to accommodate isolation valves, the cryostats will need to be warmed up before transportation to the cavern.

During these final testing operations the cryostats will be commissioned, undergoing the following tests:

- leak test at ambient temperature
- pressure test with inert gas at ambient temperature:

3.1 bars $\times$ 1.25 [coeff. for gas pressure test] = 3.9 bars for the end-caps

3.2 bars $\times$ 1.25 [coeff. for gas pressure test] = 4.0 bars for the barrel

- leak test at low temperature during cooling down
- measuring of stresses and displacements during cooling and filling with LAr.

14.4.1 The cooling plant

The principle of the cooling unit in the West Hall is the same as the one for the cavern described in Chapter 3. It uses helium or argon gas as the cooling medium. In the case where a single cooling unit should be considered for the West Hall and the cavern, a revised scheduling of the operations should be studied, to ensure, at all times, the compatibility between the cryogenics installation in the cavern and the ongoing cooling-downs in the West Hall. This is equally true for all elements which should be shared in both locations. If this is not possible, these elements should be duplicated.

14.4.2 The implementation in the West Hall

To reproduce the same conditions of operation as in the cavern, the pressurization of the LAr in the cryostat is obtained by charging a 2.5 m high column with LAr. For this purpose, the expansion vessel of the barrel cryostat is used for the test of the first end-cap and of the barrel, then the expansion vessel of the second end-cap is used.

A detailed layout of the cryogenic system in the hall will be produced in the future, as soon as the final implementation of the toroids and cryostats in the experimental hall is agreed upon.

14.4.2.1 Cryolines

The overall layout of the external and proximity cryogenics in the West Hall is different than the one in the cavern. Consequently, the safety and the emptying cryo-lines are made specifically. Depending on the final schedule of the ATLAS installation in the cavern, the flexible cryo-lines of one end-cap (~ 30 m long) could possibly be used for the connection between the cryostats and the liquid nitrogen storage tank.

14.4.2.2 Vacuum pumps

The intention is to use the same vacuum pumps in the West Hall as in the cavern for the flushing and purging of the cryo-lines and of the cryostats.

14.4.2.3 Liquid nitrogen and liquid argon supply

The cooling capacity needed for the tests is about 10 kW, corresponding to about 320 l/h of liquid nitrogen. A liquid nitrogen storage tank of a capacity of 30,000 litres will be located close to the test area, to supply the cooling unit and the cryostats. The final liquifier will be used.

The pressurization of the liquid nitrogen will be directly obtained from the storage tank internal pressure so that no circulator is needed.

The LAr will be taken directly from the vendor trailer and possibly returned, following the same contracts as arranged for the filling and emptying of the RD-3 cryostat.

14.5 Cool-downs and electronic tests

14.5.1 Cool-down procedure and controls

The identical procedure for cool-down and controls is applied in the West Hall and in the cavern. It includes the following operations:

- flushing, purging
- cooling down
- filling
- running
- emptying
- warming up

The details of each of these operations are to be found in Chapter 3, Section 3.

The controls will be organized the same way as in the cavern.

14.5.2 Electronics tests

The tests of the electronics are fully described in the Chapter 10, Section 7.2.

14.5.3 Possibility of X5 beam test of end-cap C

The assembly of both end-caps will be done in the year 2001 in the West Area at CERN. Given the proximity of the X5 beam line, we envision the possibility to test in real beam conditions the performance of a full LAr end-cap, including the electromagnetic, the hadronic, and the forward calorimeters.

We first describe what will be the situation in terms of beam lines, including the necessary modifications needed to get a large experimental area.

14.5.3.1 Beam lines in the West Area and upgrades

By the end of 1998 only two beam lines will remain active in the West Area: the X5 and X7 lines. Both are secondary beam lines with a common target, which means that any modification of one of the lines will affect the other one. The X7 beam line will stay essentially unmodified, whereas X5 will be upgraded [14-3]. The present characteristics and the foreseen upgrades are summarized in Table 14-1:

Table 14-1 Present and future characteristics of X5.

Mode	Energy range (Gev)	Intensity	Particle type	$\delta p/p$
Secondary	10-250	few 10^5 per spill	e, π and μ some contamination	few per mille
Tertiary	10-250	10^3 to 10^4 dep. energy	e, π and μ	8-10 per mille

The X5 beam line is a horizontal beam line, the height with respect to the floor is 3.66 m. There is only a small range in both the vertical and the horizontal plane for a beam displacement. With the actual beam elements setting, the excursion is limited to ± 2 cm. Provision should be foreseen to move the full end-cap cryostat (250 tons) horizontally by 50 cm.

Concerning the infrastructure in the experimental zone, no detailed study has been done yet but could start around mid 1997. The installation of the cryostat would require the removal of some quadrupoles and the rearrangement of the shielding so that laterally we get a space of ± 3 m on the floor. This seems to be possible, particularly if the test would take place at the end of the proton period. With 250 GeV electrons and pions we could study the global response in the crack region, around $\eta = 3.1$, as well as the inter-calibration between the electromagnetic and the hadronic calorimeters.
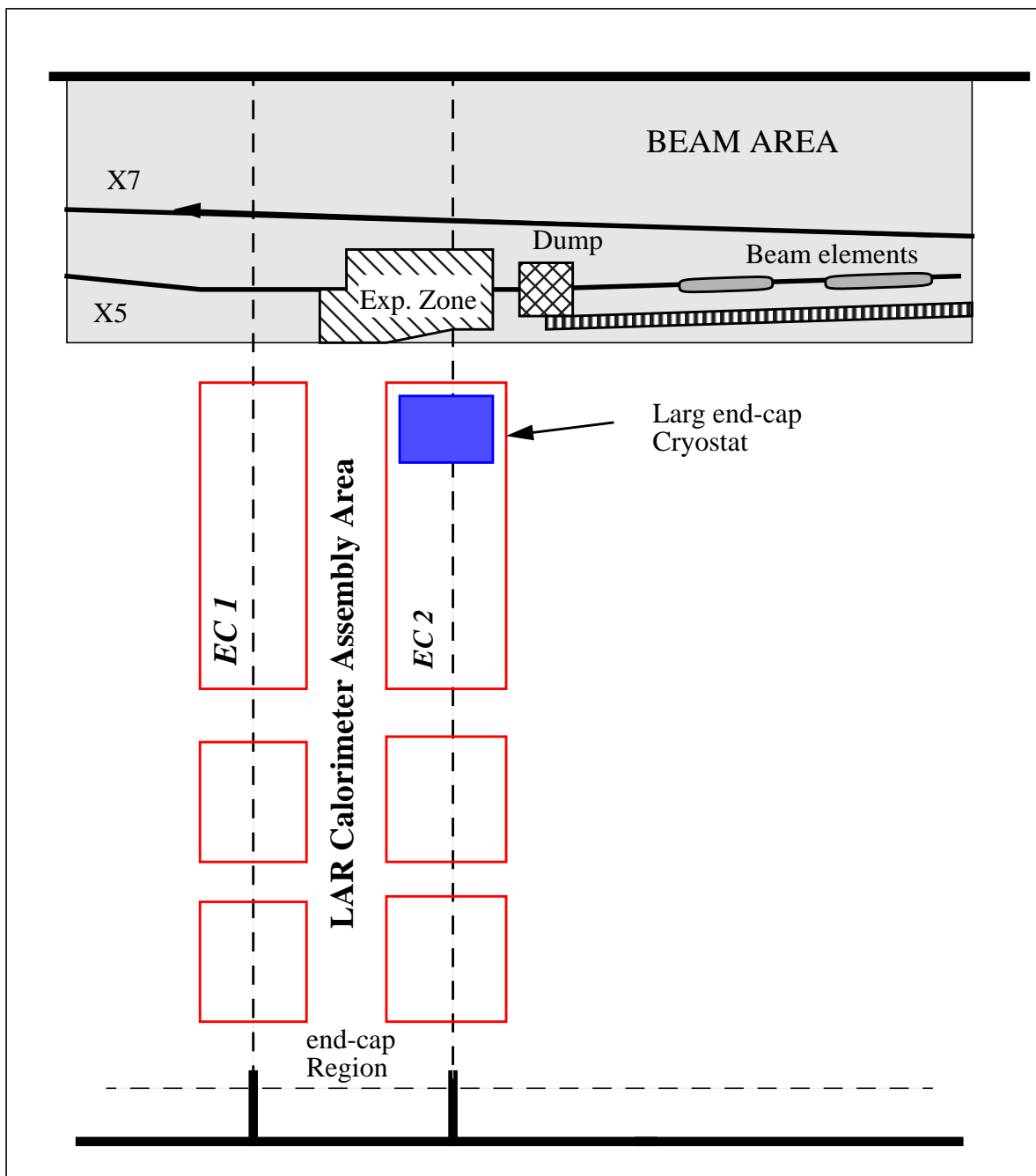
14.5.3.2 Experimental zone environment

The possible scenario would then be the following: once end-cap C is fully assembled, tested in the warm and in the cold, it will be moved, probably on a trailer, from the assembly area to the beam area (see Figure 14-3). During the displacement of the cryostat, it will be continuously connected to the cryogenic system which has to be located close enough to both the assembly and the beam area.

As already mentioned the beam height will be 3.66 m. The distance from the center of the cryostat to the external envelope, including the feedthroughs and the services is of the order of 265 ± 5 cm. This gives roughly one metre to install a platform (movable ?) below the cryostat to support (and rotate ?) it.

14.5.3.3 Schedule

The test of a full end-cap in the X5 beam line with either electrons or pions will be possible only after the completion of the warm and cold tests. According to the general assembly and installation schedule, as worked out today, these tests will start by the end of 2001. Immediately after,

Figure 14-3 Assembly and X5-X7 beam line areas in the West Hall at CERN.

i.e. around April-June 2002, we plan to bring the detectors in the X5 beam line, using a platform or a trailer. We will perform one energy scan from 5 to 250 GeV, around the horizontal zone of interest. Taking into account the time needed for the rearrangement of the zone, the installation of the cryostat, and the cooling down and warming up if we have to disconnect from the cryogenics, the total operation will take approximately three months. In the case where the cryostat would be installed on a movable platform, it will stay on it for the overall length of the operations.

14.6 Schedule

The final assembly schedule, Figure 14-4, is determined by two factors:

- the cryogenics system in the West Hall is designed to control a single cryostat at a time. Therefore the cool-downs, cold tests and warm-ups of the three cryostats have to be performed sequentially

- at present, the proton test beam periods are scheduled from say April to October. In order to be able to beam test the first end-cap in the X5 beam, as discussed before, it should be cold, filled with LAr, debugged, and ready to accept beam in this summer period.

- Although shown from January 2001, the assembly of the first half-cylinder of the barrel will be started as soon as enough calorimeter modules are ready from the production chain.

- It should be pointed out that no specific provision has been introduced in the schedule of this final phase for catastrophic measures, such as the obligation to reopen a cryostat for repair. This fact explains why the cold test periods are kept so long.

14.7 Cost, manpower, resources and responsibility sharing

14.7.1 Cost

The provisional overall cost of the integration issues for the barrel and the end-caps is included in the ATLAS COST PLANNING, see Table 14-2. Specifically the costs for final assembly are:
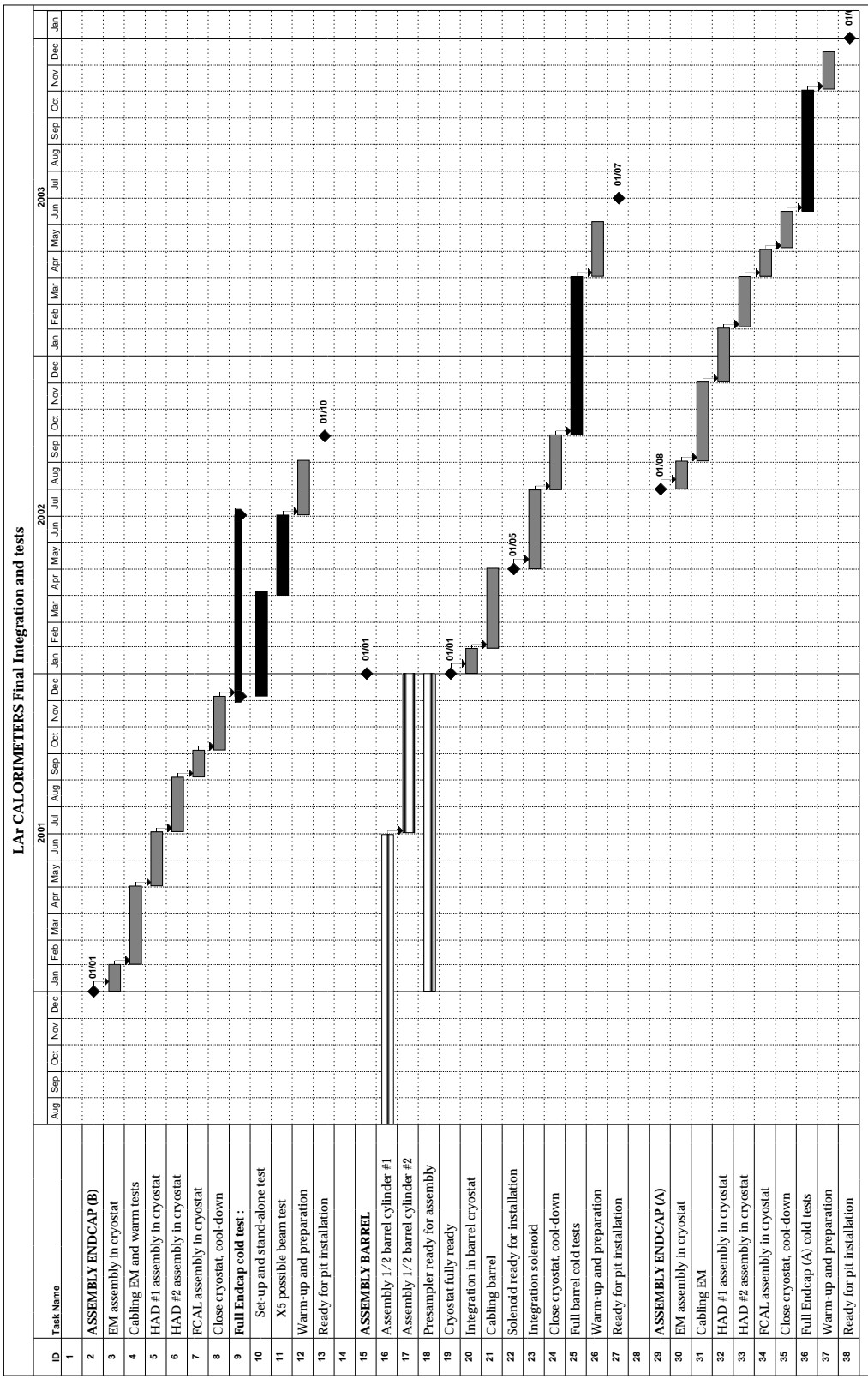
Table 14-2 Assembly costs.

Item	Cost (kCHF)
Barrel assembly	180
End-caps	
EMEC assembly	450
HEC assembly	495
FCAL integration	150

14.7.2 Manpower and resources

During the final assembly period, it is expected that the Collaboration Institutes, being freed from the main construction of the elements of the detectors themselves, will be able to gather enough manpower at CERN in order to ensure this phase of the operations.

Some help will be available from the CERN team involved in the LAr detector.

Figure 14-4 Final assembly and test schedule.

14.7.3 Sharing of responsibilities

14.7.3.1 Hall infrastructure

The general implementation of the LAr cryostats and sub-detectors in the hall including all services is a CERN responsibility, in agreement and with the help of the LAr community. This includes the general layout in Building 180, the access doors, the implementation of the external cryogenics, the use of the cranes, the clean rooms, and all necessary services. The management of the entire space will be done by the ATLAS Technical Coordination in collaboration with the teams involved in the toroidal magnets and the LAr cryostats who share the assembly hall.

The common items, shared between the magnets and the LAr cryostats, such as parts of the external cryogenics, will be managed by the Cryogenics group of the LHC division at CERN. The LAr external cryogenics is the responsibility of the CERN LHC Cryogenics group. The final sharing of the entire cryogenics complex involving the proximity cryogenics, the controls and monitoring is to be further discussed within the Collaboration, internally, and with the Cryogenics group.

14.7.3.2 Barrel integration

The integration of the barrel system is concerned with the three elements: presampler, EM calorimeter and cryostat. ISN-Grenoble and KTH-Stockholm are responsible for all integration aspects of the presampler, CEA-Saclay for the integration aspects of the EM calorimeter, and Brookhaven Nat. Lab. (BNL) / Rochester University for the cryostat.

14.7.3.3 End-caps integration

The boundary between the specific sub-detector responsibilities and the responsibility towards common final integration, to be shared amongst the different sub-detectors and the cryostat managing Institute, is placed at the completion of the detector wheels, electromagnetic and hadronic, including the assembly tables, and completion of the full FCAL. All toolings and assembly work needed up to the wheels completion or up to the full assembly of the FCAL is the responsibility of the sub-detector teams alone.

All tooling to support the cryostat as well as the tooling to handle and support the flanges of the cryostat is in the hands of the Institute responsible for the cryostat[LAL-Orsay]. The Institute is also responsible for:

- the support frame in front of the cryostat to place the wheels before their integration
- the extension of the rails of the cryostats
- the push/pull mechanism to introduce the wheels inside the cryostat, on the rails.

Some common tooling has to be shared between the electromagnetic and hadronic detector communities:

- the rotator to move the stacking tables from their horizontal position to the vertical one
- the lift fixtures for the different wheels
- any other intermediate support structure if needed.

14.8 References

14-1   The ATLAS Collaboration, CERN/LHCC/95-59: ATLAS Test beam Requirements, 16 Oct. 1995.

14-2   V Vuillemin: Clean rooms for calorimeter construction, to be published.

14-3   Lau Gatignon et al., Introduction to the X5 beam, CERN/SL, www address http://wwwcern.cern.ch/~gatignon/X5manual.html.

15 Installation, commissioning, running, access, and repair

15.1 Installation

15.1.1 Requirements

The installation of the three LAr cryostats impose several requirements on the cranes carrying large pieces from the surface to the ground of the pit. The heaviest object, as far as the LAr complex is concerned, to be lowered down into the experimental zone is the full end-cap. Its total weight is estimated at the moment to be between 264 and 272 tons. The internal detectors weighs 217 tons, the cryostat itself, including the cables and feedthroughs, weighs 31 tons. The remaining 24 tons are needed for the lifting jigs. The two cranes will have to be coupled and synchronized. The required lifting capacity of each crane is 140 tons.

The cryostats together with their internal detectors will be assembled in a remote hall and transported on special trailers to the surface buildings of the zone. They will have to be installed on the trailer with jacks because of their weight, which is greater than the crane's capabilities of the final assembly hall. Transportation tests have been carried out between Building 182 and LEP point 1. No acceleration beyond 0.1 m/s^2 has been observed either horizontally or vertically [15-1], and therefore no damage should occur to the fragile internal elements of the calorimeters during their transportation on the trailers. To ensure this, acceleration will be monitored during transport. During the transportation and installation phases, all cryostats will be kept at warm temperature and filled with clean, dry, neutral gas to properly ensure the cleanliness of the internal elements and to prevent any future pollution of the LAr.

The external diameters of the cryostats are 5.8 m, including the feedthroughs. However, for the barrel, the outside bus bar of the solenoid will go beyond the outside diameter of the cryostat vertically by another 1.3 m. Although the end-cap cryostats do not have any bus bar, another 1.3 m vertical clearance should be kept in reserve to fit the HV warm feedthrough(s) box. Vertical clearance during transport, access to the surface buildings, and the available height under the hook of the cranes should be able to accommodate these dimensions. This will definitely require a modification to the exit doors of the surface building used for final assembly. Upon arrival in the experimental area surface building, the cryostats should be unloaded from the trailer and their stand-alone support system dismounted.

From the present design, the cryostats will be brought down using the surface cranes and placed directly on the support pieces which are part of the barrel or of the extended tile calorimeter. The speed and precision of the cranes should ensure that this direct placing be carried out safely. However, if necessary, specific tooling could be envisaged to take back the load of the cryostats from the top cranes and to perform the final steps of their installation on the tiles independently of the cranes. From theoretical studies conducted for the end-cap installation, it should not be envisaged to lower the cryostats at a speed greater than 40 mm/s [15-2]. For the final positioning on the tile supports, a speed approaching 1/1000 of the nominal speed of the crane should guarantee a smooth operation. The question of the length of the cable (90 m) and of its oscillations remains. The lateral precision has to be within 1-2 mm, not only because of the required precision for positioning the cryostat from the constraints imposed by the physics data analysis, but also because the clearance in between the bulkheads of the cryostats and the extremities of the tiles is only of the order of 20 mm. This region is made very critical by the clear-

ance to the signal feedthroughs. These considerations should be taken into account in the definition of the cranes leading to an excellent synchronization of the two lifting barrels, a good precision of the brakes, and the definition of the cable elasticity.

As the installation requires the two cranes, no other operation should be scheduled at that time. Typically the operation to lower one cryostat onto the tiles should be performed within one day.

15.1.2 Sequence of installation

The installation sequence for the three cryostats follows the logic adopted for the overall ATLAS detector assembly: end-cap C, barrel, end-cap A. The sequence of availability after preassembly and testing in the surface assembly area of the cryostats follows the same logic.

Such a sequence has many advantages. The first end-cap will be ready for installation at the end of August 2002. It would be a net advantage to be able to install it as soon as possible after this date, in order to maximize the time left for the cryogenic and vacuum connections, the assembly of the readout electronics crates and water cooling, the cabling, and the necessary commissioning. Prior to the lowering of a cryostat into the cavern the following services should be installed. They should be operational before the completion of the first end-cap installation:

The external services including cryogenic facilities comprising surface and underground installations of the nitrogen refrigeration plant and interconnecting transfer lines to the proximity services (LAr, LN_2 and GN_2 transfer lines, power & signal cables and water cooling installations). This assumes that none of this equipment should be used in the assembly/test area.

It is essential that the delicate end-cap movement with the flexible cryogenics piping and the cables connected be tested as soon as possible in situ. The first time, these operations will be carried out with the cryostats and the cryogenic lines kept under room temperature neutral gas. In general, prior to cooling-down and filling with LAr, all cryostats should be filled with clean neutral gas and closed.

The barrel cryostat should be installed next. In any cryostat installation, the principle is identical: first install the necessary number of bottom tile modules in order to form a cradle and to be able to bolt the pieces supporting the cryostat to the tile modules, then lay down the cryostat and complete the tile cylinder around it. In order to install the last end-cap cryostat, the full barrel calorimeter system has to be pushed inside the toroid in its final position where the solenoid connections and cryogenics connections can be carried out. At this phase of the installation, until all connections have been performed on both sides of the barrel, the two end-caps should stay in their open position and consequently the magnet system should not be energized in this position.

Once cooled and filled with LAr, the external envelopes of the cryostats should be measured to ensure that they fall into the specified dimensions, before the cryostats are moved in their final position.

Physical installation of the LAr cryostats usually takes a few days. However, the time needed for making the connections and commissioning should be added to that, before the LAr detector is ready for beam data taking. The LAr detectors should be fully connected by the end of 2004. Debugging of the read-out could start at the end of 2003, assuming that enough general hardware from the DAQ is installed.

15.1.3 Supports and alignment

Specific handling jigs have to be designed to transport the cryostats with the cranes. These spreader bars should be able to equalize the weights of the objects across the two cranes so that the cryostats can be well positioned on the tiles in the ATLAS pit. Care should be taken to ensure that the overall weight of any cryostat (including the weight of its support system) does not exceed 280 tons.

For the barrel cryostat, the principle is to lengthen the rods which suspend the cold vessel from the warm flange of the cryostat. A tie bar will connect all four points. The cryostat rods provide a natural mechanical bond for both the cold and warm vessels of the cryostat and using them for suspension is quite adequate to ensure minimal stress on the overall structure during the crane operations.

For the end-cap, use will be made of the supports of the cryostat, that are designed to lay on the supports on the tiles. A compensation bar will also connect all four points. For the end-cap, the distribution of the weight is strongly asymmetrical, which is not the case for the barrel.

As mentioned earlier, no adjustment system is foreseen between the cryostats and the tiles, except shims. The role of the shims is to ensure that the cryostats are effectively resting on the four supporting areas, and to adjust the overall height of the full object. If any other adjustment proves to be necessary, hydraulic or mechanical jacks could be placed between the tile calorimeter and the ATLAS rail system. Although the weight of the overall calorimetry complex is much greater than the LAr detector itself, it is felt that adjusting it as a whole is better not only for long-term consistency of physics data but also because room is available there to place the jacks. The barrel and end-cap cryostat should be aligned and stable within 2 mm with respect to the beam axis, as well as longitudinally. This requires that the overall supporting system from the floor up to the tiles should be designed to guarantee such a final precision in the positioning of the three cryostats [15-3]. The overall transfer of the position of the calorimeter with respect to the beam axis will be measured by several position gauges located on the internal wall of the cryostat after the completion of the tile assembly.

Once the tile calorimeters are moved to their central region positions, the precision of their spatial position, and consequently of the cryostats, with respect to the beam axis, should be maintained and monitored.

15.1.4 Cryogenic connections

For each side of the barrel cryostat or for each end-cap, several cryogenics pipes have to be connected (either with stainless steel welds made with an argon torch or by flanges) and tested:

- 2 LN_2 and GN_2 connections [flexible pipes in case of the EC's, rigid for the barrel] between the valve box and the cryostats
- - 1 drain line for LAr
- - 1 large diameter safety line [flexible for the end-caps, rigid for the barrel) between the expansion vessel and the cryostat, used also for LAr filling.

At each step vacuum tightness has to be checked. All links should be under vacuum requiring that a specific sequence of pumping be applied to the lines. As soon as the flexible lines of the end-caps are connected, the moving mechanism for the end-caps should be tested.

The overall cryogenics connections are described in Chapter 3.

For the barrel, it is recommended that the connections of the solenoid be completed prior to the cryogenics ones.

15.1.5 Final connections

As mentioned in Chapter 10, the readout electronics crates are directly mounted on the signal feedthrough flanges. The crates are made of two sections: a pedestal part and the rest of the crate. The pedestal part is about 20 to 25 cm above the feedthroughs. It contains the cables from the feedthrough to the crate. This part, except in some restricted areas near the cold vessel supports used for crane attachment and the region of the supporting feet, was assembled in the CERN West Area and still remains permanently installed. The time-consuming cabling will not therefore have to be redone during installation in the pit. As the diameter of the cryostats is already very important (5.8 m), it is not clear whether the top parts of the crates attached to the pedestal partswill be able to stay connected after the cold tests in the CERN West Area for safe transportation and installation. This should however be carefully studied in order to minimize later the installation time in the experimental pit. In any case, lots of read-out cable connections will have to be realised in-situ on both sides of the barrel, as well as on the end-caps. The connections on the barrel are all fixed, when lots of connections on the end-caps are flexible to follow the movement of the cryostat away from the interaction point in case of access. At this stage of the design, these mobile connections have not all been studied yet, as the design work has concentrated on the cryogenic lines.

The following steps must be carried out in a predefined sequence:

- connect the vacuum system to all the vacuum connectors of the signal feedthroughs

- install and connect the heating system on the feedthrough bodies to prevent condensation

- for the few pedestal parts not already connected, in the region of the support rod for the cold vessel, the cables from the feedthrough pin connectors to the backplanes must be connected. Then, the remaining electronics crates will be fixed, and the electronic boards inserted

- install the crate water-cooling manifolds and connect them to the general cooling pipes

- connect the LV power cables and their water-cooling system, if these cables should be water-cooled

- connect the cables for read-out, HV, calibration, monitoring and slow controls

- connect an optical fiber around the feedthroughs and the cryostat flange for temperature detection, as advertised by safety (TIS).

After each step the connections should be tested. It is estimated that all connections and the necessary time-consuming check-outs will be finished at the latest six months after the physical installation of each cryostat. For all these connections the barrel, and the end-caps, should stay in an open position in order to have access to all the read-out crates. Such an installation is consequently orthogonal in scheduling with the overall magnet system tests and should preferably be done beforehand.

The same remark can be made for all connections of the end-caps as was made for the cryogenic flexible lines of the end-caps: whenever the whole end-cap detector is connected, the full movement of the end-caps must be tested before ATLAS detector commissioning and running, to make sure that every connection which should stay in place during the move can effectively stay connected.

15.2 Commissioning and running

15.2.1 Cryogenics

As described in Chapter 3, the cryogenic system involves several storage tanks, a cooling plant, several transfer lines, and the cryostats systems. The commissioning sequence has to be carried out according to a predefined sequence to reach the status where all components are cold, under electrical power and operational, including all the necessary controls and monitoring.

At the beginning of such an operation, all valves are closed, the lines are under low pressure, no fluid is inside and there is no power. All circuits have been sequentially vacuum tested and rinsed with argon or nitrogen until the gas analysis, especially in terms of oxygen content, is acceptable. At this time, all sensors (temperature, pressure, levels of liquid) should be working and the pressure inside the cryostat cold vessels should be correct.

The cool-down of all transfer lines, separator and storage tanks starts with LN_2 coming from the trucks on the surface. At each step, a defined sequence of valves openings and closings should be followed, allowing nitrogen gas from the boiling to escape to the surface. Pressure control valves set to 2.8 to 3 bars are provided to avoid the pressure from the entire 90 m column of liquid nitrogen from the surface to the cavern to reach the lines and the tanks. For the liquid nitrogen such a pressure from the column is 8 bars, 14 bars for the liquid argon. When the liquid nitrogen storage tank is full, the commissioning of the cooling plant can start.

The cooling plant works in a closed circuit and the oxygen content is checked. This should avoid any problem with the formation of ozone with radiation, leading to risks of explosion [15-4]. The pressure, the temperature, the speed of the turbine, and the analysis of gases are controlled. The cooling plant contains a purification stage to avoid any pollution of the cooling liquid which could lead to the above mentioned problem. After optimization of the Joule-Thompson valve between the cooling plant and the transfer tank, and the setting of the pressure inside the transfer tank, the cooling system is operational and should continue to work by itself.

15.2.2 Cool-down

For the cool-down of all liquid argon transfer lines and the tank, the procedure is similar. Cool-downs of cryostats are achieved with cold He, with the help of the internal cooling loops in order to reach a temperature of around 100 K. At this stage, a switch is quickly operated from He gas to Ar gas and a new cycle of rinsing and pumping is carried out, checking the purity of the Ar gas. When the purity of the Ar is sufficient, the cryostat can be filled with LAr and the nitrogen cooling loops are set to their regulated mode. The system is then operational.

However, if longer cooling and warming times are acceptable to keep the same temperature gradients, use of Ar gas could be considered. Cooling with Ar would allow savings in investments, but leak detection should be studied in both cases.

The complete cool-down procedure is described in the preceding chapter.

15.2.3 Electronics

The commissioning process of the electronics for the barrel (EM and Presampler) as well as of the one of the three detectors of the end-caps is a rather complicated process. It is assumed that:

- the various single boards have been fully tested in a stand-alone mode

- the crates have been assembled, filled and connected to supplies and cooling, and tested as integrated units, still in stand-alone mode

The connections should be checked as the installation proceeds, or at least per crate unit. When completed, all the electronics should be set and global connectivity and checkouts should be performed. This should include, as a minimum:

- connectivity test: firing patterns of injected charge should give the expected results. This could be performed in parallel, i.e. one channel per module simultaneously and should be such that potential miscablings or non-connections be uncovered

- dynamic range test: firing increasing values of injected charge into some channels would allow the overall dynamic range and linearity of the global system to be checked

- monitoring and cooling tests should be performed to be certain that the temperature and the power consumption of the installation remain within rated values.

15.3 Access and repair
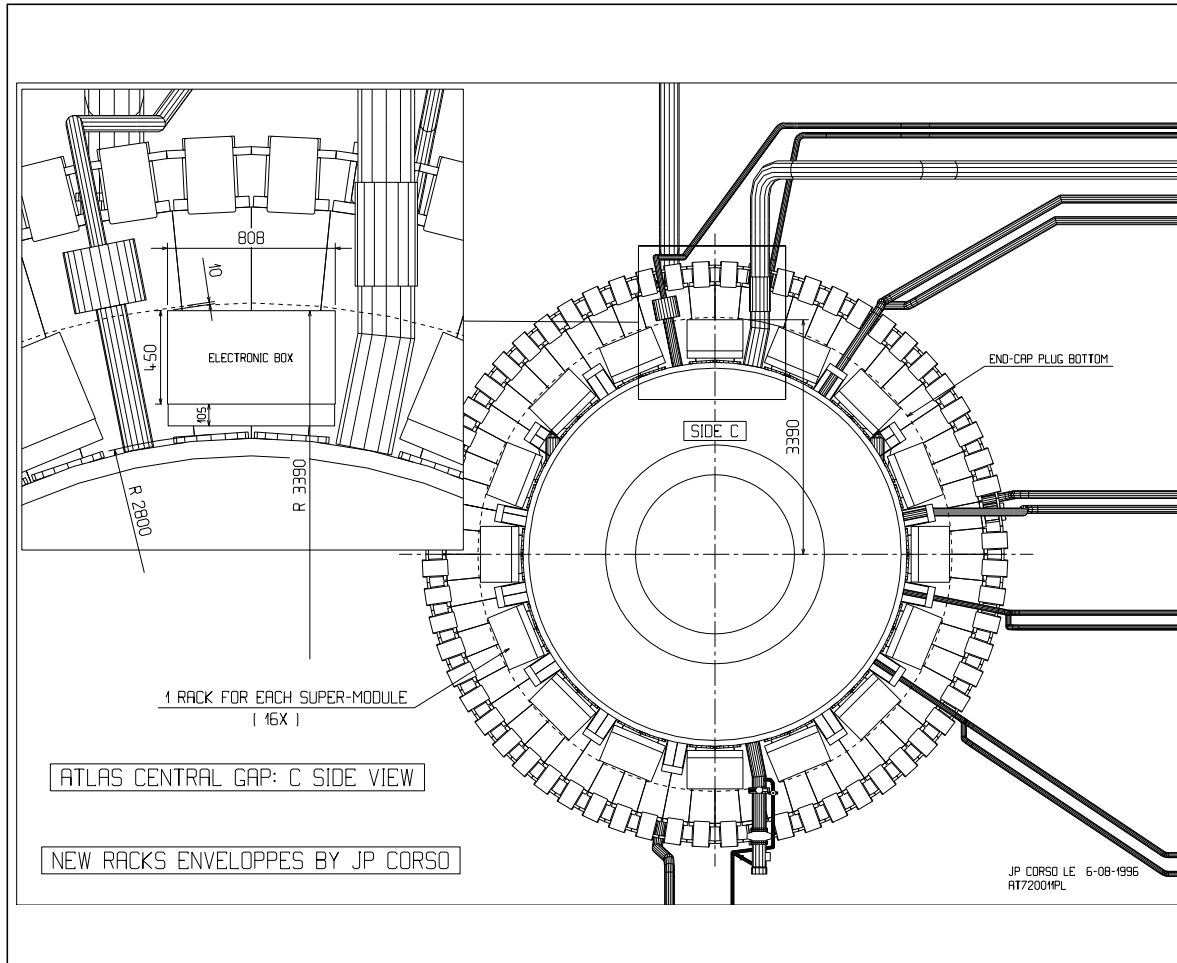
15.3.1 Requirements

For all detectors, the LAr read-out electronics are located at the periphery of the end flanges of the cryostats, directly connected to the feedthroughs by very short cables. As a consequence, any repairs or maintenance of the read-out boards, vacuum or heating systems of the feedthroughs, signal, HV or LV cabling, of the barrel requires the end-cap cryostats to be retracted by at least two meters. The separation between the central and end-cap cryostats should be sufficient to have easy access to the entire crown of the end flanges of the barrel cryostat, and to work in a convenient position (see Figure 15-1). Access to the read-out electronics of the end-caps themselves requires all the elements be moved further downstream, such as end-cap toroid, muon chambers, and shielding. Access to the electronics requires an infrastructure of gangways, still to be designed, accessible from the outside of the ATLAS detector [15-5]. A 12 m move of the end-cap would be needed to extract the inner detector along the beam, if such a scheme to remove the inner detector is chosen [15-6]. This scenario will be described in the next section.

The frequency of these interventions will depend on whether the detectors are operated during the commissioning and during the running period. During normal LHC running time, these interventions should be scheduled during the machine shutdowns. A frequency of two accesses per year seems reasonable. The possibility of more frequent access should be considered at the beginning of the running-in period of the machine, especially when the detector is in its debugging phase. During this period, the number of access could be doubled compared with stable operation time.

In order to reach the backs of the barrel and end-cap cryostats, personnel access should of course be considered, as well as the possibility of bringing equipment if any exchange of parts is needed. The crates themselves contain only backplanes and connections, and there is therefore

no need to consider their being exchanged after the debugging period. Probably any material needed could be carried by a human being. The perspective of bringing an oscilloscope inside should be considered. The question of the location of the vacuum pumps (and their possible failure) needed for the separated isolation vacuum of the feedthroughs should certainly be considered in this context, especially if the pumps are of the oil diffusion type which require routine maintenance during shutdown periods.

Figure 15-1 View of one of the extremities of the barrel cryostat, showing the cryogenics pipes and the electronics crates

Given the frequency of access, it is clear that all cryogenics pipes for the end-caps will stay connected to the cryostat when it is displaced, and be continuously filled with LAr. Emptying the liquid from the cryostat for each of these displacements, would endanger the liquid purity and could have disastrous effects on the mechanical stability of the calorimeters inside the vessels. The number of warming-ups and cooling-downs of the cryostats must be kept to a minimum, as they create a lot of stress in all the internal elements. To guarantee the safest possible operation of a liquid argon detector, there should only be one single cool-down and the detector should be kept cold and filled for the duration of the experiment.

It is equally important that the read-out electronics system stays connected during debugging and repair. It is highly desirable that the electronics be operational during the only period when the detector, being in its open configuration, can be checked, debugged and repaired. This is certainly of prime importance during all shutdown periods, in order to ensure that all channels

are in good running order during physics data taking. This implies strong constraints on all the elements connecting the end-caps to the outside world of the ATLAS detector. All these elements are designed to be flexible, for a short move of the detectors, for electronics maintenance. All read-out cables, cooling pipes and power cables, should stay connected as soon as the system has been fully checked out, with cooling pipes and power cables.

The question of the continuous connection of the water-cooling pipes, LV power cables, especially if water-cooled, should be assessed for all conditions, short and long moves of the end-caps. If it turns out that the cooling and the LV power of the end-cap is disconnected during the whole period of the annual shutdowns when it is in its far remote position to allow for inner detector removal, all the necessary provision must be taken to locally power the crates in which some problems have been observed. This could imply that some equipment will have to be brought inside the detector close to the back wall of the cryostats.

The problem of gaining access to the interior of the ATLAS detector (persons, equipment), the location of gangways, and the enforcement of safety rules in these half-confined or confined areas will be treated in the Technical Coordination Volume of the ATLAS TDR.

15.3.2 End-caps displacement

Two end-cap movements are considered:

- a short move, cold, of maximum 4 m to access the barrel electronics for maintenance and repair. The exact position of the end-caps should allow optimal access to both the barrel and the end-caps.

- a long move, cold also, of 12 m to allow for ID removal.

Both of these moves, as mentioned earlier, must be carried out cold and with the cryostat full of liquid or nearly full of liquid.

In both cases several interventions have to be carried out before moving the end-cap cryostat. Some of these must also be carried out in order to get to the read-out electronics installed on the back of the end-cap cryostat for maintenance or repair.

The sequence of events is as follows:

- the iron shielding around the beam tube in the forward region is removed

- some portions of the beam pipe in the very forward region might have to be taken out, depending on the scenario

- some vertical muon chambers supported by the surrounding structure are removed to allow the movement of the end-cap toroid (turret)

- the services from the muon chambers situated in between the barrel and the end-cap toroids are disconnected

- the current leads and other service lines are disconnected from the turret of the end-cap toroid

- - the vertical muon chambers on the outside of the end-cap toroid are disconnected from the services

- the end-cap toroid, the muon walls, and the shielding disks are moved back

- at this point, the end-cap cryostat can be moved, or the end-cap electronics can be accessed.

These interventions take several days. For the long move of the end-cap cryostat (12 m) for ID removal along the axial direction, the end-cap toroid must also be pushed to the side of the cavern on perpendicular rails. This additional operation is not necessary for the single access to the read-out electronics of the end-cap or the barrel.

The beam pipe and its flanges running through the inner warm vessel of the end-cap cryostat should have a diameter which size allows the cryostat to slide around it. That can be achieved with a small enough diameter pipe connected to a flange whose external diameter is less than or equal to 80 mm. Another solution, with no flange, would be to weld the corresponding portion of the beam pipe in place.

The constraint of moving the end-cap cryostat full of LAr implies that the cryogenics system stays in operation. In order to remain connected to the end-cap cryostat for both the short and long moves, the transfer lines must be flexible, at least along some length. The biggest problem is the safety line. As the expansion vessel is not in close proximity to the calorimeter, a large diameter safety line has to be routed from the top of the calorimeter, through the detector, in the limited space left by the sub-systems, to the expansion vessel. This safety line, under normal operating conditions will be full of LAr. For most of the time, this line will not move. For the move scenarios, we anticipate emptying the expansion vessel and the line. Amongst the many scenarios studied, up to now we have retained and worked on the hypothesis of a flexible line, at least for parts of its length (see Figure 15-2).
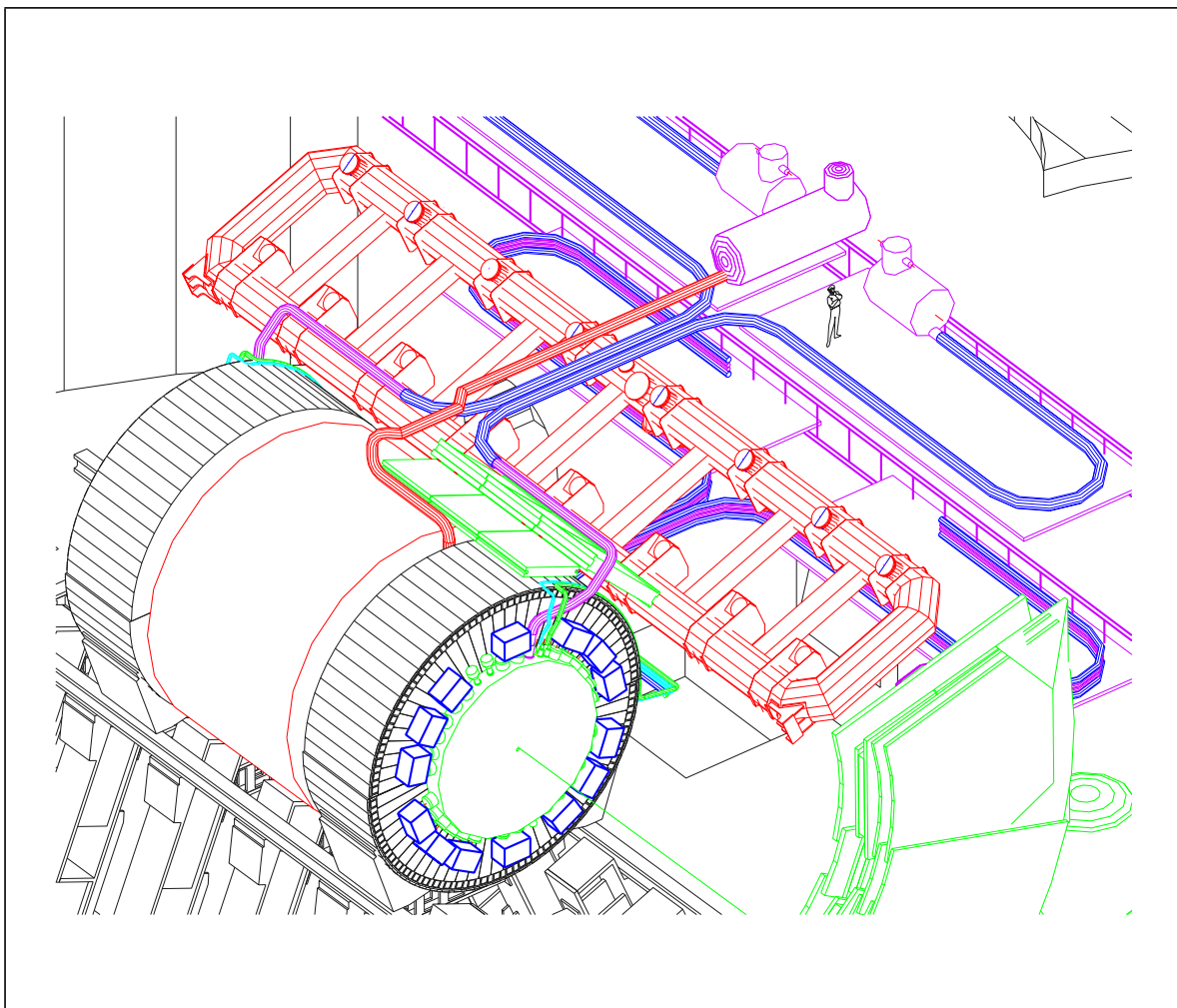
Such a line of 300 mm external diameter is uncommon and is not readily available. There are, therefore, a number of uncertainties about the bending radius and the degree of flexibility. Linked to this, a specific support structure to be assembled on the side of the cavern, motorized handling, and guide systems have to be designed. Certainly, tests of such a line and guiding systems must be carried out prior to taking any decision on the moving scenario. Fifteen metres of such a transfer line have been ordered for mechanical tests to be performed on a specifically designed bench.

Moving the other cryogenics lines for liquid nitrogen is an easier issue, as their diameters are smaller. Such lines can be purchased more easily.

All cables, signals, LV power, calibration, and HV should stay connected as much as possible for the short and long moves. This would have of course the great advantage of keeping, in the remote position or even far remote position, the entire electronics system in the same configuration of power, noise, cross-talk, and so on. This would imply that all services should remain equally connected, such as the water cooling systems for the readout crates and the power cables (if water-cooled), the vacuum for the cryostat and for the feedthroughs. This should be studied in detail for the overall design and layout of the ATLAS services, which is by far not an easy problem to solve

15.4 Major repair on calorimeters

A major repair of one of the calorimeters automatically means that the corresponding cryostat will have to be opened. This is of course a very delicate and time-consuming operation which could create an important shutdown. The biggest difficulty would be to open the barrel cryostat and to gain access to the electromagnetic calorimeter, when it is extracted from the cryostat. A similar situation would have to be faced also in the case of any repair of the solenoid. All decisions about the cold electronics of the electromagnetic calorimeters, barrel and end-caps, have been influenced by these considerations, thus minimizing the probability of such a catastrophy by placing all preamplifiers outside of the cryostat.

Figure 15-2 View of the flexible cryogenic connections of the end-caps. The flexible cryo lines pass through the ATLAS detector by the central gap in between central muon chambers.

Concerning the calorimeter, a major repair would be the failure of the HV system over several areas, mechanical break-downs during cooling, rupture of a sizeable fraction of the connections. For the cryostats, leaks detected when cold, rupture of the feedthroughs vacuum, mechanical problems during cool-down would constitute major repairs. The case of the solenoid will be described in the corresponding TDR.

In order to master all possible problems of the detectors/cryostats systems, it was decided to carry out extensive cold tests in the assembly buildings as described in the previous chapter. In terms of schedule, it means that in essence all LAr detectors and cryostats will have to be ready at least one year earlier than the other sub-systems. All the schedules should allow for this and LAr construction should be allowed to start early enough. In the assembly hall, the cryostats, together with the solenoid and the detectors, will undergo their first cool-down. Major problems, if any, should appear at this stage. The cryostats could then be reopened in the clean area of the assembly building. It is certainly mandatory to demonstrate that all parts are functioning according to specifications before the detectors are installed in the cavern. However, the cryostats will be installed warm, and will have to go through a second cool-down after their installation in the cavern. This is not desirable but, at this stage, it is unavoidable.

The probability of major repairs of the LAr calorimeters should therefore be considered as a quite exceptional circumstance. Although all measures will have been taken to avoid it, scenarios for repairing the barrel and the end-caps must be demonstrated as being possible, although difficult to achieve in practice and involving major shutdowns. As the geographical position of the barrel and of the end-caps is quite different in the cavern, these two cases are discussed separately.

15.4.1 Barrel calorimeter

Any repairs to be made inside the barrel cryostat for the cryostat complex itself, for the calorimeter or for the solenoid, will be extremely difficult and lead to a very long shutdown. Such a situation will only be envisaged for very large repairs. A comparable situation for ATLAS would be to have a major problem with one of the barrel toroid coils.
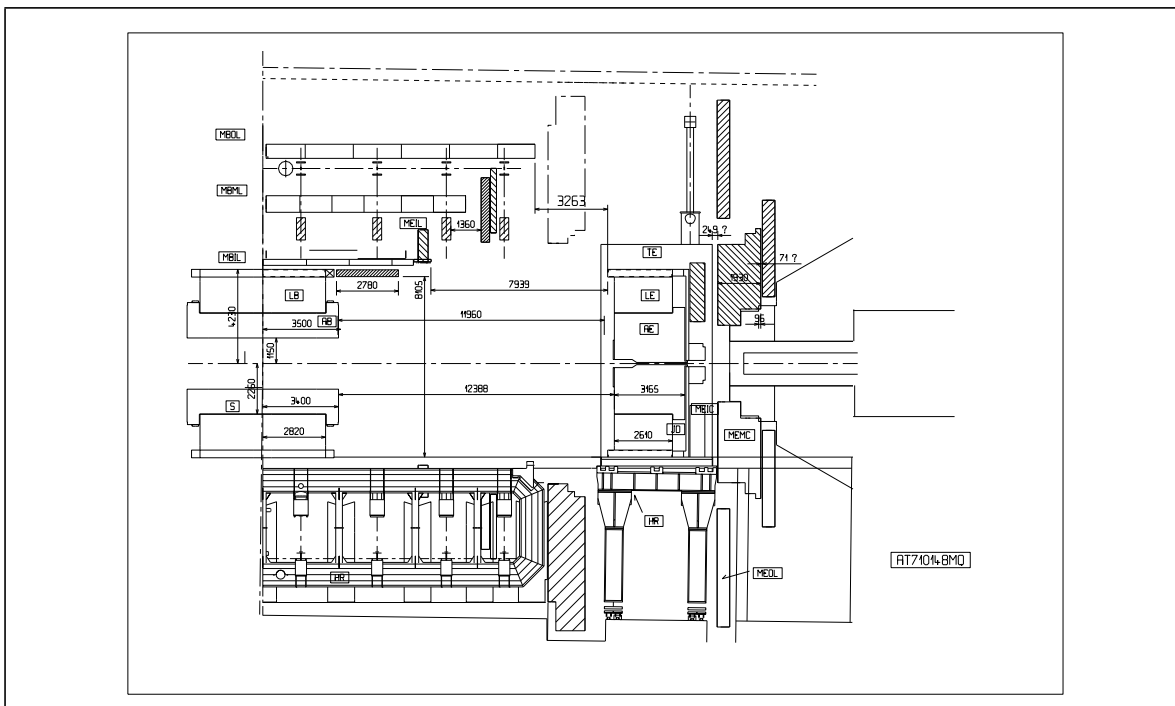
Two possibilities can, at least in principle, be envisaged to repair the barrel detector: bring it back upstairs or repair it in-situ. In both cases, the inner detector has to be removed first from the inside of the cryostat after its disconnection from all signal cables and cooling pipes.

To take the barrel cryostat upstairs implies the following steps:

- all external connections of the solenoid have to be broken

- all cryogenics, signals, cooling, vacuum connections of the barrel have to be removed

- the read-out electronics around the feedthrough locations have to be taken apart, leaving only the pedestal part of the crates connected to the feedthroughs

- the ATLAS detector should be fully opened on the side of the main access shaft, and enough room should be available to bring back the full barrel under the shaft. (Some detectors will have to be brought to the surface)

- the mechanism used to install the barrel in the centre of the experiment should be able to retract it from there

- all the top modules of the tile calorimeter should be removed and brought back to the surface.

- The cryostat can then be lifted up.

During such an intervention, the ATLAS detector would be totally inoperational as all internal and forward elements would be dismantled except the magnets and part of the muon system. To minimize the time when the LHC machine would be inoperational, the removal of the barrel cryostat should be programmed to coincide within the yearly shutdown, perhaps slightly extended. Repairs on the cryostat or on the calorimeter could then by performed at the surface. The detector would then be re-installed during the next LHC machine shutdown.

Opening the cryostat in situ, without moving it, faces four major problems: the room needed radially and transversally to the beam axis, the amount of heavy mechanical structures to be brought inside the toroid, the absence of crane access leading to complicated mechanisms to handle the cryostat covers, the solenoid if necessary and the calorimeter, the cleanliness of the entire area should be guaranteed (see Figure 15-3). The situation where repairs would have to be implemented on the side of the solenoid connections is the most complicated. In this case, the solenoid would have to be either removed or at least disconnected to open the cold vessel of the cryostat. Due to the presence of a central flange on the outer radius of the cold vessel, it is not possible to remove the calorimeter from one side only. All these difficult questions should be

Figure 15-3 Side view of the ATLAS detector showing the EC toroid magnet and the EC cryostat recessed from their original positions. The ID has been removed. The dimensions of the access gap between the toroid and the EC cryostat, as well as the size of the internal free area which could be used in case of repair of the barrel in-situ are given.

discussed and a scenario should be defined with the ATLAS Technical Coordination. The fact that the ATLAS rail system will be inclined should not be forgotten either.

Alternative scenarios could also be studied such as: bringing back the entire barrel on one side of the cavern. This will provide enough axial room along the beam to operate the long I-beam needed for removal of the solenoid. On the other hand, other detectors, such as some forward muon chambers, could also be removed. Larger pieces of mechanical structures could then be brought in.

In order to be able to open the cryostat in-situ, one should also be able to guarantee that one will be able to close it again. It should then be asserted that no unknown mechanical deformations could happen during cool-down, transportation, lowering down in the pit or due to the inclined position in the interaction area. The answers to all these questions could not be developed in the time given for the delivery of this TDR and should therefore be undertaken in the future.

15.4.2 End-cap calorimeters

Concerning internal repair to be made inside the end-cap cryostat, the situation is different in many aspects from the case of the barrel. Two scenarios can be envisaged: opening the cryostat and extracting the detectors in the cavern, or taking apart the full Extended Tile calorimeter in order to take the cryostat to the surface. At the moment, the baseline for such action is to bring the cryostat back to the surface, transport it to the assembly hall in the CERN West Area and perform all repairs there, in clean conditions. In any event, this scenario can be envisaged only when major repairs are necessary.

Each end-cap, as a whole, can be retracted from the coverage of the barrel toroid and is then accessible by the surface cranes either by the main or by the smaller access shaft. For this, the end-cap toroid should be rolled into its side position, on the perpendicular rails, as for the ID axial removal, and the muon wall between the end-cap cryostat and the end-cap toroid should be removed. All connections from the end-cap should be removed, including all cryogenics pipes, after warming up the detector. The entire upper structure of the extended tiles should be dismantled and removed. At this point, the end-cap can be lifted up by the same means as used during its installation. The time estimate for such operation is a few months.

15.5 Installation schedule

The LAr installation schedule, Figure 15-4, and consequently all LAr schedules are not accurate to better than two months. This reflects the inherent uncertainty of all long-term schedules and the fact that the final integrated ATLAS schedule for installation in the cavern is not at present known in full detail. This schedule will have to be rewieved when all inputs from ATLAS are known. The final installation schedule will then be published in the ATLAS volume 19, Installation, Overall Safety Issues and Schedule.

Although not specifically shown in the chart, it is assumed that several items will be ready whenever needed:

- the services should be available much earlier than the cryostats installation, i.e. safety services, control system.

- all LAr piping passing through the centre gap of the experiment has to be installed before the muon chambers installation

- enough hardware in the TRIGGER/DAQ system has to be installed to test the calorimeters as soon as the cables are connected.

The LAr installation schedule is linked with the final assembly schedule and the full cold tests of the cryostats. As mentioned earlier, due to the single cryogenic system installed in the West Hall, all cryostats have to be tested sequentially. These tests are time-consuming. It is not possible to advance arbitrarily the installation of one of the cryostats, for example the second end-cap, without modifying the overall final assembly schedule and consequently the milestones for the construction of the detectors. .

15.6 References

15-1   P.Beynel / TIS, TIS/GS/PB/cg/94-189: Mesures de vibrations sur remorque
             articulée-tractée Nicolas, 19 Dec. 1994.

15-2   L.Nikita, A.Pleskach, ATLAS Internal Note, LARG-NO- (1996) : Les problèmes de la
             descente du calorimètre "LAr END-CAP" dans le puits, 10 July 1996.

15-3   F.Butin, ATL-GE-CERN-EDH-0001 : A   system analysis of support structures, 5 July 1996.

15-4   C.R.Gregory, C.W.Nuttall, CERN/AT/95-06 (DI), CERN TIS-CFM/95-06 : Explosion risks
             in cryogenic liquids exposed to ionising radiation, 28 March 1995.

15-5   ATLAS TDR, vol. 19 : Installation, Overall Safety Issues and Schedule, to be published.

15-6   Atlas Technical Coordination, Minutes of meetings, PPE/BN/date_TIE.
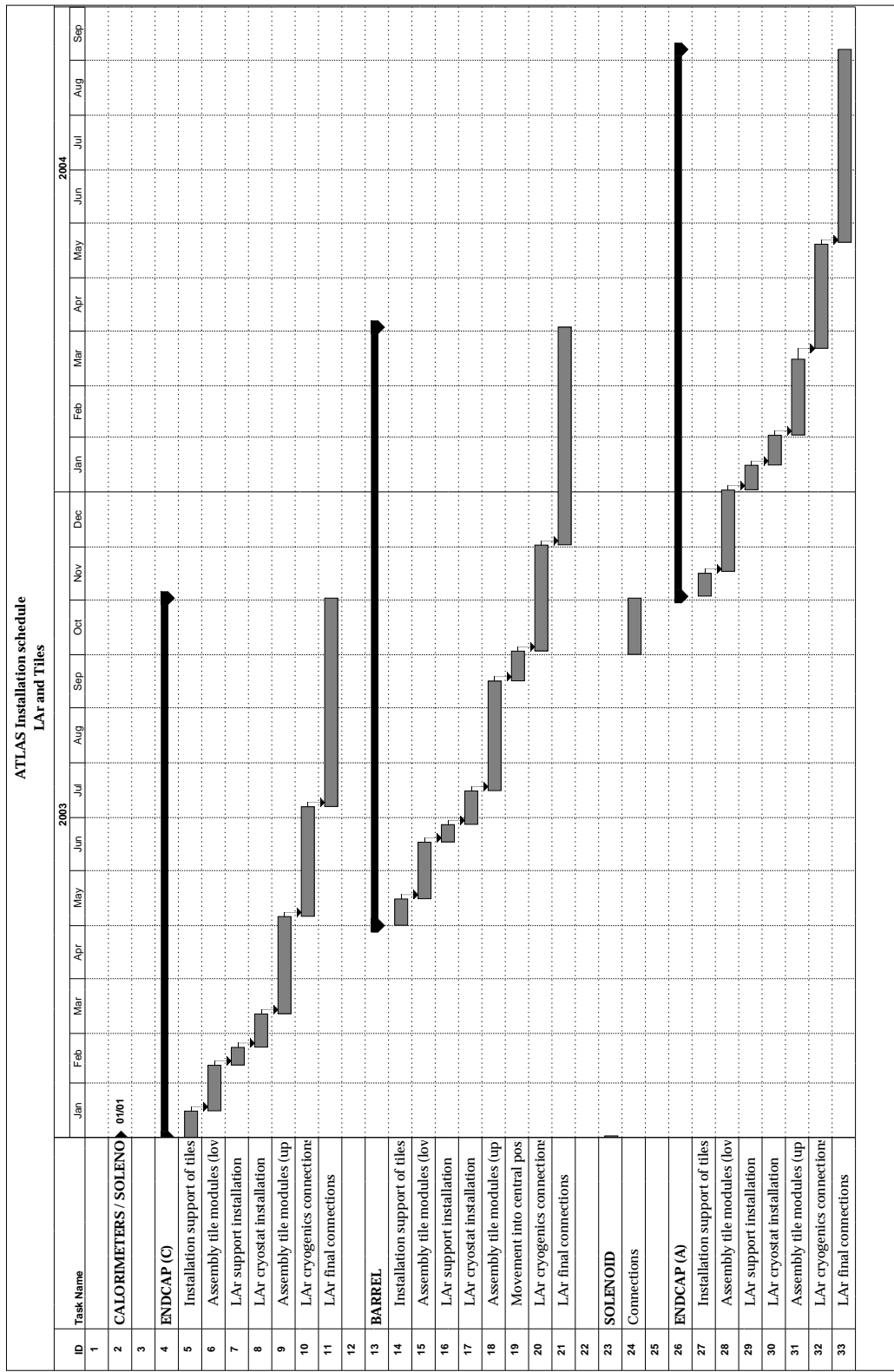
Figure 15-4 LAr installation schedule.
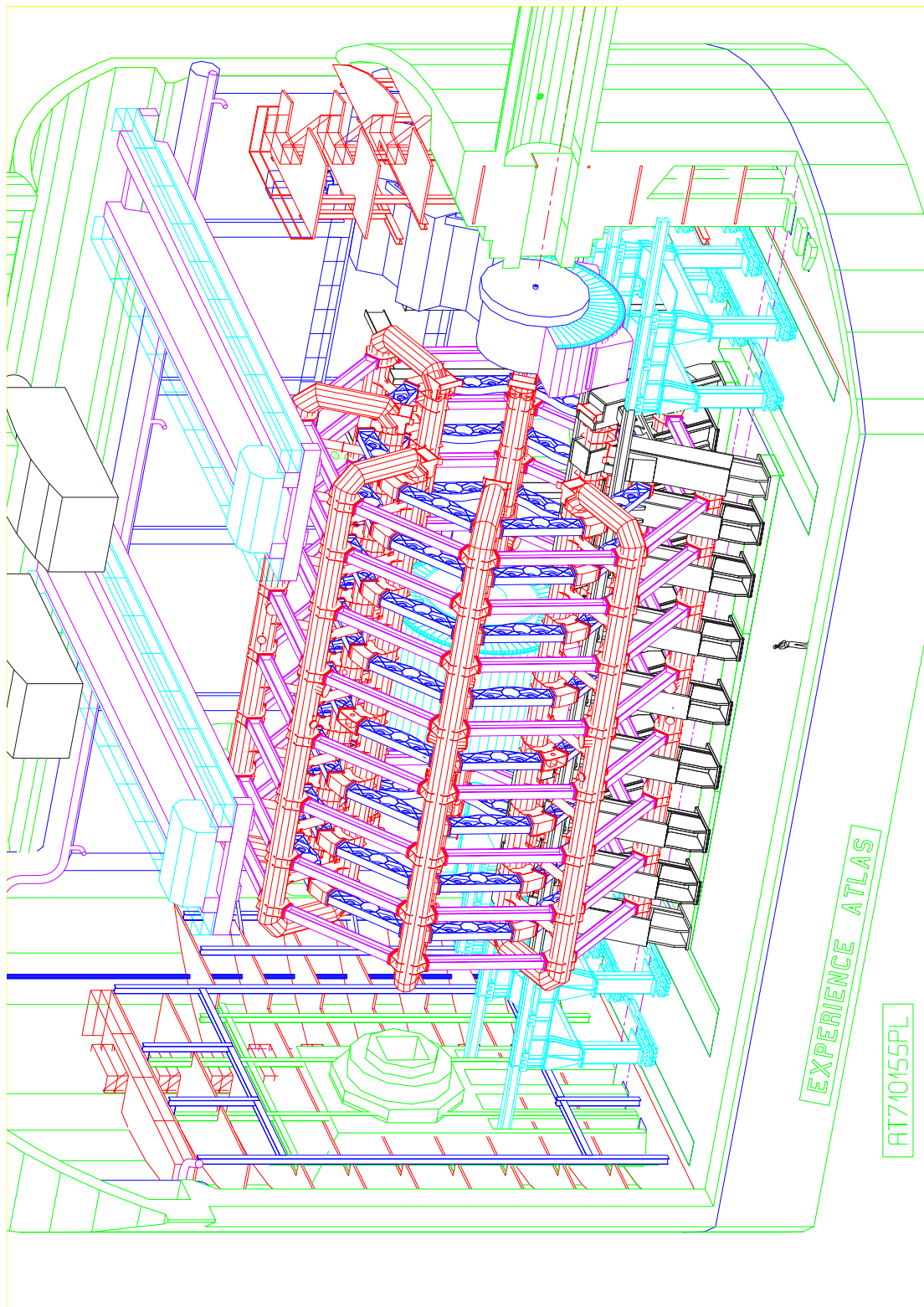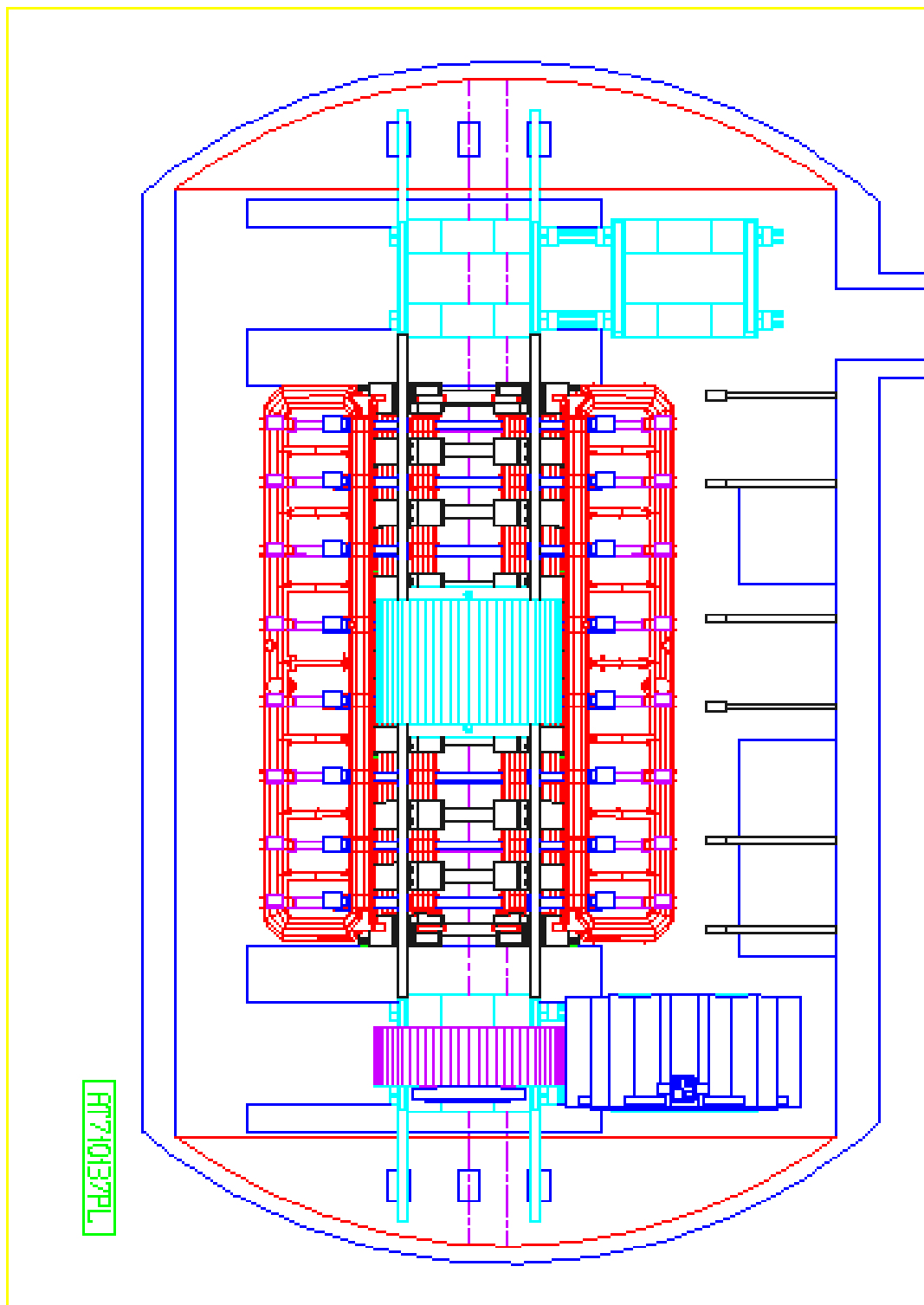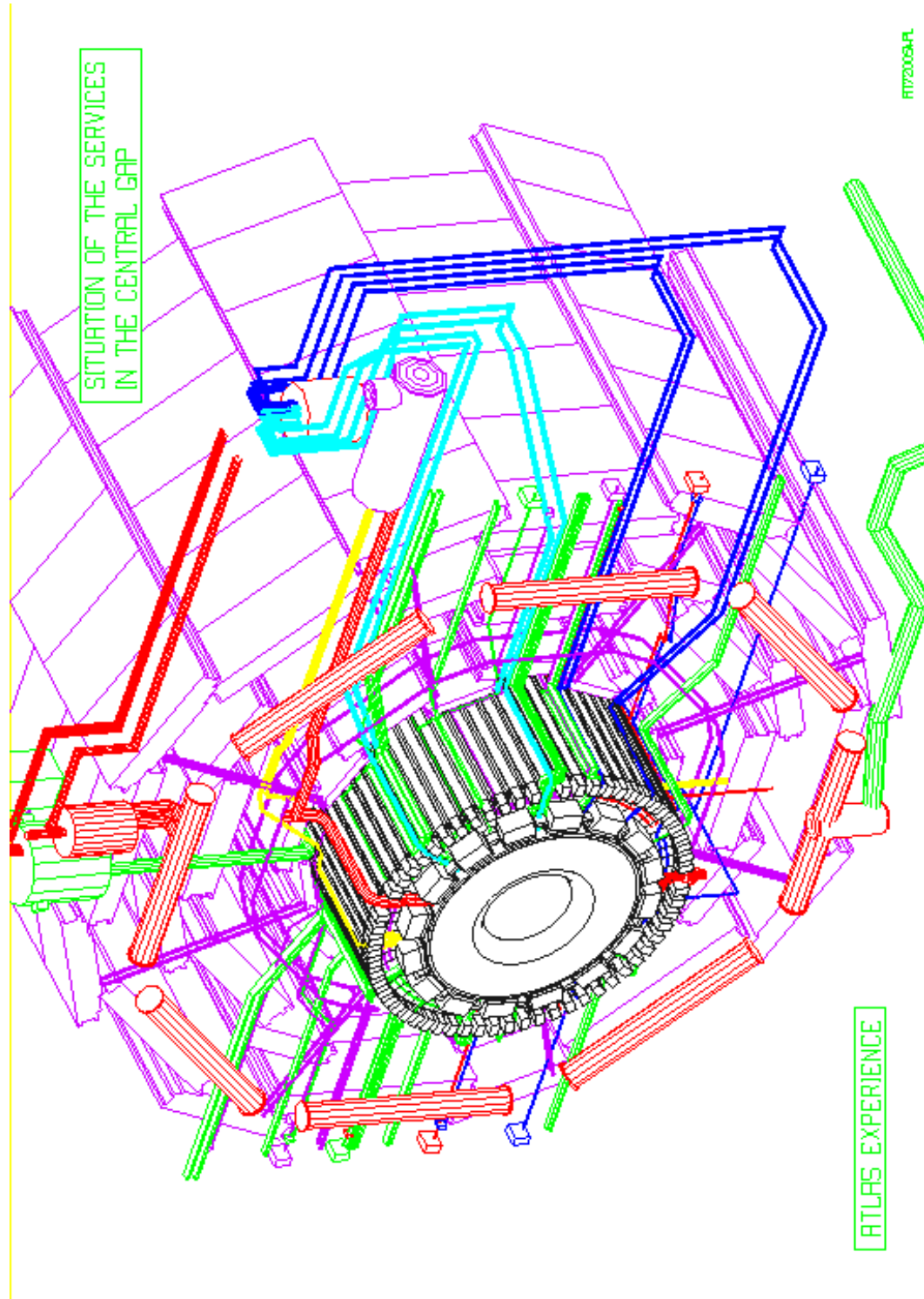
Figure 15-i View of the ATLAS experiment during the assembly of one calorimeter end-cap.

Figure 15-ii Top view of the ATLAS experiment showing the barrel and one end-cap cryostat assembled.

Figure 15-iii General view of the services passing through the central ATLAS gap, in between muon chambers.
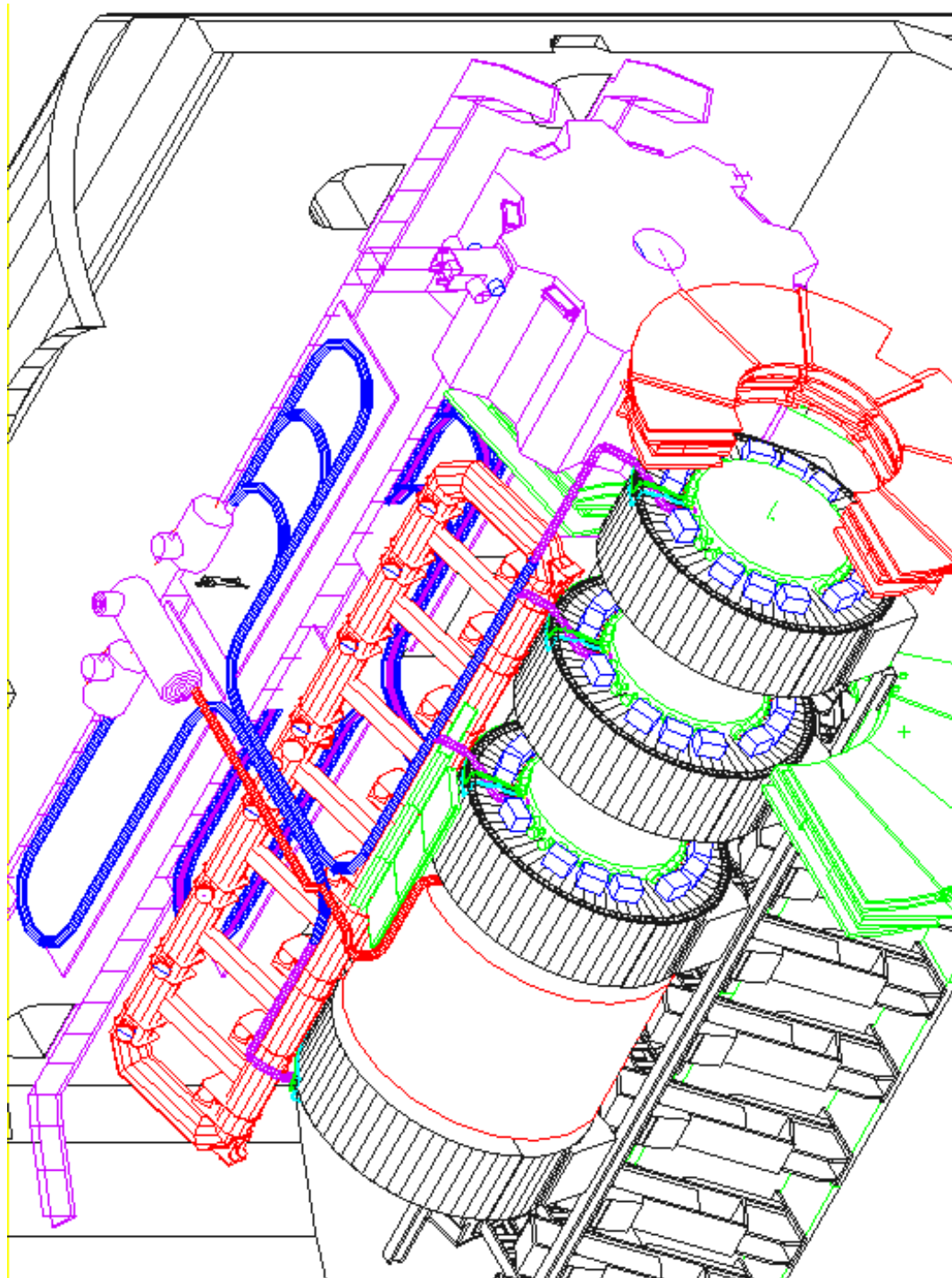
Figure 15-iv Principle of the movement of one end-cap calorimeter showing the evolution of the pass of the flexible cryogenic lines.

16 Master schedule and LAr PBS

16.1 Master schedule

The present main LAr schedule, Figure 16-i to Figure 16-v, is a summary of the detailed schedules which are part of the precedent chapters. The accuracy of such a schedule cannot be considered better than a few months. The present schedule will have to be revisited in view of the definitive general installation schedule.

The main features of the LAr schedule are:

- a design period of the detectors which comes to an end at the time of the present TDR

- a one year period for building modules zero

- a construction period, of three years for the barrel, of four years for both endcaps

- a final assembly and tests - warm and cold - period taking two years

- the installation period in the cavern

Given the rather long time reserved for the overall cold tests of detectors and cryostats, the construction of the LAr calorimeters should start earlier than for most other detectors.

16.2 LAr Product Breakdown Structure (PBS)

16.2.1 Introduction

The full list of the LAr Institutions, and the people involved, is given in Appendix D.

The LAr Extended PBS, Figure 16-1 and Table 16-1, uses the following abbreviations:

// : the Institute(s) on the left, right-side of the // are responsible for half of the PBS item.

C.F. : ATLAS Common Fund

Alberta: Centre for Subatomic Physics, University of Alberta, Edmonton

Annecy: Laboratoire d'Annecy-le-Vieux de Physique des Particules (LAPP), Annecy-le-Vieux

Arizona: University of Arizona, Tucson, Arizona

British (or B.) Columbia: Dept. of Physics , University of British Columbia, Vancouver

Brookhaven: Brookhaven National Laboratory (BNL), Upton, New York

Canada: Alberta, British Columbia, Carleton, Montréal, Toronto, TRIUMF, Victoria

Carleton: University of Carleton / C.R.P.P., Carleton

Casablanca: Universités Hassan II, Casablanca et Mohamed V, Rabat, Morocco

CERN: European Laboratory for Particle Physics (CERN), Geneva

Columbia: Nevis Laboratory, Columbia University, Irvington, New York

Dallas: Department of Physics, Southern Methodist University, Dallas, Texas

JINR : Joint Institute for Nuclear Research (JINR), Dubna

Germany: Heidelberg, Mainz, Munich MPI, Wuppertal

Grenoble: Institut des Sciences Nucléaires de Grenoble, IN2P3-CNRS-Université Joseph Fourier

Heidelberg : Institut für Hochenergiephysik der Universität Heidelberg

IN2P3: Annecy, Grenoble, Marseille, Orsay, Paris

ITEP: Institute for Theoritical and Experimental Physics, Moscow

Kosice: Institute of Experimental Physics of the Slovak Academy of Sciences, Kosice

Madrid: Physics Department, Universidad Autónoma de Madrid, Madrid

Mainz: Institut für Physik, Universität Mainz

Marseille: Centre de Physique des Particules de Marseille, IN2P3-CNRS, Marseille

Milano : Dipartimento di Fisica dell'Universitá di Milano e I.N.F.N., Milano

Montreal: Group of Particle Physics, University of Montreal,Montreal

Moscow FIAN : P.N.Lebedev Institute of Physics, Moscow

Munich MPI: Max-Planck-Institut für Physik, München

Novosibirsk: Budker Institute of Nuclear Physics (BINP), Novosibirsk

Orsay: Laboratoire de l'Accélérateur Linéaire, IN2P3-CNRS, Orsay

Paris: LPNHE, Universités de Paris VI et VII, IN2P3-CNRS, Paris

Pittsburgh: University of Pittsburgh, Pittsburgh, Pennsylvania

Protvino: Institute for High Energy Physics (IHEP), Protvino

Rochester: Department of Physics and Atronomy, University of Rochester, Rochester, New-York

Saclay: CEA, DSM/DAPNIA, Centre d'Etudes de Saclay, Gif-sur-Yvette

Stockholm KTH: Royal Institute of Technology (KTH), Stockholm

Toronto: Department of Physics, University of Toronto, Toronto

TRIUMF: TRIUMF, Vancouver

US: Arizona, Brookhaven, Columbia, Dallas, Pittsburgh, Rochester

Victoria: Dept. of Physics and Astronomy, University of Victoria, Victoria

Wuppertal : Fachbereich Physik, Bergische Universität, Wuppertal

16.2.2 Extended PBS
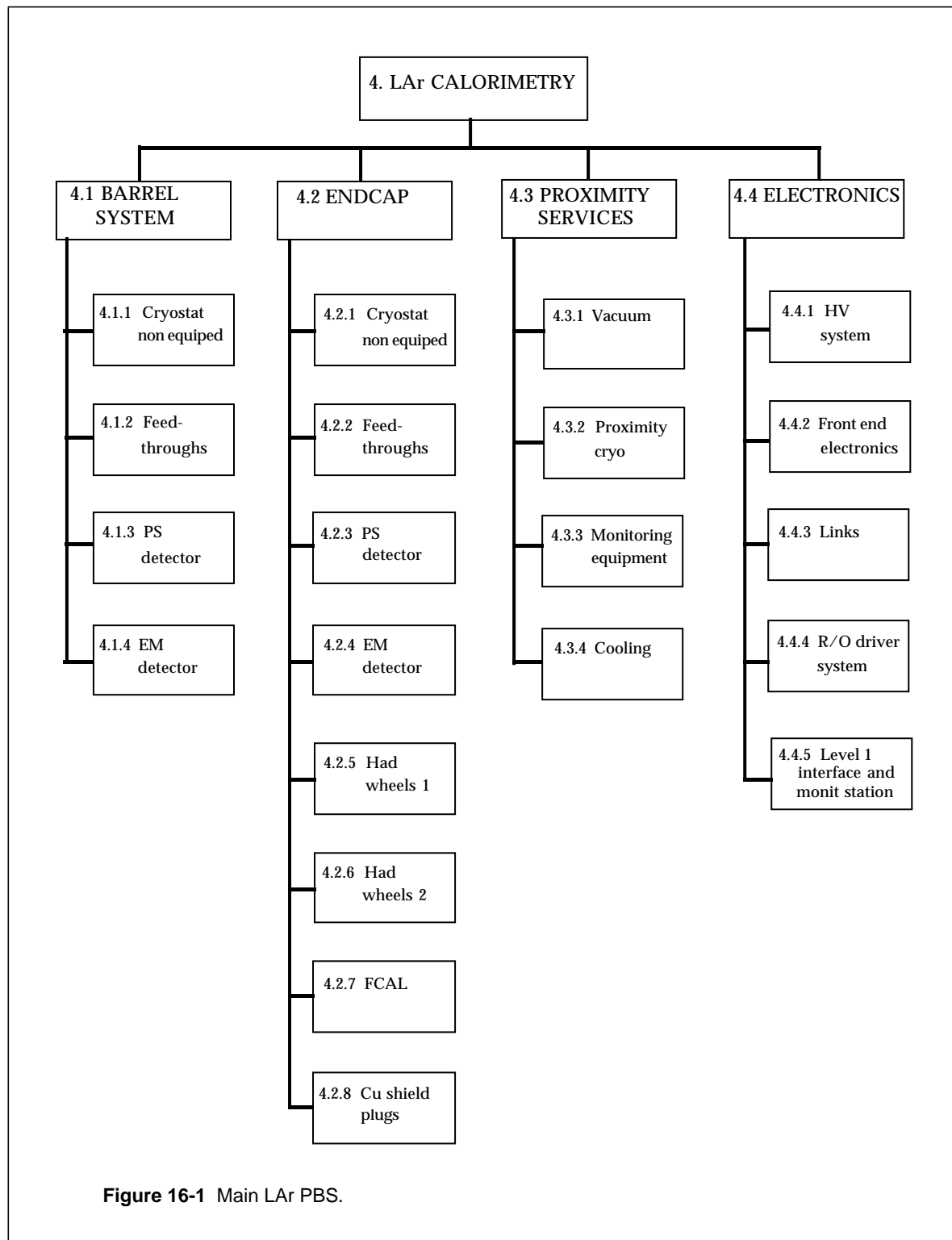
Figure 16-1 Main LAr PBS.

Figure 16-2

Table 16-1 The LAr Detector Extended Product Breakdown Structure

PBS No.	PBS ITEM	List of related items	Resp.Institutes
4.	LAr CALORIMETRY		
4.1	BARREL		
4.1.1	Cryostat non equipped	Engineering	Rochester ∕ C.F.
4.1.1.1	Warm vessel	Support beam	C.F.
		Support columns	C.F.
		Spreader bars	C.F.
		Support struct. for half cold	C.F.
		Support struc. for warm bulkheads	C.F.
		Support structure for cryostat	C.F.
4.1.1.1.1	Outer warm cylinder		C.F.
4.1.1.1.2	Inner warm cylinder		C.F.
4.1.1.1.2.1	Final cylinder		C.F.
4.1.1.1.2.2	Support ledge for I.D.		C.F.
4.1.1.1.2.3	Spare unit for shipping		C.F.
4.1.1.1.3	Bulkheads		C.F.
4.1.1.1.4	Accessories		C.F.
4.1.1.1.5	Transition ledge		C.F.
4.1.1.2	Cold vessel		C.F.
4.1.1.2.1	Outer cold cylinder		C.F.
4.1.1.2.1.1	Half outer cold cylinder (safety line side)		C.F.
4.1.1.2.1.2	Half outer cold cylinder (bus line side)		C.F.
4.1.1.2.2	Inner cold cylinder with bulkheads		C.F.
4.1.1.2.2.1	Half inner cold cylinder (safety line side)		C.F.
4.1.1.2.2.2	Half inner cold cylinder (bus line side)		C.F.
4.1.1.2.3	Accessories		C.F.
4.1.1.3	Support mechanisms		C.F.
4.1.1.3.1	Support sling between warm and cold vessel		C.F.

Table 16-1 The LAr Detector Extended Product Breakdown Structure

PBS No.	PBS ITEM	List of related items	Resp.Institutes
4.1.1.3.2	Alignement stops between warm and cold vessel		C.F.
4.1.1.3.3	Support legs of outer vessel		C.F.
4.1.1.4	Cryo feedthroughs		C.F.
4.1.1.5	Superinsulation		C.F.
4.1.1.6	LAr outlet valve		C.F.
4.1.1.7	Warm vessel relief valve		C.F.
4.1.1.8	Pumpout valves warm vessel		C.F.
4.1.1.9	Associated internal cryogenics		C.F.
4.1.1.9.1	Overflow vessel		C.F.
4.1.1.9.2	Overflow LAr line		C.F.
4.1.2	Feedthroughs	Engineering	Brookhaven / C.F.
4.1.2.1	Signal feedthroughs		C.F.
4.1.2.1.1	Body		C.F.
4.1.2.1.1.1	Alu ring flange		C.F.
4.1.2.1.1.2	Outer warm flange assembly		C.F.
4.1.2.1.1.3	Inner warm flange assembly		C.F.
4.1.2.1.1.4	Cold flange assembly		C.F.
4.1.2.1.1.5	Cold box assembly		C.F.
4.1.2.1.1.6	Vacuum cables		C.F.
4.1.2.1.1.7	Heater		C.F.
4.1.2.1.1.8	Temperature control		C.F.
4.1.2.1.1.8.1	Probes		C.F.
4.1.2.1.1.8.2	Cables		C.F.
4.1.2.1.1.8.3	Transmitters		C.F.
4.1.2.1.1.8.4	Controllers		C.F.
4.1.2.1.2	Pigtail cables		C.F.
4.1.2.2	HV feedthroughs	Engineering Procurement	Rochester / C.F. C.F.

Table 16-1 The LAr Detector Extended Product Breakdown Structure

PBS No.	PBS ITEM	List of related items	Resp.Institutes
4.1.3	PS detector	Integration and insertion tools	Casablanca / Grenoble / Stockholm KTH
4.1.3.1	Sectors	Assembly clean rooms	Grenoble / Stockholm KTH
		LN2 test cryostats	Grenoble / Stockholm KTH
		Test benches	Grenoble / Stockholm KTH
		Assembly tools	Casablanca/Stockholm KTH
		Storage bags / vessels	Casablanca/Stockholm KTH
4.1.3.1.1	Modules	Electrodes	Stockholm KTH
		Jigs & shims	Grenoble
		Production	Grenoble
4.1.3.1.2	Shells		Grenoble
4.1.3.1.3	Support bars		Grenoble
4.1.3.2	Cold electronics		
4.1.3.2.1	Mother-board system	Test station for MB	Grenoble
		Testing of MB	
4.1.3.2.2	Cables		Grenoble / Orsay
4.1.3.2.2.1	Signal cables		Grenoble / Orsay
4.1.3.2.2.2	Calibration cables		Grenoble / Orsay
4.1.3.2.2.3	HV cables		Grenoble / Orsay
4.1.3.3	Support rails		Grenoble
4.1.4	EM detector		
4.1.4.1	Absorbers	Assembly hall	Orsay
		Manutention tools	CERN / Orsay / Paris
		Tooling for sandwich assbly	CERN
		Bending press	CERN
		Gluing press	Orsay
		Gluing tool bars on absorbers	Orsay
		Absorber meas.tridim.equip.	Paris
		Fabrication absorbers	Orsay
		Absorber measurement	Paris
4.1.4.1.1	Lead plates	Lead specification	CERN / Orsay /Paris/ Saclay
		Lead procurement	Saclay
		Lead laminating & tooling	Saclay
		On-line thickness meas.	Paris
		U-sound meas. tooling	Paris
		U-sound measurements	Paris
		Cleaning machine lead	Orsay
4.1.4.1.1.1	Large plates (1.5 mm)		id. as 4.1.3.1.1

Table 16-1 The LAr Detector Extended Product Breakdown Structure

PBS No.	PBS ITEM	List of related items	Resp.Institutes
4.1.4.1.1.2	Small plates (1.1 mm)		id. as 4.1.3.1.1
4.1.4.1.2	Steel sheet (0.2 mm)	Steel specification Steel sheets procurement Steel laminating & tooling Cleaning	CERN / Orsay / Saclay Saclay Saclay Saclay
4.1.4.1.3	Prepreg	Prepreg specification Prepreg procurement	CERN / Orsay / Saclay Saclay
4.1.4.1.4	Bars	Design G10 bars procurement	CERN CERN
4.1.4.1.5	Misc. components		CERN
4.1.4.2	Kapton electrodes	PCB's design Bending tools Testing tools Logistics	Annecy / CERN / Paris / US Annecy Milano / Paris CERN / IN2P3 / Milano / US
4.1.4.2.1	Electrodes	Testing tools in factory PCB's procurement Bending Testing Final conditioning	Milano / Paris CERN / IN2P3 / Milano / Saclay / US Annecy Milano / Paris Milano / Paris
4.1.4.2.2	Ground contacts		
4.1.4.3	Spacers	Procurement Forming tools	Saclay Saclay
4.1.4.4	Rings		Annecy
4.1.4.4.1	External rings	Rings procurement Module assbly backbones Rings/backbones machining	Annecy Saclay Saclay
4.1.4.4.2	Internal rings		Annecy
4.1.4.5	Cooling loops on modules	Design Procurement	Annecy / Rochester / Saclay Saclay
4.1.4.6	Cold electronics		
4.1.4.6.1	Mother-board system	Test station for MB Testing of MB	Brookhaven Brookhaven
4.1.4.6.1.1	Summing boards (F+B)		Brookhaven
4.1.4.6.1.2	Signal mother boards		Brookhaven
4.1.4.6.1.3	HV mother boards		Brookhaven
4.1.4.6.2	Cables	Test station for cables	Annecy / Orsay

Table 16-1 The LAr Detector Extended Product Breakdown Structure

PBS No.	PBS ITEM	List of related items	Resp.Institutes
4.1.4.6.2.1	Signal cables		Annecy / Orsay
4.1.4.6.2.2	Calibration cables		Annecy / Orsay
4.1.4.6.2.3	HV cables		Annecy / Orsay
4.1.4.6.3	Patch panel and cable support		Annecy
4.1.4.7	Modules (32)	Module HV test system (3) Module assembly jigs (3) Handling devices (3) Module assembly halls Clean rooms Module cold test stations Module assembly & tests Electronics for cold tests Transportation	Annecy Annecy Saclay Annecy / CERN / Saclay Annecy / CERN / Saclay Annecy / Saclay Annecy / CERN / Saclay Annecy / Saclay CERN
4.1.4.8	Half-barrel (2)	Half-barrel assbly tools Half-barrel assbly & insertion	CERN / Saclay CERN / Saclay
4.2	END-CAP		
4.2.1	Cryostat non equiped	Engineering Support structure cryostat Support structure covers Spreader bar cryostat Spreader bars bulkheads Integration tools : Support structures detects Spreader bar detects Insertion support structure Push-pull system Extension rails Support structure Cu abs Spreader bar Cu abs FCAL integration tube	Orsay / Germany / C.F. C.F. C.F. C.F. C.F.
4.2.1.1	Vessels		C.F.
4.2.1.1.1	Warm vessel		C.F.
4.2.1.1.2	Cold vessel		C.F.
4.2.1.1.3	Forward structure		C.F.
4.2.1.1.4	Forward tube		C.F.
4.2.1.1.5	Warm tube		C.F.

Table 16-1 The LAr Detector Extended Product Breakdown Structure

PBS No.	PBS ITEM	List of related items	Resp.Institutes
4.2.1.1.6	Warm bulkhead		C.F.
4.2.1.1.7	Cold bulkhead		C.F.
4.2.1.1.8	Forward bulkhead		C.F.
4.2.1.1.9	Set Alu/steel transitions		C.F.
4.2.1.2	Cryo feedthroughs		C.F.
4.2.1.3	Superinsulation		C.F.
4.2.1.4	Seals kit		C.F.
4.2.1.5	Bolting		C.F.
4.2.1.6	Insulated supports		C.F.
4.2.1.7	Vacuum safety valve		C.F.
4.2.1.8	Inner LN2 cooling system		C.F.
4.2.1.9	Insulated stops		C.F.
4.2.1.10	Axial expansion bellow		C.F.
4.2.1.11	Steel supports		C.F.
4.2.1.12	Extension cylinder for signal feedthroughs		C.F.
4.2.1.13	Associated internal cryo-genics		C.F.
4.2.1.13.1	Overflow vessels		C.F.
4.2.1.13.2	Overflow LAr lines		C.F.
4.2.2	Feedthroughs	Engineering	Canada / C.F.
4.2.2.1	Signal feedthroughs		C.F.
4.2.2.1.1	Body		C.F.
4.2.2.1.1.1	Alu ring flange		C.F.
4.2.2.1.1.2	Outer warm flange assembly		C.F.
4.2.2.1.1.3	Inner flange assembly		C.F.
4.2.2.1.1.4	Cold flange assembly		C.F.
4.2.2.1.1.5	Cold box assembly		C.F.
4.2.2.1.1.6	Vacuum cables		C.F.
4.2.2.1.1.7	Heater		C.F.
4.2.2.1.1.8	Temperature control		C.F.

Table 16-1 The LAr Detector Extended Product Breakdown Structure

PBS No.	PBS ITEM	List of related items	Resp.Institutes
4.2.2.1.1.8.1	Probes		C.F.
4.2.2.1.1.8.2	Cables		C.F.
4.2.2.1.1.8.3	Transmitters		C.F.
4.2.2.1.1.8.4	Controllers		C.F.
4.2.2.1.2	Pigtail cables		C.F.
4.2.2.2	HV feedthroughs		
4.2.3	PS detector		
4.2.3.1	Sectors		
4.2.3.1.1	Modules		
4.2.3.1.2	Support system		
4.2.3.2	Cold electronics		
4.2.3.2.1	Mother-board system		
4.2.3.2.2	Cables		Orsay
4.2.3.2.2.1	Signal cables		Orsay
4.2.3.2.2.2	Calibration cables		Orsay
4.2.3.2.2.3	HV cables		
4.2.4	EMEC detector	CERN assbly clean room	CERN
		Assembly structure	Marseille
		EM EC wheel assembly	Madrid / Marseille / Novosibirsk
		Overturning tool	
4.2.4.1	Absorbers	Manutention tools	Madrid
		Tooling for sandwich stacking	Madrid
		Bending tools	Madrid
		Curing molds	Madrid
		Absorber fabrication	Madrid
		Absorber control	Madrid
4.2.4.1.1	Lead plates	Design	Madrid / Marseille
		Procurement	Madrid
		On-line thickness meas	Madrid/Paris
		U-sound meas. tooling	Madrid / Paris
		U-sound measurement	Madrid
		Out-cutting	Madrid
		Cleaning	Madrid
4.2.4.1.1.1	Large plates		id. as 4.2.4.1.1

Table 16-1 The LAr Detector Extended Product Breakdown Structure

PBS No.	PBS ITEM	List of related items	Resp.Institutes
4.2.4.1.1.2	Small plates		id. as 4.2.4.1.1
4.2.4.1.2	Steel	Design Procurement Out-cutting Cleaning	Madrid / Marseille Marseille Madrid Marseille
4.2.4.1.2.1	Large plates		id. as 4.2.4.1.2
4.2.4.1.2.2	Small plates		id. as 4.2.4.1.2
4.2.4.1.3	Prepreg	Design Procurement Out-cutting	Madrid Madrid Madrid
4.2.4.1.3.1	Large plates		id. as 4.2.4.1.3
4.2.4.1.3.2	Small plates		id. as 4.2.4.1.3
4.2.4.1.4	Bars	Design Procurement Bars production	Marseille Marseille Marseille
4.2.4.2	Kapton electrodes	PCB's design Bending tools Testing tools Logistics	CERN / Marseille Marseille Orsay / Paris CERN / IN2P3 / Milano / US
4.2.4.2.1	Electrodes	Testing tools in factory PCB's procurement Bending Testing Final conditioning	Milano / Orsay / Paris CERN / IN2P3 / Milano / Saclay / US Marseille (module 0 only) / .... Orsay / Paris Orsay / Paris
4.2.4.2.2	Ground contacts		
4.2.4.3	Spacers	Studies Procurement	Marseille Marseille
4.2.4.3.1	Inner wheel		Marseille
4.2.4.3.2	Outer wheel 1st part		Marseille
4.2.4.3.3	Outer wheel 2nd part		Marseille
4.2.4.4	Structure	Studies Procurement	Marseille Marseille
4.2.4.4.1	Outer rings		Marseille / Novosibirsk
4.2.4.4.2	Indexing rings		Marseille / Novosibirsk
4.2.4.4.3	Intermediate rings		Marseille
4.2.4.4.4	Inner rings		Marseille
4.2.4.5	Cold electronics		

Table 16-1 The LAr Detector Extended Product Breakdown Structure

PBS No.	PBS ITEM	List of related items	Resp.Institutes
4.2.4.5.1	Mother-board system	Test station for MB Testing of MB	Marseille / Madrid Marseille / Madrid
4.2.4.5.1.1	Summing boards		Marseille / Madrid
4.2.4.5.1.2	Signal mother boards		Marseille / Madrid
4.2.4.5.1.3	HV mother boards		Marseille / Madrid
4.2.4.5.2	Cables		Marseille / Orsay
4.2.4.5.2.1	Signal cables		Marseille / Orsay
4.2.4.5.2.2	Calibration cables		Marseille / Orsay
4.2.4.5.2.3	HV cables		Marseille / Orsay
4.2.4.5.3	Patch panel and cable support		Marseille
4.2.4.6	Modules	Clean rooms Handling tools Assembly supports Module assembly Module geometry control Module cabling Cold test set-up Cold tests, incl.electronics Spatula Overturning tool	Madrid / Marseille Marseille Marseille Madrid / Marseille Madrid / Marseille Madrid / Marseille Marseille Madrid / Marseille / Novosibirsk Marseille Marseille
4.2.5	HEC1		
4.2.5.1	Modules	Module assembly and test Transport Cold test at CERN Outer module connection Inner module connection Wheel assembly and test	Canada//JINR/Munich MPI Canada//JINR Canada//JINR/Munich MPI Canada//JINR Canada//JINR Canada//JINR/Munich MPI
4.2.5.1.1	Absorber structure		Canada // JINR
4.2.5.1.2	Readout structure		Canada // Moscow FIAN / Mainz
4.2.5.1.3	Bolts &clamps		Canada // JINR
4.2.5.2	Preamplifier system		
4.2.5.2.1	Motherboards		Munich MPI
4.2.5.2.2	Preamp chips		Munich MPI

Table 16-1 The LAr Detector Extended Product Breakdown Structure

PBS No.	PBS ITEM	List of related items	Resp.Institutes
4.2.5.2.3	Signal module cables		Canada // Munich MPI
4.2.5.2.4	Signal quadrant cables		Canada // Munich MPI
4.2.5.3	LV distribution		
4.2.5.3.1	LV distribution board		Munich MPI
4.2.5.3.2	LV module cables		Munich MPI
4.2.5.3.3	LV quadrant cables		Munich MPI
4.2.5.4	Calibration distribution		
4.2.5.4.1	Calib distribution board		Canada//Kosice/Mainz
4.2.5.4.2	Calib module cables		Canada//Kosice/Mainz
4.2.5.4.3	Calib quadrant cables		.... //Kosice/Mainz
4.2.5.5	HV distribution		
4.2.5.5.1	HV distribution board		Canada // Munich MPI
4.2.5.5.2	HV module cables		Canada // Munich MPI
4.2.5.5.3	HV quadrant cables		.... //Munich MPI
4.2.6	HEC2		
4.2.6.1	Modules	Module assembly and test	Canada//Munich MPI/ Protvino
		Transport	Canada//Protvino
		Cold test at CERN	Canada//Munich MPI/ Protvino
		Outer module connection	Canada//Protvino
		Inner module connection	Canada//Protvino
		Wheel assembly and test	Canada//Munich MPI/ Protvino
4.2.6.1.1	Absorber structure		Canada // Protvino
4.2.6.1.2	Readout structure		Canada //Moscow FIAN / Mainz
4.2.6.1.3	Bolts &clamps		Canada // Protvino
4.2.6.2	Preamplifier system		
4.2.6.2.1	Motherboards		Munich MPI
4.2.6.2.2	Preamp chips		Munich MPI
4.2.6.2.3	Signal module cables		Canada // Munich MPI
4.2.6.2.4	Signal quadrant cables		Canada // Munich MPI
4.2.6.3	LV distribution		
4.2.6.3.1	LV distribution board		Munich MPI

Table 16-1 The LAr Detector Extended Product Breakdown Structure

PBS No.	PBS ITEM	List of related items	Resp.Institutes
4.2.6.3.2	LV module cables		Munich MPI
4.2.6.3.3	LV quadrant cables		Munich MPI
4.2.6.4	Calibration distribution		
4.2.6.4.1	Calib distribution board		Canada//Kosice/Mainz
4.2.6.4.2	Calib module cables		Canada//Kosice/Mainz
4.2.6.4.3	Calib quadrant cables		............//Kosice/Mainz
4.2.6.5	HV distribution		
4.2.6.5.1	HV distribution board		Canada // Munich MPI
4.2.6.5.2	HV module cables		Canada // Munich MPI
4.2.6.5.3	HV quadrant cables		.............//Munich MPI
4.2.7	FCAL	Assembly Tooling : Assembly stand Storage stand	Arizona Arizona Arizona
4.2.7.1	FCAL1 (EM module)	Assembly Module carrier tool	Arizona Arizona / Carleton
4.2.7.1.1	Absorber matrix	Assembly Swaging tool	Arizona Carleton
4.2.7.1.1.1	End plates		Arizona
4.2.7.1.1.2	Absorber plates		Arizona
4.2.7.1.1.3	Dowel pins		Arizona
4.2.7.1.1.4	Fasteners		Arizona
4.2.7.1.2	Electrodes	Assembly Fibre winder tool	Arizona Carleton
4.2.7.1.2.1	Copper tubes		Arizona
4.2.7.1.2.2	Brass rods		Arizona
4.2.7.1.2.3	Quartz fibers		Arizona
4.2.7.1.2.4	Signal pins		Arizona
4.2.7.1.3	Interconnects		Arizona
4.2.7.1.3.1	Ground pins		Arizona
4.2.7.1.3.2	Kapton washers		Arizona
4.2.7.1.3.3	Brass washers		Arizona
4.2.7.1.3.4	Interconnect boards		Arizona

Table 16-1 The LAr Detector Extended Product Breakdown Structure

PBS No.	PBS ITEM	List of related items	Resp.Institutes
4.2.7.2	FCAL2 (HAD-A module)	Assembly Module carrier tool	British Columbia B.Columbia / Carleton
4.2.7.2.1	Absorber matrix	Assembly Tooling : Assembly jig Swaging tool	British Columbia B.Columbia / Carleton B.Columbia / Carleton
4.2.7.2.1.1	End plates		British Columbia
4.2.7.2.1.2	Tungsten slugs		British Columbia
4.2.7.2.2	Electrodes	Assembly Fibre winder	British Columbia B.Columbia / Carleton
4.2.7.2.2.1	Copper tubes		British Columbia
4.2.7.2.2.2	Tungsten rods		ITEP
4.2.7.2.2.3	Quatrz fibers		British Columbia
4.2.7.2.2.4	Signal pins		British Columbia
4.2.7.2.3	Interconnect boards		British Columbia
4.2.7.2.3.1	Ground pins		British Columbia
4.2.7.2.3.2	Kapton washers		British Columbia
4.2.7.2.3.3	Brass washers		British Columbia
4.2.7.2.3.4	Interconnect boards		British Columbia
4.2.7.3	FCAL3 (HAD-B module)	Assembly Module carrier tool	British Columbia Carleton /B.Columbia
4.2.7.3.1	Absorber matrix	Assembly Tooling : Assembly jig Swaging tool	British Columbia Carleton /B.Columbia Carleton /B.Columbia
4.2.7.3.1.1	End plates		British Columbia
4.2.7.3.1.2	Tungsten slugs		British Columbia
4.2.7.3.2	Electrodes	Assembly Fibre winder tool	British Columbia B.Columbia / Carleton
4.2.7.3.2.1	Copper tubes		British Columbia
4.2.7.3.2.2	Tungsten rods		ITEP
4.2.7.3.2.3	Quatrz fibers		British Columbia
4.2.7.3.2.4	Signal pins		British Columbia
4.2.7.3.3	Interconnect boards		British Columbia
4.2.7.3.3.1	Ground pins		British Columbia
4.2.7.3.3.2	Kapton washers		British Columbia

Table 16-1 The LAr Detector Extended Product Breakdown Structure

PBS No.	PBS ITEM	List of related items	Resp.Institutes
4.2.7.3.3.3	Brass washers		British Columbia
4.2.7.3.3.4	Interconnect boards		British Columbia
4.2.7.4	Cold electronics	Assembly Cable Harness jig	Arizona Arizona
4.2.7.4.1	Patch panels		Arizona
4.2.7.4.2	Cold cables		Arizona
4.2.7.4.3	Cable covers		Arizona
4.2.8	Cu shielding plugs		
4.2.8.1	Plug 1		ATLAS infrastructure
4.2.8.2	Plug 2		ATLAS infrastructure
4.2.8.3	Plug 3		ATLAS infrastructure
4.3	PROXIMITY SERVICES	Engineering	CERN / C.F. / Grenoble
4.3.1	Vacuum		C.F.
4.3.1.1	Cryostats		C.F.
4.3.1.2	Feedthroughs		C.F.
4.3.1.3	Flushing pumps		C.F.
4.3.2	Proximity cryo		C.F.
4.3.2.1	Cryo lines		C.F.
4.3.2.2	Cryo pumps		C.F.
4.3.2.3	Valve-boxes		C.F.
4.3.2.4	LAr separator		C.F.
4.3.2.5	LAr storage tanks		C.F.
4.3.2.6	Cooling-down and warming-up units		C.F.
4.3.2.7	Fittings		C.F.
4.3.2.8	Warm plumbing		C.F.
4.3.2.9	Instrumentation		C.F.
4.3.2.10	Controls		C.F.

Table 16-1 The LAr Detector Extended Product Breakdown Structure

PBS No.	PBS ITEM	List of related items	Resp.Institutes
4.3.3	Monitoring equipment		
4.3.3.1	Equipment on cryostats		
4.3.3.1.1	Purity equip system		
4.3.3.1.1.1	Monitoring cells		Mainz/......
4.3.3.1.1.2	Cables		Mainz/......
4.3.3.1.1.3	Readout		Mainz/......
4.3.3.1.2	Temperature system		
4.3.3.1.2.1	Probes		
4.3.3.1.2.2	Cables		
4.3.3.1.2.3	Readout		
4.3.3.1.3	Position gauge system		
4.3.3.1.3.1	Elements		
4.3.3.1.3.2	Cables		
4.3.3.1.3.3	Level gauges		
4.3.3.1.3.4	Readout		
4.3.3.1.4	Strain gauge system		
4.3.3.1.4.1	Elements		
4.3.3.1.4.2	Cables		
4.3.3.1.4.3	Level gauges		
4.3.3.1.4.4	Readout		
4.3.3.2	Equipment on detectors		
4.3.3.2.1	Purity equip system		
4.3.3.2.1.1	Monitoring cells		Mainz/.....
4.3.3.2.1.2	Cables		Mainz/.....
4.3.3.2.1.3	Readout		Mainz/.....
4.3.3.2.2	Temperature system		
4.3.3.2.2.1	Probes		
4.3.3.2.2.2	Cables		
4.3.3.2.2.3	Readout		
4.3.3.2.3	Position gauge system		
4.3.3.2.3.1	Elements		

Table 16-1 The LAr Detector Extended Product Breakdown Structure

PBS No.	PBS ITEM	List of related items	Resp.Institutes
4.3.3.2.3.2	Cables		
4.3.3.2.3.3	Level gauges		
4.3.3.2.3.4	Readout		
4.3.3.2.4	Strain gauge system		
4.3.3.2.4.1	Elements		
4.3.3.2.4.2	Cables		
4.3.3.2.4.3	Level gauges		
4.3.3.2.4.4	Readout		
4.3.4	Cooling		
4.3.4.1	Crate cooling		
4.3.4.1.1	Crate manifold		Brookhaven
4.3.4.1.2	Feeder lines (barrel, EC, EC retracted)		CERN
4.3.4.1.3	Long pipes		CERN
4.3.4.1.4	Pumps		CERN
4.3.4.1.5	Controls		CERN
4.3.4.1.6	Heat exchanger		CERN
4.3.4.1.7	Water tank		CERN
4.3.4.1.8	Level gauges		CERN
4.3.4.2	Power lines cooling (assume water cooling)		
4.3.4.2.1	Feeder lines manifolds		CERN
4.3.4.2.2	Controls		CERN
4.3.4.2.3	Pumps		CERN
4.3.4.2.4	Heat exchanger		CERN
4.3.4.2.5	Water tank		CERN
4.3.4.2.6	Level gauges		CERN
4.4	ELECTRONICS		
4.4.1	HV system		CERN/Stockhom KTH/.....

Table 16-1 The LAr Detector Extended Product Breakdown Structure

PBS No.	PBS ITEM	List of related items	Resp.Institutes
4.4.1.1	HV power system		CERN/Stockhom KTH/.....
4.4.1.1.1	Power supplies		CERN/Stockhom KTH/.....
4.4.1.1.2	Interface to DCS		CERN/Stockhom KTH/.....
4.4.1.2	HV cables		CERN/Stockhom KTH/.....
4.4.1.3	HV box on detector (decoupling network)		CERN/Stockhom KTH/.....
4.4.2	Front End Electronics		
4.4.2.1	Crate system		
4.4.2.1.1	Strip lines		Brookhaven/Alberta/ ....
4.4.2.1.2	Crate mechanics		Brookhaven/Alberta/ ....
4.4.2.1.3	Cooling boards Crate cooling manifold		Brookhaven/Alberta/ ....
4.4.2.1.4	Crate backplane		Brookhaven/Alberta/ ....
4.4.2.2	LV power system		Brookhaven/Alberta/ ....
4.4.2.2.1	LV power supplies		Brookhaven/Alberta/ ....
4.4.2.2.2	LV cables		Brookhaven/Alberta/ ....
4.4.2.2.3	Control		Brookhaven/Alberta/ ....
4.4.2.2.4	HEC LV		Munich MPI
4.4.2.3	Calib. pulser boards		
4.4.2.3.1	EM		Annecy / Orsay
4.4.2.3.2	HEC		Kosice / Mainz
4.4.2.3.3	FCAL		Arizona
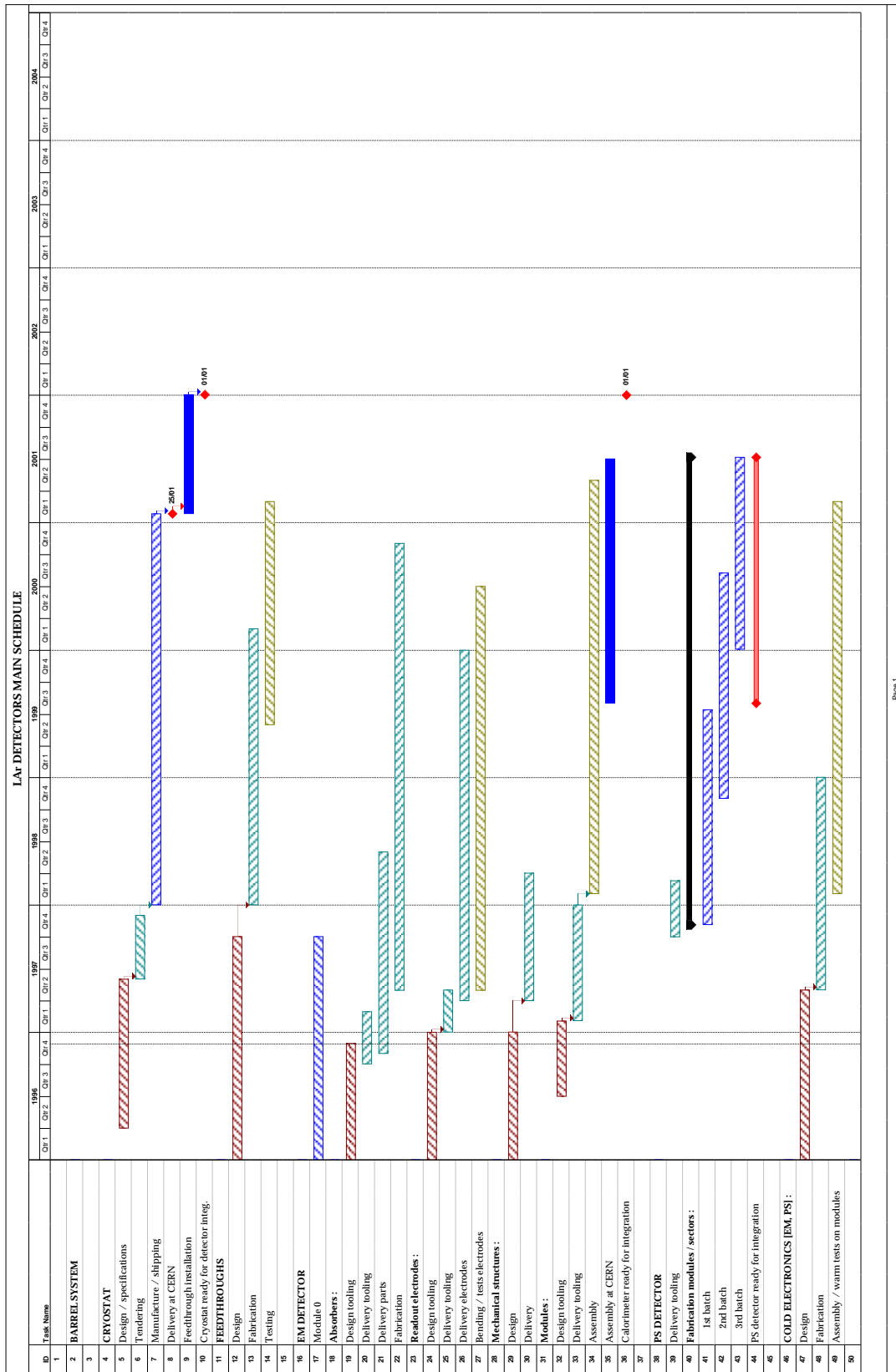
Table 16-1 The LAr Detector Extended Product Breakdown Structure

PBS No.	PBS ITEM	List of related items	Resp.Institutes
4.4.2.4	FE board		
4.4.2.4.1	EM, FCAL preamps		Arizona/Brookhaven / Milano
4.4.2.4.2	Shapers		
4.4.2.4.2.1	EM, FCAL		Grenoble / Orsay
4.4.2.4.2.2	HEC		JINR / Munich MPI
4.4.2.4.3	Layer sums and cables to TB		
4.4.2.4.3.1	EM, FCAL		Pittsburgh
4.4.2.4.3.1	HEC		Munich MPI
4.4.2.4.4	SCA's		Columbia / Orsay / Saclay
4.4.2.4.5	Address generators		Alberta
4.4.2.4.6	Boards		Alberta /Columbia / Brookhaven / Orsay
4.4.2.4.7	ADC's		id. as 4.4.2.4.6
4.4.2.5	Tower builder and driver for link to level 1 room		
4.4.2.5.1	EM calorimeters		Saclay
4.4.2.5.2	HEC		Munich MPI
4.4.2.5.3	FCAL		Arizona
4.4.2.6	Crate controllers		Paris / Saclay
4.4.3	Links		
4.4.3.1	Links to ROD's (incl. drivers + receivers circuits and optical fibers		Marseille / Stockholm KTH / ....
4.4.3.2	Links to level 1		
4.4.3.2.1	EM		Saclay
4.4.3.2.2	HEC		
4.4.3.2.3	FCAL		Arizona
4.4.3.3	TTC		Paris / Saclay
4.4.3.4	Control link		
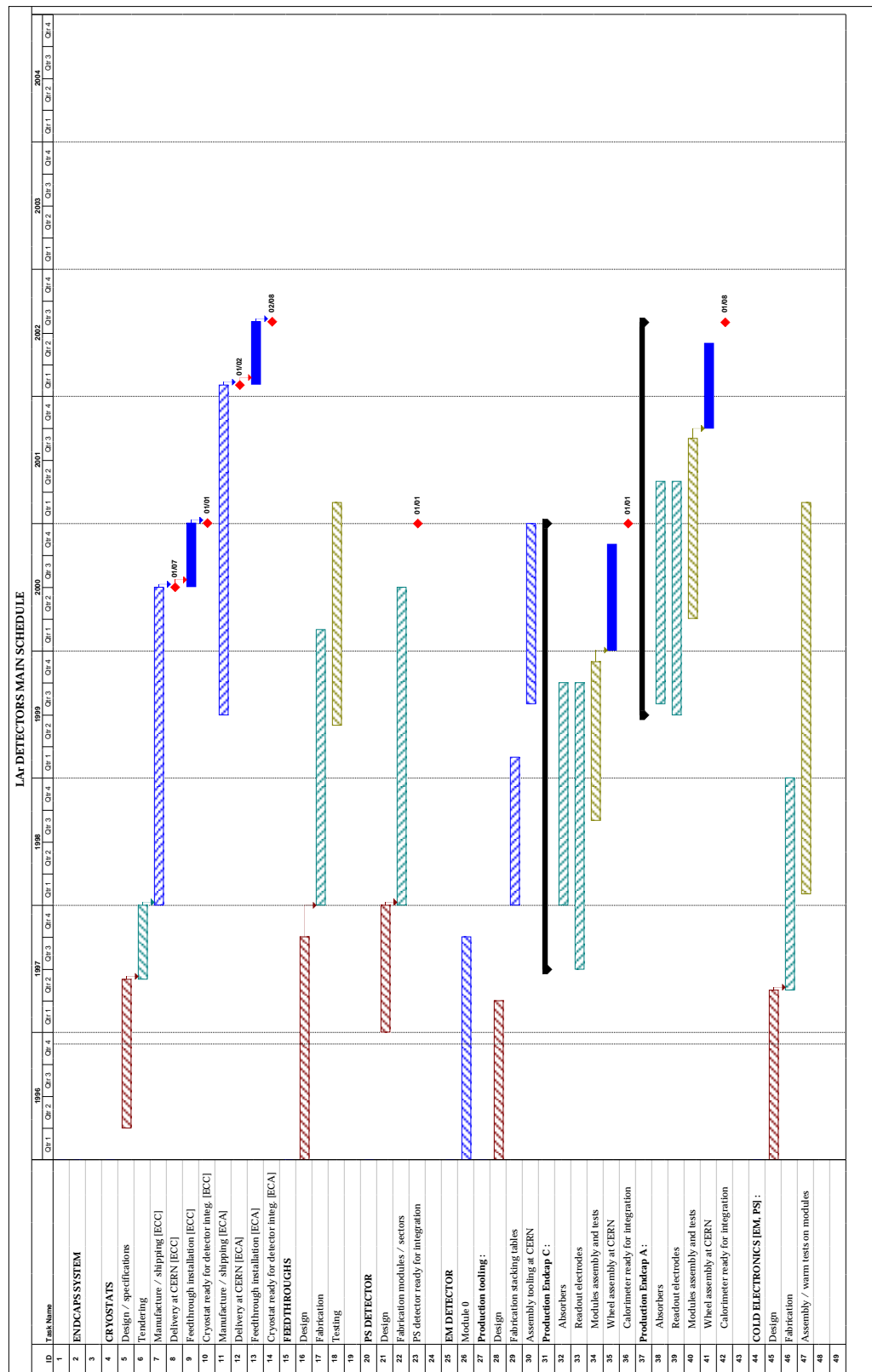
Table 16-1 The LAr Detector Extended Product Breakdown Structure

PBS No.	PBS ITEM	List of related items	Resp.Institutes
4.4.4	R/O Driver System (incl. digital filtering)		Annecy/Columbia/Dallas /Marseille/ Munich MPI (HEC)
4.4.4.1	ROD crate and PS		id. as 4.4.4
4.4.4.2	ROD board		id. as 4.4.4
4.4.4.3	Control		id. as 4.4.4
4.4.5	Level 1 interface and monitoring station		Heidelberg / Pittsburgh

Figure 16-i LAr main schedule.

Figure 16-ii LAr main schedule, contn'd.
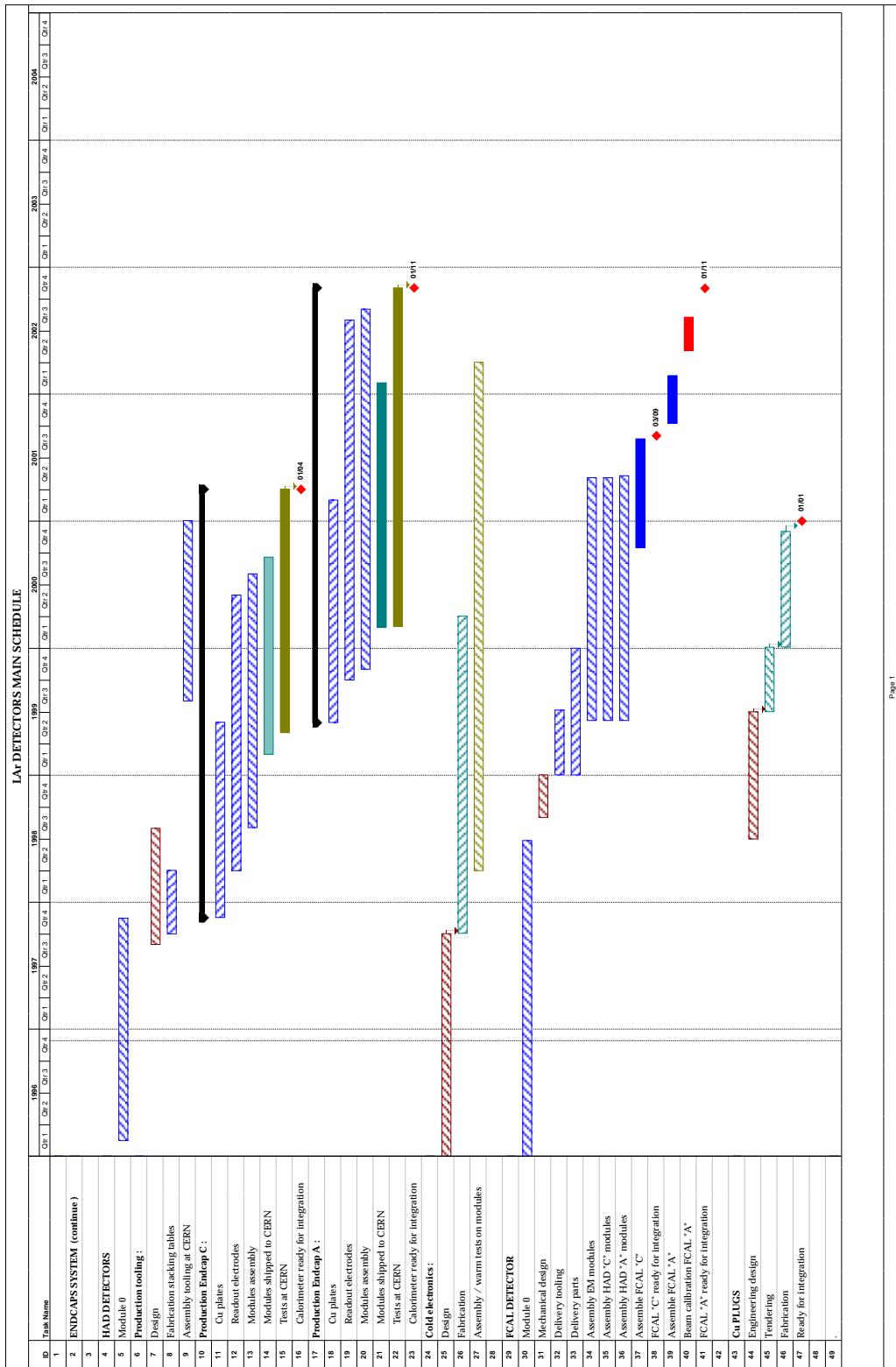
Figure 16-iii LAr main schedule (contn'd).
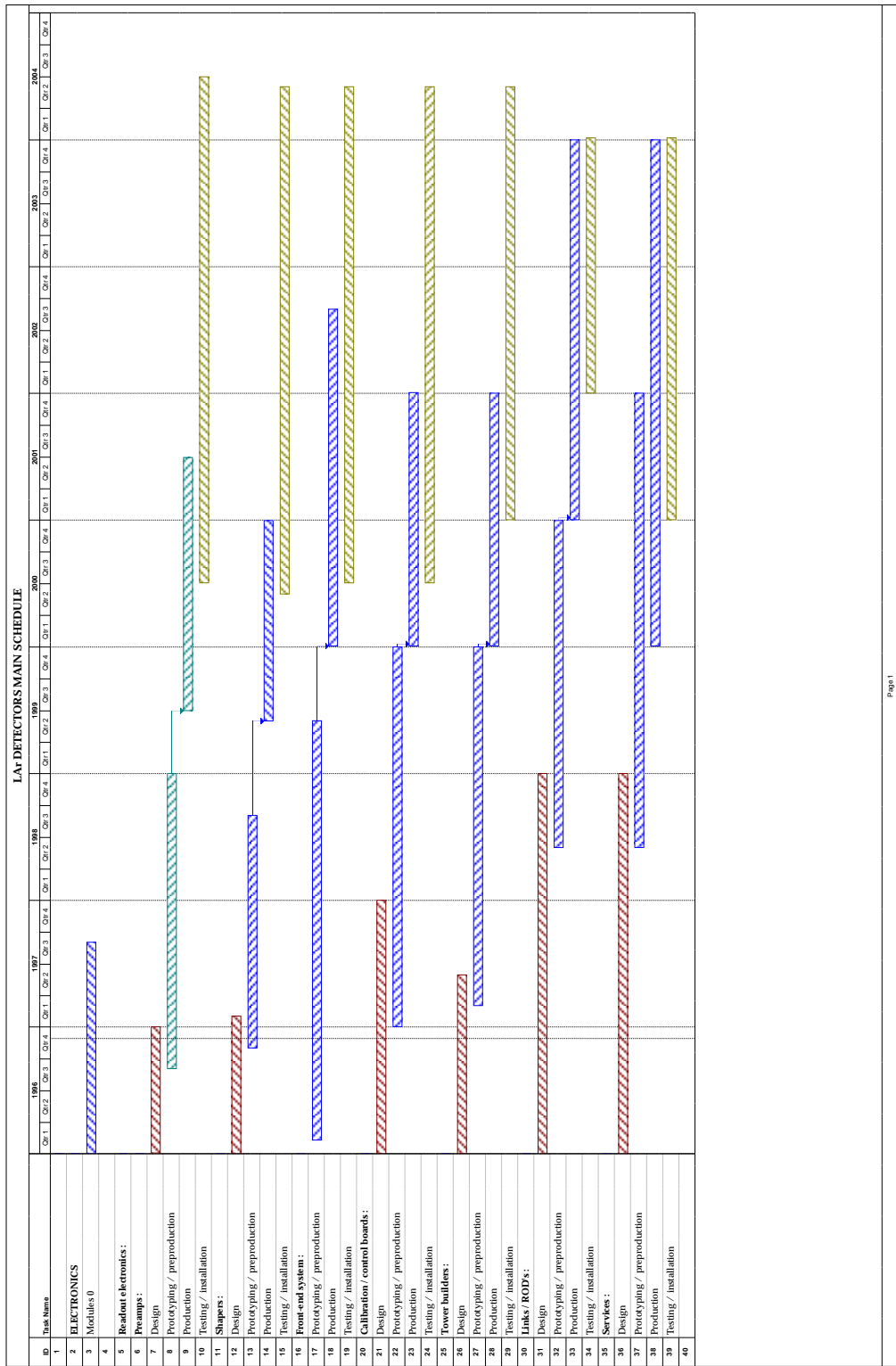
Figure 16-iv LAr schedule (contn'd).
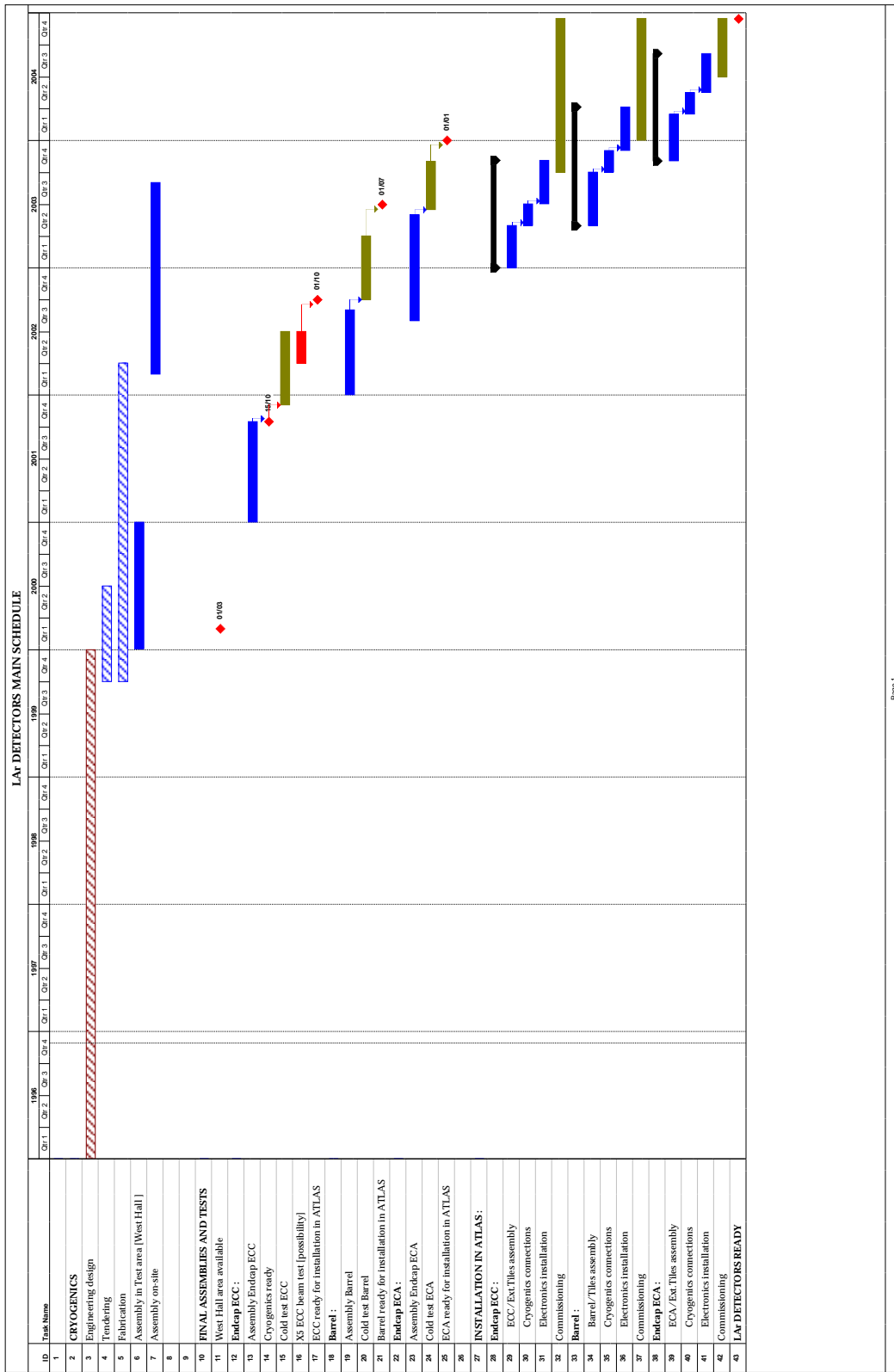
**Figure 16-v** LAr schedule (contn'd).

A Liquid argon properties
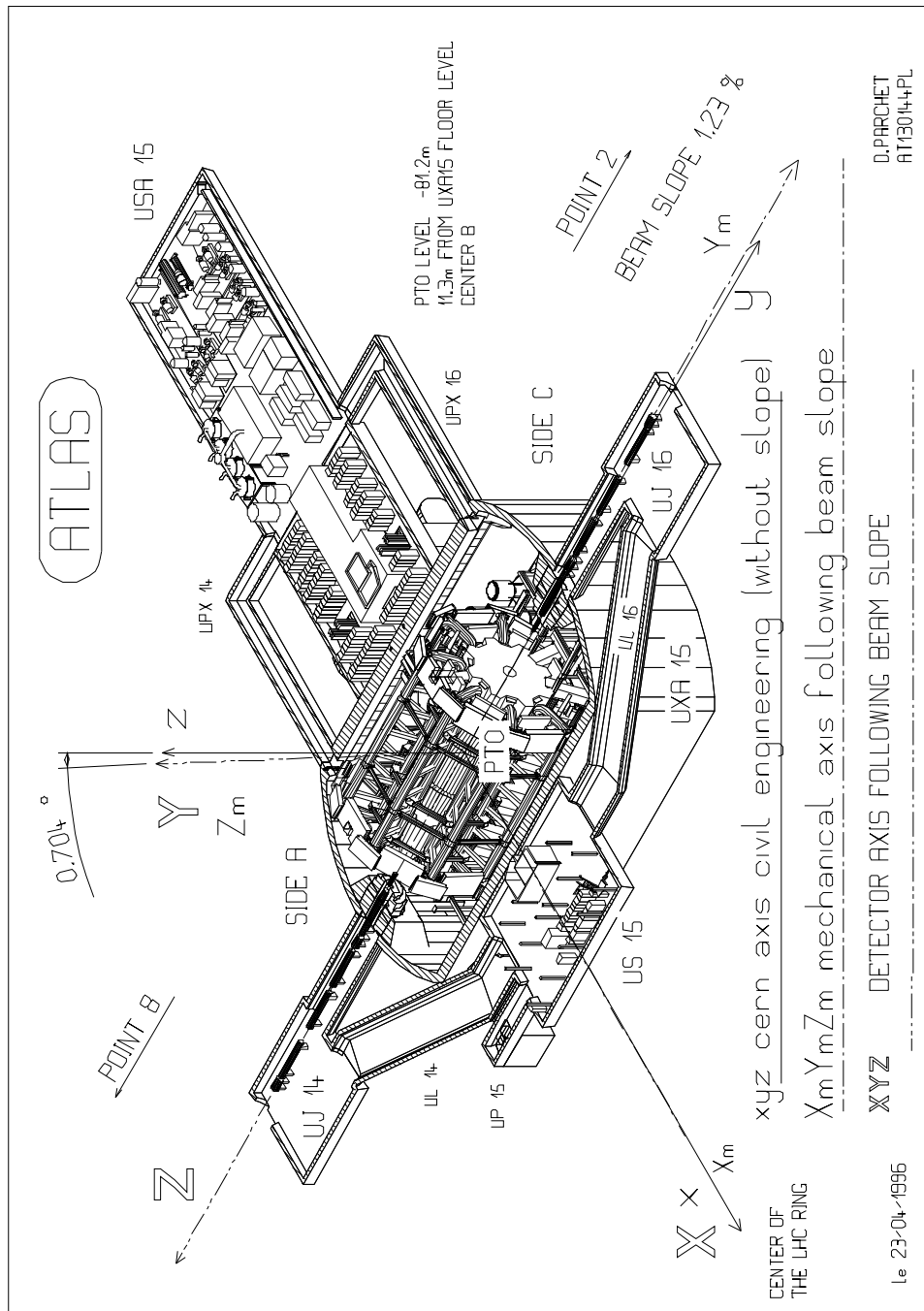
Table A-1 General properties of liquid argon.

PROPERTY	VALUE
Atomic number	18
Atomic weight (u)	39.94
Atomic diameter (Å)	3.42
Radiation length (cm)	14.2
Absorption length (cm)	83.6
Molière radius (cm)	10.1
Critical energy (MeV)	30.5
$< \Delta E_{mip}$ (1 cm) $>$ (MeV)	2.1
W-value (1 MeV electrons) (eV/ion-pair)	23.3
Fano factor	0.107
Electron mobility at bp (m^2 V^{-1} s^{-1})	0.048
Ion mobility at bp ($\times 10^5$) (m^2 V^{-1} s^{-1})	0.016
Oxygen trapping constant ($\times 10^{14}$) (m^2 V^{-1})	1.5
Dielectric constant	1.6
Heat capacity (C_p) (cal mol^{-1} K^{-1})	10.05
Thermal conductivity ($\times 10^3$) (cal s^{-1} cm^{-1} K^{-1})	30
Triple point temperature (K)	83.78
Triple point pressure (atm)	0.679
Triple point density (g cm^{-3})	1.14
Critical point temperature (K)	150.85
Normal boiling point (bp) (K)	87.27
Liquid density at bp (g cm^{-3})	1.40
Heat of vaporization at bp (cal mol^{-1})	1557.5
Gas/liquid ratio	784.0
Temperature (K) :	Pressure (bars)
87.15	1.0
89.3	1.25
91.8	1.6
94.2	2.0
96.8	2.5
Temperature (K) :	Density (g cm^{-3})
87.15	1.395
89.3	1.381
91.8	1.365
94.2	1.350
96.8	1.333

B ATLAS axis system

Figure B-1 shows the ATLAS detector installed at point 1. It describes the axis system used in this volume (detector axis following the beam slope). It also describes the +z side, referenced throughout the text as A-side, and the -z side, referenced as C-side.

Figure B-1 ATLAS installation at point 1. Definition of the axis system used (Detector Axis), and of side A (+z) ad side C (-z).

C Acronyms used

One list below the acronyms used in the Technical Design Report, by alphabetical order.

Table C-1 List of acronyms used.

A	
ADC	Analog to digital converter
ASIC	Application specific integrated circuit
B	
BCID	Beam crossing identification
BCK	Back section of the EM calorimeters
C	
CMRR	Common mode rejection ratio
CODAP	Code Français de construction des appareils à pression non soumis à l'action de la flamme.
CTLB	Control board
CTP	Central trigger processor
D	
DAC	Digital to analog converter
DCS	Detector control system
DSP	Digital Signal Processing
E	
EC	End-cap
ED	Electro-deposited
EM	Electromagnetic calorimeter
EMEC	Electromagnetic end-cap calorimeter
EMI	Electromagnetic interference
EST	Electrostatic transformer
F	
FCAL	Forward calorimeter
FCAL1	Forward calorimeter section 1
FCAL2	Forward calorimeter section 2
FCAL3	Forward calorimeter section 3
FDR	Fast digital read-out
FEA	Finite element analysis

Table C-1 List of acronyms used.

FEB	Front-end board
FEC	Front-end crate
FPGA	Field programmable gate array
FRT	Front section of the EM calorimeter
FT	Feedthrough
G	
GHe	Helium gas
H	
HEC	Hadronic calorimeter
HEC1	Forward calorimeter first wheel
HEC2	Forward calorimeter second wheel
HD	High-ductility
HEC	Hadronic end-cap calorimeter
HRL	High resistive layer
HV	High voltage
I	
ID	Inner detector
IP	Interaction point
L	
LAr	Liquid argon
LARG	Liquid argon calorimeter
LCS	Local control system
LHe	Liquid helium
LN_2	Liquid nitrogen
LSB	Least significant bit
LUT	Look-up table
LV	Low voltage
LVDS	Low voltage differential signaling
LVDT	Linear variable differential transformer
M	
MID	Middle section of the EM calorimeter
MWPC	Multi-wire proportional chamber
O	

Table C-1 List of acronyms used.

ODH	Oxygen deficit hazard
P	
PA	Preamplifier
PBS	Product breakdown structure
PECL	Positive emitter-coupled logic
PI	Polyimide
PLD	Programmable logic device
PRT	Platinum resistance thermometer
PS	Presampler
R	
RA	Roll-annealed
ROB	Read-out board
ROD	Read-out driver
ROC	Read-out crate
S	
SCA	Switch capacitor array
SB	Service board
SS	Stainless steel
T	
TC	Technical coordination
TDR	Technical Design Report
TTC	Timing, trigger and control

D Members of the ATLAS LAr Collaboration

Azerbaijan Republic
Institute of Physics, Azerbaijan Academy of Science, Baku
Abdinov O.B., Mekhdiyev R.R., Usubov Z.U.

Brazil
Instituto de Fisica, Universidade de Sao Paulo, Sao Paulo
DaSilva N.C., Dietzsch O., Leite M.A.L., Sakanoue M.H., Takagui E.M., Zandona F.

Canada
Centre for Subatomic Physics, University of Alberta, Edmonton
Armstrong W.W., Buchanan N., Gingrich D.M., Green P., Hewlett J.C., Holm L., Mc Donald W.J., Mullin S., Nickle T., Pinfold J.L., Schaapman J., Soukup J.

Department of Physics and Astronomy, University of British Columbia, Vancouver
Axen D., Mayer J.K., Orr R.S.

University of Carleton/C.R.P.P., Carleton
Armitage J., Dixit M., Dubeau J., Estabrooks P., Losty M., O'Neil M., Oakham G.

Group of Particle Physics, University of Montreal, Montreal
Azuelos G., Ben El Fassi A., Depommier P., Leon-Florian E., Leroy C., Lorazo B., Martin J.P., Marullo F., Roy P., Savard P.

Department of Physics, University of Toronto, Toronto
Bailey D.C., Bhadra S., Martin J.F., Sinervo P.K., Stairs G.G., Trischuk W.

TRIUMF, Vancouver
Astbury A., Birney P., Hodges T., Langstaff R., Lenckowski M., Oram C., Roberts W., Rosvick M., Wellisch H.P.

Departement of Physics and Astronomy, University of Victoria, Victoria
Bishop S., Fincke-Keeler M., Honma A., Keeler R., Lefebvre M., O'Neil D., Poffenberger P., Roney M., Sobie R.

CERN
European Laboratory for Particle Physics (CERN), Geneva
Baisin L., Chevalley J.L., Dell'Acqua A., Gianotti F., Haug F., Hervas L., Marin C.P., Pailler P., Passardi G., Poggioli L., Vuillemin V.

France
Laboratoire d'Annecy-le-Vieux de Physique des Particules (LAPP), IN2P3-CNRS, Annecy-le-Vieux
Aubert B., Bazan A., Beaugiraud B., Bohner G., Boniface J., Caille M., Colas J., Dromby G., Eynard G., Girard C., Jezequel S., Le Flour T., Lecoq J., Lesueur J., Linossier O., Massol N., Minard M.N., Moynot M., Nicoleau S., Perrodo P., Ricadonna X., Sauvage G., Thion J., Wingerter I., Zitoun R., Zolnierowski Y.

Institut des Sciences Nucléaires de Grenoble, IN2P3-CNRS-Université Joseph Fourier, Grenoble
Andrieux M.L., Ballon J., Collot J., Dzahini D., Ferrari A., Guerre-Chaley B., Hostachy J.Y., Laborie G., Martin Ph., Pouxe J., Rabier C., Rey-Campagnolle M., Rossetto O., De Saintignon P., Wielers M.

Centre de Physique des Particules de Marseille, IN2P3-CNRS, Marseille
Dargent P., Dinkespiler B., Djama F., Etienne F., Fassnacht P., Henry-Couannier, Karst P., Le Van Suu A., Martin L., Martin O., Mirea A., Monnier E., Nagy E., Nicod D., Olivetto C., Sauvage D., Tisserant S., Toth J.

Laboratoire de l'Accélérateur Linéaire, IN2P3-CNRS, Orsay
Augé E., Belot G., Blaquière M., Bouchel M., Boucrot J., Breton D., Chollet C., Coulon J-P., De la Taille C., Delebecque P., Fayard L., Fournier D., Gonzales J., Grivaz J-F., Hrisoho A., Iconomidou-Fayard L., Imbert P., Jacquier Y., Lavigne B., Mace G., Martin-Chassard G., Merkel B., Nikolic I., Noppe J-M., Parrour G., Petroff P., Puzo P., Richer J-P., Schaffer A-C., Seguin-Moreau N., Serin L., Tisserand V., Tocut V., Unal G., Vales F., Veillet J-J., Vernay E.

LPNHE, Universités de Paris VI et VII, IN2P3-CNRS, Paris
Astesan F., Bezamat J., Blouzon F., Canton B., Castera A., David J., Imbault D., Lacour D., Le Dortz O., Nayman P., Rossel F., Savoy-Navarro A., Schwemling P., Treguier Y., Vincent P., Vallereau A.

CEA, DSM/DAPNIA, Centre d'Etudes de Saclay, Gif-sur-Yvette
Belorgey J., Bernard R., Borgeaud P., Chalifour M., De Girolamo P., Delagnes E., Desages F., Giacometti J., Heitzmann J., Huet M., Lottin J-P., Lugiez F., Mansoulié B., Molinié F., Pailler P., Pascual J., Pelle J., Perrin P., Renardy J.F., Schwindling J., Simion S., Taguet J.P., Teiger J., Walter C.

Germany
Institut für Hochenergiephysik der Universität Heidelberg, Heidelberg
Geweniger C., Hanke P., Kluge E.-E., Mass A., Putzer A., Tittel K., Wunsch M.

Institut für Physik, Johannes-Gutenberg Universität Mainz, Mainz
Buchholz P., Hoelldorfer F., Jakobs K., Kleinknecht K., Koepke L., Marschalkowski E., Merle K., Othegraven R., Renk B., Schaefer U., Schue Y., Walkowiak W.

Max-Planck-Institut für Physik, München
Aderholz M., Brettel H., Cwienk W.D., Fent J., Kiryunin A., Kurchaninov L., Laskus H., Lindenmaier M., Oberlack H., Schacht P., Schmuecker H., Stenzel H., Striegel D., Tribanek W.

Fachbereich Physik, Bergische Universität, Wuppertal
Braun H.M., Lenzen G.

Italy
Dipartimento di Fisica dell' Universitá di Milano and I.N.F.N., Milano
Battistoni G., Bonivento W., Camin D., Cavalli D., Costa G., Fedjakin N., Ferrari A., Mandelli L., Mazzanti M., Perini L., Resconi S., Sala P.

Kazakhstan
High-Energy Physics Institute of the Kazakh Academy of Sciences, Almaty
Boos E., Pokrovsky N., Zhautykov B.

Morocco
Faculté des Sciences Aïn Chock, Université Hassan II, Casablanca, and Université Mohamed V, Rabat
Chakir H., Cherkaoui R., Hoummada A., Saadi H., Sayouty E.

Russia
Institute for Theoretical and Experimental Physics (ITEP), Moscow
Artamonov A., Epchtein V., Gorbunov P., Gurin R., Jemanov V., Khovansky V., Koutchenkov A., Kruchinin S., Maslennikov A., Ryabinin M., Shatalov P., Tsoukerman I., Zaitsev V., Zeldovich S.

P.N., Lebedev Institute of Physics, Moscow
Akimov A., Baranov S., Belov M., Blagov M., Gavrilenko I., Komar A., Konovalov S., Kopytine M., Mouraviev S., Popov L., Shikanyan A., Shmeleva A., Snesarev A., Speransky M., Sulin V., Tikhomirov V., Vassilieva L., Yakimenko M.

Budker Institute of Nuclear Physics (BINP), Novosibirsk
Akhmadaliev S., Chekhtman A., Kolachev G., Kozlov V., Maslennikov A., Shaldaev E., Snopkov R., Tikhonov Y.

Institute for High Energy Physics (IHEP), Protvino
Bogoliubsky M.Yu., Chekulaev S.V., Denisov S.P., Dushkin A.Yu., Gapienko V.A., Gilitsky Yu.V., Khmelnikov V.A., Kiryunin A.A., Konstantinov V., Kurchaninov L.L., Levitsky M.L., Mikhailin V.N., Minaenko A.A., Moiseev A.M., Onuchin V.A., Pleskach A.V., Popov A., I., Shein I.V., Solodatov A.P., Sytnik V.V., Tsyupa Yu., Zaets V.G.

JINR
Joint Institute for Nuclear Research, Dubna
Cheplakov A., Gogiberidze G., Golikov V., Golubykh S., Kakurin S., Kazarinov M., Kekelidze V., Kukhtin V., Lazarev A., Louschikov V., Matafanov V., Metreveli Z., Neganov A., Obudovskij V., Salihagic D., Samoilov V., Savin I., Serotchkine E., Shilov Y., Usov Y.

Slovak Republic
Institute of Experimental Physics of the Slovak Academy of Sciences, Kosice
Ban J., Bruncko D., Chytracek K., Ferencei J., Jusko A., Kladiva E., Kocper B., Strizenec P.

Spain
Physics Department, Universidad Autónoma de Madrid, Madrid
Barreiro F., Del Peso J., Garcia G., Labarga L., Romero P., Scheel C.

Sweden
Royal Institute of Technology (KTH), Stockholm
Akerman D., Carlson P., Clement C., Leven S., Lund-Jensen B., Pearce M., Soderqvist J., Vanyashin A.

United States of America
University of Arizona, Tucson, Arizona
Cheu E., Johns K., Loch P., Rutherfoord J., Savine A., Shaver L., Shupe M., Steinberg J., Tompkins D.

Brookhaven National Laboratory (BNL), Upton, New York
Citterio M., Densig F., Farrel J., Gibbard B., Gordeev A., Gordon H., Graf N., Hoffmann A., Kotcher J., Lissauer D., Ma H., Makowiecki D., Murtagh M.J., Paige F., Protopopescu S., Radeka V., Rahm D.C., Rajagopalan S., Rescia S., Sexton K., Stumer I., Takai H., Wolnierwicz K.

Nevis Laboratory, Columbia University, Irvington, New York
Cartiglia N., Cunitz H., Dodd J., Gara J., Leltchouk M., Parsons J., Seman M., Shaevitz M., Sippach W., Willis W., Zhang L.

University of Pittsburgh, Pittsburgh, Pennsylvania
Cleland W.E., Rabel J.

Department of Physics and Astronomy, University of Rochester, Rochester, New York
Bazizi K., England D., Ginther G., Glebov V., Haelen T., Lobkowicz F., Slattery P., Ward Ch.

Department of Physics Southern, Methodist University, Dallas, Texas
Coan T.E., Olness F., Skwarnicki T., Stroynowski R., Teplitz V.

This document has been prepared with Release 5 of the Adobe FrameMaker® Technical Publishing System using the Technical Design Report template prepared by Mario Ruggier of the Information and Programming Techniques Group, ECP Division, CERN, according to requirements from the ATLAS collaboration.

To facilitate multiple author editing and electronic distribution of documents, only widely available fonts have been used. The principal ones are:

Running text:	Palatino 10.5 point
Chapter headings:	Helvetica Bold 18 point
2nd, 3rd and 4th level headings:	Helvetica Bold 13, 11.5 and 10.5 point respectively
Figure and table captions:	Helvetica 9 point